Design Studies for the Beam-dump Experiment DarkMESA

DISSERTATION

zur Erlangung des Grades
„Doktor der Naturwissenschaften“

am Fachbereich Physik, Mathematik und Informatik
der Johannes Gutenberg-Universität
in Mainz

vorgelegt von
MIRCO CHRISTMANN
geb. in Kaiserslautern

Institut für Kernphysik
Johannes Gutenberg-Universität

Mainz, den 08. Dezember 2022

Tag der mündlichen Prüfung: 04. Mai 2023

Erstgutachter: Univ.-Prof. Dr. Achim Denig

Abstract

At the Institute for Nuclear Physics in Mainz the new electron accelerator MESA will go into operation within the next years. In the extracted beam operation – with up to 155 MeV of beam energy and 150 µA of beam current – the P2 experiment will measure the weak mixing angle in electron-proton scattering. The high-power beam-dump of this experiment and the 20 000 hours of operation time are ideally suited for a parasitic dark sector experiment – DarkMESA.

The experiment is designed for the detection of light dark matter. The model studied here is based on the coupling of dark matter to a massive vector particle, the dark photon γ'. It can potentially be produced in the P2 beam-dump by a process analogous to photon Bremsstrahlung and can then decay in dark matter particle pairs $\chi\overline{\chi}$ – if kinematically allowed. A fraction of them scatter off electrons or nuclei in the DarkMESA calorimeter, located in a well shielded area outside of the MESA hall. This thesis covers an evaluation of the accessible dark matter parameter space with a `MadGraph` and `Geant4` simulation.

For the calorimeter, high-density PbF_2 and lead glass SF5 Cherenkov radiators, and photomultipliers from previous experiments will be used. In Phase A a prototype with 25 PbF_2 crystals and in Phase B $\sim$2000 PbF_2 and SF5 crystals with a total active volume of 0.7 m^3 are planned. The characterization of the crystals in laboratory and beam-time studies was part of this work, as well as the comparison of the experimental data with simulation studies. During a MAMI beam-time the suitability of these materials has been proven.

For the prototype stage, a hermetic veto system with two layers of plastic scintillators and 1 cm of lead shielding is currently under development and a similar concept is foreseen for Phase B. In this thesis, the possibilities of background suppression with these concepts were investigated in simulation studies.

The experimental setup was optimized and further concepts were investigated. An additional off-axis detector can further extend the accessible parameter range. This concept was evaluated in the context of this work as well as the possibilities of a negative-ion time projection chamber filled with CS_2 at low pressure serving as dark matter detector – DarkMESA-DRIFT. With the nuclear recoil threshold being in the keV range, the accessible parameter space can be extended to higher dark matter masses. The space to further increase the active volume of DarkMESA in a Phase C, based on traditional technologies or following an innovative concept, was also studied.

The ability to perform experiments with different detector concepts and detection methods at one experimental site is a great advantage of the beam-dump experiment at MESA.

Contents

Introduction

"Dark Matter", *"Dark Energy"*, or *"Dark Photon"*. For many people these are terms from the field of science fiction.

"What is that supposed to be!"

"There's no such thing!" ***"That's just another weird invention!"***

"Wasn't there once an episode of Star Trek? ***"Never heard of it!"***

...or was that Star Wars, because of dark...?"

Even the building blocks of the matter surrounding us are not conceivable for many people. The problem: these building blocks are not so easy to see with the bare eye. Molecules and atoms, can be made visible with electron microscopes. However, to resolve the building blocks of atoms, the elementary particles, high-energy particle beams are necessary.

Electron, proton, and neutron, most know from school, with quarks, leptons, and bosons it is already a little bit more difficult. Quarks might be known by some, but more from the German television show with the same name or from the breakfast table.

But: With these particles of the standard model, a term like *"science fiction"* is rarely used. Why are there differences? As well as those from the dark sector, one cannot touch these particles.

The difference is quite obvious: Scientists *"from the big underground ring in the Alps"* have already found these standard model particles. And if you search for them in the internet, you will find the complete profile with mass, charge, spin and maybe even a nice picture. With the details like GeV, MeV, sometimes also a c^2, one has some difficulty, but that will have its truth, because it is written there.

"But dark...? Anyway! There is no exact data."

There is already a lot of astrophysical evidence for the existence of dark matter or at least for the necessity to extend the standard model. But the statement is true, exact data were not found. Whether the mass of dark matter equals the mass of a jumbo jet, a pin head, or is beyond the scale of particle physics, nobody knows yet. The simple reason is, that particles of the dark sector could not be found experimentally up to now. The possible mass range seems to be infinitely large and the interaction with already known particles is extremely small. It's a bit like fishing in a huge lake with only one fish. And the fish has no particular interest in the bait we offer it. But nevertheless, and to stay with the metaphoric language, researchers around the world are trying to drain the lake further and further and to find the optimal bait. Perhaps it will soon be said:

"There will be the Nobel Prize for it." ***"Impressive. Their persistence has paid off."***

"Dark matter? I heard about that on the news yesterday."

"How could it have remained undiscovered for so long?"

The DarkMESA experiment has set its goal to further drain the lake. Or maybe DarkMESA has the right bait at hand?

Outline

The thesis starts with Chap. 1 and a discussion of evidence for the existence of dark matter (DM). Dark sector models, some experimental approaches and their sensitivities are also presented.

In Chap. 2 the Mainz Microtron (MAMI), which is used for DarkMESA material studies, and the associated experiments, which are also of particular interest for DarkMESA, are introduced, followed by a detailed description of the Mainz Energy-recovering Superconducting Accelerator (MESA) currently under construction. In addition to DarkMESA, the P2 and the Mainz Gas Injection Target Experiment (MAGIX) will be operated at this accelerator and all three are discussed. MAGIX will employ an energy recovery mode, while P2's beamline will end in a beam-dump. This then serves as a DM source for DarkMESA.

Chap. 3 first introduces the main tools used in the simulation studies – `Geant4` and `MadGraph`. Their most important functions are described before the individual modules of the DarkMESA simulation are introduced. Many parameters of the simulation can be controlled via a steering file. The simulation includes light yield studies of individual detectors, efficiency studies of veto systems, and the evaluation of the DarkMESA expected reach. For the latter, simulation of DM production in the beam-dump and detection in the DarkMESA calorimeter are included. A study of the MAGIX trigger veto system shows the synergies of both experiments.

In addition to necessary theoretical and technical details, two beam-times at the MAMI accelerator are the central focus of Chap. 5. Detectors were built from various materials, in particular Cherenkov radiators, and their properties were investigated with beam electrons of up to 14 MeV energy. The results are compared with a simulation study. The experimental neutron response of these detectors is also discussed.

With the results of Chap. 5 and a few optimization studies, a staged approach for the DarkMESA calorimeter is presented in Chap. 6. There will be a prototype Phase A followed by a full calorimeter setup using $\sim 2\,000$ PbF_2 and lead glass (PbGl) crystals of type SF5 in Phase B.

The expected backgrounds are studied in Chap. 7. Both beam-related and beam-unrelated backgrounds are investigated, and the veto systems for both DarkMESA phases are designed accordingly.

In Chap. 8 the relevant theory for a beam-dump experiment like DarkMESA is discussed in more detail. The simulation results for DM production and detection, and the expected reach for Phase A and B are presented. A few concepts for an extension of the measurable parameter space are also discussed.

The last Chap. 9 summarizes all the results and gives an outlook on future developments for the DarkMESA project.

My credits go to the Helmholtz Institute Mainz and HGS-HIRe for their financial and scientific support in context of this thesis.

1. Dark sector physics

Astrophysical observations suggest that the universe does not only consist of the visible (baryonic) matter. About five times that amount of mass is assigned to dark matter (DM), which has not been found experimentally yet.[1] The experiments at the new particle accelerator MESA will support the research efforts in the search for dark sector particles. The theoretical considerations relevant for the discussions in this thesis are presented in the following and are based on Luca Doria's habilitation [4]. Natural units ($\hbar = c = 1$) are used.

1.1. Evidence for dark matter (DM)

Already in 1933 with astrophysical investigations of the Coma cluster Fritz Zwicky came to the conclusion that the so-called "dark matter" (normal, non-luminous matter at that time) must be present in much larger amount than the luminous matter [5]. The apparent velocities of the individual galaxies in the Coma cluster vary so significantly that these values can only be explained if the mean density of the Coma cluster is at least 400 times larger than the value obtained by observations of visible matter. Single galaxies with intrinsic velocities in the order of $1\,000 - 2\,000\,\mathrm{km\,s^{-1}}$ have not yet been observed, which practically excludes the alternative theory of the Coma cluster flying apart over time.
Later in 1978 Vera Rubin et al. studied the rotation curves of high-luminosity spiral galaxies [6]. The results showed a discrepancy between the observations and the expected behavior due to Newton's law of gravitation:

$$\begin{aligned} F_{\mathrm{cent}} = F_{\mathrm{grav}} \Leftrightarrow \frac{mv^2(R)}{R} &= G\frac{mM(R)}{R^2} \\ \Rightarrow v(R) &= \sqrt{G\frac{M(R)}{R}} \quad . \end{aligned} \tag{1.1}$$

Fig. 1.1 shows the observed rotational velocities (black curves) depending on the distance from the galactic center. It can be seen that the observed velocities in outer galaxy regions are more or less constant, which contradicts the blue curve obtained from Kepler's law. An explanation for this disagreement could be that a large part of the present matter is not visible and therefore not observed.
Studies on larger cosmological scales also suggest the existence of invisible DM. The Wilkinson Microwave Anisotropy Probe (WMAP) satellite in 2001–2010 [7] and even more precisely the Planck surveyor satellite in 2009–2013 [8,9] measured the temperature fluctuations in the universe, the so-called cosmic microwave background (CMB). It provides insight into the structure formation

[1] By far the largest part is assigned to the even more mysterious dark energy (69.11(62) %), but its description is beyond the scope of this thesis. For more details, please refer to [1–3].

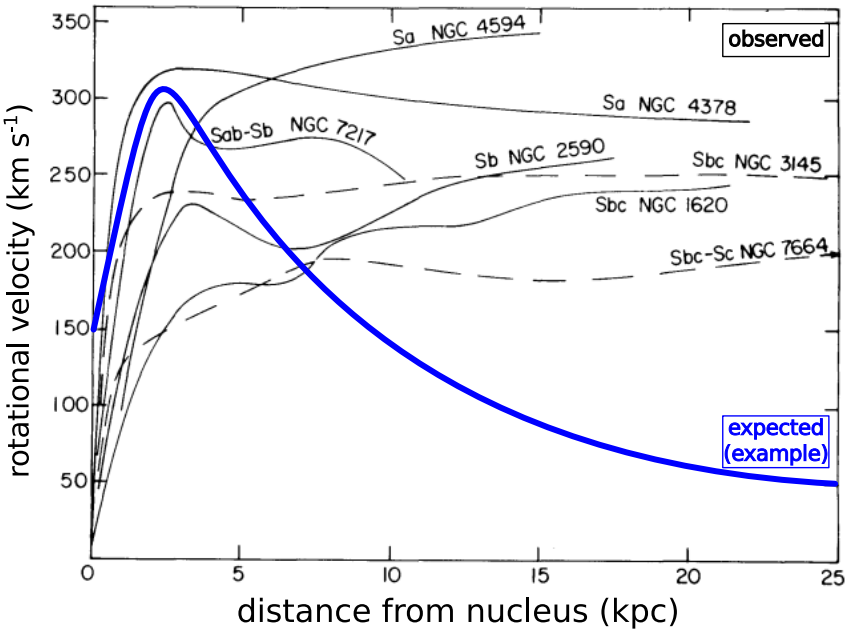

Figure 1.1.: Rotation curves of spiral galaxies measured by Vera Rubin et al. The observed rotational velocities (black) are shown together with an example for an expected behavior of visible mass only (blue). (Figure adapted from [6])

and matter distribution of the universe shortly after the Big Bang. The cosmological lambda cold dark matter (ΛCDM) model used in the analysis of the CMB includes dark energy as well as cold DM and is based on the Friedmann-Lemaître-Robertson-Walker (FLRW) metric. From the acquired power spectrum of the angular temperature fluctuations as function of the multipoles l, this model yields the matter content of the universe. Besides a more accurate value for the expansion rate of the universe (Hubble constant $H_0 = 67.74(46)\,\mathrm{km\,s^{-1}\,Mpc^{-1}}$), it was also confirmed that the universe is nearly flat ($\Omega_\mathrm{k} \sim 0$). With the Planck data the following density parameters of the universe were obtained:[2]

$$\begin{aligned} \Omega_\mathrm{c} + \Omega_\mathrm{b} + \Omega_\mathrm{r} + \Omega_\mathrm{k} + \Omega_\Lambda &= 1 \quad , \\ \Omega_\mathrm{c} &= 0.258\,9(57) \quad , \\ \Omega_\mathrm{b} &= 0.048\,6(10) \quad , \\ \Omega_\mathrm{r} &\sim 10^{-4} \quad , \\ \Omega_\mathrm{k} &\sim 0 \quad , \\ \Omega_\Lambda &= 0.691\,1(62) \quad , \end{aligned} \tag{1.2}$$

with Ω_c the cold DM density, Ω_b the baryonic density, Ω_r the radiation density (photons and relativistic neutrinos), Ω_k the curvature of the universe, and Ω_Λ the dark energy density.
These results are consistent with the previously described observations of Vera Rubin on rotational curves of galaxies. Also many other cosmological observations like galaxy clusters dynamics, gravitational lensing [10,11], Type Ia supernova distance measurements [12,13], and spectroscopic methods [14] are consistent.

[2] $\Omega_\mathrm{x} = \rho_\mathrm{x}/\rho_0$, with ρ_0 being the critical density.

1.2. Freeze-out and DM candidates

In the early time of the universe, Standard Model (SM) and DM particles were in equilibrium. As the universe expands with time, it becomes less likely that annihilation or creation of DM occurs. After some time, the rates of these processes have decreased so far that the DM density remains constant. The fraction of DM (n_χ) after this freeze-out process is given by

$$n_\chi \Gamma = H \quad , \tag{1.3}$$

where $\Gamma = \langle \sigma \left(\chi\chi \rightarrow \mathrm{SM} \right) v_\chi \rangle$ is the averaged annihilation rate, with v_χ being the DM velocity, and H the expansion rate. In the relativistic (hot) DM case the DM number density is:

$$n_{\mathrm{rel}} \sim T^3 \quad \text{if} \quad m_\chi \ll T \quad . \tag{1.4}$$

In the non-relativistic (cold) DM case the DM number density is:

$$n_{\text{non-rel}} \sim (m_\chi T)^{3/2} \, e^{-m_\chi / T} \quad \text{if} \quad m_\chi \gg T \quad . \tag{1.5}$$

In the radiation-dominated era ($\rho \sim T^4$) the Hubble parameter can be written as $H \sim T^2 / M_{\mathrm{P}}$, with M_{P} being the Planck mass. For the cold DM case (Eq. 1.5) and defining $x = m_\chi / T$, the freeze-out condition can be written as

$$\sqrt{x} e^{-x} = \frac{1}{m_\chi M_{\mathrm{P}} \, \sigma} \quad . \tag{1.6}$$

This freeze-out process is shown in Fig. 1.2. The DM number density n normalized to the entropy

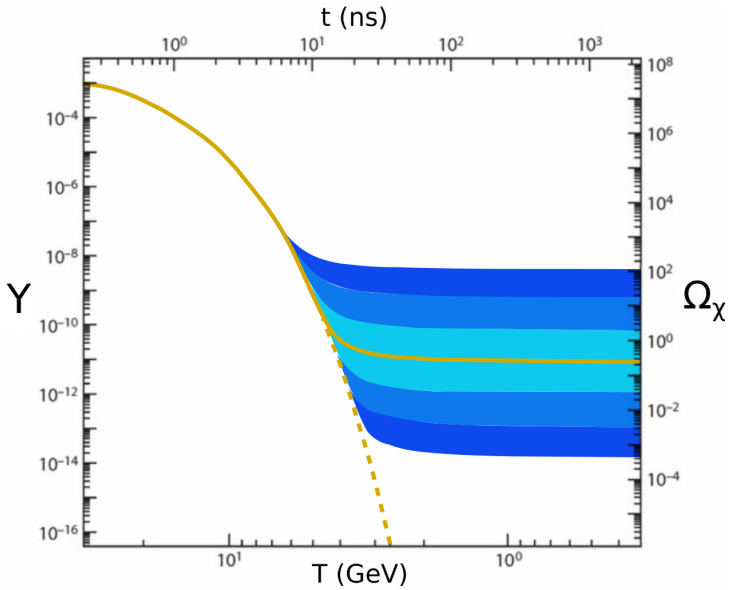

Figure 1.2.: The thermal freeze-out process. The DM number density n normalized to the entropy density s ($Y = n/s$) is shown as a function of the time (temperature) of the universe. After a phase of equilibrium, the annihilation rate drops exponentially and when reaching $n_\chi \Gamma = H$ the DM freezes out. The blue curves represent the freeze-out for different values of $\langle \sigma v_\chi \rangle$ and are solutions of the Boltzmann equation [15] for an expanding universe. Figure adapted from [16].

density s ($Y = n/s$) is shown as a function of the time and the temperature of the universe. If Eq. 1.3 is valid, DM freezes out and Y is constant again. The blue curves represent different values of $\langle \sigma v_\chi \rangle$ and are solutions of the Boltzmann equation [15] for an expanding universe

$$\dot{Y} = \langle \sigma v_\chi \rangle s \left(Y_{\mathrm{eq}}^2 - Y^2 \right) \quad . \tag{1.7}$$

Cold DM is the source for effects on a galaxy scale and hot DM for the mass surrounding whole galaxy clusters. Hot DM alone cannot explain the structure of the CMB, while cold DM, for example, excludes non-baryonic but not cold neutrinos. The non-relativistic behavior and a thermal origin of DM leads to a lower DM mass limit of $\sim 10\,\mathrm{keV}$, since small scale structures are observable in the universe. A higher limit of $\sim 10\,\mathrm{TeV}$ exists because of violation of perturbative unitarity [17].
Prominent DM candidates in this mass range are weakly interacting massive particles (WIMPs) and light dark matter (LDM) particles. The former are located in the mass range above $\sim$10 GeV and LDM below $\sim$1 GeV. For a non-thermal origin of DM and a mass range from $10^{-22}\,\mathrm{eV}$ up to $\sim$keV, axion-like particles (ALPs) are possible DM candidates [18]. Other candidates are the lightest neutralino [19] predicted by supersymmetry (SUSY) theories, the Kaluza-Klein photon or neutrino [20, 21] from theories of new physics at the electroweak breaking scale, and gravitinos [22]. A variety of other theories come without new particles: a selection are the enhanced occurrence of black holes, normal-matter non luminous compact objects, modifications to the law of gravity [23], and the associated relativistic extensions [24]. Superheavy DM ($\sim 10^{13}\,\mathrm{GeV}$), so-called WIMPzillas, with cosmological origin in the inflationary phase of the universe are also predicted in theoretical models [25].

1.3. Light dark matter (LDM) and dark sector models

The dark sector is discussed in detail for LDM. The possible dark sector models, which are classified by the type of mediator (portals) and the type of DM particle, are presented. A specific model for the nature of the DM particle is described for the massive vector particle γ' – the so-called *dark photon*.

If thermal dark matter is assumed to interact via the weak interaction, it would need to have a mass greater than 2 GeV: this is the so-called Lee-Weinberg limit [26]. If the mass of these DM particles is smaller, the annihilation cross-section $\langle \sigma v_\chi \rangle$ will be too small, resulting in an overproduction of DM. However, LDM can exist under the condition that there are still undiscovered light mediators, which are neutral under the SM gauge groups. If restrictions for the Lagrangian, such as gauge and Lorentz symmetries of the SM are respected, it is possible to introduce portals for these new interactions. Renormalizability must also be assumed and the portals can be represented by SM gauge singlet operators

$$\hat{\mathcal{O}} = H^\dagger H,\, LH,\, B_{\mu\nu} \quad , \tag{1.8}$$

where H is the Higgs field, L a lepton doublet, and $B_{\mu\nu}$ the hypercharge field strength tensor. The mediator field can be a scalar ϕ, a fermion N, or a vector particle A'.

These three cases provide thermal relic density limits which can be seen as targets to be reached by DM experiments. For the visualization of experimental reaches, they are also indicated in the $y - m_\chi$ parameter spaces (see Chap. 8) as so-called *thermal relic targets*. The portals are now introduced in detail.

Higgs portal. The mediator is a scalar ϕ. The couplings $\phi H^\dagger H$ and $\phi^2 H^\dagger H$ are renormalizable and consistent with the symmetries. For fermionic DM particles χ, the Lagrangian of a simple model based on the Higgs portal is

$$\mathcal{L}_\phi = g_\mathrm{D}\phi\chi\overline{\chi} + \frac{1}{2}m_\phi^2\phi^2 + aH^\dagger H\phi\frac{m_f}{v}\overline{f_\mathrm{L}}f_\mathrm{R} + \mathrm{h.c.} \quad . \tag{1.9}$$

In this equation g_D is the DM scalar coupling, a a coupling constant, v the Higgs vacuum expectation value, and f a SM fermion. After symmetry breaking, the mixing between the scalar and the fermions is $g_\mathrm{mix} = \sin\theta_{H\phi}/v$, where $\theta_{H\phi}$ is the Higgs−scalar mixing angle. Two cases depending on the mass must now be distinguished. For $m_\chi < m_\phi$ *direct annihilation* of DM particles into SM fermions via the scalar ϕ is possible:

$$\chi\chi \longrightarrow \phi \longrightarrow ff \quad . \tag{1.10}$$

For LDM ($m_\chi \lesssim 1\,\mathrm{GeV}$ and $m_f \ll v$) the mixing angle is so large that branching ratios for rare decays are not consistent with precision meson decay experiments anymore. In the second case $m_\chi > m_\phi$, in addition to the direct annihilation, a *secluded annihilation* is allowed:

$$\chi\chi \longrightarrow \phi\phi \quad . \tag{1.11}$$

The scalars can decay into SM particles afterwards. In this case a dependency of g_mix is missing and there is no thermal target to be tested experimentally. In the case of *direct annihilation* the thermal target variable

$$y = g_\mathrm{D}^2 \sin\theta_{H\phi}\left(\frac{m_f}{v}\right)^2\left(\frac{m_\chi}{m_\phi}\right)^4 > \langle\sigma v\rangle_\mathrm{relic} m_\chi^2 \quad , \tag{1.12}$$

can be probed by experimental searches.

Fermion portal. The coupling to the SM can be realized with the Lagrangian

$$\mathcal{L}_L \sim a_\nu LHN \quad , \tag{1.13}$$

where a_ν is a Yukawa coupling and the fermion N is a right-handed neutrino. For a thermal DM origin a sub-GeV mass of the fermion is required, which results in a too small Yukawa coupling for achieving thermalization in the early universe [16]. Therefore, a fermionic mediator is only possible in a narrow mass range if the thermal DM origin is excluded [27].

Vector portal. Very promising candidates are new vector particles A'. A new gauge group $U(1)_\mathrm{D}$ in the so-called dark sector could interact with SM particles through vector mediator(s).

One could be the so-called dark photon. The Lagrangian for such a simple model is

$$\mathcal{L}_{A'} \sim \underbrace{-\frac{1}{4}F'_{\mu\nu}F'^{\mu\nu}}_{A' \text{ field}} + \underbrace{\frac{\varepsilon_{\mathrm{Y}}}{2}F'_{\mu\nu}B_{\mu\nu}}_{\text{kinetic mixing}} + \underbrace{\frac{m_{A'}^2}{2}A'_{\mu}A'^{\mu}}_{A' \text{ mass}} + \underbrace{g_{\mathrm{D}}A'_{\mu}J^{\mu}_{\chi}}_{A'-\chi \text{ interaction}} + \underbrace{g_{\mathrm{Y}}B_{\mu}J^{\mu}_{\mathrm{Y}}}_{\text{SM hypercharge}} \quad . \tag{1.14}$$

J^{μ}_{χ} is the DM current, the dark photon field is

$$F'_{\mu\nu} = \partial_{\mu}A'_{\nu} - \partial_{\nu}A'_{\mu} \quad , \tag{1.15}$$

and the coupling constant of the dark photon is

$$g_{\mathrm{D}} = \sqrt{4\pi\alpha_{\mathrm{D}}} \quad , \tag{1.16}$$

where α_{D} is the dark fine structure constant. J^{μ}_{Y} is the hypercharge current, ε_{Y} the SM hypercharge, and the hypercharge field is

$$B_{\mu\nu} = \partial_{\mu}B_{\nu} - \partial_{\nu}B_{\mu} \quad . \tag{1.17}$$

Electroweak symmetry breaking leads to a dark photon mixing with the SM photon and the Z boson:

$$\frac{\varepsilon_{\mathrm{Y}}}{2}F'_{\mu\nu}B_{\mu\nu} \longrightarrow \frac{\varepsilon}{2}F'_{\mu\nu}F_{\mu\nu} + \frac{\varepsilon_{\mathrm{Z}}}{2}F'_{\mu\nu}Z_{\mu\nu} \quad , \tag{1.18}$$

where $\varepsilon = \varepsilon_{\mathrm{Y}}/\cos\theta_{\mathrm{W}}$, $\varepsilon_{\mathrm{Z}} = \varepsilon_{\mathrm{Y}}/\sin\theta_{\mathrm{W}}$ and θ_{W} is the weak mixing angle. The coupling of A' with DM and the SM photon is obtained after mass diagonalization:

$$\underbrace{g_{\mathrm{D}}A'_{\mu}J^{\mu}_{\chi}}_{A'-\chi \text{ interaction}} + \underbrace{g_{\mathrm{Y}}B_{\mu}J^{\mu}_{\mathrm{Y}}}_{\text{SM hypercharge}} \longrightarrow A'_{\mu}\left(g_{\mathrm{D}}J^{\mu}_{\chi} + \varepsilon e J^{\mu}_{\mathrm{EM}}\right) \quad , \tag{1.19}$$

where J^{μ}_{EM} is the electromagnetic current of the SM. Again the direct annihilation case with $m_{A'} > m_{\chi}$ gives a clear thermal target for experiments:

$$y = \varepsilon^2\alpha_{\mathrm{D}}\left(\frac{m_{\chi}}{m_{A'}}\right)^4 \quad . \tag{1.20}$$

Different DM candidates corresponds to different choices of dark currents: complex scalar DM, Majorana DM, pseudo–Dirac DM.

Vector mediators and possible DM particles. In the following, the focus is on the promising vector mediators. The possible cases discussed here are Dirac fermions, Majorana fermions, and scalar particles. The current J^{μ}_{χ} and the annihilation cross-section $\langle\sigma v_{\chi}\rangle$ for the three cases are summarized in Tab. 1.1.

- **Dirac fermion:** In analogy to electrons, the DM particle χ is a Dirac fermion with mass m_{χ}. The abundance of the DM particle χ and the anti-DM particle $\overline{\chi}$ could be symmetric or asymmetric. The symmetric case is ruled out by CMB measurements [16], while the asymmetric case is not [28]. The abundance of $\overline{\chi}$ could be suppressed by factors of $\sim e^{-\langle\sigma v_{\chi}\rangle}$,

similar to SM matter/ anti-matter cases.

- **Majorana fermion:** In this case the DM particles χ_1 and χ_2 have a mass difference $\Delta = m_2 - m_1 > 0$. If $m_{A'} > m_1 + m_2$ (direct annihilation) χ_2 is unstable and decays via
$$\chi_2 \longrightarrow \chi_1 \, f\overline{f} \quad .$$
For the direct annihilation both particles are necessary and decay via
$$\chi_1\chi_2 \longrightarrow A' \longrightarrow f f \quad .$$
If the mass deviation is small compared to the DM masses, the annihilation cross-section $\langle\sigma v_\chi\rangle$ is the same in the Dirac and Majorana fermion case.

- **Scalar:** For the direct annihilation of two scalar DM particles
$$\chi\chi \longrightarrow A' \longrightarrow f f \quad ,$$
the DM velocity v_χ is present in the annihilation cross-section $\langle\sigma v_\chi\rangle$, giving an enhanced thermal target compared to the fermion case.

DM particle		**current J^μ_χ**	**annihilation cross-section $\langle\sigma v_\chi\rangle$**
Dirac fermion	$\chi\overline{\chi}$	$\overline{\chi}\gamma^\mu\chi$	$\propto \varepsilon^2\alpha_\mathrm{D}\frac{m_\chi^2}{m_{A'}^4} \sim \frac{y}{m_\chi^2}$
Majorana fermion	$\chi_1\chi_2$	$\chi_1\gamma^\mu\chi_2 + \mathrm{h.c.}$	
Scalar	$\chi\chi$	$i(\chi^*\partial^\mu\chi - \chi\partial^\mu\chi^*)$	$\propto \varepsilon^2\alpha_\mathrm{D}\frac{m_\chi^2 v_\chi^2}{m_{A'}^4} \sim \frac{y v_\chi^2}{m_\chi^2}$

Table 1.1.: Current J^μ_χ and thermally averaged cross-section for DM annihilation $\langle\sigma v_\chi\rangle$ for vector mediators and three kinds of DM particle. y is the dimensionless combination of model parameters.

Yield expectations. The theoretical model parameters can be linked to the DM production yields. If $m_{\gamma'} < 2\,m_\chi$ the production takes place off-shell via virtual dark photon. The DM yield is $\sim \alpha_\mathrm{D}\varepsilon^2/m_\chi^2$ and the DM scattering in the detector scales with $\sim \alpha_\mathrm{D}\varepsilon^2/m_{\gamma'}^2$ resulting in the total yield:
$$Y = Y_\chi \times Y_\mathrm{D} \sim \frac{\alpha_\mathrm{D}^2\varepsilon^4}{m_\chi^2 m_{\gamma'}^2} \quad . \tag{1.21}$$
However, in the simulation studies presented in this thesis, the second case is assumed, where $m_{\gamma'} > 2\,m_\chi$ and a real production of the dark photon takes place, decaying directly into a DM pair. In this case, the DM yield is $\sim \alpha_\mathrm{D}\varepsilon^2/m_{\gamma'}^2$ and the DM scattering in the detector scales with the same value $\sim \alpha_\mathrm{D}\varepsilon^2/m_{\gamma'}^2$ as in the first case, resulting in:
$$Y = Y_\chi \times Y_\mathrm{D} \sim \frac{\alpha_\mathrm{D}^2\varepsilon^4}{m_{\gamma'}^4} \quad . \tag{1.22}$$
What becomes obvious here is that for the expected low coupling constant ε and the fourth power, reduced yields are to be expected. However, by using modern accelerators with high beam currents and dense targets, this effect can be compensated.

1.4. Experimental LDM search

Due to the nature of DM, highly sensitive experiments with almost perfect background suppression methods are required. Direct detection experiments try to detect DM particles recoil against nuclei (or electrons). Depending on the nucleus, the scattering rates of direct spin-independent searches gain a factor of A^2 or Z^2, while spin-dependent searches do not benefit from this factor. That is why the former searches reach higher sensitivities. For DM masses below $\sim 1\,\mathrm{GeV}$, it is difficult to detect nuclear recoils. The nuclear recoil energy limit can be calculated with

$$E_R \lesssim \frac{\mu^2 v_\chi^2}{m_{\mathrm{nucl}}} = \left(\frac{m_\chi\, m_{\mathrm{nucl}}}{m_\chi + m_{\mathrm{nucl}}}\right)^2 \frac{v_\chi^2}{m_{\mathrm{nucl}}} \quad . \text{[29]} \tag{1.23}$$

For a DM particle with a mass of $m_\chi = 1\,\mathrm{GeV}$ and assuming a DM halo velocity of $v_\chi = 300\,\mathrm{km\,s^{-1}}$ (see Fig. 1.1) the maximum recoil energy is $E_\mathrm{R} \approx 250\,\mathrm{eV}$. For typical detection media such as liquid Xenon ($m_{\mathrm{nucl}} \approx 122\,\mathrm{GeV}$ [30]) the value is even lower with $E_\mathrm{R} \approx 8\,\mathrm{eV}$. Producing DM with an accelerator has the advantage that DM energy can be higher than the one of halo DM and therefore the mass and threshold limitations of direct detection techniques can be overcome. There are also indirect detection techniques, which try to detect SM particles from a DM decay or DM annihilation. Some of the searches for LDM that have been performed or are still ongoing are presented in the following.

Underground science laboratories. Cryogenic Rare Event Search with Superconducting Thermometers (CRESST)-II searched for the elastic scattering of DM particles in $CaWO_4$ crystals with cryogenic detectors. CRESST-II extended the reach of direct detection experiments to the sub-GeV region and enhanced the sensitivity in the LDM–WIMP transition area [31]. CRESST-III improved the reach even further into the sub-GeV range [32]. The resulting sensitivities for CRESST and the following experiments are presented in Fig. 1.3.
Super Cryogenic Dark Matter Search (SuperCDMS) at SNOLAB will use two different types of cryogenic detectors and two target materials will be used for the direct detection of low mass ($< 10\,\mathrm{GeV}$) particles via nuclear recoil. The setup will be operated in the underground laboratory SNOLAB. The sensitivity will be sufficient for sub-GeV DM and better sensitivities in the mass range up to 10 GeV are projected [33].
These experiments improve the sensitivity in the transition region from LDM to WIMP mass. Since these experiments are optimized for the DM-nucleon recoil only, it is difficult for them to go even deeper into the LDM domain.
The following experiments are also designed for detecting DM-electron recoils. Experiments in this lower DM mass range are DArk Matter In CCDs (DAMIC) at SNOLAB and Sub-Electron-Noise Skipper-CCD Experimental Instrument (SENSEI) in the MINOS cavern at Fermi National Accelerator Laboratory (Fermilab). Both use CCD silicon detectors and achieved high sensitivities in a wide range of sub-GeV DM masses. DAMIC established the best direct detection limits for DM–electron scattering in the range of 600 keV to 6 MeV [34]. SENSEI increased the experimental sensitivity in the range of 500 keV to 10 MeV [35] even further.

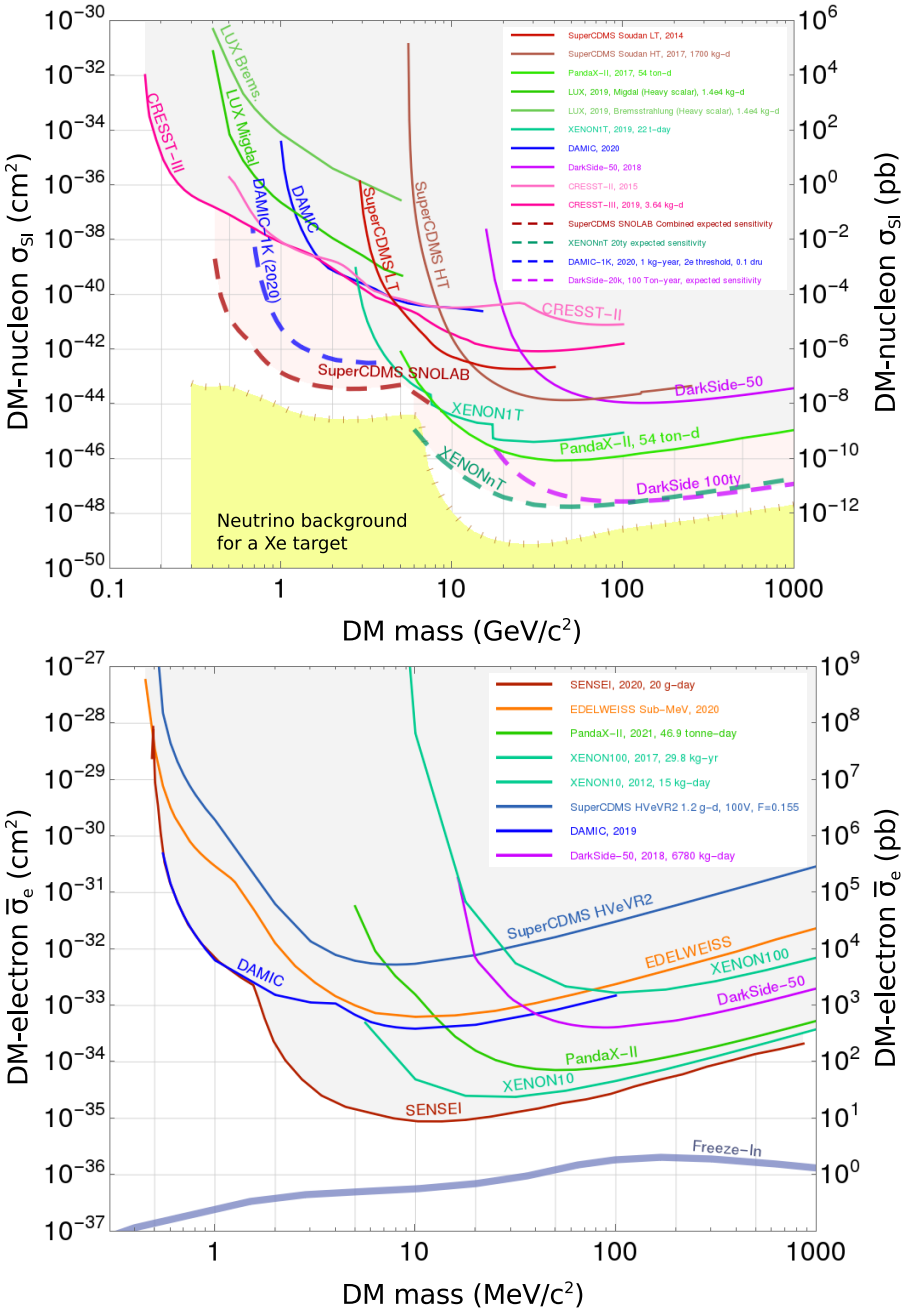

Figure 1.3.: Current sensitivities of spin-independent direct DM searches. The solid lines are results and the dashed lines are projections of experiments. The DM-nucleon cross-section σ_{SI} [31, 32, 36–44] (top) and the DM-electron cross-section $\overline{\sigma_{\mathrm{e}}}$ [34, 35, 45–50] (bottom) are shown for the world leading experiments.[3]

High-intensity accelerators. Another generation of experiments tries to produce LDM with accelerators and detect particles involved in the processes with suitable experimental setups. The A' EXperiment (APEX) [51] at Thomas Jefferson Laboratory (JLab) is searching for a sub-GeV vector boson[4] produced via scattering of 2.26 GeV beam electrons on a tantalum foil. The scattered e^+e^- pairs are measured with a spectrometer setup and new limits were established

[3] Plots created with the `Dark Matter Limit Plotter v5.17` (as from Dec 21, 2021) provided by the SuperCDMS collaboration.

[4] Whether other authors call it a light spin-1 boson, heavy photon or dark photon, A', or γ', all are denoted γ' throughout this thesis.

during an APEX test run in the mass range from 175 to 250 MeV. APEX demonstrated, that fixed-target experiments can explore new parameter space in search for LDM. The sensitivities of APEX and the following experiments are shown in Fig. 1.4.

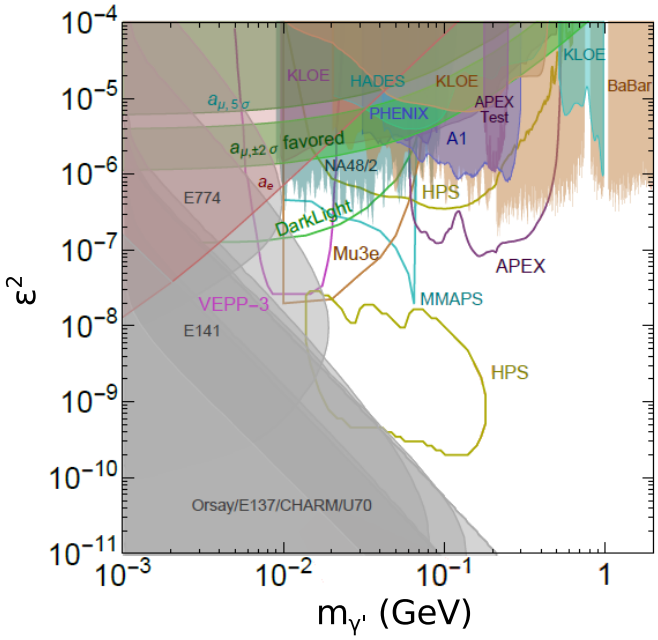

Figure 1.4.: $\varepsilon^2 - m_{\gamma'}$ parameter space for visible dark photon decays $\gamma' \longrightarrow e^+e^-$. The projected sensitivities of the JLab experiments APEX, Heavy Photon Search (HPS), and DarkLight are shown with solid lines. Results from completed experiments, including an APEX test run, are shown with shaded areas. Figure from [52].

Another fixed target experiment searching for the e^+e^- decay of a massive gauge boson at JLab is HPS [53]. The main components of HPS, which receives an 1.1 to 11 GeV electron beam with a current up to 250 nA, are a silicon tracker and an electromagnetic calorimeter. With a sensitivity in the 20 MeV to 1 GeV mass range, new stringent exclusion limits are set by HPS.
DarkLight [54, 55] is a future experiment, which will be operated at ARIEL. With a 31 MeV (upgrade 50 MeV) electron-linac, DarkLight will target an energy range, which appears to be of particular interest due to striking results from the ATOMKI Collaboration. They produced excited states of ^{8}Be* and measured the angular distribution of e^-e^+ pairs. An excess was found for a wide opening angle around 140°. The opening angle, the asymmetry, and the invariant mass are consistent with the decay of a new particle with a mass of $16.7 \pm 0.35\,(\text{stat}) \pm 0.5\,(\text{sys})$ MeV [56]. For the excited states of ^{4}He* a result as in the ^{8}Be* case was found leading to a mass of $16.84 \pm 0.16\,(\text{stat}) \pm 0.2\,(\text{sys})$ MeV [57, 58]. This particle could be a light neutral boson – the so-called X17.

Beam-dump experiments. Another class of experiments has been exploited in recent years to search for dark sector particles – beam-dump experiments. These also use high intensity accelerators, but in contrast to the previous approaches, the beam-dump serves as DM source and the DM detectors can be placed outside the accelerator halls, well shielded from beam-related SM background. DarkMESA will be such an experiment and the experimental setup is described in Sec. 2.2.3 and Chap. 6. The underlying theory, further beam-dump experiments and their expected reach are discussed in Chap. 8.

2. The accelerator facility in Mainz

With particle accelerators, researchers have an instrument at their disposal that can accelerate charged particles with the help of electromagnetic waves to high kinetic energies and thus almost to the speed of light. They are used in fundamental research as well as industry and medicine. In this chapter the extensive experimental possibilities at the Institute for Nuclear Physics in Mainz (KPH) are presented. Both the existing infrastructure with the Mainz Microtron (MAMI) and its experiments, as well as the future expansion with the Mainz Energy-recovering Superconducting Accelerator (MESA), which is currently under construction. All experimental setups with a connection to DarkMESA, whether they are explicitly related to the construction or operation of DarkMESA, are presented.

2.1. MAMI – The Mainz Microtron

With MAMI, there is a reliable experimental facility in-house, which was used several times for DarkMESA material studies. For instance, lead fluoride (PbF_2) Cherenkov radiators used in the A4 experiment were studied. The results are discussed in Chap. 5. Moreover, in the future MAMI will be important to experimentally study DarkMESA prototypes. In addition to laboratory background studies with cosmic radiation, MAMI offers the possibility to investigate the veto and calorimeter behavior due to beam-induced backgrounds like neutrons or photons.

A general overview and the operation principle of MAMI is presented in Sec. 2.1.1 and the experimental possibilities are discussed in Sec. 2.1.2.

2.1.1. Accelerator overview

MAMI is a multistage recirculating electron accelerator, first proposed in 1976 by H. Herminghaus in collaboration with K. H. Kaiser [59]. Fig. 2.1 shows the underground floor plan of the KPH, with the MAMI accelerator and the experiments X1, A1, A2, and A4 [60].
Initially a 2.1 MeV Van-de-Graaff injector served as a source for the beam electrons with 2.1 MeV and a maximum current of 65 µA and no polarized electrons were available. The first three stages are based on continuous wave (CW) Race Track Microtrons (RTMs). Each uses one linear acceleration stage, composed of radio frequency (RF) cavities, multiple times. This is obtained by bending the beam electrons with two 180°-magnets after each acceleration. The beam frequency is $\nu_{\mathrm{RF}} = 2.45\,\mathrm{GHz}$. Thus the time structure of the electron beam is so short that detectors of the various experiments observe a continuous flow of electrons and no pulsed bunches. The increase of energy for each recirculation is

$$\Delta E = \frac{ecB}{2\pi} \cdot \lambda_{\mathrm{RF}} \qquad \text{with} \quad \lambda_{\mathrm{RF}} = \frac{c}{\nu_{\mathrm{RF}}} \quad . \tag{2.1}$$

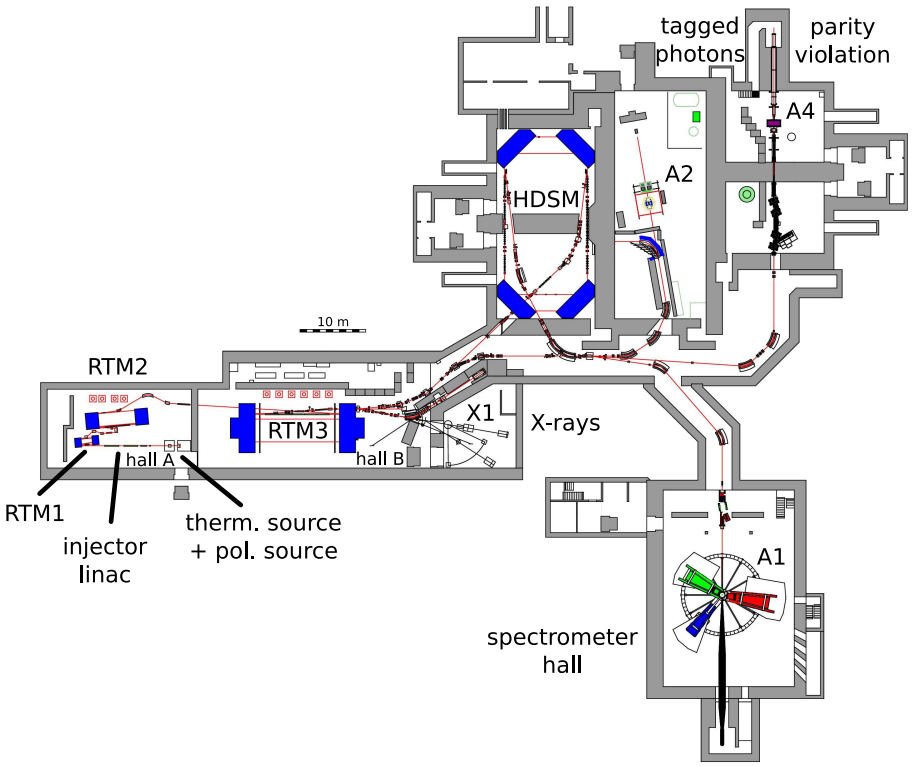

Figure 2.1.: Floor plan of the MAMI accelerator facility. In hall A the electrons from a thermal or polarized source are preaccelerated in the injector linac to a kinetic energy of up to 3.5 MeV. The energy can be increased up to 14 MeV after RTM1 and up to 180 MeV after RTM2. In hall B is located the RTM3 with a maximum energy of 855 MeV. From there the electron beam can be guided to the experimental halls (X1, A1, A2, and A4) or be further accelerated up to 1 604 MeV with the HDSM before being used at the experimental sites. Additional test beam stations relevant for DarkMESA are located close behind RTM1 and RTM3. Figure adapted from [60].

RTM1 went into operation 1979 and RTM2 in 1983. Both together with the Van-de-Graaff injector are called MAMI-A. Energies of up to 180 MeV were achieved.
With the progressive development of MAMI and the decision to build RTM3 the previous MAMI setup was moved to its present day position in hall A and RTM3 with its two 450 t magnets was build in the separate hall B. During this relocation the Van-de-Graaff injector was replaced by a 3.5 MeV CW linac, where the electrons already reach 99.2 % of the speed of light. For unpolarized electrons a 100 keV thermal electron source is used. The now better access to the injector also makes it possible to use a source for polarized electrons. They can be produced with a source that exploits the photoelectron emission of semiconductors: GaAsP cathodes are irradiated by a He-Ne-laser [61]. In 1990 this so-called MAMI-B setup went into operation. The design beam energy reached a maximum of 855 MeV and the design current for unpolarized electrons rose to a maximum of 100 µA. For polarized electrons, currents larger than 30 µA with a polarization better than 85 % can be achieved today. For MAMI-B the energy spread is better than 13 keV and the beam position can also be kept precisely constant (±200 µm).
In 1999 the proposal for a further expansion stage was approved. With higher electron energy also the diameter of the magnet pole faces of the RTMs increase: the magnets become larger, heavier, and more expensive. To reach the desired beam energy of 1.5 GeV two 2 200 t magnets would have been necessary. So it was not feasible nor affordable to increase the beam energy

further with a fourth RTM. Instead, a Harmonic Double-Sided Microtron (HDSM) with more compact 90°-bending magnets was suggested [62]. The stage uses four such dipole magnets and the beam can be recirculated up to 43 times. Two normal conducting linacs are placed opposite to each other between two dipoles. Despite the rising electron beam energy, for each recirculation $\sim 15\,\mathrm{MeV}$, the electrons are guided through the same two linacs. The power consumption was reduced to a quarter by using one of the linacs with a frequency of 4.90 GHz, twice the MAMI frequency. This four stages of MAMI provide physicists with a high-performance accelerator for a variety of experiments, especially to study the structure of matter in the subatomic range. Experimental setups of the past and present are introduced in the next subsection.

	RTM1	**RTM2**	**RTM3**	**HDSM**
beam energy (MeV)	14.86	180	855	1508
energy spread (keV)	1.2	2.8	13	110
magnetic field strength (T)	0.1	0.5	1.3	$0.95 - 1.5$
no. of turns	18	51	90	43
mass per magnet (t)	1.3	40	450	250

Table 2.1.: Some key parameters of the three Race Track Microtrons (RTMs) and the Harmonic Double-Sided Microtron (HDSM).

2.1.2. Experiment overview

The locations of the experiments described in the following are also indicated in Fig. 2.1. First, a rough overview of the experiments is given, before their significance for DarkMESA is discussed.

X1 - X-ray radiation. The X1 Collaboration was initiated in 1991 to study alternative sources for excellent x-rays, which arise by the interaction of the MAMI electron beam with various targets. Also magnetic undulator structures are used to produce x-rays. The research of X1 is of interest in a wide range of fields, like physics, material sciences, biology, and medicine. [63]

A1 - Electron scattering. With its three spectrometer setup, A1 allows electron scattering experiments with a coincident detection of involved particles. Particles can be resolved with a momentum resolution better than 0.01 %, a 3 mrad angle resolution, and a timing resolution of 500 ps. This allows precise studies of the structure of atomic nuclei. For instance, A1 contributed to the proton radius puzzle with a measurement of the proton charge radius through precise cross-section measurements in the elastic electron-proton scattering on hydrogen [64, 65]. A1 has also contributed with an exclusion limit in the field of dark sector physics: a search for the decay products e^+e^- of a hypothetical light $U(1)$ gauge boson γ' produced via electromagnetic Bremsstrahlung was performed [66]. The resulting limit was already indicated in Fig. 1.4. The scattering chamber and targets are exchangeable and it is possible to carry out experiments with the MAGIX gas jet target (Sec. 2.2.1) already at A1.

A2 - Real photon experiments. Instead of using the MAMI electron beam directly, at A2 photons are generated in a Bremsstrahlung process. These photons arise, when beam electrons

(E_{e^-}) hit the heavier atomic nuclei in a Møller radiator. The Glasgow photon tagger spectrometer allows the determination of the scattered electron's energy E'_{e^-} and hence the photon's energy is:

$$E_\gamma = E_{e^-} - E'_{e^-} \quad . \tag{2.2}$$

For the full energy range a resolution of $\Delta E_\gamma = 2\,\mathrm{MeV}$ is obtained. The tagger microscope allows the study of tight energy ranges ($\sim 80\,\mathrm{MeV}$), improving the energy resolution by a factor of three [67]. The tagged photons are not influenced by the magnetic field and can be forwarded to a target in the center of the Crystal Ball (CB) calorimeter [68]. Together with the Two Arm Photon Spectrometer (TAPS) detector installed as forward wall and internal detectors, this setup can distinguish between charged and neutral particles. A direct measurement of the helicity dependence of the total photoabsorption cross-section on the proton was carried out at A2 [69] and A2 contributes to baryon resonance searches with a variety of photon scattering experiments [70].

A4 - Parity violation (completed). A4 investigated the structure of nucleons, which is more complex than just the valence quarks composition. In addition, there are gluons and quark-antiquark pairs known as sea quarks. The additional flavor contributions were investigated with the A4 experiment. MAMI delivered a beam of polarized electrons, which were scattered off hydrogen or deuterium targets. The scattered electrons were detected with a total absorbing lead fluoride (PbF_2) calorimeter. This cylindrical calorimeter was segmented with 1022 tapered crystals in seven different lengths between 150.0 and 185.4 mm. The front surfaces cover $26 \times 26\,\mathrm{mm}^2$, while the back surfaces are $30 \times 30\,\mathrm{mm}^2$ in size. This setup allowed the measurement of tiny contributions to the parity violation asymmetry in the weak interaction. [71, 72]

This brief overview is now linked to the upcoming DarkMESA experiment. What possibilities do MAMI and these experiments offer for DarkMESA?

- **Reutilization.** The A4 experiment is now completed and there is the opportunity to reuse the crystals in the DarkMESA setup including the optical readout and parts of the electronics. More than 1 000 PbF_2 crystals with a total active volume of $0.13\,\mathrm{m}^3$ are available.

- **Background studies.** In many solid-target experiments at A1, a significant background radiation is generated, e.g. by neutrons, which are particularly suitable for studies of a prototype veto system. Without disturbing the regular beam operation, a prototype could be placed next to the A1 target or the beam-exit-pipe. Furthermore, the tagged photons of A2 could be used for additional background studies.

- **Material studies.** Beside the experiments, MAMI offers experimental sites behind RTM1 (up to 14.86 MeV) and RTM3 (up to 855 MeV). Both have already been used for calorimeter crystal and veto scintillator studies in this work and will be used again for future development studies. Small detectors could also be tested at certain positions inside of the A1 spectrometers. The existing measuring tools in the spectrometers allow the exact determination of particle tracks.

In the more than four decades of operation, MAMI has offered and still offers versatile experimental possibilities. Nevertheless, or especially because of the long experience, the desire to perform even more precise measurements in a lower energy range arose. Together with new high-precision experiments, the new MESA accelerator was finally developed.

2.2. MESA – A new electron accelerator in Mainz

The Mainz Energy-recovering Superconducting Accelerator (MESA) [73] is currently under construction at the Institute for Nuclear Physics located at the Johannes Gutenberg University Mainz. It will operate in parallel to the existing MAMI accelerator and in direct proximity to it. Both, the experience and the infrastructure of the institute, like the mechanical, accelerator, vacuum, and electronics workshops, can therefore be easily and fully exploited. MESA and its experiments will be placed in emptied MAMI halls and a newly build hall extension. In this way, the construction effort is reduced and the original A4 beam-dump can be used further. The hall and its maintenance building will be finished in 2022 and the assembly of the accelerator and also the experiments in their final position will start shortly after. The first MESA beam for the experiments is expected in 2024.

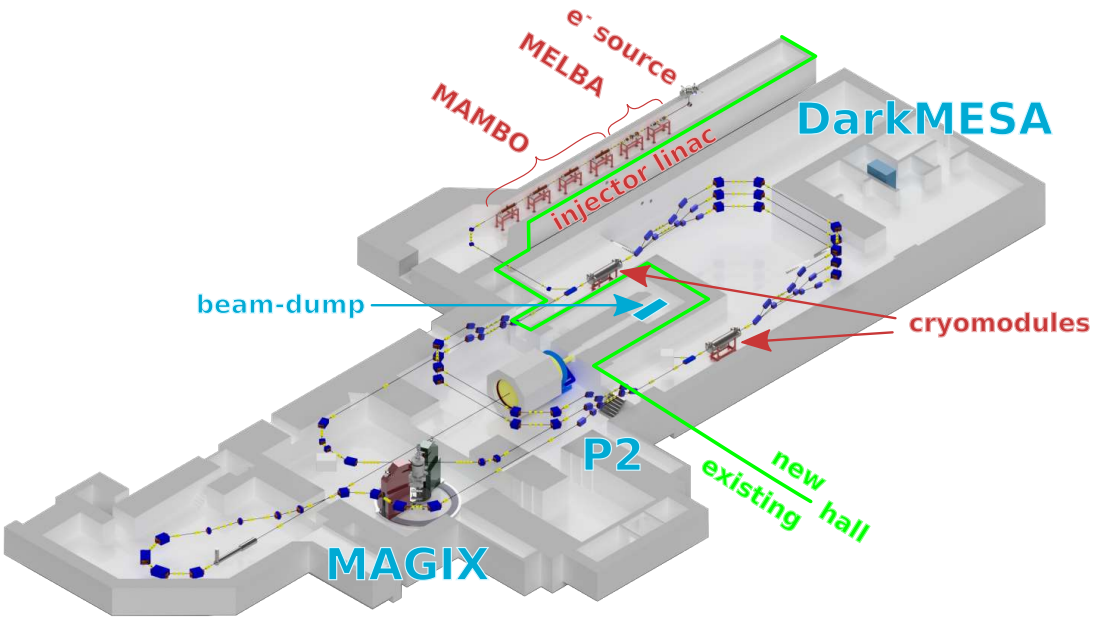

Figure 2.2.: Overview of the MESA accelerator facility. The existing and new parts of the MESA hall are shown. The electron beam from the injector linac gains up to 25 MeV when passing a cryomodule and is guided to the main experiments MAGIX and P2. The DarkMESA experiment is placed in the extension of the P2 beam-dump. Adapted from the original CAD drawings created by Daniel Simon [74, 75].

MESA will be the world's first energy-recovering accelerator to perform fundamental research in physics experiments. Due to the energy range covered with a higher beam intensity than with MAMI, new high-precision experiments will be realized.
The layout of MESA and its experiments can be seen in Fig. 2.2. Like MAMI, it is a CW electron accelerator with a frequency of 1.3 GHz. Depending on the beam mode and experiment, different sources for electron production are used. In the case of polarized electrons: a polarized inverted

DC photogun. The MESA Low-energy Beam Apparatus (MELBA) manages the transport and spin manipulation of the low energy electrons up to the chopper-buncher sections for the beam injection. Immediately afterwards the normal conducting Milli AMpere BOoster (MAMBO) is used for pre-acceleration up to 5 MeV beam energy. After the pre-acceleration the beam is recirculated in the main linac up to three times, depending on the beam mode. In Fig. 2.2, shown in blue are the dipole magnets for the beam transport and in yellow the quadrupole magnets for beam focusing. In each recirculation the electrons pass two ELBE-type superconducting cryomodules [76]. Each of them contains two TESLA/XFEL 9-cell superconducting RF cavities inside, where the electrons gain up to 12.5 MeV of energy in each cavity.
The first mode is the energy-recovering linac (ERL) mode. In this mode the electrons are recirculated two times and gain up to 105 MeV energy. The beam interacts with a (pseudo) internal target, reaching luminosities in the order of $10^{-35}\,\mathrm{cm}^{-2}\,\mathrm{s}^{-1}$. Most of the beam electrons pass through the target undisturbed and their energy is returned stepwise to the cavities. The beam current reaches up to 1 mA with the possibility of a later upgrade to 10 mA, which is two orders of magnitude higher than the MAMI current. At this high beam current, it is not possible to use polarized electrons due to the short lifetime of the photocathodes. The experiment in the energy-recovering linac (ERL) mode is called MAGIX and is described in detail in Sec. 2.2.1.
The other mode is the so-called extracted beam (EB) mode. There, a high precise and stable beam of 85 % polarized electrons is generated and interacts with a liquid or solid target. The beam current is 150 µA and by using GaAs/ GaAsP superlattice photocathodes twelve days runtime without replacement are estimated for the P2 experiment. For this extracted beam (EB) mode experiment the beam energy is up to 155 MeV after three recirculations. The high dense targets do not allow energy-recovering and the electron beam has to be stopped after the experiment in the beam-dump. This beam-dump in turn serves as target for the third experiment, the DarkMESA experiment, which is placed in the extension of the P2 beam-axis in a dedicated room outside of the MESA hall.

2.2.1. Energy-recovering linac (ERL) mode

In the ERL mode, the beam is guided to the MAGIX experiment after two circulations. The electrons reach an energy of up to 105 MeV and a maximum beam current of 1 mA[1].

MAGIX - A versatile fixed target experiment

The physic studies with MAGIX aim to achieve a particularly high level of precision, which is why multiple scattering of involved particles has to be avoided. Beam electrons enter the MAGIX windowless scattering chamber and interact with the particles of the gas jet target. The scattered electrons can be detected with the two identical magnet spectrometers STAR and PORT. They are mounted rotatable around the interaction point. A sliding seal setup allows the connection of the spectrometers and the scattering chamber without any window. The magnet optics is defined by a quadrupole and two dipoles, which focus the scattered electrons on the focal plane. A short drift time projection chamber (TPC) based on gas electron multipliers (GEMs) covers the size of the entire focal plane and is used to determine the particle tracks. With the information of

[1] Possibility of a later upgrade to 10 mA.

position and drift time, angle and momentum of the particle can be deduced. The momentum resolution will be $\Delta p/p < 10^{-4}$ and the angular resolution $\Delta\theta < 0.2°$. A highly efficient trigger and veto system selects physics events and rejects backgrounds.

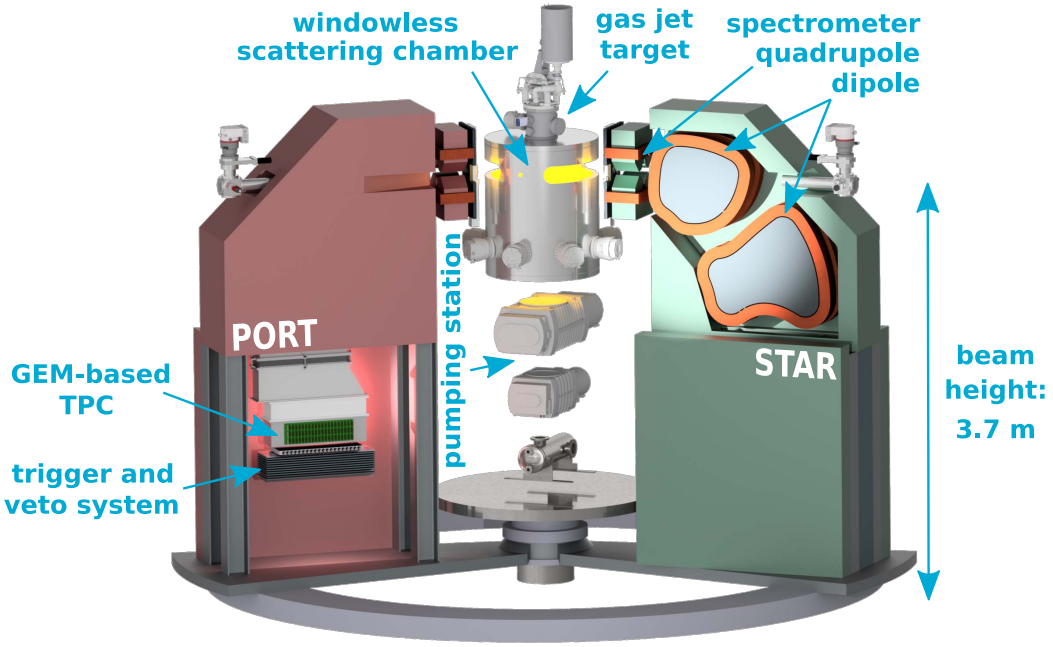

Figure 2.3.: Overview of the MAGIX setup. The MESA electron beam enters the windowless scattering chamber and interacts with the internal gas jet target. With the two identical magnetic spectrometers STAR and PORT, scattered particles are focused to focal planes and close to them they are detected with GEM-based TPCs. A trigger and veto system assists in the assignment of detected particles. [77]

Interaction - Scattering chamber and gas jet target. The MESA electron beam enters the windowless scattering chamber, where it can interact with a target gas (Fig. 2.4). The target was developed by the University of Münster and has been designed for a wide range of different gases. In the cold head the gas is cooled down (e.g. 40 K for hydrogen) and enters the scattering chamber through a Laval nozzle, which is specially designed for the various target gases. In this cold state, the hydrodynamics of the Laval nozzle allow a stable beam for several millimeters. Below the interaction point, the gas is pumped away through a catcher. So the vacuum inside of the scattering chamber is not significantly worsened by the target gas. An areal target thickness of $> 10^{18}$ atoms/cm^2 allows a luminosity of $\mathcal{O}\left(10^{35}\,\mathrm{cm}^{-2}\,\mathrm{s}^{-1}\right)$ [78]. Several silicon strip detectors are mounted inside of the scattering chamber for studies, where the knowledge on the recoil target particles is needed [79].

Detection - Spectrometers and short drift TPC. Scattered electrons can leave the chamber through the magnetic spectrometers STAR and PORT, located left and right of the beam-line. They are connected to the chamber with a sliding seal, which allows a windowless connection and an angular range from 15° to 165° with respect to the beam-axis. For smaller angles, an additional detector uses the first MESA dipole after the scattering chamber. This Zero Degree Tagger (ZDT) is able to measure at forward angles below 0.5° [80]. The magnetic spectrometers have a quadrupole-dipole-dipole configuration and are designed to focus electrons with same momenta to the same point in a horizontal focal plane (Fig. 2.5 left). The scattering angle could

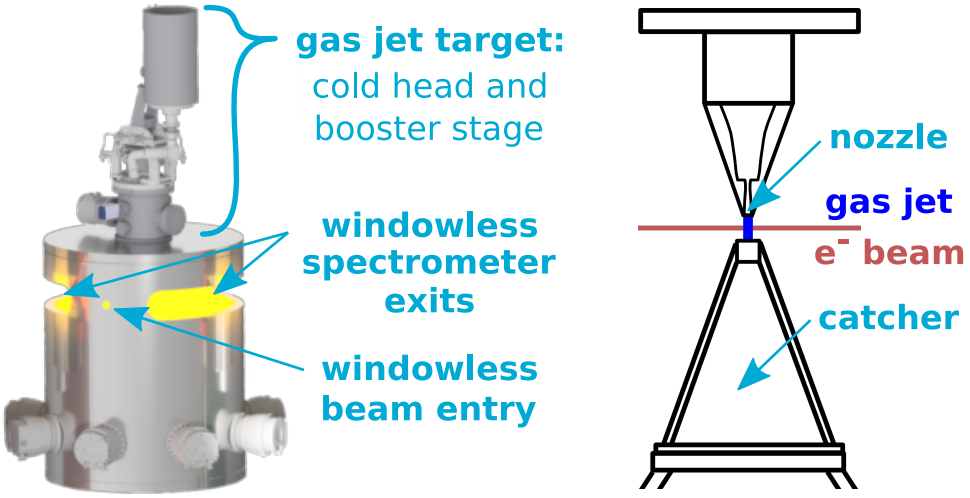

Figure 2.4.: CAD drawing of the MAGIX scattering chamber (left) and sketch of the MAGIX gas jet target (right). The MESA electron beam enters the scattering chamber through a windowless entry and interacts with the gas jet of a target developed by the University of Münster [78]. The cold head and an additional nitrogen booster stage serve for the necessary gas cooling. A laval nozzle allows a stable beam and in order to keep the surrounding vacuum stable, the target gas is pumped away directly after the interaction through a catcher. Scattered particles can leave the chamber through windowless openings in direction of the spectrometers.

be determined by measuring in a second plane, but two stacked detectors are not the best choice due to the additional material budget. With a short drift TPC this disadvantage is eliminated and full trajectories can be obtained. Only a thin foil between the spectrometer vacuum and the gas filled TPC is necessary.
The TPC is located below the magnets inside of a lead housing. Its active volume covers the full focal plane and is filled with a gas mixture, containing Argon as counting gas. A schematic working principle is shown in Fig. 2.5 (right).

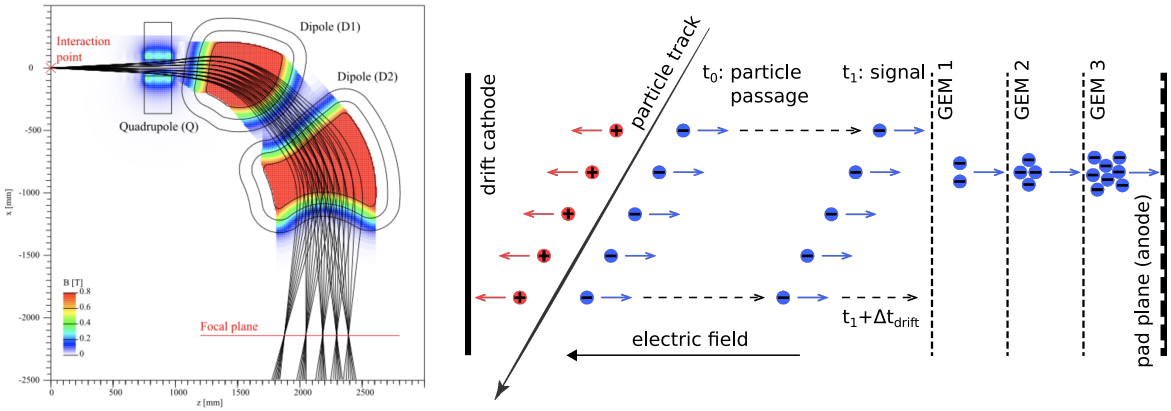

Figure 2.5.: Magnetic field map of the MAGIX spectrometers (left) and TPC detection principle (right). Trajectories of scattered electrons are shown in black. The dipole edges are designed to focus particles with same momenta, but distinct scattering angle, to the same point in a horizontal focal plane. A short drift TPC is located there. The applied electric fields and a GEM detector readout, allow the detection principle shown on the right.

A strong electric field is applied between a drift cathode and an anode. An amplification stage with three GEM foils and the readout plane is located there. All scattered beam electrons pass

between cathode and anode. On its track, an incoming particle can ionize multiple gas atoms of the TPC's counting gas (at the time t_0). Due to the electric field, ions drift to the cathode and electrons towards the amplification stage. Strong electric fields inside the holes of the GEM foils, lead to further ionization and an electron avalanche. In a pad plane, the charge of the electrons is measured. Due to the particle's path, time differences in the signal detection can occur. The first signal is detected at the time t_1 and for an ionization closer to the cathode a time $t_1 + \Delta t_{\text{drift}}$ is observed. From these drift times and the x-y-positions in the pad plane, momenta and scattering angle can be determined.

Selection - The MAGIX trigger and veto system. The trigger and veto system is located directly below the TPC, in the same lead housing. This system is intended to distinguish between real and background events with high precision. In a first trigger layer (T1) 22 plastic scintillator bars with a rhomboid base and 150 mm length are connected to Plexiglas® light guides and photomultiplier tubes (PMTs) on both sides. Beneath, a layer of 10 mm thick plastic scintillator serves as second trigger (T2) and first veto (V1). This first veto and the two following veto layers (V2, V3) are separated by multiple lead shielding layers from each other. A tray system allows flexible replacement, interchange, or removal of veto and lead layers.[2] Light in the veto layers is collected with silicon photomultipliers (SiPMs) on both short sides. The distinction principle of the full setup is shown in Fig. 2.6. The largest majority of scattered beam electrons will leave a signal in the trigger layers T1 and T2, while leaving no signal in the veto layers V2 and V3. Due to their energy, most of the cosmic muons leave a signal in all four layers. Background radiation from neutrons can lead to signals in all layers, but these signals do not correlate in time. The high efficiency of the trigger veto system allows a precise event selection without losing too many real events.[3]

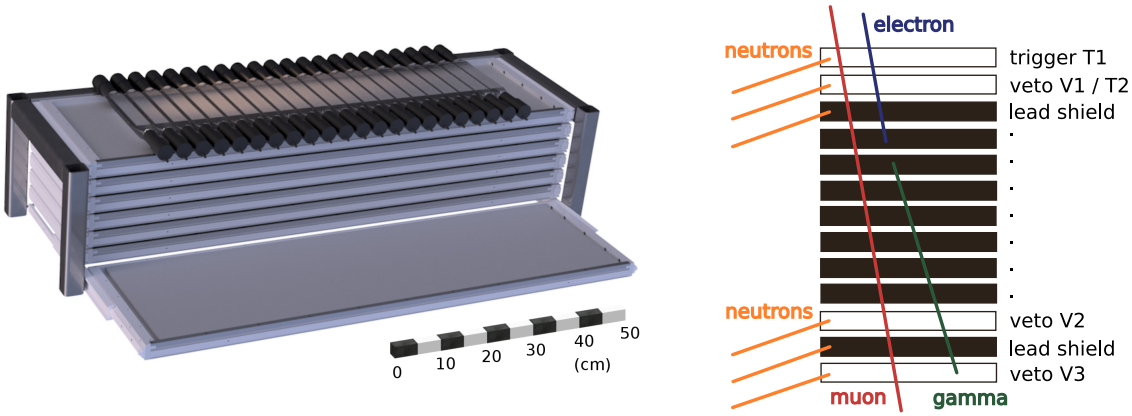

Figure 2.6.: CAD drawing (left) and working principle (right) of the MAGIX trigger and veto system. The trigger plane T1 is read out on both sides. All trigger and veto layers are made of plastic scintillator. Each tray can be filled with two 1 cm thick lead or scintillator layers. For scattered beam electrons, this concept allows a high trigger efficiency $\mathcal{O}\left(10^{0}\right)$, while the veto response probability is below $\mathcal{O}\left(10^{-4}\right)$.

[2] Additional detectors can also be used with this tray system. A MAGIX shower detector made of SF5 lead glass is briefly discussed in the outlook in Chap. 9.

[3] An initial MAGIX trigger veto simulation study was prepared based on the DarkMESA simulation framework and is presented in Sec. 4 along with initial results.

Physics program. Due to its high precision and flexibility in terms of both, the usable target gases and the detection possibilities of scattered electrons and recoil nuclei, MAGIX is suitable for a wide range of innovative experiments:

- In elastic electron-proton scattering, high precision measurements of the magnetic and electric form factors in the low Q^2 range are foreseen.
- Measurements of astrophysical relevance, like the stellar nucleosynthesis $^{12}\mathrm{C}\,(\alpha,\gamma)\,^{16}\mathrm{O}$ reaction. This can be realized by measuring the electro-disintegration reaction $^{16}\mathrm{O}\,(e,e'\alpha)\,^{12}\mathrm{C}$.
- High precision measurements of electron scattering on few-nucleon systems allow a systematic study of new aspects of few-body physics.
- Searches for dark photons in the low mass region are foreseen. In electron scattering off a heavy target nucleus, dark photons could be produced radiatively, decaying into electron pairs and being detected by the MAGIX spectrometers.

2.2.2. Extracted beam (EB) mode

After three circulations in the EB mode, the beam is guided to the P2 experiment. The electrons reach an energy of up to 155 MeV and a beam current of 150 µA. Since this mode is also of great relevance for DarkMESA, the P2 experiment is discussed in more detail.

P2 - A parity-violating electron scattering experiment

The goal of P2 is a high precision measurement of the weak charge of the proton $Q_{\mathrm{W}}(p)$ at $Q^2 = 4.5 \times 10^{-3}\,\mathrm{GeV}^2$ [81]. This value can be determined by looking at the parity violating elastic electron-proton scattering at a low momentum transfer.
In the unification of the weak with the electromagnetic interaction, both mix with a proportion given by the electro-weak mixing angle, also known as Weinberg-angle Θ_{W}. The mediators of the weak interaction are the W^+, W^-, and Z^0 gauge bosons. Their mass values were determined experimentally [82–84] and the today's world average [85] is:

$$m_{\mathrm{W}} = 80.379 \quad \pm\ 0.012 \quad \mathrm{GeV} \tag{2.3}$$

$$m_{\mathrm{Z}} = 91.1876 \ \pm\ 0.0021\,\mathrm{GeV} \quad . \tag{2.4}$$

The calculations in [86] show that:

$$\sin^2(\Theta_{\mathrm{W}}) = 1 - \frac{m_{\mathrm{W}}^2}{m_{\mathrm{Z}}^2} \approx 0.223 \quad . \tag{2.5}$$

This value corresponds to the lowest order of perturbation theory and it also depends on the energy scale and the renormalization scheme ($\mu = \sqrt{|Q^2|}$). The Weinberg-angle is connected with the weak charge of the proton and without radiative corrections the following formula is given:

$$Q_{\mathrm{W}}(p) = 1 - 4\sin^2(\Theta_{\mathrm{W}}) \quad . \tag{2.6}$$

For the determination of the electro-weak mixing angle the relative precision at P2 will be $\sim 0.14\,\%$. This is 10 times better than for the weak charge:

$$\frac{\Delta \sin^2(\Theta_\mathrm{W})}{\sin^2(\Theta_\mathrm{W})} = \frac{1-4\sin^2(\Theta_\mathrm{W})}{4\sin^2(\Theta_\mathrm{W})} \cdot \frac{\Delta Q_\mathrm{W}(p)}{Q_\mathrm{W}(p)} \approx 0.1 \cdot \frac{\Delta Q_\mathrm{W}(p)}{Q_\mathrm{W}(p)} \quad . \tag{2.7}$$

The corrections for $\sin^2(\Theta_\mathrm{W})$ have to be considered accurately, especially because of the impact for $Q_\mathrm{W}(p)$. For the desired precision, a maximum statistical uncertainty in the order of 10^{-9} is allowed. This uncertainty can be reached with a total of

$$N = \frac{1}{[\mathcal{O}(10^{-9})]^2} = \mathcal{O}(10^{18}) \quad , \tag{2.8}$$

elastic scattering events. The measurement time is planned to be around 20 000 h. To reach the necessary number of events in the given time, a sufficient high beam current and a long target are needed. An overview of the experimental setup can be seen in Fig. 2.7 and the main components are explained in the following.

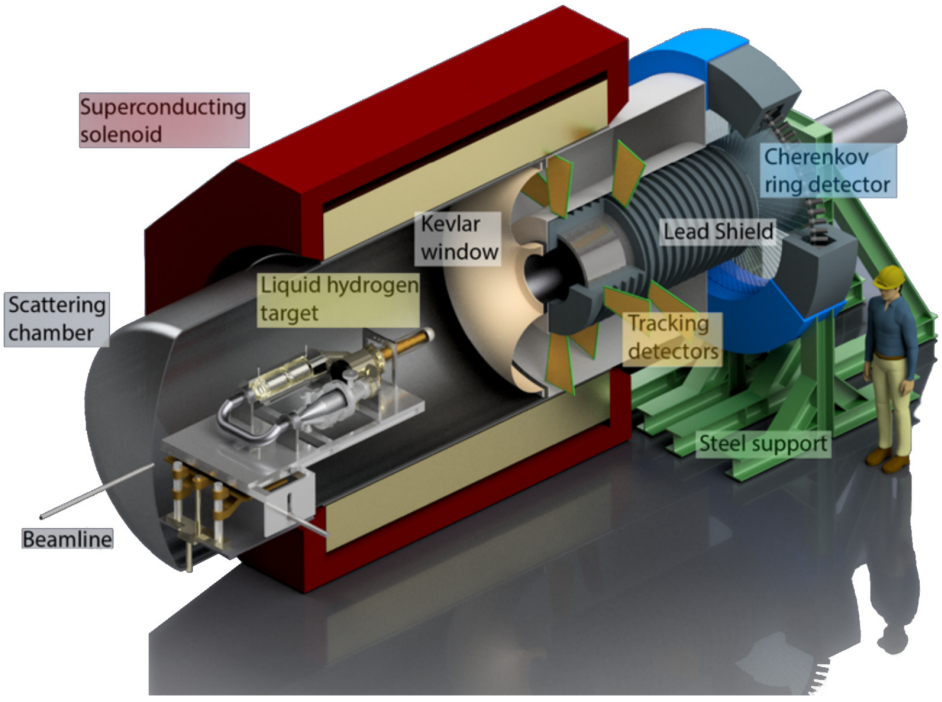

Figure 2.7.: Overview of the P2 experiment: Inside of the scattering chamber a liquid hydrogen ($l\mathrm{H}_2$) target is placed. The trajectories of the scattered electrons are identified with the tracking detectors at lower beam current and the energy deposit is measured in the Cherenkov ring detector. For the distinction of the particle origin the magnetic field of the solenoid and the tracking detectors are needed. Figure adapted from [81].

The beam current delivered from MESA will be 150 µA (compared to $I_\mathrm{max} \approx 20\,\mu\mathrm{A}$ for polarized electrons at MAMI) and it was decided to use an in-beam direction 600 mm long liquid hydrogen ($l\mathrm{H}_2$) target (yellow in Fig. 2.7), which corresponds to the design of the target cell of the G0 experiment [87]. Thereof the estimated P2 luminosity is

$$L_\mathrm{P2} = \frac{I_\mathrm{beam}}{e} \frac{\rho_\mathrm{target}}{m_\mathrm{p}} l_\mathrm{target} = 2.38 \times 10^{39}\,\mathrm{cm}^{-2}\,\mathrm{s}^{-1} \quad , \tag{2.9}$$

where I_{beam} is the MESA beam current, e the elementary charge, ρ_{target} the density of the $l\text{H}_2$ target, m_{p} the proton mass, and l_{target} the target length. This implies a high rate of elastic scattering events in the $l\text{H}_2$ target. The detection of single events would only be possible with a very high segmentation of the detector ($\mathcal{O}(10^4)$), which requires a lot of effort and is associated with high costs. Therefore the setup is simplified by using an integrated measurement. This is possible by using 82 Cherenkov detectors arranged in a cylindrical circle (blue in Fig. 2.7). For the radiator material a high light output and an outstanding radiation hardness are the main criteria. Spectrosil 2000 [88] fulfills those requirements. The spatial separation of the elastic electron-electron scattering events and the elastic electron-proton scattering events is possible with a magnetic field, since the energies of the final states strongly differ, even for relatively small angles (Fig. 2.8).

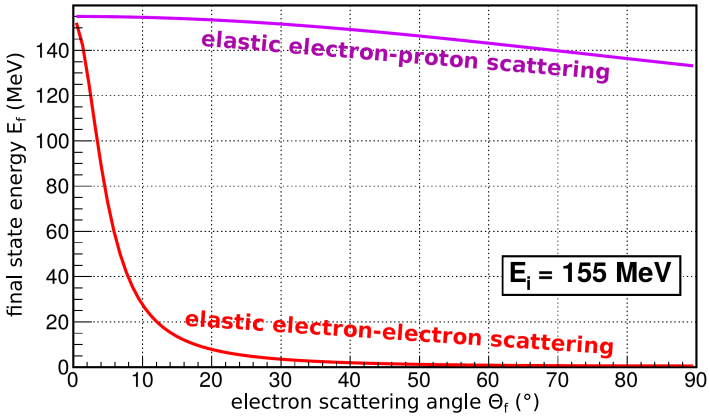

Figure 2.8.: Final state energies (E_{f}) of the elastic electron-proton and electron-electron scattering depending on the electron scattering angle (Θ_{f}). Figure adapted from [86].

The magnetic field also serves for focusing the electrons from the elastic electron-proton scattering to the Cherenkov detectors and offers the advantage of discrimination between photons from Bremsstrahlung in the target and final state electrons from elastic electron-proton scattering. In the P2 concept a superconducting solenoid was chosen (red in Fig. 2.7), where a 180° spin flip can be obtained by reverting the current. The solenoid covers a larger range of azimuth angles than a toroid and reduces the measurement time. Thus the eventually occurring polarization of the $l\text{H}_2$ target has to be taken into account when determining $Q_{\text{W}}(p)$. For the determination of the Q^2-distribution the exact knowledge of the particle trajectories inside of the magnetic field is needed. Inside of a helium filled chamber these are measured with tracking detectors (orange in Fig. 2.7) at a reduced beam current. Therefore the four independent module systems based on high voltage monolithic active pixel sensors (HV-MAPS) [89] are used in coincidence with the Cherenkov detectors. The lead shield protects the Cherenkov detectors from photons coming from the target.

Because of the accuracy P2 aims for, the beam of polarized electrons has to be monitored carefully. Three independent measurements of the polarization can be performed with a double Mott polarimeter at 100 keV and a single Mott polarimeter at 5 MeV for long time stability measurements, and a Hydro-Møller polarimeter close to the P2 experiment with online capabilities [90]. Each has an accuracy better than $\Delta P/P = 0.01$. Due to the flip of the electrons polarization with a frequency of 1 kHz, an active beam position stabilization is needed. A system of logging

and active corrections with analog feedback loops like in the A4 experiment [91] or an online measurement of helicity correlations for all parameters, a so-called feed-forward suppression, are possible. The helicity correlates with the six beam parameters, position (x, y), angle (x', y'), intensity or beam current (I), and beam energy (E), at the target. The fluctuations in these parameters contribute to the apparative asymmetry A^{app}, which should be kept small. MESA is planning a 210° return-arc followed by the 2.5 m long Hydro-Møller polarimeter. A 10 m section between the Hydro-Møller and the P2 target is reserved for the beam stabilization and other diagnostic tools.

The parameters can be monitored and stabilized with cavity beam monitors. With a beam current monitor (BCM) the beam intensity and phase are measured, one beam position monitor (BPM) measures the position (x, y) and in combination with a second BPM also the angles (x', y') can be determined. The beam energy is measured with two beam phase cavity monitors, which are placed before and after the deflecting magnet of the return-arc, where the longitudinal dispersion is at a maximum. The time difference of two electrons with different energies and therefore deviating trajectories can be determined. The time difference can be monitored and minimized by the accelerator crew to stabilize the beam energy. This is a critical parameter, because a helicity correlated change of 1 eV at MESA has a 23 % effect at P2. For a relative energy change of 10^{-5} a change in the path length of 0.1 mm can be routinely achieved. This corresponds to a RF phase difference of 0.14°, which has to be detected in a 0.5 ms helicity window. This is doable and the uncertainty does not exceed the maximum value of $\Delta A^{\text{app}} = 0.1$ ppb [81].

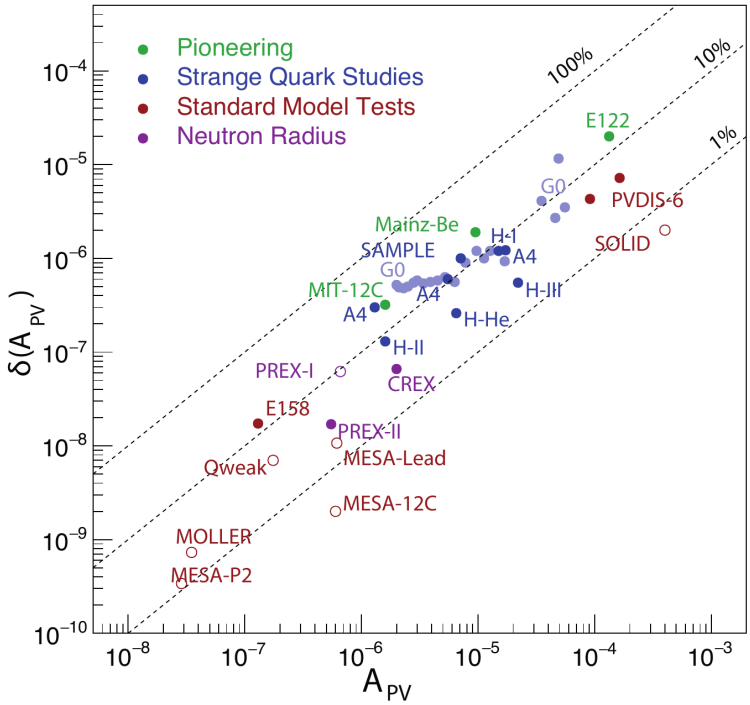

Figure 2.9.: Shown is the absolute amount of the parity violating asymmetry A_{PV} and its precision $\delta(A_{\text{PV}})$ for various electron scattering experiments. The solid points mark the values of past experiments and the blank circles the predicted values of future experiments. MESA-P2 marks the P2 experiment with the 600 mm $l\text{H}_2$ target and MESA-12C the P2 setup with a ^{12}C target [92]. The predicted value for MESA-P2 is -39.94×10^{-9} with 1.4 % precision, the smallest asymmetry measured by now. For detailed information about the other experiments see [93–104]. Figure from [81].

When looking at the absolute amount of the parity violating asymmetry

$$A_{\mathrm{PV}} = \frac{\sigma_+ - \sigma_-}{\sigma_+ + \sigma_-} \quad , \tag{2.10}$$

and its precision $\delta(A_{\mathrm{PV}})$ compared to other experiments (Fig. 2.9), the predicted value for P2 with the $l\mathrm{H}_2$ target is -39.94×10^{-9} with 1.4 % precision and the smallest asymmetry measured by now. For the electro-weak mixing angle, this means that the measurement of P2 is located in an energy range where such a high precision has not been achieved so far (Fig. 2.10).

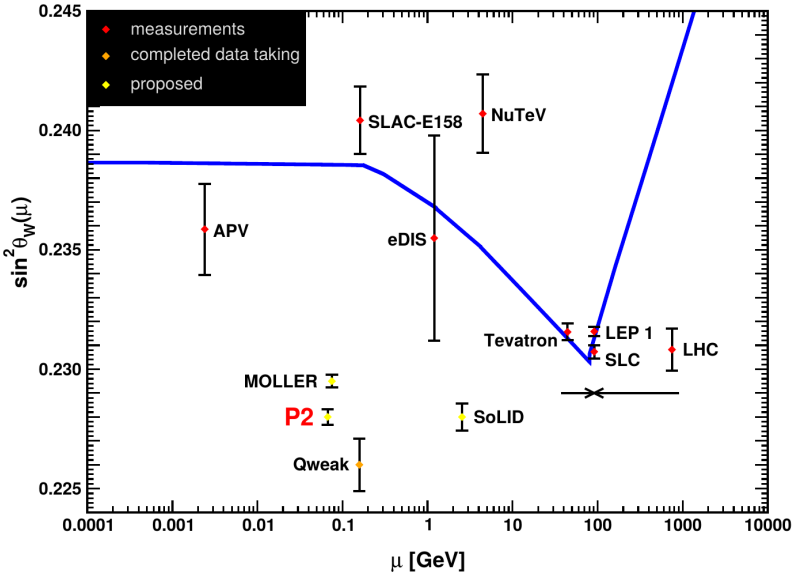

Figure 2.10.: The electro-weak mixing angle in dependence from the energy scale $\mu = \sqrt{|Q^2|}$ is shown. The blue curve shows the behavior in the $\overline{MS}$-renormalization scheme. The red marks show the concluded experiments and their error bars. On the low energy scale the error bars are relatively high compared to the Tevatron, LEP1, and SLC results. The P2 experiment will contribute with a high precision measurement at lower energies. For the experiments that are not yet completed, the position on the y-axis is arbitrary. Figure from [81].

Only a small part of the beam electrons are scattered in the target so that the P2 experiment can detect them. The majority leaves the experiment via a beam-exit-pipe and has to be stopped in a beam-dump.

The P2 beam-dump

Since the P2 beam-dump is essential for the DarkMESA experiment, it is discussed in detail, with some physical properties relevant to other parts of this thesis. This beam-dump was already used in the A4 experiment and thus designed for higher electron beam energies than expected for P2. It is therefore able to stop almost all MESA beam electrons at an early stage in the beam-dump. Its structure is shown in Fig. 2.11. Particles leaving the P2 target in the direction of the beam-dump pass through about 12 m of vacuum before reaching the beam-dump. The jacket of the beam-dump consists of an aluminum magnesium alloy (AlMg_3). A pipe system is used to pump water into the front part for cooling. The pipe is constructed in such a way that the water jet at an angle of 30° is directed to the center of the front surface, where most of the particles are

expected. This first hemisphere is almost completely filled with water, which is separated by a perforated metal plate from the cylindrical part of the beam-dump filled with aluminum pellets. The cooling water can now flow through the perforated plate, but vice versa the aluminum pellets cannot reach the front part. The cooling water flows around the entire aluminum filling and leaves the beam-dump through the rear tube which is again separated from the tube volume by a perforated plate. Two copper plates with a total thickness of 117 mm, one of which is completely and the other partially within the $AlMg_3$ coating, complete the beam-dump.

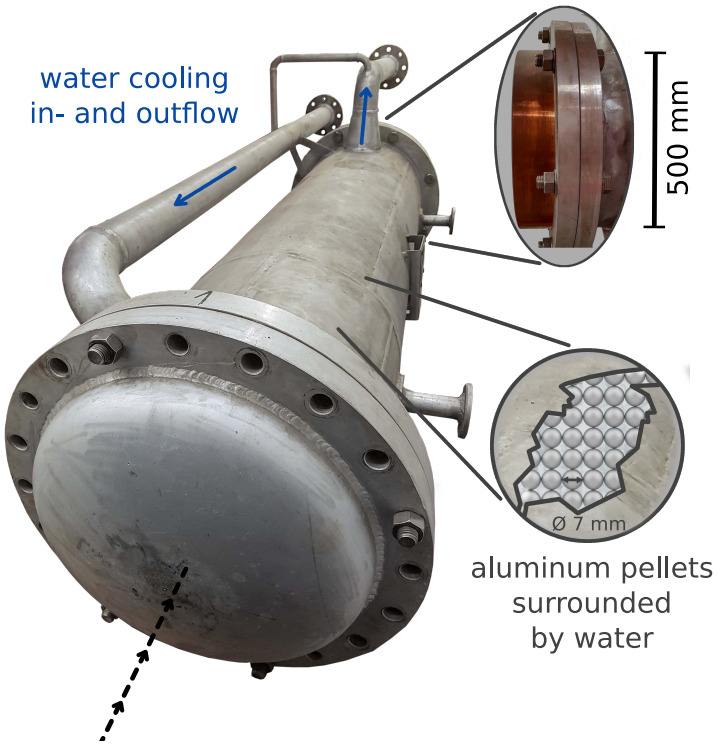

Figure 2.11.: Picture of the A4 beam-dump that is used in the P2 experiment. The jacket made of $AlMg_3$ is filled with aluminum pellets and water is pressed through it for cooling. The beam-dump has a total length of 2.1 m with a copper block at the rear end.

In the following, the total radiation length has to be determined first. Due to a lack of information regarding the mass of the aluminum pellets, a maximum filling was assumed, which corresponds to the densest close-packing of equal spheres of 74 %. The other 26 % is assumed to be water. The physical properties in Tab. C.1 of Appx. C.1 were used to determine the total radiation length of the P2 beam-dump in Tab. 2.2.

	material	**length (mm)**	**radiation length (X_0)**
coating	$AlMg_3$	65	0.71
water	H_2O	133	0.37
tube	74 % Al/ 26 % H_2O	1787	16.15
copper plates	Cu	117	8.14
$\sum$			25.37

Table 2.2.: Total radiation length of the P2 beam-dump for particles, which cross the beam-dump exactly in the middle along the z-axis.

For simplification only the radiation length for particles that pass through the beam-dump exactly in the middle is calculated. This is appropriate because the curvature of the front surface and the water inflow pipe lead only to slight fluctuations. In Tab. 2.2, summarized under the item "coating" are all traversed $AlMg_3$ areas. This are 12 mm at the entry and 35 mm immediately in front of the copper plates, plus the 8 mm perforated plate and parts of the inflow water pipe with a wall thickness of 5 mm. Together with the water, the aluminum pellets rushed around by water and the copper plates, the total radiation length is $25.37\,X_0$.

This P2 beam-dump in combination with the stable beam conditions and the long measurement time allows DarkMESA to use it for a parasitic dark sector experiment.

2.2.3. DarkMESA – A beam-dump experiment

The third experiment at MESA is DarkMESA, the topic of this thesis, and a very brief introduction is given here. After more aspects of the experiment have been elaborated in this thesis, a detailed discussion follows in Chap. 6. DarkMESA is positioned on the beam-axis of the P2 experiment in a separate room outside the accelerator hall. The P2 beam-dump described in Sec. 2.2.2 can be regarded as the target of this experiment – a source for DM particles.
The assumption is that LDM interacts with the SM through a (massive) dark photon γ' coupling with strength ε. For the generation of these DM particles, a simple theory of dark Bremsstrahlung can be used first. In this theory a dark photon γ' could be produced in a process analog to electromagnetic Bremsstrahlung in the beam-dump. The dark photon can then decay invisibly into a pair of DM particles $\chi\overline{\chi}$ (Fig. 2.12 a). The coupling between dark photon and DM is described by the dark fine structure constant α_D.

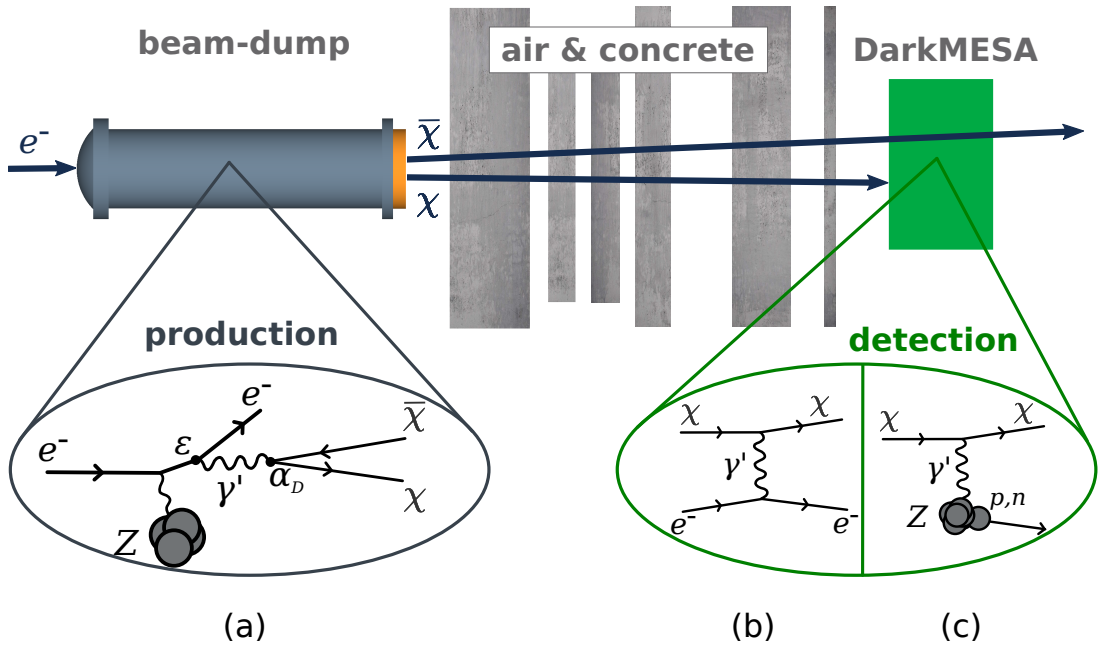

Figure 2.12.: Schematic (not to scale) overview of the beam path including the Feynman graphs for production and detection. Feynman graph of the dark photon γ' production in a dark Bremsstrahlung process and following decay into DM particles $\chi\overline{\chi}$ in the beam-dump (a). Feynman graph for the detection possibilities of electron recoil (b) and nucleon recoil (c) in a DarkMESA detector.

Between the beam-dump and the DarkMESA detector location there are about 15 m of air and a total of 8.15 m of concrete. Due to the low interaction probability, the DM particles can pass through air and concrete undisturbed, while all other SM particles are stopped. A fraction of this DM particles could then scatter off electrons or nucleons in the DarkMESA detector. These recoil particles could then be detected. Depending on the detection principle, electron recoil (Fig. 2.12 b) or nucleon recoil (Fig. 2.12 c) is possible.

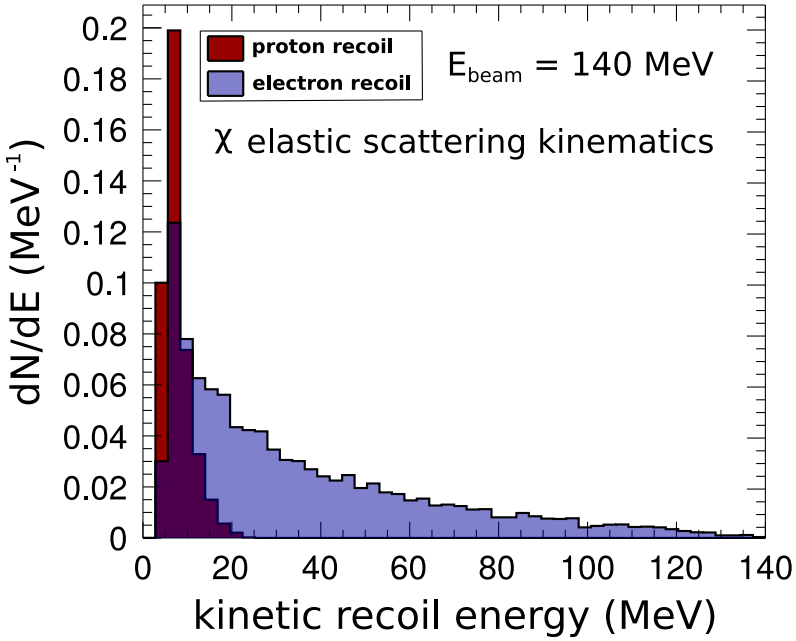

Figure 2.13.: Expected kinetic energy distribution of the recoil particles for proton or electron recoil. This simplified simulation assumed a primary energy of 140 MeV. The energy loss in the P2 target is already taken into account.

In Fig. 2.13 a simple simulation study shows the kinetic energy distribution of recoil particles for both cases. For proton recoil a sharp peak at about 10 MeV is predicted, whereas for electron recoil a much broader spectrum is expected. A detection threshold has to be assumed, below which the recoil of DM events is no longer detectable. At the beginning of this studies, the threshold value was not known. It was decided to develop a detector concept that measures the electron recoil, since for same threshold significantly more events would be lost with proton recoil. The use of a traditional calorimeter, which can measure the deposited energy, seems to be the natural choice. The initial experience of the Beam Dump Experiment (BDX) at JLab was also used as a first step [105].

Based on this considerations, a suitable concept for the DarkMESA experiment is now developed in this work. A constraint is the limited amount of space (12 m^2 floor space) in the dedicated DarkMESA room. Since the total number of scattering centers in the detector is decisive for the detection probability of DM events, materials of high density must be preferred. Based on simulation and material studies, a detector is developed which can make a significant contribution to the search for DM. For this purpose, the overall concept is optimized on both the production side (MESA, P2, beam-dump) and the detection side (DarkMESA DM detector). All beam-related and beam-unrelated backgrounds have to be considered and reduced as much as possible. The parasitic location to P2 gives DarkMESA the big advantage, that measurements with and

without the DM beam are possible without relocation or modifications of DarkMESA. The beam-off periods of P2 can be used to study beam-unrelated backgrounds. Thus, data can be collected almost continuously without relying on beam schedules.

In the following Chap. 3, the basics of the DarkMESA simulation are presented before the results of material studies follow in Chap. 5. Based on these results, a stage-like DarkMESA detector concept is presented in Chap. 6. This concept is completed by background studies in Chap. 7 and the reachable exclusion limits in Chap. 8.

3. The DarkMESA simulation framework

After the remarks at the end of Chap. 2 about the possibility of a dark sector experiment behind the P2 beam-dump, the possible concepts need to be investigated further. Instead of directly realizing the concepts experimentally, a simulation framework based on `MadGraph` [106] and `Geant4` [107–109] was developed. In particular, the simulation should provide information on whether this experiment can make a significant contribution to the search for LDM.
The chapter starts with a general discussion of the simulation tools used, with reference to the processes in the subsequent DarkMESA simulation. Since several physical aspects related to DarkMESA are investigated in the simulation, these parts of the simulation can be controlled individually. An user who is performing simulation studies, can control the basic components of the simulation via a so-called *steering file*, without having to recompile the code. This steering file is reduced to the most necessary and useful settings, but can be expanded by the user optionally. The use and content of this file is introduced in Sec. 3.2. After that, the simulation is discussed in more detail. The processes in the simulation for the most important cases are presented in the Secs. 3.3 to 4. It should be noted that the results of the simulation studies are not yet covered in this chapter.

3.1. Simulation tools

For the simulations to be carried out, two tools are mainly used. The `MadGraph` event generator handles the production of dark photons in the beam-dump and their decay into DM particles. However, most of the simulation is carried out within the `Geant4` environment, for tracking particles through matter. Both make use of `ROOT`, a framework for data analysis. The scope and purpose of `MadGraph` and `Geant4` are described in more detail below.

3.1.1. MadGraph

`MadGraph/MadEvent` in version 4.4.17 [106, 110] is a Monte Carlo (MC) event generator and is used to simulate physical processes. Existing or new hypothetical physics models can be used. The simulation and event generation is performed on parton level and additional program codes can extend this processes up to the level of detector interactions. The core processes compute the tree-level and next-to-leading order cross-sections on parton level. The programs full name is `MadGraph5_aMC@NLO` and is written in `FORTRAN`. The final events are obtained in the Les Houches Event (LHE) format [111]. A full discussion of `MadGraph`'s capabilities is omitted here. Only the components needed for the simulations in this thesis are presented in Sec. 3.5.3.

3.1.2. Geant4

Geant4 is a simulation tool developed at CERN and released for the first time in 1998. Geant stands for geometry and tracking. The software is used in many research areas and is regularly developed further and maintained by the Geant4 Collaboration. Now available is version 11.0 (first released 10 December 2021), but in this work version 10.4 (first released 8 December 2017) has been used. The tool is based on the object-oriented programming language C++. The user is also provided with program examples for a wide variety of application cases, which can serve as a starting point for own simulations.
Geant4 enables the user to simulate any particle (leptons, mesons, baryons, ions, quarks, messenger particles, but also user-defined particles) or whole particle showers in a wide energy range. Any place within a predefined world volume can be set as the starting point of the particle trajectory. In addition, the particle can also be given a momentum or a fixed time, for example. The user sets the entire geometry (detailed or simplified) in the world volume, including the corresponding materials and their properties. In a physics list all processes for the particle interactions are defined. Depending on the use case, high or low energy physics for example, a different list may be more appropriate. The user can select a predefined physics list or create an own list. Now the particles can be tracked through the entire world volume and the data of sensitive detector parts can be stored in a desired file format. Since it is C++ code, analysis routines or cut values can be programmed directly where it is needed.
The whole process can be started in a graphical environment, where all geometries and tracks are displayed. This is suitable for a still manageable number of particles and for debugging. Tracking can take a particularly long time, if optical properties of materials are considered or when a large number of high energy particles has to be tracked through several components. For the Eljen EJ-200 scintillators used in this work, for example, the scintillation yield is in the order of 10 000 optical photons for a 1 MeV electron [112]. In that case the track of each optical photon through the media (reflections and refractions) is traced until it is absorbed or interrupted by some condition programmed by the user. Here, the graphical environment is only useful for individual primary particles, but not for a high number of tracks. A pure terminal input and output is available for these computationally intense simulations. For the Geant4 installation procedure and when building own programs or existing examples, there are differences depending on the operating system and compiler used. Please refer to the "Geant4 Installation Guide" [113] and the "Geant4 User's Guide for Application Developers" [114].[1]

The basic structure of a Geant4 simulation is always the same. For a better understanding of the structure even for the less experienced user, please refer to Appx. A.1. In addition to the basic structure, the placement of geometries and the tracking process are discussed there using a simple example. For the more experienced user, the specifics of the DarkMESA simulation are discussed directly.

[1] For the default Debian GNU/Linux installation used in the MAGIX-DarkMESA working group, a guide for installation and usage of this simulation package is attached in Appx. A.2.

3.2. The steering file

The DarkMESA simulation is a `Geant4` simulation that can cover different physics applications. In order to give the user the possibility to call the part of the simulation that is currently needed and also to set parameters without having to recompile the code, a so-called "steering file" has been developed, which is read at the beginning of a simulation. First the functionality of this file and its integration into the overall simulation is presented. Later in this chapter, different applications of the simulation are shown without presenting the simulation results.

The steering file allows the user to change important parameters of the simulation quickly and with no need to recompile the code. When executing the simulation, an additional argument that specifies the steering file to be used (here: `steering.xml`) is provided. The file layout is made in such a way that the value of each variable is between a start and an end tag. These are uniformly structured in a `<variableName>value</variableName>` form. In addition, the variables are sorted by application category and provided with comments. The value of the variable can be of the data types `G4String`, `G4double`, `G4int`, or `G4bool`. In order to read them correctly, the simulation was extended by the files `BDXSteering.cc/.hh`. In these files, there is the member function `LoadSteering()`, which controls the reading of the data into the corresponding variables. To do this, the `steering.xml` file is read into a `std::stringstream buffer` and searched for the corresponding tags. There is a `createSteeringDataType()` function for each data type. The function `get_str_between_two_str()` used in it returns a `G4String` that has to be converted according to the desired data type. As an example, the function to read an integer variable is shown here:

```
G4int BDXSteering::createSteeringInt(G4String input, G4String name) {
  G4String start_delim = "<"+name+">";
  G4String stop_delim = "</"+name+">";

  G4String value = get_str_between_two_str(input, start_delim, stop_delim);

  return atoi(value.c_str());
}
```

All variables are generated as public variables (`G4DataType variable;`) and in `LoadSteering()` they are read in sequence.

```
variable = createSteeringDataType(buffer.str(), "variable");
```

The `LoadSteering()` function has to be called once at the beginning of `main.cc`. After that, all variables from the steering file are available to the simulation. The value of a variable can now be called in the simulation using

```
(BDXSteering*) fSteering->variable   .
```

This type of programming allows the less experienced user to run simulations without the need to change the program code. In addition, even without extensive programming knowledge, further variables of the simulation can be set via the steering file easily. A complete list of the variables that are set in this steering file is not given here. If necessary, the parameters are explained

when needed. At the moment the file comprises more than 180 parameters. Although these are all commented, it can be confusing for the inexperienced user. For this reason, the following procedure is suggested. If one parameter has been proven to be optimal during the execution and analysis of simulation parts, the parameter should be set with an initial value at the beginning of `LoadSteering()`. Thus a simplified and an extended steering file can be made available to the user. In addition, example steering files for the main use cases are provided.

Before individual parts of the simulation are presented, it is now necessary to show how these different parts can be reached. The two variables `primaryType` and `primaryPos` are essential for this. They determine which primary particles are generated at which location inside of the world volume. As in the example in Appx. A.1, a simple `G4ParticleGun` is used. Particle type, momentum direction, energy, and position are set with the steering file. It is also possible to read all the parameters line by line from an external list. These two modes seem to be sufficient. However, since different objectives of the simulation also require access to different simulation components, it has shown that it makes sense to have a larger variety of generator types and generator positions to choose from. The most important of these are the following:

Main primary generator types

- **Free choice** of particle type, energy, and momentum,
- **DM particles** $\chi\overline{\chi}$ from four-vector list generated with `MadGraph`,
- **recoil electrons** from four-vector list generated with the $\chi\overline{\chi}$ run in `Geant4`,
- **cosmic-ray particles** generated with the cosmic-ray shower library (CRY).

Main primary generator positions

- **Free choice** of position,
- 5 mm in front of **P2 target**,
- one X_0 in **beam-dump**,
- at beginning of **DarkMESA detectors**,
- **cosmic-ray layer** above DarkMESA,
- **beam-time positions**,
- **random or central** in detector crystal,
- **screening** of scintillator modules.

The simulation excludes unreasonable combinations of type and position. In this case an error message is displayed to the user. These two variables can be used to access the basic parts of the simulation presented in the following Secs. 3.3 to 3.5. They do not only determine the particle generation in the `PrimaryGeneratorAction()`, but frequently decide about the running of processes in the `RunAction()`, `EventAction()`, and `SteppingAction()`.

3.3. Light output simulation of detector prototypes

Right at the beginning of the DarkMESA project the question of suitable detector materials came up. Since only limited space is available for DarkMESA, optical materials with high density were considered: the higher the material density, the better the detection probability per volume.

The chosen materials – PbF_2, $Bi_4Ge_3O_{12}$ (BGO), and the PbGl types SF5, SF6, and SF57HTU from Schott – were studied during two beam-times at MAMI in July and December 2018 with a 14 MeV electron beam, see Chap. 5. The experimental results obtained should be compared with a simulation study.
For this study, optical processes are included in the simulation. First these processes are registered in a physics list, see Appx. A.3.1. Energy deposition in an optical material for which additional optical properties have been defined is accompanied by the generation of optical photons. Their path through the simulation environment is fully simulated using the defined processes. The most important processes are the reflection and refraction at boundaries, the absorption in the material, and the Rayleigh scattering on sufficiently small and distant particles.

Primary generator. Since this simulation is based on the real conditions at the 14 MeV MAMI experimental site, energy and particle type (14.86 MeV electrons) are fixed.[2] The starting point of the beam is assumed to be almost point-like. The angle between the electron beam and the detector can be adjusted to simulate a lateral impact. With a given beam-time date and detector type, the correct positions are chosen from a database. The gun position, 10 mm in front of the flange, and the momentum direction are dynamically calculated and set according to the lateral angle of impact with a function in the `PrimaryGeneratorAction()` file.

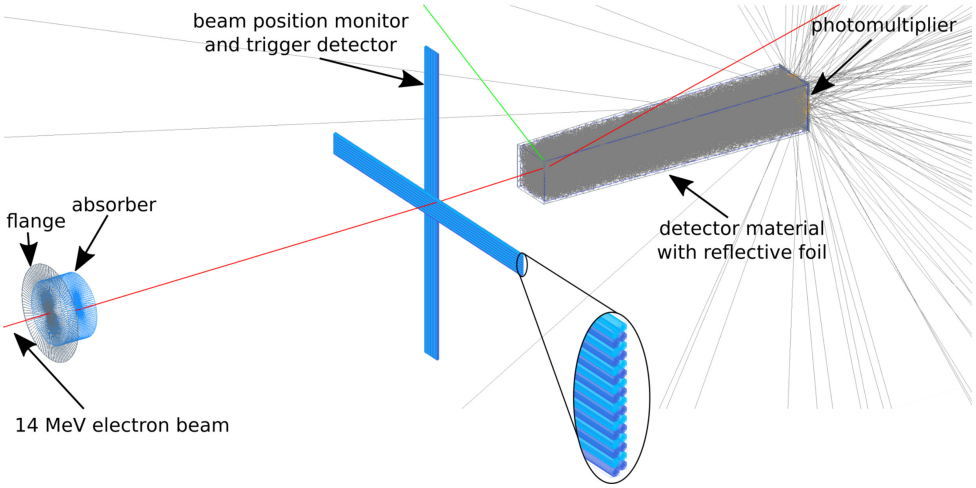

Figure 3.1.: `Geant4` construction layout of the 14 MeV MAMI beam-time simulation. The visualization of all trajectories due to a single 14 MeV beam electron is shown. Electrons (red), gamma rays (green), and optical photons (grey) are shown. The layers of one fiber bundle are shown enlarged.

Geometries and placement. The detector material is surrounded by a thin layer of air and a reflective aluminum foil. An exception is only the frontal surface of the photomultiplier tube (PMT), which connects directly to the detector material. Optionally, a fiber detector, used as a trigger and beam position monitor, the 200 µm thick aluminum flange at the end of the beam pipe, and absorber plates for energy reduction behind the flange can be switched on. The necessary physical volumes can be seen in Fig. 3.1. Flange and absorber are simple geometric shapes – `G4Tubs()` were chosen. These can be switched on and off via the steering file and the absorber thickness can be varied. Another useful `Geant4` function is used for the fiber detector.

[2] This part of the simulation can be accessed by choosing `primaryType = 4` (14 MeV electrons) and `primaryPos = 4` (beam-time position).

It should consist of horizontally and vertically running fiber bundles. Each bundle consists of two layers of 16 fibers each. The fibers themselves are again created from `G4Tubs()`, but not every fiber is placed individually. The logical volume of a single fiber is created – position and rotation are not included, physical volumes are required for each fiber layer. The two layers of a fiber bundle are created as `G4Trd()`. The physical volumes are generated according to the position and orientation of the fiber bundle. Since the fiber layers in a bundle are supposed to mesh, the physical volumes also overlap. These four volumes serve as the mother volume of the fibers. The fibers are generated in these volumes in the desired number as `G4PVReplica()`.

```
...
G4Tubs* solidFiberSingle =
  new G4Tubs("Fiber", 0.*mm, rFiber, lFiber, 0.*deg, 360.*deg);
G4LogicalVolume* logicFiberSingle =
  new G4LogicalVolume(solidFiberSingle,          //its solid
                      fiber,                     //its material
                      "Fiber");                  //its name

G4Trd* solidFiberReplicaMotherX =
  new G4Trd("FiberMother", 16*rFiber, 16*rFiber, rFiber, rFiber, lFiber);
G4LogicalVolume* logicFiberReplicaMotherX1 =
  new G4LogicalVolume(solidFiberReplicaMotherX,  //its solid
                      air,                       //its material
                      "LayerX1");                //its name
  new G4PVPlacement(rotationFiberX,              //rotation
                    posFiberSingleX1,            //at position
                    logicFiberReplicaMotherX1,   //its logical volume
                    "LayerX1",                   //its name
                    logicEnv,                    //its mother volume
                    false,                       //no boolean operation
                    0,                           //copy number
                    checkOverlaps);              //overlaps checking

G4VPhysicalVolume* FiberX1 =
  new G4PVReplica("FiberX1",                     //its name
                  logicFiberSingle,              //its logical volume
                  logicFiberReplicaMotherX1,     //its mother volume
                  kXAxis,                        //replica axis
                  16,                            //number of replicas
                  rFiber*2,                      //width
                  0);                            //offset
...
```

For the construction of the detector made of the respective material, a thin air layer, a 20 µm reflective foil, and a PMT, the boolean `G4SubtractionSolid()` class is helpful. This allows to subtract geometric shapes from each other. The solid detector material (`solidDarkMESADetector`) and a simplified PMT (`solidDarkMESADetectorPMT`) are created. The PMT is only simulated as a 2 mm thick circular disc. The material choice corresponds to the front glass of the PMT. This allows to simulate the optical transition from the detector material to the PMT.[3] The photocathode itself is not placed as a geometric element. Their function is mathematically included in the simulation. For the surrounding air volume one creates the same geometric shape as for the detector material with slightly larger dimensions (`solidReflectiveFoilAir`), corresponding to the air layer thickness of 1 mm and the same for the reflective foil (`solidReflectiveFoilTmp`).

[3] The optical grease lying between detector and PMT is omitted here, since the optical properties are very similar.

Then `solidReflectiveFoilAir` is subtracted from `solidReflectiveFoilTmp`:

```
G4VSolid* solidReflectiveFoilTmp2 =
  new G4SubtractionSolid("ReflectiveFoilTmp2",        //its name
                         solidReflectiveFoilTmp,      //solid A
                         solidReflectiveFoilAir,      //solid B
                         0,                           //rotation
                         G4ThreeVector(0.,0.,0.));    //trans vector
```

To finalize the reflective foil (`solidReflectiveFoil`), the PMT element is subtracted from `solidReflectiveFoilTmp2`. There the displacement of the two elements has to be taken into account. At the end one has to place only the `solidDarkMESADetector`, the `solidDarkMESAPMT`, and the `solidReflectiveFoil` in the world volume.[4]
When placing the elements it is necessary to consider the optional mode of a lateral impact. In the simulation the detector always remains fixed and the axis consisting of beam, flange, absorber, and fiber detector can be rotated around the detector. This axis can be shifted in two additional dimensions and the intersection with the detector can be chosen exactly (Fig.3.2).

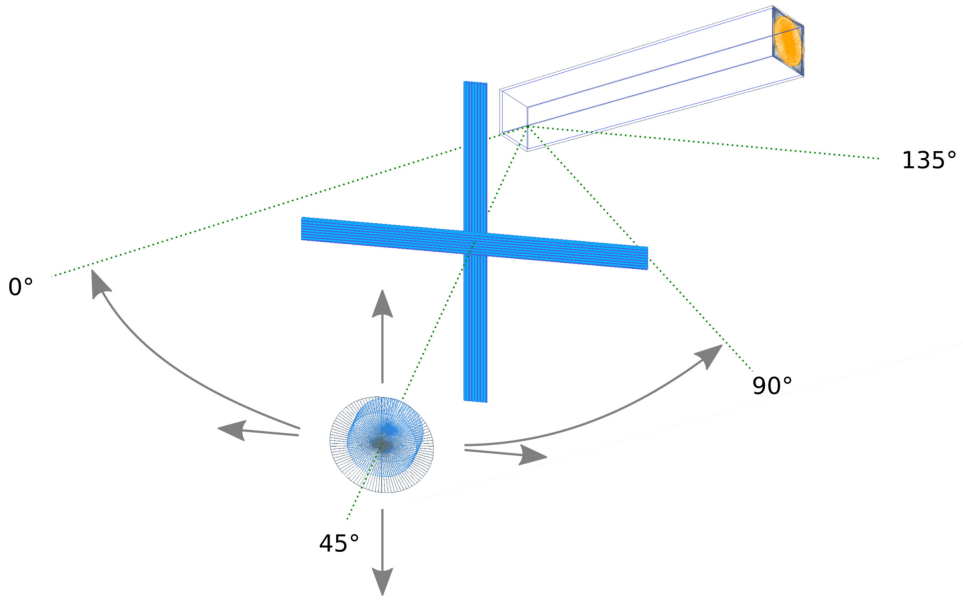

Figure 3.2.: Realization of the lateral impact mode. The beam-axis with flange, absorber, and fiber detector can be rotated around the fixed detector. With two additional directions of movement, the beam-axis can be aligned to any point of the detector side surfaces.

Optical processes. Additional optical properties must be assigned to all relevant materials. For each material a `G4MaterialPropertiesTable()` is created first. Properties can then be assigned to this table. These can be individual constants, but also wavelength- or energy-dependent distributions. For each material (`G4Material* material`) one has to assign at least a refractive index spectrum (`"RINDEX"`) and an attenuation length spectrum (`"ABSLENGTH"`).[5]
For most materials in this study, these parameters are largely sufficient. An exception is the detector material BGO. Unlike the Cerenkov detector materials, BGO is a scintillating material. Therefore, scintillation properties must be included. This includes at least a `"FASTCOMPONENT"`

[4] Since, the world volume material is air, it is not necessary to place the air layer. It was also dispensed with packing the detectors in black foil, as no unwanted light sources are present in the simulation.
[5] If the attenuation length spectrum is not provided by the user, the values are set to infinity automatically.

spectrum, which describes the wavelength-dependent scintillation intensity, as well as the decay time (`"FASTTIMECONSTANT"`) and the scintillation light yield (`"SCINTILLATIONYIELD"`). For BGO this is implemented as follows.[6]

```
// Setting optical material properties for BGO
myMPT = new G4MaterialPropertiesTable();

const G4int nEntries = 7;
G4double photonEnergy[nEntries] =
  {4.13*eV, 3.54*eV, 3.10*eV, 2.76*eV, 2.48*eV, 2.25*eV, 2.07*eV};
G4double refIndex[nEntries] =
  {2.43, 2.29, 2.22, 2.17, 2.14, 2.12, 2.11};
G4double absorption[nEntries] =
  {10*mm, 380*mm, 1400*mm, 2300*mm, 3470*mm, 3730*mm, 3990*mm};
G4double fComp[nEntries] =
  {0.00, 0.01, 0.06, 1.00, 0.13, 0.07, 0.00};

myMPT->AddProperty("RINDEX", photonEnergy, refIndex, nEntries);
myMPT->AddProperty("ABSLENGTH", photonEnergy, absorption, nEntries);
myMPT->AddProperty("FASTCOMPONENT", photonEnergy, fComp, nEntries);
myMPT->AddConstProperty("SCINTILLATIONYIELD",8000./MeV);
myMPT->AddConstProperty("FASTTIMECONSTANT", 300.*ns);

material->SetMaterialPropertiesTable(myMPT);
```

The optical properties are now defined for all materials. To track optical photons correctly, information about the material surfaces is still missing. Components of the same material do not necessarily have to have the same surface properties. Therefore, the surface texture for all relevant logical volumes is defined individually via the `G4OpticalSurface()` package. Once a set of optical properties has been created, it can be assigned to an existing surface. To select the desired surfaces, the `G4LogicalSkinSurface()` and `G4LogicalBorderSurface()` classes are available. In the first case, the entire surface of the logical volume is used. In the second case, another logical volume is given and the optical properties are applied to the boundary between the two volumes. Both particle directions must be considered here, resulting in two `G4OpticalSurfaces`. With this concept, each surface of a volume can be provided with different optical properties. This is not possible with the `G4LogicalSkinSurface()`.
The most important properties of the boundaries are the surface type, finish, model, and polish value. The `dielectric_dielectric` type is used for all materials except the aluminum foil, which is of type `dielectric_metal`. With this setting the reflectivity of the foil is 100 % by default, but a complex refractive index or the reflectivity can be set as a property in the `G4MaterialPropertiesTable()` optionally. As surface finish a variety of options can be selected, such as a perfectly smooth surface (`polished`) or a rough surface (`ground`). Furthermore, front- or backpainted options can be used, as well as mechanical and chemical processes of surface treatment. The way how the reflection and refraction at the volume surfaces has to be treated is chosen with the model option. In this study the original `glisur` model from `Geant3` was used.[7] This model assumes that the surface consists of many micro-facets. Each time an optical photon

[6] The number of `nEntries` in the BGO code snip was reduced for presentation purposes only. A reasonable large number of data points describes the behavior more accurately, while local dips are also accounting.

[7] A second model, that is often used, is the `unified` model. Although this was not used in this thesis, a comparison of the two models should be considered in future simulations. Both models are described compactly in [115].

is reflected at the surface, the orientation of a micro-facet is calculated. For this calculation an average surface normal vector is chosen, depending on the finish type. For the `polished` finish, a second vector dependent on the surface polish value (`polish` = 0.0 to 1.0, where 1.0 means perfectly polished) is defined by the random selection of a point on a sphere with the radius 1−`polish`.[8] This second vector is placed at the top of the first vector. Together they define the orientation of the micro-facet. A specular reflection is calculated from this. For a PbF_2 crystal, the surface texture could be created with the following code:

```
G4OpticalSurface* opCrystalSurface =
  new G4OpticalSurface("CrystalSurface");
opCrystalSurface->SetType(dielectric_dielectric);
opCrystalSurface->SetFinish(ground);
opCrystalSurface->SetModel(glisur);
opCrystalSurface->SetPolish(0.93);

G4LogicalSkinSurface* crystalSurface =
  new G4LogicalSkinSurface("CrystalSurface", logicCrystal, opCrystalSurface);

G4OpticalSurface* opticalSurface = dynamic_cast <G4OpticalSurface*>
  (crystalSurface->GetSurface(logicCrystal)->GetSurfaceProperty());
```

No optical properties were defined for the parts on the rotatable beam-axis (flange, absorber, fiber detector), since their function for the simulation only depends on the energy loss and scattering of the beam particles.

Beam monitor and output. During the simulation the following parameters are logged by default or as extended option (⋆):

- Number of trigger layers hit (N_{TrgX} and N_{TrgY}),
- position of detector hit[9] (X_{hit}, Y_{hit}, Z_{hit}),
- particle energy of detector hit (E_{hit}),
- total optical photons at PMT (N_{tot}),
- number of detected optical photons (N_{det}),
- (⋆) total energy deposited in detector (E_{dep}),
- (⋆) total step length of energy depositing particles in detector (l_{dep}),
- (⋆) place of origin and wavelength for each optical photon (X_{OP}, Y_{OP}, Z_{OP}, λ_{OP}).

The fiber detector serves as a simple beam position monitor. No single fiber hits are counted. When a particle passes through one of the four trigger layers the counter of the corresponding layer is set to 1. N_{TrgX} and N_{TrgY} can thus take the values 0, 1, or 2 respectively. This is sufficient to simulate the logic of trigger layers as it was handled during the beam-times.[10]
When the beam electron or a secondary particle reaches the reflective foil of the detector for the first time, its position (X_{hit}, Y_{hit}, Z_{hit}) and current energy (E_{hit}) are stored. In the case where a particle with higher energy hits the foil afterwards, the values are replaced.
Due to particles penetrating the detector, energy deposition can now occur which, due to the

[8] For `ground` finish, a `polish` value of 1.0 means maximum roughness and the radius of the sphere is the `polish`.
[9] In the case of more than one particle hitting the detector, the position and energy is set to the values according to the particle with the highest energy.
[10] However, this does not affect the ability to select a smaller region-of-interest (ROI) by reducing the number of constructed fibers and the trigger layer size.

defined optical properties, is associated with the production of optical photons. Optionally it is possible to output both the total energy deposit and the corresponding total step length, as well as the place of origin and the wavelength of each optical photon.
The trajectories of the optical photons are now fully simulated by `Geant4`. The tracking can only end in two ways: either absorption occurs within the material or the photon leaves the detector material in the direction of the PMT.[11] This must result in a transmission of the photon from detector material to PMT volume, a reflection at this point does not stop the tracking. In case of a transmission, the track of the corresponding optical photon is immediately terminated and a statistical probability for the detection of the photon is calculated based on its wavelength and the quantum efficiency of the PMT version used. After the complete tracking, the total number of photons arriving at the PMT (N_{tot}) and the number of photons finally detected (N_{det}) is logged. The data is stored either in `ASCII` files or in `ROOT` trees and the further analysis takes place outside of the `Geant4` environment.

This simulation part allows the comparison of beam-time data with simulations. On the one hand, the simulation can be used as a prediction for upcoming beam-times, but it can also be used to calibrate the measured data after a beam-time. This is done by translating the measured charge spectra into the number of detected optical photons.

3.4. Efficiency determination of DarkMESA veto systems

The next part of the simulation is supposed to investigate several aspects of a concept for background suppression. The largest background is expected to be from cosmic radiation. The DarkMESA detector signals induced by cosmic radiation have to be identified and sorted out. Various veto concepts can be tested on a small scale and successful concepts can then be adapted to the entire DarkMESA detector.

Considerations. The construction principle for the individual detectors from Sec. 3.3 is used again. The only difference is that several individual detectors can be simulated as modules. In addition, a generator for cosmic particles, and veto concepts are required. The principle described here anticipates the veto concepts that are presented in Chap. 7. Without going into the exact details, these concepts consist of large scintillators and absorbers. The materials and optical properties of the scintillators are created according to the known principle from Sec. 3.3. It is important that each single detector volume and scintillator layer has its own explicit name, since a statement about the signal in each individual module should be made during particle passage. Since high-energy particles passing through a scintillating material produce optical photons in the order of several 10 000, it is not practicable for this part of the simulation to rely on an exact tracking of all optical photons. The trajectories of the cosmic particles through the different modules and the energy deposit are now important and an exact value for the light output of each module is only subordinate.[12] Thus, for an efficient simulation of cosmic events, a small

[11] Optionally, exceeding a specified time period after the trigger signal or the first detected photon may also lead to the end of the tracking.
[12] For some particles, the energy deposition is not enough. Neutrons, for example, can have a high energy deposition, but it may be associated with only a few or no optical photons at all, depending on the material (see Sec. 5.6).

adjustment is made. Although all materials retain their optical properties, the optical photons are not tracked through the entire volume. When the optical photons are generated, the track is terminated immediately afterwards. Thus, only an absolute number of generated optical photons for each module is obtained.[13]
For this simulation part the important new elements to be described are the cosmic-ray generator and the positioning of the scintillator and absorber panels, as well as the analysis of the obtained data.

The cosmic-ray generator. The cosmic-ray shower library (CRY) is used to create the primary cosmic-ray particles and runs directly in `Geant4`. CRY uses detailed data tables. The important parameters for the generation can be set directly via a setup file. While there are parameters for excluding certain secondary particles, the most important settings are:

- `latitude` in degree – set to 50° for the location in Mainz,
- `altitude` in m – three possible values (0, 2 100, and 11 300 m) – set to 0 m, which equals sea level,
- `subboxLength` in m – particles are created in a square with this side length; data tables for 1, 3, 10, 30, 100, and 300 m are available – depending on the desired size, the next larger table must be selected for values in between,
- `nParticlesMax` – cosmic showers with more particles are shortened to this number of particles,
- `date` – the solar activity (eleven year cycle) is taken into account by a date, e.g. 12-31-2022.

The generator is included in the `GeneratePrimaries (G4Event* anEvent)` function in `BDXPrimaryGeneratorAction()`. The user settings have to be read in as `std::string` and together with a second argument for the location of the data tables a `CRYSetup()` is created. This setup is then reported to the `CRYGenerator()`. The `genEvent()` function fills the `std::vector<CRYParticle*>*vect` with all necessary event information. Within a `for`-loop the information is passed on to the `fParticleGun`. Depending on the vector size, which corresponds to the number of particles in one cosmic shower, the `fParticleGun` is filled multiple times. The vector has to be emptied with `vect->clear()` before the next cosmic shower.

```
std::string setupString;
std::vector<CRYParticle*> *vect;
G4ParticleTable* particleTableCRY = G4ParticleTable::GetParticleTable();
...                         //read in string from setup file
CRYSetup* setup = new CRYSetup(setupString,fSteering->crySetupData);
CRYGenerator* gen = new CRYGenerator(setup);

vect->clear();              //clear content of vector
gen->genEvent(vect);        //pass event information to vector
for (unsigned j=0; j<vect->size(); j++) {
```

[13] Nevertheless, if an statement about the number of detected optical photons is desired, it is still possible to obtain this information via a separate simulation part. There a particle of the desired type is generated with a random position and momentum within the module under investigation. The energy is randomly selected from a predefined energy range. The output is a two-dimensional histogram, which links the number of photons produced with the number of photons detected.

```
    fParticleGun->SetParticleDefinition(particleTableCRY->FindParticle(
        (*vect)[j]->PDGid()));
    fParticleGun->SetParticleEnergy((*vect)[j]->ke()*MeV);
    ...                    //calculate random position in a given plane
    fParticleGun->SetParticlePosition(G4ThreeVector(xpos,ypos,zpos));
    fParticleGun->SetParticleMomentumDirection(G4ThreeVector((*vect)[j]->u(),
        (*vect)[j]->w(), (*vect)[j]->v()));
    fParticleGun->SetParticleTime((*vect)[j]->t());
    fParticleGun->GeneratePrimaryVertex(anEvent);
}
```

Without further detector components, it is already possible to obtain the spectrum of cosmic particles at sea level in Mainz. It is also possible to simulate the laboratory or MESA hall ceiling between the cosmic-ray generator and the veto detector system to obtain the spectrum at the experimental site. This is only done in a simplified way by summing up all concrete ceilings above the experiment to one layer of concrete. Neither the complete laboratory building nor the MESA hall and the overburden is simulated. In a more precise setup, lateral cosmic particles pass through more material before reaching the laboratory or DarkMESA room, but a full simulation of the environment was not considered at this time. Simulating the path of a sufficiently large number of cosmic particles through multiple volumes is not practical at this point. To do this, the particles have to be generated in a larger plane and most of them do not even reach the laboratory or DarkMESA room. This would result in an unnecessary long simulation time.

Placement of components. The first component to be placed is the veto system. According to the size of the selected veto system, the size of the CRY generator (`subboxlength`) is also selected. To keep the simulation simple, only the scintillator and lead absorber panels are placed – the holding structure is neglected in the simulation. In the veto concept described here, there are an inner and an outer veto layer, consisting of six scintillator plates each. The layout was chosen so that each of the four larger plates (top, bottom, left, right) and each of the two smaller plates (front, back) have the same dimensions. Thus, apart from necessary cable entries, there are only two differently sized scintillator plates per veto layer.
The positioning and rotation of the individual plates within the simulation environment is based on a few variables and can therefore be easily adjusted. In addition to the size of the scintillator plates, the x-y-z position of the top plate is set. Since the holding structure is neglected, additional variables must be used to set the distance between the plates. There is a separate distance value for inner and outer veto (`scintiGapIV` and `scintiGapOV`), which regulates the distance between the large plates. Furthermore, the distance to the front and the back plate can be set with `scintiGapCap`. From these variables the position of each plate can be calculated and with a corresponding rotation all veto elements are placed. In a similar way, absorber layers can be placed between the inner and outer veto layer, or at the innermost position, directly around the calorimeter. It is possible to activate both absorber layers at the same time.
Next, the calorimeter has to be placed within the veto system. The module size is based on the number of detector layers in x, y, and z direction specified in the steering file. By querying these values in three nested `for`-loops, the crystals are generated at the correct positions. For a prototype, the full setup may look like in Fig. 3.3.

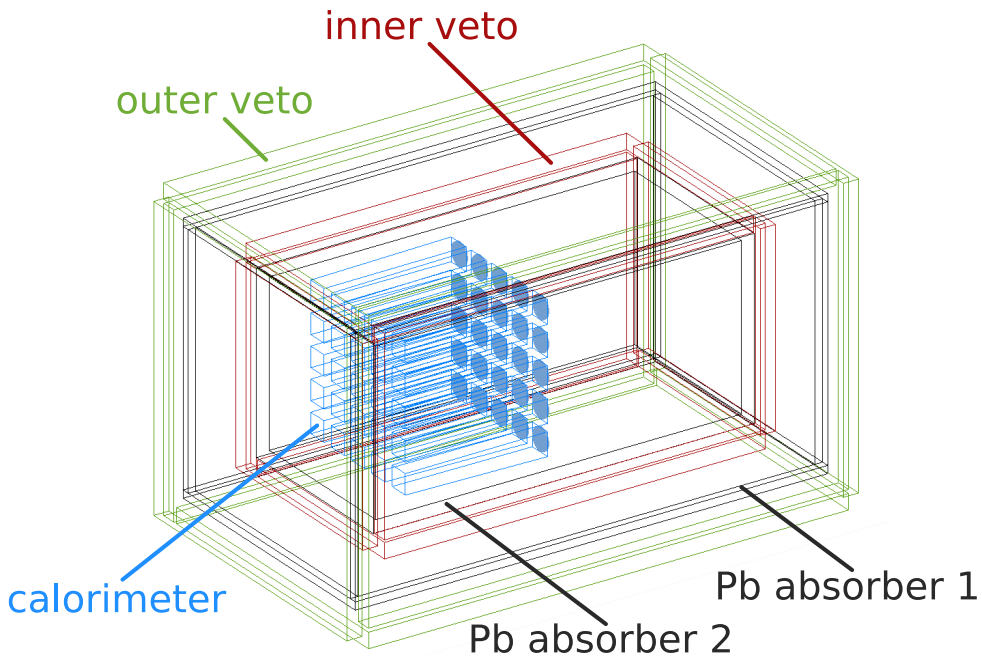

Figure 3.3.: Implementation of a prototype setup in the `Geant4` environment. Outer veto (green), inner veto (red), PbF_2 crystals with PMTs (blue), and two optional layers of lead absorbers (black).

Output and efficiency determination. For each cosmic generator event, the raw data of the primary cosmic-ray, the individual veto plates, and the calorimeter crystals are stored in three sub-folders of a `ROOT` file.

For the primary cosmic particle an event number, the particle type, and the energy is saved. For each veto and each calorimeter crystal, multiple branches are filled. They specify whether the respective element has been crossed by a particle and if so the deposited energy, the track length, and the number of optical photons generated in this element is recorded. In addition, particle type and energy of the particle responsible for the largest energy deposition in the element is saved. This is not necessarily the primary cosmic particle. Also the timestamps for the first and the last generated optical photon is stored.

Since all these branches are created for each element, the file becomes larger with the number of calorimeter elements. This is one of the reasons for having a simplified output option. With this option the most important information about selected events can be stored in an `ASCII` file to allow an immediate analysis and to speed up the simulation process. Especially one can set a minimum for the number of calorimeter crystals hit along with energy deposition limits for the veto layers. This allows to focus on specific events of interest. Under the condition that at least one calorimeter crystal responded, one can now look at the efficiency for certain veto conditions.

3.5. Full simulation of the DarkMESA experiment

This section shows how the expected reach of the DarkMESA experiment can be calculated with the help of several simulation parts.

Since DarkMESA is parasitic to the P2 experiment, the beam-dump of the P2 experiment can be considered the particle source for DarkMESA. The first objective of this simulation is to obtain the position and energy information of the particles in the beam-dump. For this purpose, the

155 MeV MESA electron beam is simulated immediately before the P2 experiment. From the P2 experiment itself, the most important components upstream to the beam-dump are simulated. These are the $l\mathrm{H}_2$ target and the magnetic field of the superconducting solenoid.
The particles then pass through a vacuum tube which closes with the beam-dump. The beam-dump itself consists of aluminum, water, copper, and a steel cladding and has been modeled accurately in `Geant4`. The energy spectrum of electrons and positrons in the beam-dump is then used as input for a `MadGraph` simulation outside of the `Geant4` environment. This external simulation aims to estimate the production of DM particles. For each kinematics setting a list of DM four-vectors is obtained and used as a new particle generator in the `Geant4` simulation. The DM is tracked up to the DarkMESA detector and their detection probabilities are calculated.
In combination with further parameters, like operating time and detection thresholds, the exclusion limits for DarkMESA can be calculated. By choosing a suitable representation, the results can be compared with existing and proposed limits from other experiments.

3.5.1. Impact of the P2 target and magnetic field on beam electrons

The MESA electron beam is assumed to be point-like and reaches the P2 target with a fixed energy. The maximum energy is 155 MeV and it is expected to remain very stable for the duration of the experiment. Within the `Geant4` environment the 600 mm long $l\mathrm{H}_2$ target with a diameter of 100 mm can be used in two different levels of detail.[14] The first version includes only the $l\mathrm{H}_2$ in cylindrical form. The more detailed one includes the following aluminum parts: an internal conical flow diverter with a wall thickness of 0.075 mm and holes for liquid exchange, upstream a 0.125 mm thick vacuum window, downstream a hemispherical cell window, and the cell wall of 0.25 mm thickness [81]. Fig. 3.4 shows the visualization of this target in `Geant4`.

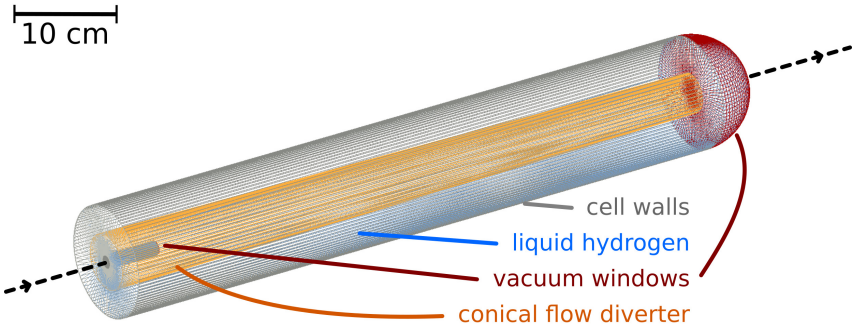

Figure 3.4.: Visualization of the detailed P2 target in `Geant4`. The $l\mathrm{H}_2$ in the cell (blue) is surrounded by thin walls (grey), and the up- and downstream vacuum windows (red). The conical flow diverter (orange) becomes narrower in beam direction. Components required for the flow of $l\mathrm{H}_2$ were not simulated.

In addition to the target, the magnetic field of the solenoid has to be included in the simulation. The used magnetic field map is called `FOPI_real` and is provided by the FOPI Collaboration [116]. The properties of the magnet are similar to those of the P2 solenoid. The data to fill the field map is stored in cylindrical coordinates. The radial- and the z-component of the magnetic field is provided. The maximum field strength is 0.7 T and compared to that the azimuthal component

[14] The distinction is of particular interest if the neutrino background has to be investigated.

is negligible small.

The additional files `Field.cc` and `Field.hh` with the function `Field()` are used to read in the field map from the `ASCII` file `./fieldmaps/FOPI_real/field.dat`. In `BDXConstruction.cc` the field is created and the properties are made available to the `G4TransportationManager()`.

```
void BDXConstruction::DefineMagneticField() {
  Field* field = new Field(scalingFactor, (char *)"FOPI_real");
  G4Mag_EqRhs* fieldEquation = new G4Mag_UsualEqRhs(field);

  G4MagIntegratorStepper* stepper = new G4HelixImplicitEuler(fieldEquation);
  G4FieldManager* fieldManager = G4TransportationManager::
      GetTransportationManager()->GetFieldManager();
  fieldManager->SetDetectorField(field);

  G4double fMinStep = 1e-3*mm; // Should be much smaller than the step limit in
       the lH2 volume
  G4double fMaxStep = 7e5*mm;  // Should not exceed the size of the world
      volume
  G4MagInt_Driver* integrationDriver = new G4MagInt_Driver(fMinStep, stepper,
      stepper->GetNumberOfVariables());
  G4TransportationManager::GetTransportationManager()->GetPropagatorInField()->
      SetLargestAcceptableStep(fMaxStep);

  G4ChordFinder* chordFinder = new G4ChordFinder(integrationDriver);
  fieldManager->SetChordFinder(chordFinder);
}
```

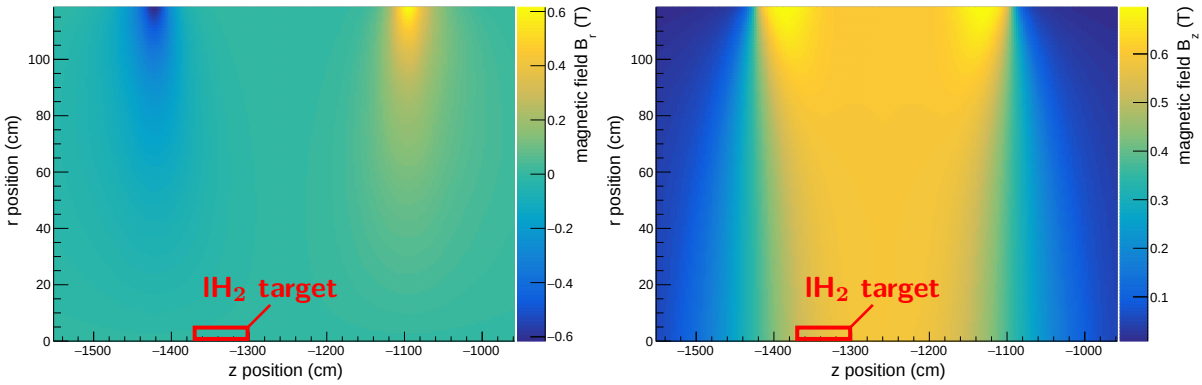

Figure 3.5.: Visualization of the magnetic field map used in the `Geant4` simulation for particle tracking through the P2 experiment. It is an approximation of the P2 solenoid corresponding to the FOPI solenoid. The radial- (left) and z-component (right) of the magnetic field are shown. The azimuthal component is negligibly small. The r position is the distance from the beam-axis and the z position corresponds to the z position in the `Geant4` environment. The position of the cylindrical $l\mathrm{H}_2$ target is shown in red.

In addition, the P2 gamma shield is simulated. It is about 2.5 m long and is made of steel and Pb. Only the Pb parts are simulated in `Geant4` and the visualization is shown in Fig. 3.6. Due to its geometry, it is important for some secondary particles on their way to the beam-dump.

The simulation of these elements ensures the correct path of the scattered particles to the beam-dump. Without these considerations, the beam of electrons would be fanned out to such an extent that 20 % of the scattered beam electrons would be stopped in the beam-exit-pipe already (see Fig. B.1 of Appx. B.1).

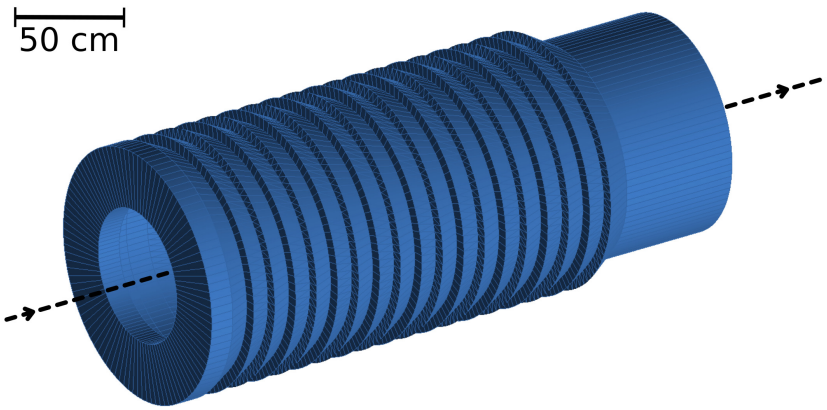

Figure 3.6.: Visualization of the P2 gamma shield in `Geant4`. Only the lead components are simulated. The steel mounting is neglected.

3.5.2. Energy and $\cos(\theta)$ distribution of e^-e^+ in the beam-dump

For a prediction of the DM production through processes of the incoming particles, the implementation of the beam-dump is of utmost importance. The P2 beam-dump was already used in the former A4 experiment and is described in Sec. 2.2.2. The shape and material composition was already discussed there and is now implemented slightly simplified into the `Geant4` simulation. The $AlMg_3$ coating of the beam-dump is composed of a spherical and several ring elements according to the dimensions shown in Fig. 3.7. The internal elements such as the water inlet and the perforated plates are neglected.

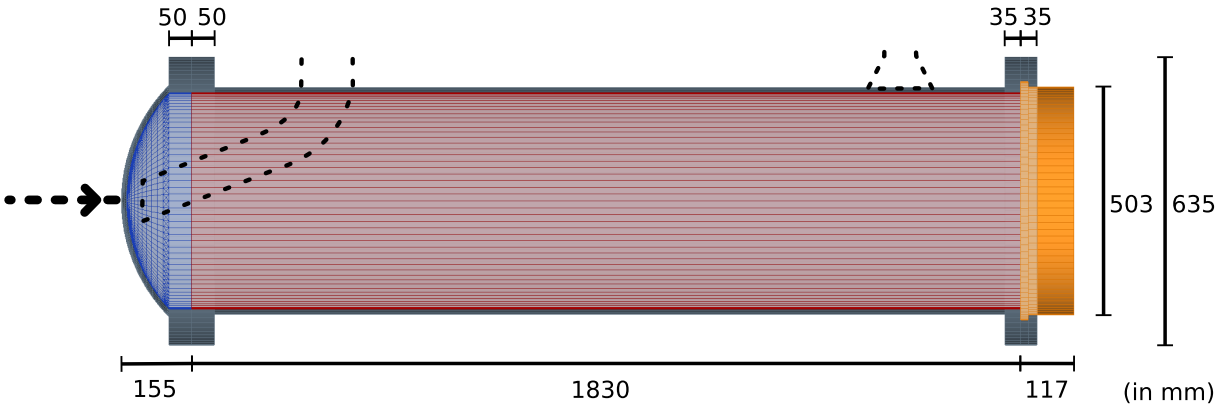

Figure 3.7.: Visualization of the P2 beam-dump in `Geant4`. The water (blue), the cylindrical part with the mixture of aluminum and water (red), and the copper plates (orange) are shown. The pipes for the water supply are indicated by dashed lines, but are not simulated in `Geant4`.

The spherical part is filled with water. Then follows the cylindrical part with the aluminum pellets and the water. Instead of simulating many small aluminum balls ($\varnothing$ 7 mm), a simplification is made and a mixture of 26 % water and 74 % aluminum as a new `G4Material()` is used for the whole tube.

For simulating the production process of DM particles χ in the beam-dump, "the differential energy spectrum of electrons and positrons as a function of the depth in the dump (in radiation length units t), normalized to the number of primary particles, $dN/dE\,(t)$" [117, p.45], is needed.

Three different methods were considered and implemented in the `Geant4` simulation:

1. Dividing the entire beam-dump along the z-axis into discs of same thickness, regardless of the material.

2. Approximation of the total radiation length of the different volumes to full radiation lengths and subsequent division of the entire beam-dump into discs with one X_0 thickness along the z-axis.

3. Calculation of the radiation length of all particles on the basis of the actual traveled path in the different materials and subsequent sorting according to full radiation lengths.

In the first approach there is no dependence on the radiation length, which already contradicts the general approaches in [118–120]. The second approach includes the radiation lengths of the different materials. The beam-dump was again subdivided along the z-axis and the radiation lengths of each volume were estimated using Tab. 2.2. The $AlMg_3$ coating in the front and the water were estimated together to one radiation length, the aluminum-water tube to 16, and the copper plates to eight radiation lengths. This approach fits relatively well with the true numbers for the P2 beam-dump, but is only valid for particles that hit and pass through the center. For most primary particles this approximation is still acceptable, but for secondary particles strong deviations can occur.[15]
For the generation of the necessary spectra, the third option was chosen, since a simulation with `Geant4` also provides the exact paths of individual particles through the different materials. For each particle the total traversed radiation length can be calculated. Then, all particles can be sorted by energy and full radiation lengths to obtain the $dN/dE\,(t)$ dependence. Despite the necessary buffering of more data, there is no relevant loss of speed. Regularly during the calculation, it is necessary to return to a previous physics process in which several particles were originated. To distinguish between the different trajectories it is important to monitor the `parentIDs` and `trackIDs`. This is an internal and continuous numbering of the tracks by `Geant4`, where the `parentID` indicates from which former track a new track (`trackID`) originates. In the `BDXSteppingAction.cc` file the entire radiation length up to the current step is determined, regardless of the particle type. In a first step, depending on the material, the radiation length in the current step is calculated. After that, the total radiation length is cached in an array corresponding to the `parentID` and `trackID` at the end of the previous step. This `parentID` and `trackID` is stored in a vector of pairs `std::pair<G4int,G4int> aPair`. Thereafter, two cases are distinguished. If both `parentID` and `trackID` match the two previous values, or if the new `parentID` matches the previous `trackID`, the track is still active and the radiation length in this step is added to the total radiation length. If these conditions are not met, the previous track is not active anymore and the tracking continues with a process that has not yet been completed. Now a cached radiation length from the position of this previous process is used (`radLenUpTo[x][y]`). The second position in the vector of pairs (at creation this was a `trackID`) is searched for the current `parentID`. Since each track originates from only one parent track, an

[15] A further problem arises if an additional target is attached in front of the beam-dump (see Sec. 6.1.1). This requires new estimations and subdivisions, which are especially difficult when the results for different target thicknesses should be compared.

unique pair is found in the `branchID` list. With this values the stored radiation length can be accessed. This corresponds to the radiation length at the location of the current process. Based on this value, the other particles are now tracked as well and the current radiation length is determined in each case.

```
G4double radLenStep;
extern G4int parentIDpre;
extern G4int trackIDpre;
extern G4double radLenTot;
G4double radLenUpTo[10000][10000];
extern std::vector<std::pair<G4int,G4int>> branchID;
std::pair<G4int,G4int> aPair;
std::vector<std::pair<G4int,G4int>>::iterator it;
struct FindPair{...};

void BDXSteppingAction::UserSteppingAction(const G4Step* step) {
  ...
  G4Track* track = step->GetTrack();
  G4int trackID = track->GetTrackID();
  G4int parentID = track->GetParentID();
  G4double stepLen = track-> GetStepLength();
  G4StepPoint* prePoint = step->GetPreStepPoint();
  G4String preLogName = prePoint->GetPhysicalVolume()->GetLogicalVolume()->
      GetName();
  ...
  if(preLogName == "Leg" || preLogName == "Water" || preLogName == "Chamber_LV"
       || preLogName == "Cu" || preLogName == "Wolfram") {
      radLenStep = stepLen/radLenMat(preLogName);
  } else {
      radLenStep = 0;
  }
  radLenUpTo[parentIDpre][trackIDpre] = radLenTot;
  aPair.first = parentIDpre;
  aPair.second = trackIDpre;
  branchID.push_back(aPair);
  if((parentID == parentIDpre && trackID == trackIDpre) || (parentID ==
      trackIDpre)) {
      radLenTot = radLenTot+radLenStep;
  } else {
      it = std::find_if(branchID.begin(), branchID.end(), FindPair(parentID));
      radLenTot = radLenUpTo[(*it).first][(*it).second]+radLenStep;
  }
  parentIDpre = parentID;
  trackIDpre = trackID;
  ...
}

G4double BDXSteppingAction::radLenMat(G4String preLogName) {
  ...
  return radiationLength;
}
```

An example for the tracking and radiation length calculation with this small code snippet can be found in Tab. 3.1.

parentID	trackID	parentIDpre	trackIDpre	branchID(1)	branchID(2)	radLenUpTo* (mm)	radLenStep (mm)	radLenTot (mm)
0	1	–1	–1	–1	–1	0.0	0.2	0.2
0	1	0	1	0	1	0.2	0.1	0.3
0	1	0	1	0	1	0.3	0.3	0.6
1	24	0	1	0	1	0.6	0.5	1.1
1	24	1	24	1	24	1.1	0.1	1.2
1	16	1	24	1	24	1.2	0.2	0.8
1	15	1	16	1	16	0.8	0.3	0.9
1	23	1	15	1	15	0.9	0.1	0.7
23	33	1	23	1	23	0.7	0.4	1.1
23	32	23	33	23	33	1.1	0.2	0.9
23	32	23	32	23	32	0.9	0.3	1.2
1	14	23	32	23	32	1.2	0.5	1.1
14	96	1	14	1	14	1.1	0.1	1.2
14	97	14	96	14	96	1.2	0.2	1.3

* `[parentIDpre][trackIDpre]`

Table 3.1.: Example for the determination of the total radiation length in the simulation. Each line is one step during the simulation. The `parentID`, `trackID`, and `radLenStep` are directly provided by the tracking algorithm of `Geant4`. They are chosen randomly for this example. All other values are determined and set according to the code snippet. It becomes clear that for same `branchIDs` the value `radLenUpTo[parentIDpre][trackIDpre]` is overwritten by a new value. For example, the total radiation length in the last row is the sum of `radLenUpTo[1][14]` and `radLenStep` in this last step (1.1 + 0.2 = 1.3).

Still being within the `BDXSteppingAction.cc`, no distinction between particle types has been made so far. When filling the histograms required by the `MadGraph` DM generator, only electrons and positrons whose steps lie within the beam-dump are important. According to their total radiation length, they are sorted into groups of whole radiation lengths. A check ensures that a track is only recorded once when the integer threshold is exceeded for the first time. Histograms for the current kinetic energy and $\cos(\theta)$ are filled for individual radiation length ranges, as well as for the entire beam-dump.

```
extern G4int radLenFilledSlice[30][10000];
G4double energy_m = track->GetKineticEnergy();
...
  if(pname == "e-" || pname =="e+") {
    if (preLogName == "Leg" || preLogName == "Water" || preLogName == "
        Chamber_LV" || preLogName == "Cu" || preLogName == "Wolfram") {
      for(int i=0; i<30; i++) {
        if(radLenTot >= i && radLenTot < i+1) {
          if(radLenFilledSlice[i][trackID] != 1) {
            radLenFilledSlice[i][trackID] = 1;
            momentumE = prePoint->GetMomentumDirection();
```

```
                cosThetaE = fabs(momentumE.cosTheta());
                // MadGraph needs the energy distribution and the cosTheta
                    distribution
                // Filling the histograms at this point
                ...
                return;
            }
        }
    }
  }
}
```

In the `EndOfRunAction()`, the final histograms are normalized according to the number of primary particles. The same binning of the energy axis must be set for both. Histograms like shown in Fig. 3.8 are obtained and can be passed to the `MadGraph` DM generator.

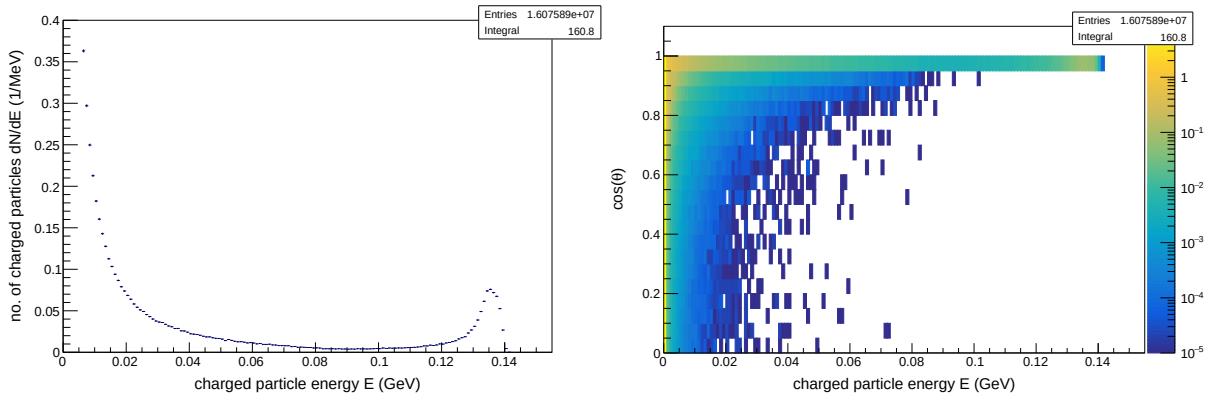

Figure 3.8.: Energy distribution (left) and $\cos(\theta)$ distribution (right) of primary and secondary electrons and positrons in the beam-dump, normalized to the number of primary electrons (100 000 in this case).

3.5.3. Production of DM particles in the beam-dump

The DM production in the beam-dump has to be simulated next. The code for this production process was provided by the BDX Collaboration, where it is used in simulations for the BDX at JLab [105]. The underlying `MadGraph` event generator was originally developed by Natalia Toro, Philip Schuster, et al. It handles the production process

$$eX \longrightarrow e'\gamma'X \longrightarrow e'\chi\overline{\chi}X \quad , \tag{3.1}$$

where X is a nucleus, γ' is the dark-photon, and $\chi\overline{\chi}$ are the two fermions from the γ' decay. The exact process of `MadGraph` event calculation is not discussed here. Reference is made to the underlying theory in Sec. 8.1 and the publication [106].
To consider showering effects in the beam-dump the `RunEventGenerator.py` script (developed by Andrea Celentano [121]) calls the `MadGraph` code multiple times with different beam energies and proper weights, which are obtained from the histograms in Fig. 3.8. The collection also includes a stand-alone detector interaction C++ program. In order to simulate complex detector systems as well, it was implemented directly into the `Geant4` simulation and is discussed in Sec. 3.5.4. The whole simulation chain is started with the scripts `singleHost.py` (single CPU) or `farm.py` (LSF-based farm). This collection of tools was used as a starting point and adapted

to the requirements of DarkMESA.

The process settings in MadGraph are mainly controlled by the three files: param_card.dat, proc_card.dat, and run_card.dat. Sample files are in Appx. A.3.2.
Some of the parameters required to create these files are specified via an entry in the run/runs.dat file. Multiple runs can be configured one after another and are entered in the form

$$\texttt{<tag>}\ \mathtt{m}_{\gamma'}\ \mathtt{m}_{\chi}\ \varepsilon\ \alpha_{\mathtt{D}}\ \mathtt{N}_{\mathtt{events}}\ \mathtt{E}_{\mathtt{beam}}\ \mathtt{L}_{\mathtt{dump}}\ \mathtt{L}_{\mathtt{x}}\ \mathtt{L}_{\mathtt{y}}\ \mathtt{L}_{\mathtt{z}}\ \#_{\mathtt{proc}} \quad .$$

After a freely choosable <tag> string the kinematics parameters $\mathtt{m}_{\gamma'}$, $\mathtt{m}_{\chi}$, ε, and $\alpha_{\mathtt{D}}$ follow. The desired number of events is chosen with $\mathtt{N}_{\mathtt{events}}$, followed by the electron beam energy $\mathtt{E}_{\mathtt{beam}}$ in GeV. Since the DarkMESA detection process is not performed in this simulation part, the following parameters are not relevant: the distance between beam-dump and detector $\mathtt{L}_{\mathtt{dump}}$, the dimensions of the detector ($\mathtt{L}_{\mathtt{x}}$, $\mathtt{L}_{\mathtt{y}}$, $\mathtt{L}_{\mathtt{z}}$), and the recoil process used ($\#_{\mathtt{proc}}$)[16].
In the singleHost.py (farm.py) script the location of the ROOT file, containing the energy and cos(θ) distribution of e^-e^+ in the beam-dump, is specified. It is executed and creates the file run_card.dat with the parameters ($\mathtt{N}_{\mathtt{events}}$, $\mathtt{E}_{\mathtt{beam}}$, $\mathtt{L}_{\mathtt{dump}}$, $\mathtt{L}_{\mathtt{x}}$, $\mathtt{L}_{\mathtt{y}}$, $\mathtt{L}_{\mathtt{z}}$, $\#_{\mathtt{proc}}$) and param_card.dat with the parameters ($\mathtt{m}_{\gamma'}$, $\mathtt{m}_{\chi}$, ε, $\alpha_{\mathtt{D}}$) by calling the corresponding function in CardsUtils.py. Next the Unix shell script run/tmp.csh is automatically created and executed. With this script, the two card files are moved to the correct path and the RunEventGenerator.py script is executed with the two card files and the ROOT file as arguments. As the calculations are performed once per energy bin, the histograms are rebinned to reduce simulation runtime and the amount of data generated. A maximum number of 20 iterations is sufficient.[17] For each bin a LHE file is created and after one kinematics setting a final LHE file is created. In this file the number of entries from each bin corresponds to the beam-dumps energy distribution.
The AnalyzeOutput.C script allows the reduction of the final LHE file for further use in Geant4. The final state four-vectors of all DM particles (PDG ID 611 or −611) together with the proper weight are written into a separate ASCII file and this can be used to fill a new primary generator in Geant4. Since the DM particles are produced in pairs, the generator consists of a ParticleGunChi() and a ParticleGunAntiChi(). The DM particle types are defined in the additional G4DarkMatter.cc/.hh files as spin-0 particles with mass $\mathtt{m}_{\chi}$, corresponding to the current kinematics.
The positioning of this new generator is simplified. For the z positioning, a position in the beam-dump is chosen where most of the e^- and e^+ are stopped. The deviations from the beam-axis in the x and y direction are neglected, since they equalize on average and have little effect due to the relatively large distance to the DarkMESA detector. According to the four-vector list, SetParticleMomentumDirection() and SetParticleEnergy() are set and a GeneratePrimaryVertex() event is generated. Histograms are created for the energy and angular distribution of all primary particles. In addition, the stepping process checks whether a detector element has been hit. The detector interaction length and time of flight (TOF) to this detector element are determined. A new and reduced ASCII file is written containing only the

[16] Recoil process ID's: 0 nothing, 1 proton elastic, 2 electron elastic, and 3 nuclear elastic.
[17] In a few cases, problems may occur at the margins of the histograms. For them, the energy range in the histograms has to be restricted. This ensures that MadGraph runs error-free, but the number of bins is correspondingly smaller.

DM particles passing through a detector element. The information about the original DM particle (four-vector) and the detector interaction length (L_{det}) are stored in this file. The visualization of the remaining particles in the `Geant4` environment is shown in Fig. 3.9.
If these particles can be detected with the DarkMESA detectors is discussed in the next subsection.

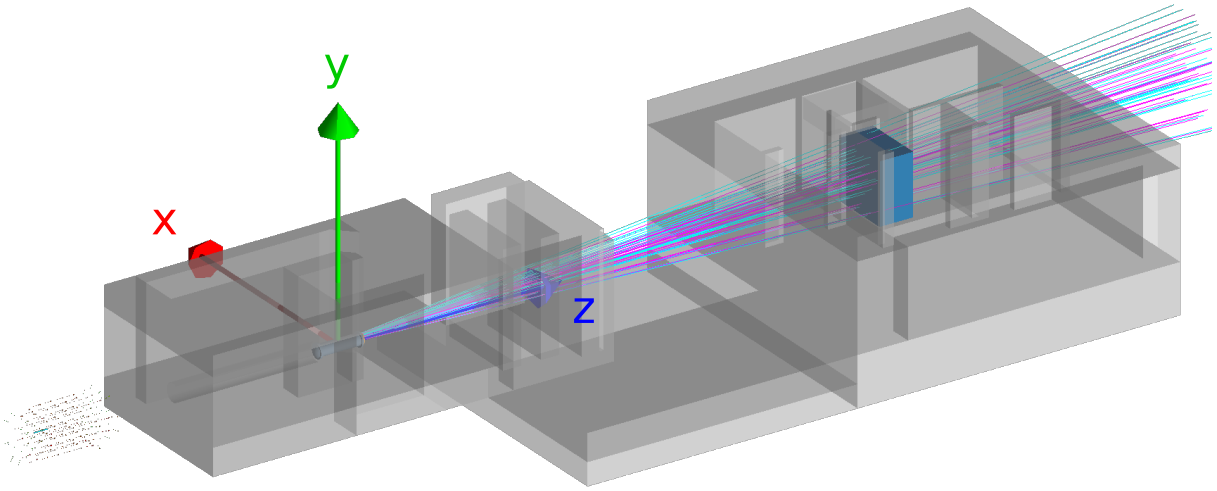

Figure 3.9.: Visualization of the MESA hall with important components used in the `Geant4` simulation. The target and the magnetic field of the P2 experiment are shown. The beam-dump is located in the center of the coordinate system. The blue block in the DarkMESA room represents the yet undefined DarkMESA detector. For a single kinematics the trajectories of the χ and $\overline{\chi}$ particles reaching the DarkMESA detector are shown in pink and turquoise. The distances along the beam-axis in `Geant4` coordinates are shown in Fig. B.2 of Appx. B.1.

3.5.4. Detection of DM particles with DarkMESA detectors

In the `EndOfRunAction()`, the reduced output file from the previous subsection is reused. Together with the weight (W), the value y is calculated at the end of the `DetSim()` function for the current kinematics ($\mathrm{m}_{\gamma'}$, m_{χ}, ε, α_{D}). This variable y is a dimensionless combination of model parameters and allows the comparison of the DM detection probabilities of various experiments.

For the analysis of the DM recoil it is possible to use three different processes – proton elastic, electron elastic, or nuclear elastic recoil. Specified via the steering file, the next steps are focused on the electron elastic recoil, whose advantages have already been shown in Sec. 2.2.3. The slight differences between the three processes are summarized in Appx. A.3.3.
In the recoil analysis process, first, 1-dim. histograms (`TF1** f_chieXsection`) associated with the calculation of cross-sections in `BDXKinUtils::Er_chieXsection()` are created once. In the energy range from zero up to the beam energy E_{beam}, 100 equidistant values for the DM particle energy E_0 are set and for each value the cross-section in the whole possible recoil energy range is calculated. Due to the recoil electron kinetic energy threshold E_{thr}, the beam energy E_{beam}, and the electron mass m_{e}, the recoil energy range is limited to

$$x_{\text{min}} = E_{\text{thr}} + m_{\text{e}} \qquad \text{and} \qquad x_{\text{max}} = E_{\text{beam}} + m_{\text{e}} - m_{\chi} \quad . \tag{3.2}$$

For the selected kinematics $m_{\gamma'} = 3\,\text{MeV}$, $m_\chi = 1\,\text{MeV}$, $\varepsilon = 0.001$, and $\alpha_\text{D} = 0.5$ the plotted cross-section functions are shown in Fig. 3.10.

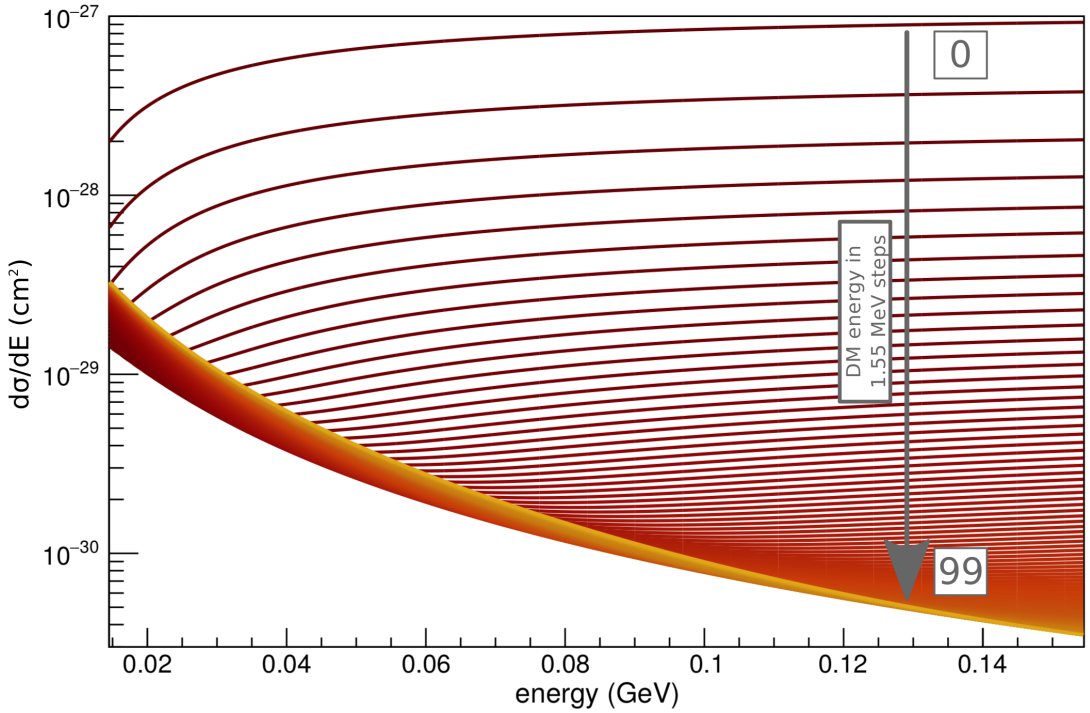

Figure 3.10.: The cross-section functions for DM particles with total energies up to 155 MeV are shown for the kinematics $m_{\gamma'} = 3\,\text{MeV}$, $m_\chi = 1\,\text{MeV}$, $\varepsilon = 0.001$ and $\alpha_\text{D} = 0.5$. Due to a recoil threshold energy of $E_\text{thr} = 14\,\text{MeV}$ and a beam energy of $E_\text{beam} = 155\,\text{MeV}$ in this case, the recoil energy range is limited to $x_\text{min} = E_\text{thr} + m_\text{e}$ and $x_\text{max} = E_\text{beam} + m_\text{e} - m_\chi$. These functions are calculated once at the beginning of the recoil analysis. The recoil energy for each DM particle can be determined with this method.

The cross-section calculation is done following the theory described in Sec. 8.1.2 and is implemented in the code as follows:

```
G4double BDXKinUtils::Er_chieXsection(G4double *x, G4double *par) {
  G4double Er=x[0];
  G4double E0=par[0];

  //The reaction is: chi(p1)+e(p2)->chi(k1)+e(k2).
  //Perform the cross-section in the lab frame, where p1=(0,0,P,E), p2=(0,0,0,
      Me), k2=(xx,yy,zz,Er)

  //1: Compute Lorentz-invariant dot products
  G4double p1p1=Mchi*Mchi;
  G4double k1k1=Mchi*Mchi;
  G4double p1p2=E0*Me;
  G4double p1k1=-0.5*(2*Me*Me-2*Mchi*Mchi-2*Er*Me);
  G4double p1k2=Me*(E0+Me-Er);
  G4double p2k1=Me*(E0+Me-Er);
  G4double p2k2=Er*Me;
  G4double k1k2=Me*E0;

  G4double k1p2=p2k1;
  G4double k2p2=p2k2;
  G4double k1p1=p1k1;
```

```
    G4double t=2*Me*Me-2*Me*Er;
    G4double s=Me*Me + Mchi*Mchi + 2*Me*E0;

    //2: the amplitude squared
    G4double  ampsq=1.0*(k1k2*p1p2 + p1k2*k1p2 - Mchi*Mchi*k2p2 - Me*Me*k1p1 + 2*
        Mchi*Mchi*Me*Me)/(pow((t-Maprime*Maprime),2));
    if (ampsq<0.0) {
        return 0;
    }

    //3: the 2 momenta in the CM frame (before/after). Since this is elastic
        scattering, they're the same!!!
    G4double p=((pow(s-Mchi*Mchi - Me*Me,2) - 4*Mchi*Mchi*Me*Me)/(4*s));
    p=sqrt(p);
    G4double k=p;

    //4: the Jacobian for the transformation cos(theta_CM) --> Recoil total
        energy in LAB frame
    G4double dcostheta = Me / (p*k);

    //5: the phase-space
    G4double S=(k/(s*p))*dcostheta;

    //6: put everything together
    G4double dsigma=ampsq*S; //in "GeV^-2 units" (and no coupling yet)
    dsigma = dsigma * Epsilon*Epsilon*4*PI*Alpha*AlphaDark;
    dsigma *=GeVm2cm2;

    return dsigma;
}
```

After these 100 histograms (`f_chieXsection`) have been created once at the beginning, the following steps are carried out for each incoming DM particle χ or $\overline{\chi}$:

1. The event counter for the total number of events $N_{\mathrm{evt,tot}}$ is increased by one.

2. According to the energy of the DM particle the cross-section function to be used is selected.

3. The maximum energy transfer $E_{\mathrm{r,max}}$ is calculated:

$$E_{\mathrm{r,max}} = \frac{2m_{\mathrm{e}}\left(E_0^2 - m_\chi^2\right)}{2E_0 m_{\mathrm{e}} + m_{\mathrm{e}}^2 + m_\chi^2} \quad . \tag{3.3}$$

   If $E_{\mathrm{r,max}} < E_{\mathrm{thr}}$ the event returns a cross-section of zero. Otherwise it is processed further.

4. A random recoil energy E_{r} between

$$x_1 = E_{\mathrm{thr}} + m_{\mathrm{e}} \qquad \text{and} \qquad x_2 = E_{\mathrm{r,max}} + m_{\mathrm{e}} \tag{3.4}$$

   is chosen and the total cross-section is computed by integrating the cross-section function between x_1 and x_2.

5. The total energy of the recoil χ is calculated:

$$E_\chi = E_0 + m_{\mathrm{e}} - E_{\mathrm{r}} \quad . \tag{3.5}$$

6. The momenta of both recoil particles are computed and the Lorentz four-vectors of the final state particles can be determined.[18]

7. The detector efficiency is taken into account by rolling a multi-sided dice, which decides, whether the event is processed further.

8. For a cross-section $\sigma_e > 0$ and a detector interaction length $L_{det} > 0$ the second event counter $N_{evt,acpt}$ is increased. The product of σ_e and L_{det} is added to W^*_{final}.

After all DM particles have been treated, one value for W^*_{final} and the final number of accepted events $N_{evt,acpt}$ are obtained. From this, the detector interactions per electron on target W_{final} are calculated:

$$W_{final} = W^*_{final}\, W\, N_{evt,acpt}\, \frac{Z_{Det}\rho_{Det}N_A}{A_{Det}}\, \frac{\rho_{Dump}N_A}{A_{Dump}}\, X_{0,Dump}\, f_{pb,cm^2} \quad , \tag{3.6}$$

where W is the weight calculated with `MadGraph`, Z_{Det} is the atomic number, $A_{Det/Dump}$ the mass number, and $\rho_{Det/Dump}$ the density of the detector and beam-dump material.[19]
$Z_{Dump} = 1$, because every nucleus in the dump counts one. N_A is the Avogadro number, $X_{0,Dump}$ the radiation length of the beam-dump material in cm. The factor f_{pb,cm^2} converts the value from pb to cm^2.
The final number of detected DM particles in a given time is obtained by multiplying this value W_{final} with the electrons on target (EOT):

$$N_\chi = W_{final}\, EOT \tag{3.7}$$

This number N_χ was determined with a fixed coupling strength ε from the initial kinematics. For the variable y, the coupling constant ε has to be scaled to a value ε_L where the number of detected DM particles corresponds to an exclusion limit with a desired confidence level (CL). For the standard confidence level of 90 %, often used in the DM community, the Poisson statistic yields:

$$N_{scaled} = N_\chi \cdot \left(\frac{\varepsilon_L}{\varepsilon}\right)^4 = 2.3 \quad . \tag{3.8}$$

For this purpose, ε_L is reduced in a loop until the number of events N_{scaled} falls below the threshold of 2.3 events.

```
for (Int_t i=0; i<1E12; i++) {
    epsL = 1/(G4double)i;
    Nscaled = Nchi * pow(epsL/fSteering->m_Epsilon,4);
    if (Nscaled<2.3) break;
}
```

[18] A more detailed description is omitted here, as the tracks of the recoil particles have not been considered further. However, the results could be used for new generators in further detector studies.
[19] For detector concepts with different active materials, averaged values depending on the volume ratio are used.

With this new ε_{L} value the variable y can be computed:[20]

$$y = \varepsilon_{\mathrm{L}}^2 \alpha_{\mathrm{D}} \left(\frac{m_\chi}{m_{\gamma'}} \right)^4 \quad . \tag{3.9}$$

Here ε_{L} is the only variable specified by the simulation. All other variables were input parameters from the chosen kinematics.

[20] When the simulation results in $N_{\mathrm{evt,acpt}} = 0$ and therefore $N_\chi = 0$ it is not possible to determine a y value with this tool. In this case y is automatically set to infinity. To avoid display problems when plotting the data of all kinematics the infinity value is set to 10^{99}.

This procedure is repeated for a whole set of kinematics with different m_χ and thus $m_{\gamma'}$ values. A `ROOT` file is created for each kinematics, and the most important information is also stored in the `BDX_log.dat` file. This file contains date, time, and path of the used `ROOT` file as well as all relevant presets and results. A simple representation of the results is obtained by plotting y against m_χ, which allows the comparison with other experiments and the theoretical thermal relic targets.

Prior to discussing the DarkMESA results obtained from these simulations, a case of application of this simulation framework for MAGIX is discussed in Chap. 4, including necessary adjustments and initial results.

4. The MAGIX trigger veto system – an application of the DarkMESA simulation

As plans for a trigger veto system for MAGIX arose, it became evident that there could be synergies with DarkMESA. A first concept, described here and in Sec. 2.2.1, was developed. Both experiments will use plastic scintillators as cosmic veto counters and the segmented MAGIX trigger plane (T1) will also be made of them. The electronics readout of both systems is developed together due to the similar dimensions and detector materials.
Since the DarkMESA simulation already contains a cosmics generator and the routines for light yield simulations including all necessary optical material properties, it is appropriate to use this framework for designing the MAGIX detectors. Among a variety of issues, the following two questions were addressed first:

1. Is the planned rhombic geometry of the trigger scintillator elements suitable? Is the light output at the corners sufficient?
2. The system must be highly efficient in the identification of beam electrons and cosmic particles. For scattered beam electrons, a trigger efficiency ~ 1 and a veto response probability $< 10^{-3}$ is desired. For cosmic muons the veto response probability should be ~ 1. Are these numbers achievable with this system? How much lead is necessary between the active veto layers to meet these conditions?

4.1. Simulation updates

Since only part of the existing DarkMESA simulation is needed for answering these questions and in order to avoid overloading it, a separate simulation was created, containing only the relevant components. The components used from the DarkMESA simulation are:

- The event processing,
- the physics list, including optical processes,
- the concept of a steering file,
- the cosmic-ray generator,
- and parts of the defined materials and their properties.

Newly included were:

- The geometry, including user parameters to be set in the steering file,
- a generator for the incoming beam electrons,
- and an extension of the event processing with output of all relevant parameters and results.

This approach aims to keep the simulation compact and user friendly. The geometry was implemented according to the initial plans. Since many parameters, including the exact size and position of the focal plane, were not yet finalized, all geometry parameters are controllable via the steering file. In these initial studies, only the basic performance of the concept was investigated. An optimization of the geometry and material of the scintillators was not performed. The dimensions of the individual parts can be found in Tab. 4.1 and further parameters in Tab. 4.2. A visualization in the `Geant4` environment is shown in Fig. 4.1.

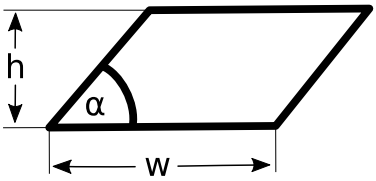

	trigger	veto	absorber
label	T1	V1/T2, V2, V3	Pb1, Pb2
count n (per layer)	20	4	1
length l (mm)	240	800	800
height h (mm)	26	10	10
width w (mm)	36	70	300
α (°)	60	60	90

Table 4.1.: Values for MAGIX trigger, veto, and absorber geometries in the `Geant4` simulation study.

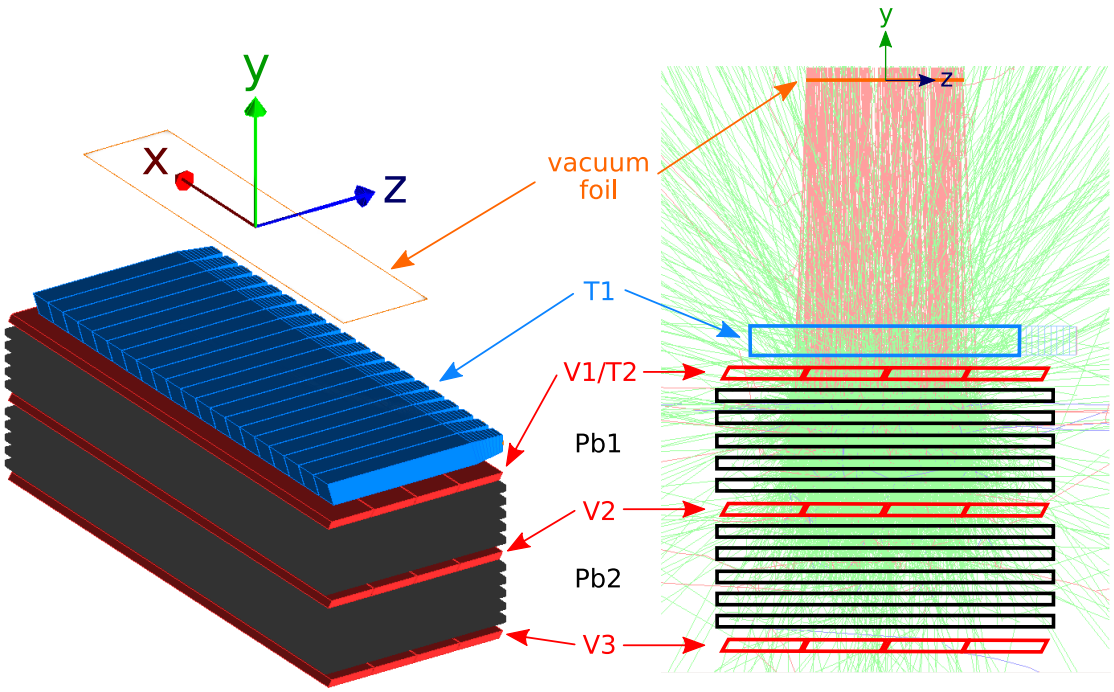

Figure 4.1.: Visualization of the MAGIX trigger veto system in the `Geant4` environment. Oblique view (left) and side view of the y-z-plane (right). A 125 µm thick Kapton vacuum foil (orange) is placed in the origin of the coordinate system. The trigger layer (blue) consists of 20 scintillator bars with coupled light guides and simplified PMTs. The three veto layers (red) consist of four bars each and are separated by multiple lead layers (black). The amount of lead was not optimized and is just for illustration in this setup. The shape of the single trigger and veto elements are rhomboid to avoid efficiency relevant gaps between the elements. In the example, 100 MeV primary electrons are tracked through the system. They are stopped soon and only secondary particles reach the veto plane V3.

[1] From the final design of the spectrometers, the incident angles of scattered beam electrons are known by now: [−16.4°, 7.3°] in dispersive and [−1.4°, 1.5°] in non-dispersive direction [122]. With this new values the sizes of absorber and veto layers will be further optimized.

scintillator	*type*	EJ 204
trigger	*readout*	one side
	light guide	yes
max. angle incoming e$^-$		10°
distance	*foil - trigger*	220 mm
	trigger - veto	10 mm
	veto - lead	10 mm
	lead - lead	10 mm

vacuum foil	*thickness*	125 µm
	width	140 mm
	length	650 mm
gap	*trigger - trigger*	250 µm
	veto - veto	1 mm
reflective foil	*type*	Teflon®
	thickness	200 µm
	air gap	100 µm

Table 4.2.: Default parameters for the initial MAGIX trigger veto study. For follow-up studies the values can be changed via the steering file.[1]

4.2. Light yield of the trigger plane

The strategy for answering each of the two main questions is a little different. For the light output study in the trigger plane the procedure is the following:

- Veto and lead layers are not relevant in this study.
- The primary particle is a 100 MeV electron with a maximum incident angle of 10° with respect to the negative y axis.
- All optical processes are turned on and the arising optical photons are tracked up to simplified 1″ Hamamatsu R1924A PMTs. Ascertained optical photons are counted.
- A scanning process along the x axis is implemented. For each position a defined number of runs is performed and the average number of detected optical photons (for each trigger element) is returned. This scan is performed for three different z positions, in the middle of the trigger bar ($z = 0$ mm), next to the light guide and PMT ($z = 100$ mm), and on the opposite side ($z = -100$ mm).
- For each trigger bar the number of detected optical photons is plotted against the x position. In addition the sum of all trigger elements is plotted.

The results in Fig. 4.2 and Appx. B.2.1 are showing a linear drop down to zero for individual trigger bars in the overlap area. At the same time the light output for the adjacent trigger increases linearly. This behavior is directly related to the amount of material traversed by the primary particle. Summing up the light output of neighboring bars does not compensate the edge effects entirely. The sharp geometry leads to a loss of optical photons at these positions. Optical photons are trapped at the corners and absorbed before reaching the PMT.
Looking at the total light output, a drop in the overlapping areas between 7.7 and 12.1 % is found. The values vary slightly for the three different z positions (see Tab. 4.3). For positions far away from the PMT the drop becomes larger. For the light arising in these corners, it is even more difficult to reach the PMT before getting absorbed. This should not be concerning, because for an optimized system the effect could be prevented by using PMTs and lightguides on both short sides. No exclusion criteria for the proposed geometry concept were found and a first laboratory prototype study was started by Sebastian Stengel.

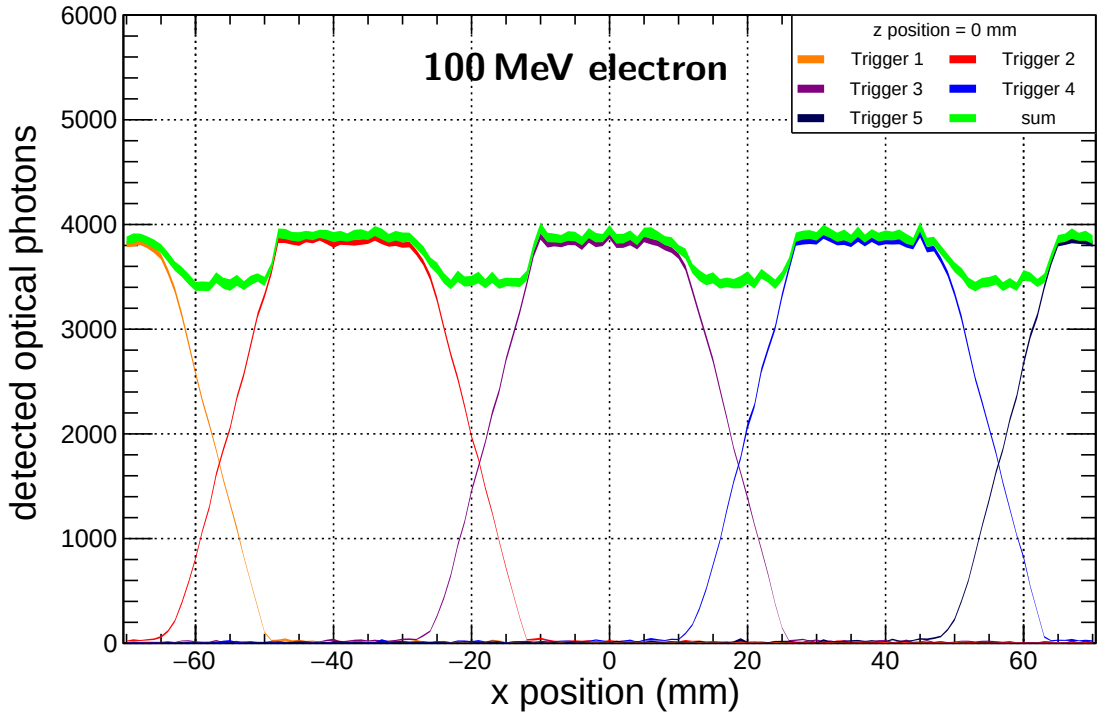

Figure 4.2.: Scan over five trigger bars along the x axis for the fixed z position of 0 mm. A 100 MeV electron with a random angle up to 10° is generated 10 mm above the trigger bar. The detected optical photons in each of the five bars are counted. This is done 1 000 times for each position and the mean values are calculated. The results are plotted for each trigger including an error band. In addition, the sum of all triggers is plotted in green.

z position	drop
-100 mm	12.08 ± 0.35 %
0 mm	10.95 ± 0.39 %
100 mm	7.67 ± 0.52 %

Table 4.3.: Decrease of light output in the overlap regions. $z = -100$ mm is opposite to the PMTs.

4.3. Veto and trigger efficiency

The second question now focuses on the whole trigger and veto concept for MAGIX. Is this concept suitable for distinguishing between beam electrons and cosmic particles? For this purpose, the following points are taken into account during the simulation:

- The primary particles to be investigated are the beam electrons scattered into the MAGIX spectrometers with the maximum expected energy of 100 MeV. In the focal plane their angle differs up to 10° from the vertical y axis. For the study of cosmic muons, muons with fixed energies of 1, 10, and 100 GeV were considered.
- Since the readout electronics for the detector elements should not be the focus yet, a complete tracking of optical photons has been omitted. Only the number of optical photons produced in the active material is considered.
- The decision whether a detector element returns a signal is determined by a predefined

threshold. The threshold is set to 100 photons for each element. The underlying consideration here is the use of silicon photomultipliers (SiPMs), which would be able to detect individual photons.[2]

- The effect of the amount of lead at the positions between the veto layers designated with Pb1 and Pb2 shall be investigated and optimized. Depending on the number of absorber plates, the veto levels are moved along the y axis. For each combination that is considered reasonable due to space conditions, a simulation run is carried out.

- The process of the simulation is the same for all configurations:
  1. A primary particle is generated at a random position 10 mm above the vacuum foil.
  2. During the tracking of this particle, the optical photons generated in each trigger and veto element are counted.
  3. Step 1 and 2 are repeated multiple times. Depending on the desired accuracy of the resulting efficiencies, several 10 000 primaries are appropriate. The results of this section are reached after 100 000 (1 000 000) events in each configuration. The veto response probability can therefore be specified up to 0.001 % (0.000 1 %).
  4. When the signal of at least one trigger bar is above the threshold, the evaluation of the veto layers is started. The combination of hit veto layers, where the four veto elements per layer are considered together (V1, V2, and V3), is considered. In total there are eight possibilities: no veto responded (no V), one veto responded (V1, V2, V3), a combination of two vetos responded (V1 && V2, V1 && V3, V2 && V3), or all three vetos responded (V1 && V2 && V3).[3] The response probabilities are calculated from these values.

For evaluation, the response probabilities of the eight veto conditions are plotted for several absorber settings. In the selection of shown plots (Fig. 4.3 (top) and Figs. B.9–B.10 of Appx. B.2.2), the thickness of Pb2 is fixed and the Pb1 thickness increases from left to right. The primary particle is a 100 MeV electron. As a precondition only events with at least one active trigger bar are evaluated. The trigger plane covers a slightly larger area than would be expected from the angular distribution of the scattered beam electrons. For this reason the simulated trigger response probability for 100 MeV electrons is between 99.997 and 100 % in all simulations. With the same method the plot for 1 GeV muons in Fig. 4.3 (bottom) was obtained. The veto inefficiency is already below 10^{-4} and for even higher muon energies of 10 GeV veto inefficiencies below 10^{-5} are achieved (Fig. B.11 of Appx. B.2.2).
The highest probability for scattered beam electrons is the condition that only veto V1 is activated. As the Pb1 absorbers get thicker, the probability approaches to 100 %. For muons on

[2] Regardless of the readout type, even a more conservative estimate of e.g. 1000 photons does not show any serious change in the results (see Fig. B.12 of Appx. B.2.2). Since the veto detectors are intended to detect minimum ionizing muons, the threshold could be set higher to exclude signals from electron shower events in the lead absorbers. A more precise assessment, required for the final concept, is beyond the scope of this initial study.

[3] Additionally, the latter case is tested with a further logic condition. It checks in the next lower veto level whether an element adjacent to the element in the previous level is triggered. Thus, the segmentation of the veto layers provides information about the direction of incidence of the particle. This could help to distinguish between scattered beam electrons and cosmic muons, and improve the veto and trigger efficiency.

the other hand, the probability is below 0.01 % for all Pb configurations. For them the highest probability with close to 100 % is reached, when all three veto levels are responding. For the 100 MeV electrons the probability for this veto condition gets smaller and smaller as one increases the amount of lead. With this two conditions one could already distinguish between the two particle types with high accuracy. In the final evaluation also the other conditions have to be taken into account and an appropriate veto and trigger condition must be established.

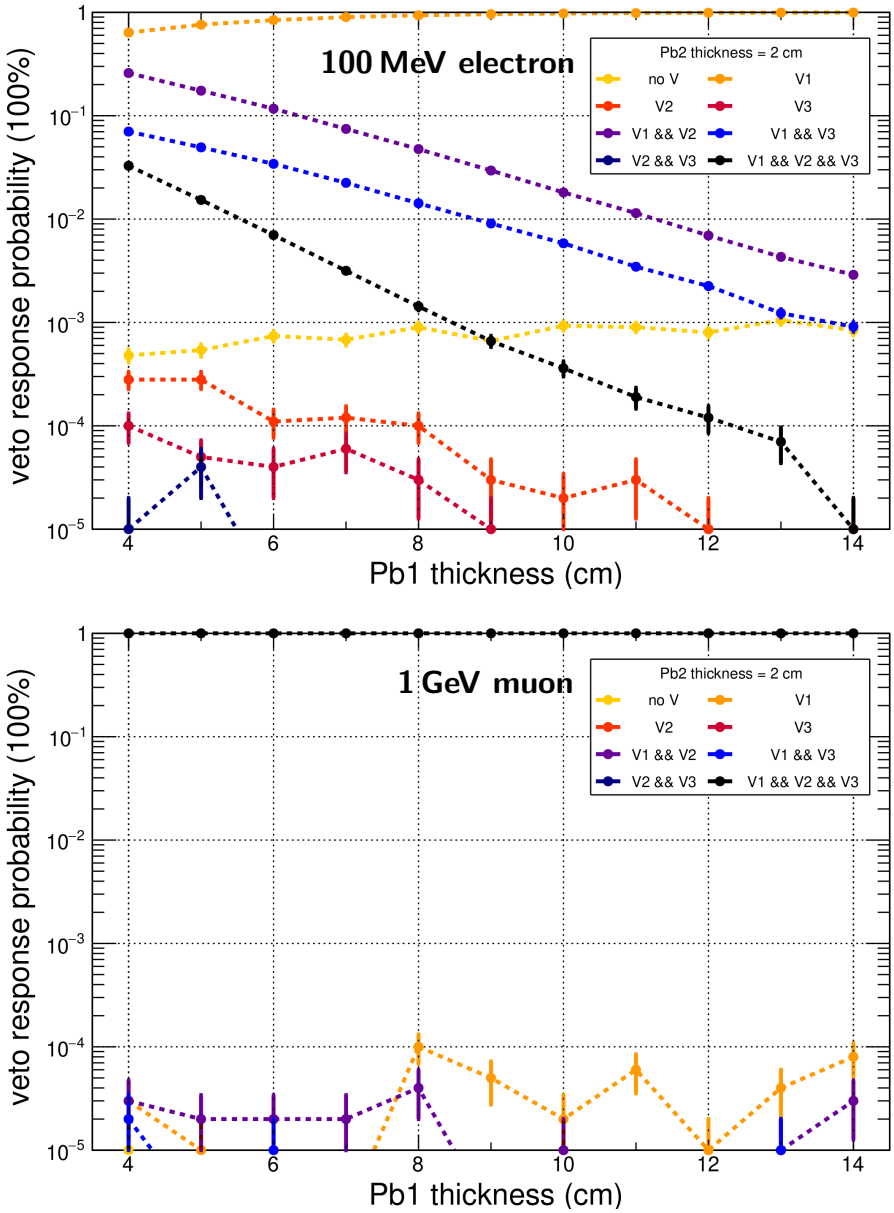

Figure 4.3.: The veto response probability for 100 MeV primary electrons (top) and 1 GeV primary muons (bottom). The eight veto conditions in dependence of the thickness of the first lead absorber layer (Pb1) are shown. The thickness of the second lead absorber layer (Pb2) is fixed to 2 cm. If at least 100 optical photons have been produced in one element, it counts as activated. Only events with at least one active trigger bar are evaluated.

For example, the conditions V1 && V2 (or V1 && V3) occur with a high probability in the 0.1 to 10 % range, but in the case of a muon theirs probability is less than 0.005 %. Since the probabilities differ in at least two orders of magnitude, these conditions can be regarded as

trigger events. Together with an appropriate amount of lead a veto efficiency smaller than the required 10^{-3} can be achieved for the scattered beam electrons. The signal height (proportional to the number of optical photons) has not yet been accurately evaluated. It is expected that especially in the veto planes V2 and V3 high signals for primary muons and low signals for primary electrons are detected. In the latter case, the signals are more likely to originate from secondary particles of a shower in the lead absorbers. A good evaluation will have a positive effect on the veto efficiency. The simulation has to be confirmed in laboratory prototype studies. A more conservative approach may also be appropriate. This would increase the measurement time, but allow a better assessment of background events.

4.4. Energy deposition

Additionally, the energy deposit in the layers can be consulted to evaluate the various Pb configurations. In Fig. 4.4 (left) the total energy deposit for the primary particles is shown for each layer. Due to the mostly perpendicular incidence of the particles in this study, the interaction length corresponds almost to the thickness of the scintillation layers. In the spectra a peak forms at the corresponding position and the peak difference between trigger and first veto is only related to these layer thicknesses, since almost no primary particle is stopped completely in the trigger detectors. For the trigger layer the peak is around 4.6 MeV and for the first veto layer the maximum is at 1.6 MeV. For the further veto levels, the secondary particles play an increasing role, since most of the primary particles are completely stopped in the Pb absorbers (Fig. 4.4 right). The relation between particle energy, interaction length, and energy deposition is no longer present. In line with the veto concept the proportion of events in which no energy is deposited is increasing sharply.

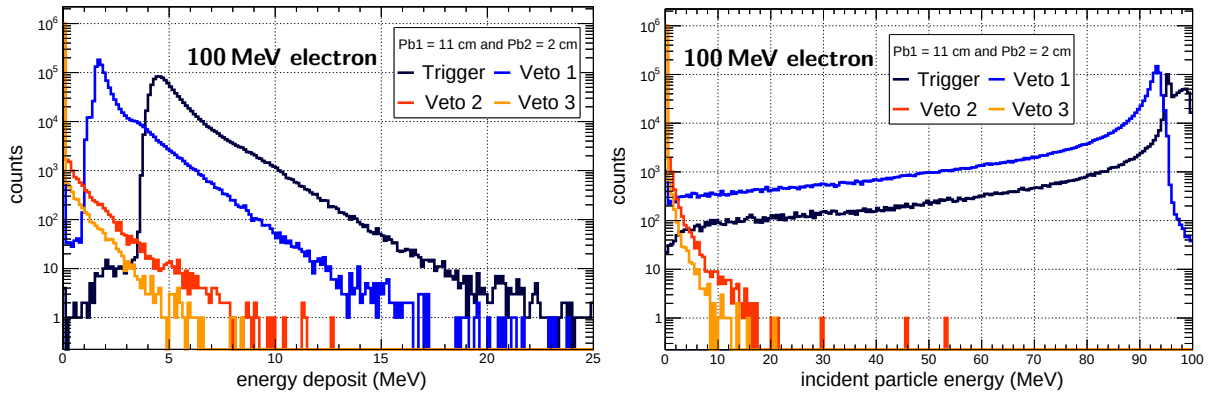

Figure 4.4.: Deposited energies (left) and incident particle energies (right) in the four distinct trigger and veto levels for 100 MeV primary electrons.

The final size and quantities of trigger and veto detectors, as well as lead absorbers, will be further investigated both experimentally and in simulation studies. In the experiment, the signals of all detector elements will be combined in a FPGA. Therefore, laboratory prototype studies are used to establish appropriate veto conditions. All these studies are already underway as part of Sebastian Stengel's doctoral thesis.

5. DarkMESA material studies

In Sec. 2.2.3 the concept of the beam-dump experiment at MESA was introduced and possible detector concepts were shown. However, no decision for a specific detector was made. Detection concepts for the detection of nucleon recoils or electron recoils were suggested and initial studies showed that designs for electron recoil detection are superior to that of nucleon recoil. The number of DM particles generated in the beam-dump (N_χ) and properties of the DarkMESA detector are decisive for the total number of generated recoil electrons

$$N^{\mathrm{e}}_{\mathrm{recoil}} = 2N_\chi P_{\chi,e} = 2\underbrace{(N_{\mathrm{e}} X_0 n_{\mathrm{T}} \sigma_{\chi\overline{\chi}})}_{\text{beam-dump}}\underbrace{(L_{\mathrm{d}} n_{\mathrm{e}} \overline{\sigma_{\chi,\mathrm{e}}})}_{\text{recoil electrons}} \quad . \tag{5.1}$$

The beam-dump material is characterized by the number of electrons on target (EOT) N_{e}, the radiation length X_0, the target density n_{T}, and the cross-section of the DM pair production $\sigma_{\chi\overline{\chi}}$. For the number of recoil electrons per incoming DM particle $P_{\chi,e}$, the detector interaction length L_{d}, the detector material density n_{e}, and the average electron recoil cross-section $\overline{\sigma_{\chi,\mathrm{e}}}$ are relevant. From Eq. 5.1 it is evident that a large active volume with a high density is desirable for a high DM detection yield.
The idea is to work with a traditional low-energy calorimeter, whereby the active volume should consist of high density materials. The material choice depends also on granularity, backgrounds, energy resolution, energy threshold for signal detection, and costs.
This total absorbing calorimeter is able to detect the transferred energy in elastic scattering of LDM particles off electrons, which depends on scattering angle and mass. In addition, any form of background above a certain electron recoil energy threshold is detected by the calorimeter.
Over a range of electron energies relevant for LDM detection, the light production of various Cherenkov radiators and inorganic scintillators was studied in beam-tests at MAMI. The crystals were all coupled to the same photo-sensor type and were wrapped in reflective foils for an optimal light collection efficiency. To complement the beam-tests, optical properties of the materials, in particular measured transmittances in the near UV and visible spectrum, were studied. The measured detector responses were also compared to MC simulations of energy-loss, light production, transport, and detection.

In the first section the mechanisms of light production are discussed and the main electronic components are presented. In Sec. 5.2 the materials studied are presented together with their transmission behavior investigated with a spectrophotometer. With the selection procedure in Sec. 5.3 suitable photomultiplier tubes (PMTs) were chosen and Sec. 5.4 presents the assembly of the prototype detectors. These prototypes were investigated in beam-times at MAMI and in Sec. 5.5 the results are presented and compared to `Geant4` MC simulations. A neutron response study follows in Sec. 5.6. The summary of all results with a decision for suitable calorimeter

materials in Sec. 5.7 also implies the next steps in detector development up to a full scale DarkMESA detector.

5.1. Theoretical and technical principles

5.1.1. Light production mechanisms

The amount of light produced in a material, when traversed by high-energy or charged particles, depends essentially on two processes: scintillation and Cherenkov radiation.

Scintillation. If the molecules of an optical transparent material are excited by ionizing radiation, the absorbed energy can be converted into light: the so-called scintillation light. Materials specifically designed as scintillators usually consist of several components to enable light transport in the visible wavelength range. For optical materials that are not primarily manufactured as scintillators, the resulting light is often in a wavelength range for which the material itself is not transparent or the wavelength is deep in the UV range, which makes the readout with photo-sensors difficult.

Cherenkov radiation. When a charged particle passes through a dielectric medium it can lead to coherent bluish-white Cherenkov radiation [123]. This can only happen, when the velocity of the particle $v = \beta c$ is larger than the phase velocity of light c_{ph} in the material.

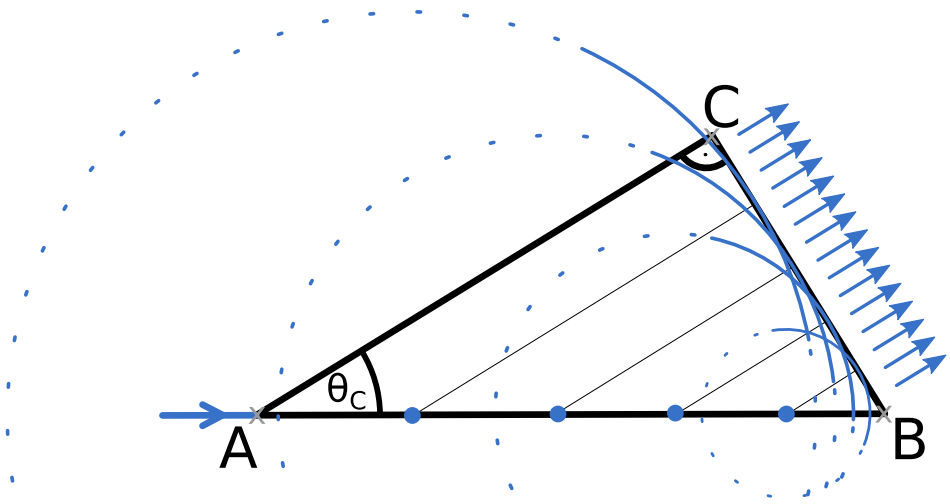

Figure 5.1.: Arising Cherenkov radiation from a charged particle with a velocity v larger than the phase velocity of light c_{ph} in the medium. The drawing is a simplified representation and actually the Cherenkov radiation is emitted in a cone.

The schematic diagram in Fig. 5.1 shows the origin of the radiation. $\overline{AB}$ is the path of a particle in the medium that meets the condition $v > c_{\mathrm{ph}}$. Points lying on this track can now be regarded as starting points of spherical wavelets. The resulting coherent wave-front lies on the line $\overline{BC}$. If the particle needs the time Δt for traveling the distance $\overline{AB}$ this results in $\overline{AB} = \beta c_0 \Delta t$. In turn, the emitted radiation has traveled the distance $\overline{AC}$ (90° to the wave front) during this time.

This results in the expression $\overline{AC} = (c_0/n)\,\Delta t$. Geometric considerations lead to the Cherenkov relation [124]

$$\cos(\theta_C) = \frac{1}{\beta n} \quad . \tag{5.2}$$

In general, Cherenkov emitters are dispersive media. This means that a wavelength-dependent emission is observed. The number of produced photons per particle path length x and per wavelength interval λ can be calculated with the Frank-Tamm formula [125]

$$\frac{dN^2}{dx d\lambda} = \frac{2\pi\alpha_{em} q^2}{\lambda^2} \cdot \sin^2(\theta_C) \quad . \tag{5.3}$$

α_{em} is the fine-structure constant and q the particle's charge in units of the elementary charge e. The four diagrams in Fig. 5.2 are showing the wavelength dependence of Cherenkov light production, transport, and detection for a given crystal material and detection system.[1] The amount of light produced by Cherenkov radiation is proportional to λ^{-2} (a). As a result, light production in the ultraviolet range is larger. Whether a material can act as a Cherenkov emitter depends on its dispersion (b) and transmission behavior (c). If the quantum efficiency of the used readout is sufficiently high in the wavelength range of the Cherenkov photons, a detection is possible (d).

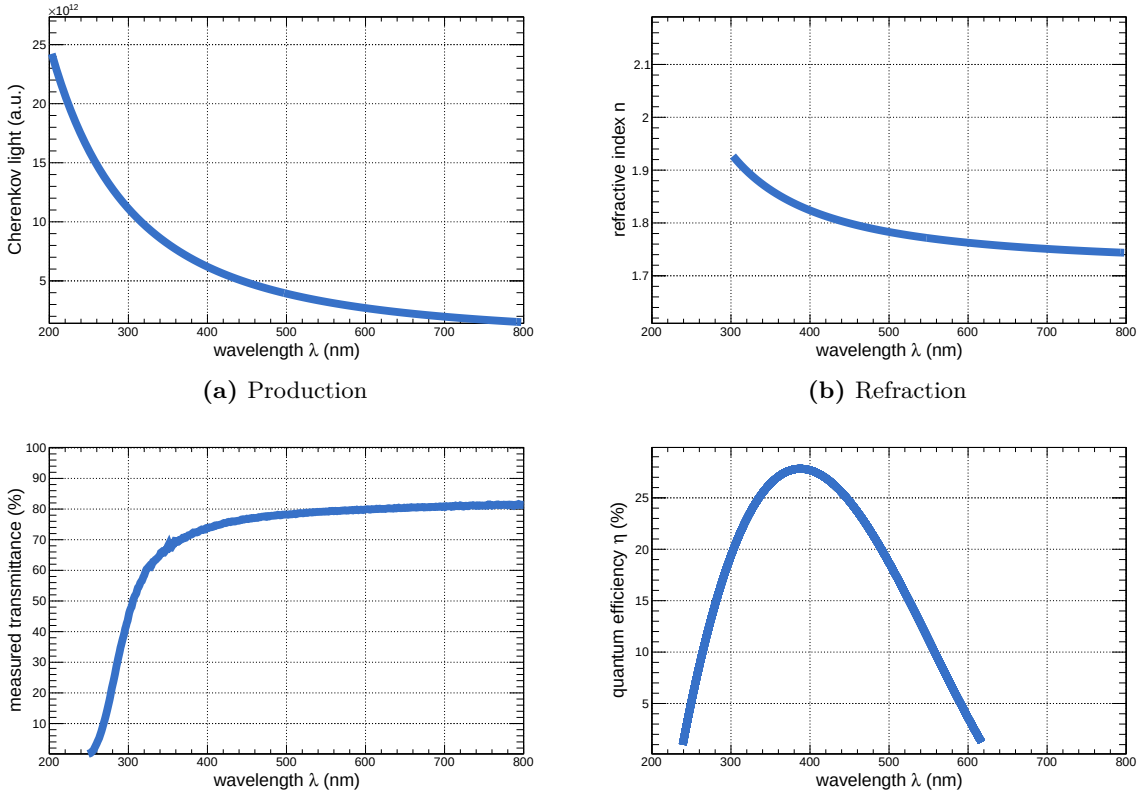

(a) Production **(b)** Refraction

(c) Transmission **(d)** Detection

Figure 5.2.: The Cherenkov light production is proportional to λ^{-2} (a). The maximum visible amount of light is determined by the refractive index (b) and the transmission (c) of the material. An efficient light readout in the corresponding wavelength range is required for the detection (d).

[1] Shown is an example for a PbF_2 crystal read out with a Philips (Photonis) XP2900/01 PMT.

5.1.2. Light detection and readout

The produced photons show a wavelength dependent distribution with a peak emission at a certain wavelength. A suitable readout with a high efficiency in the expected wavelength range has to be chosen. The PMTs used in the A4 experiment are the first choice in this work.

Photomultiplier tube (PMT). A PMT is a device that allows the conversion of photons into a measurable electronic signal. PMTs consist of a vacuum tube with an entrance window followed by a photocathode, multiple stages of dynodes, and an anode. A schematic view is shown in Fig. 5.3. When a photon overcomes the optical transition between crystal and entrance window, it reaches the photocathode. The photoelectric effect is exploited and the photon can extract a photoelectron from the photocathode. The applied voltage accelerates this photoelectron to the first dynode, where secondary electrons can be knocked out. This creates an avalanche of electrons that propagates to the last dynode, which is the readout anode. Even for individual photons, the multiplication by the dynodes is high enough to obtain a measurable signal at the anode.
Typically, the voltages of the photocathode and the individual dynodes are set with the help of a voltage divider. Through the use of specific resistor chains, an optimal multiplication of the photoelectrons and thus a good signal-to-noise ratio can be achieved.

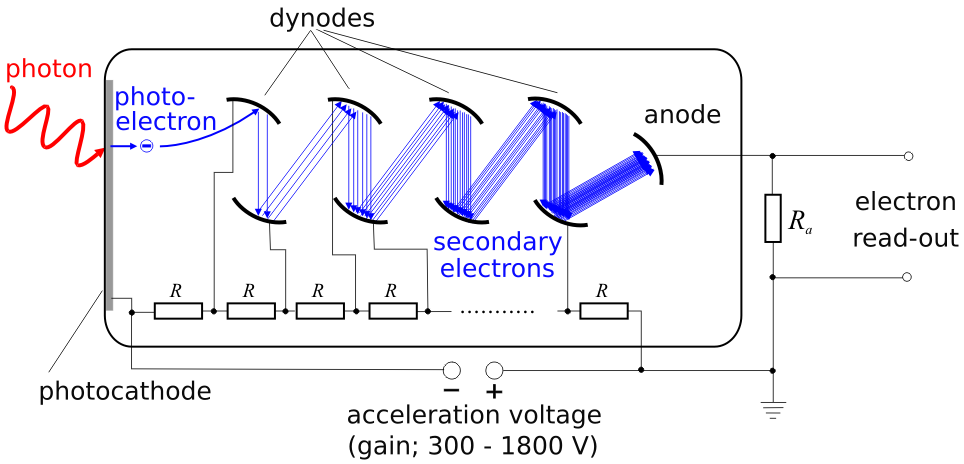

Figure 5.3.: Working principle of a photomultiplier tube (PMT). An incoming photon extracts a photoelectron from the photocathode. This photoelectron is accelerated by several dynodes and with arising secondary electrons the current at the anode is measurable. The applied acceleration voltage and a resistor chain steer the dynodes voltages for an optimal electron avalanche.

The individual signals of the PMTs can be observed with an oscilloscope, but for data acquisition and more precise analyses, devices that record the entire waveform or measure the charge of a signal pulse are used.

Sampling analog-to-digital converter (ADC). The switched capacitor digitizer CAEN V1742B [126] can fully record and store the waveform of each signal and up to 32 channels are available. It is based on the DRS4 chip developed at the Paul Scherrer Institute (PSI), which relies on 1024 capacitors in which a continous sampling of the analog signal takes place. The resolution is 12-bit with a 1 Vpp input dynamic range and a sampling frequency of 0.75 to 5 GHz

is possible. This frequency and a variable record length allow data acquisition windows from 27 to 1 364 ns. The data acquisition can be triggered with an external signal or internally with a logical linking of any number of channels. In the first case, it may be necessary to extend the signal path with delay boxes and also to change an internal post trigger value. This is required for pushing the signals back into the acquisition window.

Charge-to-digital converter (QDC). A 16-channel dual-range charge-to-digital converter (QDC) of type V965 [127] from CAEN is used to acquire the charge spectra with 12-bit resolution. The conversion is implemented in two steps. The input charge is converted to a voltage amplitude with a charge-to-amplitude converter (QAC). The following two parallel analog-to-digital converters (ADCs) allow the use of a high- and low-gain mode. In the low-gain mode a conversion of 25 fC per channel allows an input range from 0 to 100 pC. The high-gain mode has a acquisition window from 0 to 900 pC with 200 fC per channel resolution. These two modes allow a high precision for small pulses and the avoidance of saturation effects for larger pulses.

High voltage (HV) power supply. For all studies presented in this chapter the power supply of the PMTs is ensured with the CAEN V6533 [128] high voltage (HV) power supply module in VERSA-Module Euro card (VME) standard. It has six safe high voltage (SHV) channels with negative polarity and a maximum output voltage of 4 kV and output current of 3 mA. The voltage resolution is 100 mV and the hardware accuracy for the set voltages is 2 % of the full scale range (FSR). The voltage ripple at the supply voltages of the PMTs (between 1 kV and 2 kV) is typically 3 mV and 5 mV at maximum. For the beam-test studies this number of channels is sufficient. For the full prototype module, presented in Sec. 6.2.1, 25 channels are needed. Two of the iseg C040n [129] Versatile High Voltage Modules in VME Standard (VHS), with 12 SHV channels each, will be used in addition.

5.2. Calorimeter materials studied

The material studies in this chapter mainly focus on high density Cherenkov radiators. Their advantages are a short response time, directionality, and a lower sensitivity to background neutrons compared to inorganic scintillators [130]. A relevant disadvantage is their lower light yield. For the DarkMESA calorimeter, PbF_2 and lead glass (in the following denoted as PbGl) have been considered, which were investigated for their light yield. These are the high-density PbF_2 crystals of the former A4 experiment [131] in different lengths and the PbGl types SF5, SF6, and SF57HTU from Schott AG, Mainz, which differ in their PbO content. This is reflected in the variation of densities, radiation lengths, transmission edges, and refractive indices. To our knowledge, it is for the first time that the ultra-high transparent material SF57HTU, with improved transmittance especially in the blue to violet spectral range, is studied as a possible electromagnetic calorimeter material.
One of the most widely used inorganic scintillation materials in electromagnetic calorimetry in modern accelerator experiments is lead tungstate ($PbWO_4$). A large lead content and a density of $8.3\,\mathrm{g\,cm^{-3}}$ results in one of the shortest radiation lengths, $X_0 = 8.9\,\mathrm{mm}$, among the calorimeter materials. The scintillation mechanism has a fast decay time, but due to its low light output it

was not considered in this design studies [132].
Another possibility was thallium-doped Cesium Iodide (CsI(Tl)). Crystals from the former BaBar experiment [133, 134] are planned to be used by the LDM search experiment BDX at JLab [105]. CsI(Tl) has a higher light yield, but lower density compared to BGO, which is used at the Laboratori Nazionali di Frascati (LNF) in Italy by the Positron Annihilation into Dark Matter Experiment (PADME) [135]. PADME performs a dark photon search using the missing mass technique in a positron beam on a diamond target. Their active volume is composed of more than 600 BGO crystals from a dismantled end-cap calorimeter of the former L3 experiment at CERN [136, 137]. The raw material came from Soviet Union and was further processed by the Shanghai Institute of Ceramics of the Chinese Academy of Sciences (SICCAS). Two of these BGO crystals, with small corner damages, are available for the material studies and serve as reference detectors. They were kindly provided to us by . Their light output can be assumed to be sufficiently high, which can help especially during the preparation phase at the beginning of the beam-times.

	CsI(Tl)	**PbF_2**	**BGO**	**PbGl**
type	BaBar end-cap	A4 ring	L3 end-cap	various
cross-section (mm^2)	$47^2 - 60^2$	$26^2 - 30^2$	21^2	$\sim 30^2$
length (mm)	325	$150 - 185.4$	230	150
shape of blocks	tapered	tapered	cuboid	cuboid
density ($g\,cm^{-3}$)	4.53	7.77	7.13	$4.1 - 5.5$
radiation length (mm)	18.5	9.3	11.3	$16 - 26$
light yield (ph. MeV^{-1})	50 000	~ 25	10 000	~ 15
signal height (p.e. MeV^{-1})	7 600	~ 2	1 200	~ 1
peak emission (nm)	565	350	480	~ 450
signal decay time (ns)	680 (64 %) 3 340 (36 %)	prompt	300	prompt
refractive index	1.80	1.82	2.19	$1.7 - 1.9$
references	[133, 134]	[138, 139]	[136, 137]	[138, 140]

Table 5.1.: Properties of calorimeter materials that were considered in the design studies for the DarkMESA detector. Note that the light yield is dependent on the optical quality and the light collection efficiency of the detectors as well as the coupling and quantum efficiency of the photo-sensors. The peak wavelength in the emission spectrum of Cherenkov radiators depends on the transmittance of the material. More details on different PbGl types are given in Tab. 5.2.

5.2.1. General and optical properties

In the following, BGO, PbF_2, and the PbGl types SF5, SF6, and SF57HTU are further investigated. The properties of the considered calorimeter materials are listed in Tab. 5.1 and more details on different PbGl types are given in Tab. 5.2. Note that the light yield and signal height depend on the optical quality and the light collection efficiency of the detectors as well as the coupling and quantum efficiency of the photo-sensors.

	SF5	**SF6**	**SF57HTU**
length of blocks (mm)	150.5	149.5	150.5
cross-section of blocks (mm^2)	32.8 × 33.5	31.5 × 29.3	29.8 × 29.5
shape of blocks	cuboid	cuboid	cuboid
density ($g\,cm^{-3}$)	4.07	5.18	5.51
radiation length (mm)	25.5	17.0	15.5
refractive index @ 405 nm	1.71	1.86	1.91
internal transmittance @ 405 nm (%)	96	84	86

Table 5.2.: Properties of three different types of PbGl that are available from Schott [141] and that were studied in the electron beam-tests at MAMI. The internal transmittances are given for a sample thickness of 25 mm.

With $7.77\,g\,cm^{-3}$, PbF_2 has the highest density of all studied Cherenkov radiators and with $X_0 = 9.3\,mm$ it has also the shortest radiation length. The peak emission of 350 nm lies in the for Cherenkov radiation favorable UV region.

The A4 calorimeter consisted of 1022 PbF_2 crystals arranged in seven rings forming a barrel for detecting electrons of several hundred MeV energy. The blocks are tapered with an average cross-section of $26 \times 26\,mm^2$ at the front face and $30 \times 30\,mm^2$ at the rear face. Their lengths vary between 150.0 and 185.4 mm, corresponding to $16 - 20\,X_0$. These crystals have already been exposed to an electron beam and sometimes show visible radiation damage (Fig. 5.4c–d) or, in very rare cases, have slight repulsions at the corners (Fig. 5.4b). For the first prototype detectors, crystals with the least visible damages were chosen.

Cast blocks of the three PbGl types were provided by Schott AG, Mainz, for testing purposes. They are chemically composed of a mixture of PbO and SiO_2 with a low fraction of alkali metal oxides. The PbO content in all of them is above 50 % by weight and is the largest for SF57HTU (74.8 %), resulting in a density of $5.51\,g\,cm^{-3}$ and a radiation length $X_0 = 15.5\,mm$. SF6 has a PbO content of 61 %, a density of $5.18\,g\,cm^{-3}$ and $X_0 = 17\,mm$. SF5 (51 %) has the lowest PbO content and therefore a density of $4.07\,g\,cm^{-3}$ and $X_0 = 25.5\,mm$. These were cast blocks and the cast dimensions were chosen by the factory.

In order to obtain a good comparison of beam-test results even without an additional simulation, for the Cherenkov radiators blocks of comparable sizes were used. For a cross-section of $\sim 30 \times 30\,mm^2$, the maximum length was limited by SF6 to 149.5 mm. Since the shortest PbF_2 block is 150 mm long, the SF5 and SF57HTU blocks were shortened to this length. Photos of the PbGl blocks before and after cutting can be seen in Fig. B.13 of Appx. B.3.1. Due to the hardness of the material, the cutting procedure resulted in impurities. This is why it was decided not to cut all sides of the cast blocks to the same fixed values. Thus, the crystals do not have the same cross-section surfaces. Width and height vary by up to 10 %. Compared to SF57HTU, the 150 mm long PbF_2 crystal volume is 11 % smaller because of the trapezoidal shape.

The dimension of the two scintillating BGO crystals have been left like shown in Tab. 5.1. They have a smaller front surface while being longer and their volume is 24 % smaller than that of SF57HTU. Photos of the BGO crystals including some small corner damages can be seen in Fig. B.14 of Appx. B.3.1.

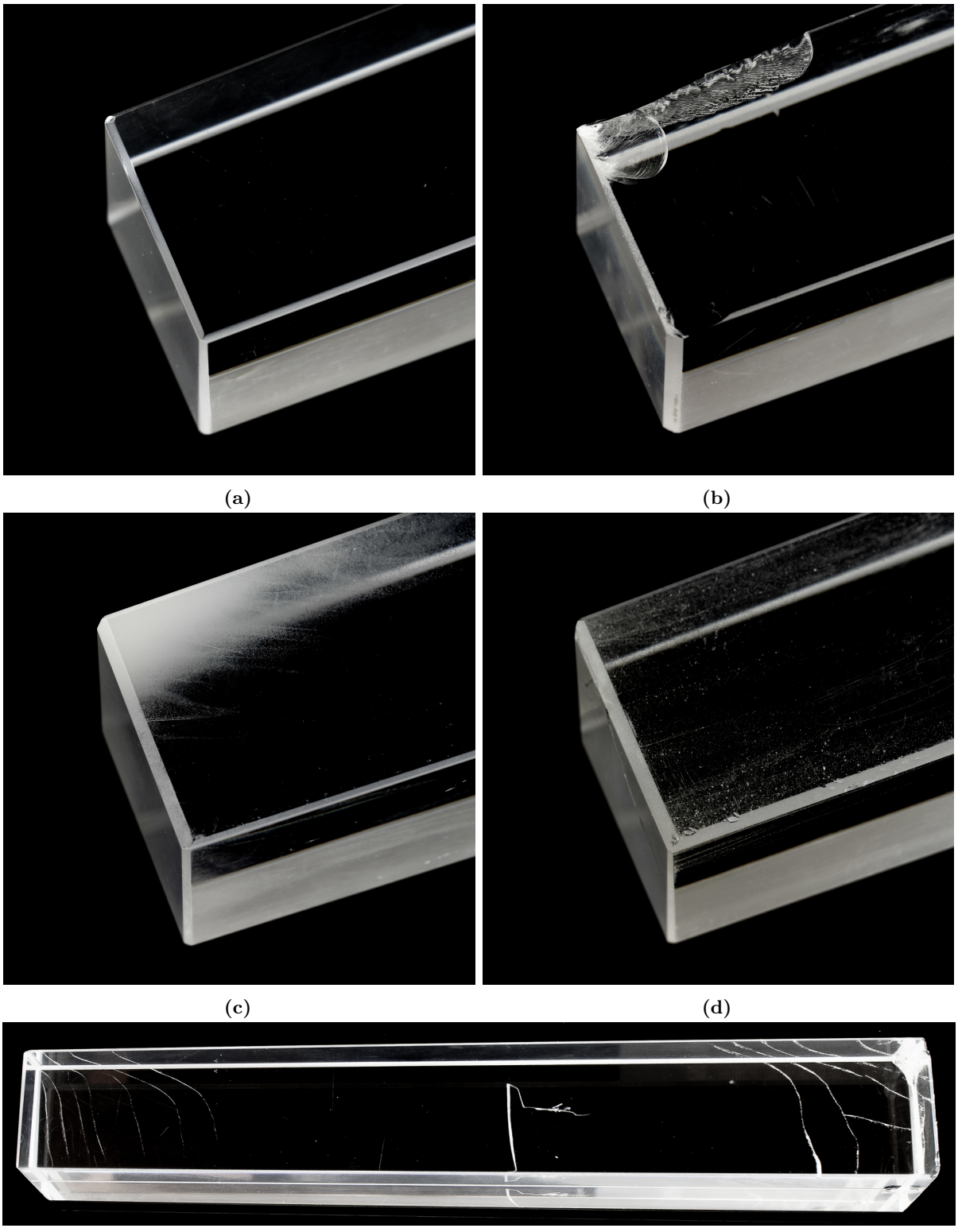

(a) **(b)**

(c) **(d)**

(e)

Figure 5.4.: Visible damages of selected PbF_2 crystals. For comparison, a damage-free crystal is shown in (a). In (b) there are repulsions at one corner. Radiation damage becomes visible through optical blurring – in the form of local clouds (c) or thin lines through large parts of the crystal (d). Tension fields in the crystal can lead to fine cracks (e).

For the BGO and PbF_2 crystals no further polishing was necessary. In the case of PbGl a rough grinding with fine water sanding paper and a polishing with Ceroxid [142] was carried out.
As shown in Fig. 5.2 in Sec. 5.1, the refractive index and the transmittance of the materials are wavelength dependent. Due to the low light yield of pure Cherenkov radiators compared to scintillating plastics or inorganic crystals, these are the key properties for the optical quality of Cherenkov radiators.
For the Cherenkov radiators the refractive indices were taken from data tables provided by Anderson et al. for PbF_2 [138] and Schott AG for the PbGl types [141]. For BGO the results from a study by Williams et al. [143] were used. The refractive indices show normal dispersion, $\mathrm{d}n/\mathrm{d}\lambda < 0$, and can be parameterized using a Sellmeier formula [144] for multiple absorption resonances:

$$n^2(\lambda) = 1 + \frac{B_1\lambda^2}{\lambda^2 - C_1^2} + \frac{B_2\lambda^2}{\lambda^2 - C_2^2} + \frac{B_3\lambda^2}{\lambda^2 - C_3^2} + \cdots \quad . \tag{5.4}$$

The parameters obtained for the four Cherenkov radiators and BGO are given in Tab. 5.3. Together with the given datapoints, the parameterization of the refractive indices in the near UV and visible spectrum are shown in Fig. 5.5.

material	B_1	C_1 (µm)	B_2	C_2 (µm)	B_3	C_3 (µm)	B_4	C_4 (µm)
PbF_2	0.67	3×10^{-4}	1.31	0.17	0.02	0.28	2007.89	796.67
SF5	1.46	0.11	0.25	0.23	0.95	10.58	–	–
SF6	1.72	0.12	0.39	0.24	1.05	10.89	–	–
SF57HTU	1.82	0.12	0.43	0.24	1.07	11.02	–	–
BGO	3.12	0.18	–	–	–	–	–	–

Table 5.3.: Parameterization of the refractive indices of PbF_2 [145], three different PbGl types [141], and BGO [143] in the near UV and optical spectrum using a Sellmeier formula for multiple absorption resonances: $n^2(\lambda) = 1 + \sum_i B_i\lambda^2/(\lambda^2 - C_i^2)$.

For the Schott PbGl types the wavelength dependent internal transmittance τ_i is also tabulated in the datasheets [141]. The values are available for two different sample thicknesses $x = 10$ and 25 mm. The characteristic light absorption length Λ_abs can be obtained from these values:

$$\Lambda_\mathrm{abs} = -\frac{x}{\ln(\tau_\mathrm{i})} \quad . \tag{5.5}$$

For PbF_2, the absorption length is also available from data of the A4 Collaboration [71].

5.2.2. Measurement of external transmittance with a spectrophotometer

Since the PbF_2 crystals have been exposed to a significant amount of radiation (up to 200 Gy) during the several years of the A4 experiment, their current transmittance should be checked. The calorimeter was built up between 1999 and 2000 and the measurement of the external transmittance of PbF_2 was carried out with the Shimadzu UV-2101PC spectrophotometer. The spectrophotometer is still available at the institute and is now used both for the important verification of selected PbF_2 crystals and for the verification of the transmittance of the new

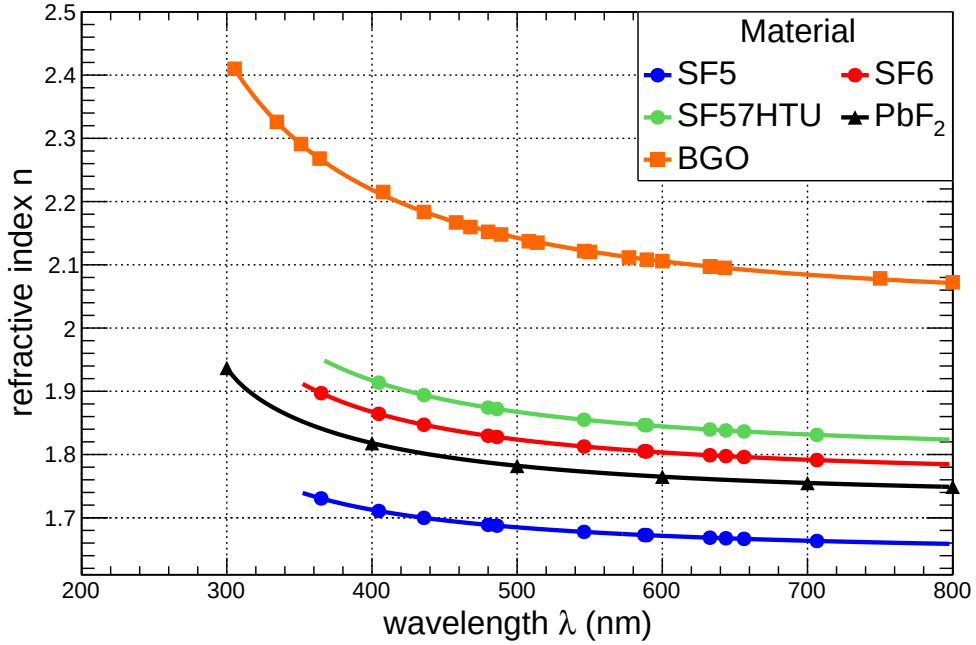

Figure 5.5.: Comparison of the refractive indices of PbF_2 [138, 145], three different PbGl types [141], and BGO [143] in the near UV and optical spectrum parameterized using a Sellmeier formula. The parameters for multiple absorption resonances are given in Tab. 5.3.

PbGl types known from the datasheets.

These measurements were carried out shortly after arrival of the PbGls from Schott. Because of the very large dimensions, the SF57HTU block was cut in size by the institutes mechanical workshop. The dimensions of the PbGl blocks at that time are given in Tab. 5.4. Not all surfaces were plane, which is why the maximum measured value is given.

material	**height h (mm)**	**width w (mm)**	**length l (mm)**
SF5	74	59	186
SF6	32	62	161
SF57HTU	42	55	164
PbF_2 (1)	26−30	26−30	150
PbF_2 (7)	26−30	26−30	185.4
BGO	21	21	230

Table 5.4.: Dimensions of the three Schott PbGl types, the PbF_2 and BGO crystals surveyed with the spectrophotometer.

For all upcoming measurements the MPC-3100 large sample compartment was attached to the spectrophotometer. This addition allows the evaluation of larger samples up to 300 mm in length. The double beam mode of the spectrophotometer employes two light beams: a reference beam and a sampling beam that passes through the sample crystals. A movable table allows the sample to be raised to the correct beam height. The light source is a halogen lamp whose beam can be

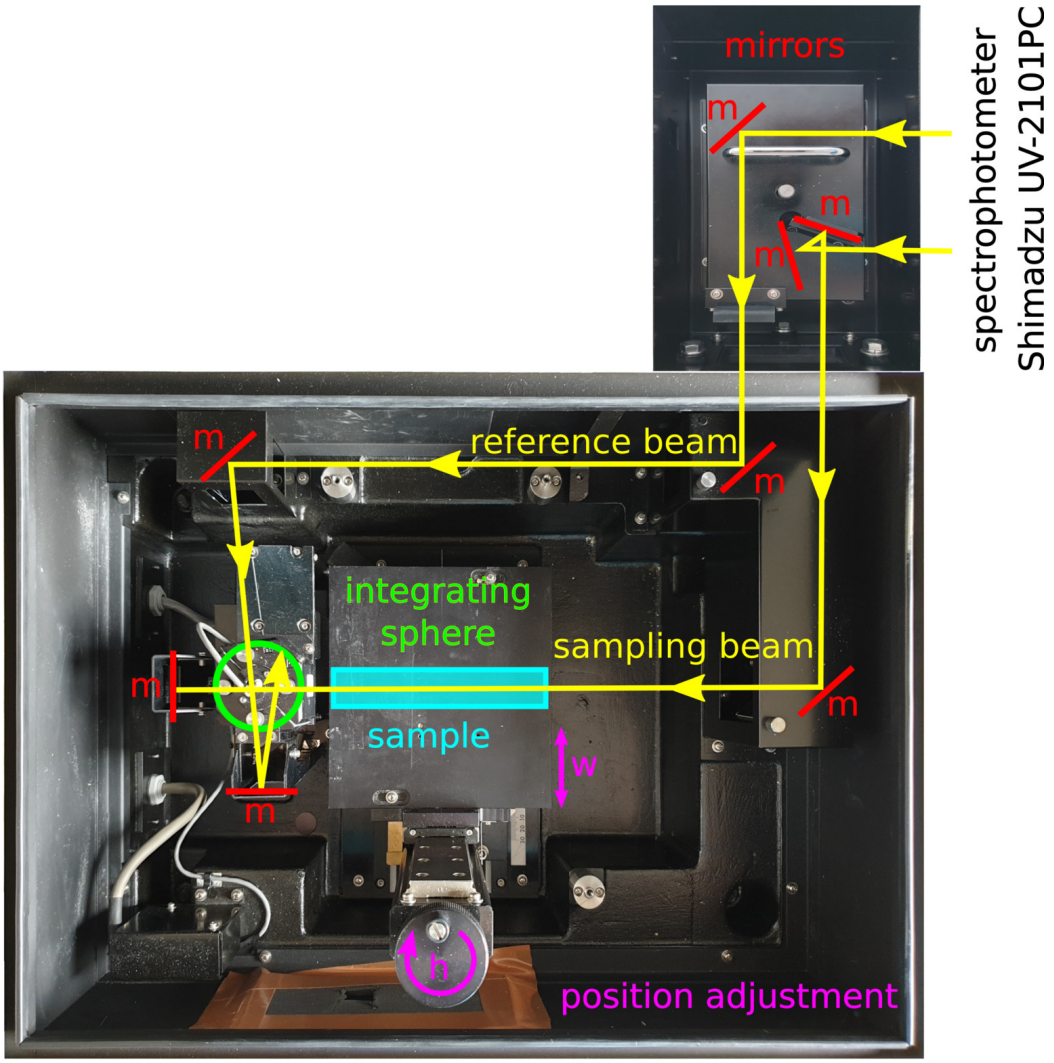

Figure 5.6.: View into the open large sample compartment of the spectrophotometer. The beam paths of the reference and sampling beam are shown and it is evident how the sample can be moved in the light beam. Two scales for width w and height h, and fixed marks on the sample plate allow repeated measurements under same conditions.

controlled with a monochromator in the wavelength range from 190 to 900 nm and a precision of 0.1 nm. The beam path can be seen from the schematic drawing of the optical system and the photo in Fig. 5.6. The two beam paths converge in an integrating hollow sphere. The sphere has a larger opening towards the sample side. This allows even the light deflected by passing through the sample to reach the inner part of the sphere. Inside, the sphere is lined with $BaSO_4$, a material that provides best reflective properties, leading to an undirected diffusion of the light inside of the sphere.

The amount of light is now measured by a PMT at the bottom of the sphere. Due to the diffuse light, the detector gives a correct result, regardless of whether it is a measurement with sample (fanned out cone of light) or without (dot-like cone of light).

The window area A covered by the PMT is $12 \times 20\,\mathrm{mm}^2$ and over the surface integral of the intensity of light $\vec{E}$ the radiation flux Φ is

$$\Phi = \iint \vec{E}\, dA \quad . \tag{5.6}$$

For the sample measurements, the beam of light should always be perpendicular to the crystal's front and rear surface. This is why in case of the tapered PbF_2 crystals the smaller side had to be raised by 2 mm when measuring along the longitudinal axis. For a measurement vertical to the axis a small deviation had to be accepted.
The data acquisition software UVPC Standard V3.52 was used to calculate the optical transmittance. Before each series of measurements, a measurement was performed without the investigated crystal and this baseline correction was loaded into the program. As a result, biases coming from the experimental system could be largely excluded.
From the reference beam, one obtains the incident radiation flux Φ_0 and from the sampling beam the transmitted radiation flux Φ_T. The ratio of the two results in the measured transmittance τ_m.
A comparison of measured transmittances along the longitudinal axis of representative samples of Cherenkov radiators and scintillating BGO is shown in Fig. 5.7a. Measurements along the shortest vertical axis are shown in Fig. 5.7b.
All materials show steep absorption edges. In both measurement setups the largest ranges of the spectrum are covered by the PbF_2 crystal, followed by BGO, and then the three PbGl types. Of these, the absorption edge of SF5 extends further into the UV range. The non-fading transmission in the deep UV range of BGO can be explained by a distortion caused by scintillation of the material – the true transmission is zero. When irradiated in deep UV, there is a small amount of scintillation light, which is in the visible range and is detected by the PMT of the spectrophotometer.
The maximum values for τ_m are between 70 and 90 %. This is not to be confused with the internal transmittance τ_i. In order to obtain τ_i, the reflection losses at the front and rear faces of the crystal have to be taken into account. This was done using the Fresnel reflectivity for a light beam with normal incidence, irrespective of polarization: $R = (1-n)^2/(1+n)^2$. Depending on the surface conditions of the crystal, the factor that approximates the losses is the reflection factor $P = (1-R)^2 = (4n)^2/(1+n)^4$. When considering an infinite series of reflections between parallel interfaces, the reflection factor becomes larger:

$$P = (1-R)^2 + R^2(1-R)^2 + \ldots = \frac{1-R}{1+R} = \frac{2n}{1+n^2} \quad . \tag{5.7}$$

For the transmittance spectra of the Cherenkov radiators considered in this study, the difference of the reflection factor including reflections to the one neglecting reflections is smaller than one percent. A complete treatment would require the correction for absorption losses of the reflected light inside the sample which changes the reflection factor to

$$P = \frac{(4n)^2}{(1+n)^4 - (n-1)^4 \exp(-2x/\Lambda_{abs})} \quad . \tag{5.8}$$

However, this correction is at the 10^{-4} level and was therefore neglected.
Using the refractive index calculated with the respective Sellmeier formula in Eq. 5.7, the reflection factor P is obtained. The measured transmission divided by this factor gives the internal transmission

$$\tau_i = \frac{\tau_m}{P} \quad . \tag{5.9}$$

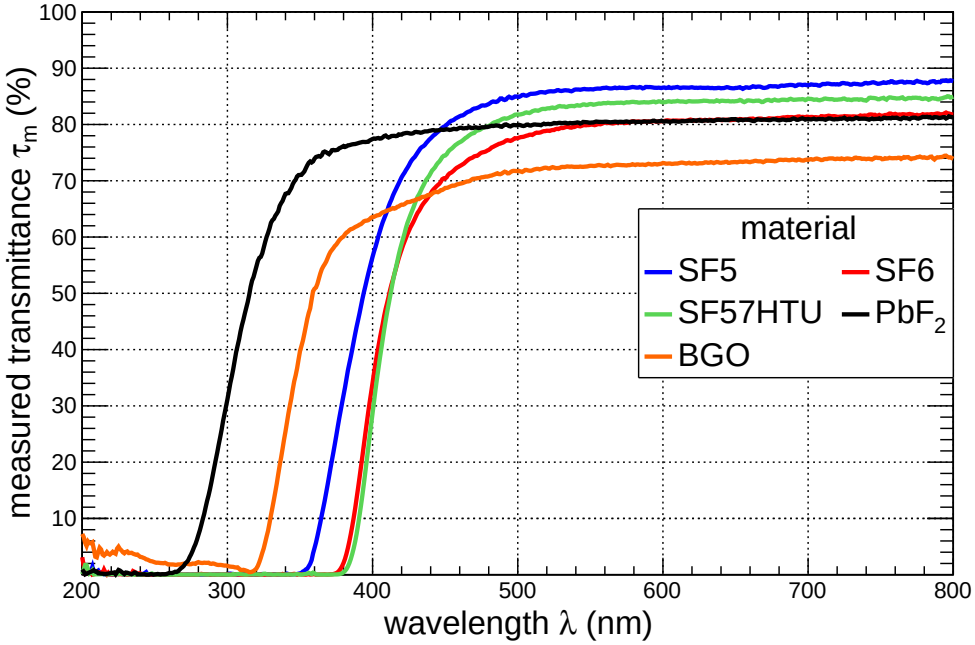

(a) Longitudinal axis

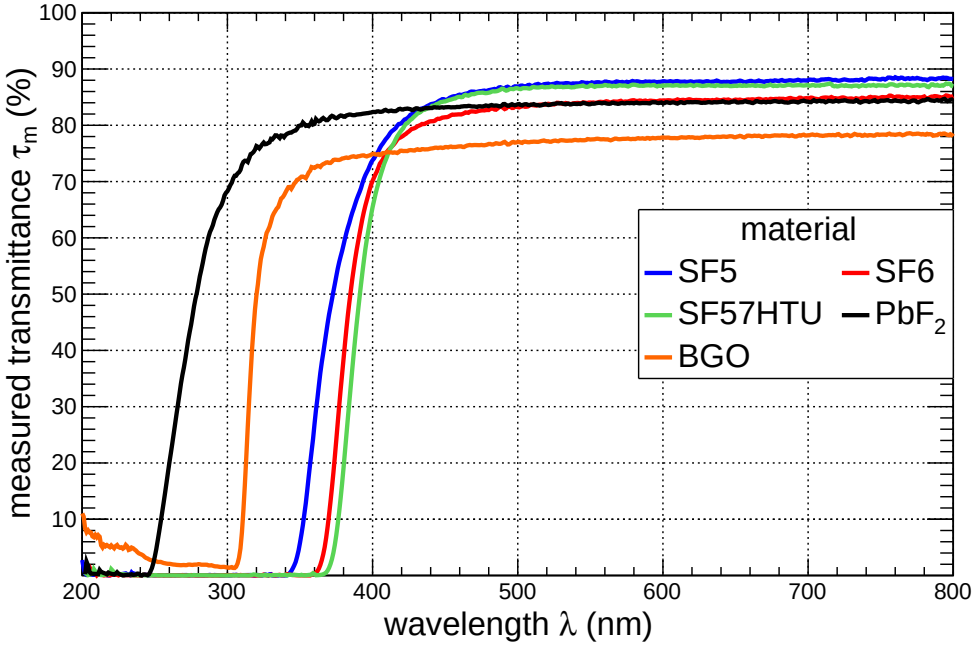

(b) Vertical axis

Figure 5.7.: Measured transmittance of PbF_2, three different PbGl types from Schott, and BGO in the near UV and optical spectrum. All data were taken with the Shimadzu UV-2101PC spectrophotometer and the MPC-3100 large sample compartment attached. The measurements were carried out for a sampling beam going through the longest crystal axis (a) and the shortest (b).

A comparison of measured and internal transmittance for all investigated materials is shown in Fig. 5.8 for a sampling beam going through the longest crystal axis. Compared to the data from a measurement of the shortest crystal axis (see Fig. B.15 of Appx. B.3.2), slightly lower values are achieved due to absorption losses and scattered light that does not reach the integrating

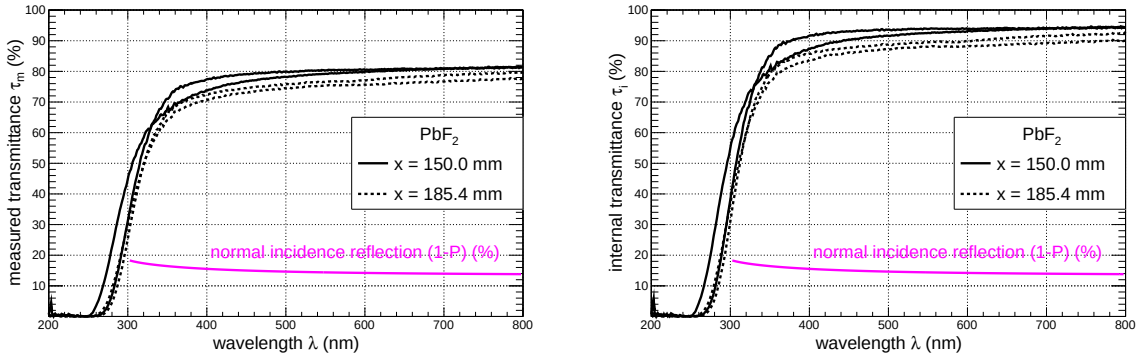

(a) τ_m for PbF_2

(b) τ_i for PbF_2

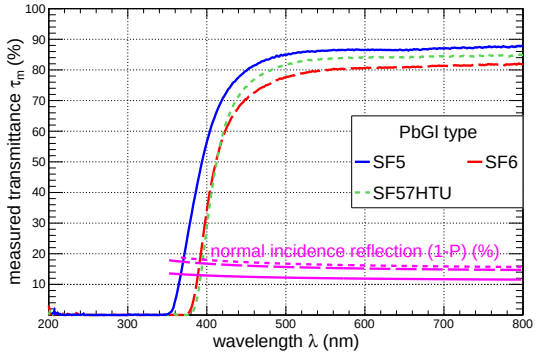

(c) τ_m for PbGl

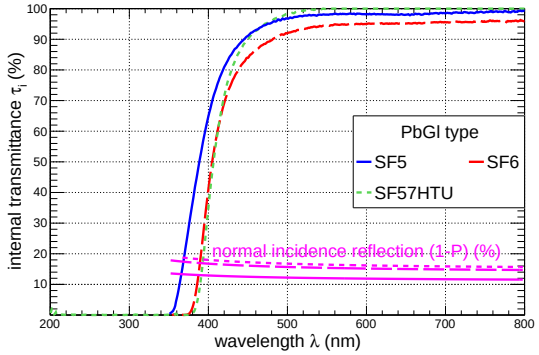

(d) τ_i for PbGl

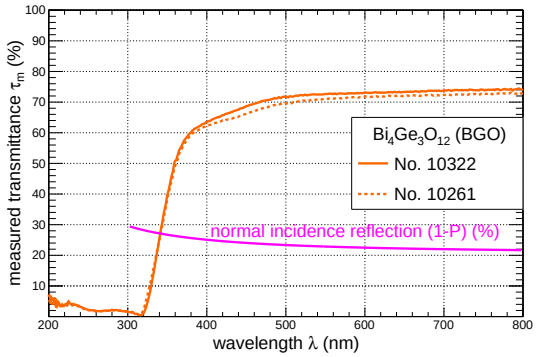

(e) τ_m for BGO

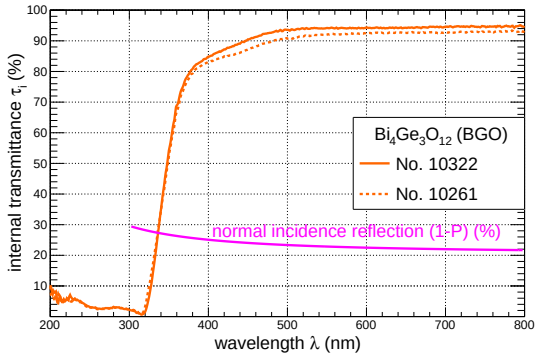

(f) τ_i for BGO

Figure 5.8.: The measured (τ_m) and calculated internal transmittance (τ_i) are shown for the measurements taken with a sampling beam going through the longest crystal axis. The normal incidence reflection ($1-P$) was calculated with the approximation in Eq. 5.7. The internal transmittance is then obtained with Eq. 5.9. For PbF_2 four crystals in two different lengths were analyzed (a–b). For each of the three PbGl types one crystal was analyzed (c–d) and for BGO two crystals of same shape were studied (e–f).

sphere. Nevertheless, for wavelengths above the transmission edges all samples show an internal transmittance better than 90 %.

The absorption length Λ_abs can finally be determined with Eq. 5.5. The results are shown in Fig. 5.9. It can be seen that for PbF_2 the absorption length rises steeply up to a wavelength of $350-400$ nm and is already above 1 m there. This is followed by a slower rise to maximum values between 2 and 3 m. An old data set from the A4 Collaboration is at the same level as the new data.

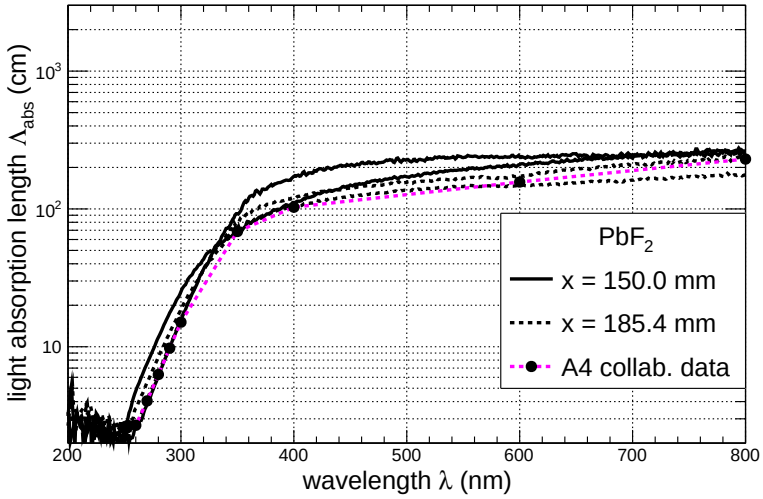

(a) Λ_{abs} for PbF_2

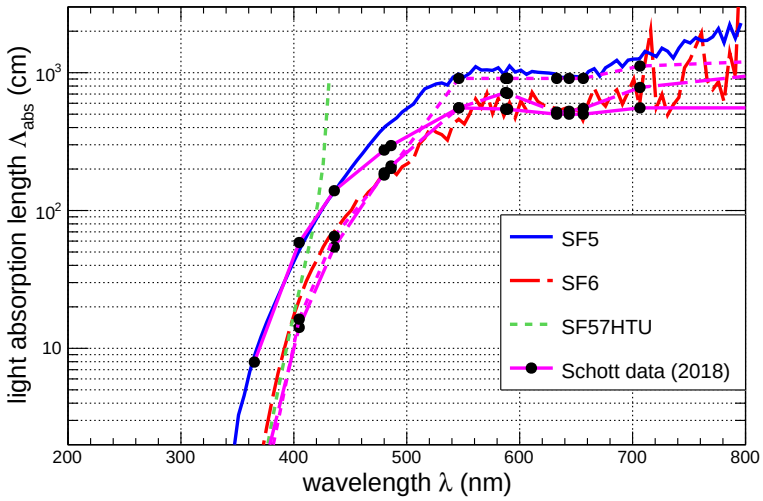

(b) Λ_{abs} for PbGl

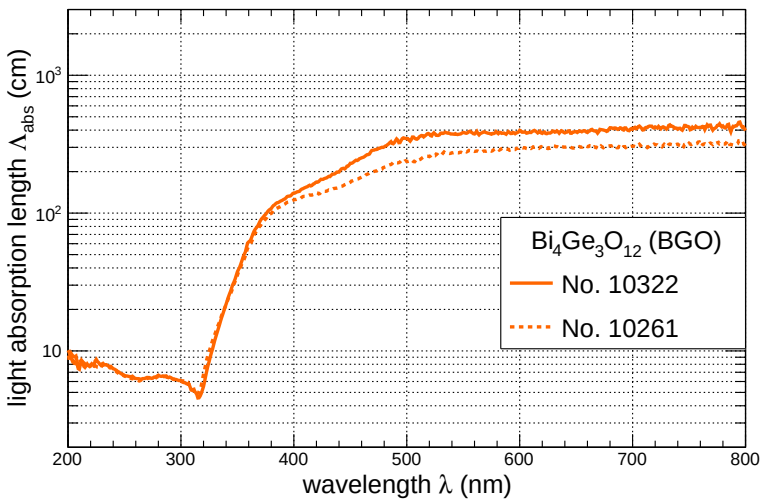

(c) Λ_{abs} for BGO

Figure 5.9.: For representative samples the light absorption length Λ_{abs} was calculated from the internal transmittance with Eq. 5.5. Former data sets for PbF_2 taken by the A4 Collaboration [71] and for the PbGl types calculated from Schott datasheets [141] are shown in magenta.

For the PbGl types a steep rise up to $500-550\,\mathrm{nm}$ can be observed, whereby the absorption length is already several meters long. At 400 nm, the value was only $0.1-0.6\,\mathrm{m}$. For SF5 and SF6 the data taken are in good approximation with the values calculated from the datasheets of the manufacturer. An exception is SF57HTU, where the data taken with the spectrophotometer shows a steeper rise and thus a high absorption length of 9 m at 430 nm already. Here it seems to be that Schott delivered an outstanding sample with better optical properties than an average sample.[2] In the case of BGO, the steep rise at about 380 nm is followed by a slightly slower rise up to 500 nm, before the absorption length remains almost constant at $3-4\,\mathrm{m}$.

5.3. Selection of photomultiplier tubes (PMTs)

The baseline idea is to build a traditional calorimeter, which is why PMTs are considered for light collection. The PMT type must be highly efficient in the expected wavelength range. The Philips (Photonis) XP2900/01 PMTs [146] with $1\,1/8''$ active diameter and 10 dynode stages were considered as first choice. In combination with PbF_2 crystals, they were used by the A4 experiment. Their bi-alkali photocathode has a maximum quantum efficiency at 420 nm and the transmittance of the borosilicate corning $801-51$ window extends below 300 nm, which matches the light spectrum of the PbF_2 radiators. For A4, the PMTs were selected with a minimal cathode corning blue sensitivity of $11\,\mu\mathrm{A/lm}$ and a white sensitivity of $90\,\mu\mathrm{A/lm}$. The typical spectral characteristics, gain curves, and key parameters can be found in Appx. C.3. The XP2900/01 also fits in size and spectral characteristics with the other crystals to be tested. The voltage dividers from Institute de Physique Nucléaire Orsay (IPN) can also be used again and the circuit diagram can be found in Fig. C.4 of Appx. C.3. Both the PMT and the voltage divider have serial numbers (SNs), which are specified in the combination $\mathrm{SN}/\mathrm{SN}_{\mathrm{PMT}}-\mathrm{SN}_{\mathrm{HV\ divider}}$ (e.g. $\mathrm{SN}/12345-678$) for each PMT. Due to the age and the about 10 000 hours in a radiation environment, the damaged PMTs and voltage dividers have to be sorted out. As part of the XVII Mainz Physics Summer Program 2019 together with , an appropriate measuring setup was developed and 25 PMTs were characterized.

Experimental setup and procedure. The bare PMT was placed in a light-tight box with a feed-through for the cables. The voltage was supplied by a CAEN V6533N module and was raised in steps of 50 V from 1 250 to 1 450 V. The PMT signals were amplified by a factor of ~ 80 with a five channel fast pre-amplifier and linear mixer. For each voltage level, data were taken with a CAEN V1742B Switched Capacitor Digitizer until at least 10 000 waveforms were recorded. The digitizer was used in self-triggering mode. The DRS4 sampling rate was set to 2.5 GHz and a record length of 256 data points was chosen. This corresponds to an acquisition window of 102.4 ns. A typical pulse of dark noise is shown in Fig. 5.10. The post trigger has been set to a level, where the pulses mainly occur in the center of the acquisition window. This allows to determine the noise level with the data in the first 20 % of the window. The noise level for each waveform was stored and for a complete run the average noise level and standard

[2] To rule out a possible mix up of materials by Schott, the density of all PbGl blocks was determined. The following values were obtained: $\rho_{\mathrm{SF5}} = 4.07(7)\,\mathrm{g\,cm^{-3}}$ ($\rho_{\mathrm{datasheet}} = 4.07\,\mathrm{g\,cm^{-3}}$), $\rho_{\mathrm{SF6}} = 5.19(14)\,\mathrm{g\,cm^{-3}}$ ($\rho_{\mathrm{datasheet}} = 5.18\,\mathrm{g\,cm^{-3}}$), and $\rho_{\mathrm{SF57HTU}} = 5.48(14)\,\mathrm{g\,cm^{-3}}$ ($\rho_{\mathrm{datasheet}} = 5.51\,\mathrm{g\,cm^{-3}}$)

deviation was calculated. Subtracting these noise levels, the charge of each pulse was determined and recorded in a histogram. The average charge amplitude for each setup was determined by a Landau distribution convoluted with a Gaussian distribution. In addition, with time stamps and event numbers, an average dark count rate was determined from each file.

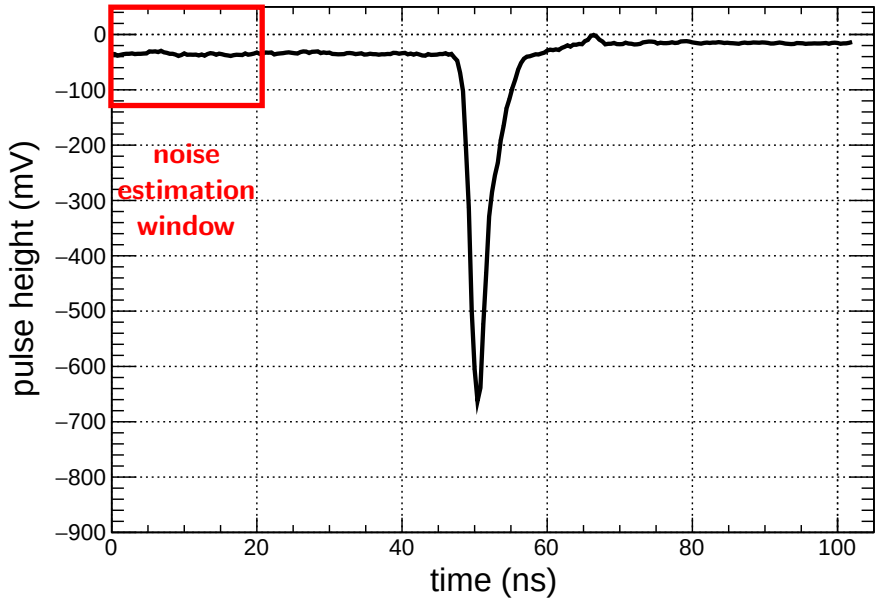

Figure 5.10.: Acquisition window with a dark count pulse. The typical pulses have a rise time of $t_{\text{rise}} < 2\,\text{ns}$ and a fall time of $t_{\text{fall}} \approx 5\,\text{ns}$. The first 20 % of the acquisition window was used for the noise level determination.

Results. The spread of the noise level is exemplarily shown for the PMT SN/26397 − 832 at voltages of 1 250 and 1 450 V (see Figs. 5.11a–b). The one sigma standard deviation is about 0.9 mV for the 1 250 V setup and about 1.3 mV for the 1 450 V setup. For all PMTs the typical values are in the range of up to 2 mV. All waveforms that deviate by more than $2\,\sigma$ from the average are not considered. Most of these contain double pulses. The charge spectra belonging to these two settings (Figs. 5.11c–d) show the increasing charge pulses with a higher voltage. The resolution σ/μ worsens for an increased voltage from 35.4(6) % to 77.9(28) %. This mean value μ corresponds to the charge amplitude for a specific supply voltage. The results for each PMT and the five supply voltages are summarized in Fig. 5.12.

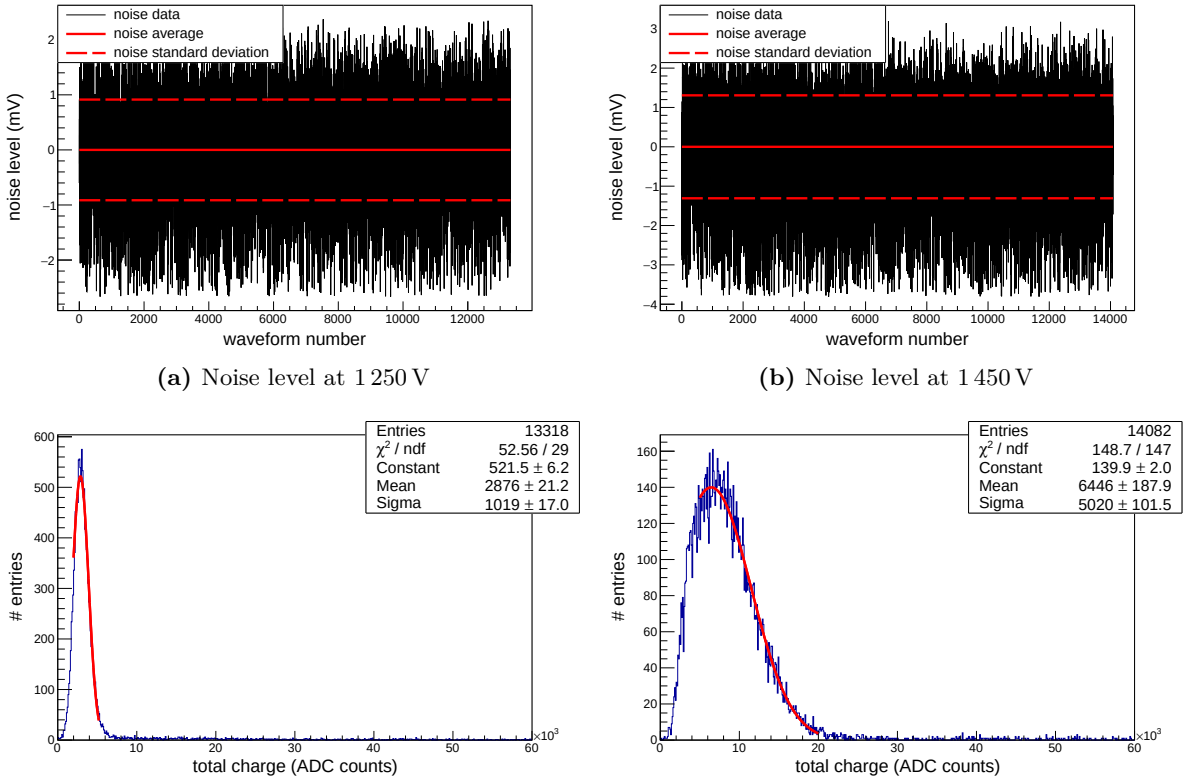

(a) Noise level at 1 250 V

(b) Noise level at 1 450 V

(c) Total charge spectrum at 1 250 V

(d) Total charge spectrum at 1 450 V

Figure 5.11.: Noisel level and total charge spectrum for a PMT voltage of 1 250 and 1 450 V.

In the future experiment, all PMTs should provide the same signal height. PMTs with significantly large (the uppermost red curve) or small amplitudes (the lowest blue curve) can therefore be discarded. By choosing a fixed charge amplitude level for all PMTs (e.g. 4000 ADC counts), individual working voltages can be set, but they are not determined at this point. The two excluded PMTs cannot reach this amplitude level within the operating voltage specified by the manufacturer. Since there are also differences in the quality of the crystals and the crystal–PMT coupling, this calibration is only carried out with the completed modules.[3]

As a second criterium, the dark count rate was monitored (Fig. 5.13). Except for one PMT, an increasing dark count rate for rising voltages was observed. This was expected and is not too severe for most of them. However, if the dark noise reaches the limit of the data acquisition[5] already at a voltage of 1 300 V, this may lead to problems in an experiment like DarkMESA, where the knowledge of all backgrounds is essential. If the dark count rate is high, but the total charge spectrum has the expected shape, these PMTs are set aside as second choice.

In total, the PMTs SN/26097 − 873 and SN/25915 − 802 were discarded due to their too high or

[3] A calibration method using the MAMI electron beam, a radioactive source, or photodiodes has to be developed. The advantage of the MAMI beam would be the reproducible results due to a precise knowledge of the beam energy, resolution, and position. If only one calibration is needed at the beginning this would be optimal. However, it should be noted that due to the long measurement time of DarkMESA, a calibration has to be performed more often. An online calibration method, e.g. by using photodiodes, would be very helpful.

[4] When this measurements were carried out, not all settings of the digitizer were optimal. The biggest limitation was the maximum number of events to be read out in one block transfer, which was set to 1 event/ch. The 1024 events/ch multi-event buffer of this model was not exploited. Therefore the bandwith was reduced and the recording rate was limited to just over 1 kHz.

[5] See footnote 4

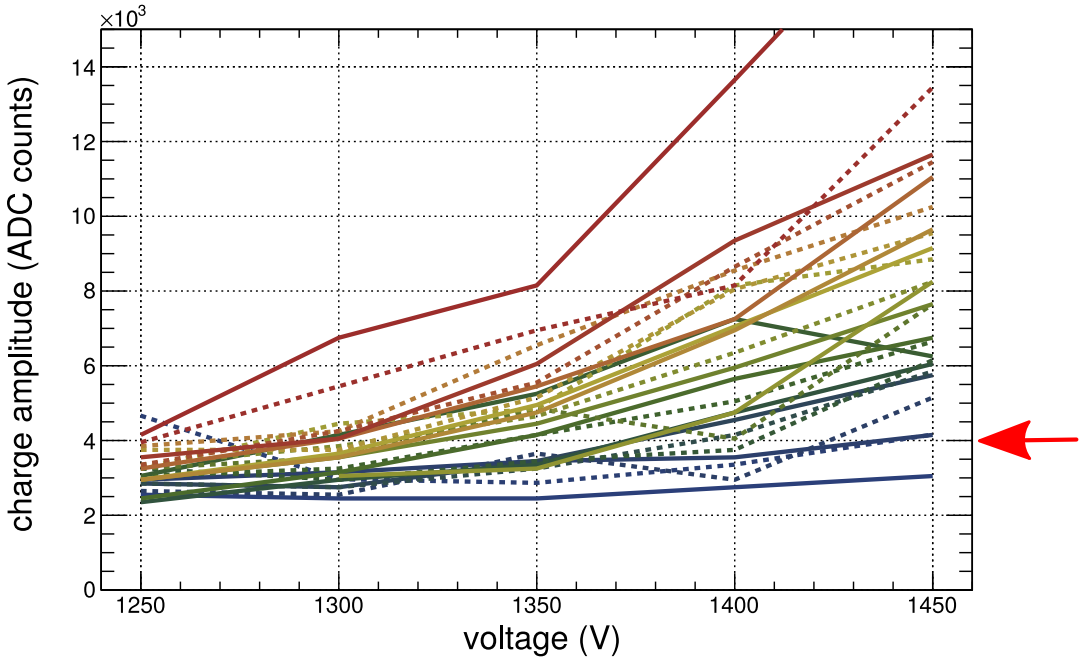

Figure 5.12.: Charge amplitude of dark counts. Each color represents a PMT and the data were taken for five different supply voltages. For the sake of clarity, the data points are not displayed and the designation of the individual PMTs has been omitted. The results and the corresponding serial numbers of PMT and HV divider can be found in Appx. B.3.3. The arrow denotes a possible charge amplitude level at 4000 ADC counts for the determination of a working voltage.

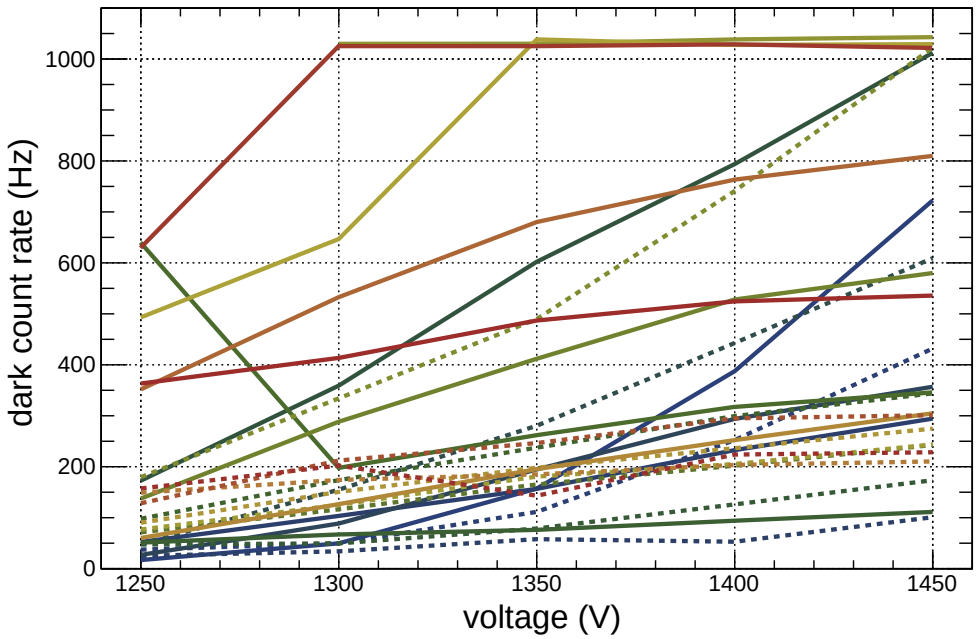

Figure 5.13.: Dark count rate obtained by using the digitizer. Each color represents a PMT and the data were taken for five different supply voltages. For the sake of clarity, the data points are not displayed and the designation of the individual PMTs has been omitted. The results and the corresponding serial numbers of PMT and HV divider can be found in Appx. B.3.3. Due to sub-optimal settings, a limitation at about 1 kHz occurs.[4]

too low charge amplitudes. In addition, PMT SN/26565 − 787 showed an unexpected spectrum with several peaks (see Fig. B.18 of Appx. B.3.3). Due to the high dark count rate, the PMTs SN/26349 − 807 and SN/26335 − 847 were set aside as second choice. This study selected 21 suitable PMTs. In addition, 10 PMTs from a similar, but not so systematic study are selected. This study was carried out beforehand to select suitable PMTs for the first beam-tests at MAMI in 2018. A larger number of PMTs was studied at a fixed PMT voltage of 1 500 V and the ones that delivered dark pulses with same signal height level were selected. This study was carried out only with the afterglow function of an oscilloscope and is less accurate than the analytical method presented before. At that time, it was considered sufficient for the upcoming beam-tests. The PMTs used for the detectors in these beam-tests could have been measured afterwards according to the principle of this section. However, this was not done, as a complete disassembly of the detector prototypes would have been necessary.

5.4. Assembly of calorimeter prototypes

In order to obtain an effective calorimeter, the following requirements must be met during assembly:

- A good coupling between crystal and PMT must be achieved,
- from the produced light the highest possible amount must reach the PMT,
- and ambient light should not be able to reach the PMT.

The best possible light output is obtained if the light can leave the crystal only in the direction of the PMT. In order to reach this ideal scenario, refractions on the other crystal surfaces must be reduced, or the light should be reflected back to the crystal immediately. Therefore, the medium surrounding the crystal should have a low refractive index to obtain a small critical angle θ_{crit} at these transition surfaces. All optical photons that arrive at an angle $> \theta_{\text{crit}}$ are reflected back into the crystal. This can be realized by a crumpled aluminum foil, which allows the combination of the good reflective properties of aluminum with the low refractive index of air. In most of the transition zones an air layer remains between the crystal and the foil (Fig. 5.14b).
An alternative is the wrapping with polytetrafluorethylen (PTFE) tape (Fig. 5.14c). At least three layers of a 0.075 mm thin Teflon® thread seal tape were used.[6] The tight fitting tape allows almost no air layer, but the refractive index is with $1.30 - 1.33$ @ 250 nm well below the values of the prototype crystals [149]. Despite the larger critical angle, total internal reflection is still possible. Due to the superior reflection properties towards aluminum, especially in the UV range, more light is trapped in the crystal [150]. For the beam-tests in this chapter, the crumbled aluminum foil was used.[7]
A good coupling between PMT and crystal must be established on the open side. The light should leave the crystal there, which is why high refraction and low internal reflection is desired. The optical grade silicone grease EJ-550 from Eljen Technology was used for the coupling [151]. The

[6] The thread seal tape is available with a width of 12 or 19 mm in construction markets. The handling of these narrow bands is complicated when detector elements become larger (e.g. scintillator panels). Glass companies also offer PTFE tapes with 50 mm width, such as BC-642 from Saint-Gobain [147]. The filtration solution company Donaldson offers PTFE membranes with custom widths as crystal wrap [148].
[7] For the setup of a multi crystal prototype calorimeter, discussed in Sec. 6.2.1, the second approach was chosen.

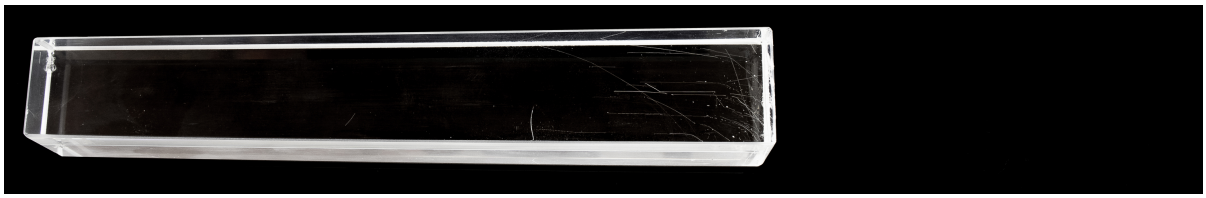

(a)

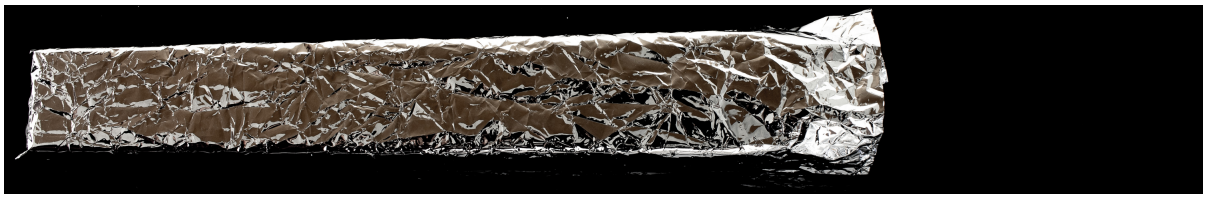

(b)

(c)

(d)

(e)

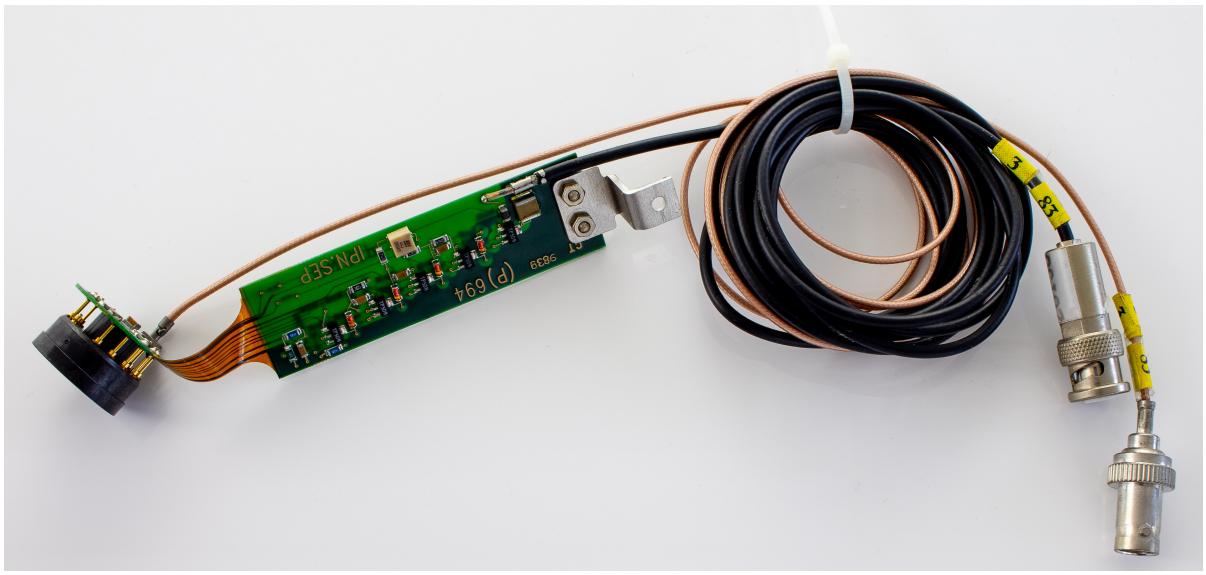

(f)

Figure 5.14.: Assembly process of calorimeter prototypes. The crystal (a) is wrapped with aluminum foil (b) or alternatively with Teflon® tape (c). The PMT is connected with optical grease to the crystal (d) and wrapped in a black light-tight foil (e). The voltage divider (f) is connected to the PMT afterwards.

refractive index ($n = 1.46$) is close to the one of the borosilicate window of the PMT ($n = 1.50$ @ 400 nm). The cut-off wavelength (10 % level) due to the window type lies at 270 nm. The optical grease limits this range negligibly. The transmission of a 0.1 mm thick EJ-550 layer is over 60 % at 285 nm and already above 90 % at 300 nm (see Appx. C.2). To achieve an uniform and stable coupling, the PMT was fixed twice with a light-tight tape running around the entire crystal (Fig. 5.14d). For best possible light tightness, the detector was wrapped in 70 µm thin opaque black foil and the edges were sealed with light-tight tape[8] (Fig. 5.14e).
When testing individual detector prototypes, the voltage dividers (Fig. 5.14f) were connected to the PMTs first. A PVC pipe with 40 mm nominal diameter (DN40) protected the PMT and voltage divider from external influences and also enhances the stability of the crystal–PMT junction (Fig. 5.15).[9] A cable tension relief was also included. For all materials proposed in Sec. 5.2 these prototype detectors were assembled using the Photonis XP2900/01 PMTs.

Figure 5.15.: Ready-to-use single crystal calorimeter prototype detector.

5.5. Electron beam-tests

The assembled calorimeter prototypes were now ready for a characterization. In order to establish the anticipated performance of the Cherenkov radiators experimentally it was necessary to carry out measurements over a range of energies relevant for the DM detection with DarkMESA. Since the results should be comparable, a reproducible experimental environment for all prototypes was foreseen. An initial characterization with cosmic radiation or radioactive sources was not performed, since the disadvantages of these two methods can be avoided with the MAMI electron beam. In comparison to cosmic-rays, the MAMI beam allows high statistics in a short time scale and a precise knowledge of particle type and energy. The divergence of the beam is almost negligible and with an additional trigger detector, also serving as beam position monitor (BPM), the point of impingement on the prototypes can be determined very precisely. Two PbF_2 prototypes (from the A4 experiment at MAMI) in a length of 150.0 and 185.4 mm, three different types (SF5, SF6, SF57HTU) of PbGl (from Schott, Mainz), and a BGO prototype (from the L3 experiment at CERN, now at LNF) were studied with the electron beam. The characterization was focused on the DarkMESA experiment. That is why beside the functional approval of the calorimeter materials, also the directional dependencies and detection thresholds were studied.

[8] 3M® Scotchrap All-Weather Corrosion Protection Tape 50 (250 µm thick)
[9] For the setup of a multi crystal prototype calorimeter, discussed in Sec. 6.2.1, all detectors without voltage dividers are placed in the support structure first. The voltage dividers, together with a 130 µm thick Kapton® pipe for shielding are connected afterwards.

5.5.1. Experimental set-up

Since energies relevant for the DM detection with DarkMESA should be studied, the full energy of MAMI is not necessary. The experimental set-up was placed at an experimental platform located in MAMI hall A, between racetrack mircotron RTM1 and RTM2 (see Fig. 5.16). At the deflection magnet, the electron beam can be extracted with an energy of 14.86 MeV.

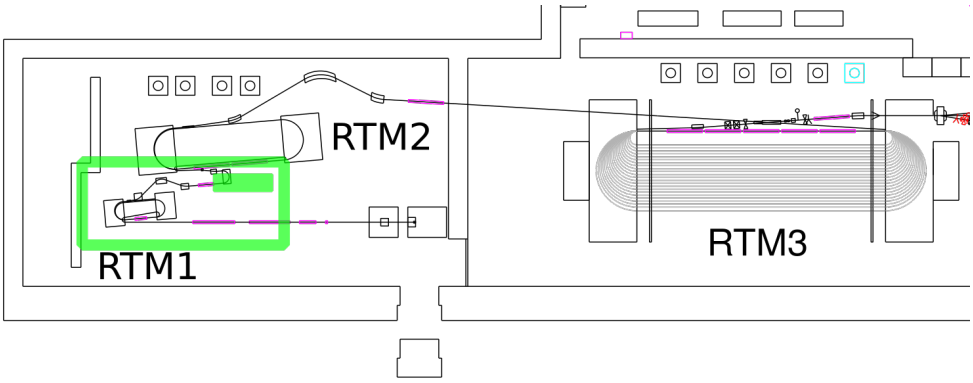

Figure 5.16.: Excerpt of the MAMI accelerator floor plan. The green line (rectangle) marks the location of the experimental setup after RTM1. At the deflection magnet between RTM1 and RTM2, the electron beam can be extracted with an energy of 14.86 MeV. An experimental platform including a beam-dump is available there.

This energy is sufficiently high and can be reduced further with energy degraders in front of the exit beam pipe. An array of six prototype detectors was mounted on a remotely steerable table so that different beam positions and different incident angles of the beam could be realized. The maximum range of motion was 143 mm for the horizontal axis and 98 mm for the vertical axis. A reference position was determined for each detector by using a laser alignment method. For the head-on measurements, the central crystal position was determined, and for the lateral measurements, the front edge of the crystal at central height represented the reference.
The data acquisition was triggered by a position sensitive detector in front of the calorimeter prototypes with a flexible active trigger area: a region-of-interest (ROI) from $0.8 \times 0.8\,\mathrm{mm}^2$ to $13.3 \times 13.3\,\mathrm{mm}^2$ was possible. This detector was made from plastic scintillating fibers of 0.83 mm diameter in two layers for one direction and two further layers in the perpendicular direction. A detailed description of this detector can be found in the Master's thesis of Manuel Mauch [152]. The average thickness of the detector was 2.4 mm corresponding to an energy-loss of 0.5 MeV for the beam electrons.
The intrinsic energy spread of the MAMI beam is $\sigma_\mathrm{B} \leq 0.01\,\mathrm{MeV}$. However, the beam left the vacuum beam pipe through an aluminum flange of 0.2 mm thickness and traversed $\sim 300\,\mathrm{mm}$ of air before hitting the detectors. The resulting energy spread of the beam was simulated and resulted in $0.07 - 0.08\,\mathrm{MeV}$, corresponding to a relative beam energy spread of $\sigma_\mathrm{B}/E_\mathrm{B} \approx 0.5\,\%$. The beam energy variation for different detector setups with different path lengths through air or detector material was found to be small. The multiple scattering in the flange increased the divergence of the 14-MeV beam to $\theta_\mathrm{B} \approx 46\,\mathrm{mrad}$ and the simulation predicted a beam-spot of approximately $x_\mathrm{B} \approx 12\,\mathrm{mm}$ width (full width at half maximum (FWHM) $\varnothing_\mathrm{B} \approx 28\,\mathrm{mm}$) for the head-on position of the detectors and $x_\mathrm{B} \approx 17\,\mathrm{mm}$ width (FWHM $\varnothing_\mathrm{B} \approx 41\,\mathrm{mm}$) for the side-on

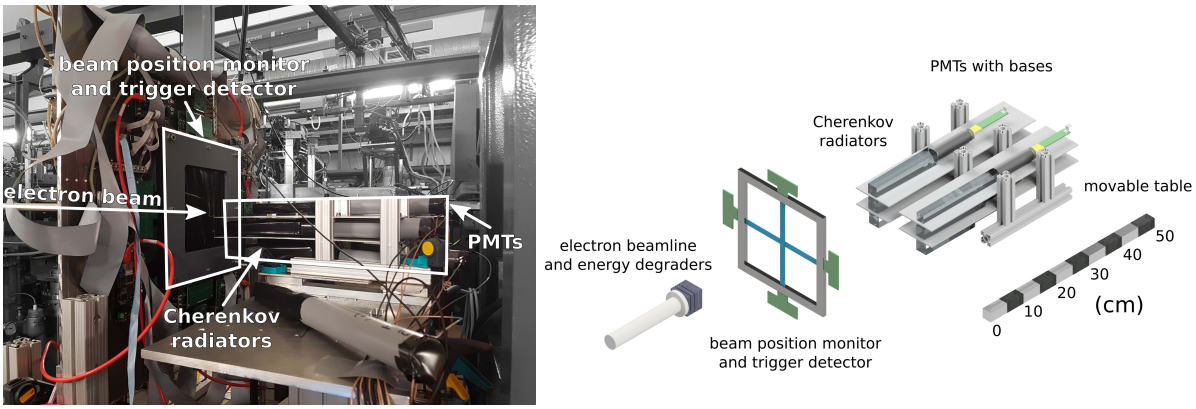

Figure 5.17.: Left: Photo of the experimental setup used for the beam-tests of calorimeter prototypes at MAMI. The electron beam entered from the left and the beam electrons were localized with a position sensitive detector that also provided the trigger signal to read out the prototype detectors. An array of six of such detectors was arranged on a remotely steerable table to realize different beam positions and different incident angles of the beam. Right: Schematics of the setup showing the relative positions of beam exit, energy degraders, crossed fiber layers, and prototype detectors.

measurements.[10]

For the data readout the CAEN V965 QDC in high-gain mode was used. All signals of the Cherenkov detectors were amplified with the Ortec Octal Fast Timing Amplifier 810 by a factor of ~ 100. With this high amplification, the appearance of too large positive signals, which are potentially harmful for the QDC, is possible. That is why the signal baselines were shifted by $-40\,\mathrm{mV}$ with a linear Fan-In-Fan-Out (LeCroy Model 428F [153]). The acquisition window of the QDC was started by a trigger signal of the fiber detector. The length of this window was set to 100 ns with a dual gate generator, which was built by the Physics Institute of the University Bonn. Time differences of the various PMT signals were compensated by delaying the corresponding signal with additional delay boxes and the signals of all Cherenkov detectors could thus be placed inside the gate. The exception are the BGO detectors. Their long signal decay times require a longer gate of 1 µs. Also the large amount of scintillating light did not require the additional amplification and the offset was reduced to $-6\,\mathrm{mV}$.

[10] This is the real MAMI beam-spot without the trigger detector. By adding a ROI as trigger condition, only a section of this beam is used for data acquisition. E.g. in the case of SF5 with a 1×1 ROI in AND logic the beam-spot used for data acquisition can be reduced to $x_\mathrm{B} \approx 6\,\mathrm{mm}$ width (FWHM $\varnothing_\mathrm{B} \approx 13\,\mathrm{mm}$). A summary of beam-spot sizes for different setups can be found in Tab. B.2 of Appx. B.3.5.

5.5.2. Simulation settings for comparison studies

A good simulation and comparison with real beam-time data allows not only the prediction of results but also the optimization of the detectors. For a replacement of the PMTs or geometrical changes to the radiators, the corresponding components do not have to be bought and tested in several versions: a thoroughly optimized version is sufficient.
In the simulation, the electron beam was generated just before an aluminum flange and, depending on the setup, passed through plastic absorbers and the fibers of the trigger detector. The ROI and the trigger logic could be set. All these components could be moved around the prototype detector in such a way that the real beam-test conditions were well met. The prototype detector itself consisted of a 20 µm reflective aluminum foil and a 1 mm air layer, surrounding the detector material, with a gap for the PMT. The borosilicate window of the PMT was simulated as a 2 mm thin disk. The radiators were always constructed as `G4Trd` objects in the simulation environment. The dimensions were set according to Tab. 5.1 and 5.2. In the case of the PbGls, this was only an approximation. There were edge damages or uneven cast side surfaces (Fig. B.13 of Appx. B.3.1). Also the BGOs had broken corners (Fig. B.14 of Appx. B.3.1), which were ignored in the simulated geometry. The detailed implementation can be found in Sec. 3.3.
All necessary materials were defined in `BDXConstruction::DefineMaterials` (Appx. B.3.4). Their optical properties were set via the `G4MaterialPropertiesTable`. In particular the properties in Tab. 5.5 were assigned to the materials and the specific values are summarized in Tab. B.1 of Appx. B.3.4. Differences when using absorption lengths from datasheets or transmittance measurements were found to be small.

		material							
		air	**foil**	**PMT**	**PbF_2**	**BGO**	**SF6**	**SF5**	**SF57HTU**
property	**RINDEX**	✓	✗	✓	✓	✓	✓	✓	✓
	ABSLENGTH	✗	✗	✓	✓	✓	✓	✓	✓
	REFLECTIVITY	✗	✓	✗	✗	✗	✗	✗	✗
	FASTCOMPONENT	✗	✗	✗	✗	✓	✗	✗	✗
	FASTTIMECONSTANT	✗	✗	✗	✗	✓	✗	✗	✗
	SCINTILLATIONYIELD	✗	✗	✗	✗	✓	✗	✗	✗
	QUANTUMEFFICIENCY[11]	✗	✗	✓	✗	✗	✗	✗	✗

Table 5.5.: Material properties set in the `G4MaterialPropertiesTable`. For the beam-time studies in this chapter an aluminum foil and a borosilicate PMT window were used. The detailed values can be found in Tab. B.1 of Appx. B.3.4.

In addition to these properties, the surface properties of the materials were implemented in the `Geant4` simulation according to the principle described in Sec. 3.3. The effects of the `polish` factor on the light output are shown in Fig. 5.18. All surface settings are summarized in Tab. 5.6.

[11] This property was not included in the `G4MaterialPropertiesTable`, but the values could be calculated with the self build `BDXSteppingAction::calc_PMTefficiency(G4double wavelength)` function. Depending on the optical photons wavelength and the result of a multi-sided dice flip a 0 or 1 was returned.

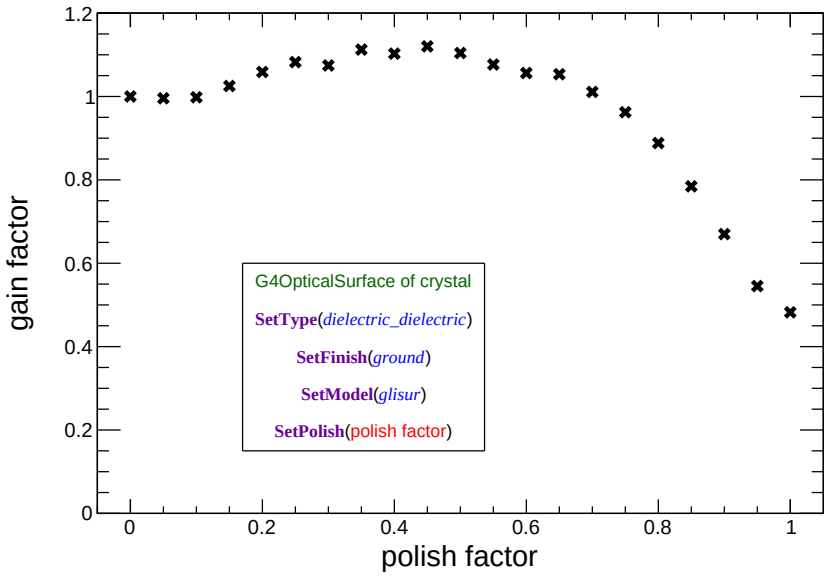

Figure 5.18.: Change in simulated light output for a rising surface roughness. Exemplarily shown for a SF5 crystal with the dimensions from the 2018 electron beam-tests (Tab. 5.2). In the `glisur` model with `ground` finish, a polish factor of 1.0 meant maximum roughness. A perfectly smooth surface (`polish` = 0.0) did not lead to the maximum light output.

	type	finish	model	polish
air [12]	dielectric_dielectric	polished	glisur	—
aluminum foil	dielectric_metal	ground	glisur	0.95
PMT window	dielectric_dielectric	ground	glisur	0.90
PbF_2	dielectric_dielectric	ground	glisur	0.93
BGO	dielectric_dielectric	ground	glisur	0.93
SF6	dielectric_dielectric	ground	glisur	0.93
SF5	dielectric_dielectric	ground	glisur	1.00
SF57HTU	dielectric_dielectric	ground	glisur	1.00

Table 5.6.: Settings for all optical surfaces used in the simulation of the 14-MeV MAMI beam-time.

In the `glisur` model with `ground` finish, a `polish` factor of 1.0 meant maximum roughness. A perfectly smooth surface (`polish` = 0.0) did not lead to the maximum light output. With `ground` finish and a `polish` factor between 1.0 and 0.7, the light output increased steadily and almost linearly. In addition to the optical examination of the surfaces, the chosen factor also included other properties. The age of the crystals, individual damage points, or the coupling of the PMT varied from detector to detector. That is why the `polish` factors had been slightly adjusted based on the beam-time data.

[12] No differences were found between the settings `ground` and `polished` for the surface finish of the air volume.

PbF_2 and BGO were the best polished crystals. SF6 had cast edges, but the best polished surface among the PbGls. The same polish value of 0.93 was set for all three. SF6 compensated the slightly worse surface by being brand new. In contrast, PbF_2 and BGO had suffered radiation damage for several years. The barely polished PbGl types SF5 and SF57HTU received a polish factor of 1.0. The surrounding aluminum foil was very smooth, but to create an air gap between crystal and foil, the foil was crumpled. Therefore, a polish factor of 0.95 was assumed for the aluminum foil. The PMT's glass window was estimated to have a value of 0.90.
Without additional absorbers, 100 000 or 1 000 000 primary electrons were simulated depending on the trigger logic and ROI. With additional plastic absorbers, this value was increased up to 5 900 000 for sufficiently high statistics.

5.5.3. Data processing

For the data evaluation, the measured QDC values were histogrammed first. It was still very common to have trigger signals without signals in the acquisition window. These events accumulated in the so called "Pedestal peak" and corresponded to a signal charge of zero. The mean of this peak was set to a QDC charge of 0 pC and the other QDC values were shifted accordingly. In the high-gain mode one QDC channel equals 200 fC. This conversion was performed and the histogram entries were normalized by the total number of events.
The measured signal peaks did not always correspond to a Gaussian curve, but were often asymmetrical. For both, measured and simulated data, the (asymmetric) distributions of the signals q in the spectra were fitted with a Crystal Ball function [154], which has a Gaussian part to describe the peak region and a power-law part on the low-energy side of the peak:

$$f(q;\alpha,n,E,\sigma_E) = \begin{cases} \exp(-\frac{(q-E)^2}{2\sigma_E^2}), & \text{for } \frac{q-E}{\sigma_E} > -\alpha \\ A\cdot(B-\frac{q-E}{\sigma_E})^{-n}, & \text{for } \frac{q-E}{\sigma_E} \leqslant -\alpha \end{cases} , \tag{5.10}$$

with $A = (n/|\alpha|)^n \cdot \exp(-|\alpha|^2/2)$ and $B = n/|\alpha| - |\alpha|$, where α, n, E, and σ_E are parameters which were fitted to the data. The relative peak width σ_E/E was determined by the width of the Gaussian component. In the measured spectra, noise was present near the pedestal at $q < 50$ pC corresponding to signals of $1-2$ photoelectrons. By limiting the fit range, the noise at small charges did not affect the extraction of the fit parameters. The uncertainties in the parameters originating from the fit were in general smaller than 1 pC.

5.5.4. Reference run with BGO prototype

Since it was not yet clear whether and how much light the Cherenkov radiators generate at an electron beam energy of 14 MeV, the basic function of the measurement setup was tested with a scintillating BGO crystal first. With a high light yield in the order of $8\,000 - 10\,000$ photons/MeV [155], a clear signal peak was expected even at the low beam energy of 14 MeV and no additional signal amplification was required. Due to the long signal decay time of 300 ns, a well-spaced gate with a length of 1 µs was chosen. For a good coverage of the 4096 available QDC channels, a PMT voltage of 1 400 V was selected. In order to record a sufficient amount of data, a trigger area of 5×5 fibers was chosen. Together with the MAMI beam current, this

corresponded to a trigger rate of about 2 kHz.
For a measurement without beam, only the pedestal peak at QDC channel 416 was visible. This is the baseline of the following BGO measurements and the corresponding channel was set as 0 pC. The detector was moved in 4 mm steps around the previously determined detector position and 90 s measurements with beam switched on were carried out. The results of the measurement of a horizontal axis going through the vertical center are shown in Fig. 5.19.

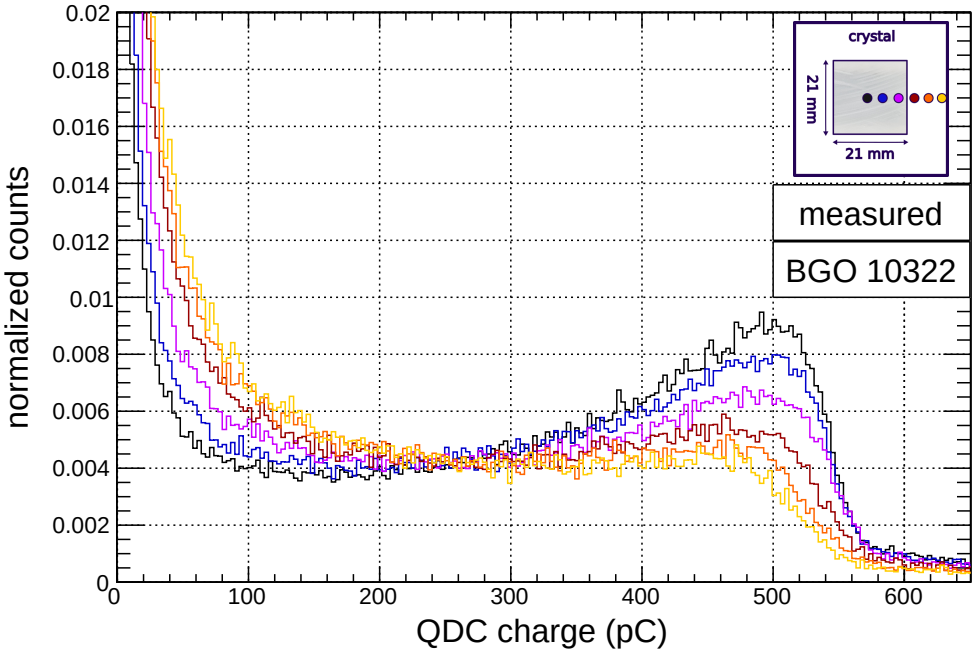

Figure 5.19.: Measured signals from a BGO detector for a 14-MeV electron beam entering the front face of the radiator at different positions with respect to the center as indicated in the insert. The FWHM of the beam was $\varnothing_B \approx 28$ mm, reduced to $\varnothing_B \approx 10$ mm with the trigger condition of the fiber detector.

A clear signal peak is visible for the central beam positions (black and blue) at about 500 pC. The height of this peak decreases towards the edge and when crossing the edge it disappears almost completely. Due to the reduced coverage of MAMI beam-spot and detector, the average deposited energy decreases and the noise events increase.
Due to a difficult comparability of these results with the other detectors, a conversion of the QDC charge into detected photoelectrons and a simulation was not performed at this point.

The functionality of the experimental setup was proven by the clear signals of the BGO detector. For the following measurements of the Cherenkov radiators, uniform basic settings should be found first.

5.5.5. Evaluation of basic settings

First some basic settings were evaluated in order to find the optimal settings for the comparison runs of the Cherenkov detector prototypes. The evaluated settings in this section are the pedestal peak position and with it the PMT high voltage setting for an optimal exploitation of the 12-bit QDCs range. Spectra for rising event rates (Wehnelt voltage) were taken and finally the impact of the ROI, defined by the trigger logic of the fiber detector, was evaluated.

Pedestal and PMT HV settings. The pedestal peak arises from trigger events, where the incident electron did not leave a signal in the crystal. Only the background noise was recorded in this case. In order to distinguish these signals from possibly very small real signals, it was necessary to record a pedestal without real signals. The MAMI beam was off and using a 10 kHz pulser[13] as random trigger for the readout of the PMT signals, spectra of the pedestal peak were recorded for all PbGl detectors at once in only 30 seconds. For the Schott SF5 prototype the spectra in Fig. 5.20 were obtained for PMT voltages from 1 200 to 1 500 V.

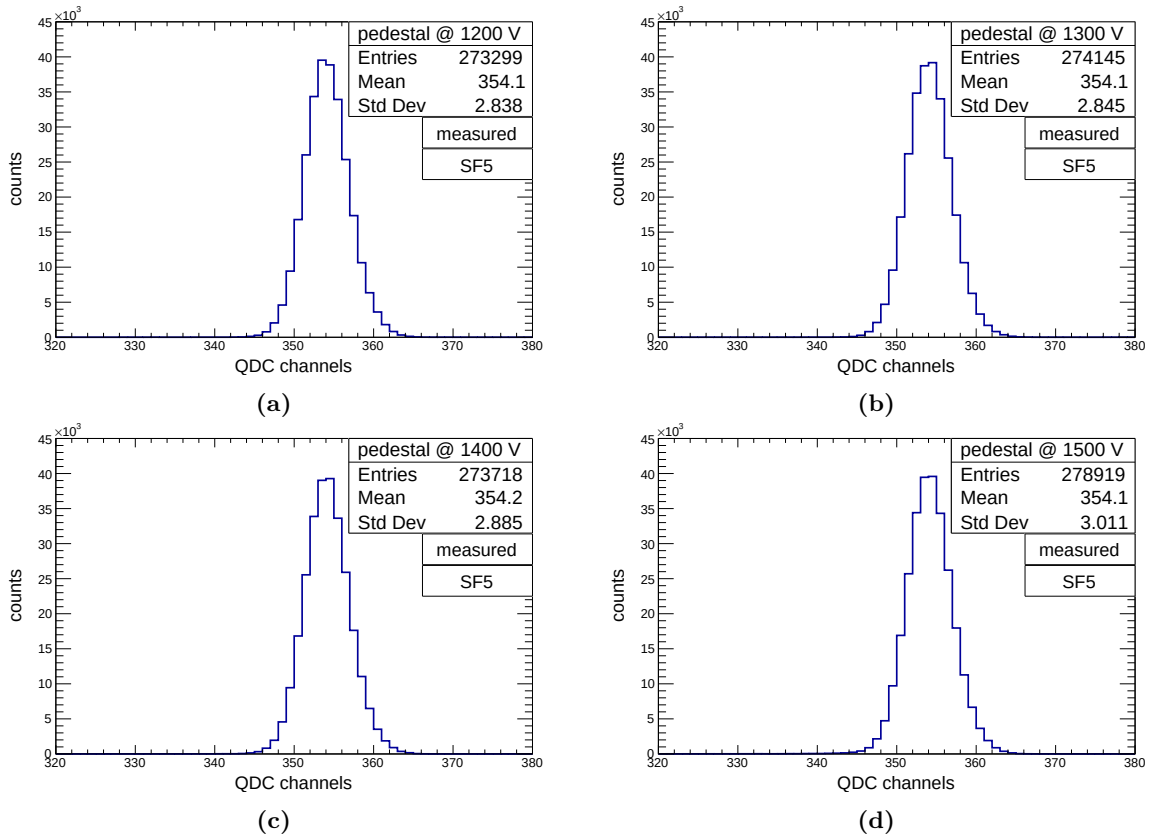

Figure 5.20.: Measured pedestal peak for the Schott SF5 detector at PMT voltages between 1 200 and 1 500 V. No shift in the peak position is visible and the pedestal peak broadens only slightly for higher PMT voltages.

The peak position was at QDC channel 354 and did not change during the four settings, but as expected with rising PMT voltage the peak slightly broadens from 2.8 to 3.0 QDC channels. The pedestal peak positions of the other PbGl detectors can be found in Fig. 5.21.
The PbF_2 measurements were carried out during the first beam-time in July 2018 and no pulser was available for the pedestal runs at that time. So the detector was triggered by the random background events of the fiber detector. Obviously these events were not so frequent and even with longer measurement times, only low statistics was acquired. The peak position was found at QDC channel 503, but the peak width for different voltages was not studied with this setup. No differences compared to the PbGl detectors were expected.

[13] The LeCroy IP-2 Instapulser® with a pulse duration of 5 ns and an amplitude of 2.5 V was used [156].

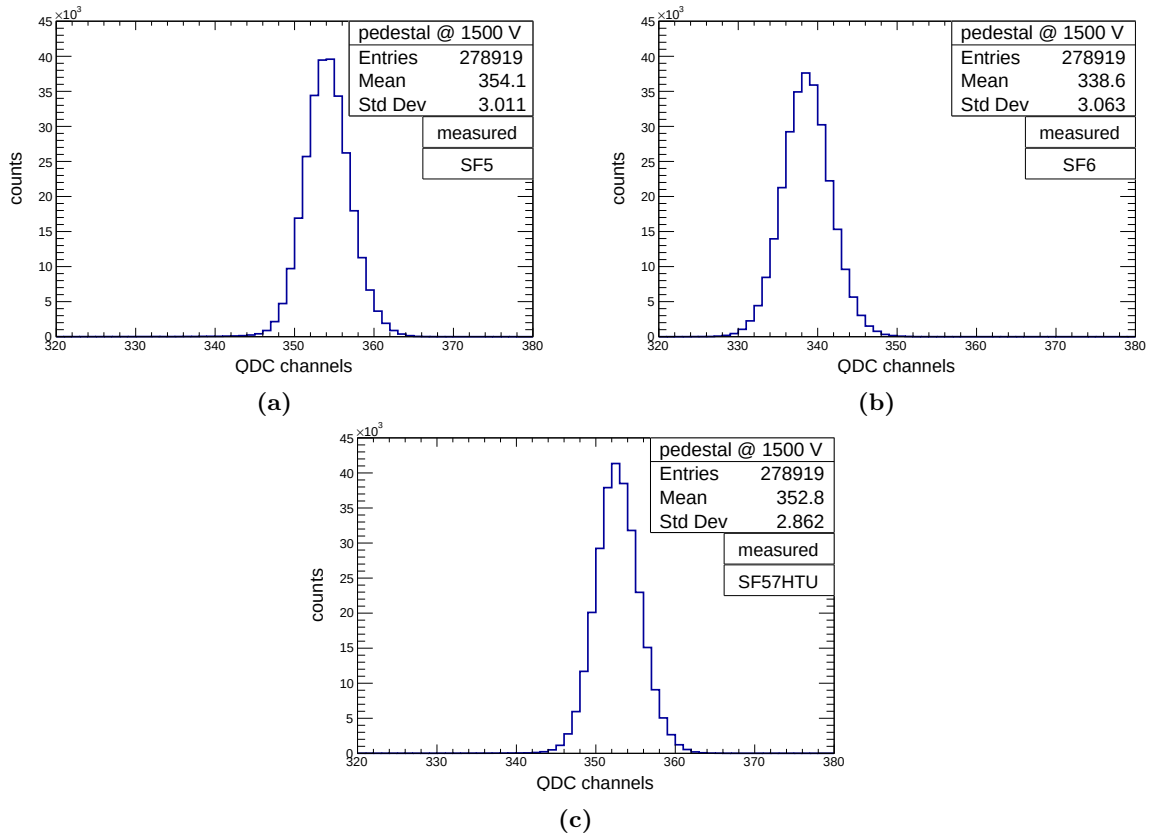

Figure 5.21.: Measured pedestal peak for PbGl detectors of type Schott SF5 (a), SF6 (b), and SF57HTU (c) at a PMT voltage of 1 500 V.

For the next steps the MAMI beam of 14-MeV was turned on. For each detector the PMT voltage was raised in the allowed working boundaries and the QDC spectra were recorded. These spectra should now cover as many of the QDC channels as possible without going into the overflow. The Ortec FTA810 amplifier was used for all Cherenkov prototypes and for a PMT HV of 1 500 V a good coverage of the QDC range was achieved (see Fig. 5.22). With this settings signals up to a charge of 747 pC[14] could be measured.

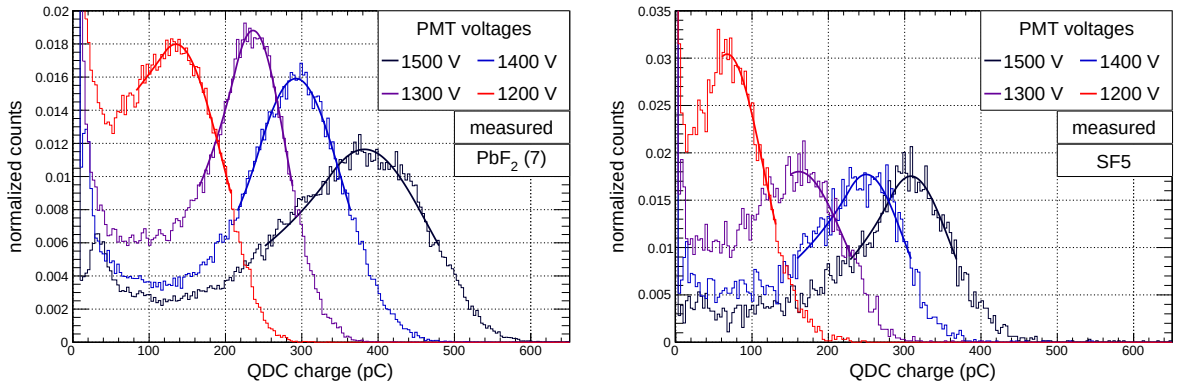

Figure 5.22.: Scan of PMT supply voltages. QDC charge spectra for PbF_2 (left) and Schott SF5 (right). The signal peaks were fitted with the Crystal Ball function.

[14] The full range of the QDC covers $4096 \times 200\,\text{fC} = 819.2\,\text{pC}$, but the pedestal value narrows the range to 747 pC. With an optional offset the full range is available again.

Wehnelt voltage scan. The MAMI accelerator uses Wehnelt cylinders for adjusting the beam intensity and focusing. A Wehnelt cylinder is an electrode with a slightly negative voltage compared to the injectors cathode. Electrons can leave the Wehnelt cylinder through a small opening at the bottom. Thus, the beam current can be set via an adjustable negative potential: the Wehnelt voltage. A translation from voltage to PMT signal rate for the following measurements is given in Tab. 5.7. An optimal beam current should be set to provide sufficient statistics within a reasonable amount of time. Since DarkMESA will be operated at low rates, the Wehnelt voltage should not be set to a level where high rate effects have an influence on the measurement. In this study, runs at different Wehnelt voltages were performed, exemplarily shown for Schott SF5 in Fig. 5.23 and PbF_2 in Fig. 5.24.

Wehnelt voltage (V)	**measured rate (Hz)**
-15.0	16
-13.0	284
-12.6	1 331
-12.4	2 850
-12.2	6 212
-12.0	12 757

Table 5.7.: Measured rates for the Wehnelt voltage (beam current) scan of PbF_2 (7) shown in Fig. 5.24.

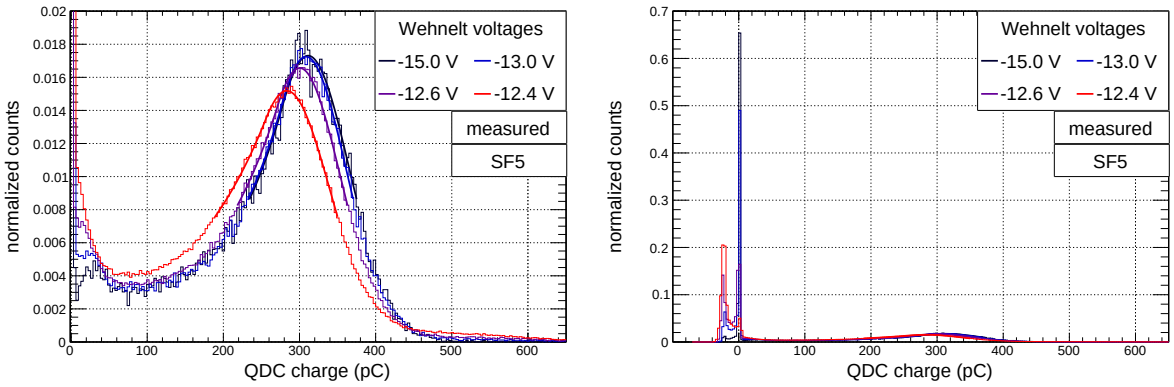

Figure 5.23.: Wehnelt voltage (beam current) scan. QDC charge spectra for Schott SF5 with a 3 × 3 ROI. Zoomed out view on the right shows the shift of baseline for higher beam currents. The signal peaks were fitted with the Crystal Ball function.

The electron beam hits the front surface of the radiators centrally. In both cases there is no large shift of the signal peak for Wehnelt voltages up to −12.6 V (1.3 kHz). At higher rates, the peak migrates to lower QDC charge values, but this is not due to a lower amount of deposited energy. When looking at the pedestal peaks in the zoomed out views in the right plots of Fig. 5.23 and 5.24, one sees a second peak forming left of the original pedestal peak. This peak increases with the rate and is a second pedestal peak. More and more signals have this baseline and therefore the signal peak moves further to the left. But why does this happen only for higher rates? Looking at the typical pulse shape of the PMT signals in Fig. 5.10 one sees that the baseline is slightly shifted upwards after the pulse. It takes a certain time for the PMT to reach the previous

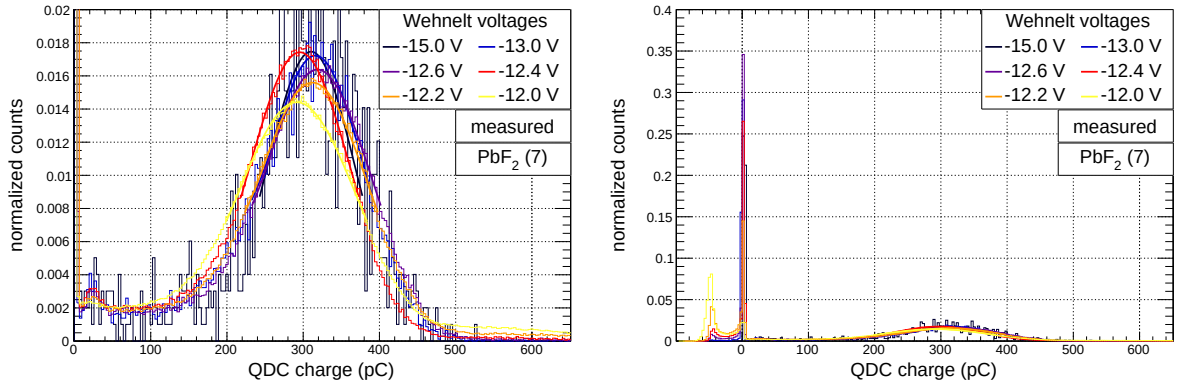

Figure 5.24.: Wehnelt voltage (beam current) scan. QDC charge spectra for PbF_2 with a 5×5 ROI connected in an OR logic. Zoomed out view on the right shows the shift of baseline for higher beam currents. The signal peaks were fitted with the Crystal Ball function.

baseline level again. With a higher rate in more and more cases the next PMT signal is so close to the prior one, that the baseline is still at this lower level. This leads to the recording of lower QDC charge values and thus to the observed behavior. In order to exclude these high-rate effects, a Wehnelt voltage of $-12.8\,\mathrm{V}$ was selected in the following series of measurements.

Region-of-interest (ROI) scan. In the next data runs the ROI covered by the fiber detector was studied. With its 32 fibers arranged in two crossed layers the maximum possible ROI is $16 \cdot d_{fiber} \times 16 \cdot d_{fiber} = 176.4\,\mathrm{mm}^2$ large. For a trigger signal, at least one fiber in each of the two layers must respond and the signals of both layers are AND-ed. By reducing the number of fibers in this trigger logic the ROI can be reduced. This reduction should allow a more precise position scan of the detectors, but on the other hand a too small ROI increases the amount of time needed for a run with sufficient high statistics. For the SF5 prototype this measurement was carried out for three ROI sizes. The QDC spectra are shown in the left plot of Fig. 5.25.

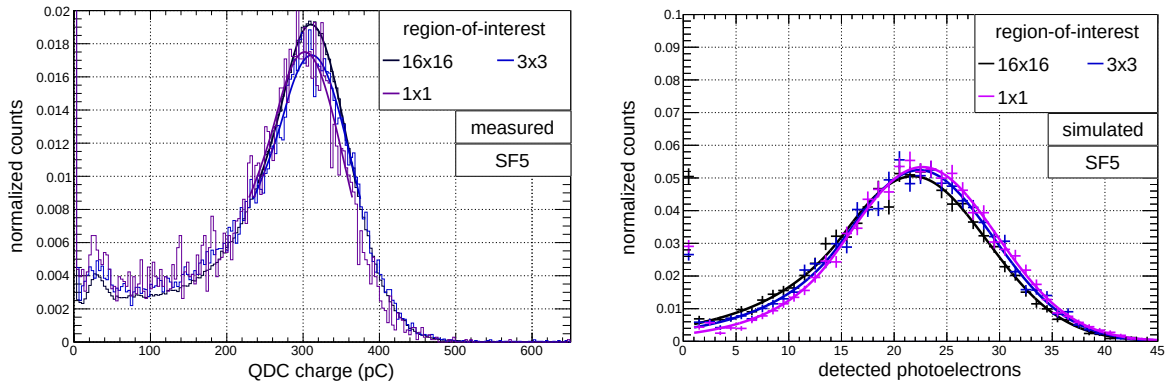

Figure 5.25.: ROI scan. Measured (left) and simulated (right) signals from the Schott SF5 detector for a 14-MeV electron beam entering the front face of the radiator. The signal peaks were fitted with the Crystal Ball function.

There are no differences in the position and shape of the signal peaks. The low statistics of the single fiber per layer ROI, especially compared to the 256 times larger ROI for 16 fibers per layer, is obvious. The simulation study in Fig. 5.25 on the right also shows that the signal peaks for all three ROI settings are close to each other. However, there is a slight tendency for the average signal height to be lower for larger ROIs. This effect can be understood even better if

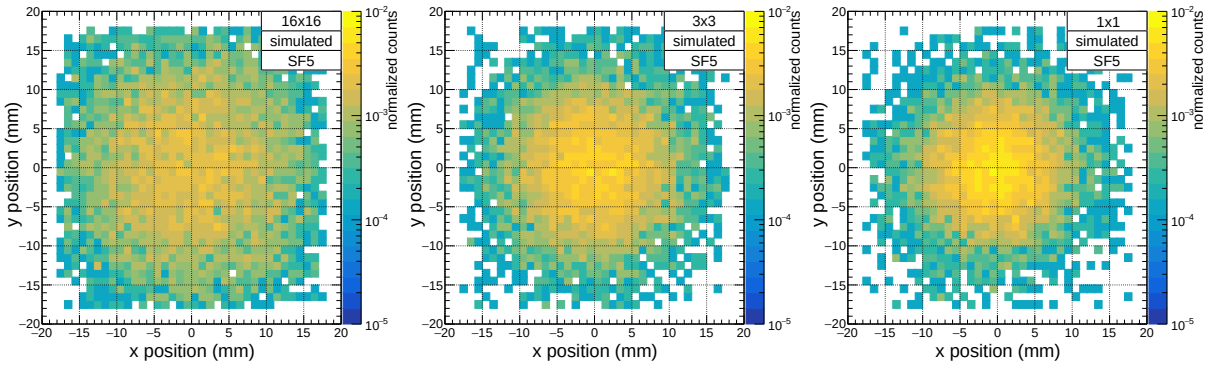

Figure 5.26.: Hitmaps of the simulated signals from the Schott SF5 detector for a 14-MeV electron beam entering the front face of the radiator. They are shown for a ROI of 16 × 16 (a), 3 × 3 (b), and 1 × 1 (c) in AND logic.

one looks at the hitmaps in Fig. 5.26. For the largest 16 × 16 ROI, the beam-spot with a FWHM of 20.16 mm is so large that several events occur in the corners of the detector, equivalent to a lower light output. For a 3 × 3 ROI, the beam-spot reduces to a FWHM of 15.09 mm and the 1 × 1 ROI can improve the FWHM to 13.35 mm even further. Due to the arising problems of higher rates, measurements with the 1 × 1 ROI and sufficient high statistics are not feasible. As a compromise in all following measurements the 3 × 3 ROI is used. The Wehnelt voltage scan for a 3 × 3 ROI (Fig. 5.23) showed no differences compared to the 1 × 1 ROI scan (Fig. 5.27).

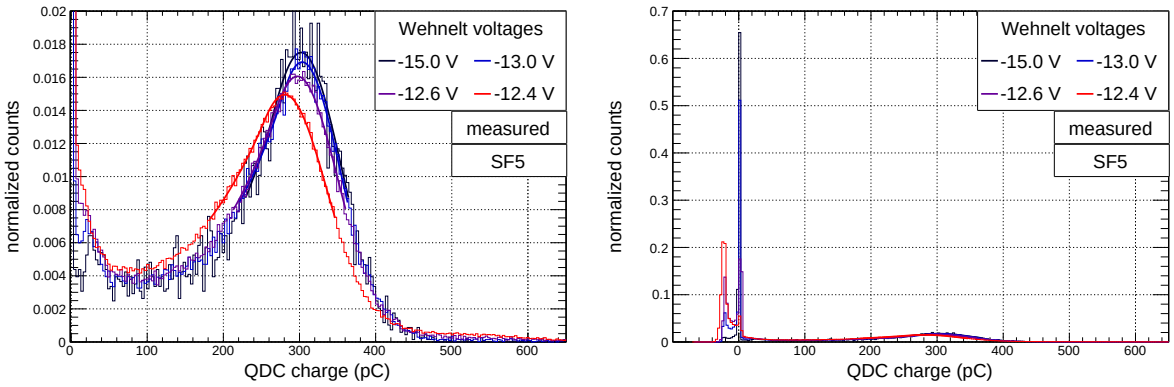

Figure 5.27.: Wehnelt voltage (beam current) scan. QDC charge spectra for Schott SF5 with a 1 × 1 ROI. Zoomed out view on the right shows the shift of baseline for higher beam currents. The signal peaks were fitted with the Crystal Ball function.

The differences in beam-spot size are not significant and the nine times larger ROI leads to a distinct reduction of measurement time. As a result of these preparatory studies, all the following measurements of the December 2018 beam-time were carried out with

- a PMT voltage of 1 500 V,
- a Wehnelt voltage of −12.8 V,
- and a 3 × 3 ROI in AND logic.

The data sets for PbF_2 were recorded during the July 2018 beam-time with different settings. Unless otherwise specified, for PbF_2 a Wehnelt voltage of −13 V and a 3 × 3 ROI in OR logic was used. A hitmap of the crucial change to an OR logic is shown in Fig. B.19 of Appx. B.3.5.

5.5.6. Response to a head-on 14-MeV electron beam

With the settings from the previous Sec. 5.5.5, the investigation of the calorimeter materials was started systematically. The detection properties of a head-on 14-MeV electron beam were studied first. With a laser alignment during the beam-time preparation, the approximate center positions of the individual detectors were already known. This method could not provide mm accuracy due to constraints resulting in a lack of space. The MAMI beam was not perfectly optimized and left the beam pipe under a certain angle during the second part of the July 2018 beam-time. For these reasons, the centers were determined experimentally. Based on the positions determined with the laser, the horizontal and vertical axes of the detectors were scanned in 4 mm steps and pulse height spectra were recorded. Both, the PbGl and the PbF_2 detectors, showed clear signal peaks for 14-MeV electrons entering the front face of the radiators, well separated from the noise. Even small displacements of the signal peaks could be resolved. For each axis a movement of the peak could be observed. When moving the remotely steerable table from left to right or top to bottom, the average pulse height increased steadily up to a certain point where it started to decrease steadily. The table positions with the maximum pulse heights were thus defined as the center of the crystal. The accuracy of the determined center was ± 2 mm. For PbF_2, SF6, and SF57HTU there were only small deviations of 4 mm compared to the laser measurement, and 8 mm for SF5.

The measured results of the three types of PbGl detectors and two PbF_2 detectors for a 14-MeV electron beam pointed at the center positions are shown in the left plot of Fig. 5.28. The PbF_2 detectors showed higher signals compared to the PbGl detectors. The largest pulse heights were found for PbF_2 (1), which had a smaller active volume compared to PbF_2 (7). Among the PbGl detectors of approximate the same shape and size, Schott SF5 performed best, followed by SF6, and SF57HTU. For SF5, the position and the slope of the absorption band between 330 and 370 nm is favorable for Cherenkov radiation, for SF57HTU the emission of Cherenkov light is restricted. The corresponding simulated signals in number of photoelectrons are shown in Fig. 5.28 on the right and the same sequence as for the measured signals was found. The number of produced Cherenkov photons increases quadratically with decreasing wavelength (Fig. 5.2a). Thus the higher light output for PbF_2 compared to the PbGl types was expected, because the transmission edge was found to be up to 100 nm deeper in the UV spectrum (Sec. 5.2.2).

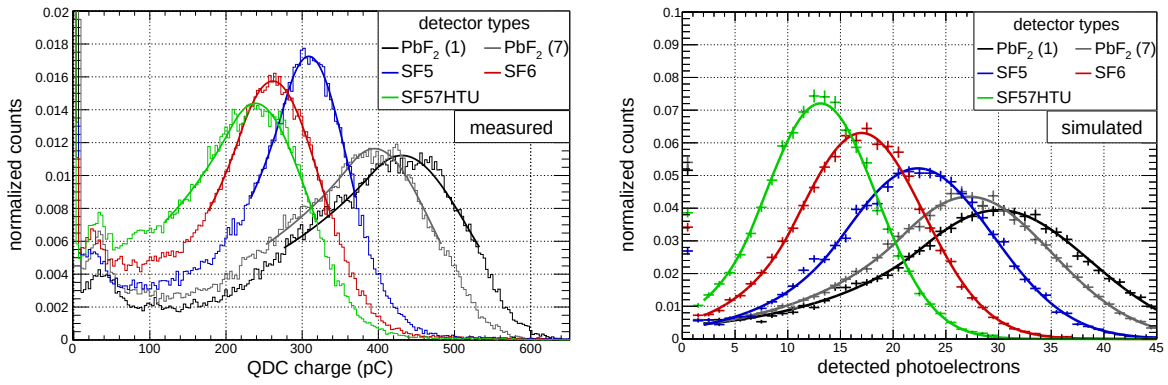

Figure 5.28.: Measured (left) and simulated (right) signals from three different types of PbGl detectors and a PbF_2 detector for a 14-MeV electron beam entering the front face of the radiators. The signal peaks were fitted with the Crystal Ball function.

Starting from the pre-determined centers, a beam-spot scan over the front faces of the radiators was performed. Due to the positioning of the crystals in the six detector array and the limited range of motion of the table, only parts of the surface were scanned. A good homogeneity in the center regions was found and for the following study it was decided to scan only the interesting edge area. For PbF_2 (7) a vertical (Fig. 5.29a) and a horizontal (Fig. B.20 of Appx. B.3.5) axis next to the center position were scanned.[15] Scans over the corners were performed for the PbGl types (Figs. 5.29b–d). The above restrictions in table movement led to the use of different corners.

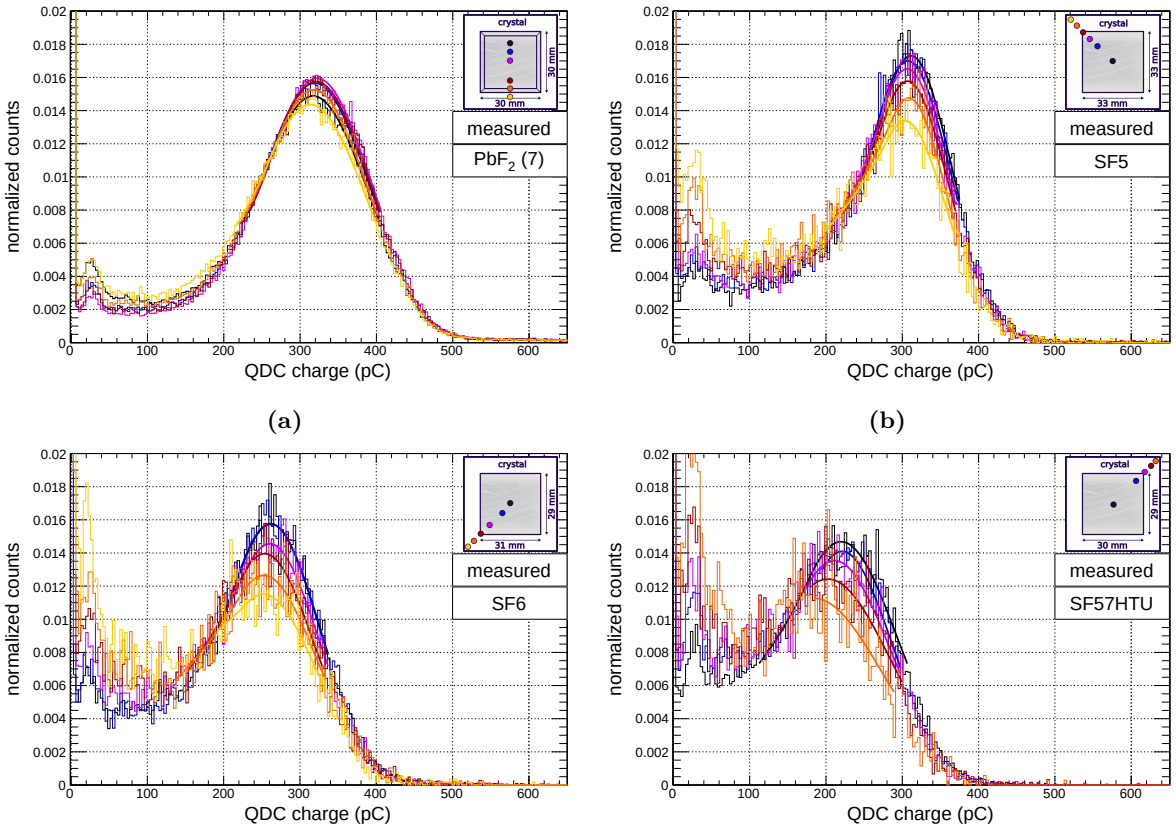

Figure 5.29.: Measured signals from a PbF_2 detector (a), and PbGl detectors of type Schott SF5 (b), SF6 (c), and SF57HTU (d) for a 14-MeV electron beam entering the front face of the radiator at different positions with respect to the center as indicated in the insert. The FWHM of the beam was $\varnothing_B \approx 28\,\text{mm}$, reduced to $\varnothing_B \approx 11\,\text{mm}$ (PbF_2) and $\varnothing_B \approx 15\,\text{mm}$ (PbGl) with the trigger condition of the fiber detector. The signal peaks were fitted with the Crystal Ball function.

In all four cases the mean QDC charge decreases slightly when moving the beam-spot to an edge or corner. When going beyond this point, the decrease becomes even stronger and a low-energy tail develops from the peak. Despite the slightly larger ROI, the uncertainty in the hit location is smaller for the PbF_2 than for the PbGl measurements, since the PbF_2 detector was closer to the fiber detector than the PbGl detectors. The trigger events without calorimeter signals or only dark count pulses increase and lead to the higher entries in the low-energy region of the spectra. This behavior was also observed in the simulated results in Fig. 5.30.

[15] This PbF_2 data was taken with a higher Wehnelt voltage of $-12.4\,\text{V}$ and a 5×5 ROI in AND logic. Also the MAMI beam was not perfectly optimized at that time. The data illustrates the edge effects of PbF_2 but is not suited for a direct comparison with the other materials.

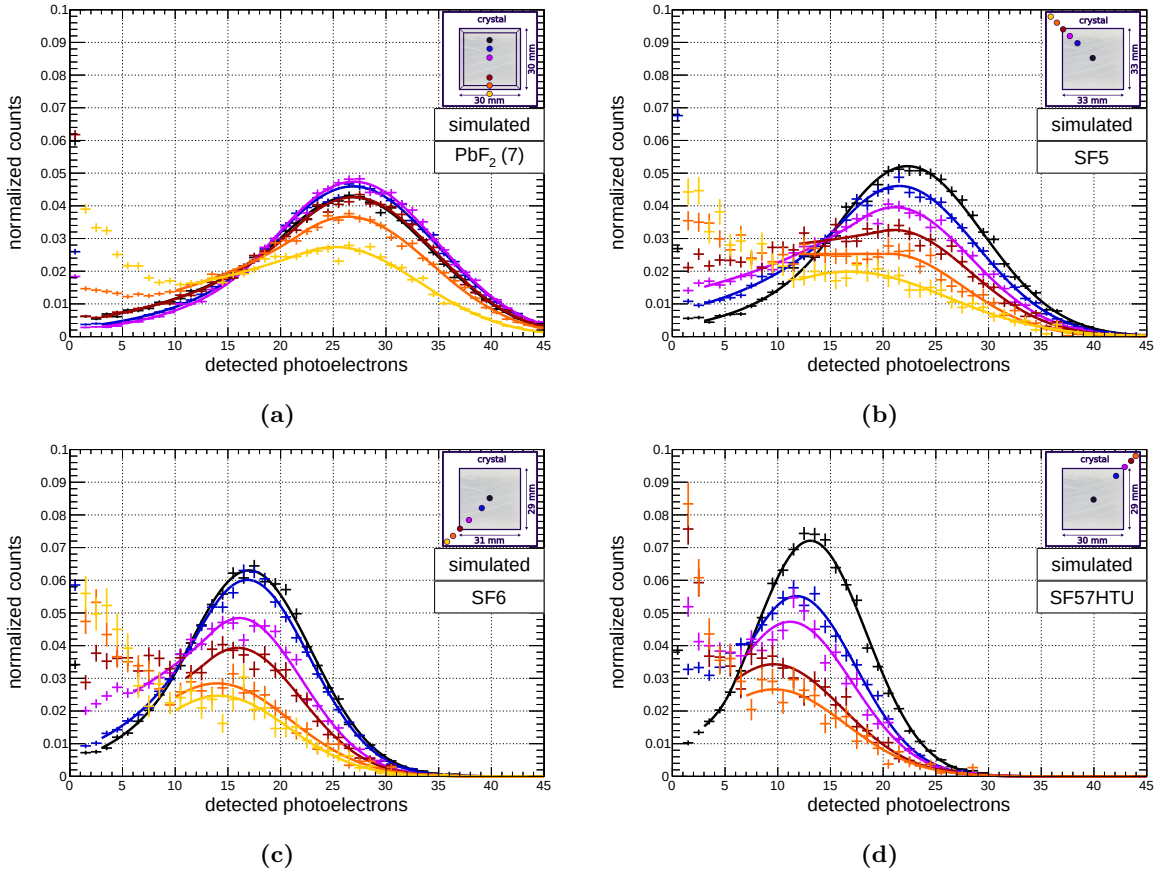

Figure 5.30.: Simulated signals from a PbF_2 detector (a), and PbGl detectors of type Schott SF5 (b), SF6 (c), and SF57HTU (d) for a 14-MeV electron beam entering the front face of the radiator at different positions with respect to the center as indicated in the insert. The FWHM of the beam was $\varnothing_B \approx 28\,mm$, reduced to $\varnothing_B \approx 11\,mm$ (PbF_2) and $\varnothing_B \approx 15\,mm$ (PbGl) with the trigger condition of the fiber detector. The signal peaks were fitted with the Crystal Ball function.

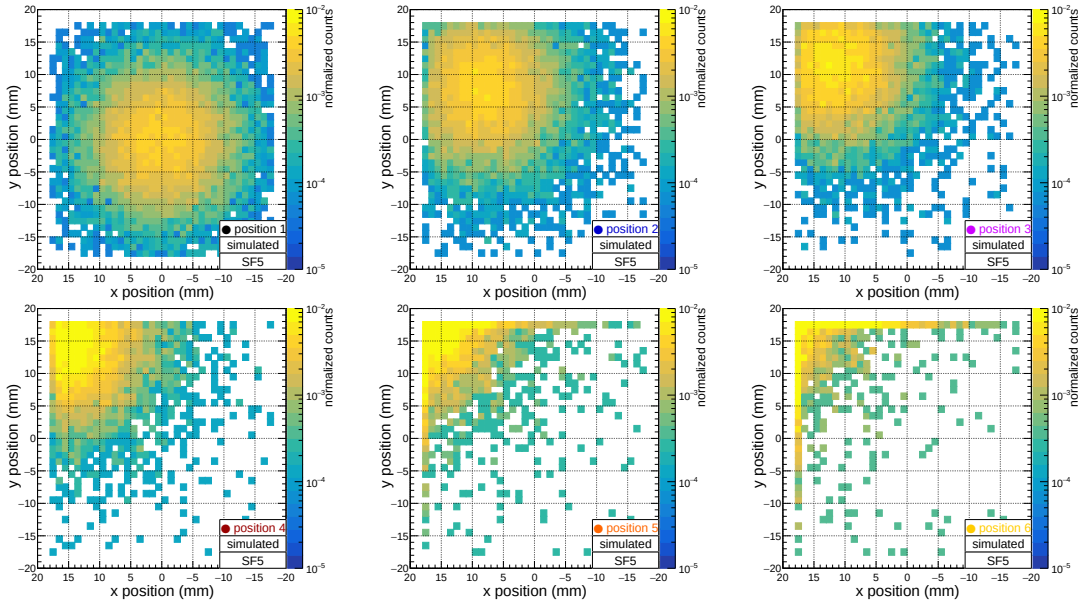

Figure 5.31.: Hitmaps of the simulated signals from the Schott SF5 detector for a 14-MeV electron beam entering the front face of the radiator at the positions measured during the corner scan.

The motion of the peak for the edge scan of PbF_2 was not as strong as for the PbGl types, since the proportion of the beam-spot on the crystal surface was not reduced as fast as with the corner scans. See Fig. 5.31 and Figs. B.21–B.23 of Appx. B.3.5.

5.5.7. Response to a side-on 14-MeV electron beam

Beam-spot scans over the side faces of the detectors were used to study their response in comparison to a head-on beam. This is especially important for Cherenkov radiators as their light is emitted in forward direction with respect to the electrons.
The detectors were rotated by 90° and due to their material density and thickness, the electron beam energy was still completely deposited inside of the crystals. The pulse height spectra for different positions on the horizontal axis, going through the vertical center of the photocathode, were analyzed. A position close to the PMT should be measured for all detectors. Almost the entire length of the PbGl detectors could be scanned. As the length of the PbF_2 (7) detector with 185.4 mm is longer than the maximum possible horizontal motion of the xy-table, no measurement was carried out in the front area in that case. All measurements in Fig. 5.32 show an increase in the average QDC charges when approaching the PMT.

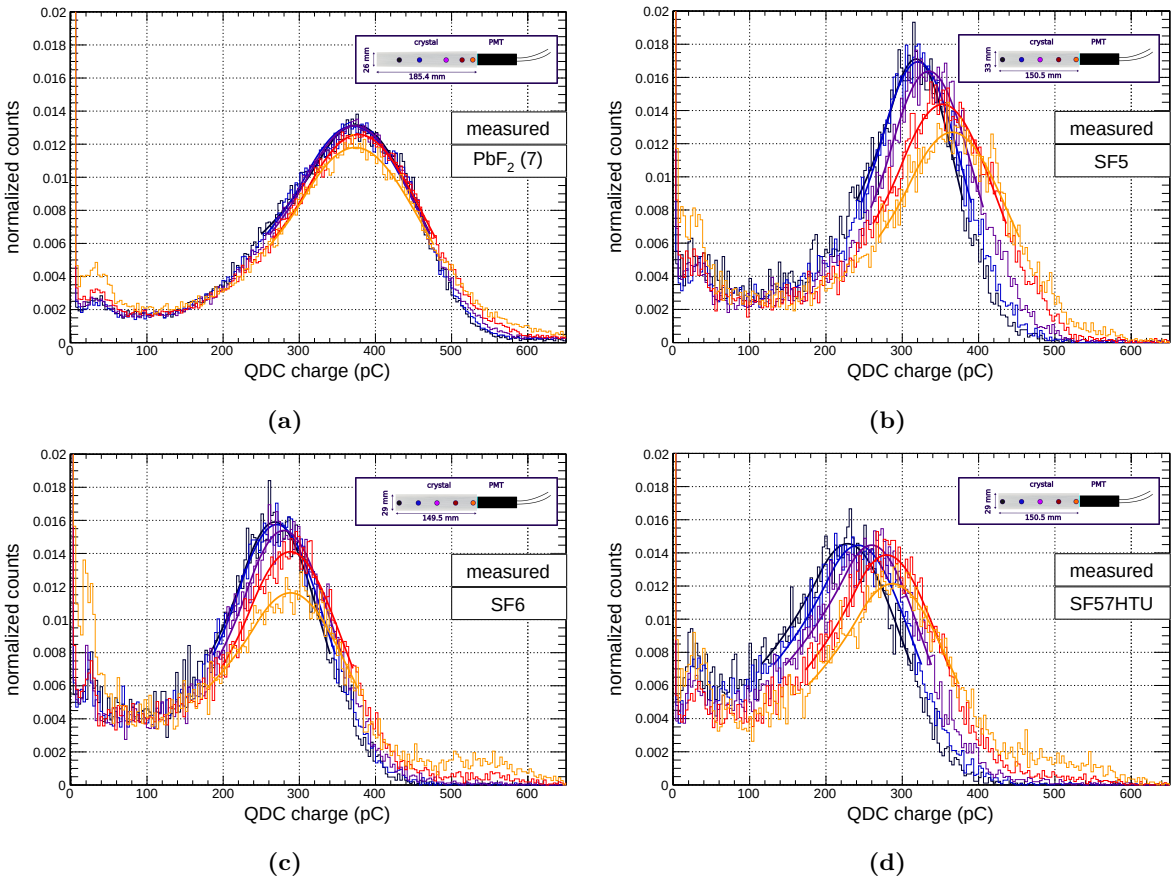

Figure 5.32.: Measured signals from a PbF_2 detector (a), and PbGl detectors of type Schott SF5 (b), SF6 (c), and SF57HTU (d) for a 14-MeV electron beam entering a side face of the detector at different distances to the PMT face as indicated in the insert. The FWHM of the beam was $\varnothing_B \approx 41$ mm, reduced to $\varnothing_B \approx 37$ mm (PbF_2) and $\varnothing_B \approx 34$ mm (PbGl) with the trigger condition of the fiber detector. The signal peaks were fitted with the Crystal Ball function.

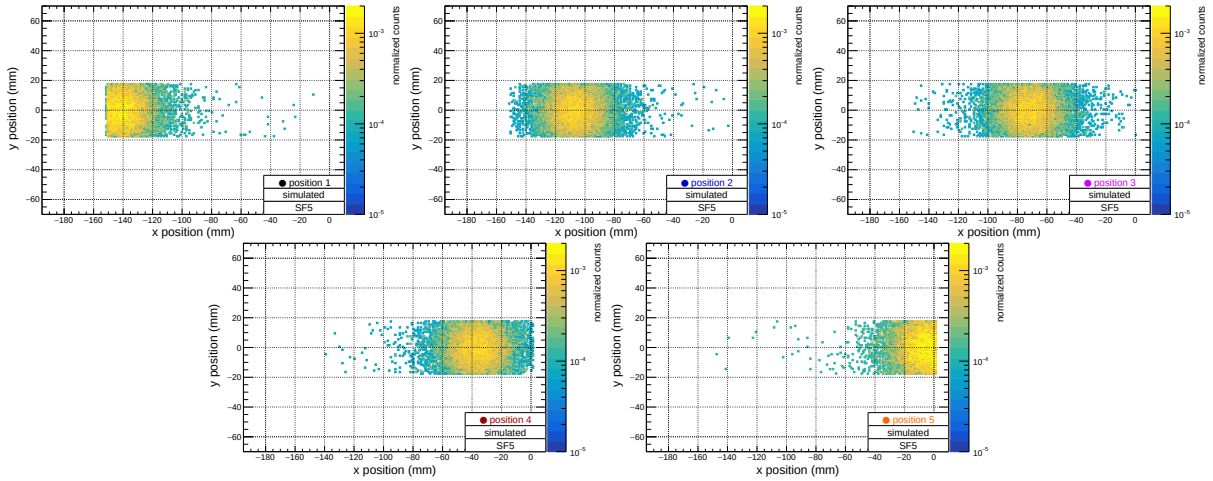

Figure 5.33.: Hitmaps of the simulated signals from the Schott SF5 detector for a 14-MeV electron beam entering the side face of the radiator at the positions measured during the 90° scan.

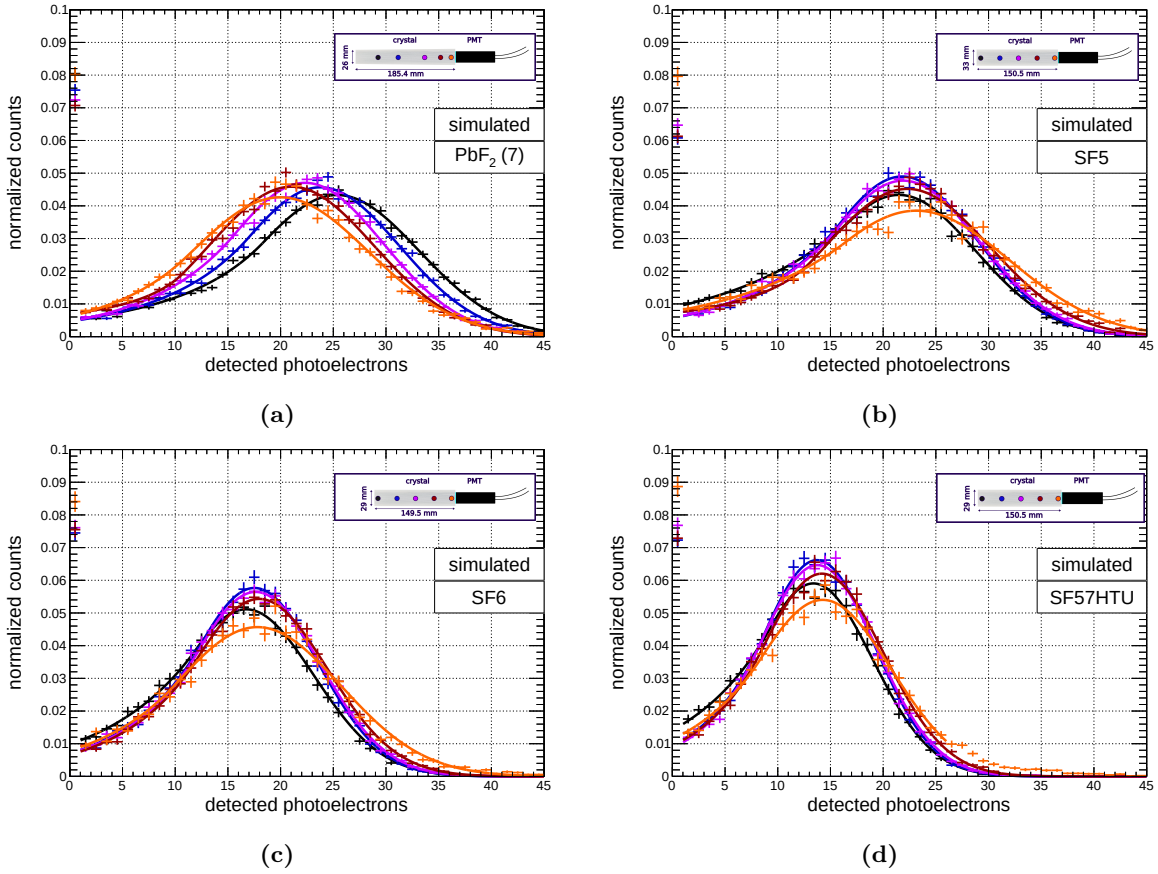

Figure 5.34.: Simulated signals from a PbF_2 detector (a), and PbGl detectors of type Schott SF5 (b), SF6 (c), and SF57HTU (d) for a 14-MeV electron beam entering a side face of the detector at different distances to the PMT face as indicated in the insert. The FWHM of the beam was $\varnothing_B \approx 41\,mm$, reduced to $\varnothing_B \approx 37\,mm$ (PbF_2) and $\varnothing_B \approx 34\,mm$ (PbGl) with the trigger condition of the fiber detector. The signal peaks were fitted with the Crystal Ball function.

This effect is associated with the increase of direct light for beam-spot positions next to the PMT. The motion of the peak is much lower in the case of PbF_2, because not only the effect of direct light has to be considered here, but the geometric shape ensures an optimized light collection in

the front areas. For the positions next to the PMT (orange spots) it is also observable that the low QDC charge entries in the histogram increase again and the height of the signal peak drops. This can be explained by the decreasing coverage of the beam-spot (simulated for example) in the bottom right plot of Fig. 5.33.
A similar effect was expected for the front positions (black spots) of the PbGl detectors and in Fig. 5.34 the simulation showed a reduced peak height for the black and orange beam positions. However, this effect was not found in the measured data. For the black spots an almost complete covering of the beam-spot on the crystal surface seems to be present. The differences between simulation and experiment can be explained by a slight shift in the alignment. Since the alignment during the experiment was carried out with the laser method, also used for the head-on measurements, a displacement below 10 mm can be assumed. In the simulation a significantly lower displacement of the signal peaks for the PbGl detectors is noticeable and for PbF_2 a higher light collection in the front area than next to the PMT can be seen. Due to the homogeneous nature of the optical elements in the simulation, the effect of direct light at a position close to the PMT is less prominent. Even for positions in the front area, the light emitted towards the PMT often reaches the photocathode on a direct or at least short way without absorption. At positions close to the PMT, the light emitted away from the PMT has a lower probability of reaching the photocathode, due to the longer path. The shape of the PbF_2 crystal further enhances this effect and part of the light remains trapped in the front part.
For the PbF_2 (7) detector, the response to a side-on beam was also studied for an incidence angle of 45° and 135° in Fig. 5.35.

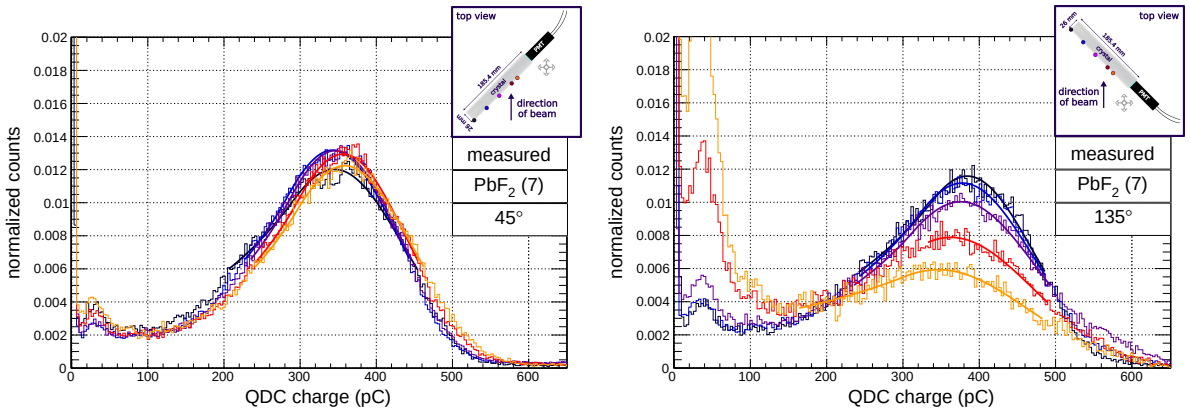

(a) **(b)**

Figure 5.35.: Measured signals from a PbF_2 detector for a 14-MeV electron beam entering a side face of the detector under an angle of 45° (a) and 135° (b) at different distances to the PMT face as indicated in the insert. The signal peaks were fitted with the Crystal Ball function.

For all positions, the 45° variant shows a minimally lower light output compared to the 90° measurement. Due to the direction of incidence towards the PMT, most of the resulting light can easily reach the photocathode. With the 135° measurement, the opposite case can be observed. The angle of incidence is directed away from the PMT and for hit locations close to the PMT, hardly any light reaches the PMT directly. Most of the optical photons have to pass through the entire crystal and a not negligible part of them gets trapped in the front area until they are totally absorbed. This results in lower pulse heights for hit positions next to the PMT.

Additionally the trigger events without or with very low signals increase. This is because the self-built crystal positioning table was not optimal for backward angles and a part of the beam was stopped in a vertical MayTec® bar. The area in front of the PMT and part of the crystal is obscured by this bar and therefore rarely hit by beam electrons, illustrated in Fig. 5.36.

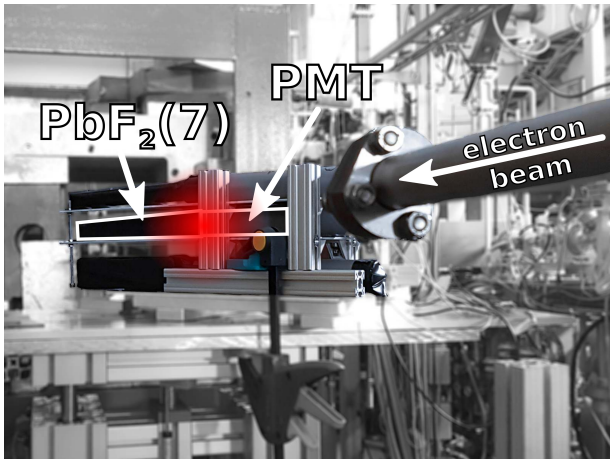

Figure 5.36.: Beam-time setup during the 135° measurements with the fiber detector temporarily removed. The studied PbF_2 (7) detector is in the middle position on the beam position table. For incoming beam electrons a part of the crystal–PMT junction is shadowed by a MayTec® bar.

Similar to the corner scans, the coverage of beam-spot and crystal is reduced. The increase of events with low pulse heights for the 135° scan at the red and orange spots is also seen in the simulation results in Fig. 5.37 and the hitmap in Fig. B.27 of Appx. B.3.5 shows this shadowing effect as well. Like for the corner scans, the influence of direct light is underestimated in the simulation and the spectra are a little further apart. In addition, it has to be assumed that the positioning during the beam-time was not perfect again.

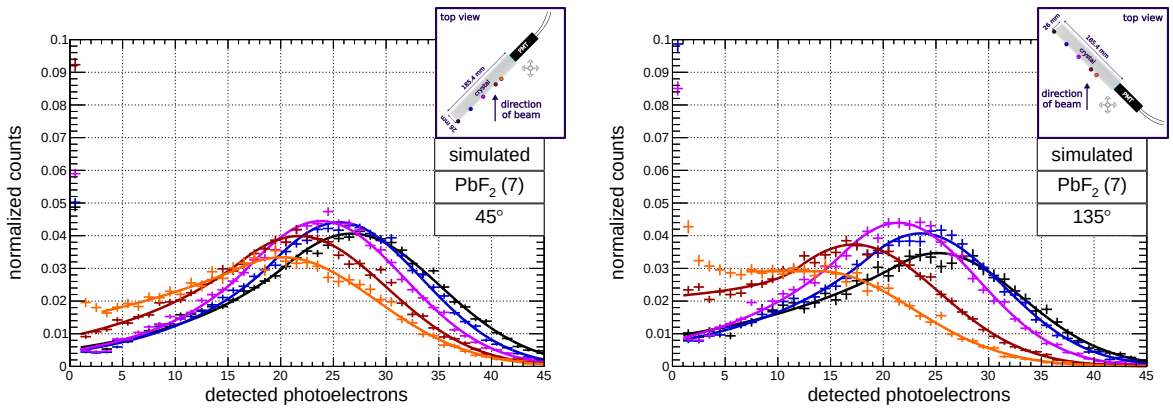

(a) **(b)**

Figure 5.37.: Simulated signals from a PbF_2 detector for a 14-MeV electron beam entering a side face of the detector under an angle of 45° (a) and 135° (b) at different distances to the PMT face as indicated in the insert. The signal peaks were fitted with the Crystal Ball function.

5.5.8. Response to an energy-degraded electron beam

The measurements until now were all performed with the maximum possible electron beam energy of MAMI, which is 14.86 MeV behind RTM1. This value was slightly reduced by the 0.2 mm aluminum flange and ~ 2.4 mm of plastic scintillating fibers (AND logic) to an average value of 14.26 MeV. In order to find out down to which electron energy a measurement of the signal peak is still possible, the beam energy was gradually reduced with polystyrene absorbers of one to several cm thickness. With a density of 1.06 g cm^{-3} the energy loss in polystyrene is 2.05 MeV cm^{-1} [30]. The simulated beam energy distributions for a PbF_2 and a PbGl setup are shown in Fig. 5.38.

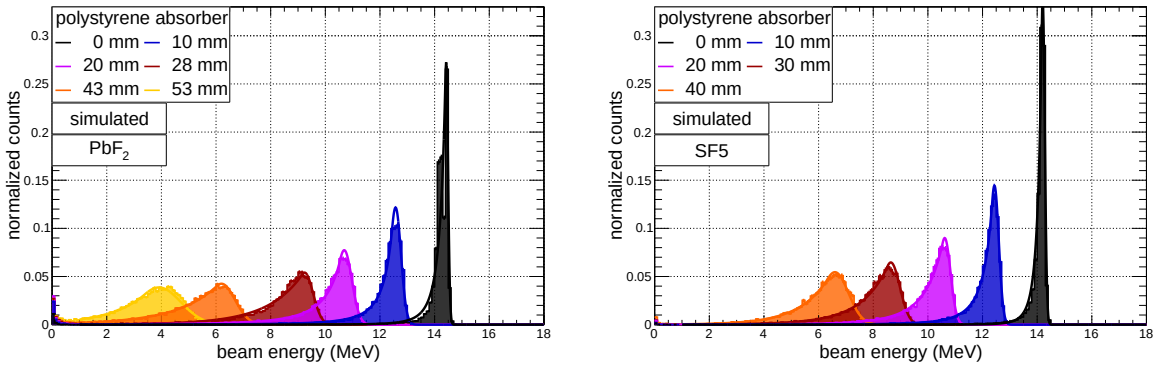

(a) **(b)**

Figure 5.38.: Simulated energy distributions of the energy-degraded electron beam for polystyrene absorbers of thicknesses up to 53 mm. The PbF_2 measurements were carried out during the July 2018 beam-time (a) and the PbGl measurements during the December 2018 beam-time (b). The beam left the vacuum beam pipe through an aluminum flange of 0.2 mm thickness followed by the energy-degraders and $270 - 320$ mm of air, ~ 2.4 mm of plastic scintillator, and additional $72 - 115$ mm of air before hitting the detectors. Variations with respect to the trigger conditions and the detector setup were found to be small. The signal peaks were fitted with the Crystal Ball function.

Each incoming beam electron was tracked in the simulation from the vacuum beam pipe through all materials and its remaining energy was determined at the first interaction point in the detector. During the July 2018 beam-time (PbF_2), only small polystyrene plates with different thicknesses were available. For the December 2018 beam-time, equal absorbers of 10 mm thickness were manufactured. For the PbF_2 energy distribution without absorbers, a double peak structure is visible. This is due to the OR trigger logic used for the PbF_2 absorber study during the July 2018 beam-time. The higher peak mainly corresponds to particle passages through two fiber layers and the lower peak to particle passages through all four fiber layers. This effect is also present in the measurements with absorber, but it is so small that it is no longer visible. These spectra depend on the absorber and the trigger settings only. Therefore, there are no differences for the two PbF_2 detectors, as well as for all PbGl detectors. The fluctuations in energy-loss lead to the increased energy spread for thicker absorbers with a relative energy spread σ_B/E_B of 0.5 % at 14 MeV to 8 % at 6 MeV. However, even after 40 mm polystyrene a very pronounced peak remains for electrons reaching the detectors. For all absorbers the beam energy spread σ_B is below 0.5 MeV, providing a sufficiently precise determination of the beam energy for the following studies.

For all the absorber thicknesses employed here, a head-on measurement was carried out for the

two PbF_2 and the three PbGl detectors. Multiple scattering in the absorbers led to a spreading of the beam-spot and the trigger rates went down. Therefore, in the case of PbF_2 starting with the 20 mm measurement, the measuring times were increased from 90 to 300 s. Additionally, starting with the 28 mm measurement, the Wehnelt voltage was increased from −13 to −12.5 V. For PbGl, starting with the 10 mm measurement, the measuring times were increased from 90 to 300 s and the Wehnelt voltage was gradually increased from −12.4 to −11.8 V.[16] In Fig. 5.39 the QDC charges for PbF_2 (1) and PbF_2 (7) are compared to an optical photon simulation study.

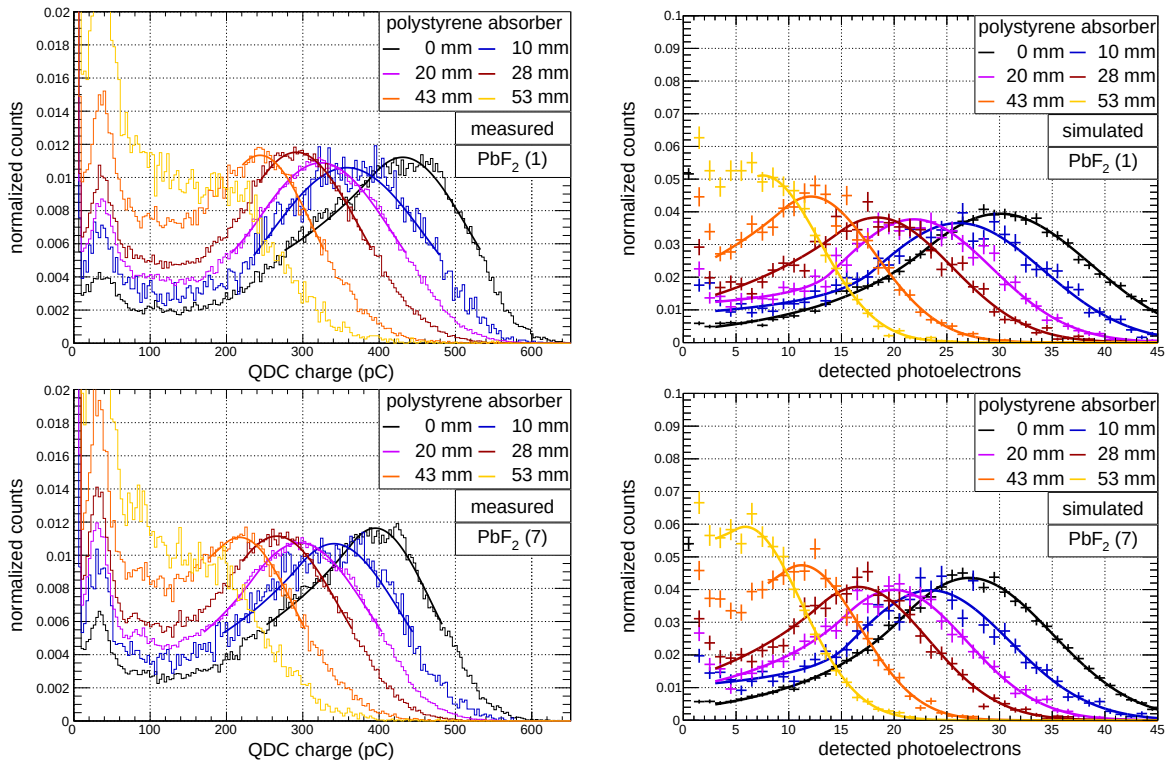

Figure 5.39.: Measured (left) and simulated (right) signals from a PbF_2 (1) (top) and a PbF_2 (7) (bottom) detector for electrons of $4-14$ MeV energy entering the front face of the radiator. The signal peaks could be resolved even below 10 MeV and were fitted with the Crystal Ball function.

The same energy deposition leads to a higher light output for PbF_2 (1) than for PbF_2 (7). For the arising optical photons it is more likely to reach the photocathode in the smaller detector volume of PbF_2 (1). Up to an absorber thickness of 43 mm (corr. to ∼6.2 MeV) the signal peak is observable. For the PbGl prototypes the results in Fig. 5.40 show a visible signal peak up to 30 mm (corr. to ∼8.6 MeV) for SF5 and SF6, and up to 20 mm (corr. to ∼10.6 MeV) for SF57HTU.

[16] A negative effect due to the change of Wehnelt voltage was not expected and also not observed, since the counting rates in the detectors do not change significantly.

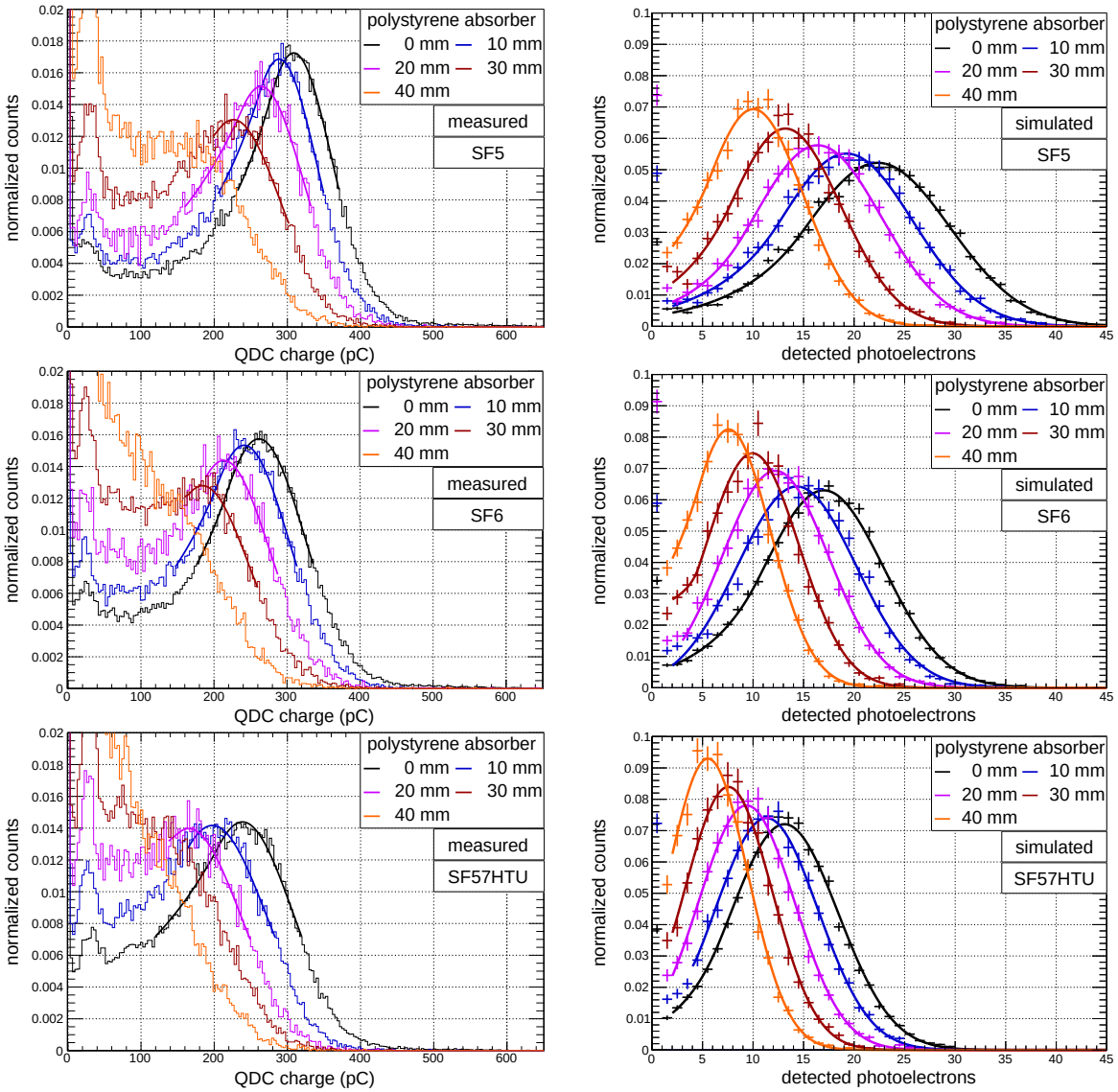

Figure 5.40.: Measured (left) and simulated (right) signals for electrons of $6-14\,\mathrm{MeV}$ energy entering the front face of the radiator for PbGl detectors of type Schott SF5 (top), SF6 (center), and SF57HTU (bottom). The signal peaks were fitted with the Crystal Ball function.

It should be recalled that the PbGl detectors have almost same size and therefore a direct comparison is possible. The best performance of the PbGl types is found for Schott SF5 again. But overall the performance of the PbF_2 detectors is even better. PbF_2 (1) compared to SF5, both with a similar active volume, show a difference of $21-37\,\%$ in the average QDC charges. With the performed Crystal Ball fits, the peak position E_{Mean} and the width of the Gaussian component σ_E of the Crystal Ball function are known for each absorber measurement – experimentally measured and simulated.

The measured versus simulated peak positions are shown in Fig. 5.41 for all materials in one plot. Below a certain material dependent energy, a consistent fit of the peak position was not possible. For these points, the beam degradation and energy straggling led to small non-linear effects and they were excluded. A linear fit yielded a calibration factor of $12.9(7)\,\mathrm{pC\,p.e.}^{-1}$. Small residuals demonstrate the robustness of the calibration.

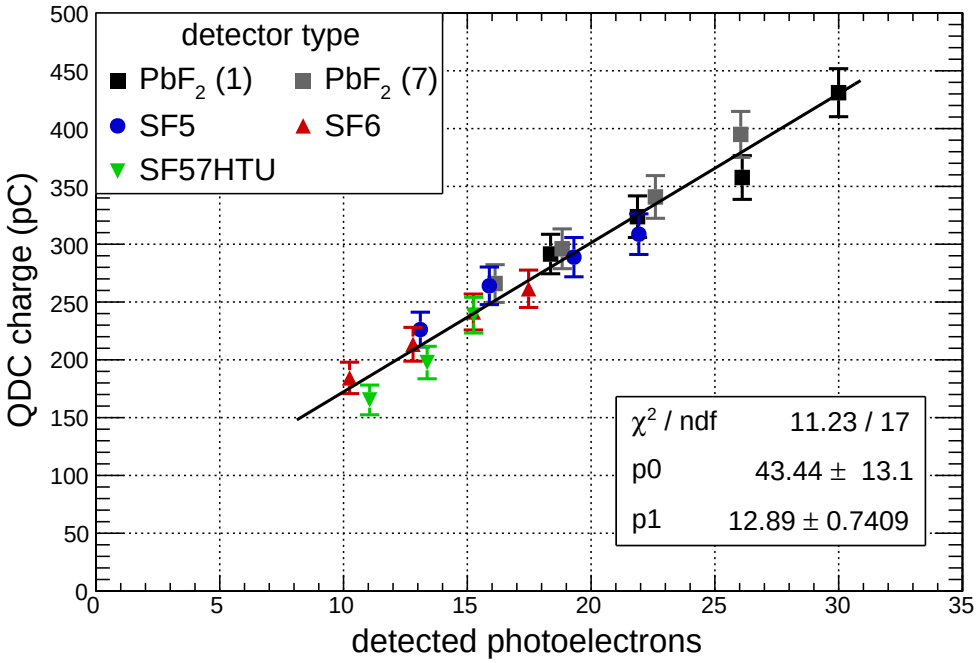

Figure 5.41.: Calibration of the measured signal heights in number of photoelectrons using the simulation. The linear fit yielded a calibration factor of 12.9(7) pC p.e.$^{-1}$ as well as small and randomly dispersed residuals.

This calibration allows the calculation of the detected photoelectrons (d_{pe}) for each absorber measurement. In Fig. 5.42 (top left) the progression of the measured number of photoelectrons with the beam energy is shown for all Cherenkov radiators. The same for the detected photoelectrons in the simulation study is shown in the top right plot. It shows a linear trend of signal height versus beam energy that is also observed in the data, demonstrating a good linearity of the measured energy response. The progression of the peaks relative energy resolution ΔE for measured and simulated data is shown in the bottom plots of Fig. 5.42. The relative energy resolution was calculated with

$$\Delta E = \frac{\sigma_E}{E_{\mathrm{Mean}}} \qquad \text{and} \qquad \Delta\left(\Delta E\right) = \sqrt{\frac{\sigma_E}{E_{\mathrm{Mean}}^2}\left(1 + \frac{\sigma_E}{E_{\mathrm{Mean}}}\right)} \quad . \tag{5.11}$$

The simulated contribution from the relative beam energy spread (shown with □ symbols in the bottom right plot) has been subtracted quadratically from the measured energy resolutions in the bottom left plot of Fig. 5.42. In contrast to the simulated data, for the measured data, four data points in total are missing. These were data runs for thicker absorbers, where the resolution of the signal peak was no longer possible. For both measured and simulated data, an improvement in the relative energy resolution can be observed with increasing beam energy. The PbF_2 (1) detector showed a nearly constant energy resolution of 32 % for all the experimental measurements with absorber. Although most of the simulated data points agree with the experimentally determined data points, some of the measured resolutions exceed the expectations of the simulation. In particular for all SF5 data points and the low beam energy measurements of the PbF_2 detectors.

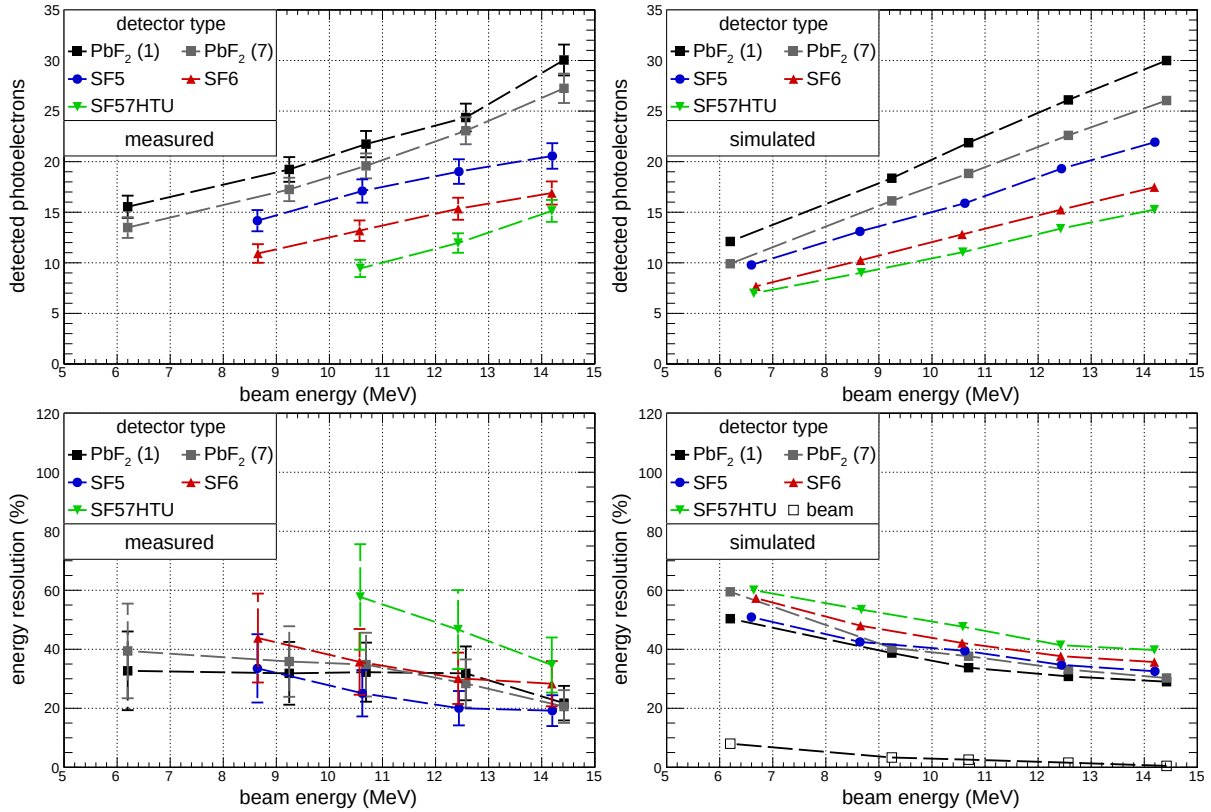

Figure 5.42.: Top: Measured (left) and simulated (right) signal heights for electrons of $6-14\,\mathrm{MeV}$ energy entering the front face of the radiators. The signal heights increase approximately linearly with energy. The materials PbF_2 and PbGl type Schott SF5 yielded more light than the types SF6 and SF57HTU. Bottom: Measured (left) and simulated (right) relative energy resolutions for these beam energies as determined by the width of the Gaussian component of the Crystal Ball function. The simulated contribution from the relative beam energy spread (shown with □ symbols) has been subtracted quadratically from the measured energy resolutions.

An average light yield $\overline{\nu_{\mathrm{yield}}}$ was then calculated for each detector type. The full dataset and the error calculation used for the values in Tab. 5.8 can be found in Appx. B.3.6. With an average value of $1.86-2.04\,\mathrm{p.e.\,MeV^{-1}}$ the PbF_2 detectors achieve values in the same range as found in the studies from Patrick Achenbach et al. [131]. The PbGl types are all below these values, with SF5 achieving the highest light output of $1.56\,\mathrm{p.e.\,MeV^{-1}}$ whereas SF57HTU achieves only 50 % light output compared to the PbF_2 detectors.

Cherenkov radiator	**light yield ($\mathrm{p.e.\,MeV^{-1}}$)**
PbF_2 (7)	1.86(7)
PbF_2 (1)	2.04(7)
SF5	1.56(6)
SF6	1.23(6)
SF57HTU	0.97(6)

Table 5.8.: Average light yield of the Cherenkov radiators, calculated with the full dataset in Appx. B.3.6.

5.6. Neutron response study

As part of a Bachelor's thesis, the response of the prototype detectors to neutrons was investigated. The most important result for this thesis is briefly outlined here. For the detailed measurement procedure and interpretation of the results, see the work of Paul Burger [130].

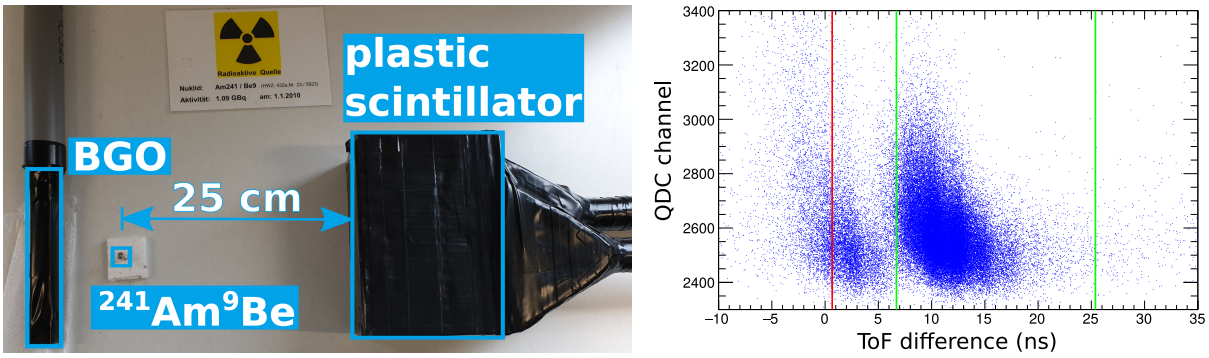

(a) (b)

Figure 5.43.: (a) Basic measurement setup with $\gamma-$detector on the left, ^{241}Am^{9}Be source in the middle, and neutron detector on the right. In this setup, a detector made of plastic scintillator served as neutron detector. (b) TOF spectrum for the setup on the left. The red line marks the theoretical TOF difference for coincident $\gamma - \gamma$ signals and the green lines mark the TOF difference for coincident n$-\gamma$ signals of 7 and 0.5 MeV neutrons.

The neutrons came from a ^{241}Am^{9}Be source, which generates prompt n$-\gamma$ pairs. 80 % of these neutrons have an energy of more than 1.5 MeV, with the maximum energy being 7 MeV. For all measurements, a BGO detector was used as $\gamma-$detector. For the detection of neutrons, first a plastic scintillator was used, which is sensitive to fast neutrons [157]. Later the plastic scintillator was replaced by the prototype detectors to be investigated. The experimental setup is shown in Fig. 5.43a and with a TOF measurement, it was possible to distinguish between coincident $\gamma - \gamma$ signals and coincident n$-\gamma$ pairs. The distance between the source and the $\gamma-$detector must be chosen sufficiently large. In Fig. 5.43b, the γ/n separation was achieved with a distance of 25 cm. The red line marks the theoretical time difference for $\gamma - \gamma$ coincidences. The green lines show the theoretical time differences calculated for 0.5 to 7 MeV neutrons. The higher energy neutrons are faster and deposit more energy in the crystals, which explains the shape of the distribution. Taking into account the spatial angles covered by the active materials, the prototype detectors showed the neutron sensitivities summarized in Fig. 5.44.

The highest response is reached by the organic scintillator made of plastic with a sensitivity of 72 %. The inorganic scintillator made of BGO shows a more than one order of magnitude lower sensitivity. The Cherenkov radiators follow with even smaller sensitivities. With 0.045 %, SF57HTU shows the lowest sensitivity, which is one order of magnitude below the PbF_2 one. Due to the low neutron detection probability found for the Cherenkov radiators, it can be assumed that neutrons will be one of the smallest background contributions. These background events can be suppressed even further with a suitable veto system made of plastic scintillators, having a factor of $180 - 1600$ higher neutron sensitivity.

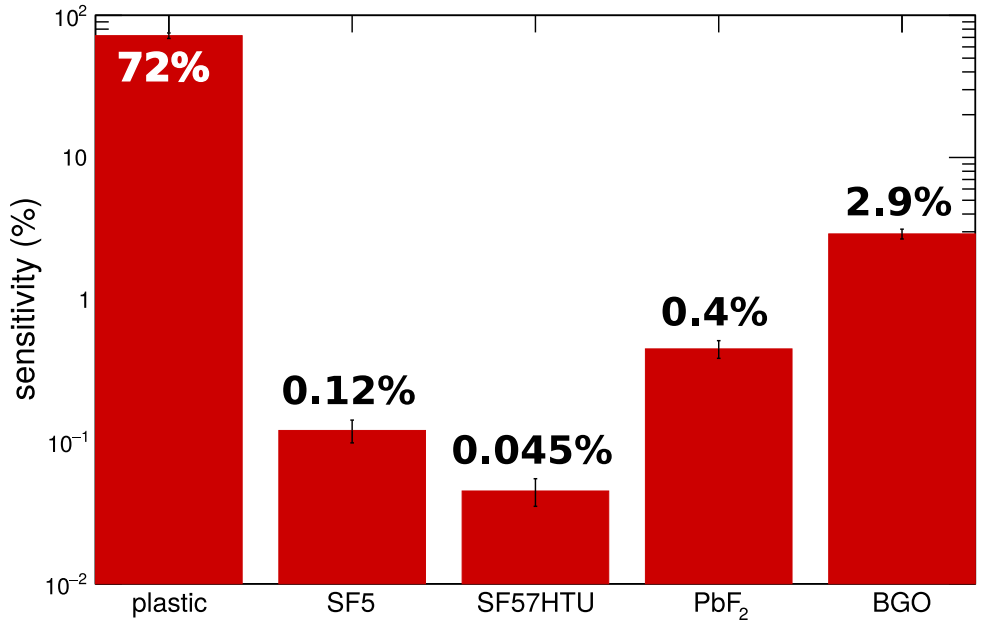

Figure 5.44.: Results of the neutron response study for the prototype detectors discussed in this chapter.[17]

5.7. Summary

The next steps in the development of the DarkMESA detector need an informed decision about the materials. It would be desirable if the chosen material fulfills most of the following points:

- A high light output for electrons,
- a small response to neutrons,
- a high material density,
- and low investment costs, at best by reusing existing materials from other experiments.

Studies with the electron beam of MAMI showed that all investigated materials are in principle suitable for the detection of electrons with a minimum energy of ∼10 MeV, but there are some differences in the average light output. With an average of 1.94 p.e. MeV^{-1}, the PbF_2 prototypes reach a twice as high light output compared to SF57HTU with 0.97 p.e. MeV^{-1}. SF6 with 1.23 p.e. MeV^{-1} and SF5 with 1.56 p.e. MeV^{-1} lie in between. Studies with fast neutrons from an $^{241}Am^9Be$ source have shown that all Cherenkov detectors have at least two orders of magnitude lower neutron response efficiencies than plastic scintillators.
Since the available volume of the DarkMESA room is also limited, a higher detection probability can be achieved by using a denser detector material. A smaller calorimeter would also reduce the size (and costs) of a veto system (Sec. 7.2).
By far the largest density of all studied Cherenkov radiators is the one of PbF_2 with 7.77 g cm^{-3}. Due to its results so far and its availability from the completed A4 experiment, PbF_2 is considered the first choice. The total quantity from the A4 experiment is limited to about 0.13 m^3.

[17] SF6 was missing in this series of measurements. A previous series of measurements under slightly different conditions showed that the neutron sensitivity of SF6 lies between those of SF5 and SF57HTU.

For a further increase of the PbF_2 detector volume, new crystals would have to be acquired. In contrast to PbF_2, the PbGl types do not have to be grown individually from a seed crystal but can be cast in blocks and cut into shape. This is associated with lower costs, which is why a PbGl detector for expanding the active volume should also be considered.
Although SF57HTU has the highest density of all PbGl types with $5.51\,\mathrm{g\,cm^{-3}}$ and showed the lowest neutron response, it was not adequate due to the lower light yield of $0.97\,\mathrm{p.e.\,MeV^{-1}}$ on average. The less dense SF5 would be the first choice due to the high light output of $1.56\,\mathrm{p.e.\,MeV^{-1}}$. Independently of this selection, it has been found that $0.72\,\mathrm{m^3}$ of Schott SF5 can be provided by the University of Münster [158–160]. The 1278 SF5 blocks were initially used in the SAPHIR calorimeter of the WA80 experiment at the CERN Super Proton Synchrotron (SPS) [161]. They have a dimension of $35 \times 35 \times 460\,\mathrm{mm^3}$ and were also re-used in the Leadglass Detector Array (LEDA) calorimeter of the WA98 experiment at CERN SPS [162]. In addition, 15 blocks (each $260 \times 142 \times 65\,\mathrm{mm^3}$) from a 2018 cast by Schott are already in Mainz.

With this two materials, PbF_2 and PbGl of type Schott SF5, the design of the DarkMESA calorimeter can start. Further optimizations and a staged approach in the construction of the full DarkMESA calorimeter are described in the following Chap. 6.

6. DarkMESA full calorimeter concept

In this chapter the DarkMESA calorimeter is described in more detail. Due to the accelerator infrastructure of MESA and structural conditions of the halls, specifications are also made for the DarkMESA experiment. Studies to improve the DM detection probabilities are presented in Sec. 6.1. Based on the results of these studies, there are limitations and specifics that need to be considered when planning the overall design. In Sec. 6.2 a staged approach for DarkMESA including a possible time line is presented.

6.1. Optimization studies on DM detection probabilities

To improve the DM detection capabilities, one can start from two considerations. On the one hand, one can try to increase the production probability of dark photons and thus also DM particles at the production side – the beam-dump. The second point is the optimization of the detector. A detection method is needed that is well suited for the detection of DM and at the same time is not too sensitive to low energy backgrounds. The dimensions of such a detector must take into account the available space in the DarkMESA room and the bearing capacity of the floor. A possible segmentation of the detector and an optimized placement in the room are investigated with a geometrical acceptance study. Here, economic factors are already taken into account and the partial re-use of existing detector systems is preferred.

6.1.1. Production side

Due to its previous use, the P2 beam-dump is not optimized for a DM experiment. A material with an even higher atomic number than aluminum ($Z = 13$) would be desirable, since the Z value enters quadratically in the cross-section of the dark photon production (see Sec. 8.1.1). Since the P2 beam-dump was already used in the A4 experiment, the location is a prohibited radiation area, where dose rates of more than 3 000 µSv are possible. Therefore a complex re-design of the beam-dump is not possible and only small and expeditious changes can be made.
A way to increase the number of generated photons, and theoretically also the number of dark photons, is to introduce a denser material as an additional absorber in the beam-dump. An up to several mm thick plate could be inserted directly in front of the existing beam-dump without major effort. The effect of using tungsten ($Z = 74$) in various thicknesses was studied in a simulation. With a density of $19.3\,\mathrm{g\,cm^{-3}}$, tungsten is a factor of seven denser than the aluminum of the beam-dump. In the γ' cross-section, a pure tungsten beam-dump would result in an improvement by a factor of 32. The additional absorber allows the high-energy beam electrons to be stopped earlier, which should result in more Bremsstrahlung photons tending to have higher energies. The simulation results in Fig. 6.1 show the total number of generated

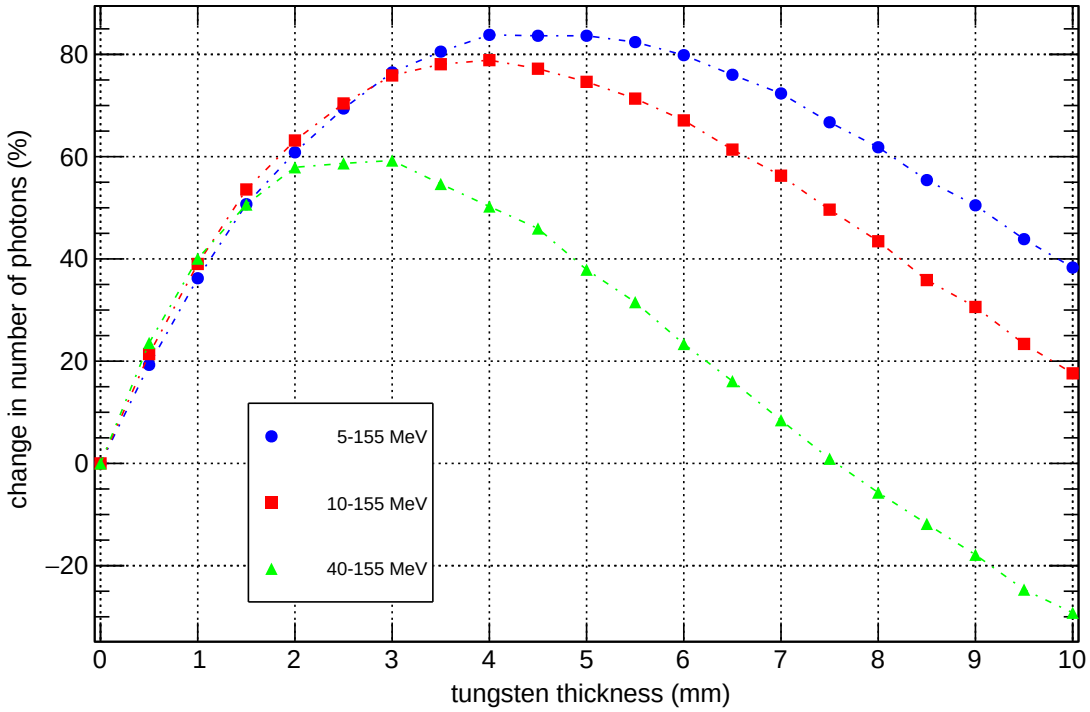

Figure 6.1.: Total number of generated photons for an up to 10 mm thick additional tungsten target, where the case without target is the reference. In blue the change for photons above 5 MeV, in red above 10 MeV, and in green above 40 MeV are shown. Since loss of high energy photons should be avoided, the target should not be chosen thicker than 3 mm.

photons in the beam-dump (N) for tungsten thicknesses up to 10 mm as a percentage change

$$\frac{N - N_0}{N_0} \cdot 100\,\% \quad , \tag{6.1}$$

with respect to the setup without tungsten (N_0). The three graphs refer to different energy ranges of the generated photons. The detailed quantity of photons for smaller energy ranges can be found in Fig. B.28 of Appx. B.4. When focusing on photons above 5 MeV the maximum number of photons is reached at 4–5 mm tungsten. If one restricts this range to high energy photons above 40 MeV, the maximum shifts to 2–3 mm. For larger thicknesses the number of photons drops again. For the overall energy range, a plate thickness of 2.5 mm seems a good choice. If new dark sector searches show that a lower energy range is preferable in the search for DM, the thickness of the target can be adjusted accordingly.

Whether this increases not only the number of Bremsstrahlung photons, but also dark photons, is not yet demonstrated. It seems not improbable that the number of dark photons is also increased by the tungsten target. In the studies in Chap. 8 this target is not included from the beginning. The change in the expected limits due to the tungsten target are discussed in Sec. 8.4.1.

6.1.2. Detection side

The largest potential for optimization is on the detector side. In the simplified MESA floor plan in Fig. 6.2 the MESA accelerator and the P2 experiment are shown. The beam-axis runs almost centrally through the marked room, whose dimensions are shown in the enlarged view on the

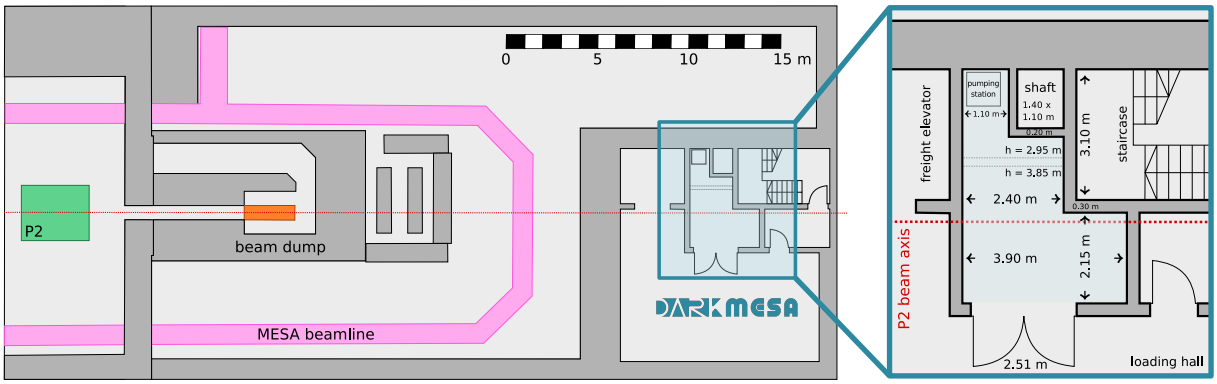

Figure 6.2.: Excerpt of the MESA accelerator hall with indicated positions of the P2 experiment (green), the P2 beam-dump (orange), the MESA beamline (magenta), and the DarkMESA room (blue). In the enlarged sketch on the right, the dimensions of the DarkMESA room are included. The P2 beam-axis is shown in red.

right. With its extended floor load capacity, this $\sim 12\,\mathrm{m}^2$ room is dedicated to DarkMESA. The detector system under development, must not exceed the room space and should include the Cherenkov crystals investigated during the material studies in Chap. 5. At this point, it is also worth recalling the decision already met in Chap. 2.2.3: a detector system optimized for detecting electron recoils is preferable to one optimized for proton recoils. An additional veto system is discussed in Chap. 7 and should also be considered while dimensioning the detector.

Available detector elements. Dimensions and properties of available crystals are listed in Tab. 6.1. The two most convincing candidates from the material studies – PbF_2 and SF5 PbGl – are available from the A4 experiment at MAMI and SAPHIR at CERN. In both cases more than 1 000 crystals and major parts of the associated electronics can be used. In addition, a total of 15 brand new Schott SF5 PbGl crystals and seven 9330B 5″ PMTs from ET Enterprises are available.[1] The other listed crystals do not play a role in the planning for the time being, but can still be considered in later phases of the DarkMESA experiment.
Not all of the more than 2 000 PbF_2 and SF5 PbGl crystals, will be used from the very beginning. Rather, a staged approach is planned to put detector elements into operation at an early stage and collect initial data.

Detector layout and positioning. Before these stages are presented in Chap. 6.2, it is important to know whether there are any restrictions on the positioning of the detector elements in the DarkMESA room. A closer look at the DM beam and in particular its angular distribution at the level of the DarkMESA room for different kinematics with $m_{\gamma'} = 3\,m_\chi$ is shown in Fig. 6.3. One can see the increasing divergence of the DM beam for larger masses m_χ, while a clear beam-spot is present for a light mass of $m_\chi = 1\,\mathrm{MeV}$. Now looking at the position of the room (marked in red), one can see that this effect plays a negligible role for the detector positioning, since the distribution of the DM particles in the room is extremely homogeneous over all kinematics. The detector can therefore be placed anywhere in the room.

[1] The order of this amount was based on the idea, to stack two blocks on top of each other and read them out with one PMT. One SF5 block remains as a spare.

material	former experiment(s)	no. of crystals	front/rear (mm^2)	length (mm)	volume (L)
BGO	L3 at CERN	600 (11 488)	21 × 21	230	0.10
PbF_2	A4 at MAMI	1 022	26 × 26 (30 × 30)	150–185.4	0.12–0.15
SF5	SAPHIR at CERN⋆	1 278	35 × 35	460	0.56
SF5	—	15	142 × 65	260	2.40
SF57	NA62LAV OPAL	896	100 × 100 (110 × 110)	370	4.08
CsI	BaBar at SLAC	820	47 × 54	325	0.83

Table 6.1.: Dimensions and properties of likely available crystals. (⋆ currently stored in Münster and available through collaboration partners.)

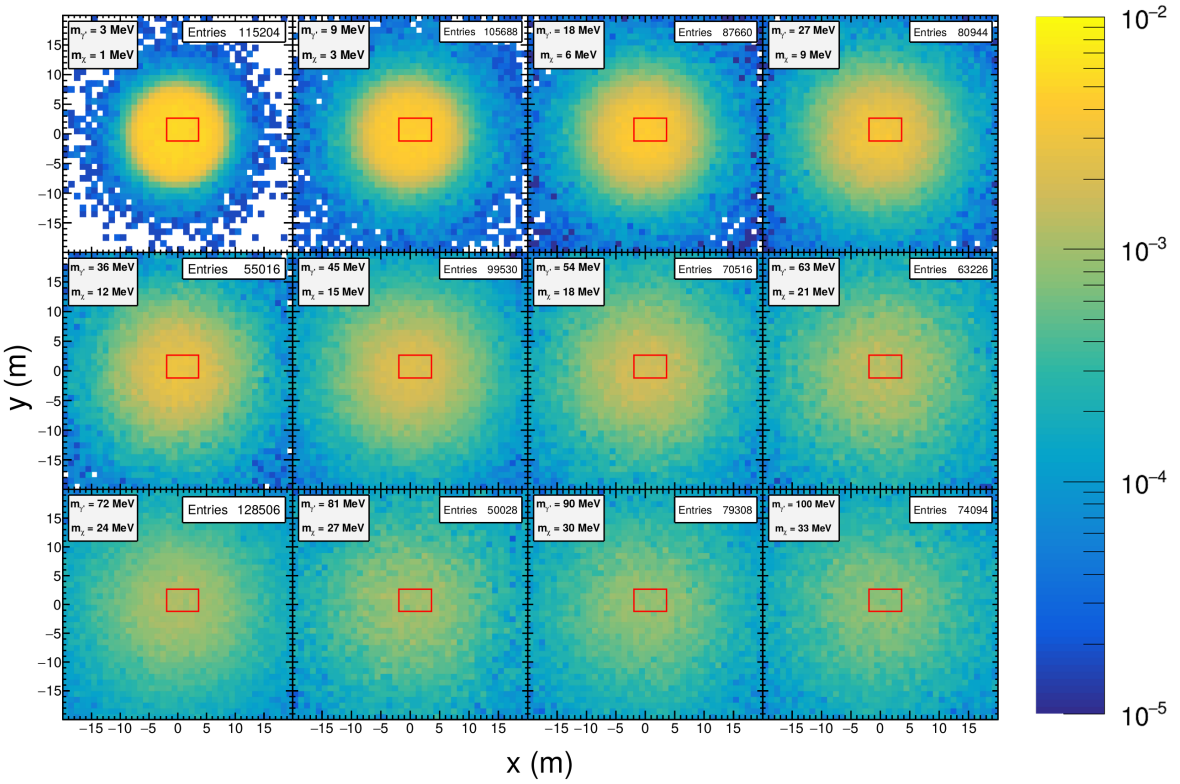

Figure 6.3.: The angular distribution of the DM particles is shown as a beam-spot at the beginning of the DarkMESA room. Shown are different kinematics with $m_{\gamma'} = 3\,m_\chi$ and rising DM mass from left to right and top to bottom. The dimensions of the DarkMESA room are indicated with a red box.

A larger detector – more scattering centers N_{det} – increases the probability for DM interactions. Whether this increase is due to a larger geometrical acceptance (enlargement in x and/or y direction) or the interaction length in the calorimeter (enlargement in z direction) has turned

out to be irrelevant. In Fig. 6.4, a look at detectors with different front surface sizes shows that for DM masses below 10 MeV only small changes in the geometrical acceptance are expected. Independently from the detector size, no significant loss in DM events has to be expected. For DM masses above 10 MeV up to 85 % fewer DM events are expected due to the smaller geometrical acceptance.

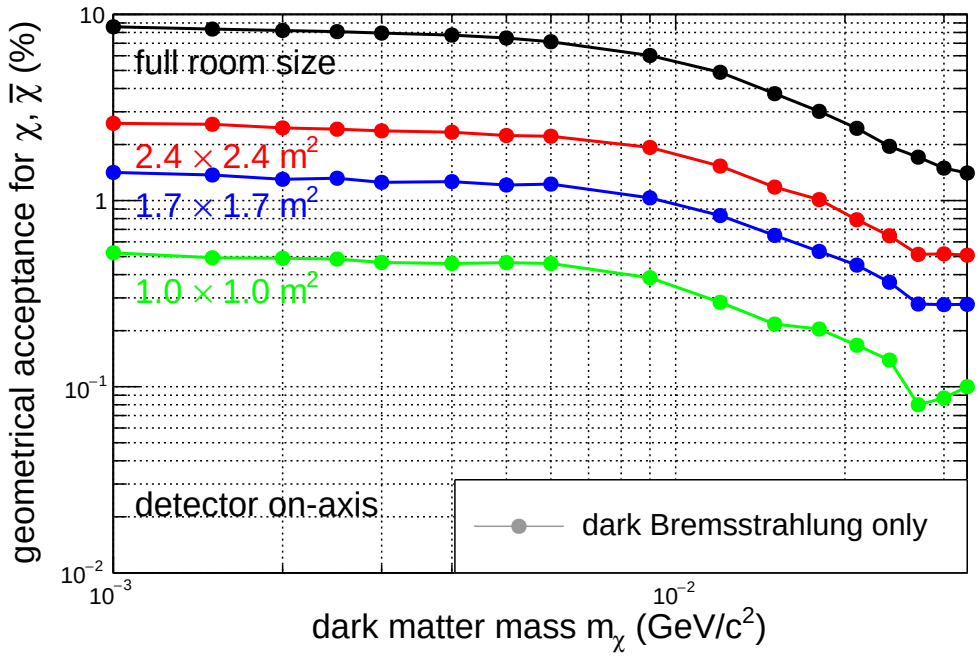

Figure 6.4.: Dependence of the geometrical acceptance on DM masses for an on-axis detector position and dark Bremsstrahlung only. The graphs show the results for detectors with fixed front surface sizes.

From these studies, there are no special requirements for the positioning of the detector elements in the DarkMESA room. However, the following functional advantages led to the preference for a wall layout:

- Exploitation of the room height,
- easy access to individual detector elements,
- enough space for electronics, including data acquisition at a workstation,
- space for new and different detection systems,
- and the possibility to rotate the calorimeter wall by 90°/180°, which may help in further background suppression.

6.2. DarkMESA staged approach

These preliminary considerations and the funding periods for MESA and DarkMESA resulted in the following staged approach for the detector design. In the years 2025 - 2028 the accelerator and the P2 experiment will be commissioned and the effective time with electron beam will be limited. Therefore a conservative plan with 2 200 h of beam is envisioned during these years. In the following periods 2 200 h of beam per year are expected. The schedules can be read in Tab. 6.2. For Phase C, the planning is not yet complete, and a conceptual design with initial studies is presented in Sec. 8.6.

stage	description	period	scheduled time	EOT
Phase A	PbF_2 prototype	1. - 3. year	2 200 h	7.42×10^{21}
Phase B	PbF_2 (A4) + SF5 (Münster)	4. - 6. year	6 600 h	2.22×10^{22}
Phase C	Phase B setup + extension	7. - 12. year	13 200 h	4.45×10^{22}

Table 6.2.: Proposed DarkMESA stages in the three funding periods. The active volume of the prototype is made of 5 × 5 PbF_2 crystals. The calorimeter in Phase B will consist of 30 × 30 PbF_2 and 32 × 32 SF5 crystals. Phase C aims to extend the active volume even further. An innovative detector system using thin radiation shielding glasses is foreseen and is presented later in Sec. 8.6.

6.2.1. Phase A – PbF_2 prototype

Since the PbF_2 crystals, PMTs, and voltage dividers are already stored in Mainz and individual crystals have already been characterized with the MAMI beam, it is natural to first build a prototype module from them. A module consisting of 25 crystals including PMTs and voltage dividers, weighing about 40 kg, is still practical enough for its characterization in the laboratory and to be used at MAMI or MESA later. This size still allows the use of a dark box to reduce the influence of ambient light. Nevertheless, the crystals are individually wrapped in Teflon® and black foil, as shown in Sec. 5.4. To achieve the highest possible active volume, only the longest PbF_2 crystals (PbF_2 (7): 185.4 mm) are used for this prototype. These are arranged in a 3D printed lattice of five by five, giving the detector a total active volume of 3.6 L. The 3D printed structures support especially the front of the crystals and the transitions to the PMTs.[2] The voltage dividers are screwed to the last 3D printed element. The data acquisition for Phase A can still be carried out using the CAEN waveform digitizer already presented in Sec. 5.1.2.[3]

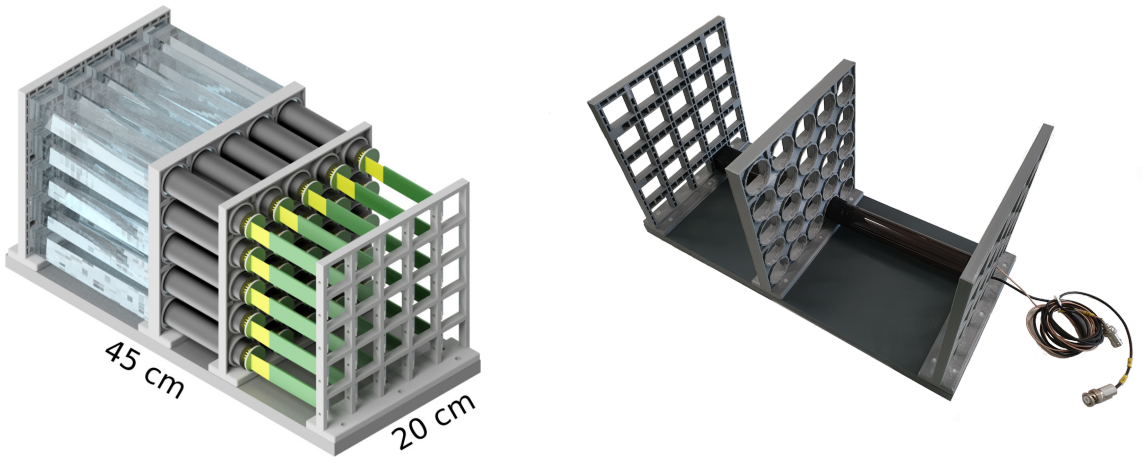

Figure 6.5.: The DarkMESA prototype in Phase A is built of 5 × 5 PbF_2 crystals and has an active volume of 3.6 L. A CAD rendering (left) and a real module during assembly (right) are shown.

[2] The first support element is divided into five pluggable levels to allow a module assembly from bottom to top. In order to be able to replace detectors of lower levels without removing overlying detectors, a revised holding structure is envisaged already.

[3] The data acquisition should be switched to the system planned for Phase B (Sec. 6.2.2) at an appropriate time already.

Together with the veto system presented in Sec. 7.2.1, this compact detector allows characterization studies in the laboratory or at MAMI already during the setup phase of MESA. With the commissioning of MESA, it allows first measurements of beam-related backgrounds and, due to large time intervals without beam, also an intensive study of beam-unrelated backgrounds, in particular the cosmogenic background reaching the DarkMESA room.

6.2.2. Phase B – Full PbF_2 and PbGl calorimeter

Based on the Phase A prototype, it is planned to build a whole wall of these modules in Phase B and thus to use all PbF_2 crystals provided by A4 except a small number of spare modules and crystals. A total of 36 of these modules will be used at the same time in the DarkMESA experiment. Their total volume is around 120 L.[4] In addition, modules made of SF5 PbGl will be used in a second wall. 64 modules with 16 crystals each, from the former SAPHIR calorimeter of the WA80 experiment, and a total volume of about 580 L will be used. The wall size is again planned in such a way that broken modules can be replaced by spare modules.

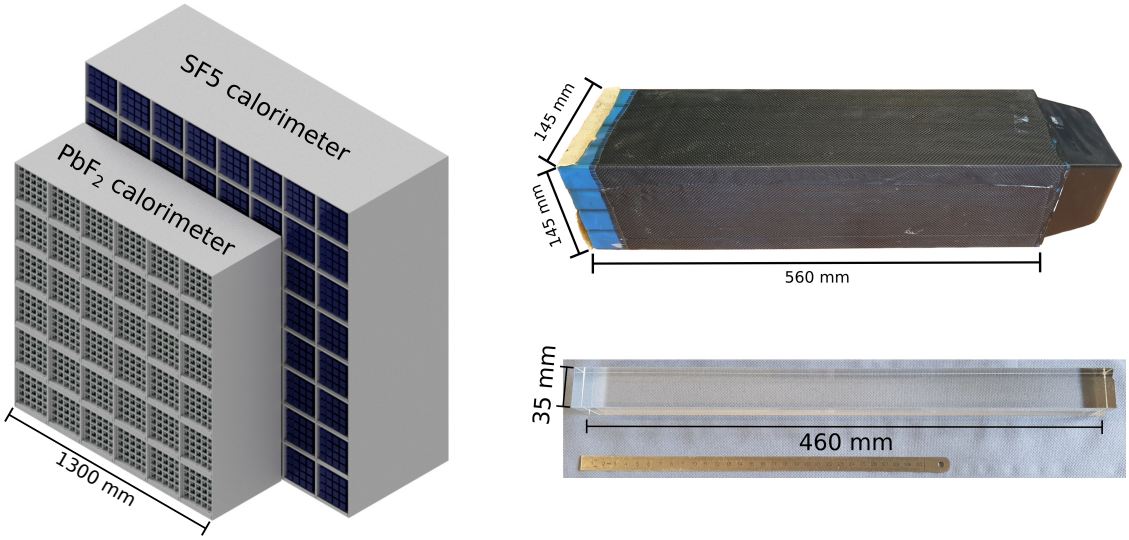

Figure 6.6.: The DarkMESA Phase B calorimeter consists of two detector walls with 1924 detectors and has an active volume of 700 L. A CAD rendering shows the PbF_2 calorimeter in front of the SF5 calorimeter (left). Four of the 4×4 SF5 PbGl modules are already in Mainz. A full module and a single crystal are shown (right).

The readout is carried out via old FEU-84 PMTs from a Russian manufacturer. Their properties can be found in Tab. C.4 of Appx. C.4. An initial characterization of fourteen PMTs during a summer student program showed no major failures. However, a replacement of all supply cables was required and a full replacement of the old devices is still under consideration. To obtain all signal information, the use of the commercial digitizer is no longer economical and practical due to the high number of channels. The data acquisition will therefore be switched to a sampling ADC developed in-house.

Already during the studies in Chap. 5, the materials to be used in the DarkMESA concept – PbF_2 and SF5 PbGl – turned out to be well suited. By increasing the detector volume, more DM

[4] The active volume of each module varies between 2.9 and 3.6 L due to various crystal lengths.

particles generated in the beam-dump and emitted forward can reach the DarkMESA detector, and the interaction probability increases. The chosen materials have good detection properties over a wide energy range of the recoil electrons. However, this also means that they are sensitive to other particles in the same energy range and above. For these two concepts of Phase A and B, the expected background is investigated in the following Chap. 7. With a suitable veto system this background events should be detected with highest efficiency.

7. Background radiation studies

Since DM particles have not yet been experimentally detected, it must be assumed that their interaction with SM particles is extremely weak. Thus, even with a search in the correct energy range, one expects very few events. In proportion, events due to secondary particles arising in the beam-dump, and in particular cosmic radiation, could be much more frequent.

These possible backgrounds are identified in Sec. 7.1. Based on this, in Sec. 7.2 a concept for their reduction in Phase A and B of the experiment is presented.

7.1. Types of background radiation to be considered

The backgrounds can be divided into two categories: one is beam-related and the other is beam-unrelated. The former category can be reduced by comparing data with and without beam. Beam-unrelated background, on the other hand, always occurs and must be eliminated completely or at least minimalized using a suitable technique.
In particular uncharged particles such as neutrons and neutrinos, belong to the first category. They could probably make it through the radiation protection walls. Also, a beam loss of the MESA accelerator near the walls closest to DarkMESA cannot be completely excluded, but should be detected by the monitoring system of MESA.
The backgrounds that are expected to be permanent are mostly from cosmic particles, since there is only $\sim 1\,\mathrm{m}$ concrete as shielding above DarkMESA. Other background signals may arise from natural radiation, especially radon from the surrounding concrete, or electronic noise from the DarkMESA readout.

7.1.1. Beam-related neutrinos and neutrons

First it shall be investigated whether a significant background by beam-related particles is to be expected for DarkMESA. For this purpose, two `Geant4` and `FLUKA` studies were performed with respect to the neutrons and neutrinos produced in the P2 experiment.

Neutrino study. For the study of beam-related neutrinos the DarkMESA simulation was used again. The detailed P2 target with the conical flow diverter was used and the `QGSP_BERT_EMV` physics list was applied to include most of the possible processes. Especially, this model uses a `Geant4` Bertini cascade for pions below $\sim 10\,\mathrm{GeV}$, resulting in more secondary particles and a better agreement with experimental data.
More than 99.9 % of the short-living pions decay into muons due to the weak interaction. Since these are responsible for the largest fraction of higher-energy neutrinos, the simulation searches

for produced pions in particular. The muons in turn decay into leptons and $\nu\overline{\nu}$ pairs.

$$\begin{aligned} \pi^+ &\longrightarrow \mu^+ + \nu_\mu \\ &\hookrightarrow e^+ + \nu_e + \bar{\nu}_\mu \end{aligned} \tag{7.1}$$

The functionality of the implemented processes was verified with a higher beam energy of 1 GeV first. For one million primary electrons, slightly more than 2 000 charged π^+ decayed into μ^+ and ν_μ. In more than 70 % of the cases, the subsequent decay of the muon into e^+, ν_e, and $\overline{\nu_\mu}$ is observed (Fig. B.29 of Appx. B.5.1). In the remaining cases, the free muon has not reached the end of its lifetime before the end of the simulation.
For the DarkMESA case the beam energy is only 155 MeV, which is slightly above the thresholds of charged pion photoproduction on nucleons, which are:

$$\begin{aligned} & 151.43\,\text{MeV} \quad \text{for} \quad \gamma + p \longrightarrow \pi^+ + n \quad , \\ \text{and} \quad & 148.45\,\text{MeV} \quad \text{for} \quad \gamma + n \longrightarrow \pi^- + p \quad . \text{[163]} \end{aligned} \tag{7.2}$$

The simulation of 40 million primary electrons in `Geant4` did not show any produced pions. Just low energy $\overline{\nu_e}$ ($< 1\,\text{MeV}$) from the β^- decay

$${}^{A}_{Z}X \longrightarrow {}^{A}_{Z+1}Y + e^- + \bar{\nu}_e \quad , \tag{7.3}$$

were observed. This is suitable as a first indication, but the small number of primary particles ($< 10^8$) compared to the $\mathcal{O}(10^{18})$ awaited in a single hour of MESA beam-time makes this study not very useful. With `Geant4` no significant increase in statistics is possible. The `FLUKA` simulation used for the estimation of the neutron background has more capabilities, but cannot simulate the full amount of beam electrons as well. For a full simulation, it is also important to keep in mind that the generated neutrinos are rarely detectable in the calorimeter, since their trajectory must pass through the calorimeter and neutrinos interact with the active detector material only via the weak interaction which results in a low detection probability. Even if no huge background is expected, together with the teams of the MESA accelerator and the P2 experiment, there is a plan to lower the beam energy below the thresholds in Eq. 7.2 to prevent a direct production of pions.

Neutron study. In a `FLUKA` simulation carried out by Luca Doria, the generation of neutrons in the P2 experiment and its beam-dump was investigated. The MESA hall was integrated into the simulation and an investigation for 10^7 beam electrons was started. One obtains the spatial distribution of all neutrons in Fig. 7.1 and recognizes that no neutron has made it through the first radiation protection wall behind the beam-dump and accordingly none could reach the room of the DarkMESA experiment. In this simulation, the number of primary particles is also relatively small, but looking at the energy distribution of the neutrons in Fig. 7.2, one sees that they are of low energy mostly and neutrons with more than 1 MeV are rare. The probability of overcoming all radiation protection walls up to DarkMESA can be estimated as very low for particles with energies above the detection threshold of DarkMESA.

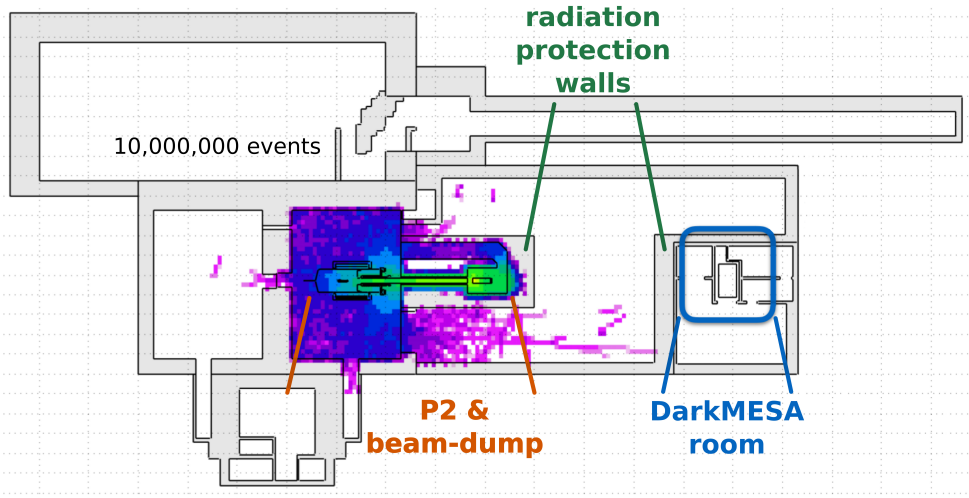

Figure 7.1.: Simulation of beam-related neutrons in the MESA halls with `FLUKA`. For 10^7 primary beam electrons no neutron reaches the DarkMESA room.

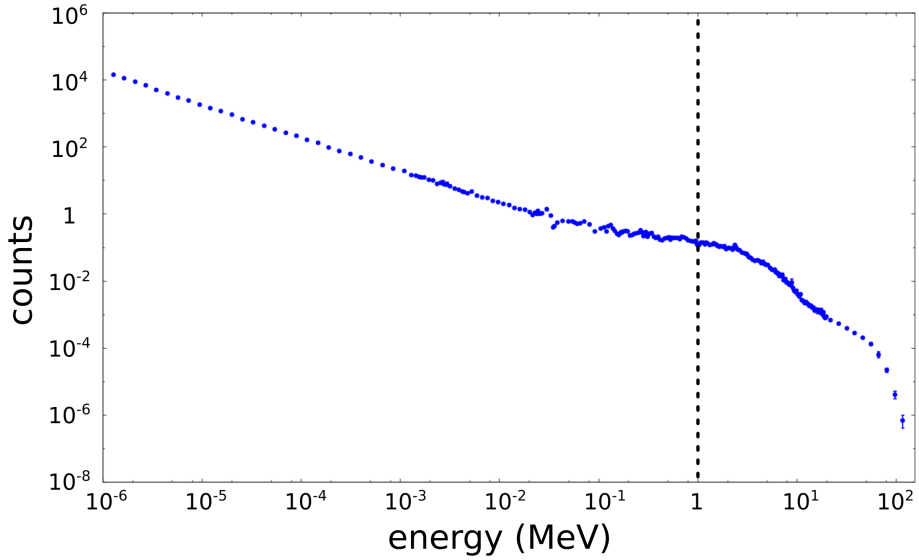

Figure 7.2.: Energy distribution of all generated neutrons from the `FLUKA` simulation in Fig. 7.1.

In addition, the calorimeter is built of materials whose neutron detection probability is low according to the study in Chap. 5.6 with 0.4 % for PbF_2 and 0.12 % for SF5 PbGl.

In the case of remaining background caused by beam-related neutrinos or neutrons, this could be suppressed by evaluating the calorimeter signals with and without MESA beam operation. Since DarkMESA is located only a few meters underground and only one meter of concrete serves as shielding above the experiment, the far greater part of neutrons and neutrinos is expected to come from cosmic-rays, which cannot be switched on and off so easily. This background must be modeled accurately in order to subtract it from the obtained calorimeter data. In [105] a possible procedure is described and for the BDX at JLab experiment $\simeq$ 5 neutrino events are predicted during the run-time of 285 days.

7.1.2. Beam-unrelated cosmic radiation

The largest background rate is expected from cosmic-rays. Burning processes in the sun and other cosmic events produce high-energy particles that are thrown into space. Most of them are captured by the Van-Allen belt surrounding the Earth. However, about 1 000 particles $\mathrm{m}^{-2}\,\mathrm{s}^{-1}$ reach the Earth's atmosphere, where further processes with the gas particles produce particle showers, which reach the Earth's surface. One primary particle can produce up to 10^{11} secondary particles. The primary radiation consists of protons (87 %), alpha particles (12 %), and heavy atomic nuclei (1 %). Neutrons, protons, and in particular pions are produced during the spallation of the gas molecules via the following processes:

$$\begin{aligned} p + p &\longrightarrow p + p + \pi^0 \quad , \\ &\longrightarrow p + n + \pi^+ \quad , \\ p + n &\longrightarrow p + n + \pi^0 \quad , \\ &\longrightarrow n + n + \pi^+ \quad , \\ &\longrightarrow p + p + \pi^- \quad . \end{aligned} \tag{7.4}$$

These pions can decay via the following processes:

$$\begin{aligned} \pi^0 &\longrightarrow \gamma + \gamma \quad , \\ \pi^+ &\longrightarrow \mu^+ + \nu_\mu \quad , \\ \pi^- &\longrightarrow \mu^- + \bar{\nu}_\mu \quad . \end{aligned} \tag{7.5}$$

The muons can reach the Earth's surface directly or decay in further processes:

$$\begin{aligned} \mu^+ &\longrightarrow \mathrm{e}^+ + \nu_e + \bar{\nu}_\mu \quad , \\ \mu^- &\longrightarrow \mathrm{e}^- + \nu_\mu + \bar{\nu}_e \quad . \end{aligned} \tag{7.6}$$

The particles resulting from these processes are those expected in the cosmics spectrum at the Earth's surface and are investigated in the following study. For the simulation a cosmics generator using CRY was implemented in the `Geant4` simulation (Sec. 3.4). The low energy solar neutrinos are not part of this generator and only the secondary neutrinos arising in Earth's atmosphere are considered.
In this study, it should be noted that only a single particle and not the full particle shower is generated as one event. This is a conservative approach, because the decay partners are not simulated, which may lead to detection mistakes in the simulation. On the other hand, these cases can also occur for large-area particle showers, where a part of the shower is flying past the detector. Therefore, this simplification should influence the results only to a small extent.
From the simulation, the energy spectrum in Fig. 7.3 is obtained for Mainz latitude on sea level. It is dominated by the muons and gammas from the decay processes in Eq. 7.5. The exact rates over the entire energy range and above a threshold energy of 10 MeV can be found in Tab. B.4 of Appx. B.5.2. This spectrum is a first indication of the particles a veto system to be developed has to deal with. In order to get a better impression of the spectrum at the DarkMESA detector,

the parts of the building above were simulated in a simplified way and the spectrum in Fig. 7.4 was obtained.

In addition to the first spectrum, the neutrinos and kaons produced in secondary processes are now included. The dominant particle species have not changed, but the rates have decreased. A comparison of the individual particle species before and after the simulated ceiling can be found in Fig. B.30 of Appx. B.5.2. In particular, the distribution of gammas has shifted to lower

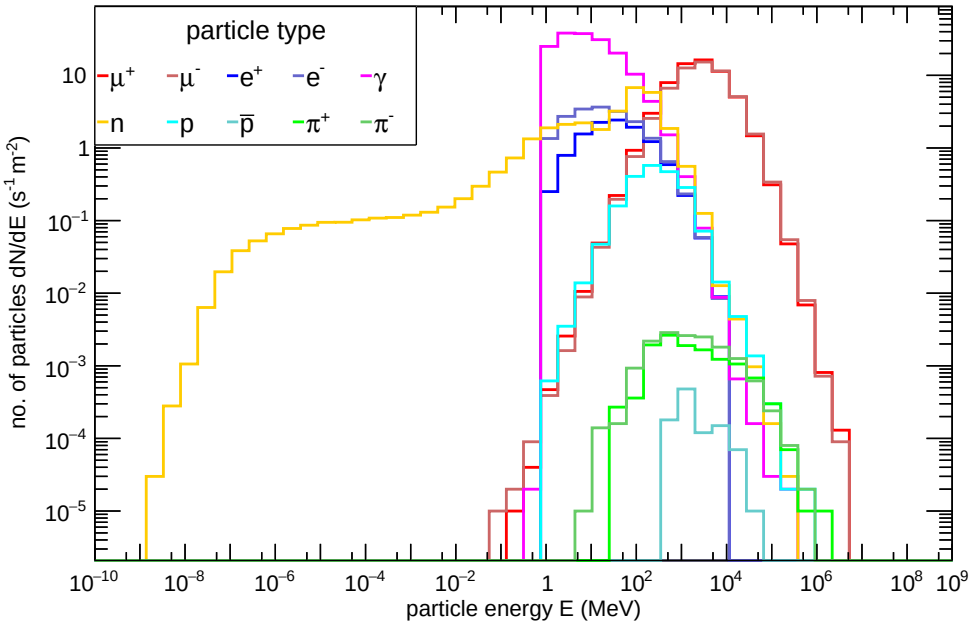

Figure 7.3.: Cosmic-ray spectrum simulated with the cosmic-ray shower library (CRY) for Mainz (sea level) at the 1st June of 2020.

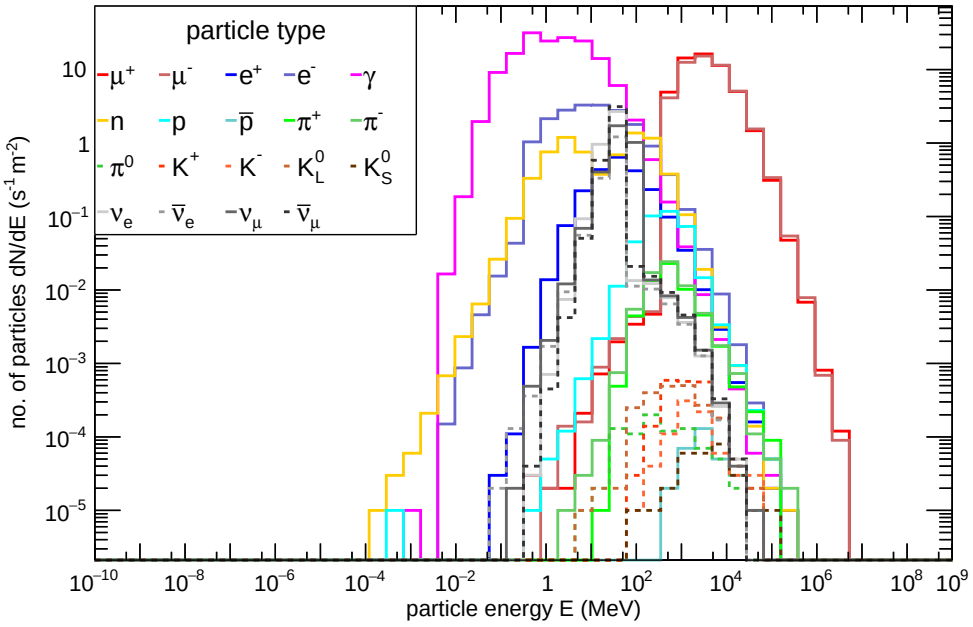

Figure 7.4.: Cosmic-ray spectrum simulated with the cosmic-ray shower library (CRY) for the DarkMESA room at the 1st June of 2020. For simplification reasons a 1 m layer of concrete was used to simulate the building parts above the DarkMESA room.

energies, and with an expected energy threshold of 10 MeV, their rate drops significantly from $165\,s^{-1}\,m^{-2}$ above ground to $23\,s^{-1}\,m^{-2}$. It also results in a drop from $30\,s^{-1}\,m^{-2}$ to $4\,s^{-1}\,m^{-2}$ for neutrons. In the muon spectra there is a sharp cut at about 400 MeV, which is due to the fact that low-energy muons are completely stopped in the concrete.
To reduce cosmic-rays even further, experiments searching for very rare events are often located very deep and well shielded underground. For DarkMESA, the shielding is limited and the suppression of this background becomes even more important.

In order to identify events in the calorimeter arising from cosmic-rays and to suppress them afterwards, these signals have to be detected in coincidence with another detector system. A veto system adapted for this purpose is presented in the following Sec. 7.2.

7.2. Concept for an efficient veto system

An efficient veto system has to enclose the calorimeter crystals hermetically and should have equally good or even better detection properties for all relevant particle types from the previous section. This approach is only possible because DM particles must have a very low interaction probability with SM particles. It is almost impossible that a DM particle detected in the calorimeter leaves a signal in a surrounding detector, too. A simplified scheme of how this might look like can be seen in Fig. 7.5.

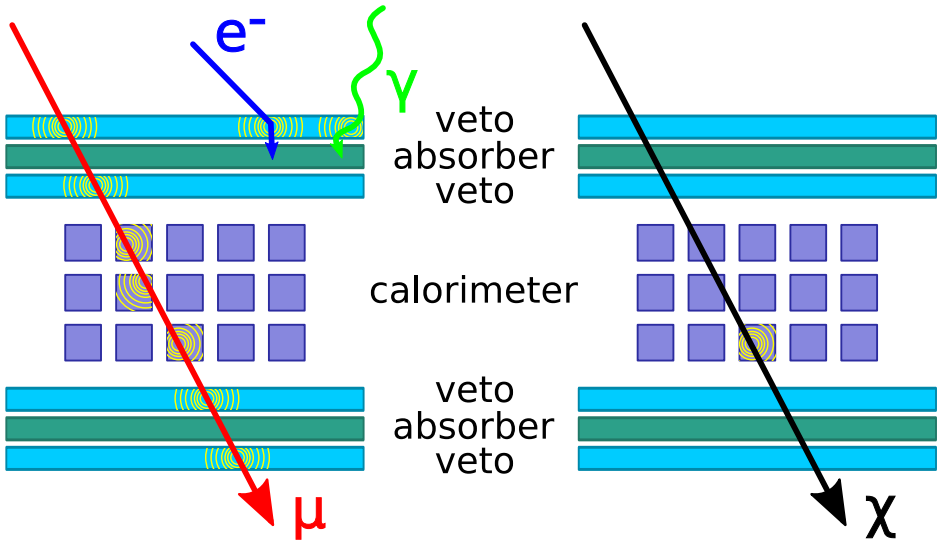

Figure 7.5.: Simplified scheme of a veto system for an enclosed calorimeter with a two veto layer setup and an intermediate absorber: on the left for particles from cosmic radiation and on the right for a DM particle.

With two veto layers and an intermediate absorber layer, events of low-energy electrons can also be distinguished from high-energy muons. The electrons are completely absorbed by one veto layer or stopped inside the absorber. The muon is a minimum ionizing particle and deposits energy in each layer leaving signals of same height. Particles close to the detection threshold of veto or calorimeter detectors can thus be stopped and identified at an early stage and the risk of leaving a signal only in one of the calorimeter crystals, like for DM, is reduced.

Selection of materials. An obvious choice of material for the veto layers are plastic scintillators, which are characterized by high light yield, easy machining, and relatively low cost. It has already been shown experimentally in Sec. 5.6 that the sensitivity of neutrons to plastic scintillators is 2–3 orders of magnitude higher than it is the case for PbF_2 or SF5.
In order to be able to also realize larger veto systems, EJ-200 from Eljen Technology was chosen, which combines a high light attenuation length of 380 cm with fast timing (0.9 ns rise time and 2.1 ns decay time). Lead is used as absorber, whose high nuclear charge ($Z = 82$) and high density (11.35 $\mathrm{g\,cm^{-3}}$) is especially beneficial for stopping gamma radiation. Lead is relatively soft, can be easily machined, and is cheap and easy to obtain. Additional secondary radiation due to Bremsstrahlung in the lead absorber must also be taken into account.

Sensitivity simulation study. In an idealized simulation, the sensitivity of EJ-200, SF5 PbGl, and PbF_2 for all particle types and energies expected in the DarkMESA room was studied. The simulation of a readout was omitted and only a block of 10×10 cm and a thickness of $z = 2$ cm was simulated. Barely above the central x-y position the incident particle is generated with momentum in z direction and a fixed energy. In each event the total number of produced optical photons is stored and after one million events the sensitivity is calculated by applying a detection limit of 100 optical photons to allow a comparison between the three materials. This was done across a broad energy range, but uncommon energies ($< 10^{-5}$ particles $\mathrm{s^{-1}\,m^{-2}}$) were neglected.
To obtain a good physical description over the wide energy range, the `QGSP_BIC_HP` physics list was used. This is especially recommended for shielding applications over all energy ranges. In particular, it contains a string model for interactions of high energy hadrons and an additional neutron package, which allows to track neutrons down to thermal energies.
The simulation results are tabulated in Tabs. B.5 and B.6 of Appx. B.5.3.
The neutron simulation results are in good agreement with the experiment, where in the investigated energy range of 0.5 to 7 MeV (with lower energies dominating), a sensitivity of 72 % was obtained for a plastic scintillator. The sensitivity for low energies of 0.1 MeV was found to be 78.948 %, for 1 MeV 49.742 %, and for 10 MeV still 18.827 %. For the SF5 PbGl, in turn, the values in this energy range were between 0.005 and 3.555 %, with the highest value for 10 MeV, which was less common in the experiment. This result is consistent with the experimental observation of 0.12 %. Consistency was also found for PbF_2.
For almost all particles, the plastic scintillator shows a higher sensitivity compared to the calorimeter materials. In contrast, the plastic scintillator becomes more and more inefficient for increasing neutron energies, while the efficiency of the calorimeter materials slightly increases again. Also for gamma particles with energies higher than 10 MeV, the plastic scintillator is less sensitive than the calorimeter crystals. A lead absorber, even in larger dimensions, is not suitable for shielding high-energy gammas. It only prevents low energy gamma particles generated in one veto layer, e.g. through Bremsstrahlung, from reaching further veto layers.

The inefficiency of the veto system for certain particle types is discussed again in a later optimization phase. First, the concept shown in Fig. 7.5 is realized for the Phase A prototype.

7.2.1. Veto system – Phase A

For the implementation of a veto system for the Phase A prototype the following requirements have to be fulfilled:

- The dimensions of the inner veto plane should allow the placement of the 5×5 PbF_2 calorimeter, a SF5 prototype[1], or future detectors of similar size. For first tests the placement of the whole system in a dark box is foreseen, which drives the wish for a compact design,
- hermetic enclosure of the calorimeter with as few gaps between elements as possible,
- holding structures must be able to support the weight,
- and easy access to the internal calorimeter and ability to replace individual scintillator plates without complete disassembly.

This resulted in the concept of a first prototype veto system shown in Fig. 7.6. Further technical drawings with exact size and the assembly concept can be found in Fig. B.31 of Appx. B.5.4.

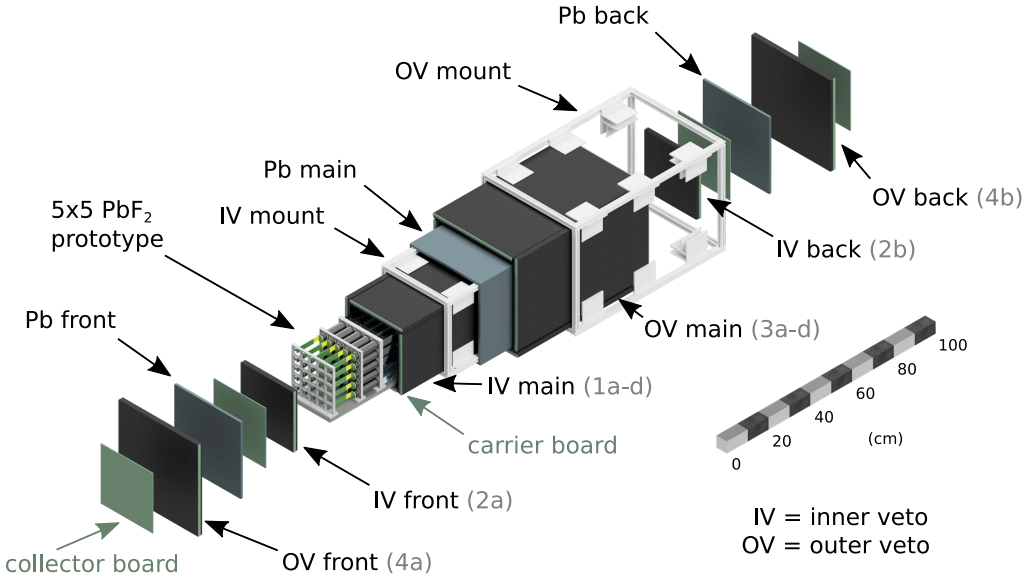

Figure 7.6.: Exploded-view CAD drawing of the veto prototype concept for the 5×5 PbF_2 Phase A prototype calorimeter with an inner and outer veto layer made of 2 cm thick EJ-200 plastic scintillator and a 1 cm thick lead layer in between. The electronic components of the readout are marked through green elements, the so-called carrier and collector boards.

A first inner veto layer tightly encloses the calorimeter, with the four large plates (1a-d) inserted into a MayTec® framework via aluminum angles. These angles also form the support base for the calorimeter block. The two smaller plates (2a-b) close off the inner veto and are held in position via small angles. A thickness of 20 mm was chosen for the EJ-200 scintillators. Lead plates are screwed to the outside of the MayTec® framework. In order to still be able to handle the prototype well, a lead thickness of only 10 mm was chosen. Nevertheless, this equals a lead

[1] At the time of design, the offer to use the SF5 crystals from SAPHIR (460 mm long) was not present. Only the usage of the shorter SF5 blocks from Schott (260 mm long) was planned. The usage of the SAPHIR crystals with the original PMTs is not possible, but a readout with SiPMs or shorter PMTs is still possible.

weight of about 100 kg and the whole prototype will thus weigh about 200-220 kg.
The entire inner veto and calorimeter block can then be inserted into another MayTec® framework, which contains the outer veto. Like for the inner veto, there are two differently dimensioned scintillator plates 3a-d and 4a-b. The dimensions are such that the length of the side to be read out is always 250 mm for the inner veto and 380 mm for the outer veto. This simplifies the development of a readout and allows the comparison of two or four plates at a time.

Readout of the scintillators. During initial beam-tests at MAMI, a 500×250 mm and 20 mm thick plastic scintillator plate was tested with and without embedded wavelength shifting (WLS) fibers. The readout was performed using four SiPMs (SensL 60035) per short side. They have a sensor of $6 \times 6\,\mathrm{mm}^2$ composed of 18980 microcells with a pixel size of $35 \times 35\,\mu\mathrm{m}^2$ allowing the detection of single photons [164]. The light collection for different scanning positions was investigated with an 855 MeV electron beam. The results of these measurements can be found in the Master's thesis of Matteo Lauß and were published in [165]. It was shown that the light collection with a WLS fiber of round geometry and 1.5 mm diameter can be improved by up to 50 % in the neighborhood of the fiber compared to the setup without fibers. However, the detection properties of such a detector are highly position-dependent and fast and accurate interpretation of the data, which is preferred at this prototype stage, becomes difficult. In addition, the insertion of the fibers requires more work and the scintillator material varies in thickness due to the milling of the grooves. Therefore, fibers were not used in the prototype and instead the number of SiPMs per side was increased from four to nine. First tests with these new readout boards have started, but a complete assembly of the prototype could not be done yet due to the present global chip crisis, so that a redesign became necessary. For this reason, no exact layout is given here. The concept foresees a carrier board that is located directly at the scintillators. With a width of only 10 mm, it is dimensioned in such a way that the respective scintillator side is only half covered and an adjacent scintillator can still rest on it. This board carries the SiPMs and a first preamplifier stage. A further amplification, the discrimination of the signals, the voltage supply, and both analog and digital outputs are on a collector board which can supply six carrier boards via flexible zero insertion force (ZIF) cables. With a total of four collector boards the readout of all twelve plastic scintillators on both sides is possible.
Each SiPM is operated with a supply voltage below 30 V, via a HV-digital-to-analog converter (DAC). For the readout of the full waveforms, the CAEN digitizer or the PANDA S-ADC can be used. The latter is an ADC under development at KPH which, in contrast to the commercial CAEN device, achieves a sampling rate of only 80 MHz, but due to the flexibility in development and lower costs per channel it is foreseen to be used at this early stage of DarkMESA. Since the exact thickness and flexibility of all cables to be fed through the veto and lead layers is not yet fully known, the implementation of a cable feedthrough has been omitted in Fig. 7.6. However, this option is already provided in the simulation, and looking at individual panels showed only slight variations in light output when the cable feedthrough is close to the readout sides (Fig. B.33 of Appx. B.5.4).

This concept was designed without a complete cosmic-ray simulation. In the following, the theoretically achievable efficiencies are determined. If there is a need for improvement, these

observations will be implemented for the prototype if possible, otherwise they will be included in the design for Phase B.

Simulation study of a single scintillator panel. In a first simulation study, a single scintillator plate ($500 \times 250 \times 20\,\mathrm{mm}^3$) is examined. This study should provide information on how many of the initially generated optical photons are detected by the SiPMs and which spatial dependencies exist. A comparison with the experimental results from Matteo Lauß' Master thesis is also possible to some extent. The scintillators are wrapped in a crumpled aluminum foil with $7 \times 7\,\mathrm{mm}^2$ cutouts for each $6 \times 6\,\mathrm{mm}^2$ SiPM. For these, a typical efficiency of 38 % according to the data sheet is assumed. Since only the percentage light yield has to be determined in this study, the type of primary particle is not yet relevant. The choice fell on 1 GeV muons generated above the scintillator at random positions. 20 000 events were generated.
The simulation result in Fig. 7.7 shows a homogeneous distribution to a great extent. The average light yield is $\sim 8.5\,\%$. Deviations from this can be found in the edge areas. There are particularly favorable positions for a higher light yield directly in front of the SiPMs, but there are also some positions with bad scattering angles resulting in a decreased light yield. Looking at the Figs. B.34 and B.35 of Appx. B.5.4, which show the light yield of the SiPMs one by one, the effects for light production directly in front of the SiPMs is evident. Furthermore, one recognizes a cone, which causes a reduced light yield for positions on the same side but further away from the SiPM.

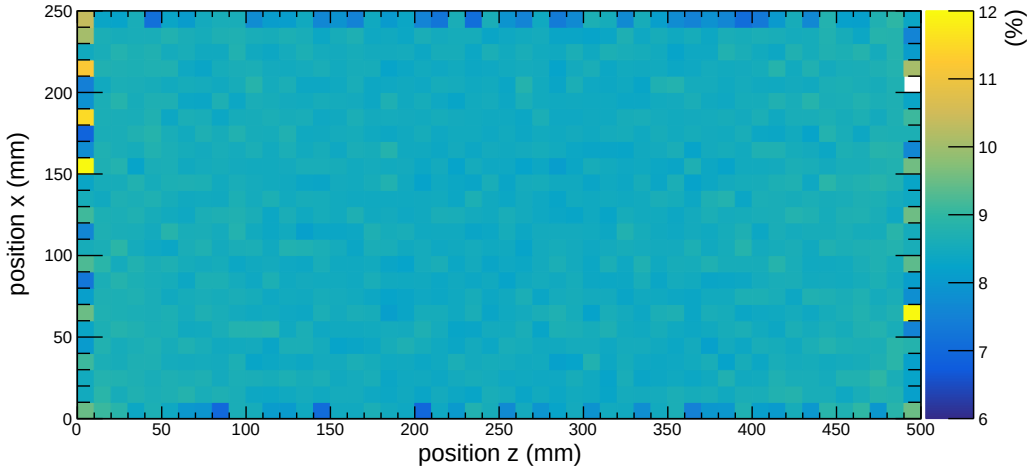

Figure 7.7.: For a 500 mm long scintillator panel, the optical photons detected in total by all SiPMs in relation to all generated optical photons, depending on the primary particle position, is shown. With exception of the edge areas, a homogeneous distribution can be found and the average value is $\sim 8.5\,\%$.

This result cannot be directly compared with available experimental data. In a next step, the light collection of the left SiPM side was distinguished from the right one and the percentage ratio on the total yield was plotted. The results are plotted both for the simulation and a laboratory experiment in Figs. 7.8 and B.32 of Appx. B.5.4. In the experiment, a ^{90}Sr source was placed on top of the scintillator at 200 different positions in a measurement grid. In 45 s long measurements the percentage light yield was calculated from the observed counting rates.
As expected, the distribution for central positions is close to 50 %. Near the actual readout side, the proportion of direct light increases and the percentage ratio on the total yield increases, while it decreases on the opposite side. The results of simulation and experiment agree qualitatively. A

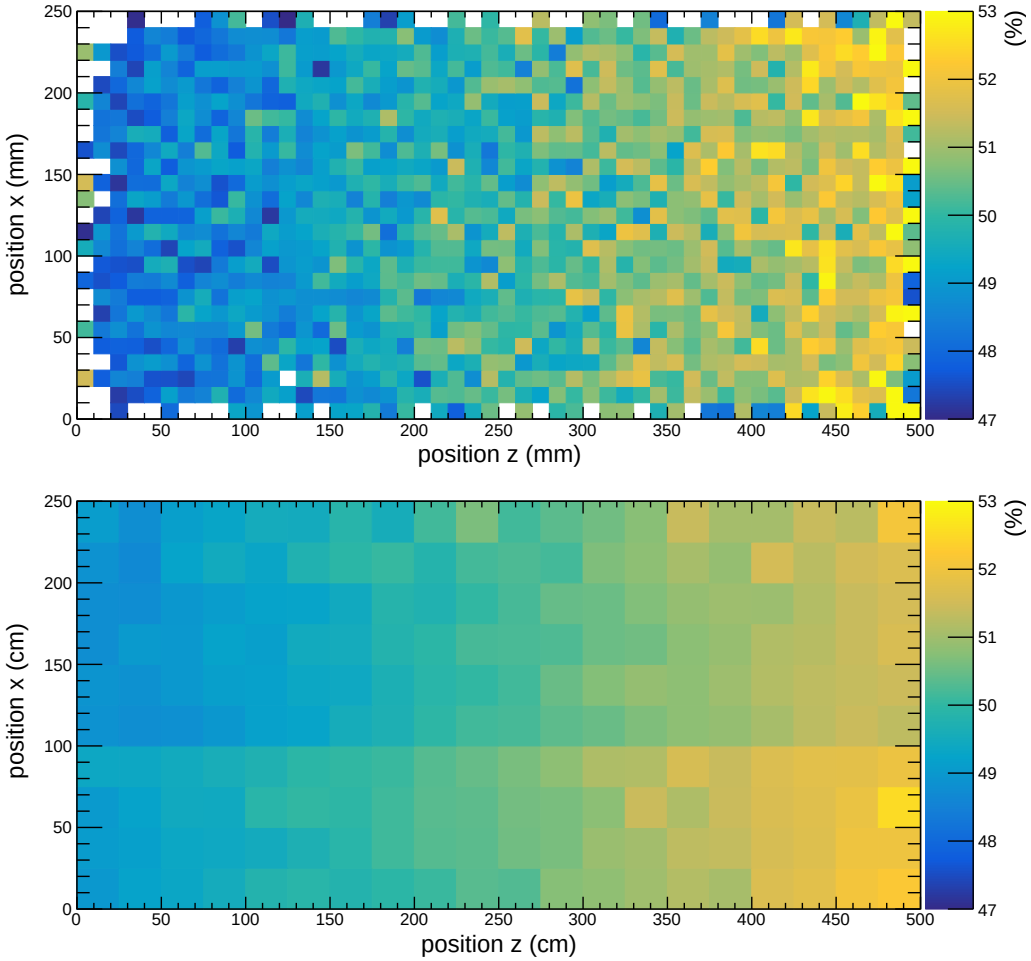

Figure 7.8.: Percentage ratio on the total yield in simulation (top) and experiment (bottom) for a readout of the nine SiPMs on the right side.

reduction of the number of bins was omitted in the case of the simulated data, because additional edge effects arise. These are due to the effects already mentioned above and are not yet visible in the experimental data due to the smaller grid.

Simulation studies of full Phase A prototype. For these studies, the simulation part described in Sec. 3.4 is used. The prototype shown in Fig. 3.3 is initially simulated with the first Pb absorber between the two veto layers only. Above the setup a layer of 1 m concrete approximates the hall ceiling and directly above, the CRY generator is placed with a size of $3 \times 3\,\mathrm{m}^2$. This can only be considered as an approximation, since incoming cosmic particles with large angles are not correctly treated. However, an even larger generator would lead to performance limits of the simulation. For the study of the complete setup, the full tracking of the produced optical photons is omitted for performance reasons, too. The number of optical photons generated is therefore calculated but only threshold values are used to decide whether this is enough for a detectable signal. The threshold to detect a real signal in a scintillator is calculated conservatively. Out of the total 18 SiPMs, half shall detect a signal of five photons on average. This corresponds to 45 photons to be detected, resulting in a threshold of 500 generated optical photons when the light yield of 8.5 % from the previous study is taken into account. Since the scintillator used in this study was of medium size, this value is also used as a good approximation

for all other panels. It corresponds to an average energy deposit of about 0.05 MeV for muons. The energy deposit in each veto layer is plotted as an example in Fig. 7.9.

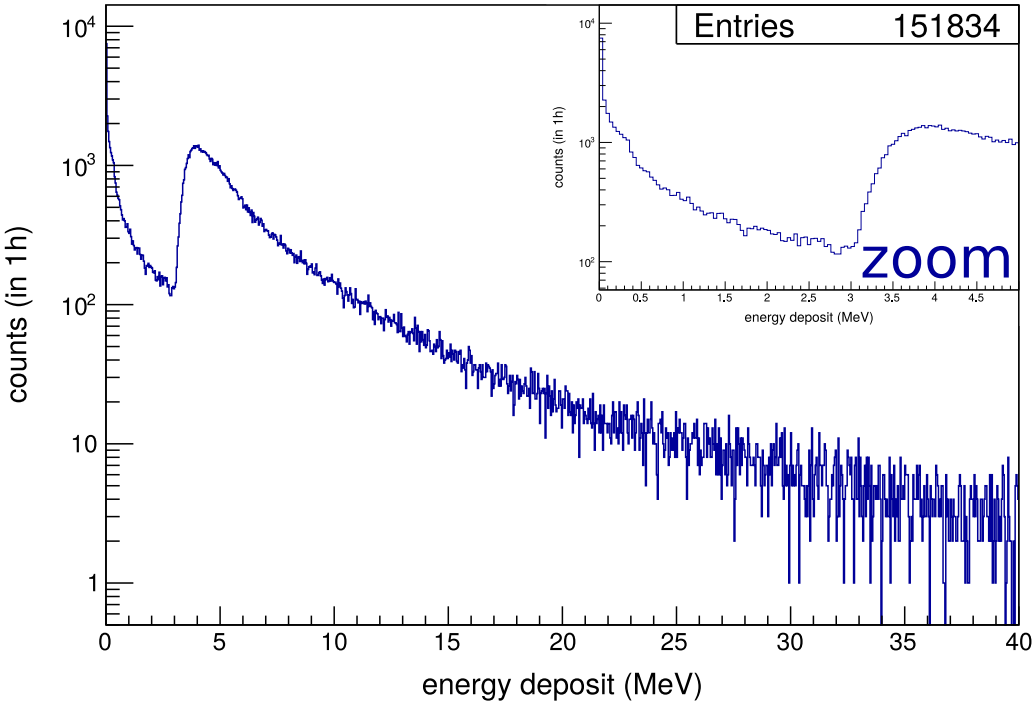

Figure 7.9.: Deposited energy of all cosmic events in all Phase A veto layers stacked in a single histogram. A peak is found at around 4 MeV and corresponds to the most common energy deposit of a minimum ionizing particle crossing a horizontal veto layer vertically from above.

With this threshold of 500 optical photons, 5.4 % of the cosmic-rays, which leave an energy deposit, are not counted as veto events. By far the largest part deposits its energy in the horizontally lying veto planes and flies through an average of 20 mm of plastic which corresponds to an energy deposition of about 4 MeV in most cases. For the energy deposition in the calorimeter crystals, the result from the experimental studies in Chap. 5 is used. Whether PbGl or PbF_2, the spectra could be resolved for an energy deposition of 10 MeV and this value is now used as energy threshold. A comparison of the spectra of energy deposit and produced optical photons shows at which point the cut has to be set in units of optical photons. In this case 10 MeV corresponds to 1 250 generated optical photons. The simulation also includes a time gate. After the first detection of an event in any detector element, a maximum time of 20 ns may elapse for further veto or calorimeter signals to be accepted.
Only events in which at least one calorimeter crystal detects a signal are of interest for the simulation. No fixed number of cosmic events is simulated but rather a simulated duration of the CRY generator is specified – one hour in this study. A calorimeter signal is not expected in every case, because of the relatively small active volume in relation to the CRY generator size. For the prototype, energy deposition and number of optical photons produced are plotted for each individual calorimeter crystal as well as for the whole module in Fig. 7.10. The three colors represent the following veto conditions:

- Blue: At least two veto layers detect a signal.
  $\longrightarrow$ Can be considered a cosmic veto event and discarded.

- Green: A maximum of one veto layer detects a signal.
  ⟶ Not clearly assignable to a cosmic veto event.

- Red: No veto layer detects a signal.
  ⟶ Inefficiency of the proposed veto system.[2]

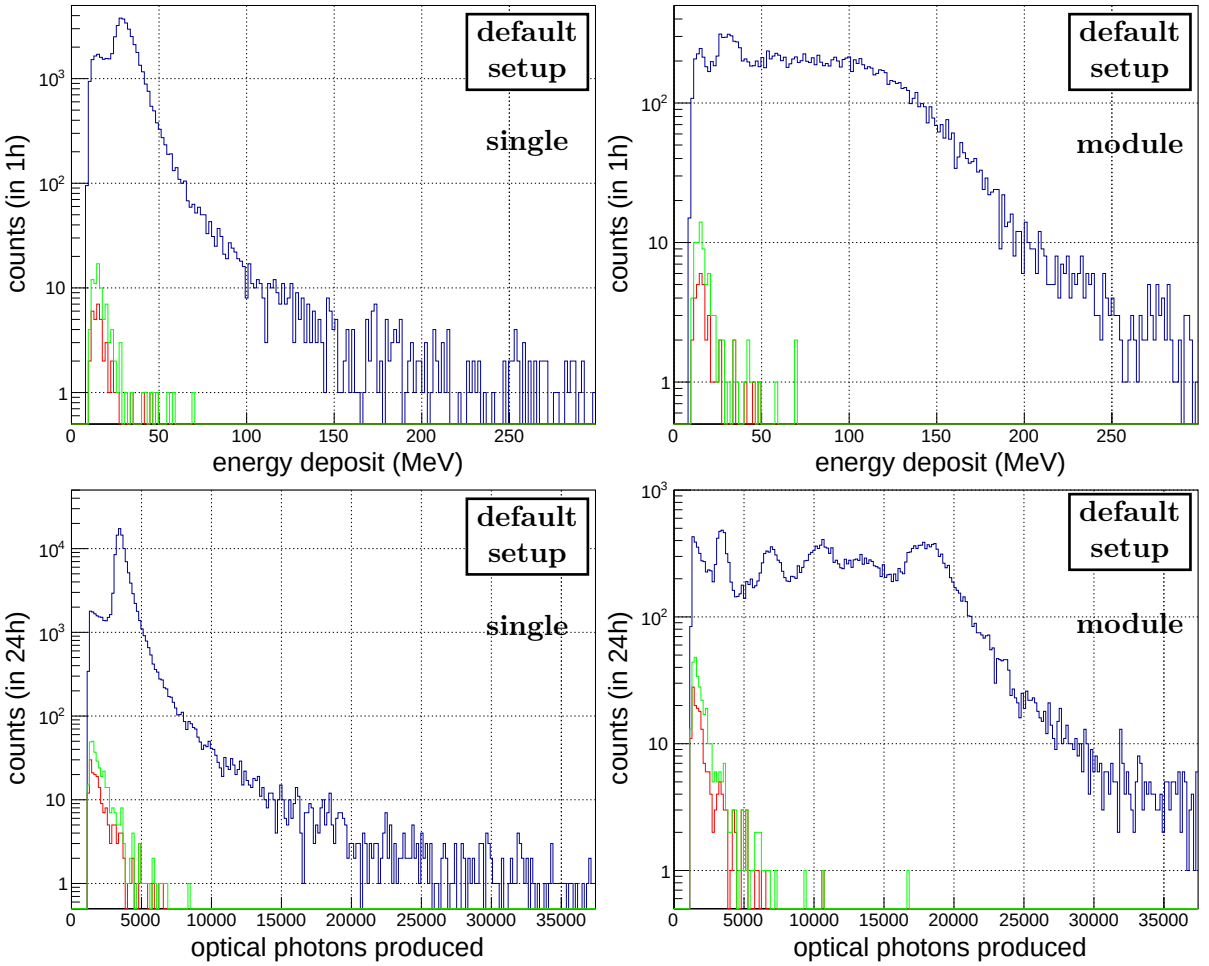

Figure 7.10.: One hour of cosmic radiation was simulated above the 1 m concrete ceiling of the DarkMESA room for the Phase A prototype. For each event detected in at least one of the calorimeter crystals, the veto condition was evaluated and the histogram corresponding to the veto condition's color was filled. This was done top for the energy deposition and bottom for the generated optical photons. On the left, the values for all individual calorimeter crystals are registered, on the right only the sum of an event is shown. The associated counts, veto inefficiencies, and rates can be found in Tab. 7.1.

For an efficient veto system, it is clear that events with green and especially red veto conditions must be strongly reduced and, at best, completely eliminated. In the case of the **default** setup, this has only been achieved to a limited extent. Almost all events with one of these two conditions, leave a signal in only one single crystal. That is why there is no great difference between the single crystal and full module histograms for these two conditions. Although they occur several orders of magnitude less frequently, the veto inefficiency is still too high at about 0.2 %. With this value, it seems unrealistic to work with the previously determined calorimeter threshold of 10 MeV. The threshold would have to be in the range of 50 MeV, which would have a negative

[2] It is important to note that the condition for zero veto events is contained in the veto conditions green and red.

impact on the energy range of DM that can be studied by DarkMESA. The obvious reasons for the poor efficiency are the different particle sensitivities of the calorimeter and veto materials used, which were studied at the beginning of Sec. 7.2. Furthermore, a larger amount of lead was omitted due to the prototype's weight. Both problems can be reduced by making small adjustments that do not change the structure of the prototype itself. The possible setups are shown in Fig. 7.11. In a first improvement step, the **calo** setup, the outermost ring of calorimeter crystals is used as additional veto and not as DM detector. Although this leads to a significant 64 % reduction in active volume in the prototype case, this change is not as significant for larger detectors. In a second step, the **ceiling** setup, a large-area veto detector is applied above the prototype. This consists of a 2 cm thick plastic scintillator directly under the concrete ceiling and a subsequent 5 cm thick lead absorber. The **both** setup combines the two improvements.

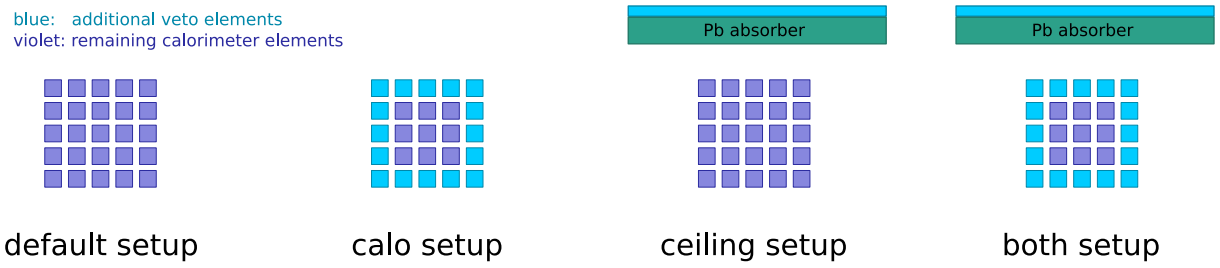

Figure 7.11.: Additional veto concepts for improvement of veto efficiency. Inner veto, outer veto, and Pb absorber are not shown, since they do not change. Beside the default setup the use of calorimeter crystals as additional veto elements and an additional veto detector at the ceiling are foreseen.

Phase A		≥ 2 veto	≤ 1 veto	0 veto	inefficiency (%)	rate (Hz)	projected counts (2 200 h)
default	**single**	48 469	88	39	8.04×10^{-2}	1.08×10^{-2}	8.58×10^{4}
	full	17 944	82	37	2.06×10^{-1}	1.03×10^{-2}	8.14×10^{4}
calo	**single**	17 476	15	4	2.29×10^{-2}	1.11×10^{-3}	8.80×10^{3}
	full	9 020	14	3	3.32×10^{-2}	8.33×10^{-4}	6.60×10^{3}
ceiling	**single**	46 711	7	2	4.28×10^{-3}	5.56×10^{-4}	4.40×10^{3}
	full	17 329	7	2	1.15×10^{-2}		
both	**single**	16 608	0	0	$< 6.02 \times 10^{-3}$	$< 2.78 \times 10^{-4}$	$< 2.20 \times 10^{3}$
	full	8 689	0	0	$< 1.15 \times 10^{-2}$		

Table 7.1.: For all four Phase A prototype setups the counts of the three veto conditions and the calculated inefficiencies, rates, and the projected counts are summarized.

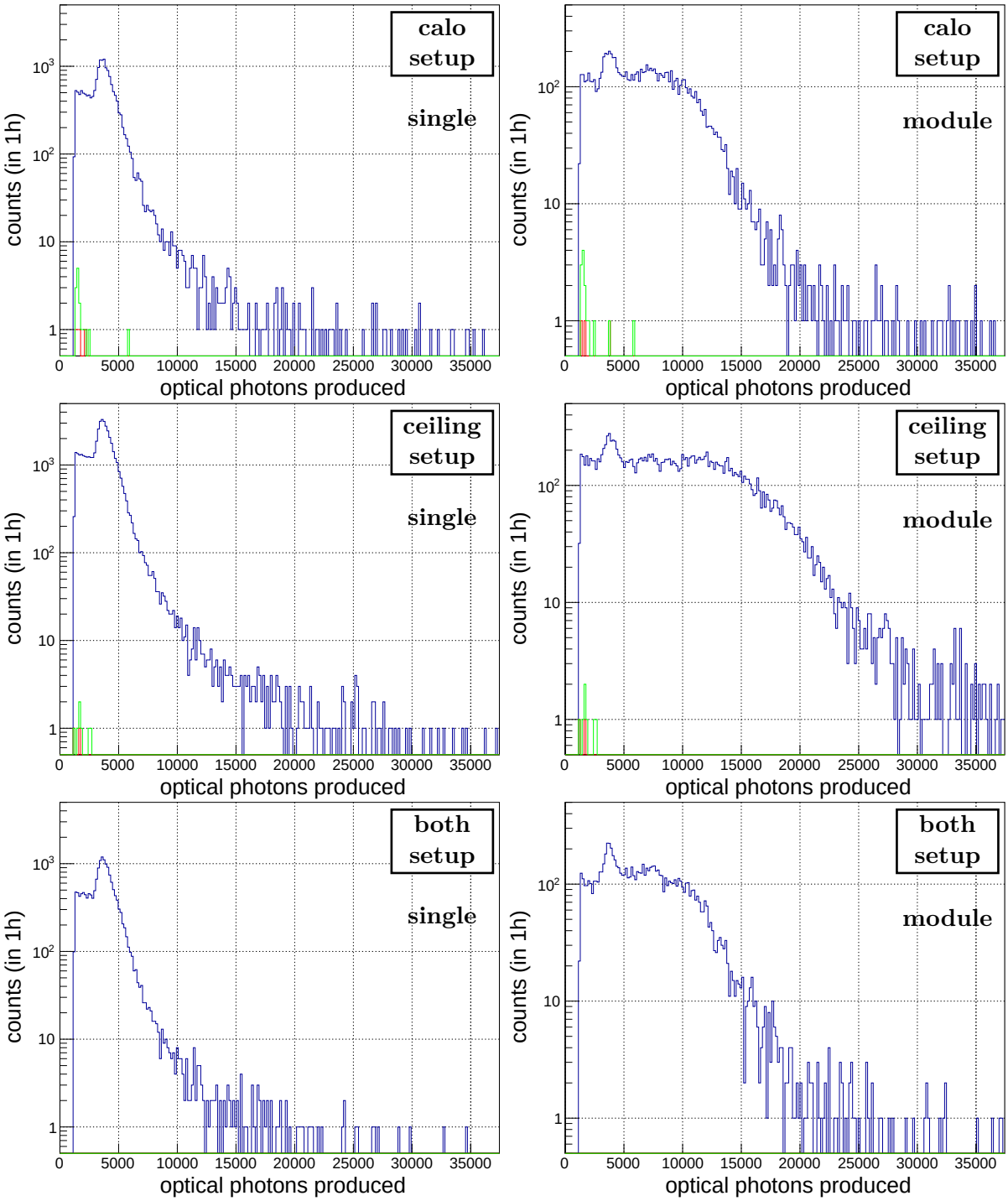

Figure 7.12.: Simulation results of the improved veto concepts for the Phase A prototype – top for the **calo** setup, middle for the **ceiling** setup, and bottom for the **both** setup. On the left, the values for all individual calorimeter crystals are registered, on the right only the sum of an event is shown. The associated counts, veto inefficiencies, and rates can be found in Tab. 7.1.

The results of these three new studies are shown in Tab. 7.1 and Fig. 7.12, where the events are histogrammed by the number of produced optical photons. It can be seen that the two additional options, both in absolute and percentage values, reduce the calorimeter signals without a veto signal present. The veto inefficiency drops from 0.206 % to 0.033 % for the **calo** setup and 0.012 % for the **ceiling** setup. No inefficiencies are found in the combination of both improvements within one hour, resulting in an upper bound of 0.012 %. The shielding effects of the additional ceiling

veto and the additional lead layer are also evident. In the simulations that include these, almost 4 % fewer cosmic particles reach one of the calorimeter crystals.
Which primary cosmic particles are responsible for these inefficiencies was also investigated within the simulation study. A separation by particle type and the number of signal-giving veto panels for the **default** setup can be found in Fig. 7.13. The events with 0 veto panels are the inefficiencies. The separation by particle type for the three improved setups can be found in Fig. B.36 of Appx. B.5.4. A comparison shows that the inefficiencies largely due to gamma particles are strongly suppressed with the ceiling veto. The inefficiencies due to low-energy electrons and positrons are almost completely removed.

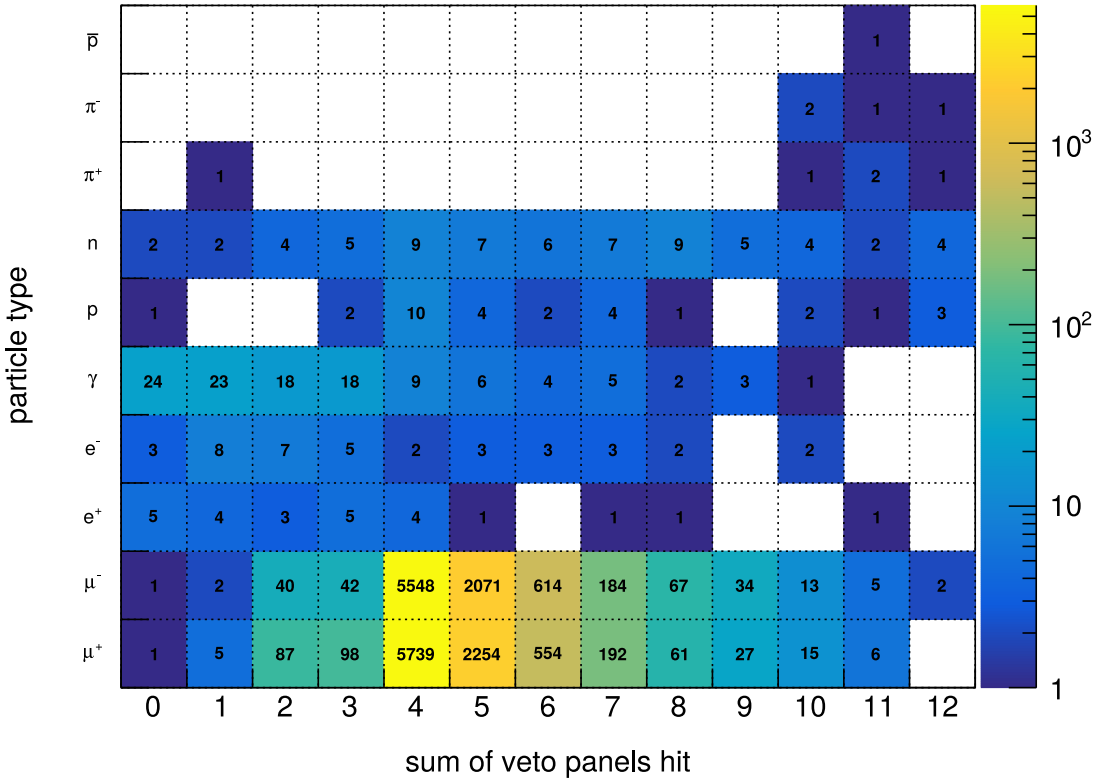

Figure 7.13.: Sum of the signal-giving veto panels separated by the primary particle type for the Phase A **default** setup. Events with no signal-giving veto panels are the inefficiencies of the system.

One way to further reduce these potentially critical particle types is to add an additional absorber layer immediately around the calorimeter. A reduction of the fraction of γ, e^+, and e^- by 35 % is observed (Tab. 7.2) and the veto efficiency is slightly improved. A thicker shielding between the veto layers is also desirable for the subsequent Phase B.

With all improvements, a good efficiency of about 99.99 % can be achieved, but due to the short simulation time of 1 h, up to 2 200 cosmic signals must still be expected in the calorimeter crystals during the entire Phase A. By measuring without beam for a similar amount of time, the background of both measurement series can be compared and further reduced. The efficiency can be further adjusted by changing the threshold values as well. For the development of Phase B additional improvements should be implemented. On the one hand, the critical particles could be reduced with a larger amount of lead. On the other hand, it has been seen that a great amount of active volume is allocated by using the outer calorimeter crystals as additional veto elements.

setup	μ^+ / μ^-	γ	n	e^+ / e^-	other
no lead absorbers	93.65 %	2.71 %	1.78 %	1.19 %	0.67 %
one lead absorber	95.04 %	1.87 %	1.64 %	0.80 %	0.65 %
two lead absorbers	96.15 %	1.18 %	1.59 %	0.52 %	0.56 %

Table 7.2.: Proportion of the different primary cosmic particles among the signals detected in the calorimeter for the three possible Phase A lead configurations.

An adaptation where the lower and perhaps some lateral crystals are used as DM calorimeters again seems appropriate. Since the logic signals of all elements will be merged via an FPGA, the decision on whether to assign them as veto or DM calorimeter element should be made in an experimental study.

7.2.2. Veto system – Phase B

For Phase B, the concept of an inner and outer veto layer is used again. Based on the previous simulation results, the lead layer in between is chosen to be 5 cm thick. Large parts of the readout electronics from Phase A will be used again and gaps in the veto layers are to be kept as small as possible. However, the six sides of each veto plane cannot consist of a single scintillator plate in this case. Each side will consist of 5–9 long scintillator panels with a fixed width of 250 mm and lengths between 1 800 and 2 258 mm. To ensure a good gap closure, the side surfaces of adjacent plates are tapered: this is the same principle as in the MAGIX trigger veto system (Fig. 4.1).

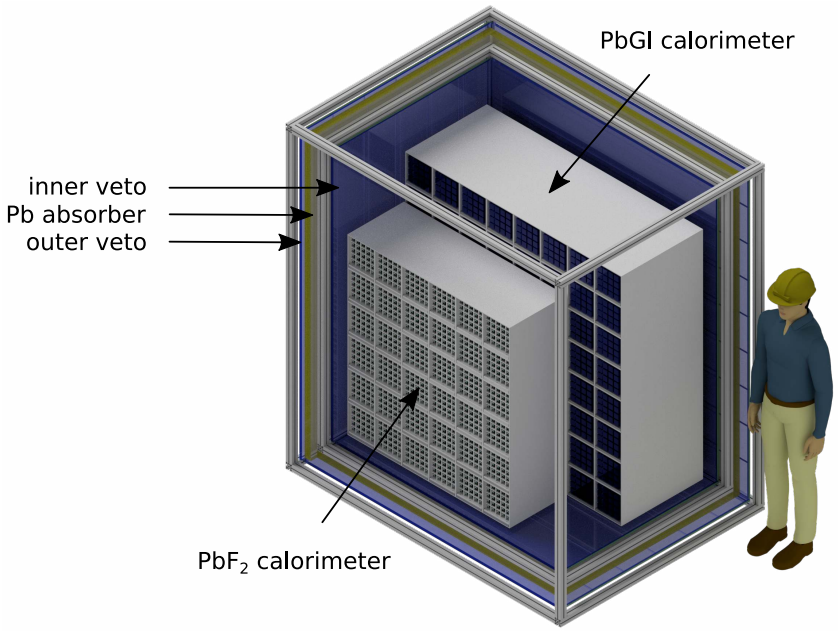

Figure 7.14.: CAD drawing of the veto concept for the Phase B PbGl and PbF_2 calorimeter with an inner and outer veto layer made of 2 cm thick EJ-200 plastic scintillator and a 5 cm thick lead layer in between. The front, top, and right veto elements are not indicated.

In Fig. 7.14 an idealized design is shown. Obviously, the lowest two veto layers will not close completely hermetically. First, the weight of the calorimeter walls and lead absorbers cannot rest on this scintillator panels, but must rest on the hall floor via support feet. Secondly, the signal and HV cables of the calorimeters must be fed out. The load capacity of the now more massive structure made of MayTec® has not yet been finalized and must be adjusted due to the increased lead amount of up to 10 t.

Simulation study of a single scintillator panel. Since the veto panels are significantly larger than the ones in the prototype study, the light yield of a 2 000 mm long panel was simulated first. The study showed a decrease of light yield from the readout to the scintillator's center by $\sim 2\,\%/100\,\mathrm{mm}$.[3] Overall an average light yield of 2.7 % was found.[4] This lower value results in a higher detection threshold of 1 600 generated optical photons, corresponding to a deposited energy of about 0.16 MeV for muons.

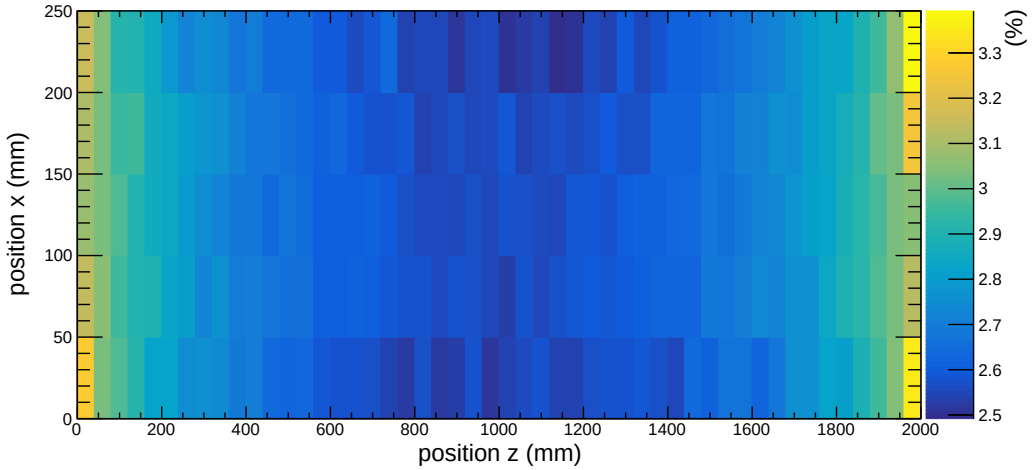

Figure 7.15.: For a 2 000 mm long scintillator panel, the optical photons detected in total by all SiPMs in relation to all generated optical photons, depending on the primary particle position, is shown. Overall an average value of $\sim 2.7\,\%$ can be found, while the value decreases by $\sim 2\,\%/100\,\mathrm{mm}$ from the readout to the scintillator's center.

Simulation studies of full Phase B setup. The procedure for this study is the same as in the previous subsection. The generator size of $3 \times 3\,\mathrm{m}^2$, the concrete ceiling, and the time period of 1 h remain the same. The threshold values for the calorimeter crystals remain at 10 MeV and 1 250 generated optical photons, respectively. Only the threshold values for the veto elements change according to the previous study to 0.16 MeV and 1 600 generated optical photons. The veto conditions and their color marking from Sec. 7.2.1 still apply. The results for the **default** setup can be found in Fig. 7.16. Due to the two orders of magnitude increase in active volume, the inefficiencies in absolute values are higher than for the Phase A prototype. However, due to the better shielded calorimeter, the percent inefficiency has already improved to 0.065 % compared to 0.206 % for the prototype. With the veto improvement options already established in the

[3] In an experimental study of a 500 mm long scintillator and four SiPMs per side, the value for the central region was found to be $5\,\%/100\,\mathrm{mm}$.

[4] The yield in the final setup could be increased by a segmentation of the veto panels, but it is also possible to use wavelength shifting fibers which were already studied in the Master's thesis of Matteo Lauß (results published in [165]).

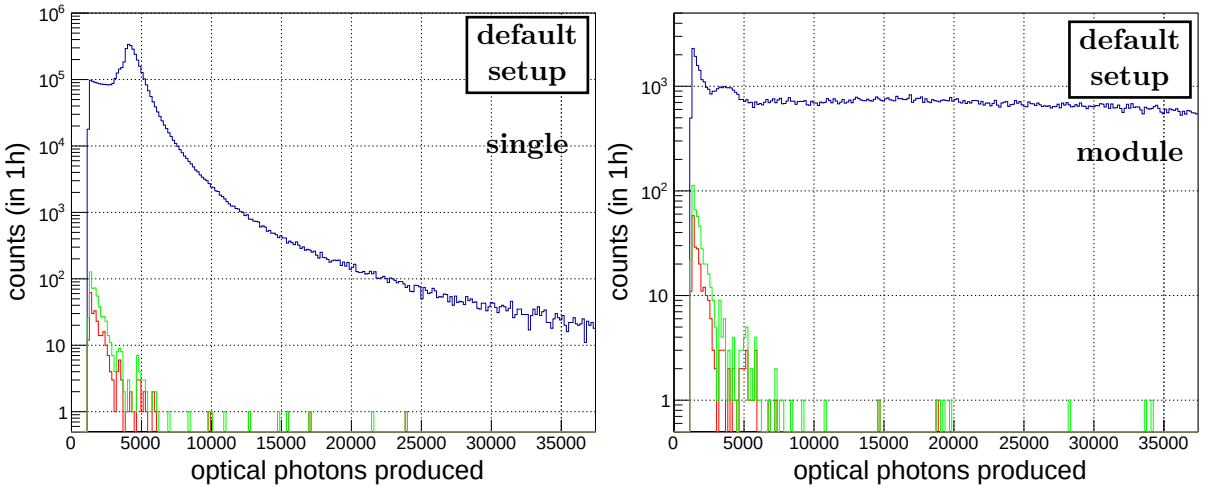

Figure 7.16.: One hour of cosmic radiation was simulated above the 1 m concrete ceiling of the DarkMESA room for the Phase B setup. For each event detected in at least one of the calorimeter crystals, the veto condition was evaluated and the histogram corresponding to the veto condition's color was filled. On the left, the values for all individual calorimeter crystals are registered, on the right only the sum of an event is shown. The associated counts, veto inefficiencies, and rates can be found in Tab. 7.3.

Phase B		**≥ 2 veto**	**≤ 1 veto**	**0 veto**	**inefficiency (%)**	**rate (Hz)**	**projected counts (6 600 h)**
default	**single**	4 356 639	576	265	6.08×10^{-3}	7.36×10^{-2}	1.75×10^{6}
	full	357 579	486	233	6.51×10^{-2}	6.47×10^{-2}	1.54×10^{6}
calo	**single**	1 788 407	98	35	1.96×10^{-3}	9.72×10^{-3}	2.31×10^{5}
	full	171 438	62	24	1.40×10^{-2}	6.67×10^{-3}	1.58×10^{5}
ceiling	**single**	4 204 137	87	33	7.85×10^{-4}	9.17×10^{-3}	2.18×10^{5}
	full	346 154	79	31	8.95×10^{-3}	8.61×10^{-3}	2.05×10^{5}
both	**single**	1 720 779	8	3	1.74×10^{-4}	8.33×10^{-4}	1.98×10^{4}
	full	165 647	6	2	1.21×10^{-3}	5.56×10^{-4}	1.32×10^{4}

Table 7.3.: For all four Phase B setups the counts of the three veto conditions and the calculated inefficiencies, rates, and the projected counts are summarized.

previous subsection, the histograms in Fig. 7.17 and the values in Tab. 7.3 are obtained.

In the case of the **calo** setup, the outermost ring of detector elements of both calorimeters is reassigned to veto elements. For the active volume, this corresponds to a loss of 12 %. It is again evident that in the case of inefficiencies almost always only one calorimeter crystal responds. Using all options, a veto efficiency of almost 99.999 % can be achieved.

Looking at the particle types involved in Fig. 7.18, one sees again that γ, e^+, and e^- are responsible for a large fraction of the inefficiencies. In particular, the veto ring of PbF_2 crystals helps to eliminate inefficiencies due to cosmic gammas. A new aspect, is the high neutron contribution, which becomes more relevant due to the now larger calorimeter even though the neutron sensitivities of the calorimeter materials are poor. With the additional veto options, the inefficiencies can be almost completely eliminated, but one should be aware of the short

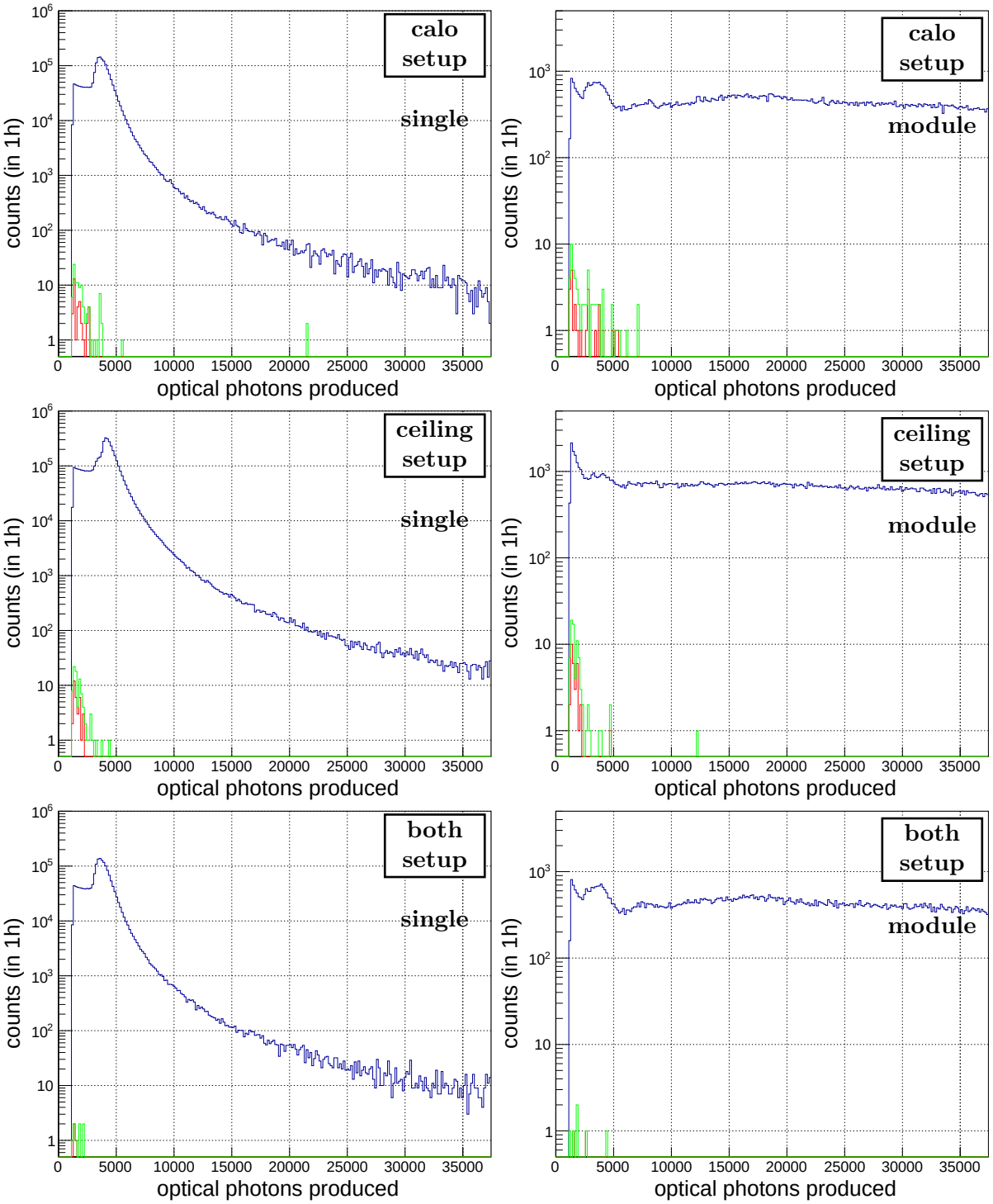

Figure 7.17.: Simulation results of the improved veto concepts for Phase B – top for the **calo** setup, middle for the **ceiling** setup, and bottom for the **both** setup. On the left, the values for all individual calorimeter crystals are registered, on the right only the sum of an event is shown. The associated counts, veto inefficiencies, and rates can be found in Tab. 7.3.

simulation time. At longer runtimes, neutral pions or kaons may also become relevant. In addition, the cosmics generator was used in simplified form, which does not reflect laterally incident events.

These two remaining events correspond to 13 200 cosmic events left as background for a MESA runtime of 6 600 h in the second funding period, and it is necessary to reduce it further. Besides

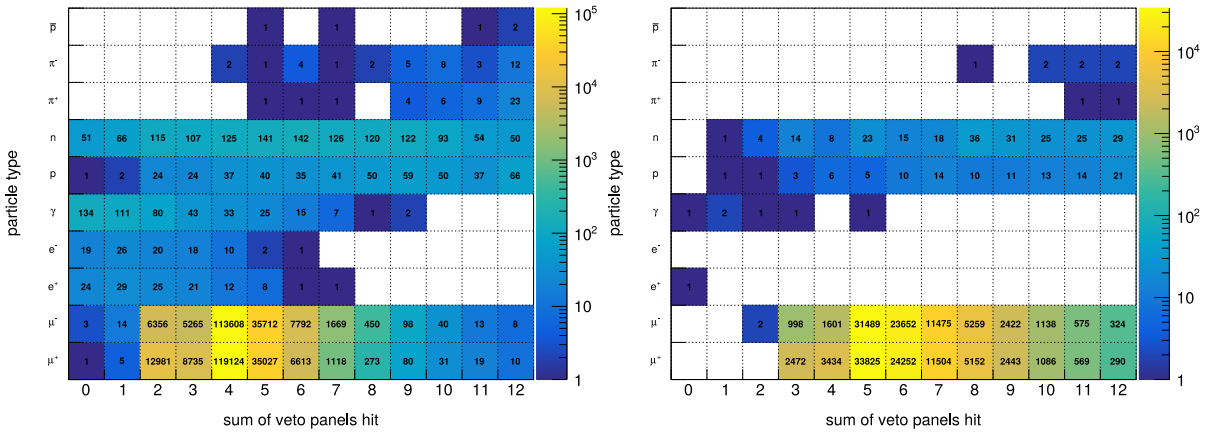

Figure 7.18.: Sum of the signal-giving veto panels separated by the primary particle type for the Phase B **default** setup (left) and **both** setup (right). Events with no signal-giving veto panels are the inefficiencies of the system. For **calo** and **ceiling** setup alone see Fig. B.37 of Appx. B.5.5.

the already described possibility to compare data sets with and without MESA beam, conclusions shall also be made by a comparison of the waveforms. Therefore, a complete acquisition of the non-vetoed signals with waveform digitizers is planned. Since the rates are very low, only moderate amounts of data are expected and it is still practicable in an experiment like DarkMESA. In case one particle type turns out to be particularly critical during the first experimental studies of the prototype, an additional and specialized veto can be considered, e.g. a gamma or neutron veto might be necessary.

These results are mainly based on simulations. Only a complete experimental study of the prototype will allow a more accurate estimate of the expected background. A further reduction by two orders of magnitude using the methods mentioned above is desirable. It may also become apparent that excessive background noise must be countered with a double-sided PMT readout of the calorimeter crystals, making a redesign of the setup necessary. So the design of Phase B should not be assumed to be final. The lower the background, the larger the parameter range that can be covered by the DarkMESA experiment. This expected reach is discussed in the following Chap. 8.

8. Expected reach

This chapter quantifies the contribution of DarkMESA to the search for DM more precisely. In Sec. 8.1, the theoretical aspects of the production of the DM particles in the P2 beam-dump and their detection in the DarkMESA calorimeter are discussed. From the results obtained in the `Geant4` study of the P2 beam-dump (Sec. 8.2) and the necessary assumptions for DarkMESA (Sec. 8.3), the first exclusion limits of DarkMESA Phase A and Phase B are obtained in Sec. 8.4. The Secs. 8.5 to 8.7 present additional concepts that can extend the covered parameter range. Included are the concept for DarkMESA-DRIFT, which can extend the parameter range with its low nuclear recoil threshold, a radiation shielding glass concept for the 13 200 h of DarkMESA Phase C, and an off-axis option for DarkMESA.

8.1. Relevant aspects of DM theory at DarkMESA

Already in Sec. 2.2.3 the theory of the DarkMESA experiment was shortly discussed. The P2 beam-dump serves as a DM source. In the simplest model a dark photon arises in a dark Bremsstrahlung process and decays into a pair of DM particles $\chi\overline{\chi}$. The DM particles can then reach the DarkMESA detector and scatter off electrons, which are then detected. In the following it is shown how the number of produced and detected DM particles can be calculated.

8.1.1. DM production

As mentioned before, the routines used in the `MadGraph` simulation are from Natalia Toro, Philipp Schuster, et al. In order to explain the processes of production and detection, a few aspects of the publication "New electron beam-dump experiments to search for MeV to few-GeV dark matter" from E. Izaguirre, G. Krnjaic, P. Schuster, and N. Toro [118] and "New fixed-target experiments to search for dark gauge forces" from J. D. Bjorken, R. Essig, P. Schuster, and N. Toro [166] are considered.

In the beam-dump, a dark photon γ' could be produced in a process analog to electromagnetic Bremsstrahlung. This dark photon couples with strength ε to the SM and can decay invisibly into a pair of DM particles $\chi\overline{\chi}$. The dark Bremsstrahlung can be calculated with the improved Weizsäcker-Williams approximation [167–169] and is described in the Appx. A of [166]. The cross-section of the γ' production is

$$\frac{d\sigma}{dx d\cos\theta_{\gamma'}} \approx \frac{8Z^2\alpha^3\varepsilon^2 E_0^2 x}{U^2}\mathcal{L}og \times \left[\left(1-x+\frac{x^2}{2}\right) - \frac{x\,(1-x)\,m_{\gamma'}^2\left(E_0^2 x\theta_{\gamma'}^2\right)}{U^2}\right] \quad , \tag{8.1}$$

where E_0 is the energy of the beam electron, $E_{\gamma'} = xE_0$ and $\theta_{\gamma'}$ is the angle between the incoming

e^- and γ' in the lab frame. Z is the nuclear charge of the beam-dump and $\alpha = 1/137$ the fine-structure constant. $\mathcal{L}og$ depends on the kinematics and various nuclear effects and lies between 5–10 for $m_{\gamma'}$ being below 500 MeV. $U(x, \theta_{\gamma'})$ is the virtuality of an average electron in this dark Bremsstrahlung process:

$$U(x, \theta_{\gamma'}) = E_0^2 x \theta_{\gamma'}^2 + m_{\gamma'}^2 \frac{1-x}{x} + m_e^2 x \quad . \tag{8.2}$$

These equations are valid for $m_e \ll m_{\gamma'} \ll E_0$ and $x\theta_{\gamma'}^2 \ll 1$. Due to this, one can neglect the electron mass and integrate over the angle:

$$\frac{d\sigma}{dx} \approx \frac{8 Z^2 \alpha^3 \varepsilon^2 x}{m_{\gamma'}^2} \left(1 + \frac{x^2}{3\,(1-x)}\right) \mathcal{L}og \quad . \tag{8.3}$$

The advantage of a beam-dump made of a material with high atomic number Z becomes evident here, since this value enters quadratically in the cross-section of the γ' production. From Eq. 8.3 it can be also seen that for most x the rate of γ' is proportional to $\alpha^3 \varepsilon^2 / m_{\gamma'}^2$. When producing a DM particle, due to the peak at $x \approx 1$, almost the entire electron beam energy is converted into dark photon energy. The γ' maximum emission angle is

$$\theta_{\gamma',\,\mathrm{max}} \sim \max\left(\frac{\sqrt{m_{\gamma'} m_e}}{E_0}, \frac{m_{\gamma'}^{3/2}}{E_0^{3/2}}\right) \quad . \tag{8.4}$$

This angle is smaller than the one between the two DM particles from the decay of the dark photon:

$$\theta_\chi \sim \frac{m_{\gamma'}}{E_0} \quad . \tag{8.5}$$

For a beam-dump with a total radiation length of T and N_e primary beam electrons with E_0, this dark Bremsstrahlung process leads to the production of N DM particles:

$$\boxed{\frac{dN}{dx} = N_e \frac{N_A X_0}{A} \int_{E_{\gamma'}}^{E_0} \frac{dE_1}{E_1} \times \int_0^T dt \mathcal{I}\,(E_1;\, E_0,\, t)\, E_0 \frac{d\sigma}{dx'}\bigg|_{x'=E_{\gamma'}/E_1}} \quad . \tag{8.6}$$

$N_A = 6.022 \times 10^{23}\,\mathrm{mol}^{-1}$ is the Avogadro number, A is the atomic mass of the beam-dump in $\mathrm{g\,mol}^{-1}$, and $\mathcal{I}$ is the energy distribution of the electrons after t radiation lengths. For $T \gg 1$, which is the case for the P2 beam-dump, most γ' are produced near the beam-dump's front and the approximation

$$N_{\gamma'} \sim EOT \times C \times \frac{\varepsilon^2 m_e^2}{m_{\gamma'}^2} \quad , \tag{8.7}$$

is valid, where $C \approx 10$ and depends on the target material.

The number of produced DM particles as well as their four-vectors are obtained from the simulation and this information can be used to calculate the number of detected DM particles from any detector concept.

8.1.2. DM detection

In the detector, a DM particle can scatter off an electron:

$$\chi + e^- \longrightarrow \chi' + e^{-\prime} \quad . \tag{8.8}$$

The corresponding cross-section has to be calculated. With $p_{1,2}$ being the initial state four-vectors and $k_{1,2}$ the final state four-vectors, the energy and momentum conservation is

$$p_1 + p_2 = k_1 + k_2 \quad , \tag{8.9}$$

and the four-vectors are

$$p_1 = \begin{pmatrix} \vec{p} \\ E_0 \end{pmatrix} \quad , \qquad p_2 = \begin{pmatrix} \vec{0} \\ m_e \end{pmatrix} \quad , \qquad k_1 = \begin{pmatrix} \vec{p'} \\ E_0' \end{pmatrix} \quad , \qquad k_2 = \begin{pmatrix} \vec{x} \\ E_r \end{pmatrix} \quad . \tag{8.10}$$

The energies are $E_0 = \sqrt{m_\chi^2 + \vec{p}^2}$ and $E_0' = \sqrt{m_\chi^2 + \vec{p'}^{\,2}}$ and E_r is the electron recoil energy. Since this is an elastic scattering in the lab frame, the electron e^- can be considered at rest and $\vec{p}$ can be set to $(0, 0, P)$. The direction of the recoil electron is given by $\vec{x} = (x_1, x_2, x_3)$. For the calculation of the Mandelstam variables s and t, the Lorentz-invariant products are computed. Since they are commutative, only the following scalar products have to be calculated:

$$\begin{aligned}
&p_1 \cdot p_1 = m_\chi^2 \quad , && k_1 \cdot k_1 = m_\chi^2 \quad , \\
&p_1 \cdot p_2 = E_0 m_e \quad , && k_1 \cdot k_2 = E_0 m_e \quad , \\
&p_1 \cdot k_1 = -\frac{1}{2}\left(2m_e^2 - 2m_\chi^2 - 2E_r m_e\right) \quad , && p_2 \cdot k_1 = m_e\left(E_0 + m_e - E_r\right) \quad , \\
&p_1 \cdot k_2 = m_e\left(E_0 + m_e - E_r\right) \quad , && p_2 \cdot k_2 = E_r m_e \quad , \\
&p_2 \cdot p_2 = m_e^2 \quad .
\end{aligned} \tag{8.11}$$

$$\begin{aligned}
s &= (p_1 + p_2)^2 = p_1 \cdot p_1 + 2 \cdot p_1 \cdot p_2 + p_2 \cdot p_2 = m_\chi^2 + 2E_0 m_e + m_e^2 \quad , \\
t &= (p_1 - k_1)^2 = p_1 \cdot p_1 - 2 \cdot p_1 \cdot k_1 + k_1 \cdot k_1 = 2m_e^2 - 2E_r m_e \quad .
\end{aligned} \tag{8.12}$$

This results in the squared scattering amplitude

$$|\mathcal{M}|^2 = \frac{(k_1 \cdot k_2)(p_1 \cdot p_2) + (p_1 \cdot k_2)(k_1 \cdot p_2) - m_\chi^2 (p_2 \cdot k_2) - m_e^2 (p_1 \cdot k_1) + 2m_\chi^2 m_e^2}{\left(t - m_{\gamma'}^2\right)^2} \quad . \tag{8.13}$$

In the center of mass (CM) frame of this elastic scattering process the momenta before and after the scattering are the same:

$$p = k = \sqrt{\frac{\left(s - m_\chi^2 - m_e^2\right)^2 - 4m_\chi^2 m_e^2}{4s}} \quad . \tag{8.14}$$

The transformation into the lab frame is done with the Jacobian $d\cos(\theta)$ and this results in the phase space factor S.

$$d\cos(\theta) = \frac{m_e}{p \cdot k} \quad , \tag{8.15}$$

$$S = \frac{k}{s \cdot p} \cdot d\cos(\theta) \quad . \tag{8.16}$$

Putting everything together, with the units converted correctly and for the electron recoil case the cross-section result is

$$\frac{d\sigma_e}{dE_r} = 4\pi\varepsilon^2\alpha\alpha_{\mathrm{D}}m_e\frac{4m_e m_\chi^2 E_r + \left[m_\chi^2 + m_e\left(E_0 - E_r\right)\right]^2}{\left(m_{\gamma'}^2 + 2m_e E_r\right)^2\left(m_\chi^2 + 2m_e E_0\right)^2} \quad . \tag{8.17}$$

For the proton recoil an additional form factor using the dipole approximation is needed. For the scattering on a nucleus the cross-section results in

$$\frac{d\sigma_{nucl}}{dE_r} = 8\pi\varepsilon^2\alpha\alpha_{\mathrm{D}}\frac{Z^2 M}{\left(m_{\gamma'}^2 + 2ME_0\right)^2} \quad , \tag{8.18}$$

where Z is the charge and M the mass of the nucleus. The cross-section for a single χ particle is calculated with

$$\sigma = \int_{x_1}^{x_2} dE_r \frac{d\sigma}{dE_r} \quad , \tag{8.19}$$

where x_1 and x_2 are the cut values of the recoil energy. The permitted ranges can be found in Tab. A.2 of Appx. A.3.3. In Fig. 2.13 it became clear that the electron recoil from Eq. 8.17 is of higher relevance for DarkMESA and is followed up for now. The formula is valid only if the energy of the incident DM particle is significantly larger than the masses of e^- and χ particles.

In order to determine the number of detected DM particles χ, the following variables are introduced to allow a simplified representation:

- The number of electrons on target is

$$EOT = \frac{I\, t_{\mathrm{meas}}}{e} \quad , \tag{8.20}$$

  where I is the MESA beam current of 150 µA in the extracted beam, t_{meas} the total measuring time, and e the elementary charge of 1.602×10^{-19} C.

- Total number of scattering centers in the detector is

$$N_{\mathrm{det}} = \frac{Z_{\mathrm{det}}\rho_{\mathrm{det}}N_A}{A_{\mathrm{det}}} \quad , \tag{8.21}$$

  where Z_{det} is the atomic number, A_{det} the mass number, and ρ_{det} the density of the detector. $N_A = 6.022 \times 10^{23}$ is the Avogadro number. An averaged value is used if more than two detector materials are involved.

- The variable

$$\sigma_{\text{final}} = N_{\text{evt}} \cdot \sum_{i=0}^{i=N_{\text{evt}}} L_i \, \sigma_i \quad , \tag{8.22}$$

  where N_{evt} is the number of events within the detector acceptance, L_i the detector interaction length, and σ_i the cross-section of the DM particle χ_i.

The number of χ particles detected in total is

$$\boxed{N_\chi = EOT \times N_{\text{det}} \times \sigma_{\text{final}} \times N_{\text{Dump}} \times X_{0,\text{Dump}} \times W} \quad , \tag{8.23}$$

where N_{Dump} is the number of nuclei in the beam-dump, $X_{0,\text{Dump}}$ the radiation length of the beam-dump material in cm, and W the event weight from the `MadGraph` cross-section calculation.

The value N_χ is the key simulation result. For a better interpretation, this value should now be related to the kinematics used in the respective case.

8.1.3. Common standard for comparing limits

The implementation of this standard in the simulation was already presented in Sec. 3.5, but is explicitly discussed again here. The number N_χ was determined with a fixed value ε, therefore the coupling constant ε has to be scaled to a value ε_{L} where the number of detected DM particles χ corresponds to a fixed number of particles N_{scaled}:

$$N_{\text{scaled}} = N_\chi \cdot \left(\frac{\varepsilon_{\text{L}}}{\varepsilon}\right)^4 \quad . \tag{8.24}$$

With this new ε_{L} value the variable y can be computed:

$$y = \varepsilon_{\text{L}}^2 \alpha_{\text{D}} \left(\frac{m_\chi}{m_{\gamma'}}\right)^4 \quad . \tag{8.25}$$

Here ε_{L} is the only variable resulting from the simulation. All other variables were input parameters of the considered kinematic in the simulation.

The $y - m_\chi$ parameter space is especially suited for comparing experimentally achievable exclusion limits in a common standard. The α_{D} value, the mass ratio $m_{\gamma'}/m_\chi$, and the confidence level (CL) must be chosen consistently for all exclusion limits to be compared. Standard values here are $\alpha_{\text{D}} = 0.5$, $m_{\gamma'} = 3\, m_\chi$, and 90 % CL. Experiments in which not all values are uniform can also be compared with each other in parts using other types of representation. Another type of representation is the $\varepsilon - m_{\gamma'}$ parameter range, which is independent of the DM mass.
All limits discussed in this chapter were calculated with the assumption $\alpha_{\text{D}} = 0.5$. Of course, the thermal relic targets would be reached faster if α_{D} were actually lower. At the same time, reaching the thermal targets in the y-limit does not mean that the corresponding particle type is completely excluded in this mass range for DM – the assumption for α_{D} may have been chosen too low. Therefore, another type of representation is used, the α_{D}-limits for the three thermal targets – pseudo-Dirac, Majorana, and Scalar. If no evidence for DM particles was found in an experiment, these limits indicate which part of the parameter range $\alpha_{\text{D}} - m_\chi$ can be excluded.

These additional representations are used in the progress of this chapter. At this point, only the existing boundaries in a y-limit representation are shown in Fig. 8.1.

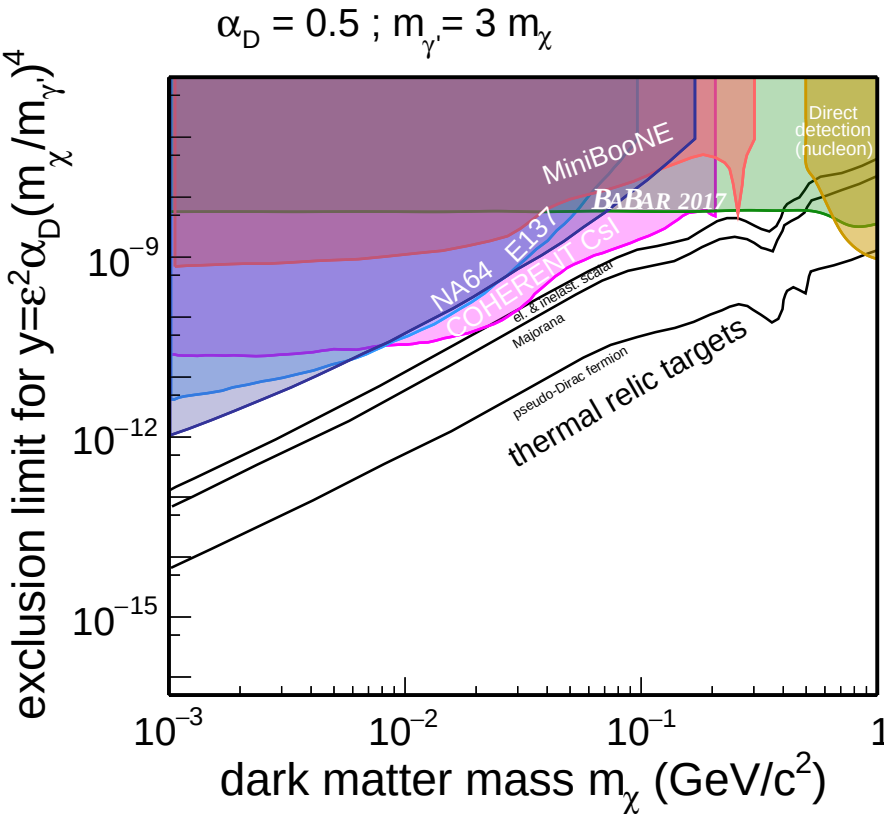

Figure 8.1.: Parameter space for dark photons decaying invisibly to $\chi\overline{\chi}$ with the DM mass m_χ on the horizontal axis and variable y, proportional to the kinetic mixing ε^2, the coupling of γ' to χ particles (α_D), and the mass ratio $(m_{\gamma'}/m_\chi)^4$, on the vertical axis. The thermal relic targets and the existing exclusion limits from various other experiments [120, 170–174] with a 90 % CL are shown.

From the existing experimental limits a selection, using similar approaches as DarkMESA, is used for the comparison with the simulation results within this thesis:

- **E137.** Results from the electron beam-dump experiment E137 at Stanford Linear Accelerator Center (SLAC) which uses an electromagnetic shower calorimeter as detector. [120]
- **NA64 (2019).** The experiment NA64 at CERN SPS uses electron or muon beams to search for dark sector particles produced by collisions with a fixed target. [170]
- **MiniBooNE.** This experiment at Fermilab, in addition to observe neutrino oscillations, searched for the DM production with an 8 GeV proton beam stopped in a steel beam-dump. The detector is made of mineral oil. [171]
- **BaBar.** It searched for events consistent with the production of spin-1 particles A' through the $e^+e^- \longrightarrow \gamma\, A'$ process. The BaBar detector was operated at the B-factory PEP-II. BaBar covers almost 4π rad and consisted of multiple detectors in a shell design. [172]
- **COHERENT CsI.** At Spallation Neutron Source (SNS) for the first time DM beyond the cosmological expectation was probed with a CsI[Na] scintillation detector and a nuclear recoil threshold of 9 keV. [173]

- **Direct Detection.** With XENON10 the proof of principle that direct detection experiments can be sensitive to DM candidates with masses in the MeV to GeV mass range was provided. [174]

In order to generate such limits for DarkMESA, some preliminary work is required.

8.2. Simulation of the P2 beam-dump as DM source

The beam electrons arriving at the beam-dump are already reduced in energy due to interactions with the P2 target and some losses in the beam pipe between the P2 experiment and the beam-dump. In a simulation study for 500 000 primary 155 MeV beam electrons, the primary and secondary electrons lose on average 17.22 MeV in the P2 target and another 2.56 MeV in the beam pipe (Figs. B.3 to B.6 of Appx. B.1). If one looks at the energy depositions in the beam-dump sorted by the particle types γ, e^-, and e^+ in Figs. 8.2 and 8.3, one sees that an average beam electron deposits 114.2 MeV through electrons in the beam-dump. 14.37 MeV are from e^+ and the contribution of γ to the energy deposition is negligible. By far the largest part of the energy is deposited immediately at the beginning of the aluminum pellets of the beam-dump, for which reason the approximation from Eq. 8.7 is valid. This point, one radiation length within the aluminum part, can be used as the origin for all DM particles with good approximation.

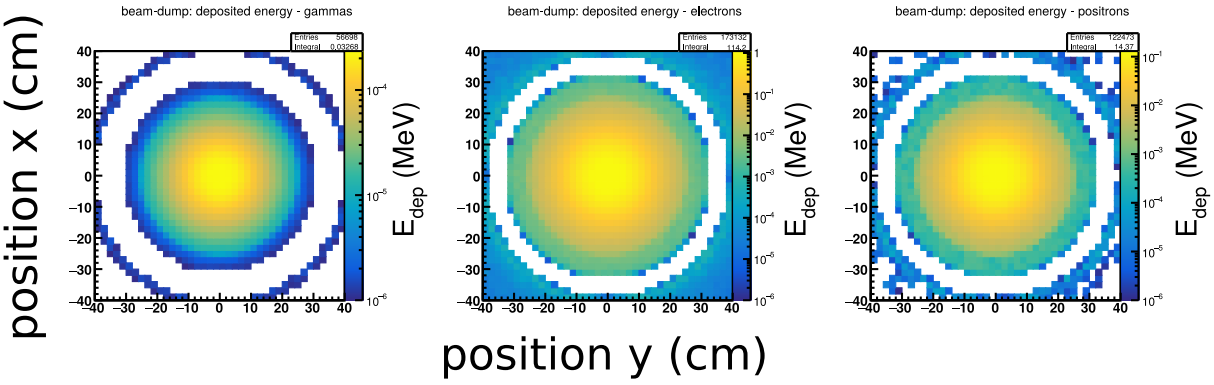

Figure 8.2.: Deposited energy of γ (left), e^- (middle), and e^+ (right) in the P2 beam-dump. The values are shown for the x and y dimension and a normalization with the total number of primary beam electrons was made.

To calculate the number of generated DM particles in the simulation, according to Eq. 8.6 one needs the energy distribution of electrons and positrons in the beam-dump as a function of the radiation length depth in the dump ($dN/dE(t)$), as well as their angular distribution. These distributions have already been discussed in Sec. 3.5.2 and the result which is further used in the `MadGraph` simulation can be found in Fig. 3.8.

As described in Sec. 3.5.3, the dark Bremsstrahlung process is now simulated in `MadGraph` and one obtains for each set of kinematics ($m_{\gamma'}$, m_χ, ε, α_D) a list of four-vectors.

In Fig. 8.4 parts of these lists are shown graphically, whereby the distance from the DM origin to the DarkMESA detector ($L_{\text{dump}} = 25\,\text{m}$) is also included.

Shown are the results for different particle masses, but always $m_{\gamma'} = 3\,m_\chi$, $\alpha_D = 0.5$, and $\varepsilon = 0.001$ as input. For light particles the time of flight to reach a DarkMESA calorimeter crystal

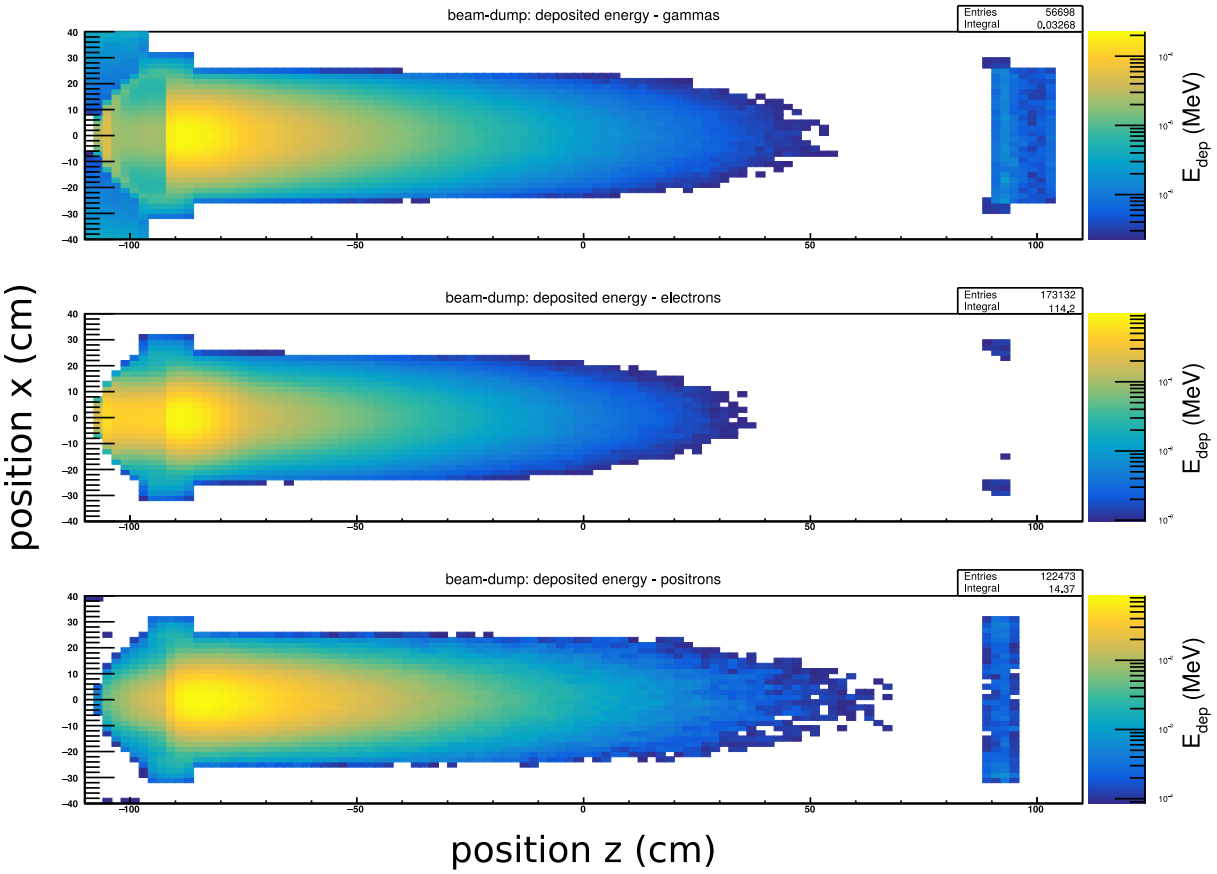

Figure 8.3.: Deposited energy of γ (top), e^- (middle), and e^+ (bottom) in the P2 beam-dump. The values are shown for the x and z dimension and a normalization with the total number of primary beam electrons was made.

is about 84 ns.[1] For higher masses, the distribution becomes broader and longer flight times are seen much more frequently. When looking at the angular distribution, one sees a plateau forming for low masses, which disappears for higher masses. To achieve a high DM flux even at high masses, the detector should be positioned ideally on (or close) to the beam-axis. The energy distributions show that the low DM energies dominate. However, a broadening of the distribution for larger masses can be observed.

The content of each four-vector list can be used to calculate one point of the DarkMESA exclusion limits. For this purpose, the detector to be investigated has to be defined and some DarkMESA specific assumptions have to be made to make the results as realistic and comparable as possible.

8.3. Assumptions for the DarkMESA exclusion limits

A brief summary of the assumptions for DarkMESA, which have been partially mentioned earlier, is now given. First, there are the kinematic assumptions. In the simplest dark sector model

[1] The sharp TOF spectrum for low DM masses may allow to further reduce the beam-unrelated background by using the time information of the beam electrons and the DarkMESA detector signals. For the MESA frequency of 1.3 GHz, the RF coincidence is only possible with a sub-ns time resolution of the DarkMESA detector system. Technically, MESA has the possibility to fill only every second bunch with electrons. Thus, a resolution of about 1.5 ns would be sufficient. This seems feasible, but needs further investigation.

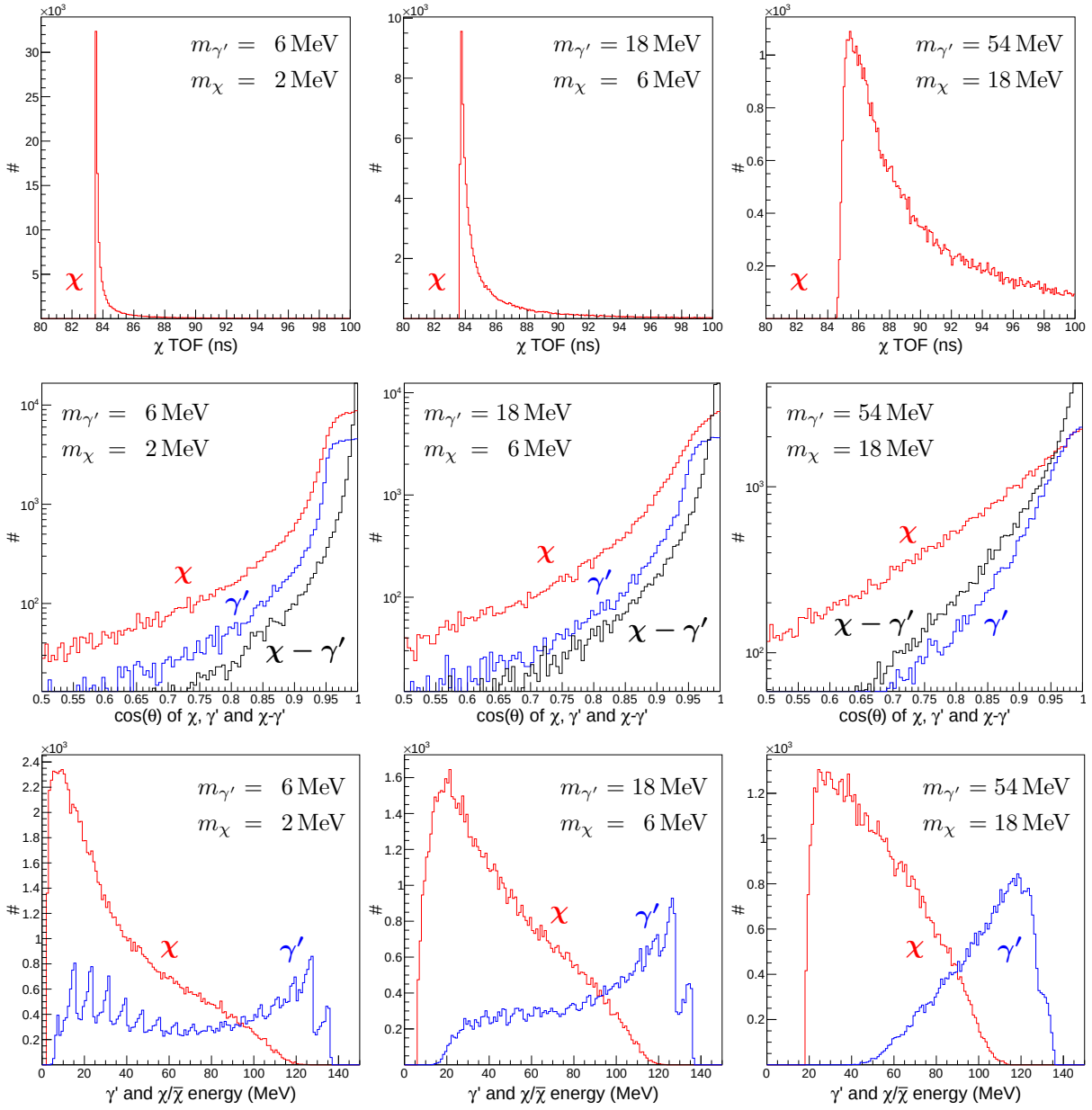

Figure 8.4.: For three different kinematics, the TOF spectra of the DM particle (top), the cos(θ) distributions (middle), and the dark photon and DM energies (bottom) are shown.[2]

only dark Bremsstrahlung is assumed. Since the dark photon mass must be at least twice as large as the DM mass, $m_{\gamma'} = 3\,m_\chi$ is chosen and the dark coupling is fixed to $\alpha_\text{D} = 0.5$. For comparability with other experiments, a CL of 90 % is always assumed here. This corresponds to the detection of at least $N_\text{sig} = 3$ DM events.[3]

The electron recoil threshold is set to $E_{e^-,\,\text{thres}} = 10\,\text{MeV}$ according to the results in Chap. 5. In a simulation study (Fig. B.42 of Appx. B.7), the detector efficiency (ϵ_det) for a PbF_2 (7) crystal was investigated . A detection efficiency of $\sim$ 95 % was obtained for the detection of at least two photoelectrons at the detection threshold of 10 MeV. An SF5 detector was studied in a smaller version only, like the one used for the beam-tests at MAMI. This achieved an efficiency

[2] For $m_{\gamma'} = 6\,\text{MeV}$ peaks occur in the γ' energy spectrum. They are artifacts caused by the binning in `MadGraph`.
[3] More precisely: $N_\text{scaled} = N_\text{sig} + N_\text{bg}$ and with $N_\text{bg} = 0$ and CL $= 0.9 \longrightarrow N_\text{sig} = -\ln(1 - \text{CL}) = 2.3$.

of almost 98 %. However, since the SF5 crystals used in Phase B are larger and are read out with a different PMT, this value may not be achieved. Therefore, the lower value of 95 % was estimated for all detectors.
Since the exact number of background events can only be approximated with the results in Chap. 7 so far and is not validated with experimental data, the number of background events is set to $N_{\mathrm{bg}} = 0$ during the studies in this chapter. This value will probably not be achievable, but via the CL parameterization study in Appx. B.6, non zero background can be added and the limits can be simply rescaled.[4] All necessary assumptions are summarized here:

- $m_{\gamma'} = 3\, m_{\chi}$
- $\alpha_{\mathrm{D}} = 0.5$
- CL of 90 % ($N_{\mathrm{sig}} = 3$)
- $E_{e^-,\,\mathrm{thres}} = 10\,\mathrm{MeV}$
- $\epsilon_{\mathrm{det}} = 95\,\%$
- $N_{\mathrm{bg}} = 0$

In the following sections, a few assumptions may be changed to show their impact or to test new concepts. When changes are made, this is explicitly pointed out.

8.4. Exclusion limits for DarkMESA Phase A and B

The ideas of the previous sections are realized and the limits of the DarkMESA Phase A and Phase B are discussed. First in the already known simple model of the dark Bremsstrahlung, then an additional process, the annihilation of positrons at beam-dump electrons is added.

8.4.1. Dark Bremsstrahlung

For calculation of the limits, the scheduled times and EOT according to Tab. 6.2 are used. For Phase A this are 2 200 h and for Phase B 6 600 h of MESA electron beam. The detectors are centered on the beam-axis in the DarkMESA room and all assumptions from Sec. 8.3 apply. This results in the limits shown in Fig. 8.5 (top). Phase A is completely within the existing limits of the other experiments. Phase B can extend the parameter range to higher DM masses as well as to higher y values and exceeds the existing limits in the low DM mass range up to $m_{\chi} = 4\,\mathrm{MeV}$. The thermal relic targets are not reached with these experimental setups and runtimes yet.
For Phase B, the effect of a variable threshold $E_{e^-,\,\mathrm{thres}}$ was investigated in Fig. 8.5 (bottom). The bold red line corresponds to the expected threshold of 10 MeV. Even with a threshold of 20 MeV, the existing limits can still be exceeded slightly. For a lower threshold of 5 MeV a close reach of the Scalar thermal targets may also be possible.[5] The expected reach using the beam-dump with an additional 2.5 mm thick tungsten target (Sec. 6.1.1) was also studied and showed slight improvements in the low mass region (see Fig. B.43 of Appx. B.8.1). As it does not fully convince, the tungsten target is not used in the following simulations anymore. This target increases the total number of photons and it should be considered again in the context of ALPs searches, which are discussed in the outlook in Chap. 9.

[4] This parameterization study can also be used to change other parameters and thus estimate new limits without having to perform extensive re-simulations.
[5] According to the results of the beam-time this seems to be realistic for PbF_2 (Sec. 5.5.8). For the (not perfectly polished) Schott SF5 crystal used there, this is not the case. With appropriate preparation and optimized readout, a lower threshold could be achieved for the PbGl calorimeter as well.

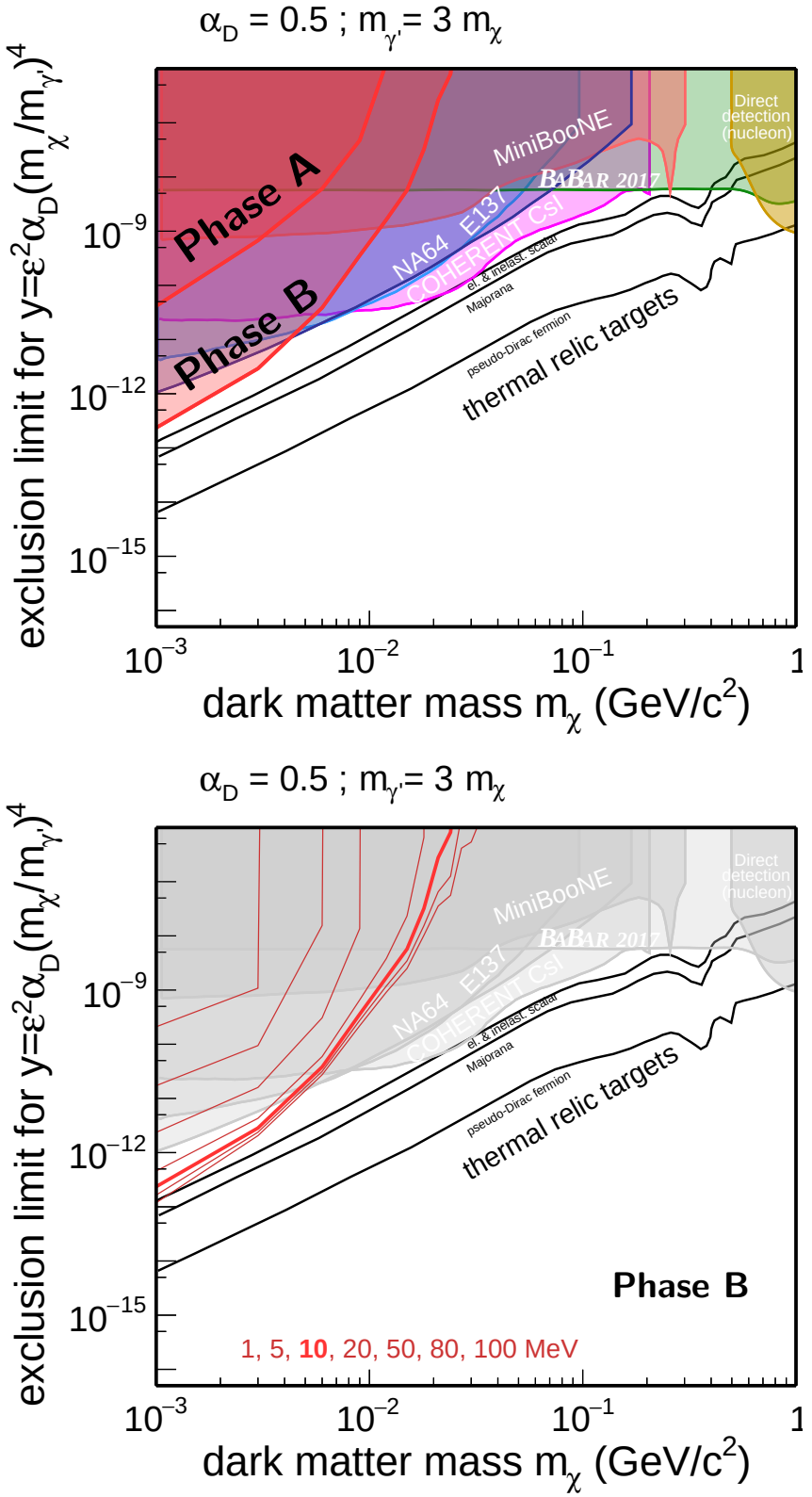

Figure 8.5.: Parameter space for dark photons decaying invisibly to $\chi\overline{\chi}$ with the DM mass m_χ on the horizontal axis and variable y on the vertical axis. The predictions for the DarkMESA Phase A and B exclusion limit with the conservatively estimated electron recoil energy threshold of 10 MeV are shown (top). The predictions for the DarkMESA Phase B exclusion limit for the indicated detection thresholds are shown (bottom). The detection efficiency is 95 % and a CL of 90 % is assumed. The EOT were set according to the time schedule in Tab. 6.2. The existing exclusion limits from various other experiments [120, 170–174] are shown.

8.4.2. Positron annihilation

The positrons produced by the electromagnetic shower in the beam-dump have been considered only for the dark Bremsstrahlung process so far. However, the positron can also produce dark photons through resonant or non-resonant annihilation of the beam-dump's atomic electrons:

$$\begin{aligned} \text{Resonant:} \qquad & e^+ + e^- \longrightarrow \gamma' \quad , \\ \text{non-resonant:} \qquad & e^+ + e^- \longrightarrow \gamma + \gamma' \quad . \end{aligned} \tag{8.26}$$

The implementation in `MadGraph` is based on the theory in "Dark photon production through positron annihilation in beam-dump experiments" from L. Marsicano et al. [175] and is already included in the event generator provided by the BDX Collaboration. Only a few theoretical steps shall be given here. The total number of dark photons per EOT is

$$N_{\gamma'} = \frac{N_A}{A} Z \rho \int_{E^R_{\min}}^{E_0} dE_e T_+ (E_e) \, \sigma (E_e) \quad , \tag{8.27}$$

where N_A is the Avogadro number, A, Z, and ρ beam-dump properties, E_0 the beam energy, and $\sigma(E_e)$ the γ' production cross-section. The cross-sections scale with $\varepsilon^2 \alpha_{\text{EM}}$ in the resonant and with $\varepsilon^2 \alpha^2_{\text{EM}}$ in the non-resonant process. Additionally

$$E^R_{\min} = \frac{m^2_{\gamma'}}{2 m_e} \quad , \tag{8.28}$$

is the minimum positron energy necessary to produce a dark photon through positron annihilation, and for a beam-dump with a total radiation length of T,

$$T_+ (E_e) = \int_0^T dt \mathcal{I}^+_e (E_1; E_0, t) \quad , \tag{8.29}$$

is the positron differential track length distribution, which requires the energy distribution of the positrons after t radiation lengths ($\mathcal{I}^+_e$).
This is a similar procedure as for the dark Bremsstrahlung. Now it is necessary to divide the simulated energy and angular distribution in the beam-dump explicitly for electrons and positrons (Fig. 8.6). The positron distribution in the beam-dump is used for the additional positron annihilation process. For the dark Bremsstrahlung process, the joint e^+e^- distribution remains. With the additional process in `MadGraph`, additional DM events could be added to the list of four-vectors. These new four-vector lists are generated for the same kinematics as in the dark Bremsstrahlung only case. Additional data points are simulated in the mass range of interest up to $m_\chi = 10\,\text{MeV}$.

The newly obtained exclusion limits can be found in Fig. 8.7. Compared to the limits without positron annihilation (dotted red), a pronounced structure appears in the region up to about $m_\chi = 5\,\text{MeV}$. The remaining curve is dominated by dark Bremsstrahlung and does not differ from the previous results. With the addition of this process, DarkMESA Phase B already reaches the Scalar and Majorana thermal relic targets.

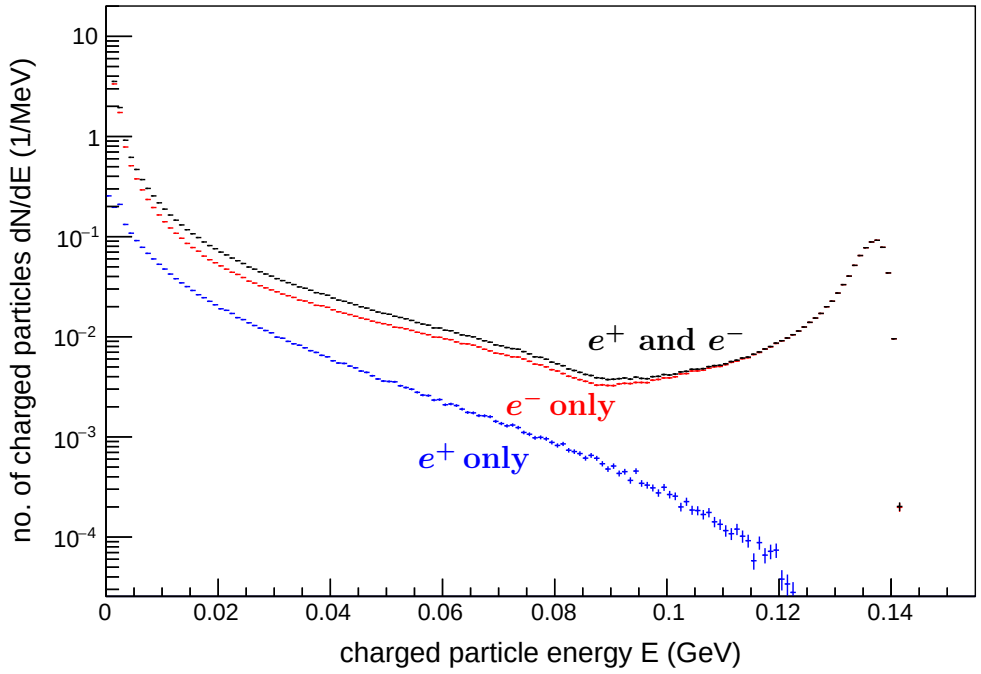

Figure 8.6.: Simulated energy distributions in the P2 beam-dump separated for e^+ and e^- (black), e^- only (red), and e^+ only (blue). 500 000 primary electrons with an energy of 155 MeV were simulated.

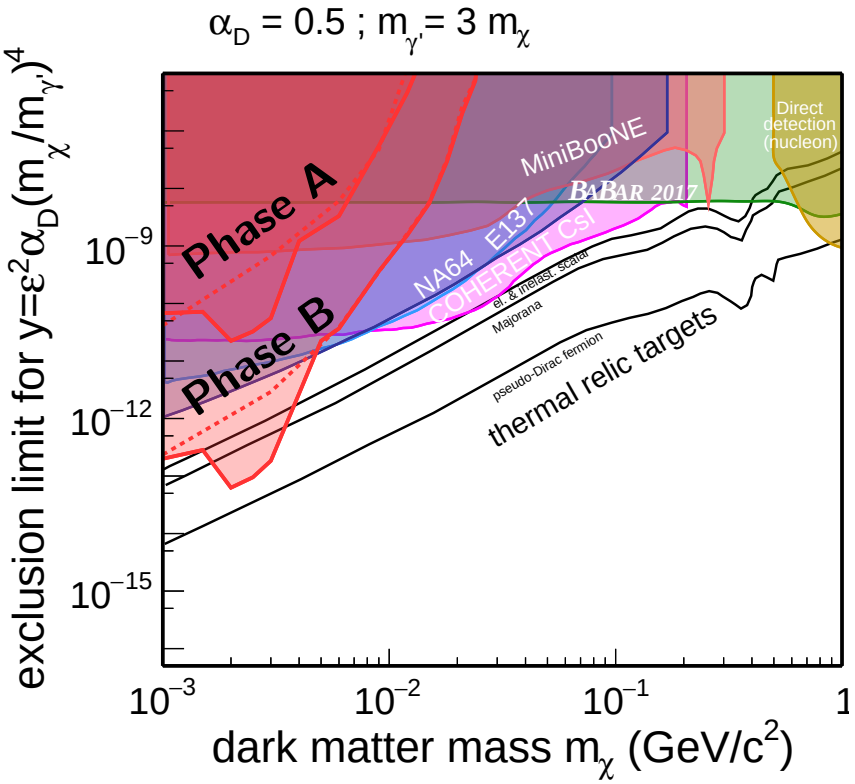

Figure 8.7.: Parameter space for dark photons decaying invisibly to $\chi\overline{\chi}$ with the DM mass m_χ on the horizontal axis and variable y on the vertical axis. The predictions for the DarkMESA Phase A and B exclusion limit with 90 % CL and positron annihilation included are shown with the red lines. Dark Bremsstrahlung only is indicated with the dotted red lines. The detection efficiency is 95 %, the conservatively estimated electron recoil energy threshold for DarkMESA is 10 MeV. The EOT were set according to the time schedule in Tab. 6.2. The existing exclusion limits from various other experiments [120, 170–174] are shown.

The limits are now discussed in other parameter spaces as well. These include the $\varepsilon - m_{\gamma'}$ range, which is independent of the DM mass, and various representations in the $\alpha_D - m_\chi$ parameter space (Fig. 8.8). In the α_D-limits one can easily see which region is covered for any chosen α_D. Even in the pseudo-Dirac case the range for a value $\alpha_D = \alpha_{EM}$ is almost completely covered. This form of representation allows a quick comparison with exclusion limits which are based on a different α_D value. The limits for values of $\alpha_D = 0.1$ are also often found in literature. These would be completely covered in the scalar case and in the other cases the exclusion limits would be closer to the thermal relic targets. However, if α_D is greater than 0.5, the targets would move further down and a longer experimental search would be needed.

The expansion of the simulation to include the positron annihilation process was able to improve the limits even further. From now on, this process is always applied.

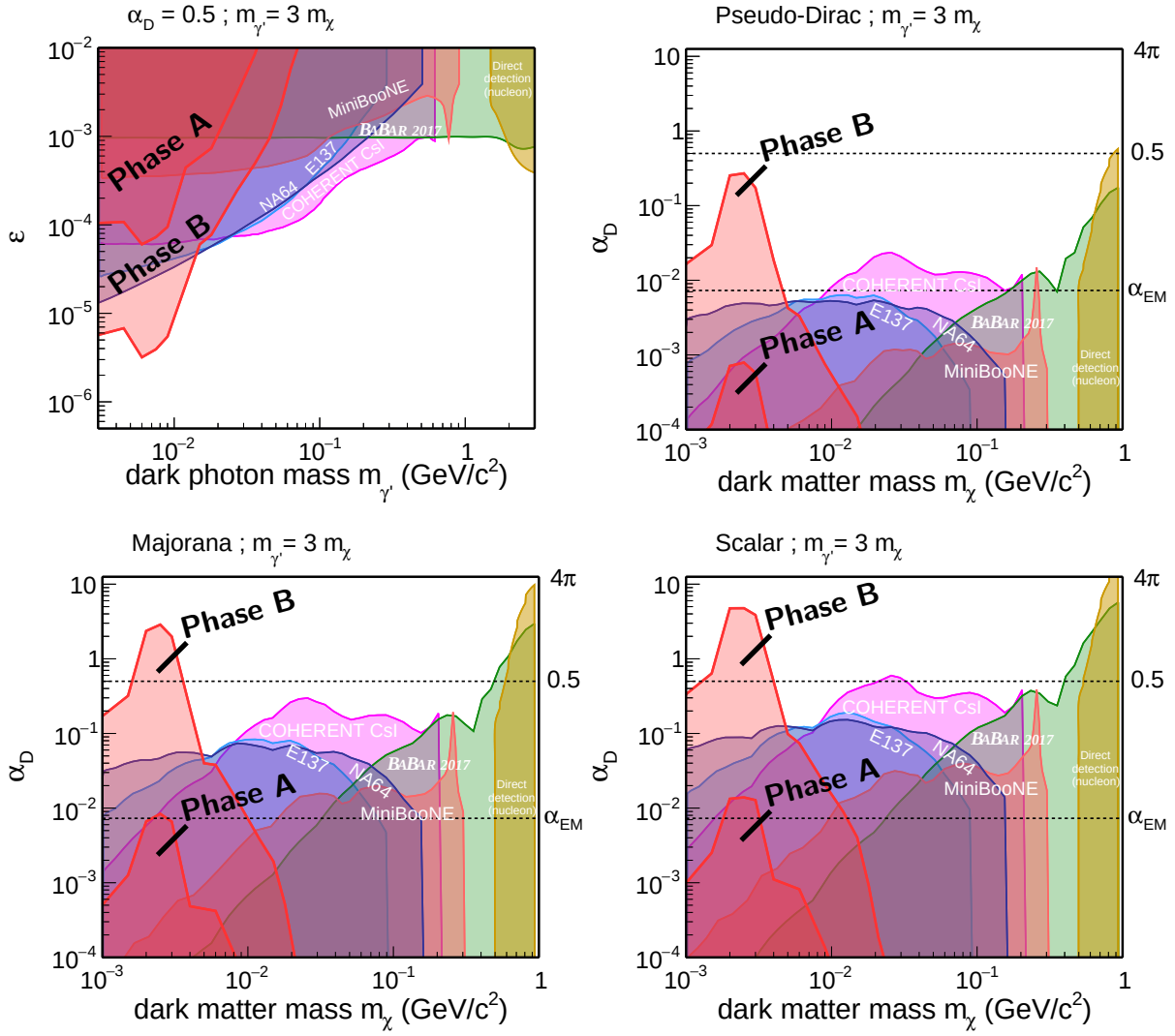

Figure 8.8.: Alternative parameter spaces for dark photons decaying invisibly to $\chi\overline{\chi}$. The ε exclusion limit (top left) and the three α_D exclusion limits – pseudo-Dirac (top right), Majorana (bottom left), and Scalar (bottom right) – are shown. The predictions for the DarkMESA Phase A and B exclusion limit with 90 % CL and positron annihilation included are shown with the red lines. The detection efficiency is 95 %, the conservatively estimated electron recoil energy threshold for DarkMESA is 10 MeV. The EOT were set according to the time schedule in Tab. 6.2. The existing exclusion limits from various other experiments [120, 170–174] are shown.

8.5. A supplementary detection method – DarkMESA-DRIFT

Already since 2014, BDX-DRIFT is considered as a complementary detector for BDX at JLab. This detector is intended to run in parallel to BDX and can extend its expected reach [176]. Through the cooperation with members of the BDX Collaboration, the idea arose to possibly use the Directional Recoil Identification From Tracks (DRIFT) detector at MESA.

A negative-ion TPC filled with CS_2 at a low pressure of 40 Torr $\approx$ 53 mbar and 1 Torr of O_2 will serve as DM detector (Figs. 8.9a–b). With the nuclear recoil threshold being in the keV range the accessible parameter space can be extended. With a particularly high resolution in the drift direction z, the detector allows to distinguish between signal and background events by measuring the root mean square (RMS) in z direction (Figs. 8.9c-d).

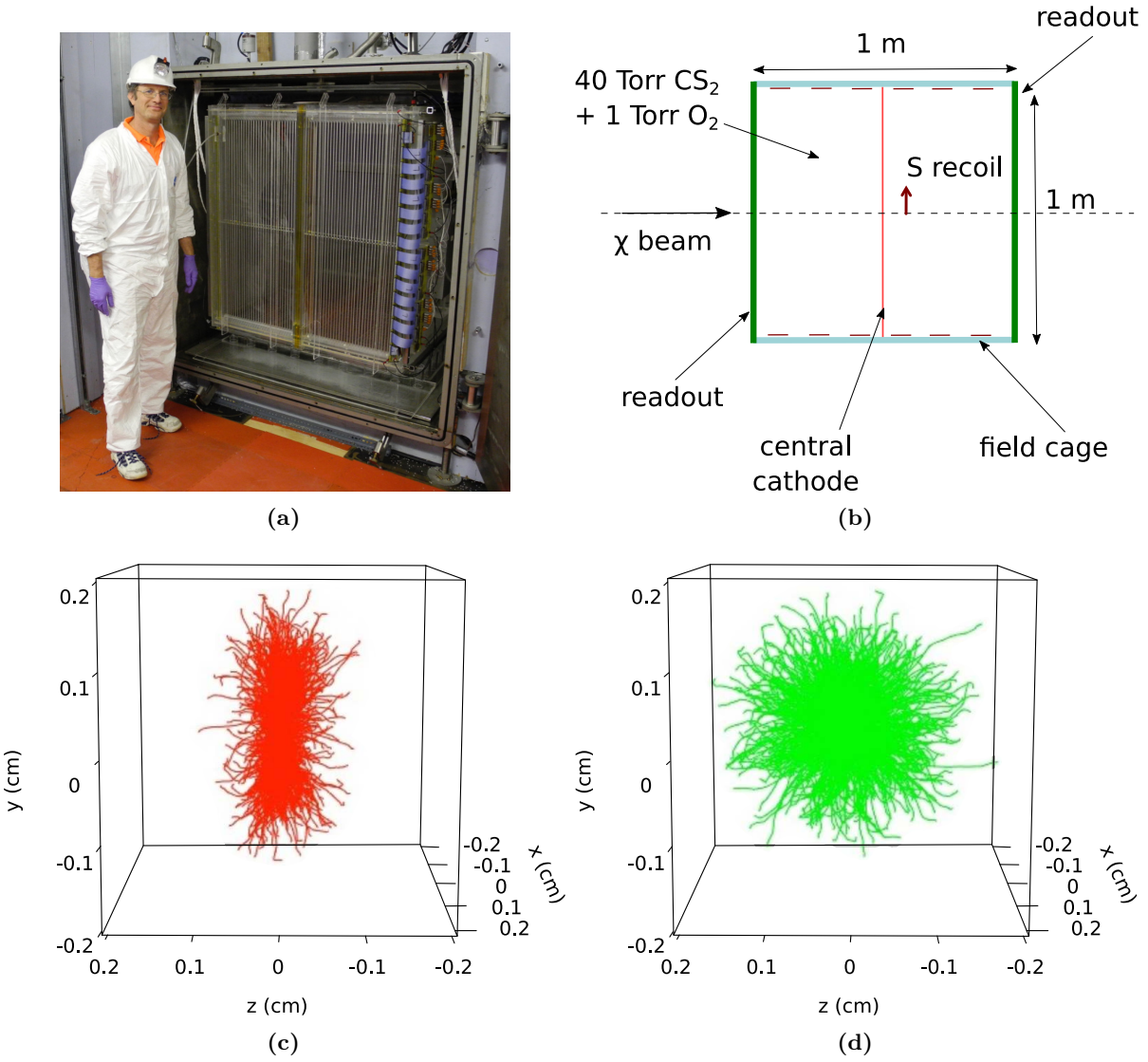

Figure 8.9.: The concept of DarkMESA-DRIFT: (a) Picture of the DRIFT detector, (b) schematic drawing of the DRIFT detector components and an incoming DM beam, (c) directional signal of 1 000 50 keV events, and (d) an isotropic background of 1 000 50 keV events [177]. The detector will be enclosed by a hermetic gadolinium wrapped neutron veto.

Since there is lack of overburden, DarkMESA-DRIFT will require an active veto system. Due to its sensitivity to neutrons in particular, the detector will be enclosed in a veto system of 30 cm thick gadolinium (Gd) wrapped plastic scintillators.

For the simulation of the limits, the same four-vector lists were used as before, with a nuclear recoil assumed for detection now. The necessary adjustments can be found in Tab. A.2 of Appx. A.3.3. The other assumptions from Sec. 8.3 still apply. With a threshold of 20 keV and a placement of the experiment in the second funding period, parallel to DarkMESA Phase B with 6 600 h beam, the limits in Fig. 8.10 are reached. Fig. B.44 of Appx. B.8.2 shows the exclusion limits for selected thresholds between 5 and 300 keV.

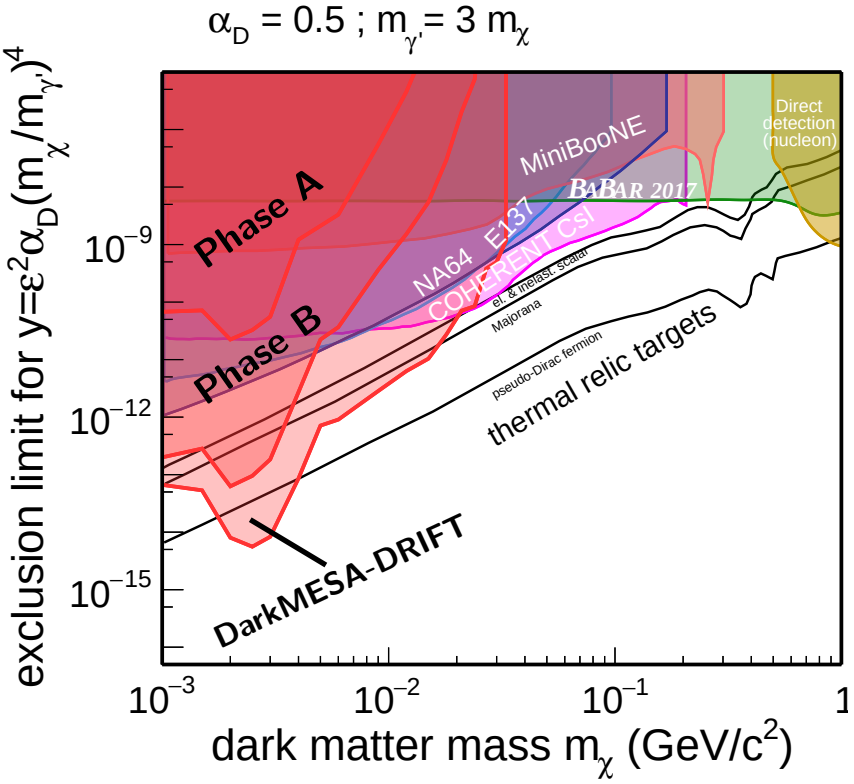

Figure 8.10.: Parameter space for dark photons decaying invisibly to $\chi\overline{\chi}$ with the DM mass m_χ on the horizontal axis and variable y on the vertical axis. The predictions for the exclusion limit with 90 % CL are shown in red. The detection efficiency is 95 %, the conservatively estimated electron recoil energy threshold for DarkMESA is 10 MeV and the nuclear recoil energy threshold for DarkMESA-DRIFT is 20 keV. The EOT were set according to the time schedule in Tab. 6.2. The existing exclusion limits from various other experiments [120, 170–174] are shown.

With the X17 [56] there is a dark photon candidate, which lies in a mass range, where the coverage by DarkMESA Phase B already decreases again. DarkMESA-DRIFT expands the covered parameter range to higher masses and offers a serious perspective in the search for the X17. Furthermore, DarkMESA-DRIFT is able to reach the pseudo-Dirac thermal relic targets in the DM mass range between 2 and 4 MeV.

8.6. Extension of active volume – DarkMESA Phase C

In Chap. 6 it was already mentioned that Phase A and B will be followed by a Phase C with a twice as high running time as Phase B. For these 13 200 h one could now continue to work with the Phase B setup, but will barely be able to increase the limits further (Fig. B.46 of Appx. B.8.3).

Another possibility would be to further increase the volume of the detector and to expand the calorimeter. Considering an extension with PbGls, in addition to the high price (2018 about €920k per m^3 Schott SF5), there is also the fact that many companies are discontinuing or have already stopped the production and further processing of lead-loaded glass. One exception is radiation shielding glass such as Schott RD50®, which is used in particular in medical applications. This is commercially available in thin sheets that can range in thickness from 5–23 mm, depending on the requested lead density value. The costs are around €250k per m^3 (as of 2022) with the density of RD50® being 25 % higher than SF5. An overview of possible materials can be found in Tab. 8.1.

	Schott RD50®	**Schott RD30®**	**Schott SF5**	**plastics**
density ($g\,cm^{-3}$)	$\geq$ 5.05	$\geq$ 3.13	4.07	1.023
PbO content (%)	$\geq$ 65	$\geq$ 22	51	–
refractive index	1.79	1.579	1.67	1.58
avg. thickness (mm)	6, 8, 9.5, 11, 12.75, 17.5, 21.5	6	variable	variable
max. size (mm^2)	2 400 × 1 100 (1 500 × 800)	2 400 × 1 300	variable	variable
costs	€250k - €285k m^{-3} (2022)	€137k m^{-3} (2022)	€920k m^{-3} (2019)	€100k m^{-3} (2018)

Table 8.1.: Proposed materials for DarkMESA Phase C. The two types of Schott radiation shielding glasses RD50® and RD30® are compared to the Schott SF5 PbGl and a typical plastic scintillator.

Thinking about a stacking of these thin plates in an innovative concept for Phase C, one could obtain additional directional information of the detected particles, since the energy of a recoil electron is not necessarily deposited in one plate only.

Phase C simulation study. A simulation is now performed to determine how many plates respond on average for the expected energy distribution of DM particles from the P2 beam-dump. The energy distribution of the recoil electrons used for this study is shown in Fig. B.45 of Appx. B.8.3. The less dense Schott RD30® and plastic scintillators were not used in this study, because the lower densities of these materials would require larger detectors to obtain the same number of scattering centers N_{det} (see Eqs. 8.21 and 8.23). This would increase both the number of readout channels and the dimensions of the veto system.[6]
In the `Geant4` simulation, the light output of individual panels was examined first before multiple panels were considered together in a second step. Settings used during the simulations are summarized in Fig. 8.11.

[6] However, if directional information or number of background events can be significantly improved with these materials, they should be studied in more detail, too.

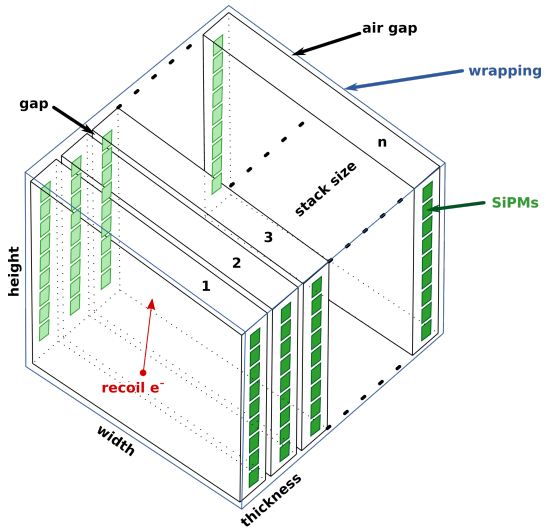

initial radiation shielding glass study	
fixed settings	
material	Schott RD50®
radiation glass **height**	250 mm
SiPMs	9 per short side; $6 \times 6\,\mathrm{mm}^2$; $\varepsilon_{\mathrm{det}} = 38\,\%$
wrapping	20 µm Teflon® foil
air gap	0.4 mm
variable settings	
radiation glass **width**	250, 500, or 1 000 mm
radiation glass **thickness**	6, 8, 9.5, 11, 12.75, 17.5, or 21.5 mm
stack size	1 or 20 elements
gap	0, 1, 2, 3, 4, or 5 mm
energy, momenta, and position of incident **recoil electron**	
full or reduced **tracking**	

Figure 8.11.: Sketch for the implementation of the initial radiation shielding glass study in `Geant4` (left) and the possible settings (right).

It should be noted that the transmission properties of the radiation shielding glasses are not fully specified by the manufacturer. At the start of experimental studies the transmittance in dependence of the wavelength has to be studied with the spectrophotometer. In the simulation, missing transmission properties were approximated by the properties of the SF5 PbGl, but the refractive index and density were set correctly according to the Schott datasheets.

Simulation study of a single panel. In a first step, the recoil electrons were used as generator starting for each electron at a different random position within the single panel. With a full tracking the percentage light output (detected optical photons/ generated optical photons) was evaluated for three different panel widths but with same thickness and height. The height was set to 250 mm, the thickness to 6 mm, and the readout was done with the already known carrier boards with nine SiPMs on the two opposite short sides. They were wrapped in 20 µm Teflon® foil with an air gap of 0.4 mm to the panels. For a width of 250 mm, the average yield was 7.5 %, 6 % for 500 mm width, and still 5 % for a width of 1 000 mm. When the thickness is increased to 21.5 mm in the case of 500 mm width, the yield drops to 3.5 % due to the reduced SiPM coverage. For the following studies with 500 mm wide panels, a hit detection threshold of 150 generated optical photons was estimated from these data. This is only an approximation, since the threshold has to be adjusted depending on the panel thickness or the number of SiPMs has to be raised.

Simulation study of a panel stack. Next, a stack of 20 panels was evaluated. With the threshold from the previous study a reduced tracking was sufficient. Thus, it is now to be determined how many plates detect a signal above the threshold. The primary particle is again generated at a random position within the 20 layers. However, this also means that it can happen that a recoil electron is generated in one of the last panels, has enough energy to leave a signal in further layers, but these do not exist. Thus, this results in an insufficient low number of triggering panels. The study is performed for panels with a width of 500 mm, a gap of 1 mm, and is repeated for all possible panel thicknesses. All are wrapped together in a single Teflon® foil.

In addition, generators with fixed electron energies of 20, 40, 60, 80, and 100 MeV are used for comparison. The results are shown in Fig. 8.12, where the mean and sigma value of the different kinematic sets are plotted against the layer thickness.

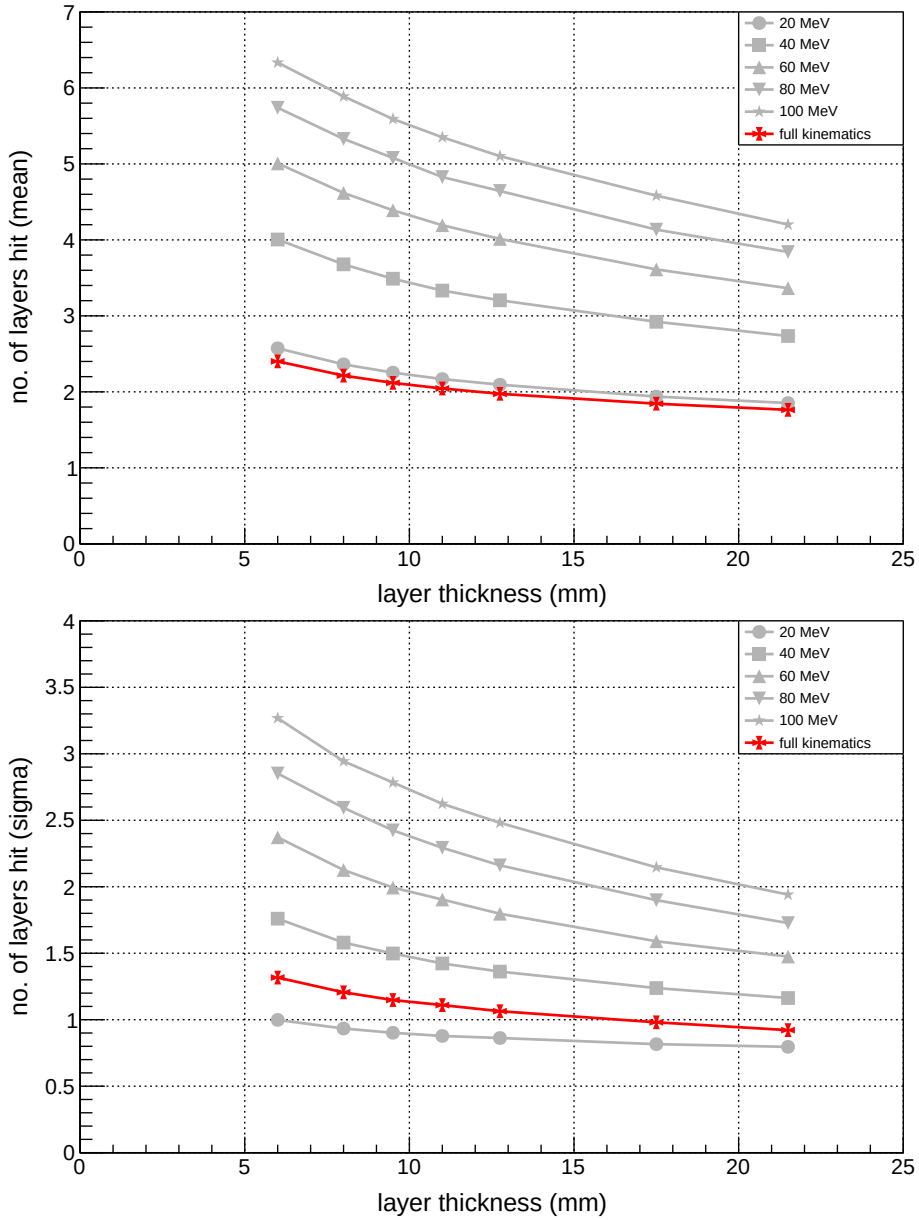

Figure 8.12.: Results of the initial radiation shielding glass study. The mean number of layers hit (top) and the associated σ (bottom) are shown for all possible layer thicknesses of Schott RD50®. The results are shown for the DarkMESA kinematics in red and for fixed electron recoil energies in grey.

As expected the average number of layers hit decreases with the layer thickness. The electron recoil distribution expected for DM particles from the P2 beam-dump is slightly below the level of the 20 MeV electrons, although the distribution is obviously broader. This result shows with an average of about 2.5 hits for the thinnest panels a not extremely high value, but the fact that in more than 80 % of the cases at least two panels react gives this setup new possibilities for the reduction of the cosmic background. Using radiation shielding glass plates and plastic scintillators in a sandwich configuration, which would reduce the number of scattering centers N_{det} per volume, but increase the average number of panels hit, is also an option. Since high-energy electrons can

be generated at the end of the stack as well, the average hit value for a stack of even more panels may increase a bit. In addition, a spacing of 1 mm between the panels has been assumed so far. This could be further reduced in experimental studies or even replaced by a thin Teflon® layer.

An initial concept for a larger detector is now used to demonstrate the new background suppression capabilities. A detector with an active volume of $1\,\mathrm{m}^3$ is proposed as a Phase C1. Many of the panels examined are stacked and, as shown in Fig. 8.13 (left), the stacks are also placed on top of each other.

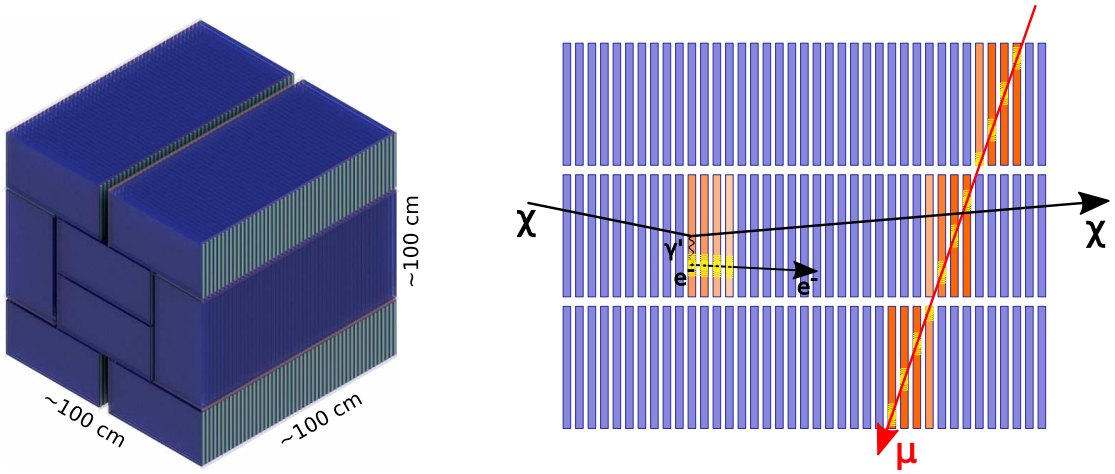

Figure 8.13.: Concept for DarkMESA Phase C1 with $1\,\mathrm{m}^3$ active volume (left), and the detection principle of a DM particle and a cosmic muon (right) are shown.

If one now looks at a cross-section with three stacks on top of each other in Fig. 8.13 (right), the differentiation possibilities become clear. A DM particle χ coming from the direction of the MESA beam leaves an electron recoil which can trigger a signal in consecutive panels in the direction of flight. For cosmic muons μ the direction of flight is different and they leave a signal in panels superimposed upon each other. Furthermore, due to the direction of flight, the track length in the panels can be extended, resulting in a higher energy deposition and thus higher signals. For this detector an adapted veto is necessary, which possibly could be slimmer as for Phase B due to the directional information given here. However, studies on the veto have not been started yet.
When looking at this concept, one directly sees the tremendous number of carrier boards required, but this readout concept has not been finalized yet. The ultra-thin design of these boards is caused by the hermetic closure of two neighboring veto plates in Phase A and B. Since in the case of Phase C1 the space is limited only in the direction of the stacked plates, the readout can be adjusted. For example, WLS bars could be attached to the readout sides, which in turn would be readout by only two SiPMs on top and bottom. This reduces the required electronics but may even increase the light yield.
Phase C1 can increase the Phase B limits and reaches the pseudo-Dirac thermal relic targets. A total of 10 MeV energy deposit was assumed as detection threshold, which still may change according to the initial experimental studies. With an even larger detector of $9\,\mathrm{m}^3$ active volume (Phase C2), the limits could be further improved and also the part below $m_\chi = 2\,\mathrm{MeV}$ dominated by dark Bremsstrahlung can reach the pseudo-Dirac targets (Fig.8.14).

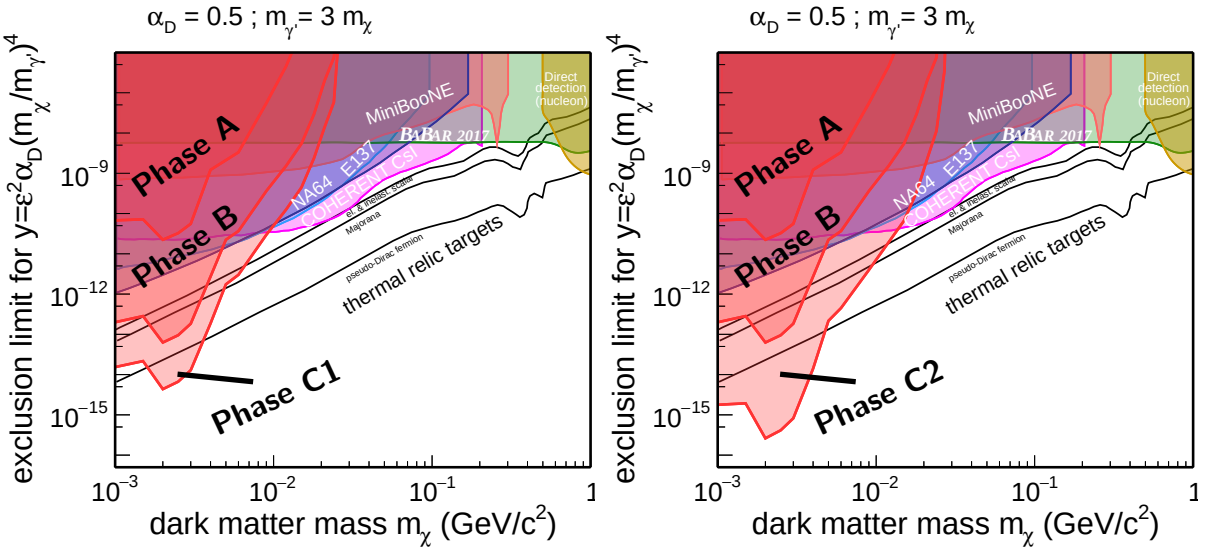

Figure 8.14.: Parameter space for dark photons decaying invisibly to $\chi\overline{\chi}$ with the DM mass m_χ on the horizontal axis and variable y on the vertical axis. The predictions for the DarkMESA Phase C1 (left) and Phase C2 exclusion limit (right) with 90 % CL and positron annihilation included are shown in red. The volume of Phase C2 is larger by a factor of 9. The detection efficiency is 95 %, the conservatively estimated electron recoil energy threshold for DarkMESA is 10 MeV. 13 200 h of MESA electron beam were assumed. The existing exclusion limits from various other experiments [120, 170–174] are shown.

8.7. DarkMESA off-axis option

During the study of positron annihilation, as in the case of dark Bremsstrahlung, the angular distribution of the resulting DM particles was investigated. It was found that for this process the maximum of the distribution is not located in the center, but depending on the mass of the particle there is a maximum close to a scattering angle $\theta_{m_\chi,\,\mathrm{max}}$. The effect is confirmed by simulations in [175] and a result is shown in Fig. B.47 of Appx. B.8.4. For masses up to $m_\chi = 4\,\mathrm{MeV}$, the formation of a ring in the beam-spot at the position of the DarkMESA room can be observed (Fig. 8.15). For higher m_χ the dark Bremsstrahlung dominates and a distribution with a central maximum is observed. In Fig. 8.15 the dimensions of the DarkMESA room are drawn with a solid red line again. It can be seen that the distribution for m_χ smaller than 4 MeV is there not as homogeneous as in the dark Bremsstrahlung only case (Fig. 6.3). To increase the DM flux, one could now move the detectors from the beam-axis further into the right corner of the room. However, this is only possible to a limited extent due to constructional conditions. Towards this corner, the room has a reduced depth, ventilation shafts and a pumping station reduce the space further (Fig. 6.2). An additional option is offered by positioning a calorimeter in a room one floor upstairs. This room would be partially available to DarkMESA and is marked with the dashed red line. This DarkMESA off-axis option is studied in the following.

In Fig. 8.16 two of the four cases – on-axis and off-axis dark Bremstrahlung only, and on-axis and off-axis positron annihilation included – are plotted in single diagrams for comparison. If one looks at the geometrical acceptance for detectors of different sizes within the DarkMESA room (top left), one recognizes that many of the potential DM particles of the positron annihilation in the low mass range are lost due to the position of the detector in the DarkMESA room. On the other hand, the loss of DM particles due to dark Bremsstrahlung is less significant for the

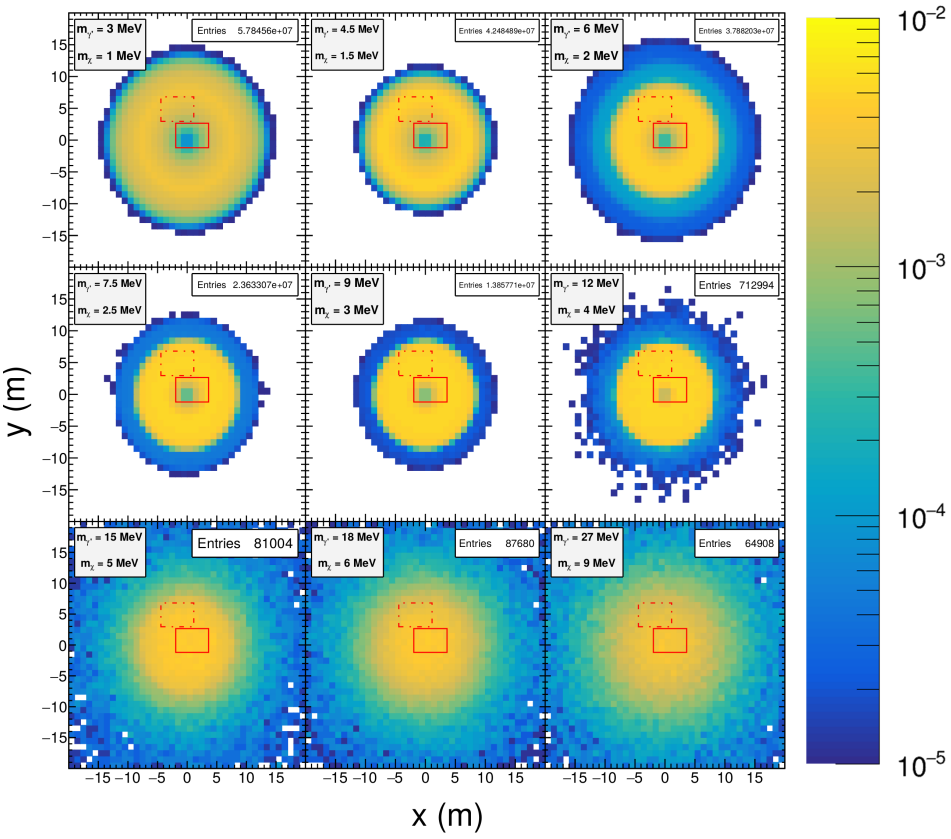

Figure 8.15.: The angular distribution of the DM particles with positron annihilation included is shown as a beam-spot at the beginning of the DarkMESA room. Shown are different kinematics with $m_{\gamma'} = 3\,m_\chi$ and rising DM mass from left to right and top to bottom. The dimensions of the DarkMESA room are indicated with a red box. The room one floor above is the DarkMESA off-axis option and indicated with a dotted red box.

off-axis room (bottom left). The comparison in the last diagram (bottom right) summarizes the differences and advantages of the two complementary detector positions. For the off-axis option the geometrical acceptance increases by up to two orders of magnitude in the low mass range. For the at first sight better positioning in the superior room, it must be taken into account that a significantly lower load capacity is possible and there is 30 cm less concrete shielding. In order to achieve the highest DM flow in the entire mass range, it is therefore advisable to position detectors in both rooms.

A first option would be to operate the DarkMESA Phase A detector at both positions. A comparison of these two options in Fig. 8.17 shows the advantage that the new position can strongly improve the exclusion limits in the mass range up to 5 MeV. Even Phase A with its low active volume and only 2 200 h beam-time manages to exceed the existing limits.[7]

This prototype detector could comfortably be operated in the off-axis room during the reconstruction phase from DarkMESA Phase A to Phase B. The weight of the Phase A setup is low enough, but for Phase B this is not the case. Alone because of the heavy lead shielding, an operation in the off-axis room is excluded. However, during the 6 600 h in this second funding period, a reduced version B2 could be operated in the off-axis room. This possible Phase B2 would consist

[7] All assuming that in the superior room the cosmic background can be lowered to the same level as in the room below by suitable additional shielding.

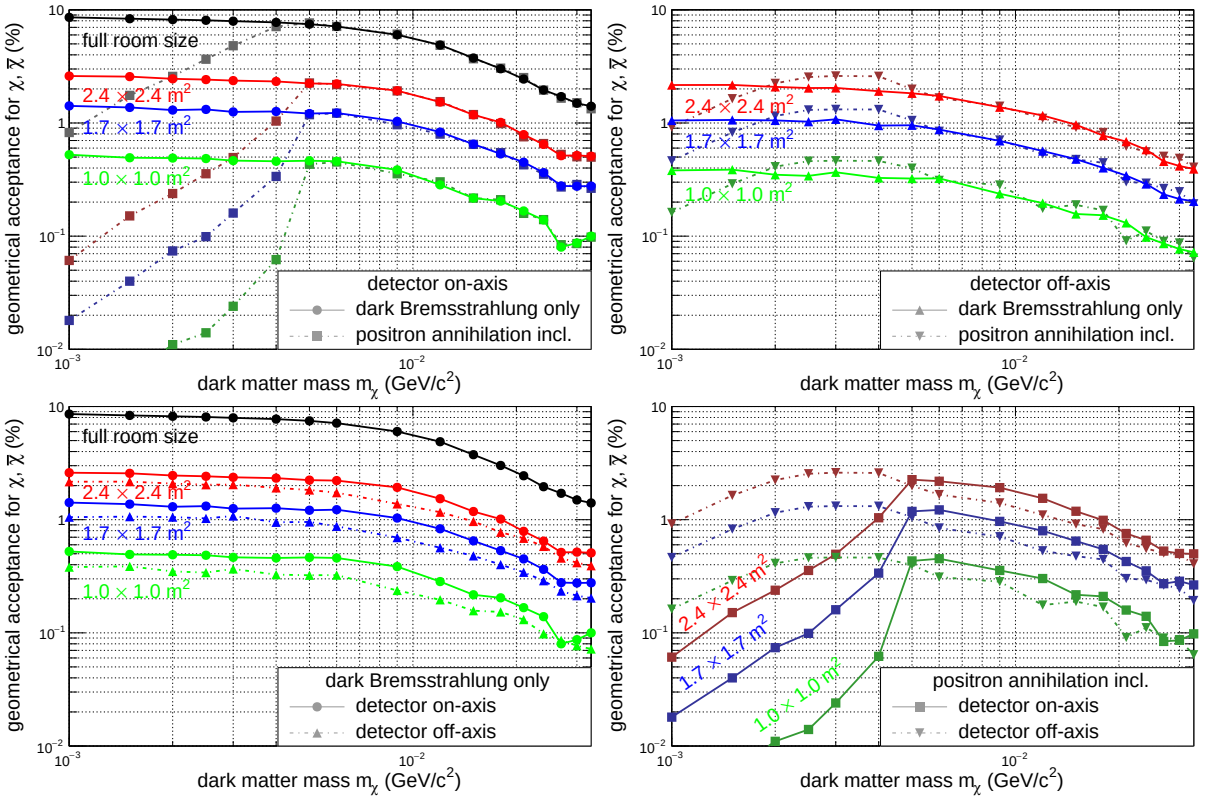

Figure 8.16.: Top: Dependence of the geometrical acceptance on DM masses for an on-axis (left) and off-axis (right) detector position for dark Bremsstrahlung only and with positron annihilation included. Bottom: Geometrical acceptance for dark Bremsstrahlung only (left) and with positron annihilation included (right) for both detector positions.

of four PbF_2 prototype modules and with its 100 crystals can achieve similar good results as Phase B at least in the narrow mass range between 2 and 4 MeV and exceed the Majorana and Scalar thermal relic targets (Fig. 8.18).

Summary. This chapter presented the exclusion limits of the well known DarkMESA Phases A and B first. By studying further concepts, a variety of dark sector experimental possibilities behind the P2 beam-dump have emerged. There is the complementary detection method DarkMESA-DRIFT. This gaseous detector has a completely different detection principle compared to the measurement of energy deposition in calorimeters. Both methods can benefit from each other. The data can be compared and results can be traced back to experiment-specific conditions. With the study of DarkMESA Phase C, the aspect of directionality from DarkMESA-DRIFT was taken up again. It is possible to increase the active volume and reduce the background issues further. Experimental studies are pending and should be started soon. The angular distribution of the DM particles from positron annihilation showed that an off-axis positioning of detectors would be a benefit for DarkMESA and an upstairs room was reserved. The several dark sector experiments at MESA can be operated in parallel, do not need dedicated beam-times, and can improve the existing exclusion limits.

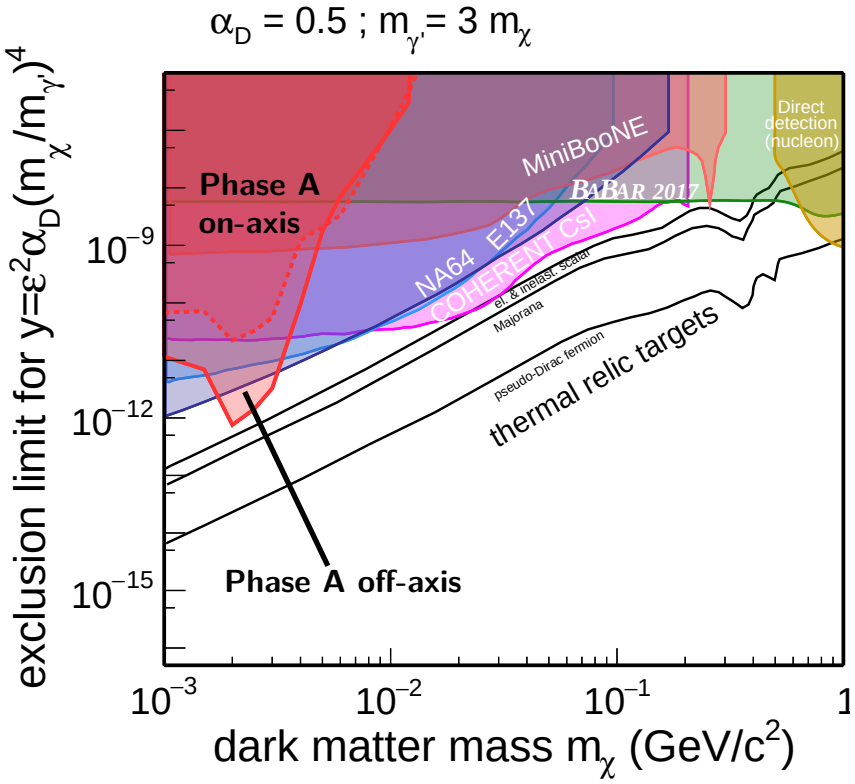

Figure 8.17.: Parameter space for dark photons decaying invisibly to $\chi\overline{\chi}$ with the DM mass m_χ on the horizontal axis and variable y on the vertical axis. The predictions for the DarkMESA Phase A on-axis and off-axis exclusion limit with 90 % CL and positron annihilation included are shown in red. The detection efficiency is 95 %, the conservatively estimated electron recoil energy threshold for DarkMESA is 10 MeV. 2 200 h of MESA electron beam were assumed. The existing exclusion limits from various other experiments [120, 170–174] are shown.

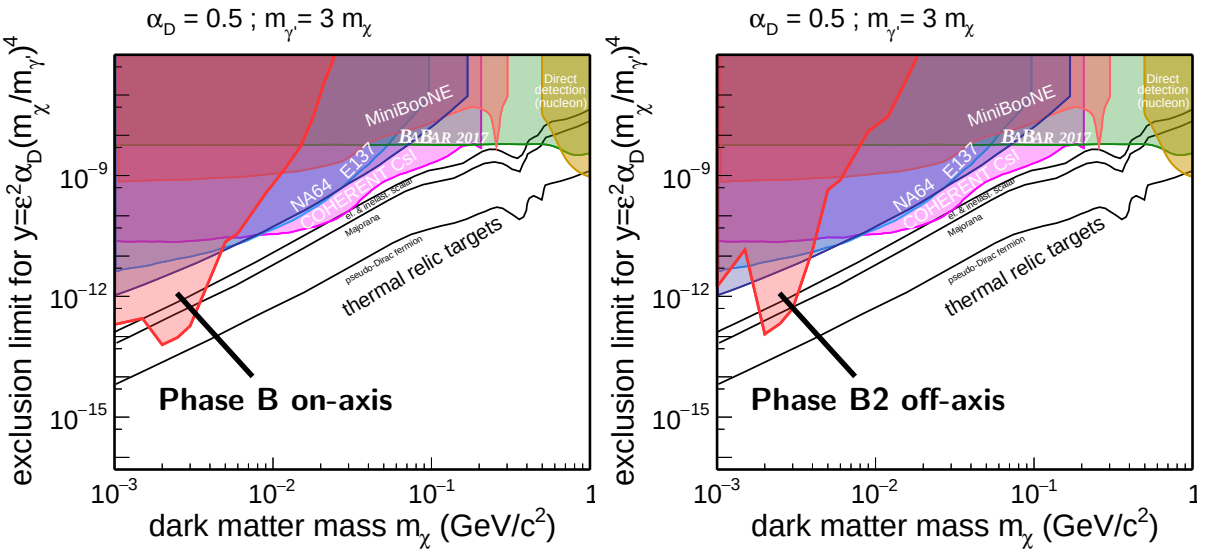

Figure 8.18.: Parameter space for dark photons decaying invisibly to $\chi\overline{\chi}$ with the DM mass m_χ on the horizontal axis and variable y on the vertical axis. The predictions for the DarkMESA Phase B on-axis (left) and the Phase B2 off-axis exclusion limit (right) with 90 % CL and positron annihilation included are shown in red. Phase B consists of 1 924 crystals, while Phase B2 comprises only 100 PbF_2 crystals. The detection efficiency is 95 %, the conservatively estimated electron recoil energy threshold for DarkMESA is 10 MeV. 2 200 h of MESA electron beam were assumed. The existing exclusion limits from various other experiments [120, 170–174] are shown.

9. Summary & Outlook

This work has demonstrated the extensive experimental capabilities in the search for dark sector particles at the new particle accelerator MESA. From simple theoretical models, via simulation studies and experimental studies, the first experimental concepts were developed and presented.

In the introduction to the dark sector in Chap. 1 the diverse astrophysical evidences for DM were presented. Besides the rotation velocities of galaxies, these are for instance the temperature fluctuations in the universe (CMB) or the dynamics of galaxy clusters. The most famous DM candidates that can explain these observations are WIMPs, LDM and ALPs. The light dark matter ($< 1\,\mathrm{GeV}$) relevant for DarkMESA and the possible dark sector models were presented and in particular the vector mediators and the possible types of DM particles were discussed. The experimental results of LDM searches in underground laboratories and at high-intensity accelerators were presented.

In Chap. 2, the existing accelerator infrastructure with MAMI and its experiments was presented first. Of particular relevance are the accelerator used for prototype studies and the already completed A4 experiment. Its PbF_2 crystals and the respective PMTs can be re-used for DarkMESA. The new accelerator MESA was also presented. The first experiment, MAGIX, will be operated in ERL mode with a beam energy of up to 105 MeV. With a high beam current of at least 1 mA, despite the lower density, the MAGIX gas jet target will achieve competitive luminosities. By avoiding foils on the path of the scattered electrons to the focal plane, precision measurements in different fields of physics will be possible. The second experiment, P2, will be operated in the EB mode and will measure the parity violating component in elastic electron-proton scattering at low momentum transfer, allowing the determination of the weak mixing angle with highest precision. The MESA beam will be stopped after this experiment in a beam-dump, which will also serve as a hypothetical source for DM particles. These particles could then be detected outside of the accelerator hall with the DarkMESA experiment. The detector concept has not been discussed at this point, only the advantage of a detector optimized for electron recoil has been shown.

For DarkMESA, a full simulation was created which is mainly based on `MadGraph` and `Geant4`. In Chap. 3 the simulation with its many facets was presented. The control of the simulation with the help of a steering file allows to activate parts of the simulation individually. The most important parts are a light yield simulation study of individual detector elements, an efficiency study of veto concepts and a complete simulation of the experiment itself. This allows to investigate the process of DM particle production in the beam-dump up to the detection in the DarkMESA experiment and to determine the expected reach for different concepts. A short study on the MAGIX trigger and veto system was also presented here, showing the synergies between the two experiments.

Potential calorimeter materials were investigated during a beamtime at MAMI and the results were presented in Chap. 5. All technical devices were presented and the processes of light production were discussed. Since a high density is desired, the study was particularly focused on the Cherenkov radiators PbF_2 and the PbGl types SF5, SF6, and SF57HTU. Transmission spectra were acquired with a spectrophotometer. This information was used to feed the simulation and the data was compared with the experimental results. The highest light yield with $1.86 - 2.04\,\text{p.e.}\,\text{MeV}^{-1}$ was obtained for PbF_2. For the PbGl types, SF5 showed the best performance with $1.56(6)\,\text{p.e.}\,\text{MeV}^{-1}$. A neutron response study showed a sensitivity of $< 0.4\,\%$ for all Cherenkov emitters.

In Chap. 6, on the production side, the possibility of increasing the number of dark photons with additional material in front of the beam-dump was investigated. A tungsten target with a thickness of 2.5 mm was considered as an option. On the detection side, the material possibilities were presented and a staged approach for DarkMESA was proposed. Starting with a prototype of 25 PbF_2 crystals in Phase A and a runtime of 2 200 h, the active volume in Phase B can be significantly increased by using about 2000 PbF_2 and SF5 PbGl crystals at a longer runtime of 6 600 h. A concept for Phase C with 13 200 h runtime has not been discussed at this point.

All these concepts require a suitable veto system, since the setup is well shielded against beam-related background, but however little shielding exists against cosmic-ray particles. In Chap. 7 the possible background sources were discussed. Initial simulation studies showed that no beam-related neutrons or neutrinos will reach the DarkMESA experiment. The simulation covered only a small time period but also for the whole experiment only a small number of events is expected, the particle energy is limited, and the sensitivity of the DarkMESA calorimeter for these particles is low. For the beam-unrelated cosmic-rays, spectra above ground and at the experimental site were simulated. To prevent calorimeter events from being wrongly identified as DM events, an efficient veto system is needed. This essentially consists of two hermetic scintillator layers and a lead layer. The scintillators are read out by SiPMs. With an additional ceiling veto and the re-definition of some calorimeter crystals as veto elements, the cosmic background could be lowered further. For the Phase A prototype, the rate was less than one event per hour, and for the much larger Phase B setup, but thicker lead shielding, about two events per hour.

For evaluating the contribution of DarkMESA to the search for DM also in comparison to other experiments, exclusion limits were introduced in Chap. 8. The theory of the production and detection of DM was presented. A simple model foresees a dark photon produced by dark Bremsstrahlung, which decays into DM. The result of a single kinematic case can be summarized in the variable y and compared with other experiments. Phase B already exceeds existing limits and could reach thermal targets by adding another DM production channel through positron annihilation. The supplementary detection method DarkMESA-DRIFT was presented and an additional coverage of the Majorana and Scalar thermal targets at higher DM masses is possible. Improvements were also achieved for DarkMESA Phase C, where a concept using thin radiation shielding glass was suggested. Another idea presented in this chapter were the detection capabilities at an off-axis position above the DarkMESA room. An additional off-axis detector can further enhance the experiment, although the size of the detector is limited due to the load capacity of the floor.

Some general ideas going beyond the scope of this thesis have been presented in the last chapter, but there are still some more ideas to consider in the near future.

- **Beam-tests at MAMI.** In addition to the already performed beam-tests of single calorimeter crystals and single veto detectors, there are also many future opportunities at MAMI. A complete or at least a slightly reduced setup of DarkMESA Phase A, should be tested in the electron beam of MAMI at various energies – initially with a reduced veto system and an active calorimeter volume of 3×3 crystals. Furthermore, a background study of the complete Phase A prototype should be carried out in the A1 spectrometer hall. The prototype could be operated during experiments with particularly high neutron fluxes. The same applies to individual 4×4 PbGl modules of the Phase B setup.

- **A shower detector for MAGIX.** The SF5 crystals of the 4×4 PbGl modules are also of particular interest for an extension of the MAGIX trigger and veto system. Within the Bachelor's thesis of Christopher Janas [178], conceptional and experimental studies for a PbGl shower detector as muon veto for MAGIX were carried out. The idea is to replace some of the (blind) lead absorbers with active PbGl detectors. At least two levels are required for the detection of a shower triggered by electrons. While muons still leave a signal in all levels, a distinction between beam electron and cosmic muon is possible in the lower levels due to the then different signal heights. While in this Bachelor's thesis only the basic functionality of the concept has been demonstrated, a complete realization of the concept is still outstanding.

- **Simulation of DM production.** The implementation of the `MadGraph` processes directly in `Geant4` is now possible [179] and will be completed in the next months as part of her PhD thesis by Saskia Plura.

- **Simulation of DM detection.** The coherent scattering on the nucleus was considered to be negligible based on a first estimate of the energy threshold. However, the material studies have shown that a threshold around 10 MeV is realistic and according to Fig. 2.13 a non-negligible fraction of proton recoil events can be expected above this threshold. This aspect could enhance the exclusion limits and should be taken into account in future studies.

- **Search for ALPs.** As part of the PhD thesis of Saskia Plura, the possibility to probe other DM models at DarkMESA will be investigated. A main point are axion searches at DarkMESA through Bremsstrahlung and Primakoff processes ($\gamma N \longrightarrow aN$). The position, energy and angle of the relevant photons in the beam-dump (Fig. B.48 of Appx. B.9) are already available and will serve as input for the simulations. The inclusion of the optional tungsten target will become more relevant again in this study.

- **Prototype status and electronics development.** In addition to the previously mentioned opportunities to characterize the veto system at MAMI, laboratory studies continue, and a PhD thesis of Matteo Lauß is in preparation. Due to delivery issues of electronic components and the several redesigns of the readout boards, the goal of his work is the

commissioning and characterization of a reduced Phase A prototype. For the data readout of the calorimeter crystals, the PANDA S-ADC will be used here, which is also foreseen in the final concept of DarkMESA. The power is still supplied by the iseg and CAEN modules and thus the number of channels is limited. A concept for the final setup should be developed soon.

- **Radiation shielding glass study for Phase C.** The material has to be studied experimentally. Similar to the simulation, one could start with single glass layers and stack them later. A beam-test at MAMI with relative low beam energy, allowing a full energy deposition in few layers, would be a good choice for this study. Since multiple panels should respond for each event, they should be very thin. The readout of thin plates could turn out to be complex and the complexity of electronic components increases. By replacing every second layer with less dense plastic scintillators, the panel thickness could be chosen slightly larger, while the same number of plates will generate a signal.

- **DarkMAMI.** Not only the P2 beam-dump might be used for a DM experiment, but also a small DM detector behind the A1 beam-dump could be an interesting option. For this purpose, one or more holes about 10 m deep might be drilled. These will allow to lower a small Cherenkov detector (possibly with an enclosing veto layer) to the level of the beam-dump (or to off-axis levels). Simulation studies for this setup have recently been started and will also be performed using the DarkMESA simulation. Due to the depth, this detector will have a better shielding against cosmic-rays. With a factor of ten higher beam energy, other DM mass regions could be probed and if necessary the detection threshold could be adjusted as well. A Bachelor's thesis will investigate the feasibility of constructing such a detector from the 460 mm long SF5 crystals and the infrastructure for lowering it into the borehole. This side project is preliminary called DarkMAMI.

The DarkMESA project is still in its early stages, but the first prototypes will be in operation at MESA soon. It is impressive to walk through the still empty accelerator halls and imagine how the MESA accelerator will be assembled here in the coming months. Especially at MAGIX, starting with the assembly of a large ring rail for the spectrometer guidance and the massive kingpin in the middle, one will quickly see how this experiment will fill large parts of its hall and when the spectrometer magnets will arrive, it will also grow in height.
The DarkMESA room could also be visited and one was imagining how it will be populated by the first prototype detectors in the near future. Starting with the first underground measurements, it is not far off that a first beam of MESA will be made available for P2 and the exciting search for DM can also start with DarkMESA.

A. Appendix A – Software

A.1. Geant4 basic structure – a simple example

With a minimalistic example, the most important parts of a `Geant4` simulation are presented. During this discussion, only excerpts of the program code are shown. In this example, the average energy loss of a 100 MeV electron during passage through 1 cm of lead (Pb) is simulated. As second material choice a sand layer (SiO_2) is investigated.

Basic structure. As usual for C++, all code modules except the `main.cc` file are divided into header files (*`.hh`) and source files (*`.cc`), which are located in the `include/` and `src/` folders. The C++ convention is that functions, classes, or variables are declared in the header file and this file is made available for the source file with an `#include` command. The mandatory files for such a `Geant4` simulation are:

- `main.cc`

- `include/ActionInitialization.hh`
- `include/DetectorConstruction.hh`
- `include/EventAction.hh`
- `include/PrimaryGeneratorAction.hh`
- `include/RunAction.hh`
- `include/SteppingAction.hh`

- `src/ActionInitialization.cc`
- `src/DetectorConstruction.cc`
- `src/EventAction.cc`
- `src/PrimaryGeneratorAction.cc`
- `src/RunAction.cc`
- `src/SteppingAction.cc`

- `init_vis.mac`
- `gui.mac`

- `vis.mac`

- `CMakeLists.txt`

- `GNUmakefile`

Every `Geant4` simulation is started via an `int main()` member function that is located in `main.cc`. In this function the mode in which the program should be started – with graphic interface or only in terminal – is defined first. This choice should be left to the user by providing an additional argument when executing the program:

```
./main vis or ./main bash
```

The `int main()` function also controls the sequence of the entire code via the `G4RunManager` class or, if several CPU cores are used, via the `G4MTRunManager` class:

```
#ifdef G4MULTITHREADED
  G4MTRunManager* runManager = new G4MTRunManager;
#else
  G4RunManager* runManager = new G4RunManager;
#endif
```

The geometries and corresponding materials are built by the user in the DetectorConstruction.cc file. The associated function is initialized next:

```
runManager->SetUserInitialization(new DetectorConstruction());
```

Also a physics list is loaded there. In this short example the Geant4 reference physics list QGSP_BERT_HP is chosen, which is recommended for shielding applications at all energies.

```
G4VModularPhysicsList* physicsList = new QGSP_BERT_HP();
runManager->SetUserInitialization(physicsList);
```

The event sequence is initiated in the main.cc file by loading the ActionInitialization() function from ActionInitialization.cc into the G4RunManager.

```
runManager->SetUserInitialization(new ActionInitialization());
```

Furthermore, a Visualization Manager and an User Interface Manager are initialized and the setting file init_vis.mac is executed when the graphical mode is selected. Preferences, such as the number of CPU cores to be used or the verbose output level, are set with this script. Also the vis.mac script, which controls the graphical representation of the example, is executed in here. For instance, the visualization driver can be chosen, the window size can be set, the colors of axes and labels adjusted, or the initial viewing angle and zoom level to the constructed components can be set. However, all these parameters can also be set with commands in the graphical environment directly. With the call of gui.mac, additional drop-down menus are created within the graphical environment. This eases the use of commonly required commands. To improve the representation, colors of geometries, particle trajectories, or the background can also be adapted with this file.

```
G4VisManager* visManager = new G4VisExecutive;
visManager->Initialize();
G4UImanager* UImanager = G4UImanager::GetUIpointer();
...
  // interactive mode
  UImanager->ApplyCommand("/control/execute init_vis.mac");
  UImanager->ApplyCommand("/control/execute gui.mac");
```

This is already the complete sequence of main(). For understanding the process in more detail, the functions DetectorConstruction() and ActionInitialization() are discussed now.

Placement of geometries. First a look into the DetectorConstruction.cc file, which is used to create geometries and materials. The Construct() function describes this buildup. All required materials are defined first – air for the surrounding world volume, as well as Pb and SiO_2 for the shielding. To generate any material, it is possible to define individual molecules in Geant4. These elements can then be used to compose materials according to their chemical formula. It is also possible to create compounds using a fractional mass. With this technique the required materials can be generated:

```
G4VPhysicalVolume* DetectorConstruction::Construct() {
  G4double z, a, fractionmass, density;
  G4String name, symbol;
  G4int ncomponents, natoms;

  a = 14.007*g/mole;
  G4Element* elN  = new G4Element(name="Nitrogen",symbol="N",z=7,a);

  a = 15.999*g/mole;
  G4Element* elO  = new G4Element(name="Oxygen",symbol="O",z=8,a);

  a = 28.085*g/mole;
  G4Element* elSi = new G4Element(name="Silicon",symbol="Si",z=14,a);

  a = 39.948*g/mole;
  G4Element* elAr = new G4Element(name="Argon",symbol="Ar",z=18,a);

  a = 207.2*g/mole;
  G4Element* elPb = new G4Element(name="Lead",symbol="Pb",z=82,a);

  density = 2.2*g/cm3;
  G4Material* SiO2 = new G4Material(name="SiO2",density,ncomponents=2);
  SiO2->AddElement(elSi, natoms=1);
  SiO2->AddElement(elO, natoms=2);

  density = 1.205*mg/cm3;
  G4Material* Air = new G4Material(name="Air",density,ncomponents=2);
  Air->AddElement(elN, fractionmass=78*perCent);
  Air->AddElement(elO, fractionmass=21*perCent);
  Air->AddElement(elAr, fractionmass=1*perCent);
  ...
}
```

This defines the element Pb, the chemical compound SiO_2, and the simplified compound air. These simple materials can also be found in the `Geant4` material database and can be selected via the `G4NistManager`:

```
G4NistManager* nist = G4NistManager::Instance();
G4Material* Air     = nist->FindOrBuildMaterial("G4_AIR");
G4Material* Pb      = nist->FindOrBuildMaterial("G4_Pb");
G4Material* SiO2    = nist->FindOrBuildMaterial("G4_SILICON_DIOXIDE");
```

This second method is much shorter, but not every material is in the database and the full control from the first method is missing.
Next, the volumes are created, starting with the world volume. The size is chosen large enough to place all necessary geometries. It serves as the mother volume for all other geometries and particles are tracked only inside this volume – at the border these tracks are aborted. The placement of a geometry is performed in three steps. First, a solid volume is created. `Geant4` provides many classes to create a wide variety of geometric shapes. Boolean operations are also possible to generate `SubtractionSolids` or `UnionSolids`. To avoid overloading this example, only the `G4Box()` class is introduced, which can define rectangular solids.

```
  G4double world_sizeXY = 1*m;
  G4double world_sizeZ  = 2*m;

  G4Box* solidWorld =
    new G4Box("World",                                    //its name
```

```
        0.5*world_sizeXY, 0.5*world_sizeXY, 0.5*world_sizeZ); //its size
```

This describes a box with a width and height of one meter, and a length of two meters. For most of the geometry classes, as well as here for `G4Box()`, half values of the requested edge lengths have to be used. No material or denotation has yet been assigned to the solid created here. This is done in the second step by generating a `G4LogicalVolume()`.

```
G4LogicalVolume* logicWorld =
  new G4LogicalVolume(solidWorld,          //its solid
                      Air,                 //its material
                      "World");            //its name
```

In the final step, the volume is placed. The `G4VPhysicalVolume()` is used for this purpose.

```
G4VPhysicalVolume* physWorld =
  new G4PVPlacement(0,                     //no rotation
                    G4ThreeVector(),       //at (0,0,0)
                    logicWorld,            //its logical volume
                    "World",               //its name
                    0,                     //its mother volume
                    false,                 //no boolean operation
                    0,                     //copy number
                    checkOverlaps);        //overlaps checking
```

For the world volume it is common to set it at a position (x=0, y=0, z=0) without an additional rotation, and obviously there is no mother volume. For all other volumes, the `G4LogicalVolume()` of the mother volume (`logicWorld`) has to be selected instead. These logical volumes can be placed and rotated at a given point inside of the world volume. The same `G4LogicalVolume()` can be called multiple times. This allows the construction of more complex geometries and the `checkOverlaps` function can minimize errors when assembling a larger number of components. It generates an error message when volumes overlap and it indicates the amount of overlap.

Stages of tracking. The simulation environment is ready. Now it is all about the particles to be examined. The user starts the simulation with the `/run/beamOn n` command, where `n` is the number of events that should go through the entire process. The process is started via the `ActionInitialization.cc` file. The `Build()` function contains all the modules to be used.

```
void ActionInitialization::Build() const {
  SetUserAction(new PrimaryGeneratorAction);

  RunAction* runAction = new RunAction;
  SetUserAction(runAction);

  EventAction* eventAction = new EventAction(runAction);
  SetUserAction(eventAction);

  SetUserAction(new SteppingAction(eventAction));
}
```

First, the `PrimaryGeneratorAction()` is called, the rest of the structure shows the nesting of `RunAction()`, `EventAction()`, and `SteppingAction()`. The sequence of these components is essential in order to understand the tracking in `Geant4`. The `PrimaryGeneratorAction()` generates a `G4ParticleGun`, which specifies the number of primary particles (per event), their

type, momentum, and energy. Several `G4ParticleGuns` can also be defined and thus an event with multiple types of particles and energies can be generated. For example, secondary particles produced in a particle shower could be used as new primary particles. In the example for a 100 MeV electron, the `G4ParticleGun` is constructed as follows:

```
PrimaryGeneratorAction::PrimaryGeneratorAction()
: G4VUserPrimaryGeneratorAction(), fParticleGun(0) {
  G4int n_particle = 1;
  fParticleGun  = new G4ParticleGun(n_particle);

  G4ParticleTable* particleTable = G4ParticleTable::GetParticleTable();
  G4String particleName;
  G4ParticleDefinition* particle
    = particleTable->FindParticle(particleName="e-");
  fParticleGun->SetParticleDefinition(particle);
  fParticleGun->SetParticleMomentumDirection(G4ThreeVector(0.,0.,1.));
  fParticleGun->SetParticleEnergy(100.*MeV);
}
```

This represents only the definition of the primary particle(s). With the `GeneratePrimaries (G4Event* anEvent)` function the generation in the simulation takes place at a given position.

```
void PrimaryGeneratorAction::GeneratePrimaries(G4Event* anEvent) {
  fParticleGun->SetParticlePosition(G4ThreeVector(0.0*m,0.0*m,-0.1*m));
  fParticleGun->GeneratePrimaryVertex(anEvent);
}
```

The particles are generated just before the absorber and this function is executed at the beginning of each event, in the `EventAction()` level. Above this level, however, there is still the `RunAction()` level. Here in the two functions

```
void RunAction::BeginOfRunAction(const G4Run* run){...}
```

and

```
void RunAction::EndOfRunAction(const G4Run* run){...}
```

commands are explicitly defined to take place before or after the entire course of all `n` events: initiating log files or histograms beforehand, and filling and closing them afterwards, for example. This level is usually executed only once, but it can also be used to customize parameters and to run a simulation multiple times, by re-calling the `/run/beamOn n` macro command. No restart of the simulation environment is needed and statistical uncertainties can be minimized. On the `EventAction()` level the progress is similar to the `RunAction()` level. Here, each of the `n` events is considered individually and before and after each of these events, commands can be executed using the

```
void EventAction::BeginOfEventAction(const G4Event* event){...}
```

and

```
void EventAction::EndOfEventAction(const G4Event* event){...}
```

functions. After running through all events `n`, the `RunAction()` level is called again. Now the processing of each event is still missing. All trajectories are simulated by using the user input information about the primary particles, the simulation environment, and the physics list. For an event, the generation of primary tracks starts and each track ends, when the kinetic energy is zero or a world boundary is reached. These tracks are stored and processed in stacks. When new secondary tracks are created, they are added to the stack. An event ends as soon as the stack has been completely processed. Due to physical processes or the indication of a minimum and maximum step length by the user, a track can consist of many steps. For these single steps the `SteppingAction()` level is responsible. One step consists of a `PreStepPoint` and a `PostStepPoint`, and has additional delta information such as energy loss or time difference. The function

```
void SteppingAction::UserSteppingAction(const G4Step* step){...}
```

can be used to steer the processing of these steps. For example, an additional break condition can be created when a certain volume or energy threshold has been reached, or a particular physical process has occurred.
To show the possibilities within the `SteppingAction()`, the example is now analyzed a little closer again. Since a pencil beam is simulated in this example (`SetParticleMomentumDirection(G4ThreeVector(0.,0.,1.));`), a Pb absorber surface of $10 \times 10\,\mathrm{cm}^2$ area with the specified thickness of 1 cm is sufficient here. It is created and placed in the `DetectorConstruction.cc` file and the associated volume name "Absorber" was chosen.
Since a `G4Step` also contains the volume information of the two points, the following condition can be established to determine the total energy deposit in the absorber material. For each `PreStepPoint`, lying inside of the absorber volume, the total energy deposited in this step is added to a variable which covers the energy deposit in one event (`eDepEvent`).

```
extern G4double eDepEvent;
void SteppingAction::UserSteppingAction(const G4Step* step) {
  G4StepPoint* prePoint = step->GetPreStepPoint();
  G4String currentVolumeName = prePoint->GetTouchableHandle()->GetVolume()->
      GetLogicalVolume()->GetName();
  G4double edepStep = step->GetTotalEnergyDeposit();
  if(currentVolumeName == "Absorber") {
      eDepEvent += edepStep;
  }
}
```

`eDepEvent` is set to zero at the beginning of each event (`BeginOfEventAction()`). Additionally the number of events is counted there, by adding +1 to `G4int nmbEvents`. At the end of each event `eDepEvent` is added to the `eDepTot` variable, which is used in multiple event runs to calculate the average energy deposit. This calculation is done by calling `G4double(eDepTot/nmbEvents)` at the end of a run (`EndOfRunAction()`). Of course, `nmbEvents` and `eDepTot` have to be reset to zero again at the `BeginOfRunAction()`.

Evaluation. How to output the raw data to files or present histogrammed results is not discussed here, as there are individual preferences. In this work, different procedures are chosen depending

on the requirement. For example, the raw data is stored in `ASCII` files or `ROOT` trees, which in turn can serve as input files in analysis programs. These programs can be written in the user's preferred programming language (in this work: Python and C++) or directly as `ROOT` macros. For some (initial) examinations a quick visual result can be helpful and the storage as graph or histogram is performed directly in the `Geant4` environment.

run no.	1 event	10 events	100 events	1 000 events	10 000 events
1	7.37 MeV	36.36 MeV	30.41 MeV	30.01 MeV	30.25 MeV
2	50.47 MeV	27.86 MeV	31.52 MeV	30.54 MeV	30.08 MeV
3	17.17 MeV	27.73 MeV	29.12 MeV	30.49 MeV	30.26 MeV
4	29.06 MeV	34.03 MeV	30.62 MeV	30.21 MeV	30.20 MeV
5	75.81 MeV	27.97 MeV	28.08 MeV	30.30 MeV	30.33 MeV
$\varnothing E_{\text{run}}$	35.98 MeV	30.79 MeV	29.95 MeV	30.31 MeV	30.22 MeV
σ_{run}	27.46 MeV	4.11 MeV	1.35 MeV	0.22 MeV	0.06 MeV

Table A.1.: Example for 1 cm Pb absorber: On average deposited energy (in MeV) for 1, 10, 100, 1 000, and 10 000 events. Five runs were carried out in each case.

When performing several runs with an increasing number of events, it becomes apparent that the statistical uncertainty decreases with the increasing number of events (see Tab. A.1). For five runs with 10 000 events each, the average energy deposition in 1 cm Pb is 30.22 MeV with a standard deviation of 0.06 MeV. Using the same procedure as for lead, an average energy deposition of 4.023 MeV with a standard deviation of 0.007 MeV is obtained for five simulations with 10 000 events. This means that at least a 7.6 cm thick SiO_2 absorber has to be used to obtain the same energy deposition as for 1 cm Pb and thus the same shielding effect.

With this example, the most basic components of a `Geant4` simulation were presented. Further components that were used in the DarkMESA simulation are briefly presented at the relevant passages in Chap. 3.

A.2. Geant4 and DarkMESA software – installation guide

This is a compact installation guide for `Geant4` and the DarkMESA software on Linux platforms. For further information – especially installation on other platforms – the user is referred to the full `Geant4` user guide provided here:

`https://geant4.web.cern.ch/support/user_documentation`

Requirements

- Software requirements:
  - `CMake3.3` or higher,
  - C++ compiler and standard library supporting the C++11 standard.
- (Optional) software requirements for visualization:

  - Qt user interface and visualization: Qt4.6 or higher,
  - X11 OpenGL visualization: X11 headers and libraries, OpenGL or MesaGL headers and libraries.
- Additional packages in case of the standard "MAGIX-Debian PC" installation:
  - libx11-dev,
  - libxmu-dev,
  - libgl1-mesa-dev.

Geant4.10.04 installation

- Download Geant4.10.04 and optional data files from https://geant4.web.cern.ch/support/download.
- Unpack the Geant4.10.04 source files to .../source/geant4.10.04.
- Create a build folder .../build/geant4.10.04-build.
- Unpack data files to $CMAKE_INSTALL_PREFIX/share/Geant4-10.04.0/data.
- It is recommended to use the cmake-gui to build Geant4. The necessary settings can be found in Fig. A.1. The installation of an external CLHEP library (version 2.3.3.0 or higher) is possible, but no requirement. Otherwise Geant4 uses an internal version which is built and used by default. In order to be able to have a visualization of the simulation environment, it is recommended to activate the GEANT4_USE_OPENGL_X11 option.
- Configure and generate the CMake commands.
- In the folder .../build/geant4.10.04-build do: make -jN[1] and sudo make install.

MadGraph BDXEventGenerator installation

- From https://github.com/JeffersonLab/BDXEventGenerator download the lastet BDXEventGenerator. No further installation is necessary.

Remarks

- Install your ROOT version with -DCMAKE_CXX_STANDARD=11 flag, e.g.: cmake -DCMAKE_CXX_STANDARD=11 -DCMAKE_INSTALL_PREFIX=<installdir> <sourcedir>.
- Environmental variables of Geant4, ROOT, and the MadGraph event generator, have to be made accessible via the export command in the .bashrc file. In addition, the files .../bin/thisroot.sh and .../bin/geant4.sh have to be sourced there.

The simulations were performed on a Debian GNU/Linux 9 (Stretch) 64-bit system with the g++ Version Debian 6.3.0-18+deb9u1, and Geant4.10.04 and ROOT 6.12/04 installed. No problems were found when using the upgrades Debian GNU/Linux 10 (buster), Geant4.10.06, and ROOT 6.22/09.

A.3. DarkMESA simulation – code snippets

A.3.1. Physics list

Electromagnetic processes: The Geant4 example nanobeam in the advanced category served as a basis. For a deeper understanding of the individual commands, please refer to [114].

[1] N is the number of threads to be used.

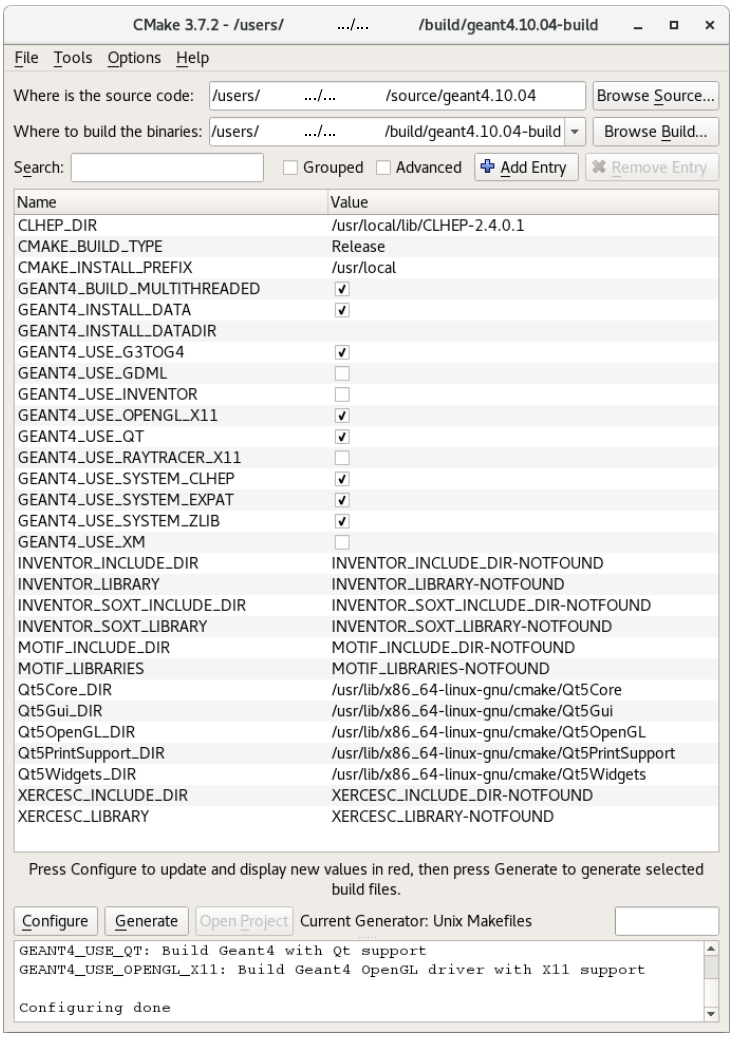

Figure A.1.: `CMake` settings during `Geant4.10.04` installation. Beside the `build` and `source` directories, the installation of the `Geant4` data sets and the correct visualization routines are set. Optionally, a link with Autodesk Inventor or a multithreaded mode can be activated.

```
...
void BDXPhysicsList::ConstructEM() {
  G4PhysicsListHelper* ph = G4PhysicsListHelper::GetPhysicsListHelper();
  auto particleIterator=GetParticleIterator();
  particleIterator->reset();
  while((*particleIterator)()) {
    G4ParticleDefinition* particle = particleIterator->value();
    G4String particleName = particle->GetParticleName();

    if (particleName == "gamma") {
      // Construct processes for gamma
      G4PhotoElectricEffect* photoelectriceffect = new G4PhotoElectricEffect();
      ph->RegisterProcess(photoelectriceffect, particle);
      ph->RegisterProcess(new G4ComptonScattering(), particle);
      ph->RegisterProcess(new G4GammaConversion(), particle);

    } else if (particleName == "e-") {
      // Construct processes for electron
```

```
      ph->RegisterProcess(new G4eMultipleScattering(), particle);
      ph->RegisterProcess(new G4eIonisation(), particle);
      ph->RegisterProcess(new G4eBremsstrahlung(), particle);

    } else if (particleName == "e+") {
      // Construct processes for positron
      ph->RegisterProcess(new G4eMultipleScattering(), particle);
      ph->RegisterProcess(new G4eIonisation(), particle);
      ph->RegisterProcess(new G4eBremsstrahlung(), particle);
      ph->RegisterProcess(new G4eplusAnnihilation(), particle);

    } else if (particleName == "mu+" || particleName == "mu-") {
      // Construct processes for muon
      G4MuMultipleScattering* msc = new G4MuMultipleScattering();
      msc->AddEmModel(0, new G4WentzelVIModel());
      ph->RegisterProcess(msc, particle);
      ph->RegisterProcess(new G4MuIonisation(), particle);
      ph->RegisterProcess(new G4MuBremsstrahlung(), particle);
      ph->RegisterProcess(new G4MuPairProduction(), particle);
      ph->RegisterProcess(new G4CoulombScattering(), particle);

    } else if (particleName == "alpha" || particleName == "He3") {
      ph->RegisterProcess(new G4hMultipleScattering(), particle);
      ph->RegisterProcess(new G4ionIonisation(), particle);

    } else if (particleName == "proton") {
      ph->RegisterProcess(new G4hMultipleScattering(), particle);
      ph->RegisterProcess(new G4hIonisation(), particle);
      ph->RegisterProcess(new G4hBremsstrahlung(), particle);
      ph->RegisterProcess(new G4hPairProduction(), particle);
      ph->RegisterProcess(new G4StepLimiter(), particle);

    } else {
      if ((particle->GetPDGCharge() != 0.0) && (particle->GetParticleName() !=
          "chargedgeantino") && !particle->IsShortLived()) {
        // All others charged particles except geantino
        ph->RegisterProcess(new G4hMultipleScattering(), particle);
        ph->RegisterProcess(new G4hIonisation(), particle);
      }
    }
  }
}
...
```

Optical processes: The `Geant4` example `optical/OpNovice` in the `extended` category served as a basis. For a deeper understanding of the individual commands, please refer to [114].

```
...
void BDXPhysicsList::ConstructOp() {
  fCerenkovProcess = new G4Cerenkov("Cerenkov");
  fCerenkovProcess->SetMaxNumPhotonsPerStep(fMaxNumPhotonStep);
  fCerenkovProcess->SetMaxBetaChangePerStep(10.);
  fCerenkovProcess->SetTrackSecondariesFirst(true);
```

```
    fScintillationProcess = new G4Scintillation("Scintillation");
    fScintillationProcess->SetScintillationYieldFactor(scintillationYieldFactor);
    fScintillationProcess->SetTrackSecondariesFirst(true);
    fAbsorptionProcess = new G4OpAbsorption();
    fRayleighScatteringProcess = new G4OpRayleigh();
    fMieHGScatteringProcess = new G4OpMieHG();
    fBoundaryProcess = new G4OpBoundaryProcess();

    fCerenkovProcess->SetVerboseLevel(fVerboseLevel);
    fScintillationProcess->SetVerboseLevel(fVerboseLevel);
    fAbsorptionProcess->SetVerboseLevel(fVerboseLevel);
    fRayleighScatteringProcess->SetVerboseLevel(fVerboseLevel);
    fMieHGScatteringProcess->SetVerboseLevel(fVerboseLevel);
    fBoundaryProcess->SetVerboseLevel(fVerboseLevel);

    // Use Birks Correction in the Scintillation process
    if (G4Threading::IsMasterThread()) {
      G4EmSaturation* emSaturation =
              G4LossTableManager::Instance()->EmSaturation();
      fScintillationProcess->AddSaturation(emSaturation);
    }

    auto particleIterator=GetParticleIterator();
    particleIterator->reset();
    while((*particleIterator)()) {
      G4ParticleDefinition* particle = particleIterator->value();
      G4ProcessManager* pmanager = particle->GetProcessManager();
      G4String particleName = particle->GetParticleName();
      if (fCerenkovProcess->IsApplicable(*particle)) {
        pmanager->AddProcess(fCerenkovProcess);
        pmanager->SetProcessOrdering(fCerenkovProcess,idxPostStep);
      }
      if (fScintillationProcess->IsApplicable(*particle)) {
        pmanager->AddProcess(fScintillationProcess);
        pmanager->SetProcessOrderingToLast(fScintillationProcess, idxAtRest);
        pmanager->SetProcessOrderingToLast(fScintillationProcess, idxPostStep);
      }
      if (particleName == "opticalphoton") {
        G4cout << " AddDiscreteProcess to OpticalPhoton " << G4endl;
        pmanager->AddDiscreteProcess(fAbsorptionProcess);
        pmanager->AddDiscreteProcess(fRayleighScatteringProcess);
        pmanager->AddDiscreteProcess(fMieHGScatteringProcess);
        pmanager->AddDiscreteProcess(fBoundaryProcess);
      }
    }
  }
  ...
```

A.3.2. MadGraph setting files

The following **proc_card.dat** file includes the physics processes to be generated.

```
#*********************************************************************
#                        MadGraph/MadEvent                           *
#                    http://madgraph.hep.uiuc.edu                    *
#                                                                    *
#                         proc_card.dat                              *
#                                                                    *
# This file is used to generate the code for a specific process.     *
# Some notation/conventions:                                         *
#                                                                    *
# 0. Do not modify the TAGS and their order.                         *
# 1. hash/pound is a comment.                                        *
# 2. The number after the @ is used as an identifier for the class   *
#    of processes. It can be any positive integer.                   *
# 3. The number of lines for the max couplings depends on how many   *
#    different classes of couplings are present in the model         *
#    In the SM these are just two: QED (which include EW) and QCD    *
# 4. Write "end_coup" after  the couplings list,                     *
#    to tell MG that the couplings input is over.                    *
# 5. Write "done" after the proc list to                             *
#    to tell MG that the proc input is over.                         *
# 6. Some model names available at present are:                      *
#    sm     =  Standard Model                                       *
#    smckm =  Standard Model with Cabibbo matrix                    *
#    mssm   =  Minimal Supersymmetric Standard Model                *
#    2hdm   =  Generic Two Higgs Doublet model                      *
#    heft   =  Higgs EFT (+Standard Model)                          *
#    usrmod =  User Model                                           *
# 7. Don't leave spaces between the particles name in the            *
#    definition of the multiparticles.                               *
#*********************************************************************
#*********************************************************************
# Process(es) requested : mg2 input                                  *
#*********************************************************************
# Begin PROCESS # This is TAG. Do not modify this line

e- N+ > e- N+ f+ f-      # Radiative
QCD=0              # Max QCD couplings
QED=1              # Max QED couplings
QFD=0
QND=1
QWD=9
QDS=2
end_coup           # End the couplings input

done               # this tells MG there are no more procs

# End PROCESS  # This is TAG. Do not modify this line
#*********************************************************************
# Model information                                                  *
#*********************************************************************
# Begin MODEL  # This is TAG. Do not modify this line
fixedAP2
```

```
# End   MODEL  # This is TAG. Do not modify this line
#*********************************************************************
# Start multiparticle definitions                                    *
#*********************************************************************
# Begin MULTIPARTICLES # This is TAG. Do not modify this line
P uu~cc~dd~ss~gf+f-
J uu~cc~dd~ss~gf+f-
L+ e+mu+
L- e-mu-
vl vevm
vl~ ve~vm~
# End  MULTIPARTICLES # This is TAG. Do not modify this line
```

The following **param_card.dat** file includes the adjustable parameters for the physics processes.

```
#*********************************************************************
#                        MadGraph/MadEvent                           *
#                    http://madgraph.hep.uiuc.edu                    *
#                                                                    *
#                         param_card.dat                             *
#                                                                    *
#   Les Houches friendly file for the SM parameters of MadGraph      *
#        Spectrum and decay widths produced by SMCalc                *
#                                                                    *
#  Please note the following IMPORTANT issues:                       *
#                                                                    *
# 0. REFRAIN from editing this file by hand! Some of the parame-     *
#    ters are not independent                                        *
#    (such as G_Fermi, alpha_em, sin(theta_W),MZ,MW) and serious     *
#    problems might be encountered (such as violation of unitarity   *
#    or gauge invariance).  Always use a calculator.                 *
#                                                                    *
# 1. alpha_S(MZ) has been used in the calculation of the parameters  *
#    but, for consistency, it will be reset by madgraph to the       *
#    value expected IF the pdfs for collisions with hadrons are      *
#    used. This value is KEPT by madgraph when no pdf are used       *
#    lpp(i)=0 .                                                      *
#                                                                    *
#  2. Values of the charm and bottom kinematic (pole) masses are     *
#     those used in the matrix elements and phase space UNLESS they  *
#     are set to ZERO from the start in the model (particles.dat)    *
#     This happens, for example,  when using 5-flavor QCD where      *
#     charm and bottom are treated as partons in the initial state   *
#     and a zero mass might be hardwired in the model definition.    *
#                                                                    *
##*********************************************************************
Block MODSEL # Select Model
 0  1  #  0  1  =  SM
Block SMINPUTS      # Standard Model inputs
 1  1.27900000E+02  #  alpha_em(MZ)(-1)  SM  MSbar
 2  1.16600000E-05  #  G_Fermi
```

```
 3  1.18000000E-01  #  alpha_s(MZ)  SM  MSbar
 4  9.15445065E+01  #  Z  mass  (as  input  parameter)
Block MGYUKAWA     # Yukawa masses m/v=y/sqrt(2)
#    PDG          YMASS
 5  4.20000000E+00  #  mbottom  for  the  Yukawa  y_b
 4  1.25000000E+00  #  mcharm  for  the  Yukawa  y_c
 6  1.74300000E+02  #  mtop  for  the  Yukawa  y_t
 15  1.77700000E+00  #  mtau  for  the  Yukawa  y_ta
Block MGCKM     # CKM elements for MadGraph
 1   1     9.75000000E-01   # Vud for Cabibbo matrix
#===========================================================
# QUANTUM NUMBERS OF NEW STATE(S) (NON SM PDG CODE) IF ANY
# (see below for masses and decay tables)
# These blocks are automatically created by the MadGraph
# qnumbers.pl script from the particles.dat model file
#===========================================================
BLOCK QNUMBERS 611 # f-
 1  -3  #  3  times  electric  charge
 2  1  #  number  of  spin  states  (2S+1)
 3  1  #  colour  rep  (1:  singlet,  3:  triplet,  8:  octet)
 4  1  #  Particle/Antiparticle  distinction  (0=own  anti)
BLOCK QNUMBERS 622 # x
 1  0  #  3  times  electric  charge
 2  3  #  number  of  spin  states  (2S+1)
 3  1  #  colour  rep  (1:  singlet,  3:  triplet,  8:  octet)
 4  0  #  Particle/Antiparticle  distinction  (0=own  anti)
BLOCK QNUMBERS 623 # N-
 1  0  #  3  times  electric  charge
 2  2  #  number  of  spin  states  (2S+1)
 3  1  #  colour  rep  (1:  singlet,  3:  triplet,  8:  octet)
 4  1  #  Particle/Antiparticle  distinction  (0=own  anti)
# END of QNUMBERS blocks
#===========================================================
Block MASS      #  Mass spectrum (kinematic masses)
#       PDG       Mass
 4  1.40000000E+00  #  charm  pole  mass
 5  4.20000000E+00  #  bottom  pole  mass
 6  1.74300000E+02  #  top  pole  mass
 11  0.51109989E-03  #  electron  mass
 13  0.10565837E+00  #  muon  mass
 15  1.77700000E+00  #  tau  mass
 23  9.15445065E+01  #  Z  mass
 24  8.02673592E+01  #  W  mass
 25  1.20000000E+02  #  H  mass
 611  1.5E-3  #  FMASS  #This  is  the  chi  mass  in  GeV
 622  4.5E-3  #  APMASS  #This  is  the  A'  mass  in  GeV
 623  25.13000E+00  #  HPMASS  (aluminum)  #This  is  the  nucleus  mass  in
    GeV  (material  of  the  beam  dump)
#            PDG       Width
DECAY       611     0.00000000e+00   # ELWIDTH
DECAY       622     0.01             # APWIDTH
DECAY       623     0.00000000e+00   # HPWIDTH
```

```
DECAY         6     1.51013490E+00   # top width
DECAY        23     2.44639985E+00   # Z   width
DECAY        24     2.03535570E+00   # W   width
DECAY        25     6.79485838E-03   # H   width
#         BR            NDA        ID1        ID2
     7.00588389E-02    2           4         -4   # BR( H -> c   cbar  )
     7.61074375E-01    2           5         -5   # BR( H -> b   bbar  )
     0.00000000E+00    2           6         -6   # BR( H -> t   tbar  )
     3.65529942E-02    2          15        -15   # BR( H -> tau- tau+)
     5.84716539E-03    2          23         23   # BR( H -> Z   Z^(*))
     6.31545979E-02    2          24        -24   # BR( H -> W   W^(*))
     2.55499652E-02    2          21         21   # BR( H -> g   g    )
     1.20906932E-03    2          22         22   # BR( H -> A   A    )
BLOCK MGUSER
 1  1E-3  #  epsilon  ,mixing  coefficient
 2  0.5  #  alphaD  ,the  interaction  aprime-chi
 3  13.0000000e+00  #  Znuc  ,nuclear  charge
```

The following **run_card.dat** file includes parameter settings on the run level, e.g. cut-values. Many of the parameters in this file are used in the second part of the simulation, the detector interaction. However, this simulation is performed in the `Geant4` environment and the parameters can be ignored at this point. Due to the file length, only a small section of important parameters is shown here.

```
#*********************************************************************
#                        MadGraph/MadEvent                           *
#                  http://madgraph.hep.uiuc.edu                      *
#                                                                    *
#                         run_card.dat                               *
#                                                                    *
#  This file is used to set the parameters of the run.               *
#                                                                    *
#  Some notation/conventions:                                        *
#                                                                    *
#   Lines starting with a '# ' are info or comments                  *
#                                                                    *
#   mind the format:   value    = variable     ! comment             *
#*********************************************************************
#
#*******************
# Running parameters
#*******************
#
#*********************************************************************
# Tag name for the run (one word)                                    *
#*********************************************************************
  'VALID'     = run_tag ! name of the run
#*********************************************************************
# Run to generate the grid pack                                      *
#*********************************************************************
  .false.     = gridpack  !True = setting up the grid pack
```

```
#*********************************************************************
# Number of events and rnd seed                                      *
#*********************************************************************
 100000 = nevents ! Number of unweighted events requested
 2775 = iseed ! rnd seed (0=assigned automatically=default))
#*********************************************************************
# Collider type and energy                                           *
#*********************************************************************
...
 0.155 = ebeam1 ! beam 1 energy in GeV
...
 0.000511 = mbeam1 ! beam 1 energy in GeV
...
#*********************************
# BW cutoff (M+/-bwcutoff*Gamma)
#*********************************
 5.0 = bwcutoff
...
#*******************
# BDX cuts
...
#*******************
# Standard Cuts
...
```

A.3.3. Proton and nuclear elastic recoil

For the two recoil processes not presented in Sec. 3.5.4, the cross-section calculation changes. For proton elastic recoil the `BDXKinUtils::Er_chipXsection()` function and for nuclear elastic recoil the `BDXKinUtils::Er_chinuclXsection()` function is used:

```
G4double BDXKinUtils::Er_chipXsection(G4double *x, G4double *par) {
  G4double Er=x[0];
  G4double E0=par[0];

  //The reaction is: chi(p1)+N(p2)->chi(k1)+N(k2).
  //Perform the cross-section in the lab frame, where p1=(0,0,P,E), p2=(0,0,0,
      Mn), k2=(xx,yy,zz,Er)

  //1: Compute Lorentz-invariant dot products
  G4double p1p1=Mchi* Mchi;
  G4double k1k1=Mchi*Mchi;
  G4double p1p2=E0*Mn;
  G4double p1k1=-0.5*(2*Mn*Mn-2*Mchi*Mchi-2*Er*Mn); //A.C. Ask Eder to check
  G4double p1k2=Mn*(E0+Mn-Er);
  G4double p2k1=Mn*(E0+Mn-Er);
  G4double p2k2=Er*Mn;
  G4double k1k2=Mn*E0;

  G4double k1p2=p2k1;
  G4double k2p2=p2k2;
```

```
  G4double k1p1=p1k1;

  G4double t=2*Mn*Mn-2*Mn*Er;
  G4double s=Mn*Mn + Mchi*Mchi + 2*Mn*E0;

  //2: the amplitude squared
  G4double  ampsq=1.0*(k1k2*p1p2 + p1k2*k1p2 - Mchi*Mchi*k2p2 - Mn*Mn*k1p1 + 2*
      Mchi*Mchi*Mn*Mn)/(pow((t-Maprime*Maprime),2));
  if (ampsq<0.0) {
      return 0;
  }
  //3: the 2 momenta in the CM frame (before/after). Since this is elastic
      scattering, they're the same!!!
  G4double p=((pow(s-Mchi*Mchi - Mn*Mn,2) - 4*Mchi*Mchi*Mn*Mn)/(4*s));
  p=sqrt(p);
  G4double k=p;

  //4: the Jacobian for the transformation cos(theta_CM) --> Recoil total
      energy in LAB frame
  G4double dcostheta = Mn / (p*k); //AC: checked this formula.

  //5: the phase-space
  G4double S=(k/(s*p))*dcostheta;

  //6: the Form-Factor, using a dipole approximation.
  G4double FF=1/pow(1+(Er*Er-Mn*Mn)/Mn*Mn,2);

  //7: put everything together
  G4double dsigma=pow(FF,2)*ampsq*S; //in "GeV^-2 units" (and no coupling yet)
  dsigma = dsigma * Epsilon*Epsilon*4*PI*Alpha*AlphaDark;
  dsigma *=GeVm2cm2;

  return dsigma;
}



G4double BDXKinUtils::Er_chinuclXsection(G4double *x, G4double *par) {
  G4double Tr = x[0];
  G4double E0 = par[0];

  //1: Use eq. 38 of 1607.01390
  G4double dsigma;
  dsigma = 8*PI*Alpha*AlphaDark*Epsilon*Epsilon*Mnucl*Znucl*Znucl;
  dsigma = dsigma/(pow(Maprime*Maprime+2*Mnucl*Tr,2)); // this is in GeV^-3

  //2: convert in cm2 / GeV
  dsigma *= GeVm2cm2;

  return dsigma;
}
```

In the functions inside of the `BDXKinUtils.cc` file also the following values change:

- Maximum recoil energy range (x_{min} and x_{max}),
- maximum energy transfer ($E_{\mathrm{r,max}}$),
- real recoil energy range (x_1 and x_2),
- and total energy of the recoil χ (E_χ).

The correct formulas for all three recoil processes can be found in Tab. A.2. For the proton elastic recoil an effective binding energy correction is also performed.

	electron elastic	**proton elastic**	**nuclear elastic**
x_{min}	$E_{\mathrm{thr}} + m_{\mathrm{e}}$	$E_{\mathrm{thr}} + E_{\mathrm{binding}} + m_{\mathrm{n}}$	E_{thr}
x_{max}	$E_{\mathrm{beam}} + m_{\mathrm{e}} - m_\chi$	$E_{\mathrm{beam}} + m_{\mathrm{n}} - m_\chi$	$E_{\mathrm{beam}} - m_\chi$
$E_{\mathrm{r,max}}$	$\frac{2m_{\mathrm{e}}\left(E_0^2 - m_\chi^2\right)}{2E_0 m_{\mathrm{e}} + m_{\mathrm{e}}^2 + m_\chi^2}$	$\frac{2m_{\mathrm{n}}\left(E_0^2 - m_\chi^2\right)}{2E_0 m_{\mathrm{n}} + m_{\mathrm{n}}^2 + m_\chi^2}$	$\frac{2m_{\mathrm{nucl}}\left(E_0^2 - m_\chi^2\right)}{2E_0 m_{\mathrm{nucl}} + m_{\mathrm{nucl}}^2 + m_\chi^2}$
x_1	$E_{\mathrm{thr}} + m_{\mathrm{e}}$	$E_{\mathrm{thr}} + E_{\mathrm{binding}} + m_{\mathrm{n}}$	E_{thr}
x_2	$E_{\mathrm{r,max}} + m_{\mathrm{e}}$	$E_{\mathrm{r,max}} + m_{\mathrm{n}}$	$E_{\mathrm{r,max}}$
E_χ	$E_0 + m_{\mathrm{e}} - E_{\mathrm{r}}$	$E_0 + m_{\mathrm{n}} - E_{\mathrm{r}}$	$E_0 + m_{\mathrm{nucl}} - E_{\mathrm{r}}$

Table A.2.: Formulas used in the simulation for the calculation of electron, proton, and nuclear elastic recoil processes.

B. Appendix B – Supplements

B.1. Simulation studies along the P2 beam-line

Fig. B.1 shows the focussing effect of the P2 solenoid. Without the magnetic field more than 22 % of the beam electrons are stopped in the beam-exit-pipe already. Components on the path from the P2 target to DarkMESA, implemented in `Geant4`, are shown in Fig. B.2. The deposited energies of γ, e^-, and e^+ in the P2 target and the beam-exit-pipe are shown in Figs. B.3–B.6.

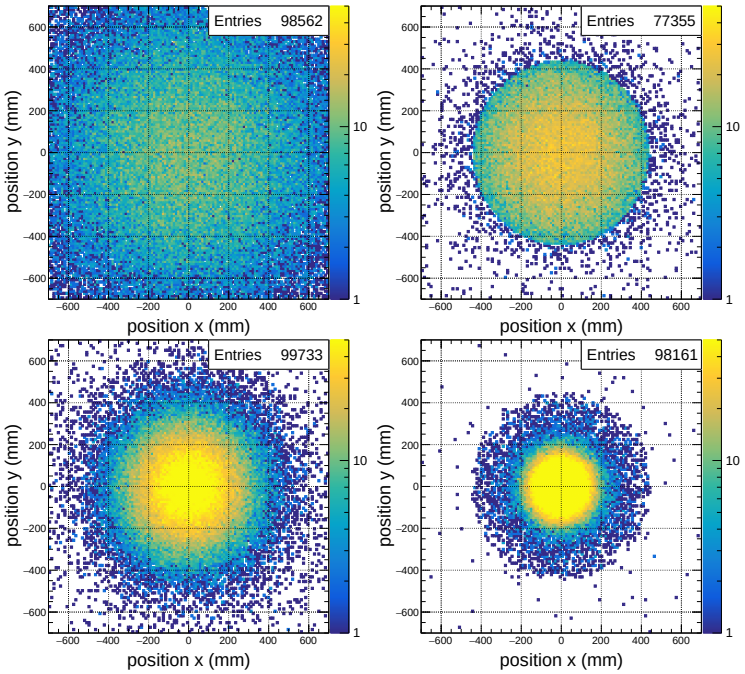

Figure B.1.: Top: Hitmap for 100 000 primary beam electrons without the solenoids magnetic field for a position 7 m before (left) and at the beam-dumps beginning (right). Bottom: Same with the magnetic field turned on for a position 7 m before (left) and at the beam-dumps beginning (right).

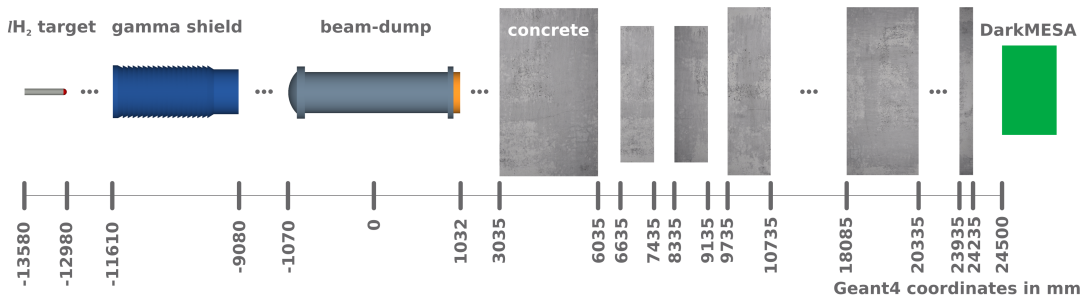

Figure B.2.: Simplified floor plan of the MESA hall with the most relevant components along the beam-axis. The coordinates used in the `Geant4` environment are given. The grey blocks symbolize the concrete walls. The components and their distances are not to scale.

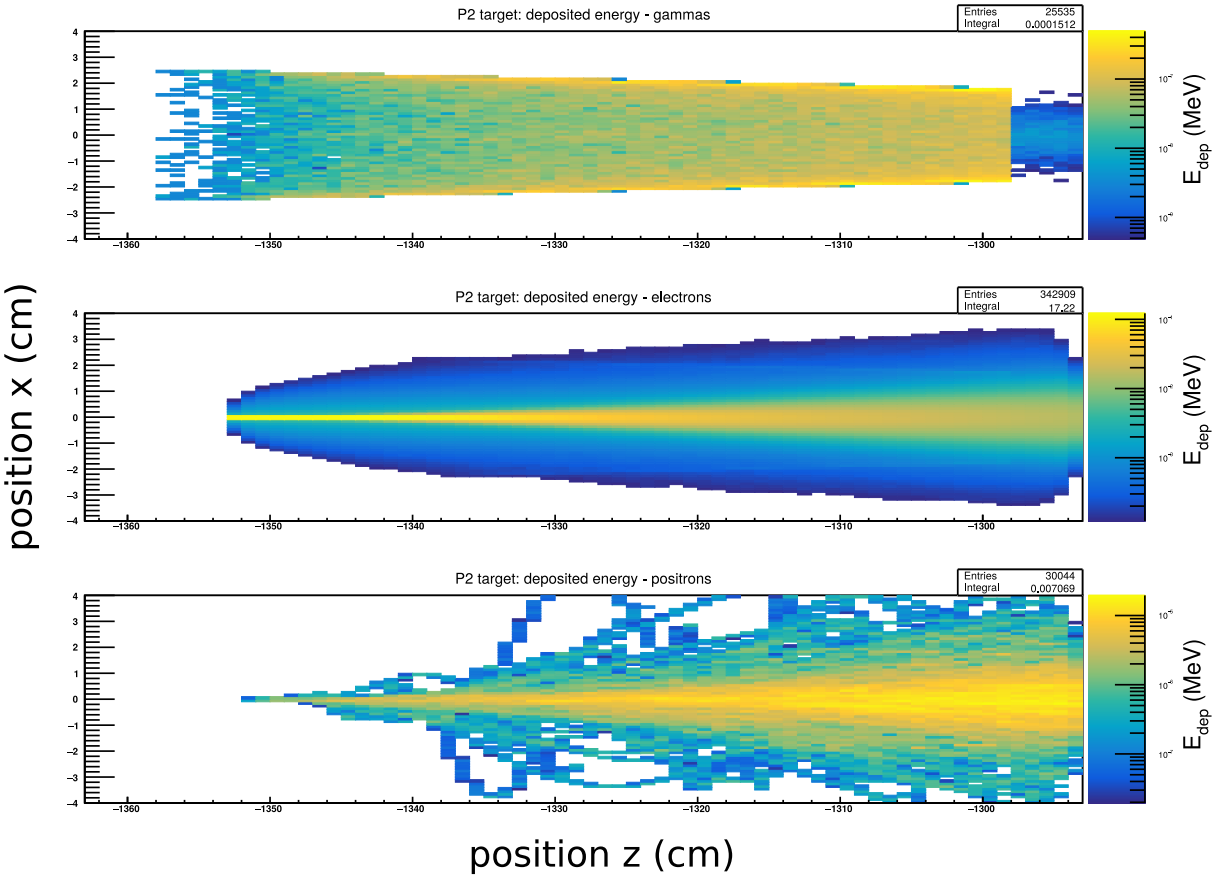

Figure B.3.: Deposited energy of γ (top), e^- (middle), and e^+ (bottom) in the P2 target. The values are shown for the x and z dimension and a normalization with the total number of primary beam electrons was made.

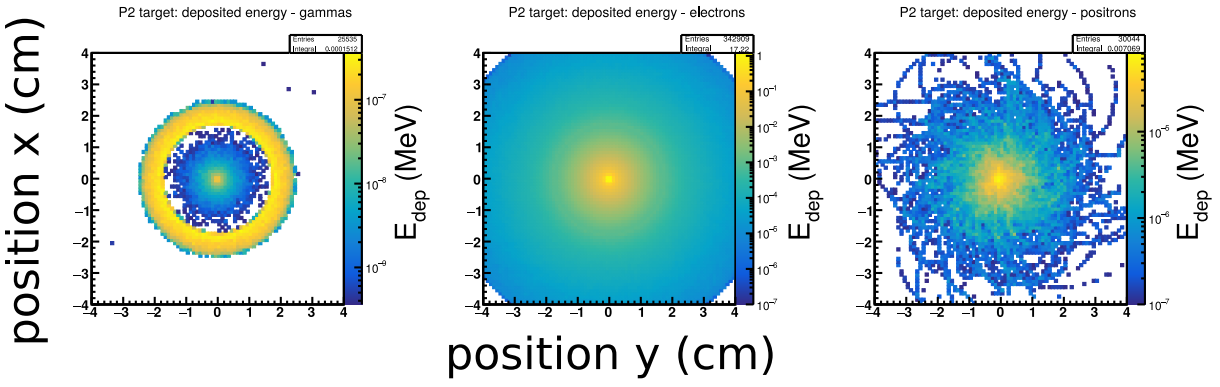

Figure B.4.: Deposited energy of γ (left), e^- (middle), and e^+ (right) in the P2 target. The values are shown for the x and y dimension and a normalization with the total number of primary beam electrons was made.

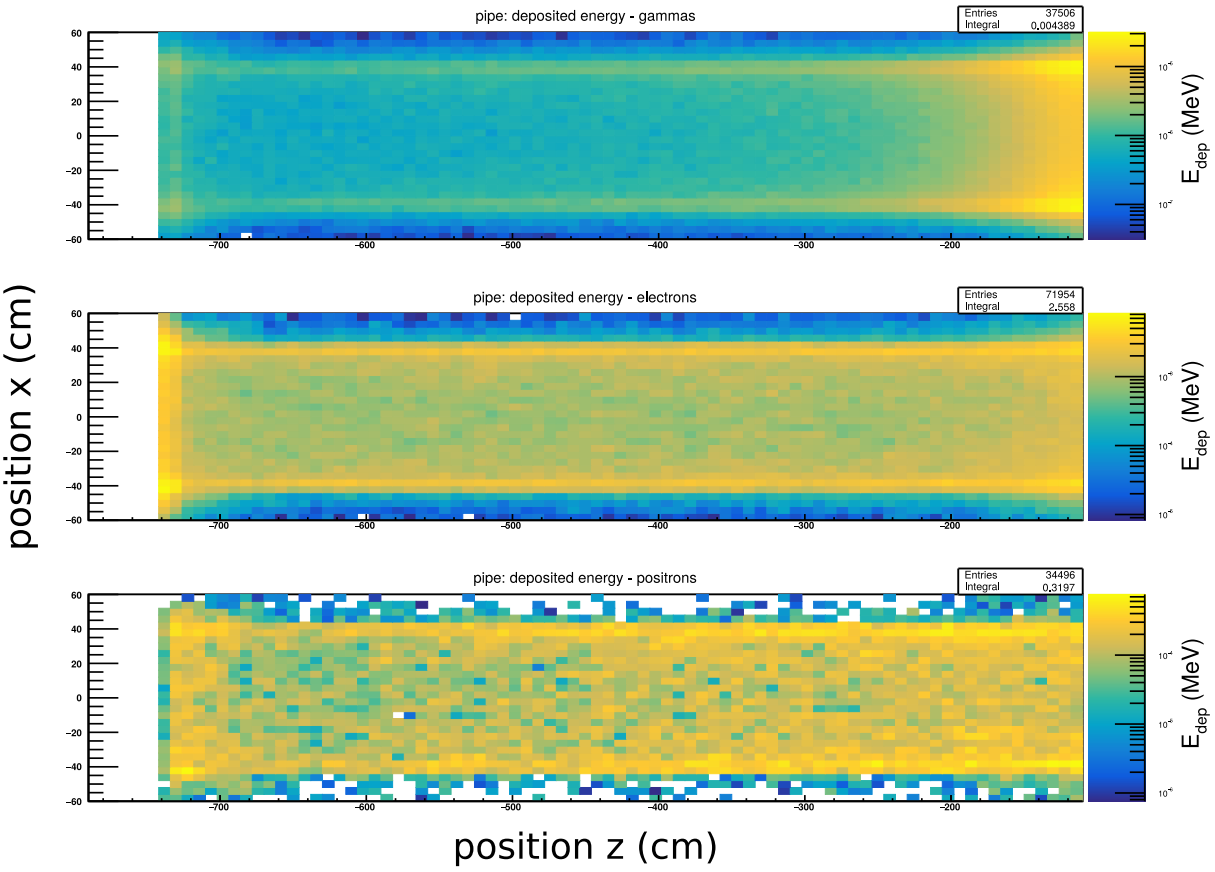

Figure B.5.: Deposited energy of γ (top), e^- (middle), and e^+ (bottom) in the beam pipe. The values are shown for the x and z dimension and a normalization with the total number of primary beam electrons was made.

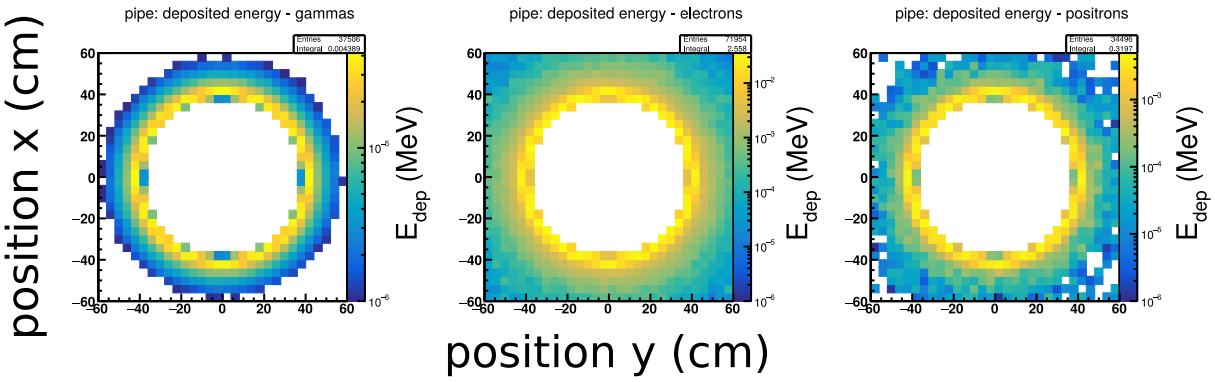

Figure B.6.: Deposited energy of γ (left), e^- (middle), and e^+ (right) in the beam pipe. The values are shown for the x and y dimension and a normalization with the total number of primary beam electrons was made.

B.2. MAGIX simulation studies

B.2.1. Trigger scan for additional z positions

Two additional scans of the trigger layer were performed at positions next to the PMT ($z = 100\,\text{mm}$, Fig. B.7) and opposite the PMT ($z = -100\,\text{mm}$, Fig. B.8).

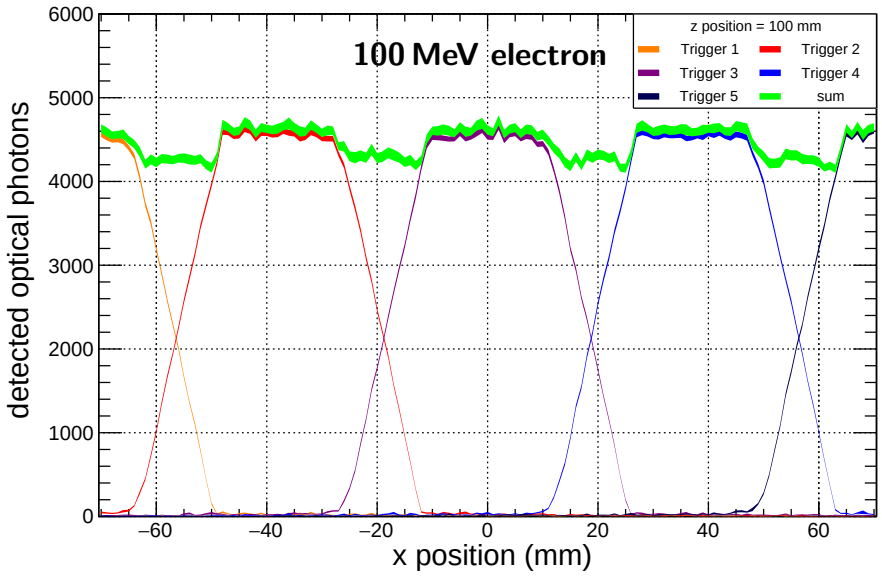

Figure B.7.: Scan over five trigger bars along the x axis for the fixed z position of 100 mm.

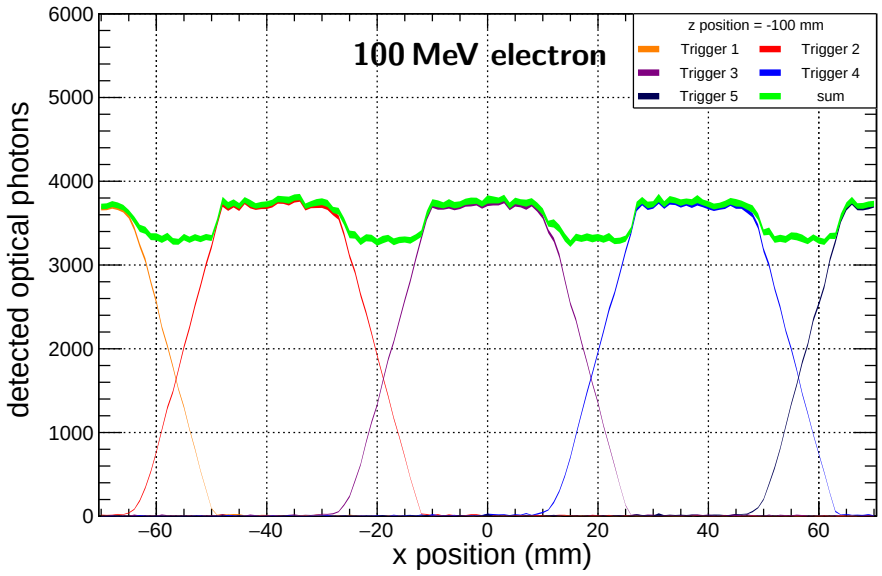

Figure B.8.: Scan over five trigger bars along the x axis for the fixed z position of −100 mm.

B.2.2. Additional veto response studies

The veto response probability for additional absorber configurations are shown in Figs. B.9–B.10. One study for 10 GeV muons is shown in Fig. B.11. The dependency on the photon cut value is shown for one electron setting in Fig. B.12.

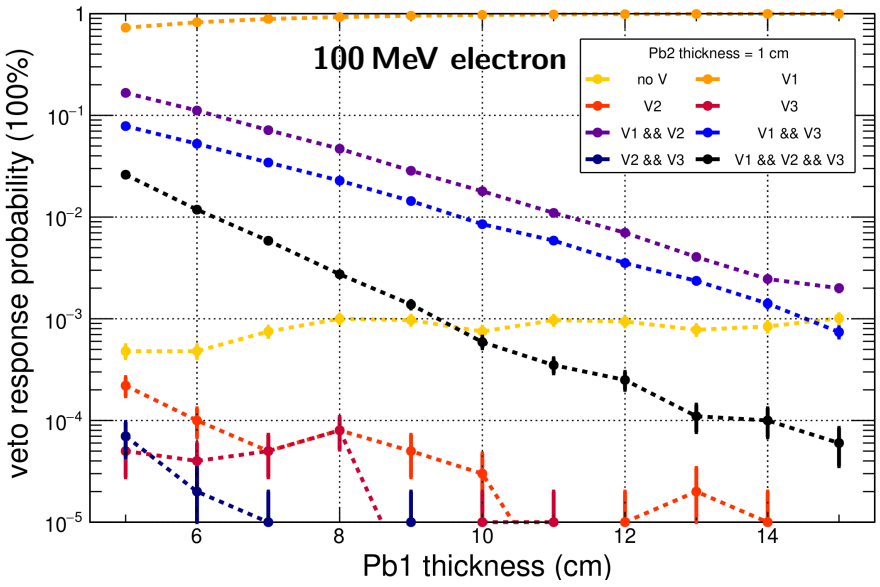

Figure B.9.: The veto response probability for 100 MeV primary electrons. The eight veto conditions in dependence of the thickness of the first lead absorber layer (Pb1) are shown. The thickness of the second lead absorber layer (Pb2) is fixed to 1 cm.

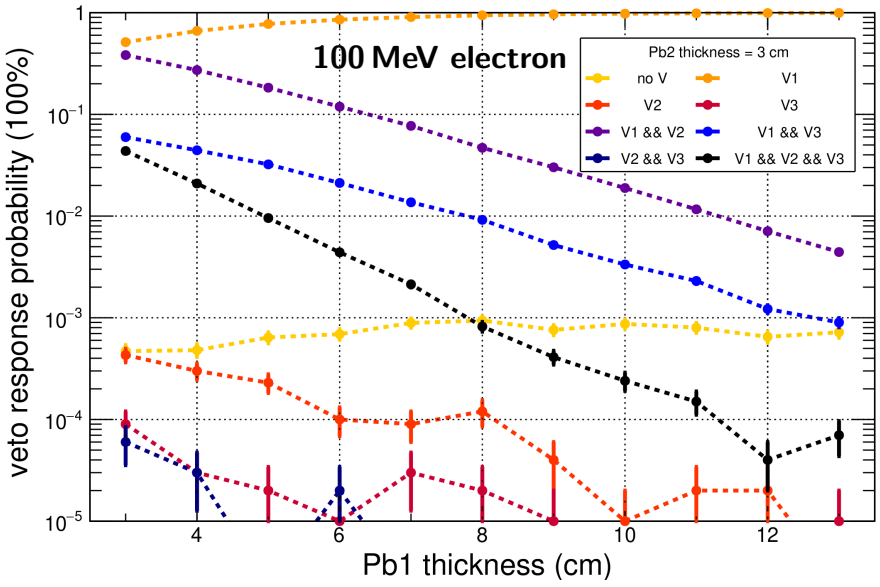

Figure B.10.: The veto response probability for 100 MeV primary electrons. The eight veto conditions in dependence of the thickness of the first lead absorber layer (Pb1) are shown. The thickness of the second lead absorber layer (Pb2) is fixed to 3 cm.

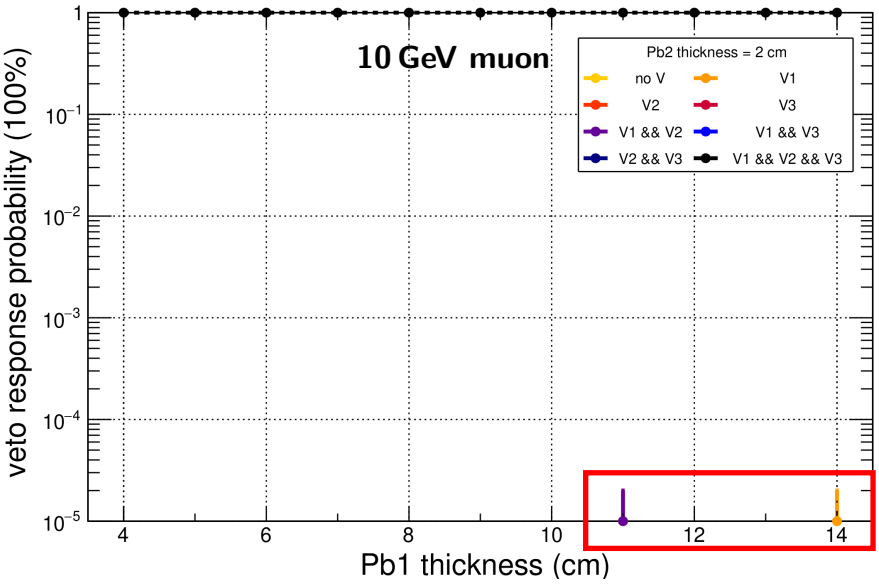

Figure B.11.: The veto response probability for 10 GeV primary muons. The possible veto conditions in dependence of the thickness of the first lead absorber layer (Pb1) are shown. The thickness of the second lead absorber layer (Pb2) is fixed to 2 cm. If at least 100 optical photons have been produced in one element, it counts as activated. Only events with at least one active trigger bar are evaluated.

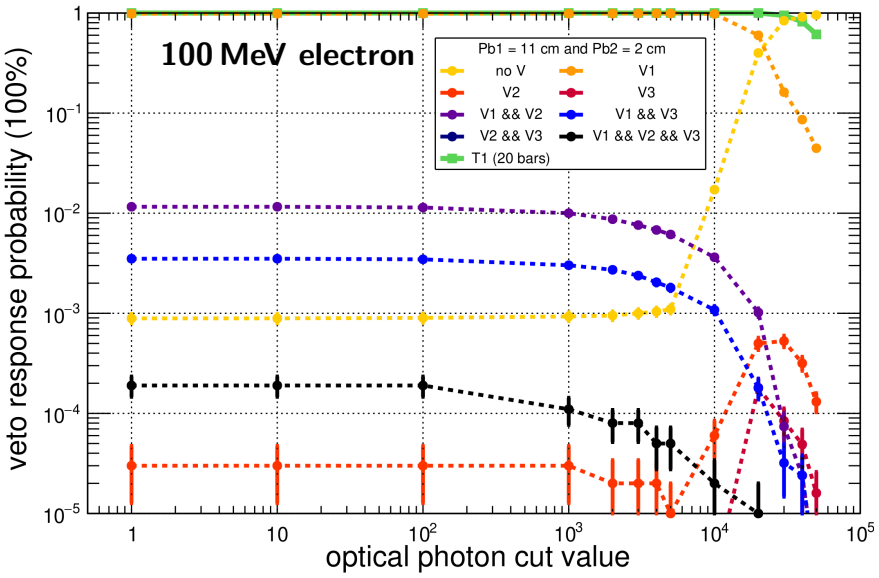

Figure B.12.: The veto response probability (100 MeV electrons) for the eight veto conditions in dependence of the optical photon cut value. The absorber layer configuration is fixed to Pb1 = 11 cm and Pb2 = 2 cm. Since there is a drop in the trigger response probability for higher cut values, it is also plotted here (green).

B.3. DarkMESA material studies

B.3.1. Photos of prototype crystals

The condition of the diverse crystals for the material studies at MAMI is shown in Figs. B.13–B.14.

(a) Schott SF5 – before cutting

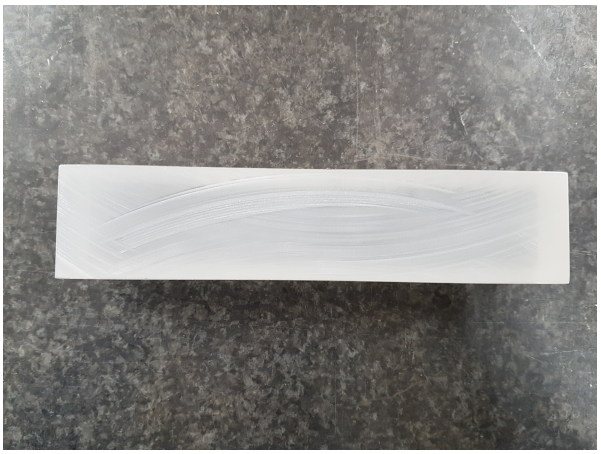

(b) Schott SF5 – after cutting

(c) Schott SF6 – before cutting

(d) Schott SF6 – after cutting

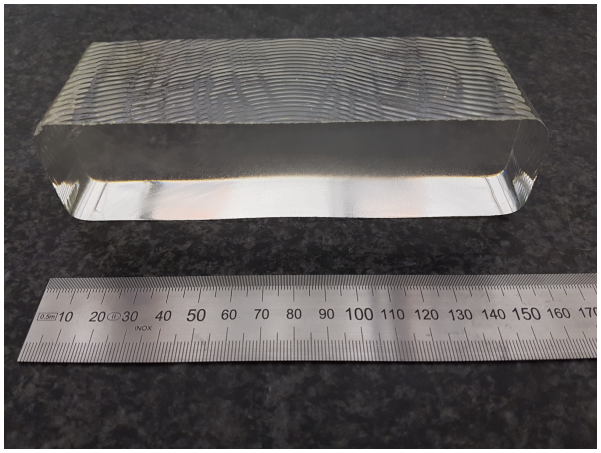

(e) Schott SF57HTU – before cutting

(f) Schott SF57HTU – after cutting

Figure B.13.: Photos of the PbGl materials – SF5 (top), SF6 (middle), and SF57HTU (bottom) – before and after cutting by the mechanical workshop. Not all edges were completely machined, as material damages occurred.

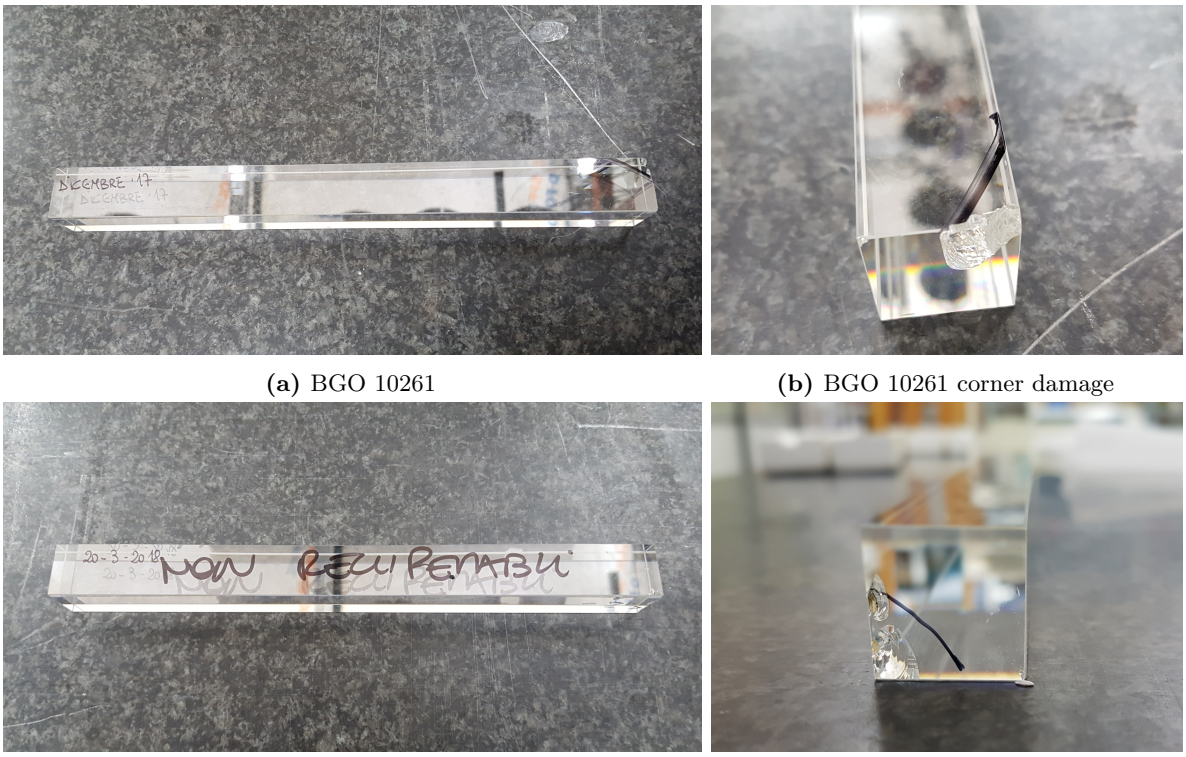

(a) BGO 10261

(b) BGO 10261 corner damage

(c) BGO 10322

(d) BGO 10322 corner damage

Figure B.14.: Photos of the BGO crystals – BGO 10261 (top) and BGO 10322 (bottom). The crystals have a length of 230 mm with a base area of $21 \times 21\,\mathrm{mm}^2$. The small corner damages are shown in the right plots. The PMTs were connected to the opposite side.

B.3.2. Transmittance spectra

Transmittance spectra taken for an additional crystal axis are shown in Fig. B.15 for all crystals studied in this thesis.

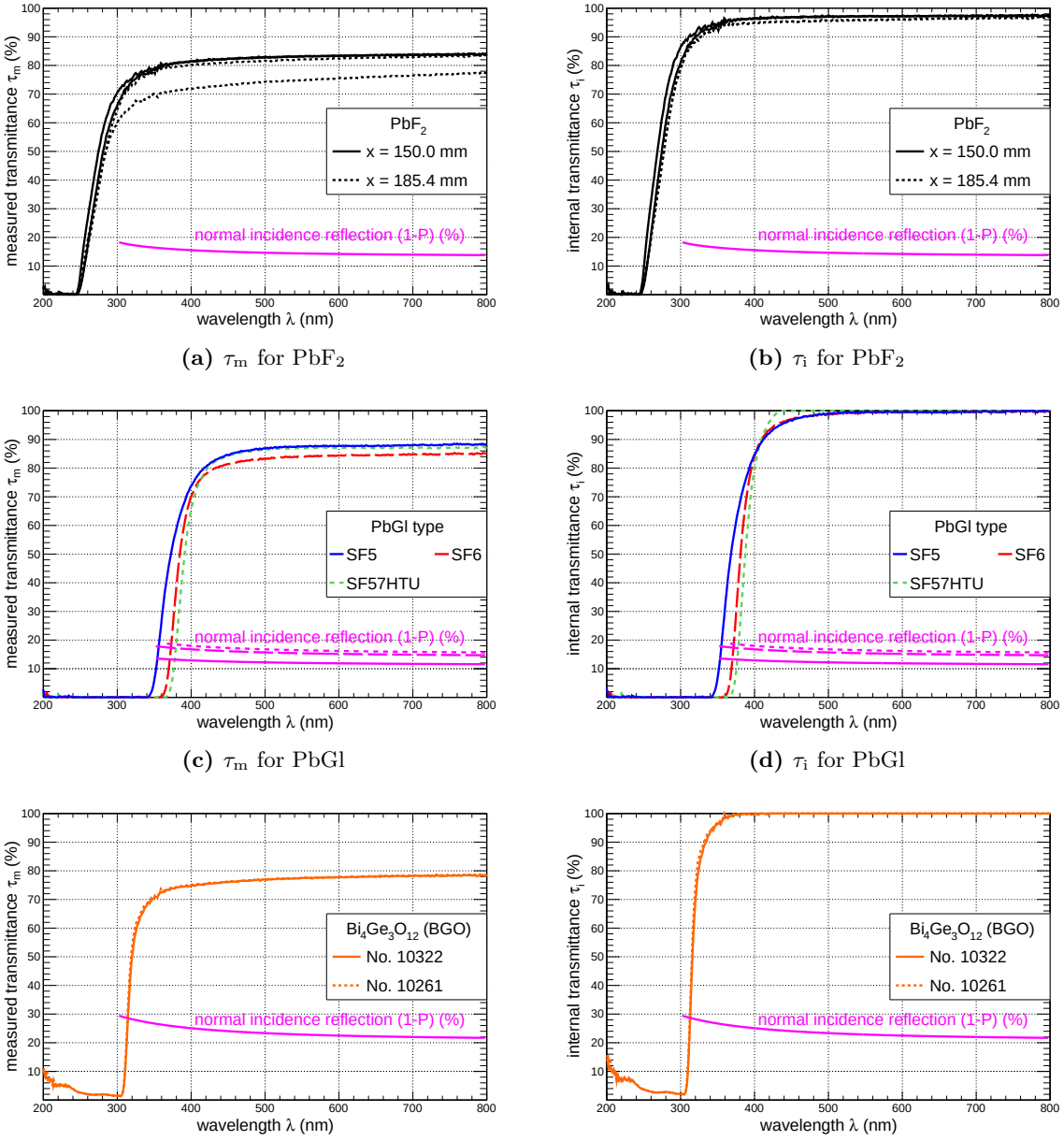

(a) τ_m for PbF_2 **(b)** τ_i for PbF_2

(c) τ_m for PbGl **(d)** τ_i for PbGl

(e) τ_m for BGO **(f)** τ_i for BGO

Figure B.15.: The measured (τ_m) and calculated internal transmittance (τ_i) are shown for the measurements taken with a sampling beam going through the shortest crystal axis. The normal incidence reflection $(1 - P)$ was calculated with the approximation in Eq. 5.7. The internal transmittance is then obtained with Eq. 5.9. For PbF_2 four crystals in two different lengths were analyzed (a–b). For each of the three PbGl types one crystal was analyzed (c–d) and for BGO two crystals of same shape were studied (e–f).

B.3.3. PMT selection

The individual plots for all 25 PMTs studied in Sec. 5.3 are shown in Figs. B.16–B.17. The combination SN/26565 – 787 showed the strange behavior in Fig. B.18 and was sorted out.

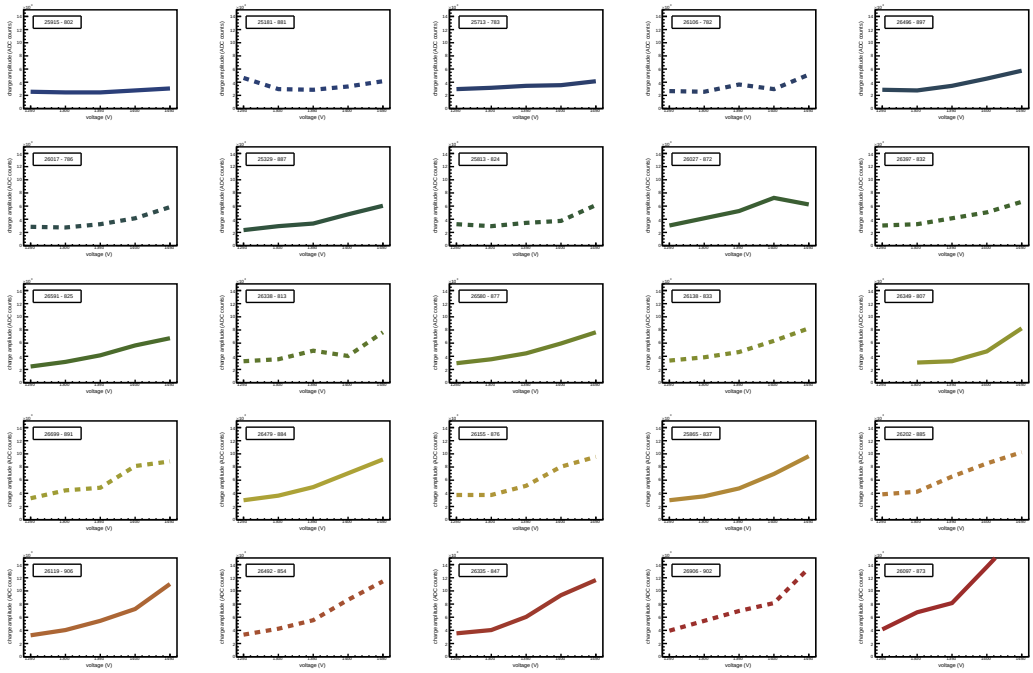

Figure B.16.: Charge amplitude of PMT dark counts as function of the supply voltages. The results for 25 PMTs are shown with the corresponding serial number of PMT and HV divider. For clarity reasons, the data points are linked.

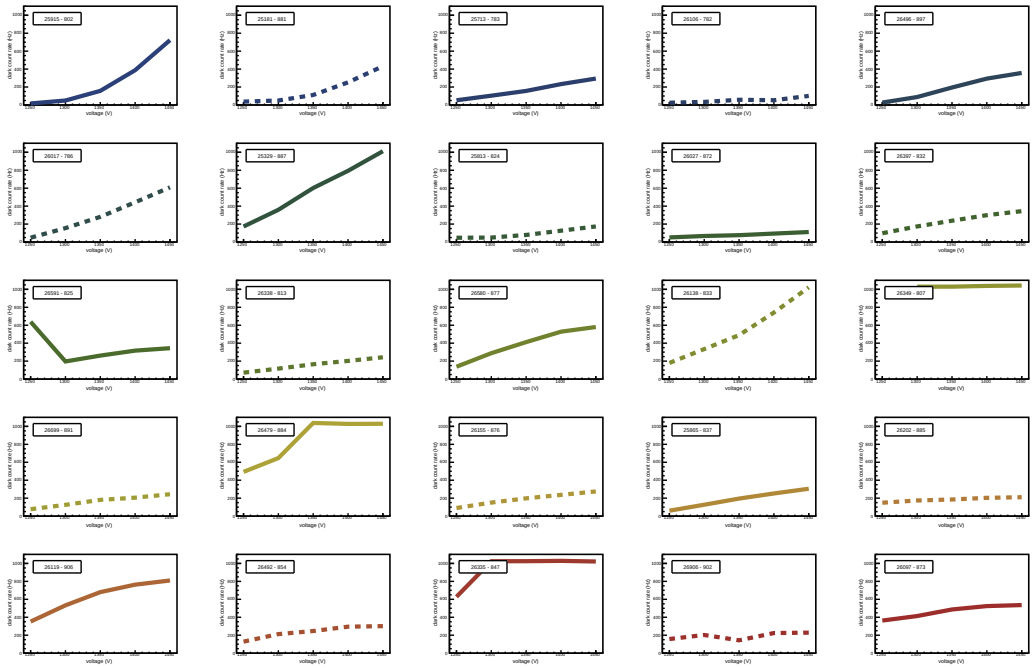

Figure B.17.: Dark count rate as function of the supply voltage. The results for 25 PMTs are shown with the corresponding serial number of PMT and HV divider. For clarity reasons, the data points are linked. Due to suboptimal settings, a limitation at about 1 kHz occurs.

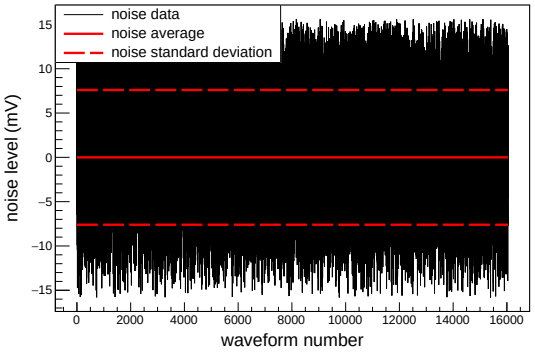

(a) Noise level at 1 250 V

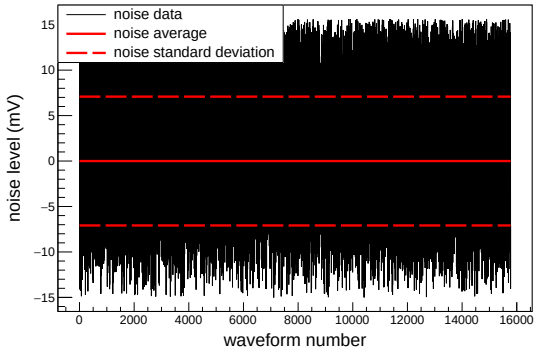

(b) Noise level at 1 450 V

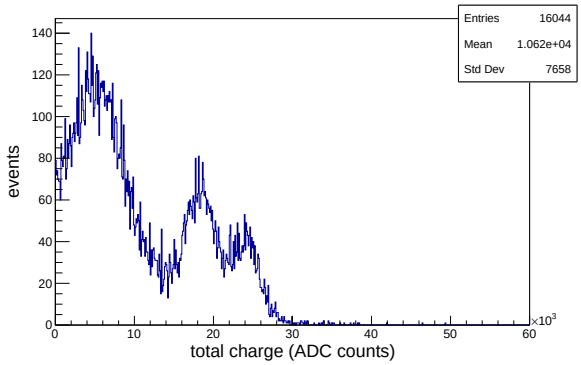

(c) Total charge spectrum at 1 250 V

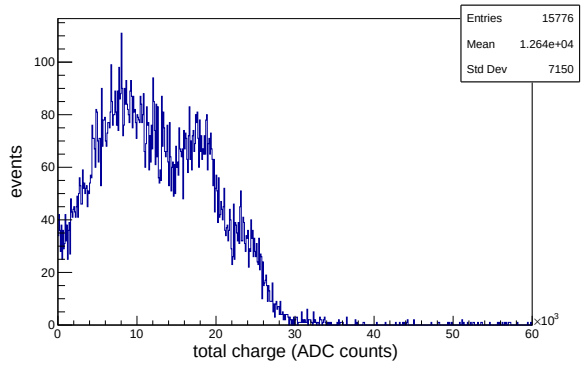

(d) Total charge spectrum at 1 450 V

Figure B.18.: A high noise level and several peaks in the total charge spectrum indicate a defect of PMT SN/26565 – 787.

B.3.4. Beam-time simulation settings

Not all necessary materials are already available in the `Geant4` material database. The code excerpt shows their implementation. Since in this study not only energy loss in matter but also light production is studied, a couple of materials must be given further properties, shown in Tab. B.1.

Code snippet of the material definitions relevant for the beam-time studies

```
void BDXConstruction::DefineMaterials() {
  G4NistManager* nist = G4NistManager::Instance();

  G4Material* air = nist->FindOrBuildMaterial("G4_AIR");
  G4Material* al = nist->FindOrBuildMaterial("G4_Al");
  G4Material* BGO = nist->FindOrBuildMaterial("G4_BGO");

  G4double z, a, fractionmass, density;
  G4String name, symbol;
  G4int ncomponents, natoms;

  a = 1.008*g/mole;
  G4Element* elH  = new G4Element(name="Hydrogen", symbol="H", z= 1., a);

  a = 10.81*g/mole;
  G4Element* elB  = new G4Element(name="Boron", symbol="B", z= 5., a);

  a=12.01*g/mole;
  G4Element* elC  = new G4Element(name="Carbon", symbol="C", z=6., a);

  a = 15.999*g/mole;
  G4Element* elO  = new G4Element(name="Oxygen", symbol="O", z= 8., a);

  a = 18.998403163*g/mole;
  G4Element* elF  = new G4Element(name="Fluorine", symbol="F", z= 9., a);

  a = 22.98976928*g/mole;
  G4Element* elNa  = new G4Element(name="Sodium", symbol="Na", z= 11., a);

  a = 26.9815385*g/mole;
  G4Element* elAl  = new G4Element(name="Aluminum", symbol="Al", z= 13., a);

  a = 28.0855*g/mole;
  G4Element* elSi  = new G4Element(name="Silicon", symbol="Si", z= 14., a);

  a = 39.0983*g/mole;
  G4Element* elK  = new G4Element(name="Potassium", symbol="K", z= 19., a);

  a = 47.867*g/mole;
  G4Element* elTi  = new G4Element(name="Titanium", symbol="Ti", z= 22., a);

  a = 74.921595*g/mole;
  G4Element* elAs  = new G4Element(name="Arsenic", symbol="As", z= 33., a);
```

```
a = 207.2*g/mole;
G4Element* elPb  = new G4Element(name="Lead", symbol="Pb", z= 82., a);

// Creating K2O
density = 2.35*g/cm3;
G4Material* K2O = new G4Material(name="K2O", density, ncomponents=2);
K2O->AddElement(elK, natoms=2);
K2O->AddElement(elO, natoms=1);

// Creating Na2O
density = 2.27*g/cm3;
G4Material* Na2O = new G4Material(name="Na2O", density, ncomponents=2);
Na2O->AddElement(elNa, natoms=2);
Na2O->AddElement(elO, natoms=1);

// Creating PbO
density = 9.53*g/cm3;
G4Material* PbO = new G4Material(name="PbO", density, ncomponents=2);
PbO->AddElement(elPb, natoms=1);
PbO->AddElement(elO, natoms=1);

// Creating SiO2
density = 2.2*g/cm3;
G4Material* SiO2 = new G4Material(name="SiO2", density, ncomponents=2);
SiO2->AddElement(elSi, natoms=1);
SiO2->AddElement(elO, natoms=2);

// Creating PbF2
density = 7.77*g/cm3;
G4Material* PbF2 = new G4Material(name="PbF2", density, ncomponents=2);
PbF2->AddElement(elPb, natoms=1);
PbF2->AddElement(elF, natoms=2);

// Creating Schott SF5
density = 4.07*g/cm3;
G4Material* SF5 = new G4Material(name="SF5", density, ncomponents=4);
SF5->AddMaterial(PbO, fractionmass=51*perCent);
SF5->AddMaterial(SiO2, fractionmass=46.3130*perCent);
SF5->AddElement(elTi, fractionmass=2.0239*perCent);
SF5->AddElement(elAs, fractionmass=0.6631*perCent);

// Creating Schott SF57HTU
density = 5.51*g/cm3;
G4Material* SchottSF57HTU = new G4Material(name="SF57HTU", density,
    ncomponents=4);
SchottSF57HTU->AddMaterial(PbO, fractionmass=74.0*perCent);
SchottSF57HTU->AddMaterial(SiO2, fractionmass=24.0*perCent);
SchottSF57HTU->AddMaterial(Na2O, fractionmass=1.0*perCent);
SchottSF57HTU->AddMaterial(K2O, fractionmass=1.0*perCent);
```

```
    // Creating Schott SF6 (simplified)
    density = 5.18*g/cm3;
    G4Material* SF6_simplified = new G4Material(name="SF6_simplified", density,
        ncomponents=2);
    SF6_simplified->AddMaterial(PbO, fractionmass=68.7*perCent);
    SF6_simplified->AddMaterial(SiO2, fractionmass=31.3*perCent);

    // Creating Polystyrene
    density = 1.06*g/cm3;
    G4Material* Polystyrene = new G4Material(name="Polystyrene", density,
        ncomponents=2);
    Polystyrene->AddElement(elC, natoms=8);
    Polystyrene->AddElement(elH, natoms=8);

    // Creating PMT window (Borosilicate)
    density= 2.23*g/cm3;
    G4Material* Borosilicate = new G4Material(name="Borosilicate", density,
        ncomponents=6);
    Borosilicate->AddElement(elB, fractionmass=0.040064);
    Borosilicate->AddElement(elO, fractionmass=0.539562);
    Borosilicate->AddElement(elNa, fractionmass=0.028191);
    Borosilicate->AddElement(elAl, fractionmass=0.011644);
    Borosilicate->AddElement(elSi, fractionmass=0.377220);
    Borosilicate->AddElement(elK, fractionmass=0.003321);
}
```

Material properties relevant for the beam-time studies

Depending on the optical photons energy (respectively the optical photons wavelength) the properties from Tab. 5.5 are set for the various materials. The values used in the simulation are tabulated for wavelengths between 250 nm and 2 500 nm in steps of 5 nm. A reduced list is attached in Tab. B.1. Independent from the wavelength, for BGO the `FASTTIMECONSTANT` is 300 ns and the `SCINTILLATIONYIELD` is 8 000 MeV^{-1}.

wavelength (nm)	energy (eV)	RINDEX	REFLECTIVITY	RINDEX	ABSLENGTH (mm)	QE	RINDEX	ABSLENGTH (mm)	RINDEX	ABSLENGTH (mm)	FASTCOMPONENT	RINDEX	ABSLENGTH (mm)	RINDEX	ABSLENGTH (mm)	RINDEX	ABSLENGTH (mm)
		air	Al foil	borosilicate			PbF_2		BGO			SF6		SF5		SF57HTU	
2500	0.50	1.000273	0.98	1.49	24	0.000	1.73	0	2.03	0	0.000	1.75	0	1.63	60	1.79	0
2400	0.52	1.000273	0.98	1.49	35	0.000	1.73	0	2.03	0	0.000	1.75	0	1.63	73	1.79	0
2300	0.54	1.000273	0.98	1.49	50	0.000	1.73	0	2.04	0	0.000	1.75	123	1.63	94	1.79	164
2200	0.56	1.000273	0.98	1.49	79	0.000	1.73	0	2.04	0	0.000	1.75	189	1.63	138	1.79	264
2100	0.59	1.000273	0.98	1.49	107	0.000	1.73	0	2.04	0	0.000	1.76	256	1.64	181	1.79	365
2000	0.62	1.000273	0.98	1.49	135	0.000	1.73	0	2.04	0	0.000	1.76	322	1.64	225	1.79	466
1900	0.65	1.000273	0.98	1.50	465	0.000	1.73	0	2.04	0	0.000	1.76	708	1.64	511	1.80	1142
1800	0.69	1.000273	0.98	1.50	925	0.000	1.73	0	2.04	0	0.000	1.76	1230	1.64	900	1.80	2063
1700	0.73	1.000273	0.97	1.50	1385	0.000	1.73	0	2.04	0	0.000	1.76	1752	1.64	1290	1.80	2984
1600	0.77	1.000273	0.97	1.50	1844	0.000	1.73	0	2.04	0	0.000	1.76	2274	1.64	1679	1.80	3905
1500	0.83	1.000273	0.97	1.50	2607	0.000	1.73	0	2.04	0	0.000	1.76	3375	1.64	2181	1.80	5167
1400	0.89	1.000273	0.97	1.50	4079	0.000	1.73	0	2.04	0	0.000	1.77	5855	1.65	2946	1.80	7240
1300	0.95	1.000274	0.96	1.50	5550	0.000	1.74	0	2.05	0	0.000	1.77	8335	1.65	3711	1.81	9312
1200	1.03	1.000274	0.95	1.50	7021	0.000	1.74	0	2.05	0	0.000	1.77	10814	1.65	4476	1.81	11384
1100	1.13	1.000274	0.95	1.51	8493	0.000	1.74	0	2.05	0	0.000	1.77	13294	1.65	5242	1.81	13457
1000	1.24	1.000274	0.93	1.51	8492	0.000	1.74	0	2.06	0	0.000	1.78	13187	1.65	5548	1.81	13757
900	1.38	1.000275	0.89	1.51	7511	0.000	1.74	0	2.06	0	0.000	1.78	11355	1.66	5548	1.82	12875
800	1.55	1.000275	0.87	1.51	6529	0.000	1.75	2880	2.07	3969	0.000	1.78	9524	1.66	5548	1.82	11993
780	1.59	1.000275	0.88	1.51	6333	0.004	1.75	2703	2.07	3970	0.000	1.79	9157	1.66	5548	1.82	11817
760	1.63	1.000275	0.88	1.51	6137	0.008	1.75	2526	2.08	3972	0.000	1.79	8791	1.66	5548	1.83	11640
740	1.68	1.000275	0.88	1.51	5940	0.012	1.75	2349	2.08	3974	0.000	1.79	8425	1.66	5548	1.83	11464
720	1.72	1.000276	0.89	1.51	5744	0.016	1.75	2172	2.08	3976	0.000	1.79	8059	1.66	5548	1.83	11287
700	1.77	1.000276	0.89	1.51	5548	0.021	1.76	1995	2.08	3977	0.000	1.79	7513	1.66	5548	1.83	10899
680	1.82	1.000276	0.90	1.51	5042	0.025	1.76	1818	2.09	3979	0.000	1.79	6593	1.66	5402	1.83	10072
660	1.88	1.000276	0.90	1.51	4536	0.029	1.76	1641	2.09	3981	0.000	1.80	5674	1.67	5256	1.84	9244
640	1.94	1.000276	0.90	1.51	4536	0.033	1.76	1464	2.10	3983	0.000	1.80	5226	1.67	5120	1.84	9091
620	2.00	1.000277	0.90	1.52	4536	0.037	1.76	1287	2.10	3984	0.000	1.80	5733	1.67	4991	1.84	9091
600	2.07	1.000277	0.91	1.52	4764	0.041	1.76	1110	2.11	3986	0.000	1.80	6602	1.67	5262	1.84	9091
580	2.14	1.000277	0.91	1.52	4991	0.064	1.77	1107	2.11	3883	0.026	1.81	6884	1.67	5548	1.85	9091
560	2.21	1.000278	0.91	1.52	5318	0.087	1.77	1104	2.12	3779	0.052	1.81	6104	1.68	5548	1.85	9091
540	2.30	1.000278	0.91	1.52	5416	0.109	1.77	1101	2.12	3676	0.078	1.81	5210	1.68	5273	1.86	8372
520	2.38	1.000278	0.91	1.52	4976	0.132	1.78	1098	2.13	3572	0.104	1.82	4058	1.68	4356	1.86	6015
500	2.48	1.000279	0.91	1.52	4536	0.155	1.78	1095	2.14	3469	0.130	1.82	2906	1.68	3440	1.87	3658
480	2.58	1.000280	0.92	1.52	3988	0.178	1.79	1092	2.15	3000	0.478	1.83	1875	1.69	2556	1.87	1809
460	2.69	1.000280	0.92	1.52	3440	0.201	1.79	1089	2.17	2532	0.826	1.84	1272	1.69	2032	1.88	1284
440	2.82	1.000281	0.92	1.53	3254	0.223	1.80	1086	2.18	2119	0.812	1.85	670	1.70	1505	1.89	760
420	2.95	1.000282	0.92	1.53	3440	0.246	1.81	1083	2.20	1759	0.436	1.86	339	1.70	909	1.90	402
400	3.10	1.000283	0.92	1.53	3217	0.269	1.82	1080	2.22	1400	0.060	1.87	126	1.71	491	1.92	144
380	3.26	1.000284	0.92	1.53	1441	0.266	1.83	1084	2.24	1080	0.040	1.88	58	1.72	195	1.93	64
360	3.44	1.000285	0.92	1.54	659	0.263	1.85	1088	2.27	619	0.020	1.90	0	1.73	60	1.96	0
340	3.65	1.000287	0.92	1.54	175	0.260	1.86	927	2.31	248	0.005	1.93	0	1.75	13	1.99	0
320	3.87	1.000289	0.92	1.55	38	0.257	1.89	602	2.36	86	0.000	1.97	0	1.77	0	2.03	0
300	4.13	1.000292	0.92	1.55	8	0.254	1.94	276	2.43	13	0.000	2.02	0	1.80	0	2.10	0
280	4.43	1.000295	0.92	1.56	3	0.169	1.97	146	2.52	1	0.000	2.12	0	1.85	0	2.23	0
260	4.77	1.000299	0.92	1.57	3	0.072	2.00	34	2.65	0	0.000	2.37	0	1.94	0	2.61	0

Table B.1.: Shortened list of wavelength dependent values used for the beam-time simulation studies of the optical photon processing. A full list in steps of 5 nm is used in the simulation and whenever needed intermediate points are calculated with a simple line method.

B.3.5. Additional MAMI beam-time results

Further results of the material studies, in particular simulated hitmaps can be found in the following Figs. B.19–B.27. Tab. B.2 summarizes important beam-time parameters dependent on the crystal under study.

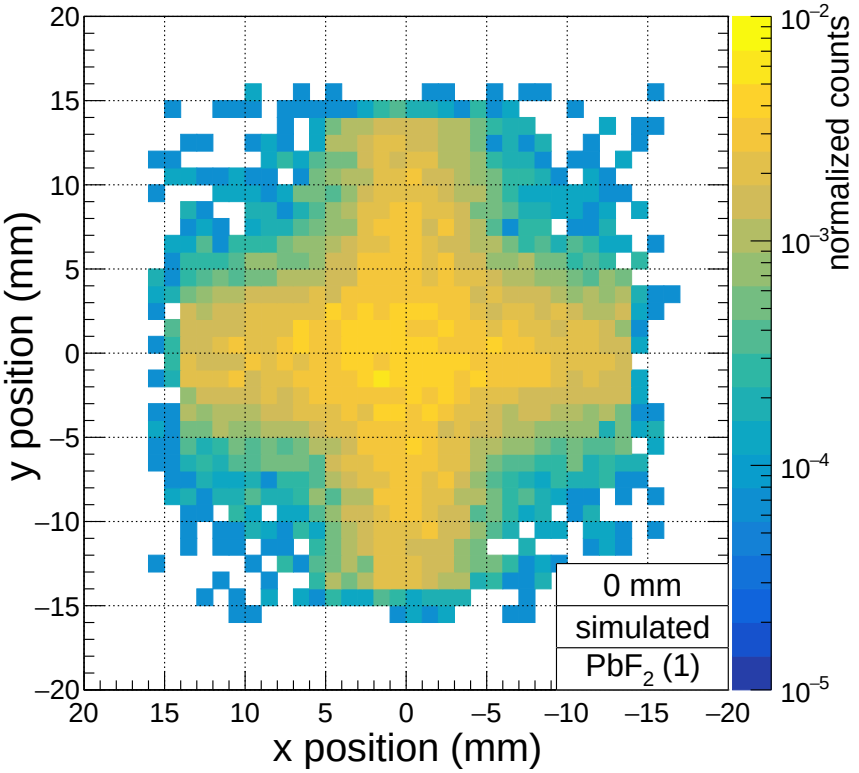

Figure B.19.: Hitmap of the simulated signals from the PbF_2 (7) detector for a 14-MeV electron beam entering the front face of the radiator. The trigger was used in an OR logic with a 3 × 3 ROI.

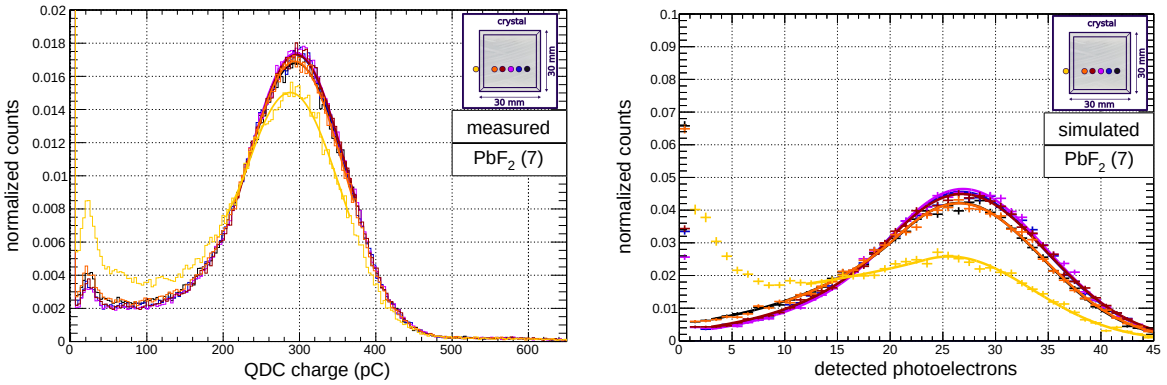

(a) **(b)**

Figure B.20.: Measured (left) and simulated (right) signals from a PbF_2 detector for a 14-MeV electron beam entering the front face of the radiator at different positions with respect to the center as indicated in the insert. The FWHM of the beam was $\varnothing_B \approx 28\,mm$, reduced to $\varnothing_B \approx 19\,mm$ with the trigger condition of the fiber detector. The signal peaks were fitted with the Crystal Ball function.

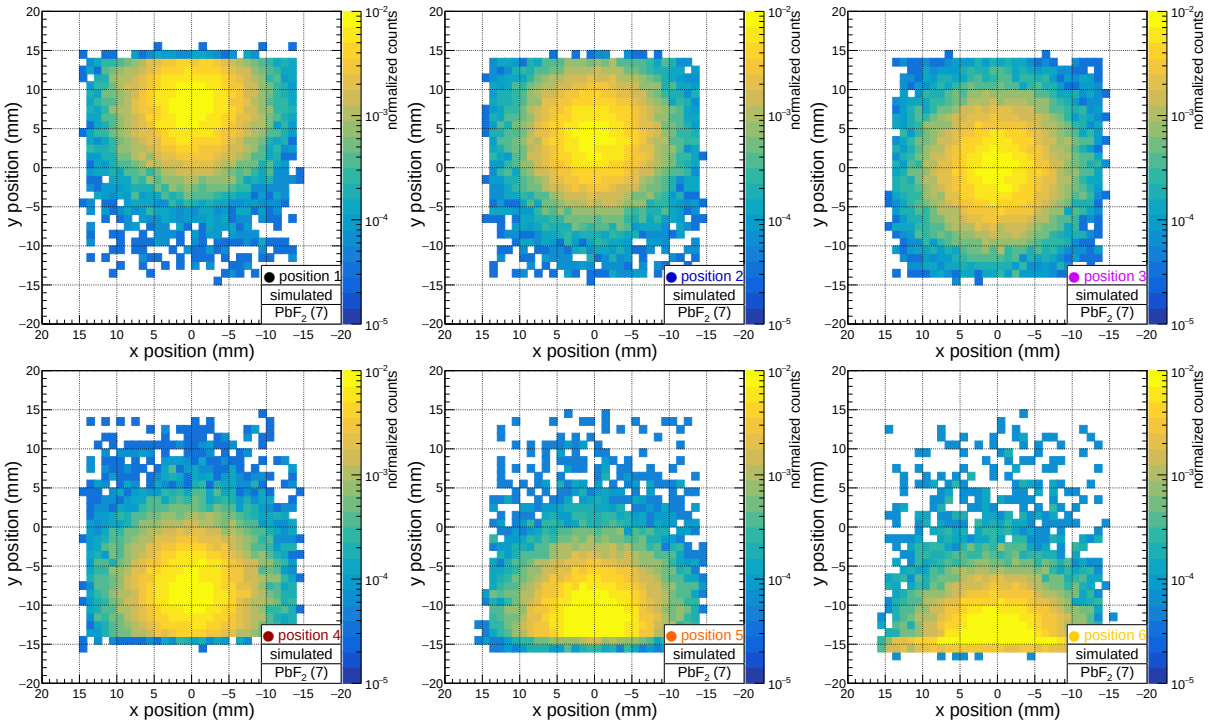

Figure B.21.: Hitmaps of the simulated signals from the PbF_2 (7) detector for a 14-MeV electron beam entering the front face of the radiator at the positions measured during the corner scan.

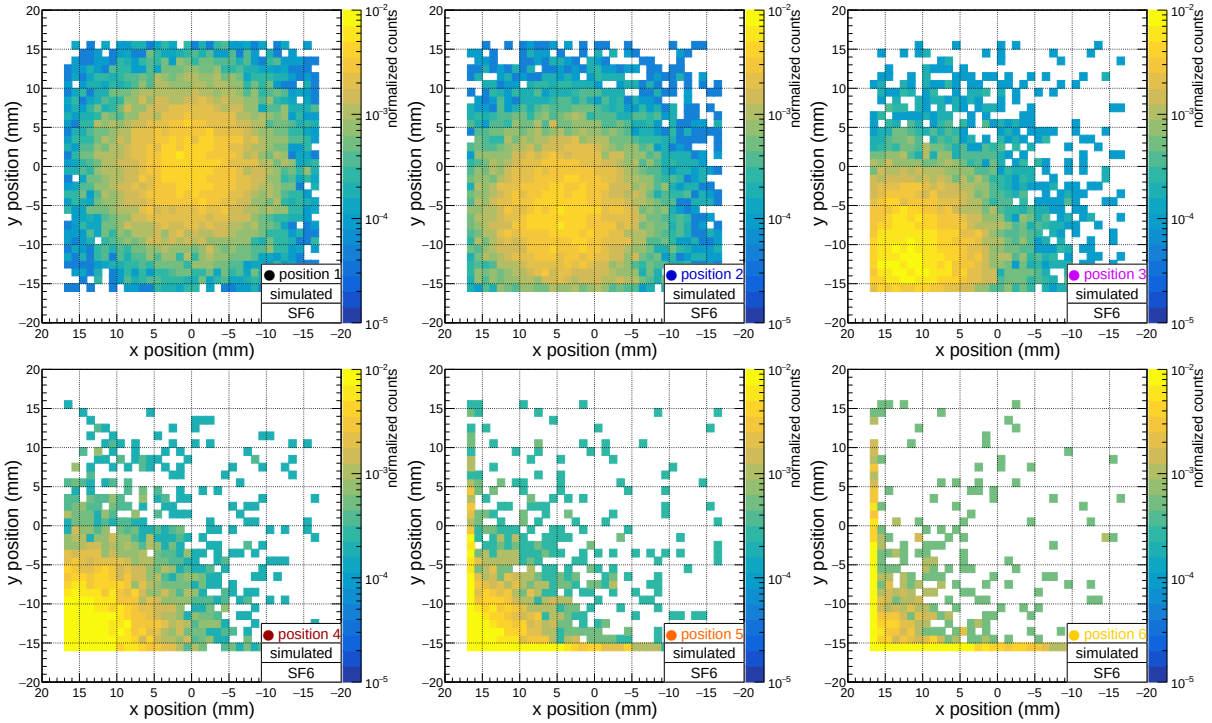

Figure B.22.: Hitmaps of the simulated signals from the Schott SF6 detector for a 14-MeV electron beam entering the front face of the radiator at the positions measured during the corner scan.

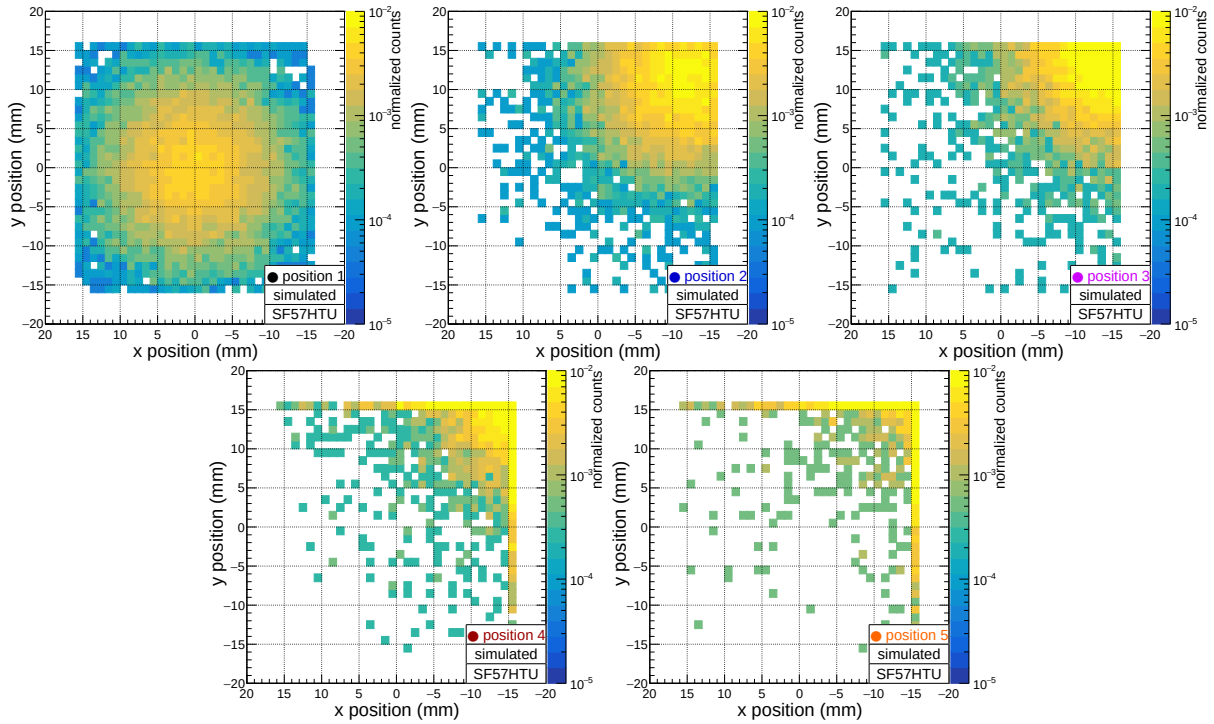

Figure B.23.: Hitmaps of the simulated signals from the Schott SF57HTU detector for a 14-MeV electron beam entering the front face of the radiator at the positions measured during the corner scan.

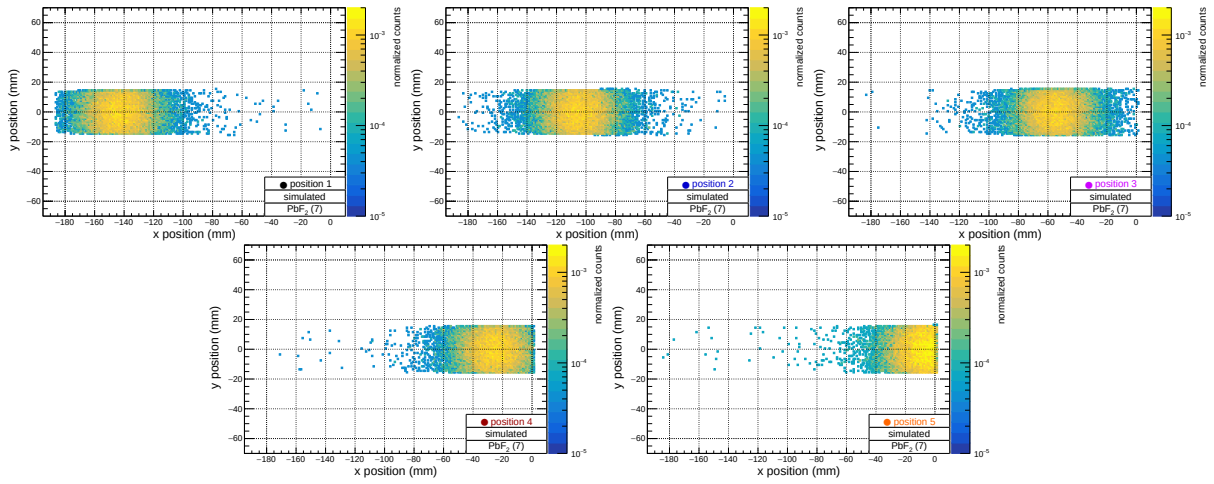

Figure B.24.: Hitmaps of the simulated signals from the PbF_2 (7) detector for a 14-MeV electron beam entering the side face of the radiator at the positions measured during the 90° scan.

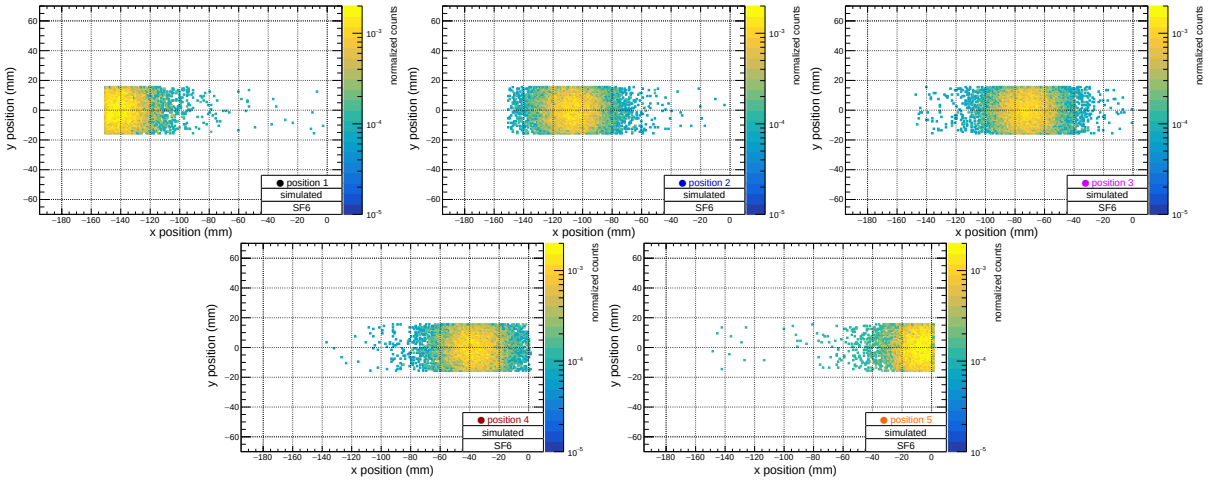

Figure B.25.: Hitmaps of the simulated signals from the Schott SF6 detector for a 14-MeV electron beam entering the side face of the radiator at the positions measured during the 90° scan.

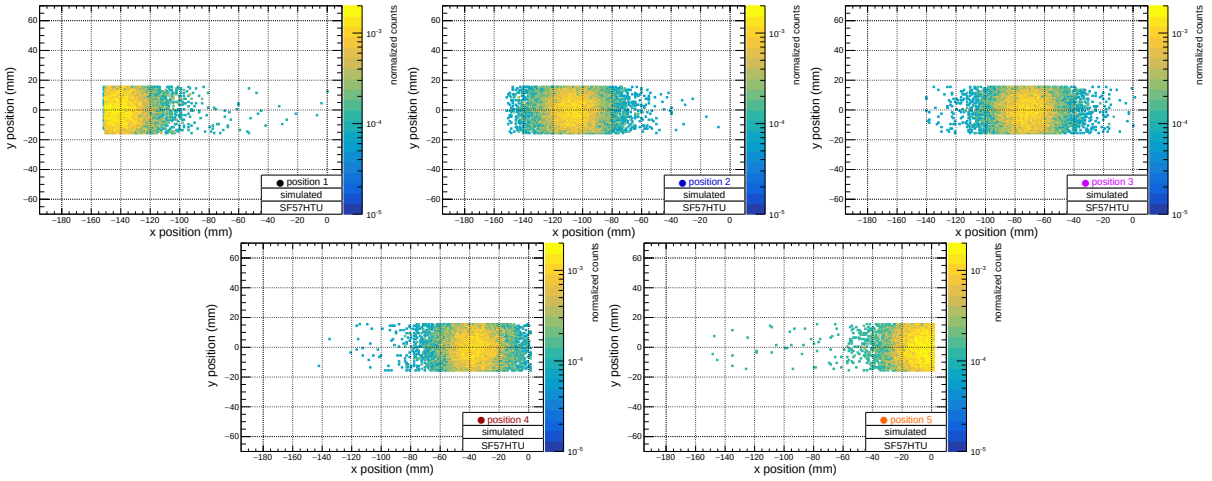

Figure B.26.: Hitmaps of the simulated signals from the Schott SF57HTU detector for a 14-MeV electron beam entering the side face of the radiator at the positions measured during the 90° scan.

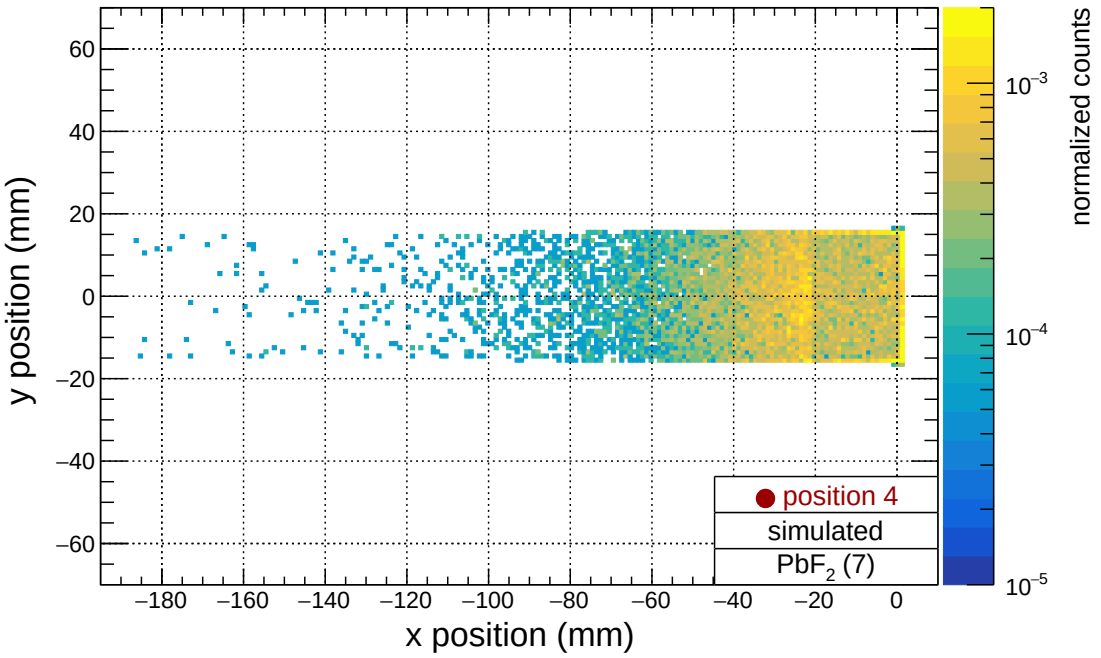

Figure B.27.: Hitmap of the simulated signals from the PbF_2 (7) detector for a 14-MeV electron beam entering the side face of the radiator with an angle of 135° at a position next to the PMT. A part of the beam-spot is shadowed by a MayTec® bar next to the setup.

	ROI	**logic**	**angle** (°)	$d_{\text{Fla-Fib}}$ (mm)	$d_{\text{Fib-Cry}}$ (mm)	$(x_B \mid \varnothing_B)_{\text{orig}}$ (mm)	$x_B \mid \varnothing_B$ (mm)
BGO	5 × 5	AND	0	320	73	12.17 | 28.66	4.39 | 10.34
PbF_2 (7)	5 × 5	AND	0	320	72	12.14 | 28.59	4.47 | 10.53
PbF_2 (7)	3 × 3	OR	0	320	72	12.14 | 28.59	7.87 | 18.53
PbF_2 (7)	5 × 5	AND	90	320	265	16.57 | 39.02	15.70 | 36.97
PbF_2 (1)	3 × 3	OR	0	320	76	12.26 | 28.87	8.27 | 19.47
SF5	16 × 16	AND	0	270	115	11.92 | 28.07	8.56 | 20.16
SF5	3 × 3	AND	0	270	115	11.92 | 28.07	6.41 | 15.09
SF5	1 × 1	AND	0	270	115	11.92 | 28.07	5.67 | 13.35
SF5	3 × 3	AND	90	270	245	17.50 | 41.21	14.28 | 33.63
SF6	3 × 3	AND	0	270	115	11.92 | 28.07	6.46 | 15.21
SF6	3 × 3	AND	90	270	245	17.50 | 41.21	14.19 | 33.41
SF57HTU	3 × 3	AND	0	270	115	11.92 | 28.07	6.40 | 15.07
SF57HTU	3 × 3	AND	90	270	245	17.50 | 41.21	14.48 | 34.10

Table B.2.: Overview of flange to fiber-detector ($d_{\text{Fla-Fib}}$) and fiber-detector to crystal ($d_{\text{Fib-Cry}}$) distances, full MAMI beam-spot sizes at the detector locations ($(x_B \mid \varnothing_B)_{\text{orig}}$), and the beam-spot sizes resulting from the trigger logic ($x_B \mid \varnothing_B$). x_B are the beam-spot widths and $\varnothing_B$ the FWHMs.

B.3.6. Calculation of detected photoelectrons (d_{pe}) and light yield (ν_{yield})

	E_B (MeV)	E_{QDC} (pC)	d_{pe} (p.e.)	ν_{yield} (p.e. MeV^{-1})
PbF_2 (7)	14.42(1)	395.0(3)	27.3(19)	1.89(13)
PbF_2 (7)	12.57(1)	340.9(8)	23.1(17)	1.84(13)
PbF_2 (7)	10.69(1)	296.1(2)	19.6(15)	1.83(14)
PbF_2 (7)	9.24(1)	266.0(3)	17.3(14)	1.87(15)
PbF_2 (1)	14.42(1)	431.1(3)	30.1(20)	2.09(14)
PbF_2 (1)	12.57(1)	357.7(10)	24.4(17)	1.94(14)
PbF_2 (1)	10.69(1)	323.8(2)	21.8(16)	2.03(15)
PbF_2 (1)	9.24(1)	291.5(3)	19.2(15)	2.08(16)
SF5	14.20(1)	308.7(2)	20.6(16)	1.45(11)
SF5	12.44(1)	288.8(3)	19.0(15)	1.53(12)
SF5	10.62(1)	264.0(5)	17.1(14)	1.61(13)
SF5	8.64(1)	226.2(4)	14.2(13)	1.64(15)
SF6	14.20(1)	261.4(2)	16.9(14)	1.19(10)
SF6	12.44(1)	241.4(3)	15.4(13)	1.23(11)
SF6	10.62(1)	213.4(6)	13.2(13)	1.24(12)
SF6	8.64(1)	184.4(5)	10.9(12)	1.26(14)
SF57HTU	14.20(1)	238.6(3)	15.1(13)	1.07(09)
SF57HTU	12.44(1)	197.7(4)	12.0(12)	0.96(10)
SF57HTU	10.62(1)	165.3(7)	9.4(12)	0.89(11)

Table B.3.: Number of detected photoelectrons (d_{pe}) and light yield (ν_{yield}) calculated with the calibration from Fig. 5.41, the simulated electron beam energy (E_B), and the measured QDC charge (E_{QDC}).

For the calculation of the values in Tab. B.3 the following formulas were used. E_B and E_{QDC} are the values from the Crystal Ball fits to the simulated beam energies and measured QDC spectra in Sec. 5.5.8. The errors were calculated with

$$\Delta E_B = \frac{\sigma_B}{\sqrt{N_B}} \qquad \text{and} \qquad \Delta E_{QDC} = \frac{\sigma_{QDC}}{\sqrt{N_{QDC}}} \quad . \tag{B.1}$$

In this error calculation, N_{QDC} is not the total number of entries in the measured spectrum, but the number of entries in the range used for the Crystal Ball fit. For the conversion of QDC charge to number of detected photoelectrons, the fit parameters $p_0 = 43.44(1310)$ and $p_1 = 12.89(74)$

from the calibration in Fig. 5.41 were used.

$$d_{\mathrm{pe}} = \frac{E_{QDC} - p_0}{p_1} \qquad \text{and} \qquad \Delta d_{\mathrm{pe}} = \sqrt{\left(\frac{\Delta E_{QDC}}{p_1}\right)^2 + \left(-\frac{\Delta p_0}{p_1}\right)^2 + \left(-\frac{E_{QDC} - p_0}{p_1^2}\Delta p_1\right)^2} \quad . \tag{B.2}$$

The light yield ν_{yield} in photoelectrons per MeV energy deposit is

$$\nu_{\mathrm{yield}} = \frac{d_{\mathrm{pe}}}{E_B} \qquad \text{and} \qquad \Delta\nu_{\mathrm{yield}} = \sqrt{\left(\frac{\Delta d_{\mathrm{pe}}}{E_B}\right)^2 + \left(-\frac{d_{pe}}{E_B^2}\Delta E_B\right)^2} \quad . \tag{B.3}$$

In Tab. 5.8 the average light yield of n values was calculated with

$$\overline{\nu_{\mathrm{yield}}} = \frac{1}{n}\left(\nu_1 + \cdots + \nu_n\right) \qquad \text{and} \qquad \Delta\overline{\nu_{\mathrm{yield}}} = \sqrt{\left(\frac{\Delta\nu_1}{n}\right)^2 + \cdots + \left(\frac{\Delta\nu_n}{n}\right)^2} \quad . \tag{B.4}$$

B.4. DarkMESA optimization studies

Optimization studies on the production side of the DarkMESA experiment include a tungsten target and additional results are shown in Fig. B.28.

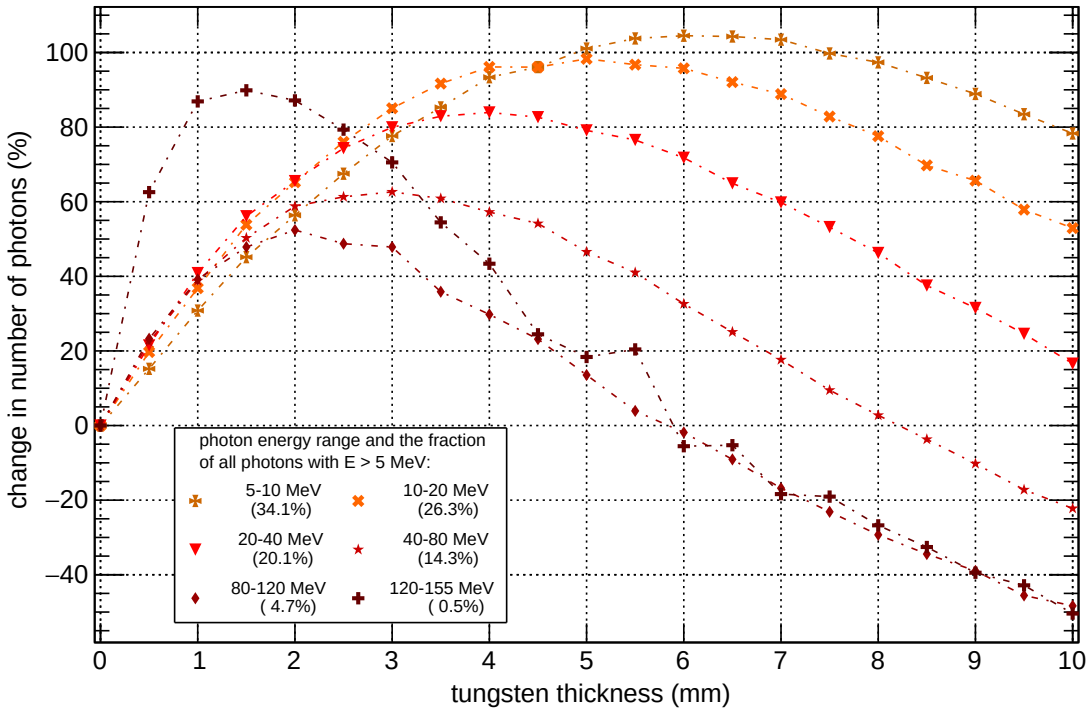

Figure B.28.: Total number of generated photons for an up to 10 mm thick additional tungsten target, where the case without target is the reference. The energy ranges are smaller than in Fig. 6.1 and with increasing energy the graphs maximum moves to the left. One must also note that the proportion of the energy range falls from almost 35 % at 5-10 MeV to less than 1 % at 120-155 MeV. Thus, to maximize photon counts for energies below 80 MeV, the choice of a 2-3 mm thick target is optimal. If it later turns out that a lower energy range is preferable in the search for DM, the thickness of the target can be adjusted accordingly.

B.5. DarkMESA background studies

Additional results of the study of beam-related and beam-unrelated background radiation are shown in Secs. B.5.1–B.5.3. Supplements to the Phase A and B veto studies are presented in Secs. B.5.4–B.5.5.

B.5.1. Neutrino study

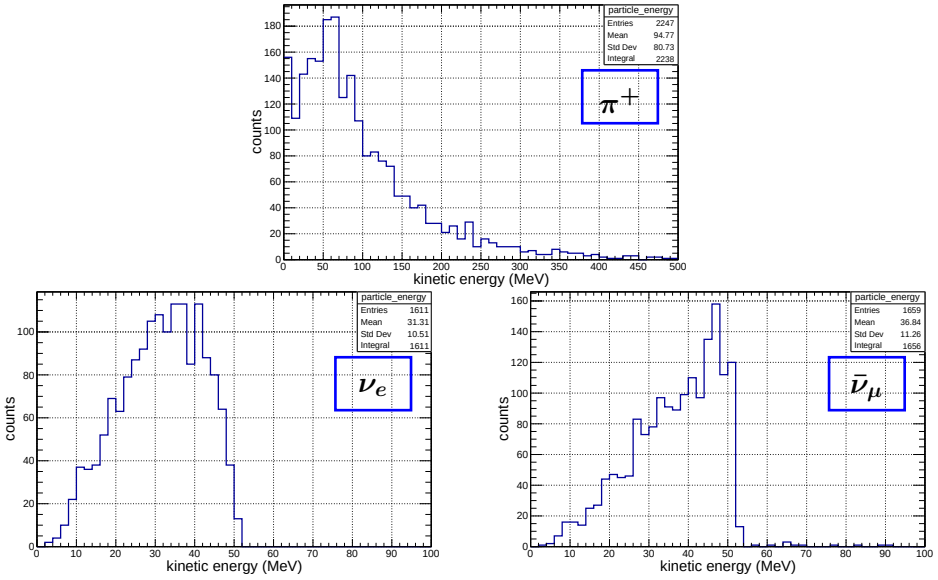

Figure B.29.: `Geant4` pion decay functionality check for a 1 GeV electron beam. Energy distribution of π^+ particles (top) and the subordinate decay products ν_e and $\bar{\nu}_\mu$ (bottom).

B.5.2. Cosmogenic background study

	full rate ($s^{-1}\,m^{-2}$)		above 10 MeV rate ($s^{-1}\,m^{-2}$)	
particle	**sea level**	**under ground**	**sea level**	**under ground**
$\mu^{+/-}$	114.925	101.665	114.903	101.665
e^+	11.057	2.101	8.627	1.811
e^-	18.500	18.048	11.309	9.054
γ	164.743	153.796	68.076	23.187
n	30.187	7.092	19.936	4.035
p	2.020	0.362	2.004	0.361
$\bar{p}$	0.001	2.7×10^{-4}	0.001	2.7×10^{-4}
$\pi^{+/-/0}$	0.027	0.119	0.027	0.119
$K^{+/-/0}$	–	0.004	–	0.004
ν	–	12.154	–	11.888

Table B.4.: Particle rates obtained from a CRY and `Geant4` simulation for Mainz at sea level and under ground in the DarkMESA room. The values were calculated for the full energy spectra on the left and a detection threshold of 10 MeV on the right. $K^{+/-/0}$ and ν considered as secondary particles only.

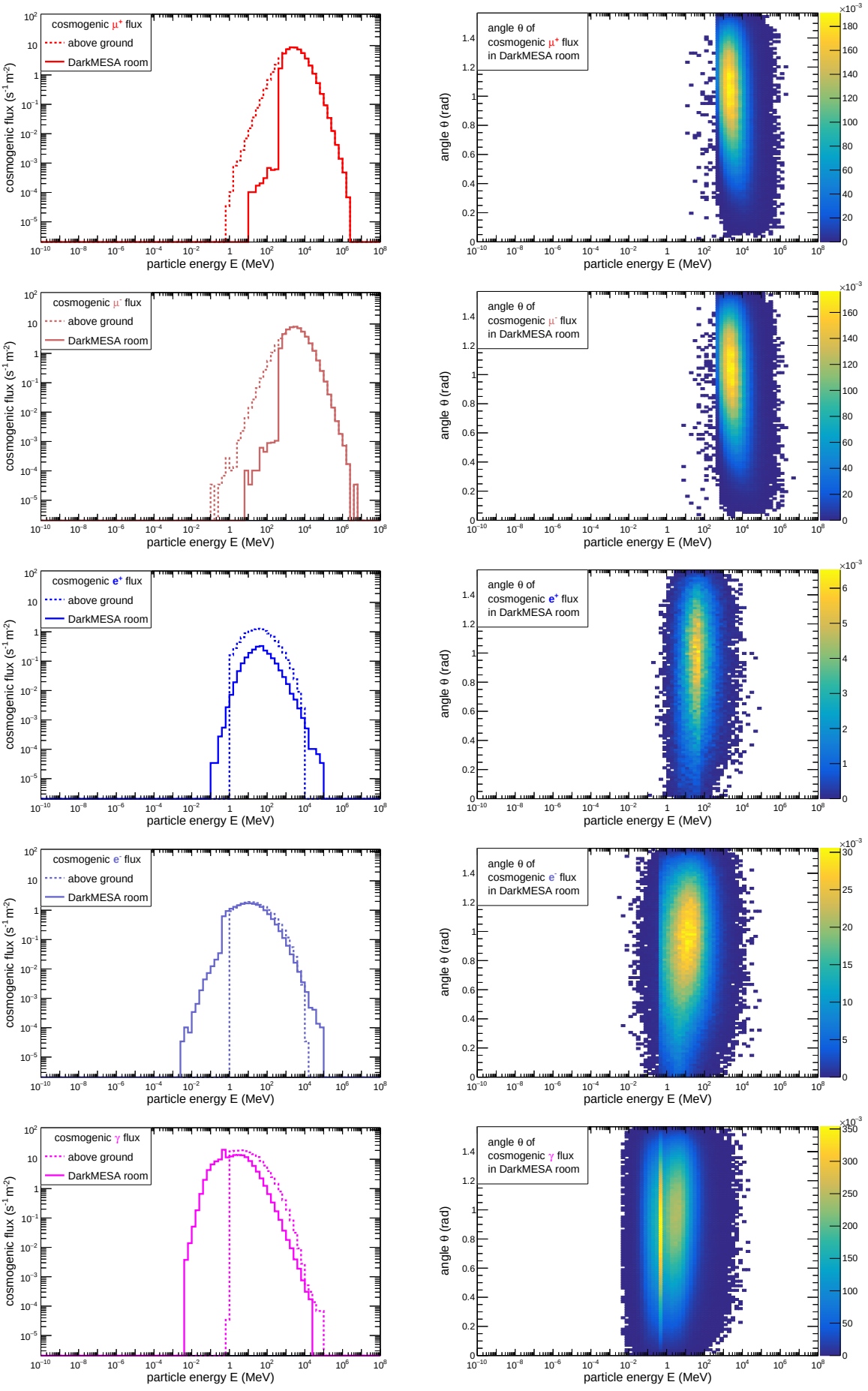
cosmogenic μ⁺ flux
above ground
DarkMESA room
cosmogenic flux (s⁻¹ m⁻²)
particle energy E (MeV)
angle θ of
cosmogenic μ⁺ flux
in DarkMESA room
angle θ (rad)
cosmogenic μ⁻ flux
angle θ of
cosmogenic μ⁻ flux
cosmogenic e⁺ flux
angle θ of
cosmogenic e⁺ flux
cosmogenic e⁻ flux
angle θ of
cosmogenic e⁻ flux
cosmogenic γ flux
angle θ of
cosmogenic γ flux

Figure B.30.

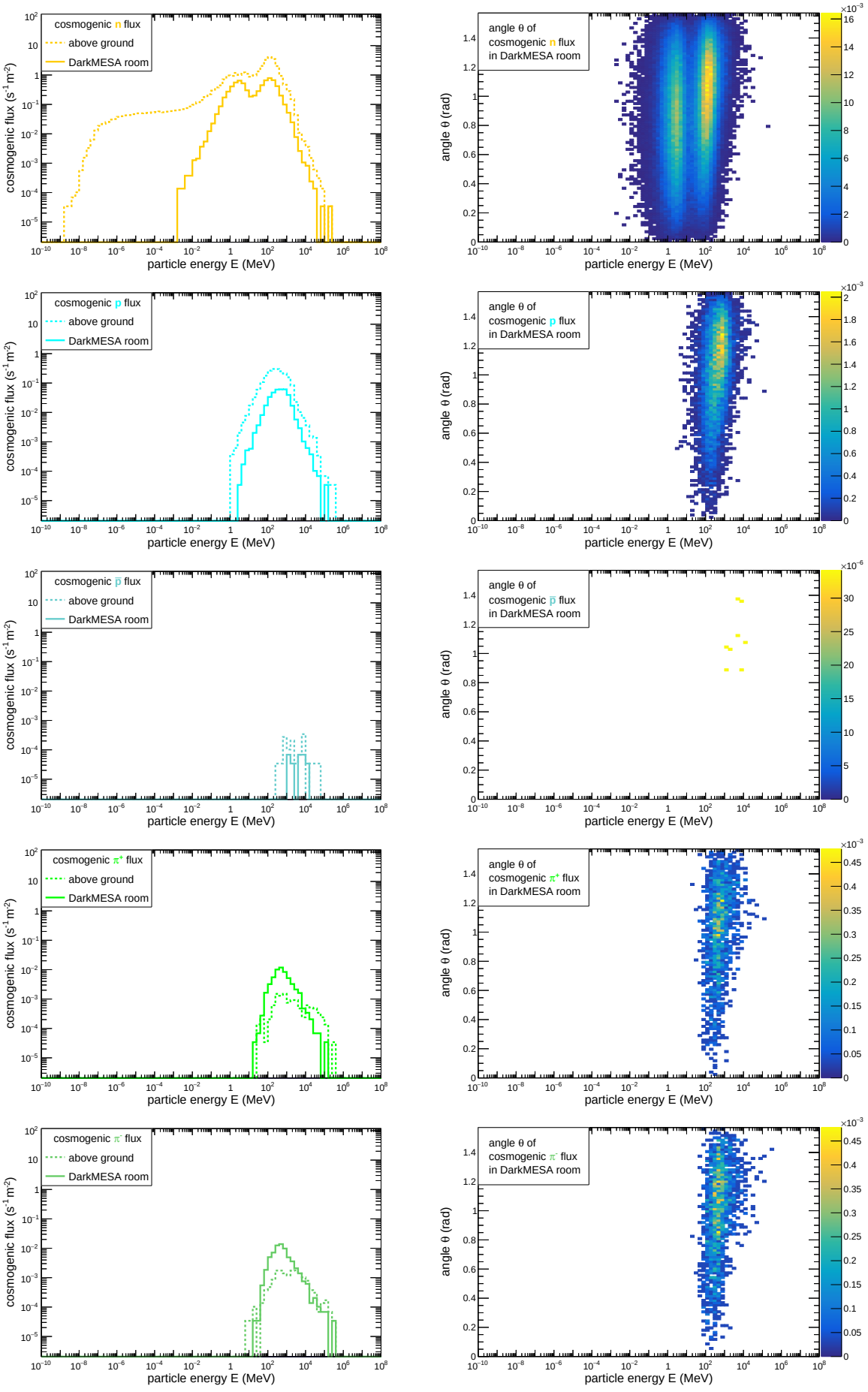

Figure B.30.: (continued)

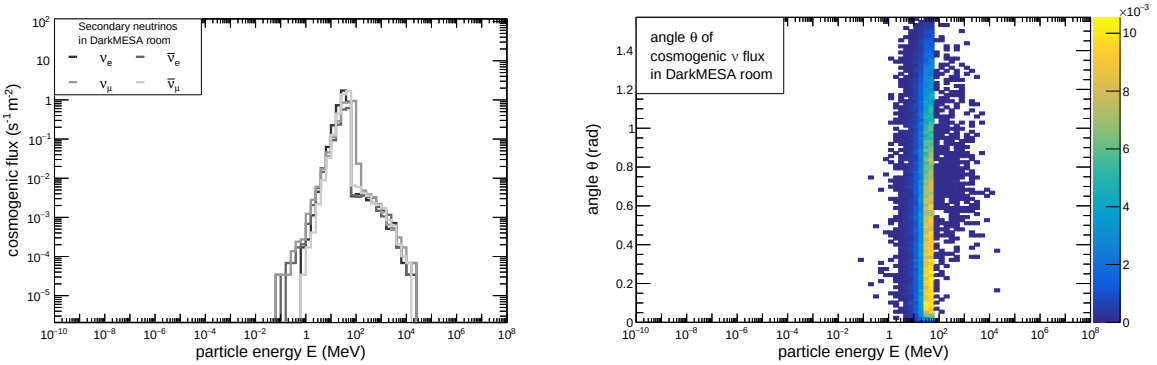

Figure B.30.: (continued) Left: Shown are the energy distributions sorted by the cosmogenic particle type. The doted lines mark the distributions for the sea level of Mainz at the 1st June of 2020. The solid line shows the expected distribution in the DarkMESA room, where the building above was taken into account. A 1 m layer of concrete was used to simulate these building parts in a simplified way. In the case of the neutrinos only the distributions for the DarkMESA room are shown. Right: The angular distribution as a function of the particle's energy in the DarkMESA room is shown.

B.5.3. Sensitivity study of proposed materials

EJ-200	**primary particle energy (MeV)**							
	10^{-3}	10^{-1}	1	10^{1}	10^{2}	10^{3}	10^{5}	10^{7}
μ^+				99.999	100.000	100.000	100.000	100.000
μ^-				99.999	100.000	100.000	100.000	100.000
e^+		99.867	99.972	99.993	99.998	100.000	100.000	
e^-	< 0.000	99.877	100.000	100.000	100.000	100.000	100.000	
γ	< 0.000	18.840	13.132	4.164	2.870	3.344	3.456	
n	3.071	78.948	49.742	18.827	5.143	3.782	3.527	
p			100.000	100.000	100.000	100.000	100.000	
$\bar{p}$						100.000	100.000	
π^+				100.000	100.000	100.000	100.000	
π^-				100.000	99.999	100.000	100.000	
π^0				5.444	7.311	7.532	7.841	
K^+			98.035	99.475	99.917	100.000	100.000	
K^-			98.060	99.474	99.922	99.999	100.000	
K^0_L			6.163	2.441	1.377	2.109	1.966	
K^0_S			66.891	72.915	63.749	25.836	2.471	
ν		< 0.000	< 0.000	< 0.000	< 0.000	< 0.000	< 0.000	

Table B.5.: Simulated sensitivity of EJ-200 plastic scintillator for all particle types and energies awaited in the DarkMESA room. Uncommon energies ($< 10^{-5}$ particles $s^{-1}\,m^{-2}$) were excluded, and a detection limit of 100 optical photons produced in the material was set to allow the comparison of results with SF5 PbGl and PbF_2 in Tab. B.6.

SF5	**primary particle energy (MeV)**							
	10^{-3}	10^{-1}	1	10^{1}	10^{2}	10^{3}	10^{5}	10^{7}
μ^+				99.910	100.000	100.000	100.000	100.000
μ^-				64.753	100.000	100.000	100.000	100.000
e^+		<0.000	73.758	99.761	99.971	99.996	100.000	
e^-	<0.000	<0.000	67.955	99.943	99.998	100.000	100.000	
γ	<0.000	<0.000	5.330	24.381	35.447	42.592	43.787	
n	0.132	0.191	0.005	3.555	2.420	5.291	6.118	
p			<0.000	0.662	3.316	99.964	100.000	
$\bar{p}$						99.984	100.000	
π^+				99.821	99.558	99.974	100.000	
π^-				49.592	99.512	99.973	100.000	
π^0				48.686	60.911	65.562	68.382	
K^+			65.328	95.302	1.099	99.966	100.000	
K^-			79.182	89.550	9.519	99.964	100.000	
K^0_L			7.646	3.909	2.663	4.957	5.069	
K^0_S			84.069	92.180	81.426	33.764	5.742	
ν		<0.000	<0.000	<0.000	<0.000	<0.000	<0.000	

PbF_2	**primary particle energy (MeV)**							
	10^{-3}	10^{-1}	1	10^{1}	10^{2}	10^{3}	10^{5}	10^{7}
μ^+				99.794	100.000	100.000	100.000	100.000
μ^-				76.890	100.000	100.000	100.000	100.000
e^+		<0.000	38.579	99.697	99.982	99.998	100.000	
e^-	<0.000	<0.000	11.863	99.850	99.994	99.999	100.000	
γ	<0.000	<0.000	0.913	49.640	70.108	78.692	79.894	
n	0.003	0.303	0.008	4.958	5.756	8.578	8.886	
p			<0.000	0.684	5.994	99.979	100.000	
$\bar{p}$						99.995	100.000	
π^+				99.754	99.589	99.979	100.000	
π^-				78.004	99.506	99.978	100.000	
π^0				82.013	90.195	94.646	95.850	
K^+			68.430	91.642	6.631	99.971	100.000	
K^-			92.228	96.721	16.487	99.977	100.000	
K^0_L			9.311	5.882	4.959	8.854	8.729	
K^0_S			92.091	98.412	86.786	39.306	9.545	
ν		<0.000	<0.000	<0.000	<0.000	<0.000	<0.000	

Table B.6.: Simulated sensitivity of SF5 PbGl (top) and PbF_2 (bottom) for all particle types and energies awaited in the DarkMESA room. Uncommon energies ($<10^{-5}$ particles $s^{-1}\,m^{-2}$) were excluded, and a detection limit of 100 optical photons produced in the material was set to allow the comparison of results with EJ-200 plastic scintillator in Tab. B.5.

B.5.4. Supplement to the Phase A prototype studies

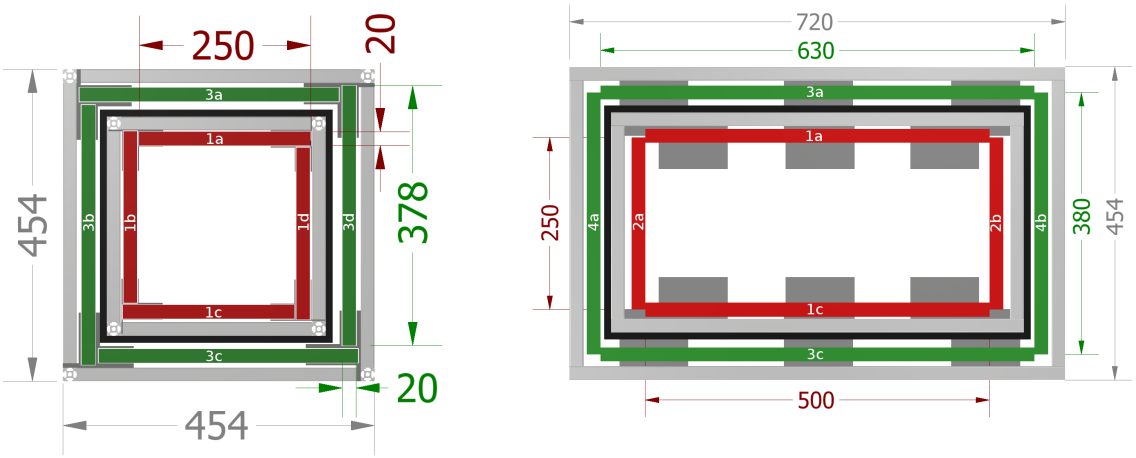

Figure B.31.: Front view (left) and side view (right) of the veto prototype concept. Shown are the outer veto (green), the inner veto (red), the lead absorber (black), and the mounting made of aluminum profiles and angles (grey). Each veto layer has a label for identification and the dimensions are in mm.

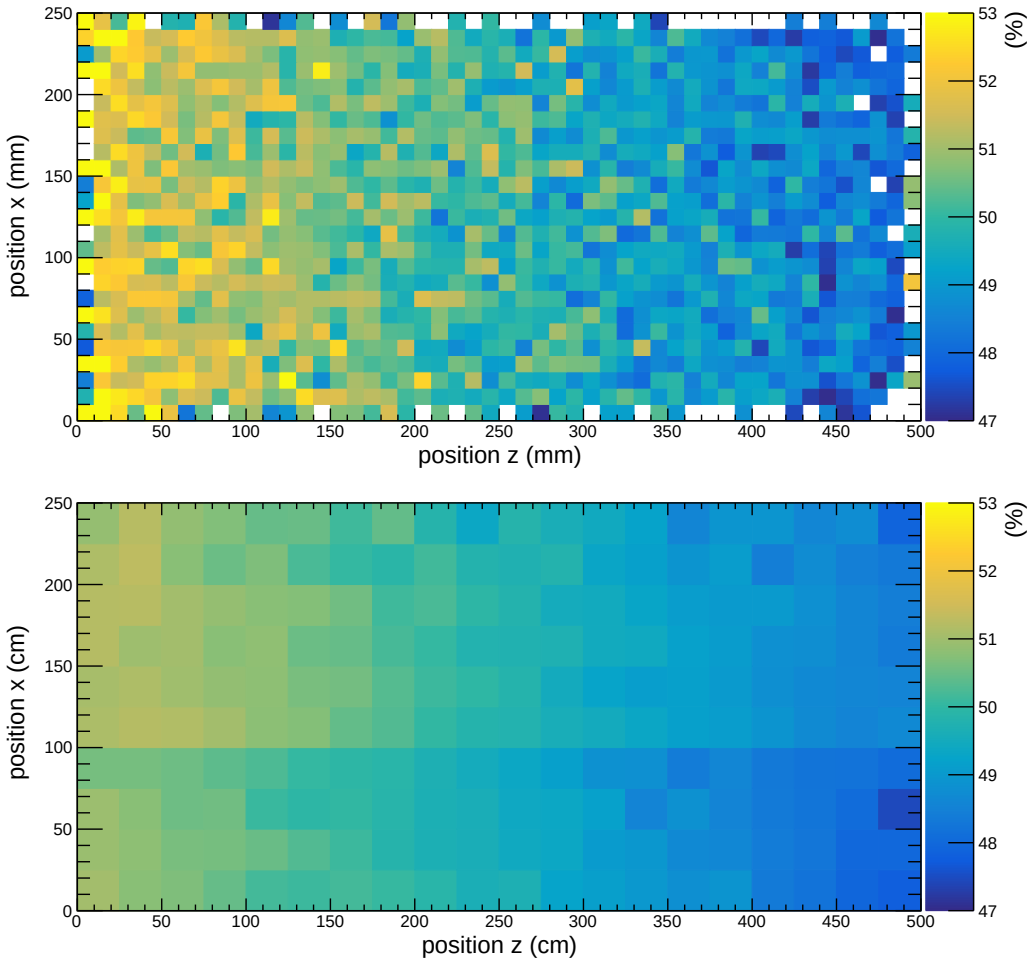

Figure B.32.: Percentage ratio on the total yield in simulation (top) and experiment (bottom) for a readout of the nine SiPMs on the left side.

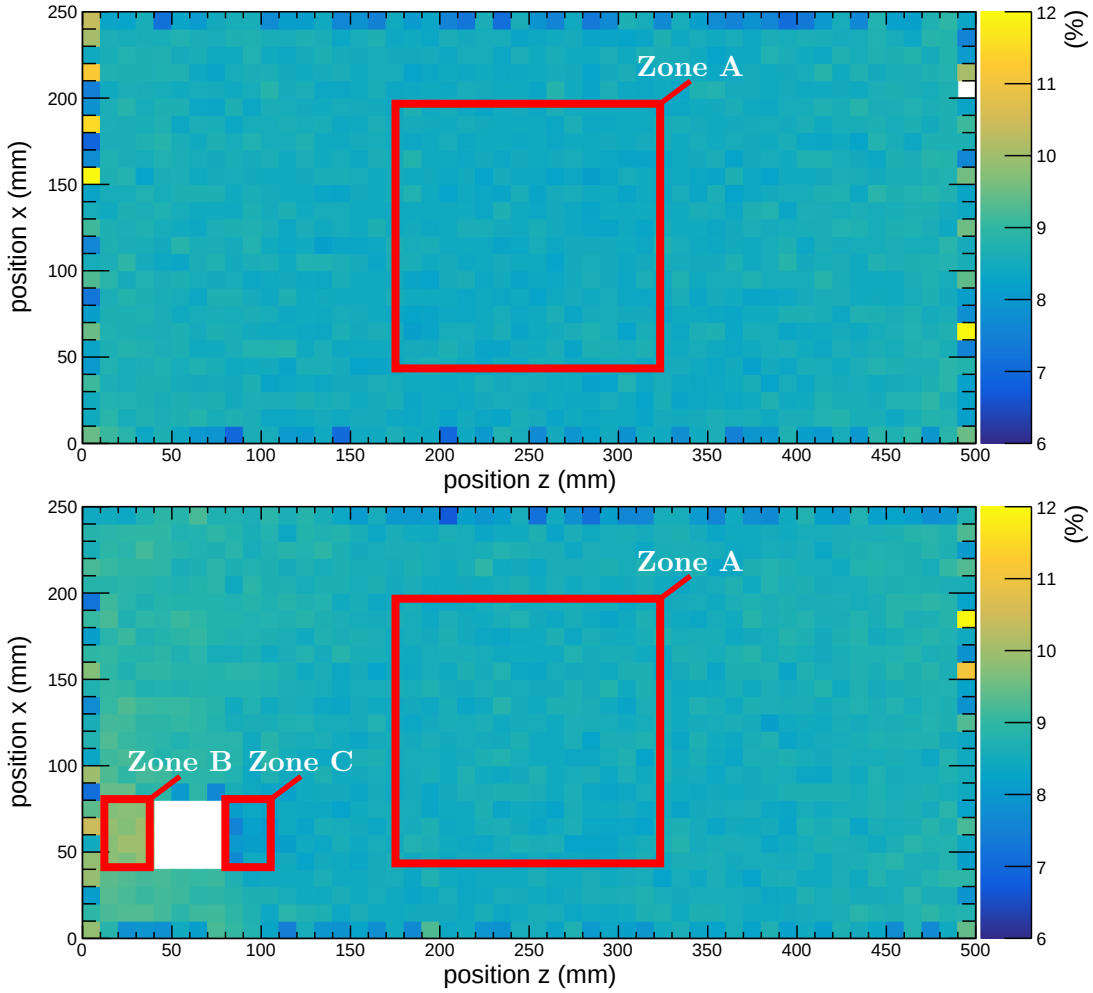

Figure B.33.: For a 500 mm long scintillator panel without cable entry (top) or with 16 cm^2 quadratic cable entry (bottom), the optical photons detected in total by all SiPMs in relation to all generated optical photons, depending on the primary particle position, is shown. With exception of the edge areas, a homogeneous distribution can be found and the average value in Zone A is ∼8.5 % for both cases. Including the cable entry the value increases to ∼9.8 % in Zone B and decreases to ∼8.1 % in Zone C. For hits in Zone B, the reflections at the cable entry lead to a higher light output of the SiPMs next to it, while the opposite SiPMs are partially shadowed. Zone C, in turn, is shaded from the left side and due to the longer path of light to the right side, an overall loss is observed.

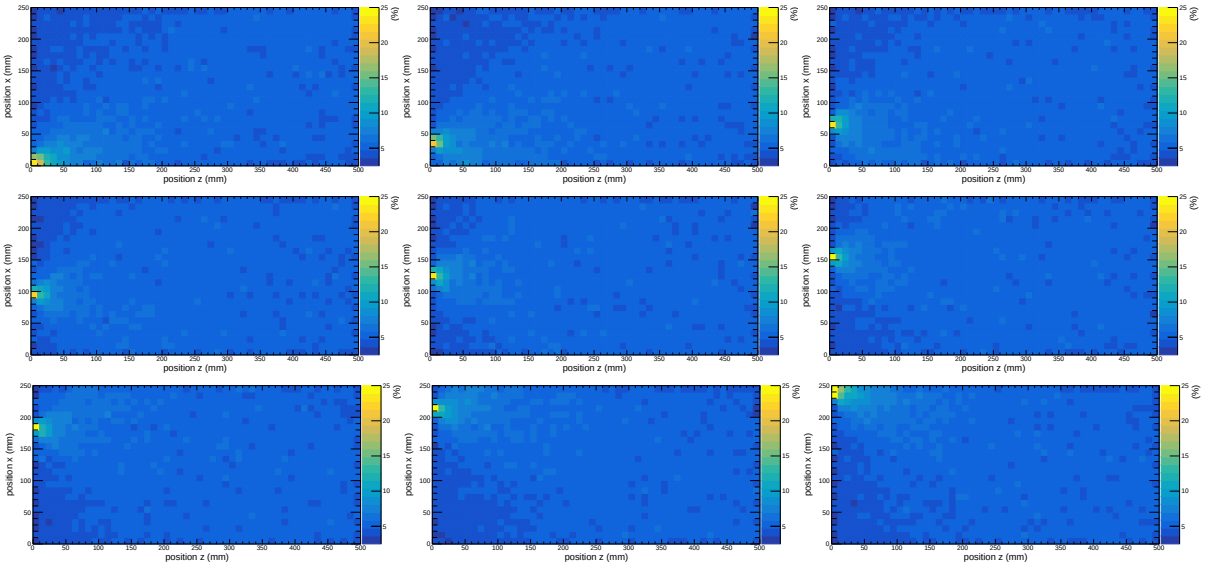

Figure B.34.: Optical photons detected by SiPM L1 (top left) to L9 (bottom right) in relation to all detected optical photons, depending on the primary particle position.

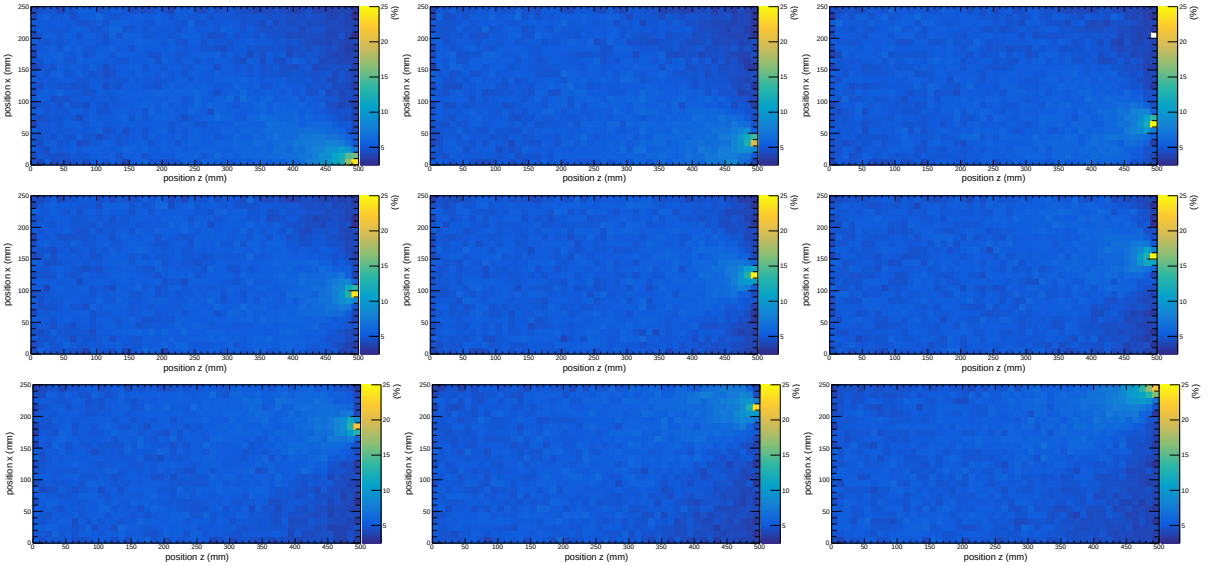

Figure B.35.: Optical photons detected by SiPM R1 (top left) to R9 (bottom right) in relation to all detected optical photons, depending on the primary particle position.

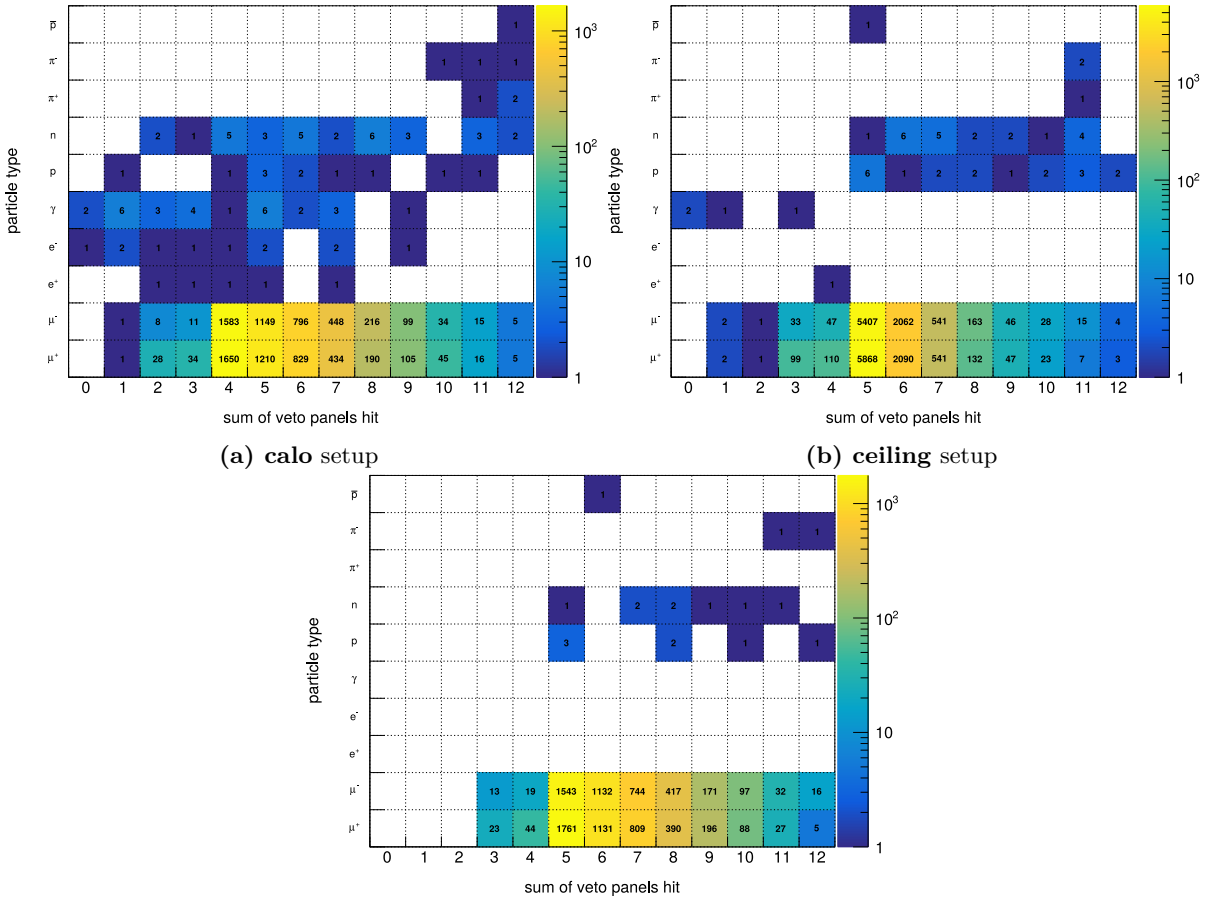

(a) calo setup

(b) ceiling setup

(c) both setup

Figure B.36.: Sum of the signal-giving veto panels separated by the primary particle type for the improved Phase A veto concepts – **calo** setup (a), **ceiling** setup (b), and **both** setup (c).

B.5.5. Supplement to the Phase B studies

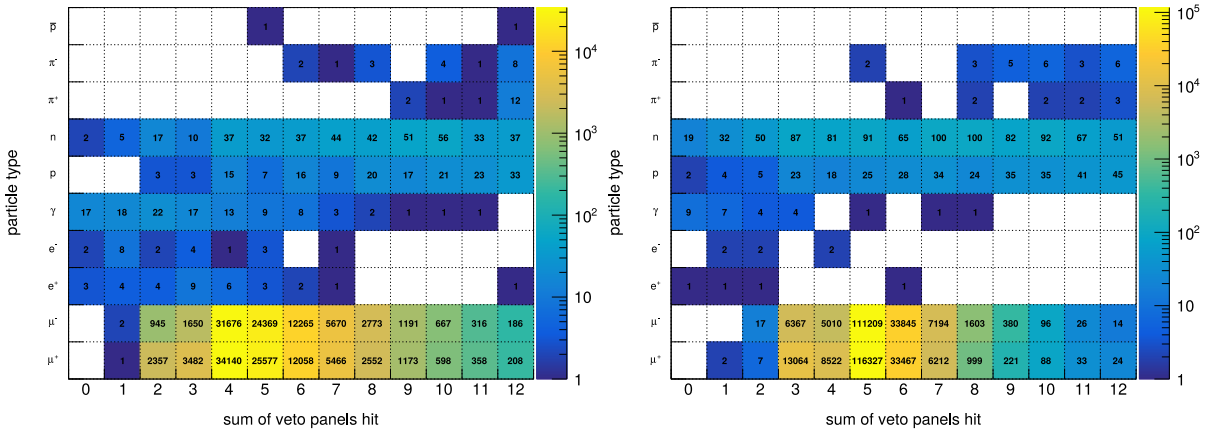

Figure B.37.: Sum of the signal-giving veto panels separated by the primary particle type for the improved Phase B veto concepts – **calo** setup (left) and **ceiling** setup (right).

B.6. DarkMESA parameterization study

For having some estimations regarding the expected reach of proposed setups without a full simulation, the following parameterization study was performed.

In order to evaluate the effects on the expected reach when changing a variable by a factor x, the scaling factor β is introduced. The value of the resulting thermal target variable y' is $\beta \cdot y$, with y being the original value. When changing $\alpha_{\mathrm{D}} \to \alpha'_{\mathrm{D}} = x \cdot \alpha_{\mathrm{D}}$, y trivially changes by the factor $\beta = x$. A change in the number of detected DM particles N_χ is also changing the scaled ε_L value. With the substitutions $N_\chi \to N'_\chi = x \cdot N_\chi$ and $\varepsilon_{\mathrm{L}} \to \varepsilon'_{\mathrm{L}}$ follows from Eq. 8.24:

$$N_{\mathrm{scaled}} = N_\chi \cdot \left(\frac{\sqrt[4]{x}\varepsilon'_{\mathrm{L}}}{\varepsilon} \right)^4 \quad , \tag{B.5}$$

and it follows

$$\varepsilon'_{\mathrm{L}} = \frac{1}{\sqrt[4]{x}} \cdot \varepsilon_{\mathrm{L}} \quad . \tag{B.6}$$

For the new y' value follows:

$$y' = \beta \cdot y \quad \text{with the scaling factor} \quad \beta = \frac{1}{\sqrt{x}} \quad . \tag{B.7}$$

To estimate the new y value due to a change in measurement time or detector material this scaling factor $\beta = 1/\sqrt{x}$ can be used. A change in detector volume or electron recoil threshold is accompanied by a change in σ_{final} and has to be computed by the simulation.

In the following considerations the PbF_2 calorimeter with 30 × 30 crystals of averaged size (PbF_2 (4)), a measurement time of 10 000 h, and an energy threshold of 14 MeV is the reference calorimeter and has the scaling factor $\beta = 1$. The detector efficiency was set to 95 % and $N_{\mathrm{scaled}} = 9$ which corresponds to a CL of ∼99.99 %.

B.6.1. Scheduled time and detector material

For a change in measurement time or detector material the scaling factor $\beta = 1/\sqrt{x}$ can be used. A time reduction to 25 % (2 500 h) hence means a worse y' value with $y' = 2 \cdot y$. For the detector material the scaling factors are shown together with material dependent values in Tab. B.7.

material	$(Z/A)_{\mathrm{det}}$	ρ_{det} (g cm^{-3})	N_{det}	scaling factor β
PbF_2	0.40784	7.77	19.08×10^{23}	1
BGO	0.42065	7.13	18.06×10^{23}	1.028
SF57	0.42101	5.51	13.97×10^{23}	1.169
SF57HTU	0.42101	5.51	13.97×10^{23}	1.169
SF6	0.42101	5.18	13.13×10^{23}	1.205
CsI	0.41570	4.51	11.29×10^{23}	1.300
SF5	0.42101	4.07	10.32×10^{23}	1.360
Polystyrene	0.53768	1.06	3.43×10^{23}	2.359
CS_2	0.49934	0.07*	0.21×10^{23}	9.532

Table B.7.: Scaling factor when changing the detector material. (*at 40 Torr)

B.6.2. Detector volume

To estimate the scaling factor β for a change of the detector volume, it becomes a little more complicated, since the detector volume only occurs indirectly in Eq. 8.23. A change in the detector volume is accompanied by a change in the detector acceptance and therefore a change in σ_{final}, which is computed by the simulation.
In order to obtain a scaling factor here, the y value was determined for a single detector type and a single kinematics, with different detector sizes. PbF_2 and the kinematics – $m_{\gamma'} = 3\,\text{MeV}$, $m_\chi = 1\,\text{MeV}$, $\alpha_D = 0.5$, $\varepsilon = 0.001$ – were selected. The size of the detector was increased according to the real conditions in the DarkMESA room and the detector center was placed close to the beam-axis. Boundary conditions such as crystal and module spacings were met. The volume was expanded evenly in the X and Y directions, but there was no increase along the beam-axis Z. The 30 × 30 detector serves as a reference again and the following values were obtained:

no. of crystals	V_{det} (L)	volume ratio	y	scaling factor β
50 × 50	326.98	2.778	5.07×10^{-13}	0.336
45 × 45	264.85	2.250	6.29×10^{-13}	0.417
40 × 40	209.27	1.778	7.90×10^{-13}	0.523
35 × 35	160.22	1.361	1.04×10^{-12}	0.689
30 × 30	117.71	1	1.51×10^{-12}	1
25 × 25	81.75	0.694	1.99×10^{-12}	1.318
20 × 20	52.32	0.444	3.02×10^{-12}	2
15 × 15	29.43	0.250	4.75×10^{-12}	3.146
10 × 10	13.08	0.111	1.06×10^{-11}	7.020
5 × 5	3.27	0.028	4.02×10^{-11}	26.623

Table B.8.: Scaling factor when changing the detector volume.

With a fit to these simulation results (Fig. B.38) a formula for the scaling factor β is received.

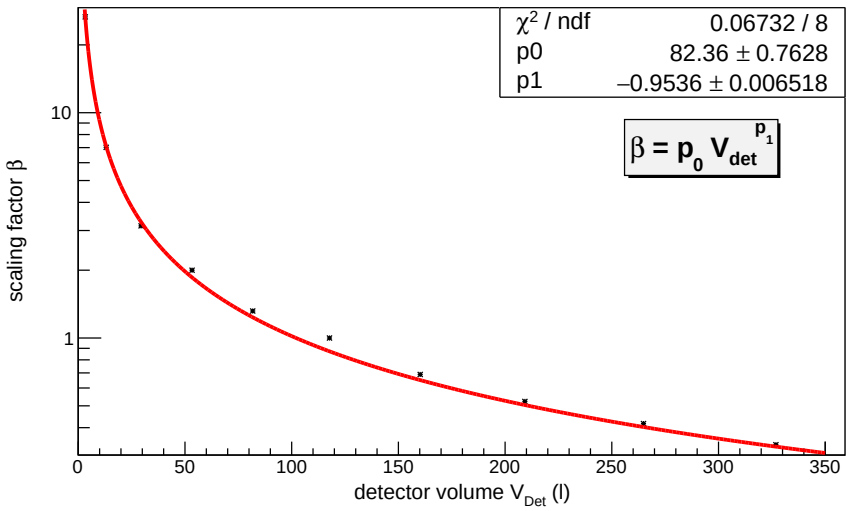

Figure B.38.: Simulated scaling factor β in dependence of the detector volume V_{det}. A fit in the form $\beta = p_0 {V_{\text{det}}}^{p_1}$ was performed.

The reference detector volume obtained from the fit $\beta = p_0 {V_{\text{det}}}^{p_1}$ is

$$V_{\text{det}}\left(\beta = 1\right) = p_0^{-1/p_1} \quad . \tag{B.8}$$

For the β calculation of a volume x times larger or smaller, it follows:

$$\beta = x^{-0.95} \quad . \tag{B.9}$$

B.6.3. Electron recoil threshold

In order to obtain a scaling factor for the electron recoil threshold, the same procedure was followed. Several simulations with different energy thresholds were performed for the 30 × 30 PbF_2 reference calorimeter. An energy threshold of 14 MeV was the reference in this case.

E_{thr} (MeV)	y	scaling factor β
0	5.19×10^{-13}	0.344
5	8.14×10^{-13}	0.539
10	1.18×10^{-12}	0.781
14	1.51×10^{-12}	1
20	2.19×10^{-12}	1.450
25	2.96×10^{-12}	1.960
30	3.97×10^{-12}	2.629
40	6.50×10^{-12}	4.305
50	1.06×10^{-11}	7.020
60	1.88×10^{-11}	12.450
70	3.19×10^{-11}	21.126
80	6.62×10^{-11}	43.841
90	1.64×10^{-10}	108.609
100	7.55×10^{-10}	500.000

Table B.9.: Scaling factor when changing the electron recoil threshold.

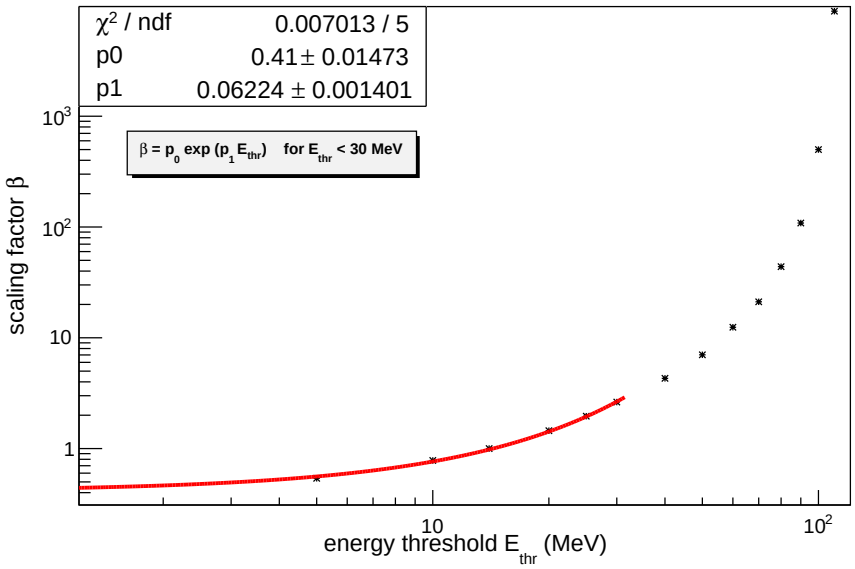

Figure B.39.: Simulated scaling factor β in dependence of the energy threshold E_{thr}. A fit in the form $\beta = p_0 \exp\left(p_1 E_{\text{thr}}\right)$ was performed in the range up to 30 MeV.

The reference energy threshold obtained from the fit $\beta = p_0 \exp(p_1 E_{\text{thr}})$ is

$$E_{\text{thr}}(\beta = 1) = -\frac{\ln(p_0)}{p_1} \quad . \tag{B.10}$$

For the β calculation of an energy threshold x times larger or smaller, it follows:

$$\beta = 0.41^{1-x} \quad . \tag{B.11}$$

B.6.4. Detector efficiency

In order to obtain a scaling factor for the detector efficiency, the same procedure was followed. Several simulations with different detector efficiencies were performed for the 30 × 30 PbF_2 reference calorimeter. A detector efficiency of 95 % was the reference in this case.

ε_{det} (100 %)	y	scaling factor β
1.00	1.43×10^{-12}	0.924
0.95	1.54×10^{-12}	1
0.90	1.55×10^{-12}	1.002
0.85	1.67×10^{-12}	1.082
0.80	1.77×10^{-12}	1.145
0.75	1.97×10^{-12}	1.275
0.70	2.10×10^{-12}	1.358
0.65	2.25×10^{-12}	1.460
0.60	2.45×10^{-12}	1.585
0.55	2.47×10^{-12}	1.602
0.50	2.80×10^{-12}	1.814
0.45	3.07×10^{-12}	1.986
0.40	3.25×10^{-12}	2.103
0.35	4.31×10^{-12}	2.794
0.30	4.71×10^{-12}	3.054
0.25	6.01×10^{-12}	3.896
0.20	7.17×10^{-12}	4.646
0.15	1.11×10^{-11}	7.183
0.10	1.89×10^{-11}	12.215
0.05	4.27×10^{-11}	27.643
0.00	∞	∞

Table B.10.: Scaling factor when changing the detector efficiency.

The reference detector efficiency obtained from the fit $\beta = p_0 \, {\varepsilon_{\text{det}}}^{p_1}$ is

$$\varepsilon_{\text{det}}(\beta = 1) = p_0^{-1/p_1} \quad . \tag{B.12}$$

For the β calculation of a detector efficiency x times larger or smaller, it follows:

$$\beta = x^{-1.02} \quad . \tag{B.13}$$

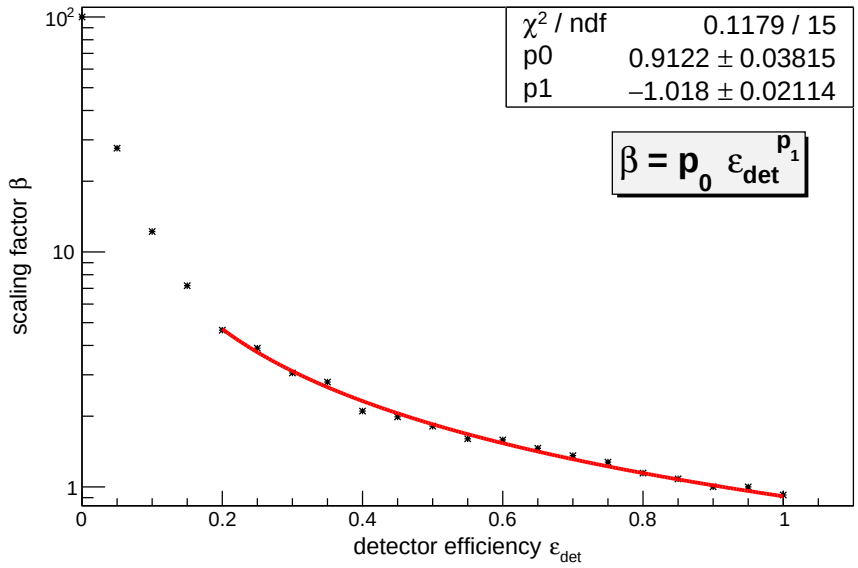

Figure B.40.: Simulated scaling factor β in dependence of the detector efficiency $\varepsilon_{\mathrm{det}}$. A fit in the form $\beta = p_0\,{\varepsilon_{\mathrm{det}}}^{p_1}$ was performed in the range $\varepsilon_{\mathrm{det}} > 20\,\%$.

B.6.5. Confidence level

In order to obtain a scaling factor for the confidence level, the same procedure was followed. Several simulations with different number of particles N_{scaled} were performed for the 30 × 30 PbF_2 reference calorimeter and the same kinematics. $N_{\mathrm{scaled}} = 9$ was the reference in this case.

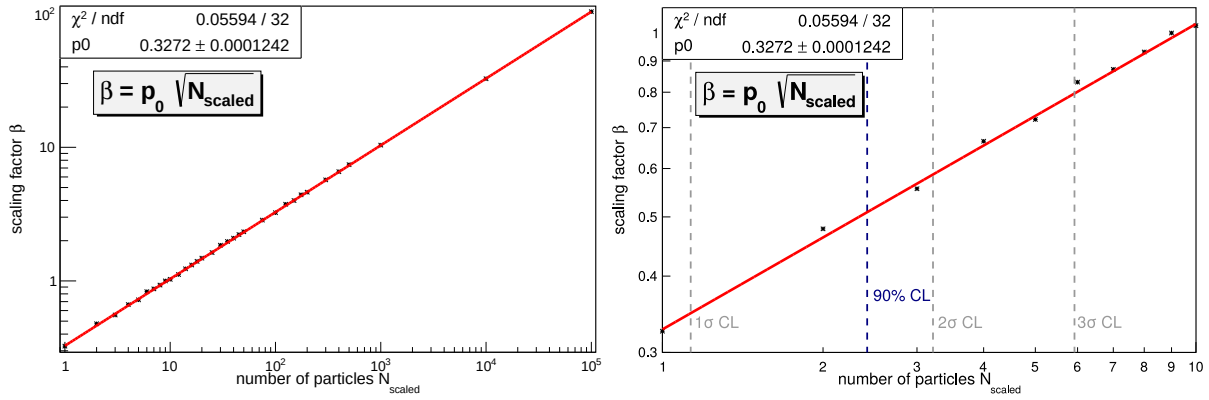

Figure B.41.: Simulated scaling factor β in dependence of the confidence level expressed by the number of particles N_{scaled}. A fit in the form $\beta = p_0\,\sqrt{N_{\mathrm{scaled}}}$ was performed. On the right an enlargement of the left plot is shown and confidence levels are marked. Note that $N_{\mathrm{scaled}} \in \mathbb{N}$ and therefore the confidence levels are exceeded for the next larger N_{scaled}.

The reference detector efficiency obtained from the fit $\beta = p_0\,\sqrt{N_{\mathrm{scaled}}}$ is

$$N_{\mathrm{scaled}}\,(\beta = 1) = p_0^{-2} \quad . \tag{B.14}$$

For the β calculation of a detector efficiency x times larger or smaller, it follows:

$$\beta = \sqrt{x} \quad . \tag{B.15}$$

With the expected number of events $N_{\mathrm{scaled}} = N_{\mathrm{sig}} + N_{\mathrm{bg}}$ and a desired observation of $N_{\mathrm{obs}} =$

N_{scaled}	y	scaling factor β
1	4.97×10^{-13}	0.325
2	7.30×10^{-13}	0.478
3	8.49×10^{-13}	0.556
4	1.02×10^{-12}	0.665
5	1.10×10^{-12}	0.722
6	1.27×10^{-12}	0.831
7	1.33×10^{-12}	0.872
8	1.42×10^{-12}	0.931
9	1.53×10^{-12}	1
10	1.57×10^{-12}	1.028
12	1.71×10^{-12}	1.117
14	1.88×10^{-12}	1.232
16	2.01×10^{-12}	1.316
20	2.26×10^{-12}	1.481
30	2.83×10^{-12}	1.851
40	3.19×10^{-12}	2.090
50	3.56×10^{-12}	2.333
100	4.95×10^{-12}	3.241
200	7.05×10^{-12}	4.615
500	1.13×10^{-11}	7.413
1 000	1.59×10^{-11}	10.385
10 000	4.98×10^{-11}	32.591
100 000	1.58×10^{-10}	103.486

Table B.11.: Scaling factor when changing the number of particles N_{scaled}.

$1 + N_{\text{bg}}$ the following probability is obtained from Poisson statistics:

$$P_{N_{\text{scaled}}}(N_{\text{obs}}) = \frac{(N_{\text{scaled}})^{N_{\text{obs}}}}{N_{\text{obs}}!} \cdot \mathrm{e}^{-N_{\text{scaled}}} \quad . \tag{B.16}$$

In the reference case the components of N_{scaled} are $N_{\text{sig}} = 9$ and $N_{\text{bg}} = 0$. Without backgrounds the desired observation is $N_{\text{obs}} = 1$ and the formula simplifies to:

$$P_{N_{\text{scaled}}}(N_{\text{obs}} = 1) = N_{\text{scaled}} \cdot \mathrm{e}^{-N_{\text{scaled}}} \quad . \tag{B.17}$$

Since exclusion limits are considered in this parameterization study, it must be assumed that no DM event was observed. It applies $N_{\text{obs}} = 0$,

$$P_{N_{\text{scaled}}}(N_{\text{obs}} = 0) = \mathrm{e}^{-N_{\text{scaled}}} \quad , \tag{B.18}$$

and the confidence level results in

$$\text{CL} = 1 - P_{N_{\text{scaled}}} \quad . \tag{B.19}$$

In Fig. B.41 (right) the required number of particles N_{scaled} for a 1σ (68.27 %), 2σ (95.45 %), and 3σ (99.73 %) confidence level are labeled. The 90 % limit, which is commonly used in the DM community, is also marked.

If one assumes non zero background the confidence levels change. Assuming the same number of background counts $N_{\mathrm{bg}} = 9$ and signal counts $N_{\mathrm{sig}} = 9$ the desired observation is $N_{\mathrm{obs}} = 1{+}9 = 10$. The expected number of events is $N_{\mathrm{scaled}} = 9 + 9 = 18$. This results in a confidence level of 98.50 % compared to 99.89 % for the case without backgrounds. If the exclusion limits are to be given with the reference confidence level, the limits worsen by a factor of $\beta = 1.401$.

B.6.6. Summary

A summary of all obtained scaling factors can be found in Tab. B.12.

variable				
change	**original**		**new**	**scaling factor β**
dark coupling	α_{D}	$\longrightarrow$	$x \cdot \alpha_{\mathrm{D}}$	x
time	EOT	$\longrightarrow$	$x \cdot EOT$	$1/\sqrt{x}$
material	N_{det}	$\longrightarrow$	$x \cdot N_{\mathrm{det}}$	$1/\sqrt{x}$
volume	V_{det}	$\longrightarrow$	$x \cdot V_{\mathrm{det}}$	$x^{-0.95}$
threshold	E_{thr}	$\longrightarrow$	$x \cdot E_{\mathrm{thr}}$	0.41^{1-x}
detector efficiency	$\varepsilon_{\mathrm{det}}$	$\longrightarrow$	$x \cdot \varepsilon_{\mathrm{det}}$	$x^{-1.02}$
confidence level	N_{scaled}	$\longrightarrow$	$x \cdot N_{\mathrm{scaled}}$	$\sqrt{x}$

Table B.12.: Overview of the formulas obtained for the scaling factor β. The scaling factor for a change in α_{D} was obtained directly from Eq. 8.25. For a change in time and material the formula was obtained from the dependencies in Eq. 8.23. For volume, threshold, detector efficiency, and confidence level a fit of the simulated data was necessary.

B.7. Detector efficiency study

The detector efficiency for possible detection thresholds was studied for PbF_2 and the PbGl type SF5 with a simulation in Fig. B.42.

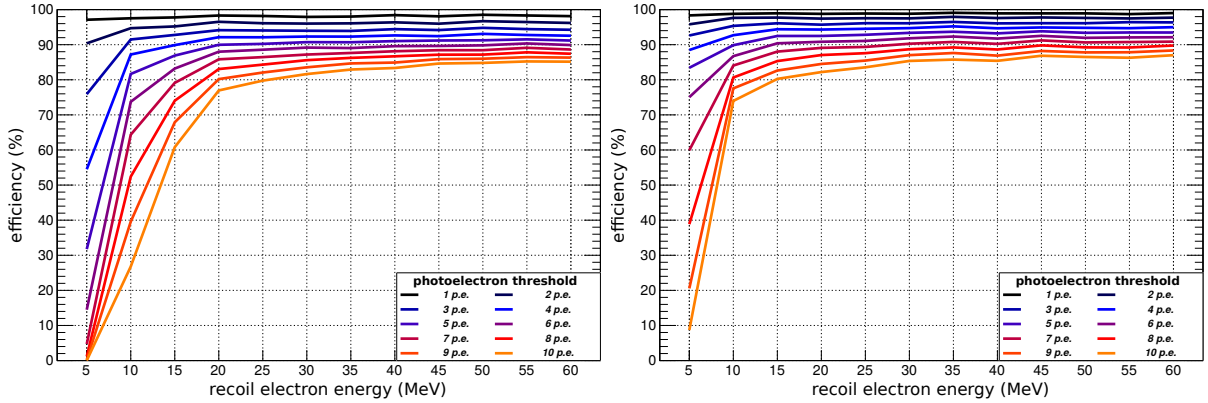

Figure B.42.: Detector efficiency study for PbF_2 (left) and Schott SF5 (right). For fixed electron recoil energies the detection efficiency was simulated. The detection threshold was set to values between 1 and 10 photoelectrons. For a electron recoil threshold of 10 MeV and a photoelectron threshold of 2 p.e. an efficiency of 95 and 98 % is achieved.

B.8. DarkMESA enhancement studies

For the extension of the DarkMESA experiment presented in Chap. 8, additional study results are shown here. The influence of a tungsten target on the exclusion limits (Fig. B.43) and the predictions for DarkMESA-DRIFT and diverse detection thresholds (Fig. B.44) are shown. For the radiation shielding glass study of Phase C the energy distribution used for the particle generator (Fig. B.45) is shown together with the exclusion limit for the Phase C alternative of following up the Phase B setup (Fig. B.46). The angular distribution of dark photons in positron annihilation (Fig. B.47) shows the additional capabilities of an off-axis detector.

B.8.1. DarkMESA with additional tungsten target

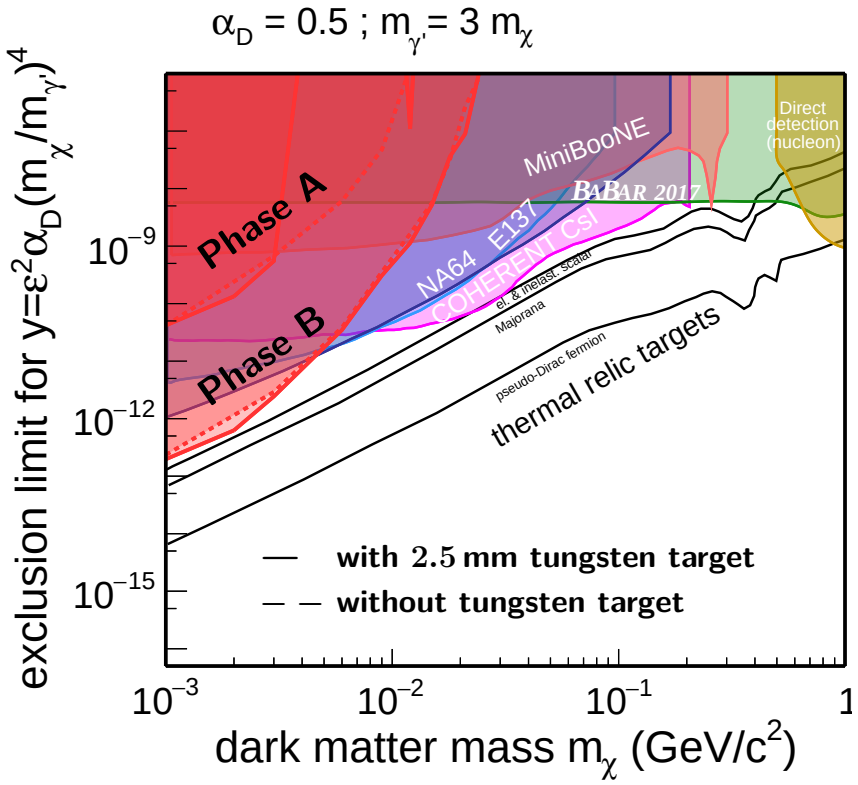

Figure B.43.: Parameter space for dark photons decaying invisibly to $\chi\overline{\chi}$ with the DM mass m_χ on the horizontal axis and variable y on the vertical axis. The predictions for the Phase A and Phase B setup with a 2.5 mm thick tungsten target as addition to the beam-dump are indicated with the solid red lines. The reference limits without tungsten are shown as dashed red lines. 90 % CL, dark Bremsstrahlung only and a detection efficiency of 95 % are assumed.

B.8.2. DarkMESA-DRIFT study

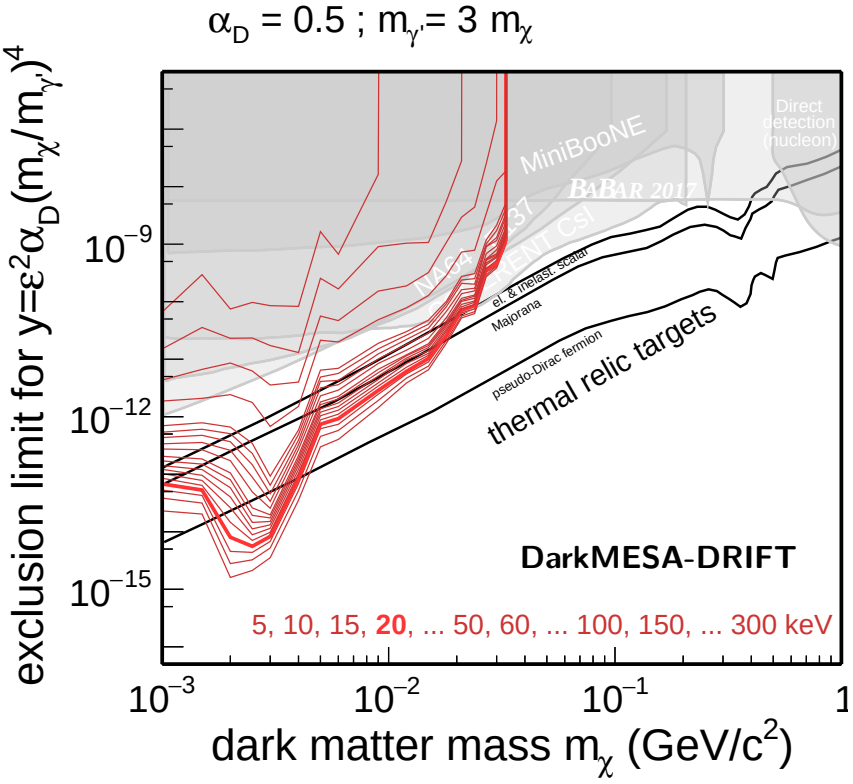

Figure B.44.: Parameter space for dark photons decaying invisibly to $\chi\overline{\chi}$ with the DM mass m_χ on the horizontal axis and variable y on the vertical axis. The predictions for the DarkMESA-DRIFT exclusion limit are shown for the indicated detection thresholds with 90 % CL, positron annihilation included and a detection efficiency of 95 %. 6 600 h of MESA electron beam were assumed.

B.8.3. DarkMESA Phase C study

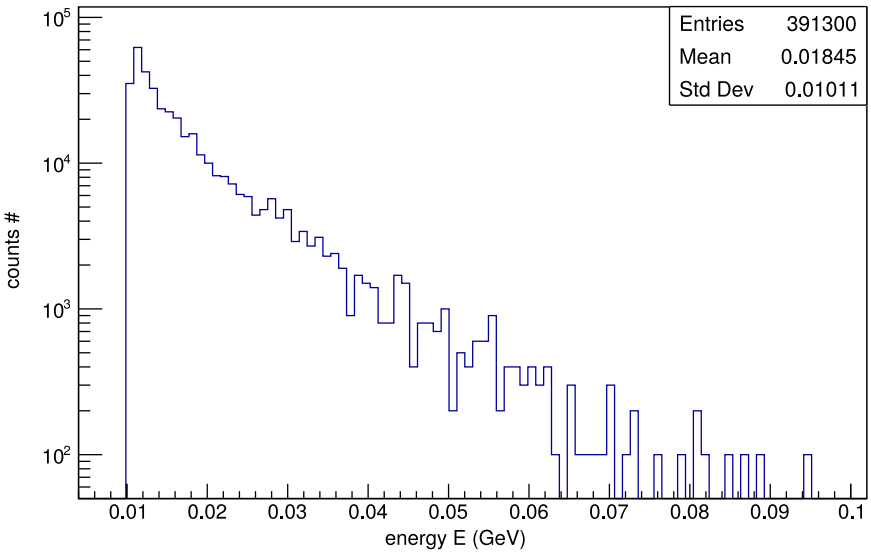

Figure B.45.: Energy distribution of recoil electrons in the initial radiation shielding glass study obtained from all kinematics used for the exclusion limit calculations.

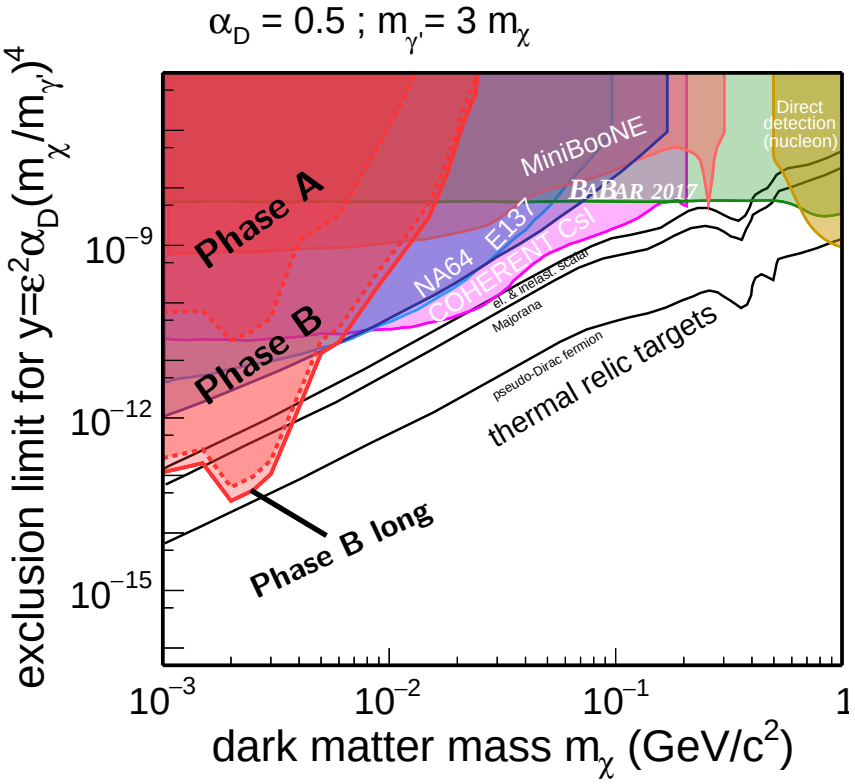

Figure B.46.: Parameter space for dark photons decaying invisibly to $\chi\overline{\chi}$ with the DM mass m_χ on the horizontal axis and variable y on the vertical axis. The predictions for the Phase B setup running also in Phase C with a total of 19 800 h is indicated with the solid red line. 90 % CL, positron annihilation, and a detection efficiency of 95 % are assumed.

B.8.4. DarkMESA off-axis study

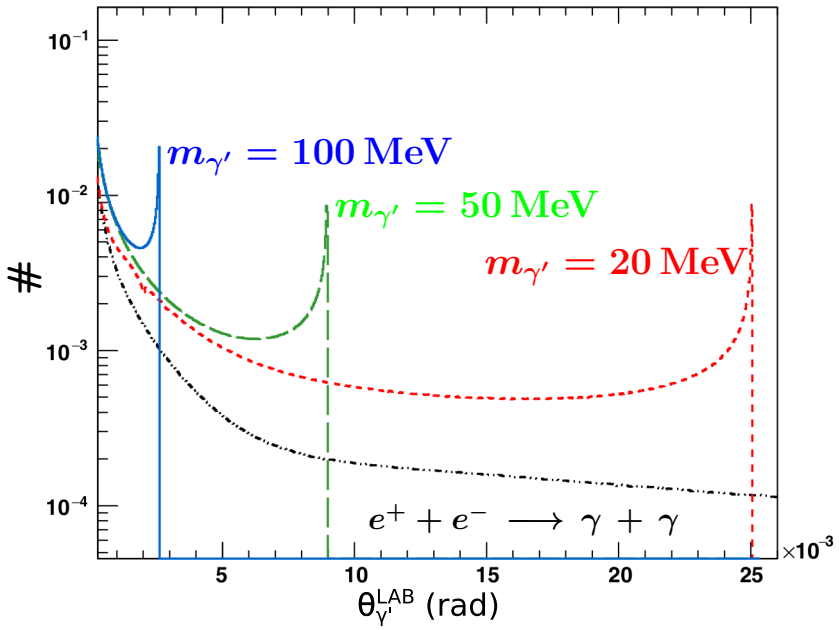

Figure B.47.: Angular distribution for dark photons produced in the non-resonant positron annihilation $e^+ + e^- \longrightarrow \gamma + \gamma'$ for 20 GeV positrons and different dark photon masses $m_{\gamma'}$. Photons produced in the process $e^+ + e^- \longrightarrow \gamma + \gamma$ are shown as comparison in black. (adapted from Fig. 3 in [175])

B.9. Axion searches at DarkMESA

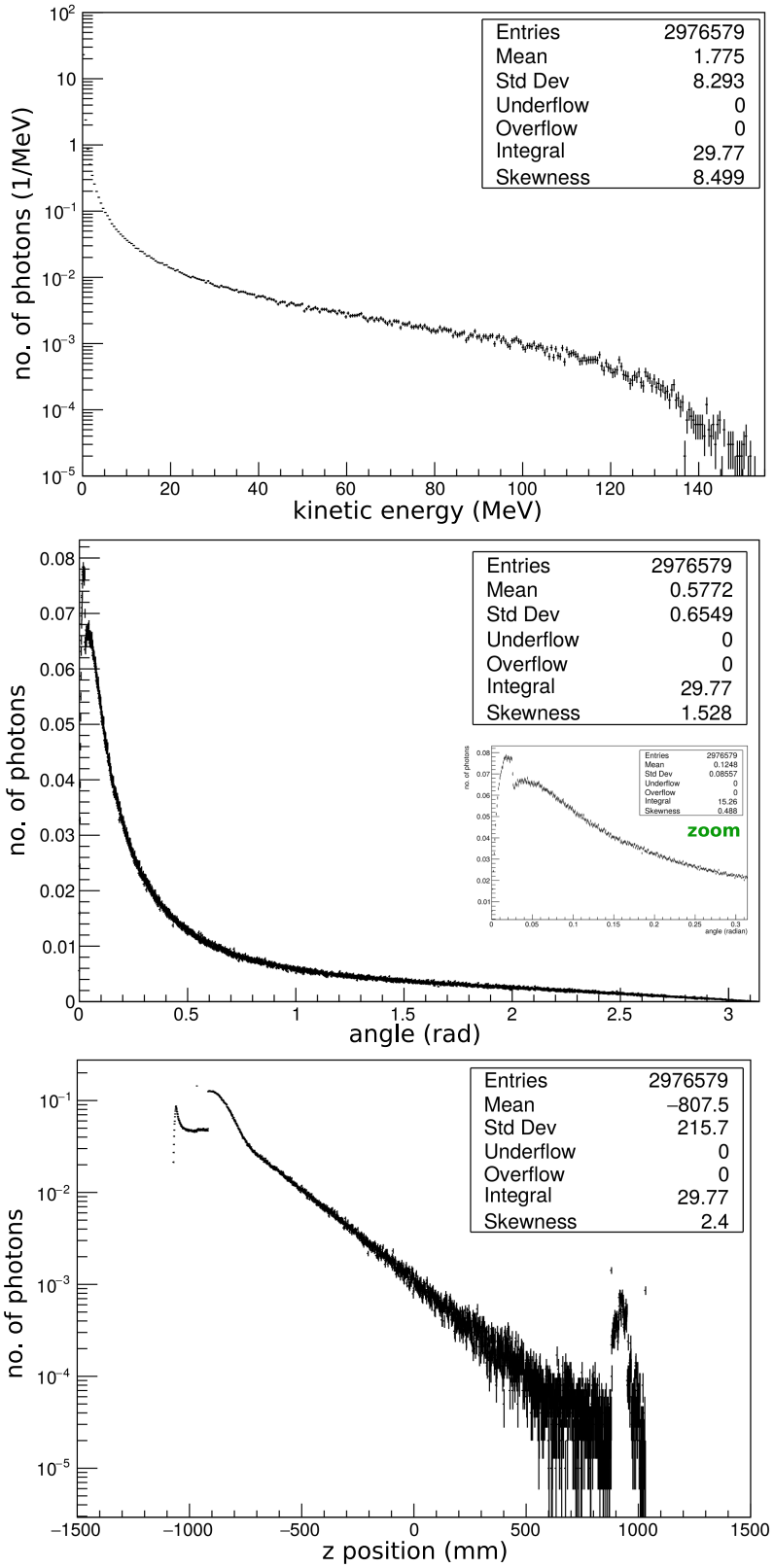

Figure B.48.: Energy (top), angular (middle) and position distribution (bottom) for photons arising in the P2 beam-dump. The simulation comprises 100 000 beam electrons with an energy of 155 MeV. The highest energy photons are generated at the very beginning of the beam-dump. The dominant low-energy photons are mostly emitted at an angle < 0.5 rad.

C. Appendix C – Datasheets

C.1. Properties of materials on the P2 – DarkMESA beam-axis

material	specific gravity ρ	critical energy E_{crit} (MeV)		mean excitation energy I	radiation length X_0	radiation length X_0
	($\mathrm{g\,cm^{-3}}$)	for e^-	for e^+	(eV)	($\mathrm{g\,cm^{-2}}$)	(cm)
$AlMg_3$	2.698	—	—	—	24.75	9.172
H_2O	1.000	78.33	76.24	79.7	36.08	36.08
Al	2.699	42.70	41.48	166.0	24.01	8.897
Cu	8.960	19.42	18.79	322.0	12.86	1.436
H_2(lq)	0.0708	278.02	271.50	21.8	63.04	890.4
air (dry)	0.0012	87.92	85.97	85.7	36.62	30390
concrete	2.300	49.90	48.50	135.2	26.57	11.55
W	19.30	7.97	7.68	727.0	6.76	0.3504

Table C.1.: Physical properties of materials crossed by beam electrons or DM particles on the way from the P2 target to the DarkMESA detectors. Taken from Atomic & Nuclear Properties (PDG) [30].

C.2. EJ-550 optical grade silicone grease

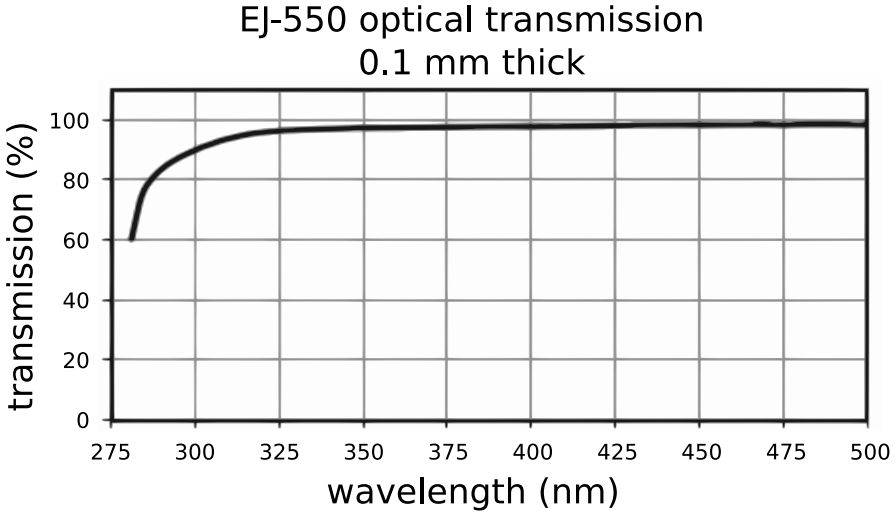

Figure C.1.: Optical transmission for a 0.1 mm thick EJ-550 layer with a specific gravity of $1.06\,\mathrm{g\,cm^{-3}}$ and a refractive index of 1.46. [151]

C.3. Photonis XP2900/01 PMTs

Some data of the PMTs already used in the A4 experiment can be found in Tab. C.2 and Figs. C.2–C.3. The data of the voltage divider used can be found in Fig. C.4 and Tab. C.3.

XP2900/01		
focused dynode structure with 10 stages		
cathode luminous sensitivity		85 μA/lm
cathode blue sensitivity	typ.	11 μA/lmF
cathode radiant sensitivity		85 mA/W @ 425 nm
gain	typ.	9.1×10^5
	max.	1.0×10^7
supply voltage	typ.	1100 V
	max.	1800 V
anode dark current	typ.	1 nA
	max.	5 nA
time response	rise	1.9 ns
	FWHM	3 ns
pulse height resolution		7.7 %

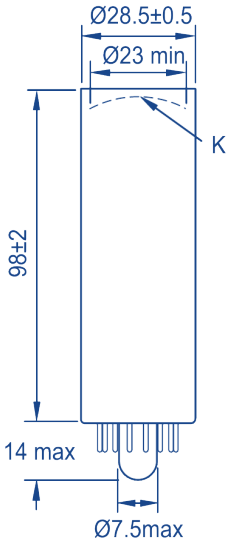

Table C.2.: Key parameters (left) and dimensions in mm (right) of the Photonis XP2900/01 photomultiplier tubes. [146]

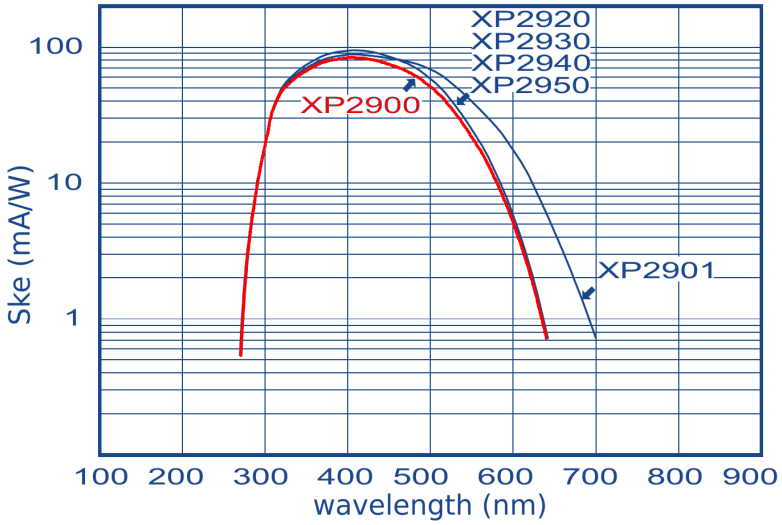

Figure C.2.: Typical spectral characteristics of the Photonis XP2900 PMTs. The wavelength dependent cathodes radiant sensitivity (Ske) is shown. This value gives the ratio of the photocathodes current to the luminous power. It is directly related to the quantum efficiency (QE) with QE (%) = 124 × Ske (mA/W) / λ (nm). [146]

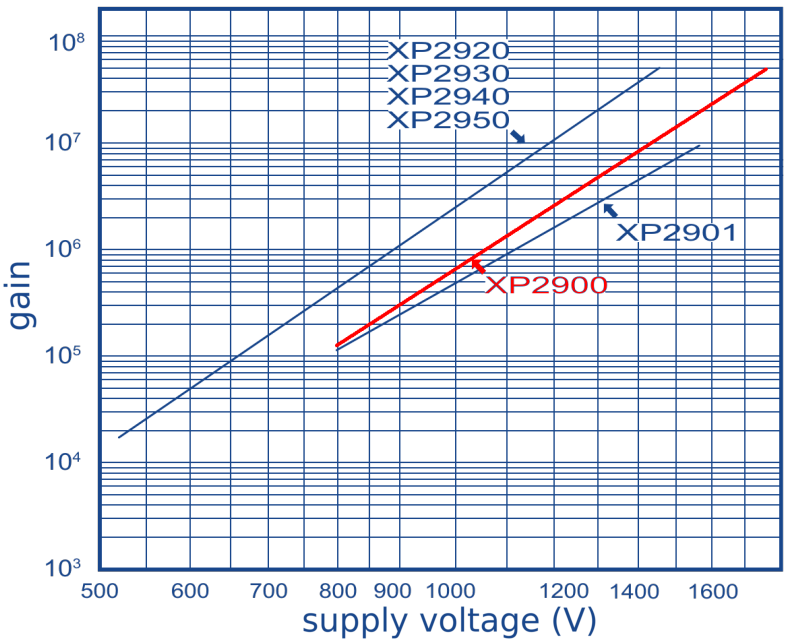

Figure C.3.: Typical gain curves of the Photonis XP2900 PMTs. [146]

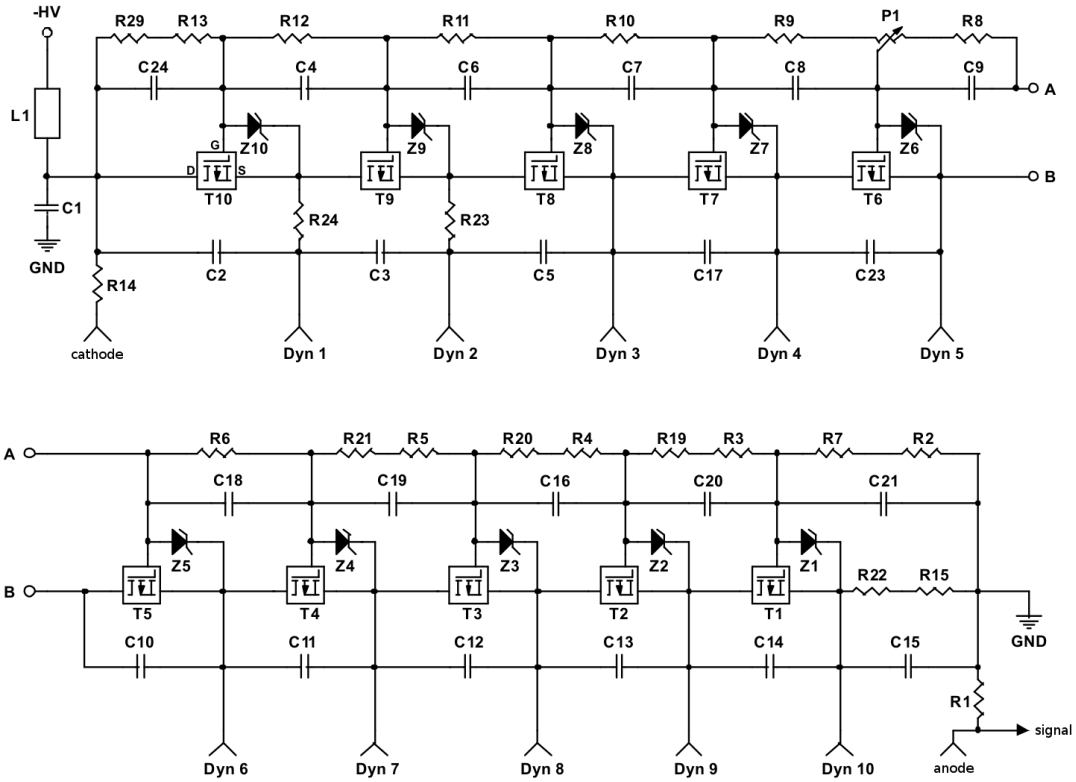

Figure C.4.: Circuit diagramm – Active stabilized high voltage divider from IPN. [180]

component	manufacturer	type	description	quantity	circuit diagram
capacitor	Vitramon	1206	15 pF 500 V 5 % NPO BN	5	C2, C3, C5, C17, C23
		1206	4.7 nF 500 V 5 % X7R BN	12	C4, C6-9, C13, C16, C18-21, C24
		1206	10 nF 500 V 5 % X7R BN	1	C14
		1206	470 pF 500 V 5 % X7R BN	1	C10
		1206	1 nF 500 V 5 % X7R BN	1	C11
		1206	2.2 nF 500 V 5 % X7R BN	1	C12
		1210	22 nF 500 V 5 % X7R BN	1	C15
	Tekelec	2020	1 nF 4 kV 20 % X7R BN	1	C1
resistor	Philips	0603	470 Ω 5 % 200 ppm	1	R1
		1206	3.3 MΩ 5 % 200 ppm	5	R2, R4, R6, R22, R29
		1206	2 MΩ 5 % 200 ppm	1	R21
	KOA	0603	1 kΩ 5 % 200 ppm	2	R23, R24
		1206	4.3 MΩ 5 % 200 ppm	3	R7, R13, R15
		1206	2.4 MΩ 5 % 200 ppm	3	R8, R10, R12
		1206	3.9 MΩ 5 % 200 ppm	1	R11
		1206	10 MΩ 5 % 200 ppm	1	R14
		1206	1.3 MΩ 5 % 200 ppm	1	R9
		1206	5.1 MΩ 5 % 200 ppm	2	R3, R19
		1206	3 MΩ 5 % 200 ppm	2	R5, R20
potentiometer	Beckman		44JR2M 2 MΩ 10-turn	1	P1
inductance	Murata	1206	BLM31 A700 SPTM00-03	1	L1
z-diode	Philips	SOD 80	BZV55C16 16 V	10	Z1-10
transistor	Supertex	SOT 89	TP2540-N8 (P-MOSFET)	10	T1-10

Table C.3.: List of components – Active stabilized high voltage divider from IPN. [180]

C.4. FEU-84 PMTs

For the FEU-84 PMTs the level of official information is low. Different types were manufactured and the exact identifiers have been lost. That is why the key parameters are reprinted from a diploma thesis by Georg Schepers in Münster [159]. His work dealt with the PbGl calorimeter in its present form, of which several modules are already available in Mainz.

FEU-84	
cathode luminous sensitivity	$\geq 8 \times 10^{-5}\,\mathrm{A\,lm^{-1}}$
supply voltage for luminous sensitivity of $100\,\mathrm{A\,lm^{-1}}$	$\leq 1\,700\,\mathrm{V}$
dark current for this supply voltage	$\leq 2 \times 10^{-7}\,\mathrm{A}$
spectral sensitivity at 694 nm	$\geq 3 \times 10^{-3}\,\mathrm{A\,W^{-1}}$
sensitivity threshold	$\leq 10^{-8}\,\mathrm{W}$
number of dynodes	12
cathode material	SbNaKCs (S-20)
emission wavelength (max.)	420 nm
spectral sensitivity at this emission wavelength	$70\,\mathrm{mA\,W^{-1}}$
quantum efficiency at this emission wavelength	20 %

Table C.4.: Key parameters of the FEU-84 PMTs. [159]

List of Figures

List of Tables

Abbreviations

ΛCDM	Lambda Cold Dark Matter
ADC	Analog-to-Digital Converter
AlMg$_3$	Aluminum Magnesium Alloy
ALP	Axion-Like Particle
APEX	A' EXperiment
ARIEL	Advanced Rare Isotope Laboratory
ATOMKI	Institute for Nuclear Research, Debrecen, Hungary
BCM	Beam Current Monitor
BDX	Beam Dump Experiment
BGO	$Bi_4Ge_3O_{12}$
BPM	Beam Position Monitor
CAD	Computer-Aided Design
CB	Crystal Ball
CCD	Charge-Coupled Device
CERN	Conseil Européen pour la Recherche Nucléaire
CL	Confidence Level
CM	Center of Mass
CMB	Cosmic Microwave Background
CPU	Central Processing Unit
CRESST	Cryogenic Rare Event Search with Superconducting Thermometers
CRY	Cosmic-Ray shower Library
CsI(Tl)	Thallium-doped Cesium Iodide
CW	Continuous Wave
DAC	Digital-to-Analog Converter
DAMIC	DArk Matter In CCDs
DC	Direct Current
DM	Dark Matter
DN40	40 mm Nominal Diameter
DRIFT	Directional Recoil Identification From Tracks
EB	Extracted Beam
EOT	Electrons On Target
ERL	Energy-Recovering Linac
FAIR	Facility for Antiproton and Ion Research
Fermilab	Fermi National Accelerator Laboratory
FLRW	Friedmann-Lemaître-Robertson-Walker
FOPI	4π
FPGA	Field Programmable Gate Array
FSR	Full Scale Range
FWHM	Full Width at Half Maximum
GEM	Gas Electron Multiplier
HDSM	Harmonic Double-Sided Microtron
HGS-HIRe	Helmholtz Graduate School for Hadron and Ion Research
HPS	Heavy Photon Search
HV	High Voltage
HV-MAPS	High Voltage Monolithic Active Pixel Sensors
IPN	Institute de Physique Nucléaire, Orsay, France
JLab	Thomas Jefferson Laboratory

KPH	Institute for Nuclear Physics in Mainz
LDM	Light Dark Matter
LEDA	Leadglass Detector Array
LEP	Large Electron-Positron collider
lH$_2$	Liquid Hydrogen
LHE	Les Houches Event
LNF	Laboratori Nazionali di Frascati
LSF	Load Sharing Facility
MAGIX	Mainz Gas Injection Target Experiment
MAMBO	Milli AMpere BOoster
MAMI	Mainz Microtron
MC	Monte Carlo
MELBA	MESA Low-energy Beam Apparatus
MESA	Mainz Energy-recovering Superconducting Accelerator
MINOS	Main Injector Neutrino Oscillation Search
PADME	Positron Annihilation into Dark Matter Experiment
PANDA	antiProton ANnihilation at DArmstadt
PbF$_2$	Lead Fluoride
PbGl	Lead Glass
PbWO$_4$	Lead Tungstate
PDG	Particle Data Group
PMT	Photomultiplier Tube
PSI	Paul Scherrer Institute
PTFE	Polytetrafluorethylen
PVC	Polyvinyl Chloride
QAC	Charge-to-Amplitude Converter
QDC	Charge-to-Digital Converter
QE	Quantum Efficiency
RF	Radio Frequency
RMS	Root Mean Square
ROI	Region-Of-Interest
RTM	Race Track Microtron
SENSEI	Sub-Electron-Noise Skipper-CCD Experimental Instrument
SHV	Safe High Voltage
SICCAS	Shanghai Institute of Ceramics of the Chinese Academy of Sciences
SiPM	Silicon Photoultiplier
SLAC	Stanford Linear Accelerator Center
SLC	Stanford Linear Collider
SM	Standard Model
SN	Serial Number
SNOLAB	Sudbury Neutrino Observatory Laboratory
SNS	Spallation Neutron Source
SPS	Super Proton Synchrotron
SuperCDMS	Super Cryogenic Dark Matter Search
SUSY	Supersymmetry
TAPS	Two Arm Photon Spectrometer
TOF	Time Of Flight
TPC	Time Projection Chamber
UV	Ultra Violet
VHS	Versatile High Voltage Module in VME Standard
VME	VERSA-Module Euro card
WIMP	Weakly Interacting Massive Particle
WLS	Wavelength Shifting
WMAP	Wilkinson Microwave Anisotropy Probe
ZDT	Zero Degree Tagger
ZIF	Zero Insertion Force

Bibliography

[1] V. Sahni and A. Starobinsky, "Reconstructing Dark Energy," *International Journal of Modern Physics D*, vol. 15, no. 12, pp. 2105–2132, Dec. 2006. [Online]. Available: https://doi.org/10.1142/S0218271806009704

[2] A. Silvestri and M. Trodden, "Approaches to Understanding Cosmic Acceleration," *Reports on Progress in Physics*, vol. 72, no. 9, p. 096901, Aug. 2009. [Online]. Available: https://doi.org/10.1088/0034-4885/72/9/096901

[3] D. Huterer and D. L. Shafer, "Dark energy two decades after: Observables, probes, consistency tests," *Reports on Progress in Physics*, vol. 81, no. 1, p. 016901, Dec. 2017. [Online]. Available: https://doi.org/10.1088/1361-6633/aa997e

[4] L. Doria, "Search for New Physics with Intense Pion and Electron Beams," Habilitation thesis, Johannes Gutenberg Universität, Institut für Kernphysik Mainz, Sep. 2018, Accessed: Dec 8, 2022. [Online]. Available: https://www.staff.uni-mainz.de/doria/Hab.pdf

[5] F. Zwicky, "Die Rotverschiebung von extragalaktischen Nebeln," *Helvetica Physica Acta*, vol. 6, pp. 110–127, 1933. [Online]. Available: https://doi.org/10.1007/s10714-008-0707-4

[6] V. C. Rubin *et al.*, "Extended rotation curves of high-luminosity spiral galaxies. IV. Systematic dynamical properties, Sa through Sc," *Astrophysical Journal*, vol. 225, pp. L107–L111, Nov. 1978. [Online]. Available: https://doi.org/10.1086/182804

[7] G. Hinshaw *et al.*, "Nine-Year Wilkinson Microwave Anisotropy Probe (WMAP) Observations: Cosmological Parameter Results," *The Astrophysical Journal Supplement Series*, vol. 208, no. 2, p. 19, Sep. 2013. [Online]. Available: https://doi.org/10.1088/0067-0049/208/2/19

[8] P. A. R. Ade *et al.* (Planck Collaboration), "Planck 2015 results. XIII. Cosmological parameters," *Astronomy & Astrophysics*, vol. 594, p. A13, Sep. 2016. [Online]. Available: https://doi.org/10.1051/0004-6361/201525830

[9] N. Aghanim *et al.* (Planck Collaboration), "Planck 2018 results. V. CMB power spectra and likelihoods," *Astronomy & Astrophysics*, vol. 641, p. A5, Sep. 2020. [Online]. Available: https://doi.org/10.1051/0004-6361/201936386

[10] A. Refregier, "Weak Gravitational Lensing by Large-Scale Structure," *Annual Review of Astronomy and Astrophysics*, vol. 41, no. 1, pp. 645–668, Sep. 2003. [Online]. Available: https://doi.org/10.1146/annurev.astro.41.111302.102207

[11] R. Massey *et al.*, "The dark matter of gravitational lensing," *Reports on Progress in Physics*, vol. 73, no. 8, p. 086901, July 2010. [Online]. Available: https://doi.org/10.1088/0034-4885/73/8/086901

[12] A. G. Riess *et al.*, "Observational Evidence from Supernovae for an Accelerating Universe and a Cosmological Constant," *The Astronomical Journal*, vol. 116, no. 3, pp. 1009–1038, Sep. 1998. [Online]. Available: https://doi.org/10.1086/300499

[13] S. Perlmutter *et al.*, "Measurements of Ω and Λ from 42 High-Redshift Supernovae," *The Astrophysical Journal*, vol. 517, no. 2, pp. 565–586, June 1999. [Online]. Available: https://doi.org/10.1086/307221

[14] M. Viel *et al.*, "Cosmological and astrophysical constraints from the Lyman-alpha forest flux probability distribution function," *Monthly Notices of the Royal Astronomical Society: Letters*, vol. 399, no. 1, pp. L39–L43, Oct. 2009. [Online]. Available: https://doi.org/10.1111/j.1745-3933.2009.00720.x

[15] Y. Du *et al.*, "Revisiting Dark Matter Freeze-in and Freeze-out through Phase-Space Distribution," *Journal of Cosmology and Astroparticle Physics*, vol. 2022, no. 04, p. 012, Apr. 2022. [Online]. Available: https://doi.org/10.1088/1475-7516/2022/04/012

[16] J. L. Feng, "Dark Matter Candidates from Particle Physics and Methods of Detection," *Annual Review of Astronomy and Astrophysics*, vol. 48, no. 1, pp. 495–545, Aug. 2010. [Online]. Available: https://doi.org/10.1146/annurev-astro-082708-101659

[17] K. Griest and M. Kamionkowski, "Unitarity limits on the mass and radius of dark-matter particles," *Physical Review Letters*, vol. 64, pp. 615–618, Feb. 1990. [Online]. Available: https://doi.org/10.1103/PhysRevLett.64.615

[18] K. Choi *et al.*, "Recent Progress in the Physics of Axions and Axion-Like Particles," *Annual Review of Nuclear and Particle Science*, vol. 71, no. 1, pp. 225–252, Sep. 2021. [Online]. Available: https://doi.org/10.1146/annurev-nucl-120720-031147

[19] C. Cheung *et al.*, "Prospects and Blind Spots for Neutralino Dark Matter," *Journal of High Energy Physics*, vol. 2013, no. 5, May 2013. [Online]. Available: https://doi.org/10.48550/arXiv.1211.4873

[20] H.-C. Cheng *et al.*, "Kaluza-Klein Dark Matter," *Physical Review Letters*, vol. 89, p. 211301, Oct. 2002. [Online]. Available: https://doi.org/10.1103/PhysRevLett.89.211301

[21] G. Servant and T. M. Tait, "Is the lightest Kaluza–Klein particle a viable dark matter candidate?" *Nuclear Physics B*, vol. 650, no. 1-2, pp. 391–419, Feb. 2003. [Online]. Available: https://doi.org/10.1016/S0550-3213%2802%2901012-X

[22] F. D. Steffen, "Gravitino Dark Matter and Cosmological Constraints," *Journal of Cosmology and Astroparticle Physics*, vol. 2006, no. 09, pp. 001–001, Sep. 2006. [Online]. Available: https://doi.org/10.1088/1475-7516/2006/09/001

[23] M. Milgrom, "MOND laws of galactic dynamics," *Monthly Notices of the Royal Astronomical Society*, vol. 437, no. 3, pp. 2531–2541, Nov. 2013. [Online]. Available: https://doi.org/10.1093/mnras/stt2066

[24] J. D. Bekenstein, "Erratum: Relativistic gravitation theory for the modified Newtonian dynamics paradigm [Phys. Rev. D 70, 083509 (2004)]," *Physical Review D*, vol. 71, p. 069901, Mar. 2005. [Online]. Available: https://doi.org/10.1103/PhysRevD.71.069901

[25] D. J. H. Chung *et al.*, "Superheavy dark matter," *Physical Review D*, vol. 59, no. 2, p. 023501, Nov. 1998. [Online]. Available: https://doi.org/10.1103/PhysRevD.59.023501

[26] B. W. Lee and S. Weinberg, "Cosmological Lower Bound on Heavy-Neutrino Masses," *Physical Review Letters*, vol. 39, pp. 165–168, July 1977. [Online]. Available: https://doi.org/10.1103/PhysRevLett.39.165

[27] S. Dodelson and L. M. Widrow, "Sterile neutrinos as dark matter," *Physical Review Letters*, vol. 72, pp. 17–20, Jan. 1994. [Online]. Available: https://doi.org/10.1103/PhysRevLett.72.17

[28] K. Petraki and R. R. Volkas, "Review of asymmetric dark matter," *International Journal of Modern Physics A*, vol. 28, no. 19, p. 1330028, July 2013. [Online]. Available: https://doi.org/10.1142/S0217751X13300287

[29] C. Strandhagen, "Search for Low-Mass Dark Matter with the CRESST-II Experiment," PhD thesis, Eberhard Karls Universität Tübingen, 2016. [Online]. Available: http://dx.doi.org/10.15496/publikation-15461

[30] P. Zyla *et al.*, "Review of Particle Physics," *Progress of Theoretical and Experimental Physics*, vol. 2020, no. 8, p. 083C01, Aug. 2020. [Online]. Available: http://doi.org/10.1093/ptep/ptaa104

[31] G. Angloher *et al.* (CRESST Collaboration), "Results on light dark matter particles with a low-threshold CRESST-II detector," *The European Physical Journal C*, vol. 76, no. 1, Jan. 2016. [Online]. Available: https://doi.org/10.1140/epjc/s10052-016-3877-3

[32] A. H. Abdelhameed *et al.* (CRESST Collaboration), "First results from the CRESST-III low-mass dark matter program," *Physical Review D*, vol. 100, no. 10, p. 102002, Nov. 2019. [Online]. Available: https://doi.org/10.1103/PhysRevD.100.102002

[33] R. Agnese *et al.* (SuperCDMS Collaboration), "Projected sensitivity of the SuperCDMS SNOLAB experiment," *Physical Review D*, vol. 95, no. 8, p. 082002, Apr. 2017. [Online]. Available: https://doi.org/10.1103/PhysRevD.95.082002

[34] A. Aguilar-Arevalo *et al.* (DAMIC Collaboration), "Constraints on Light Dark Matter Particles Interacting with Electrons from DAMIC at SNOLAB," *Physical Review Letters*, vol. 123, no. 18, p. 181802, Oct. 2019. [Online]. Available: https://doi.org/10.1103/PhysRevLett.123.181802

[35] L. Barak *et al.* (SENSEI Collaboration), "SENSEI: Direct-Detection Results on sub-GeV Dark Matter from a New Skipper CCD," *Physical Review Letters*, vol. 125, no. 17, Oct. 2020. [Online]. Available: https://doi.org/10.1103/PhysRevLett.125.171802

[36] R. Agnese *et al.* (SuperCDMS Collaboration), "Search for Low-Mass Weakly Interacting Massive Particles with SuperCDMS," *Physical Review Letters*, vol. 112, p. 241302, June 2014. [Online]. Available: https://doi.org/10.1103/PhysRevLett.112.241302

[37] R. Agnese *et al.* (SuperCDMS Collaboration), "Results from the Super Cryogenic Dark Matter Search (SuperCDMS) experiment at Soudan," *Physical Review Letters*, vol. 120, no. 6, p. 061802, Feb. 2018. [Online]. Available: https://doi.org/10.1103/PhysRevLett.120.061802

[38] X. Cui *et al.* (PandaX-II Collaboration), "Dark Matter Results from 54-Ton-Day Exposure of PandaX-II Experiment," *Physical Review Letters*, vol. 119, no. 18, p. 181302, Oct. 2017. [Online]. Available: https://doi.org/10.1103/PhysRevLett.119.181302

[39] D. S. Akerib *et al.* (LUX Collaboration), "Results of a Search for Sub-GeV Dark Matter Using 2013 LUX Data," *Physical Review Letters*, vol. 122, p. 131301, Apr. 2019. [Online]. Available: https://doi.org/10.1103/PhysRevLett.122.131301

[40] E. Aprile *et al.* (XENON Collaboration), "Light Dark Matter Search with Ionization Signals in XENON1T," *Physical Review Letters*, vol. 123, p. 251801, Dec. 2019. [Online]. Available: https://doi.org/10.1103/PhysRevLett.123.251801

[41] A. Aguilar-Arevalo *et al.* (DAMIC Collaboration), "Results on Low-Mass Weakly Interacting Massive Particles from an 11 kg d Target Exposure of DAMIC at SNOLAB," *Physical Review Letters*, vol. 125, no. 24, p. 241803, Dec. 2020. [Online]. Available: https://doi.org/10.1103/PhysRevLett.125.241803

[42] P. Agnes *et al.* (DarkSide Collaboration), "DarkSide-50 532-day Dark Matter Search with Low-Radioactivity Argon," *Physical Review D*, vol. 98, p. 102006, Nov. 2018. [Online]. Available: https://doi.org/10.1103/PhysRevD.98.102006

[43] E. Aprile *et al.* (XENON Collaboration), "Physics reach of the XENON1T dark matter experiment." *Journal of Cosmology and Astroparticle Physics*, vol. 2016, no. 04, pp. 027–027, Apr. 2016. [Online]. Available: https://doi.org/10.1088/1475-7516/2016/04/027

[44] F. Ruppin *et al.*, "Complementarity of dark matter detectors in light of the neutrino background," *Physical Review D*, vol. 90, p. 083510, Oct. 2014. [Online]. Available: https://doi.org/10.1103/PhysRevD.90.083510

[45] Q. Arnaud *et al.* (EDELWEISS Collaboration), "First Germanium-Based Constraints on Sub-MeV Dark Matter with the EDELWEISS Experiment," *Physical Review Letters*, vol. 125, no. 14, p. 141301, Oct. 2020. [Online]. Available: https://doi.org/10.1103/PhysRevLett.125.141301

[46] C. Cheng *et al.* (PandaX-II Collaboration), "Search for Light Dark Matter–Electron Scattering in the PandaX-II Experiment," *Physical Review Letters*, vol. 126, no. 21, p. 211803, May 2021. [Online]. Available: https://doi.org/10.1103/PhysRevLett.126.211803

[47] R. Essig *et al.*, "New constraints and prospects for sub-GeV dark matter scattering off electrons in xenon," *Physical Review D*, vol. 96, no. 4, p. 043017, Aug. 2017. [Online]. Available: https://doi.org/10.1103/PhysRevD.96.043017

[48] D. W. Amaral *et al.*, "Constraints on low-mass, relic dark matter candidates from a surface-operated SuperCDMS single-charge sensitive detector," *Physical Review D*, vol. 102, no. 9, p. 091101, Nov. 2020. [Online]. Available: https://doi.org/10.1103/PhysRevD.102.091101

[49] P. Agnes *et al.* (DarkSide Collaboration), "Constraints on Sub-GeV Dark-Matter–Electron Scattering from the DarkSide-50 Experiment," *Physical Review Letters*, vol. 121, no. 11, p. 111303, Sep. 2018. [Online]. Available: https://doi.org/10.1103/PhysRevLett.121.111303

[50] R. Essig *et al.*, "Direct detection of sub-GeV dark matter," *Physical Review D*, vol. 85, no. 7, p. 076007, Apr. 2012. [Online]. Available: https://doi.org/10.1103/PhysRevD.85.076007

[51] S. Abrahamyan *et al.*, "Search for a New Gauge Boson in Electron-Nucleus Fixed-Target Scattering by the APEX Experiment," *Physical Review Letters*, vol. 107, no. 19, p. 191804, Nov. 2011. [Online]. Available: https://doi.org/10.1103/PhysRevLett.107.191804

[52] A. Celentano, "Dark Sector Searches at Jefferson Laboratory," *Journal of Physics: Conference Series*, vol. 770, p. 012040, Nov. 2016. [Online]. Available: https://doi.org/10.1088/1742-6596/770/1/012040

[53] A. Celentano and the HPS Collaboration, "The Heavy Photon Search experiment at Jefferson Laboratory," *Journal of Physics: Conference Series*, vol. 556, p. 012064, Nov. 2014. [Online]. Available: https://doi.org/10.1088/1742-6596/556/1/012064

[54] J. Balewski *et al.*, "The DarkLight Experiment: A Precision Search for New Physics at Low Energies," Dec. 2014. [Online]. Available: https://doi.org/10.48550/arXiv.1412.4717

[55] E. Cline *et al.* (DarkLight Collaboration), "Searching for New Physics with DarkLight at the ARIEL Electron-Linac," Aug. 2022. [Online]. Available: https://doi.org/10.48550/arXiv.2208.04120

[56] A. J. Krasznahorkay *et al.*, "Observation of Anomalous Internal Pair Creation in ^{8}Be: A Possible Indication of a Light, Neutral Boson," *Physical Review Letters*, vol. 116, p. 042501, Jan. 2016. [Online]. Available: https://doi.org/10.1103/PhysRevLett.116.042501

[57] A. J. Krasznahorkay *et al.*, "New evidence supporting the existence of the hypothetic X17 particle," Oct. 2019. [Online]. Available: https://doi.org/10.48550/arXiv.1910.10459

[58] A. J. Krasznahorkay *et al.*, "A new anomaly observed in ^{4}He supports the existence of the hypothetical X17 particle," *Physical Review C*, vol. 104, no. 4, p. 044003, Oct. 2021. [Online]. Available: https://doi.org/10.1103/PhysRevC.104.044003

[59] H. Herminghaus *et al.*, "The design of a cascaded 800 MeV normal conducting C.W. race track microtron," *Nuclear Instruments and Methods*, vol. 138, no. 1, pp. 1–12, Oct. 1976. [Online]. Available: https://doi.org/10.1016/0029-554X(76)90145-2

[60] A. Jankowiak, "The Mainz Microtron MAMI – Past and future," *The European Physical Journal A*, vol. 28, pp. 149–160, Jan. 2006. [Online]. Available: https://doi.org/10.1007/3-540-36754-3_16

[61] K. Aulenbacher *et al.*, "The MAMI source of polarized electrons," *Nuclear Instruments and Methods in Physics Research Section A: Accelerators, Spectrometers, Detectors and Associated Equipment*, vol. 391, no. 3, pp. 498–506, June 1997. [Online]. Available: https://doi.org/10.1016/S0168-9002(97)00528-7

[62] K.-H. Kaiser *et al.*, "The 1.5 GeV harmonic double-sided microtron at Mainz University," *Nuclear Instruments and Methods in Physics Research Section A: Accelerators, Spectrometers, Detectors and Associated Equipment*, vol. 593, no. 3, pp. 159–170, Aug. 2008. [Online]. Available: https://doi.org/10.1016/j.nima.2008.05.018

[63] H. Backe *et al.*, "Resonant transition radiation in the X-Ray region from a low emittance 855-MeV electron beam," *Zeitschrift für Physik A Hadrons and Nuclei*, vol. 349, pp. 87–92, Mar. 1994. [Online]. Available: https://doi.org/10.1007/BF01296337

[64] J. C. Bernauer *et al.* (A1 Collaboration), "Electric and magnetic form factors of the proton," *Physical Review C*, vol. 90, p. 015206, July 2014. [Online]. Available: https://doi.org/10.1103/PhysRevC.90.015206

[65] M. Mihovilovič *et al.*, "The proton charge radius extracted from the initial-state radiation experiment at MAMI," *The European Physical Journal A*, vol. 57, p. 107, Mar. 2021. [Online]. Available: https://doi.org/10.1140/epja/s10050-021-00414-x

[66] H. Merkel *et al.* (A1 Collaboration), "Search for Light Gauge Bosons of the Dark Sector at the Mainz Microtron," *Physical Review Letters*, vol. 106, no. 25, p. 251802, June 2011. [Online]. Available: https://doi.org/10.1103/PhysRevLett.106.251802

[67] R. Beck *et al.* (CrystalBall@MAMI and A2 Collaborations), "New results and future plans with real photons at MAMI," *Progress in Particle and Nuclear Physics*, vol. 55, no. 1, pp. 91–107, July 2005. [Online]. Available: https://doi.org/10.1016/j.ppnp.2005.01.025

[68] E. D. Bloom and C. Peck, "Physics with the Crystal Ball Detector," *Annual Review of Nuclear and Particle Science*, vol. 33, pp. 143–197, Dec. 1983. [Online]. Available: https://doi.org/10.1146/annurev.ns.33.120183.001043

[69] J. Ahrens *et al.* (GDH and A2 Collaborations), "First Measurement of the Gerasimov-Drell-Hearn Integral for ^1H from 200 to 800 MeV," *Physical Review Letters*, vol. 87, no. 2, p. 022003, June 2001. [Online]. Available: https://doi.org/10.1103/physrevlett.87.022003

[70] E. F. McNicoll *et al.* (CrystalBall@MAMI Collaboration), "Experimental study of the $\gamma p \to \eta p$ reaction with the Crystal Ball detector at the Mainz Microtron (MAMI-C)," *Physical Review C*, vol. 82, p. 035208, Sep. 2010. [Online]. Available: https://doi.org/10.1103/PhysRevC.82.035208

[71] P. Achenbach, "Aufbau eines Bleifluorid-Kalorimeters zur Messung der Paritätsverletzung in der elastischen Elektronenstreuung," PhD thesis, Johannes Gutenberg-Universität, Institut für Kernphysik, Mainz, May 2001, Accessed: Dec 8, 2022. [Online]. Available: https://www.blogs.uni-mainz.de/fb08-ag-maas/files/2017/06/achenbach.diss_.pdf

[72] AG Maas, "A4 Collaboration at MAMI," Johannes Gutenberg-University Mainz, June 2017, Accessed: Dec 8, 2022. [Online]. Available: https://www.blogs.uni-mainz.de/fb08-ag-maas/a4-collaboration-at-mami/

[73] F. Hug *et al.*, "MESA - an ERL Project for Particle Physics Experiments," *Proceedings of Linear Accelerator Conference (LINAC'16), East Lansing, MI, USA, 25-30 September 2016*, vol. 28, pp. 313–315, May 2017. [Online]. Available: https://doi.org/10.18429/JACoW-LINAC2016-MOP106012

[74] D. Simon, "Gesamtkonzept für den MESA-Teilchenbeschleuniger unter besonderer Berücksichtigung von Strahloptik und Kryogenik," PhD thesis, Johannes Gutenberg-Universität, Institut für Kernphysik, Mainz, Apr. 2021. [Online]. Available: http://doi.org/10.25358/openscience-5809

[75] D. Simon, "Autodesk Inventor data files. Institute for Nuclear Physics. Johannes Gutenberg-University Mainz," 2016.

[76] J. Teichert *et al.*, "RF status of superconducting module development suitable for CW operation: ELBE cryostats," *Nuclear Instruments and Methods in Physics Research Section A: Accelerators, Spectrometers, Detectors and Associated Equipment*, vol. 557, no. 1, pp. 239–242, Feb. 2006. [Online]. Available: https://doi.org/10.1016/j.nima.2005.10.077

[77] B. S. Schlimme *et al.* (A1 and MAGIX Collaborations), "Operation and characterization of a windowless gas jet target in high-intensity electron beams," *Nuclear Instruments and Methods in Physics Research Section A: Accelerators, Spectrometers, Detectors and Associated Equipment*, vol. 1013, p. 165668, Oct. 2021. [Online]. Available: https://doi.org/10.1016/j.nima.2021.165668

[78] S. Grieser *et al.*, "A cryogenic supersonic jet target for electron scattering experiments at MAGIX@MESA and MAMI," *Nuclear Instruments and Methods in Physics Research Section A: Accelerators, Spectrometers, Detectors and Associated Equipment*, vol. 906, pp. 120–126, Oct. 2018. [Online]. Available: https://doi.org/10.1016/j.nima.2018.07.076

[79] J. Geimer, "Aufbau eines ortsauflösenden Siliziumdetektorsystems zum Nachweis von α-Teilchen," Master's thesis, Johannes Gutenberg-Universität, Institut für Kernphysik, Mainz, June 2020.

[80] S. Lunkenheimer, "Feasibility Studies for Measuring the Astrophysical S-Factor of the Reaction $^{12}\mathrm{C}\,(\alpha,\gamma)\,^{16}\mathrm{O}$ via Electro-Disintegration at MAGIX," PhD thesis, Johannes Gutenberg-Universität, Institut für Kernphysik, Mainz, Nov. 2021. [Online]. Available: http://doi.org/10.25358/openscience-6808

[81] D. Becker *et al.*, "The P2 experiment – A future high-precision measurement of the electroweak mixing angle at low momentum transfer," *The European Physical Journal A*, vol. 54, no. 11, Nov. 2018. [Online]. Available: http://doi.org/10.1140/epja/i2018-12611-6

[82] G. Arnison *et al.* (UA1 Collaboration), "Experimental observation of isolated large transverse energy electrons with associated missing energy at s=540 GeV," *Physics Letters B*, vol. 122, no. 1, pp. 103–116, Feb. 1983. [Online]. Available: https://doi.org/10.1016/0370-2693(83)91177-2

[83] M. Banner *et al.* (UA2 Collaboration), "Observation of single isolated electrons of high transverse momentum in events with missing transverse energy at the CERN pp collider," *Physics Letters B*, vol. 122, no. 5, pp. 476–485, Mar. 1983. [Online]. Available: https://doi.org/10.1016/0370-2693(83)91605-2

[84] P. Bagnaia *et al.* (UA2 Collaboration), "Evidence for $Z^0 \to e^+e^-$ at the CERN $\bar{p}p$ Collider," *Physics Letters B*, vol. 129, pp. 130–140, Sep. 1983. [Online]. Available: http://doi.org/10.1016/0370-2693(83)90744-X

[85] M. Tanabashi *et al.* (Particle Data Group), "Review of Particle Physics," *Physical Review D*, vol. 98, p. 030001, Aug. 2018. [Online]. Available: https://doi.org/10.1103/PhysRevD.98.030001

[86] D. Becker, "Voruntersuchungen zur Messung der schwachen Ladung des Protons im Rahmen des P2-Experiments," PhD thesis, Johannes Gutenberg-Universität, Institut für Kernphysik, Mainz, Nov. 2018. [Online]. Available: http://doi.org/10.25358/openscience-3737

[87] D. Androić *et al.*, "The G0 experiment: Apparatus for parity-violating electron scattering measurements at forward and backward angles," *Nuclear Instruments and Methods in Physics Research Section A: Accelerators, Spectrometers, Detectors and Associated Equipment*, vol. 646, no. 1, pp. 59–86, Aug. 2011. [Online]. Available: https://doi.org/10.1016/j.nima.2011.04.031

[88] Heraeus Holding, "Quartz Glass for Optics - Data and Properties," Dec. 2019, Accessed: Dec 8, 2022. [Online]. Available: https://www.heraeus.com/media/media/hca/doc_hca/products_and_solutions_8/optics/Data_and_Properties_Optics_fused_silica_EN.pdf

[89] I. Perić, "A novel monolithic pixelated particle detector implemented in high-voltage CMOS technology," *Nuclear Instruments and Methods in Physics Research Section A: Accelerators, Spectrometers, Detectors and Associated Equipment*, vol. 582, no. 3, pp. 876–885, Dec. 2007. [Online]. Available: https://doi.org/10.1016/j.nima.2007.07.115

[90] K. Aulenbacher *et al.*, "The polarimetry chain for the P2 experiment," *Il Nuovo Cimento C*, vol. 035N04, pp. 186–191, July 2012. [Online]. Available: https://doi.org/10.1393/ncc/i2012-11301-y

[91] S. Baunack, "Einzelspin-Asymmetrien in der elastischen Elektron-Proton-Streuung und die Beitraege der Strange-Quarks zu den Formfaktoren des Nukleons," PhD thesis, Johannes Gutenberg-Universität, Institut für Kernphysik, Mainz, Jan. 2006, Accessed: Dec 8, 2022. [Online]. Available: https://www.blogs.uni-mainz.de/fb08-ag-maas/files/2017/06/baunack.diss_.pdf

[92] O. Koshchii *et al.*, "Weak charge and weak radius of ^{12}C," *Physical Review C*, vol. 102, p. 022501, Aug. 2020. [Online]. Available: https://doi.org/10.1103/PhysRevC.102.022501

[93] B. Mueller *et al.* (SAMPLE Collaboration), "Measurement of the Proton's Neutral Weak Magnetic Form Factor," *Physical Review Letters*, vol. 78, no. 20, pp. 3824–3827, May 1997. [Online]. Available: http://doi.org/10.1103/physrevlett.78.3824

[94] T. M. Ito *et al.* (SAMPLE Collaboration), "Parity-Violating Electron Deuteron Scattering and the Proton's Neutral Weak Axial Vector Form Factor," *Physical Review Letters*, vol. 92, no. 10, p. 102003, Mar. 2004. [Online]. Available: http://doi.org/10.1103/PhysRevLett.92.102003

[95] F. E. Maas *et al.*, "Measurement of Strange-Quark Contributions to the Nucleon's Form Factors at Q^2=0.230 $(GeV/c)^2$," *Physical Review Letters*, vol. 93, no. 2, p. 022002, July 2004. [Online]. Available: http://doi.org/10.1103/PhysRevLett.93.022002

[96] F. E. Maas *et al.*, "Evidence for Strange-Quark Contributions to the Nucleon's Form Factors at Q^2=0.108 $(GeV/c)^2$," *Physical Review Letters*, vol. 94, no. 15, p. 152001, Apr. 2005. [Online]. Available: http://doi.org/10.1103/PhysRevLett.94.152001

[97] S. Baunack *et al.*, "Measurement of Strange Quark Contributions to the Vector Form Factors of the Proton at Q^2=0.22 $(GeV/c)^2$," *Physical Review Letters*, vol. 102, no. 15, p. 151803, Apr. 2009. [Online]. Available: http://doi.org/10.1103/PhysRevLett.102.151803

[98] D. Balaguer Ríos *et al.*, "Measurement of the parity violating asymmetry in the quasielastic electron-deuteron scattering and improved determination of the magnetic strange form factor and the isovector anapole radiative correction," *Physical Review D*, vol. 94, p. 051101, Sep. 2016. [Online]. Available: http://doi.org/10.1103/PhysRevD.94.051101

[99] D. Balaguer Ríos *et al.*, "New Measurements of the Beam Normal Spin Asymmetries at Large Backward Angles with Hydrogen and Deuterium Targets," *Physical Review Letters*, vol. 119, p. 012501, July 2017. [Online]. Available: http://doi.org/10.1103/PhysRevLett.119.012501

[100] K. A. Aniol *et al.* (HAPPEX Collaboration), "Measurement of the neutral weak form factors of the proton," *Physical Review Letters*, vol. 82, no. 6, pp. 1096–1100, Feb. 1999. [Online]. Available: http://doi.org/10.1103/PhysRevLett.82.1096

[101] K. A. Aniol *et al.* (HAPPEX Collaboration), "Parity-violating electroweak asymmetry in $\vec{e}p$ scattering," *Physical Review C*, vol. 69, no. 6, p. 065501, June 2004. [Online]. Available: http://doi.org/10.1103/PhysRevC.69.065501

[102] Z. Ahmed *et al.* (HAPPEX Collaboration), "New Precision Limit on the Strange Vector Form Factors of the Proton," *Physical Review Letters*, vol. 108, no. 10, p. 102001, Mar. 2012. [Online]. Available: http://doi.org/10.1103/PhysRevLett.108.102001

[103] D. S. Armstrong *et al.* (G0 Collaboration), "Strange-Quark Contributions to Parity-Violating Asymmetries in the Forward G0 Electron-Proton Scattering Experiment," *Physical Review Letters*, vol. 95, no. 9, p. 092001, Aug. 2005. [Online]. Available: http://doi.org/10.1103/PhysRevLett.95.092001

[104] D. Androić *et al.*, "The G0 experiment: Apparatus for parity-violating electron scattering measurements at forward and backward angles," *Nuclear Instruments and Methods in Physics Research Section A: Accelerators, Spectrometers, Detectors and Associated Equipment*, vol. 646, no. 1, pp. 59–86, Aug. 2011. [Online]. Available: http://doi.org/10.1016/j.nima.2011.04.031

[105] M. Battaglieri *et al.*, "Dark matter search in a Beam-Dump eXperiment (BDX) at Jefferson Lab: an update on PR12-16-001," *JLab PAC*, vol. 45, Dec. 2017. [Online]. Available: https://doi.org/10.48550/arXiv.1712.01518

[106] J. Alwall *et al.*, "The automated computation of tree-level and next-to-leading order differential cross sections, and their matching to parton shower simulations," *Journal of High Energy Physics*, vol. 2014, no. 7, July 2014. [Online]. Available: https://doi.org/10.48550/arXiv.1405.0301

[107] S. Agostinelli *et al.*, "Geant4—a simulation toolkit," *Nuclear Instruments and Methods in Physics Research Section A: Accelerators, Spectrometers, Detectors and Associated Equipment*, vol. 506, no. 3, pp. 250–303, July 2003. [Online]. Available: https://doi.org/10.1016/S0168-9002(03)01368-8

[108] J. Allison *et al.*, "Geant4 developments and applications," *IEEE Transactions on Nuclear Science*, vol. 53, no. 1, pp. 270–278, 2006. [Online]. Available: https://doi.org/10.1109/TNS.2006.869826

[109] J. Allison *et al.*, "Recent developments in Geant4," *Nuclear Instruments and Methods in Physics Research Section A: Accelerators, Spectrometers, Detectors and Associated Equipment*, vol. 835, pp. 186–225, Nov. 2016. [Online]. Available: https://doi.org/10.1016/j.nima.2016.06.125

[110] F. Maltoni and T. Stelzer, "MadEvent: automatic event generation with MadGraph," *Journal of High Energy Physics*, vol. 2003, no. 02, pp. 027–027, Feb. 2003. [Online]. Available: https://doi.org/10.1088/1126-6708/2003/02/027

[111] E. Boos *et al.*, "Generic User Process Interface for Event Generators," Sep. 2001. [Online]. Available: https://arxiv.org/abs/hep-ph/0109068

[112] Eljen Technology, "General purpose plastic scintillator EJ-200, EJ-204, EJ-208, EJ-212," July 2021, Accessed: Dec 8, 2022. [Online]. Available: https://eljentechnology.com/images/products/data_sheets/EJ-200_EJ-204_EJ-208_EJ-212.pdf

[113] Geant4 Collaboration, "Installation Guide: For setting up Geant4 in your computing environment," Dec. 2019, Accessed: Dec 8, 2022. [Online]. Available: http://cern.ch/geant4-userdoc/UsersGuides/InstallationGuide/BackupVersions/V10.6/fo/Geant4InstallationGuide.pdf

[114] Geant4 Collaboration, "User's Guide: For Application Developers," Dec. 2019, Accessed: Dec 8, 2022. [Online]. Available: http://cern.ch/geant4-userdoc/UsersGuides/ForApplicationDeveloper/BackupVersions/V10.6/fo/BookForApplicationDevelopers.pdf

[115] M. Janecek and W. Moses, "Simulating Scintillator Light Collection Using Measured Optical Reflectance," *IEEE Transactions on Nuclear Science*, vol. 57, pp. 964–970, July 2010. [Online]. Available: https://doi.org/10.1109/TNS.2010.2042731

[116] J. Ritman *et al.* (FOPI Collaboration), "The FOPI Detector at SIS/GSI," *Nuclear Physics B Proceedings Supplements*, vol. 44, no. 1, pp. 708–715, Nov. 1995. [Online]. Available: https://doi.org/10.1016/S0920-5632(95)80107-3

[117] M. Battaglieri *et al.*, "Dark matter search in a Beam-Dump eXperiment (BDX) at Jefferson Lab," *JLab PAC*, vol. 44, pp. PR12–16–001, July 2016. [Online]. Available: https://doi.org/10.48550/arXiv.1607.01390

[118] E. Izaguirre *et al.*, "New electron beam-dump experiments to search for MeV to few-GeV dark matter," *Physical Review D*, vol. 88, no. 11, p. 114015, Dec. 2013. [Online]. Available: https://doi.org/10.1103/PhysRevD.88.114015

[119] E. Izaguirre *et al.*, "Physics motivation for a pilot dark matter search at Jefferson Laboratory," *Physical Review D*, vol. 90, no. 1, p. 014052, July 2014. [Online]. Available: https://doi.org/10.1103/PhysRevD.90.014052

[120] B. Batell *et al.*, "Strong Constraints on Sub-GeV Dark Sectors from SLAC Beam Dump E137," *Physical Review Letters*, vol. 113, no. 17, p. 171802, Oct. 2014. [Online]. Available: https://doi.org/10.1103/PhysRevLett.113.171802

[121] A. Celentano, "private communication," Nov. 2017.

[122] S. Stengel, "private communication," Aug. 2022.

[123] P. A. Cherenkov, "Visible luminescence of pure liquids under the influence of γ-radiation," *Doklady Akademii Nauk SSSR*, vol. 2, no. 8, pp. 451–454, 1934. [Online]. Available: https://doi.org/10.3367/UFNR.0093.196710N.0385

[124] J. V. Jelley, "Cerenkov radiation and its applications," *British Journal of Applied Physics*, vol. 6, no. 7, pp. 227–232, 1955. [Online]. Available: https://doi.org/10.1088/0508-3443/6/7/301

[125] I. Tamm, "Radiation Emitted by Uniformly Moving Electrons," *Journal of Physics USSR*, vol. 1, pp. 439–454, June 1939.

[126] CAEN S.p.A., "V1742 & VX1742 32+2 Channel 12bit 5 GS/s Switched Capacitor Digitizer – Manual," Apr. 2022, Accessed: Dec 8, 2022. [Online]. Available: https://www.caen.it/?downloadfile=5304

[127] CAEN S.p.A., "V965/V965A - 16/8 Channel Dual Range Multievent QDC – Manual," Jul. 2008, Accessed: Dec 8, 2022. [Online]. Available: https://www.caen.it/?downloadfile=4018

[128] CAEN S.p.A., "V6533 6 Channel 4 kV/3 mA VME HV Power Supply Module (9W) – Manual," Oct. 2019, Accessed: Dec 8, 2022. [Online]. Available: https://www.caen.it/?downloadfile=5042

[129] iseg Spezialelektronik GmbH, "Versatile High Voltage Module in VME Standard – Datasheet," Oct. 2020, Accessed: Dec 8, 2022. [Online]. Available: https://iseg-hv.com/download/SYSTEMS/VME/VHS/iseg_datasheet_VHS_en.pdf

[130] P. Burger, "Antwortverhalten von kalorimetrischen Tscherenkow-Strahlern auf Elektronen und Neutronen im MeV-Energiebereich," Bachelor's thesis, Johannes Gutenberg Universität, Institut für Kernphysik Mainz, Apr. 2019.

[131] P. Achenbach *et al.*, "Measurements and simulations of Cherenkov light in lead fluoride crystals," *Nuclear Instruments and Methods in Physics Research Section A: Accelerators, Spectrometers, Detectors and Associated Equipment*, vol. 465, no. 2-3, pp. 318–328, June 2001. [Online]. Available: https://doi.org/10.1016/S0168-9002(01)00668-4

[132] P. Lecoq *et al.*, "Lead tungstate ($PbWO_4$) scintillators for LHC EM calorimetry," *Nuclear Instruments and Methods in Physics Research Section A: Accelerators, Spectrometers, Detectors and Associated Equipment*, vol. 365, no. 2, pp. 291–298, Nov. 1995. [Online]. Available: https://doi.org/10.1016/0168-9002(95)00589-7

[133] J. Brose *et al.*, "Properties of CsI(Tl) crystals and their optimization for calorimetry of high energy photons," *Nuclear Instruments and Methods in Physics Research Section A: Accelerators, Spectrometers, Detectors and Associated Equipment*, vol. 417, no. 2, pp. 311–324, Nov. 1998. [Online]. Available: https://doi.org/10.1016/S0168-9002(98)00765-7

[134] B. Aubert *et al.*, "The BaBar detector," *Nuclear Instruments and Methods in Physics Research Section A: Accelerators, Spectrometers, Detectors and Associated Equipment*, vol. 479, no. 1, pp. 1–116, Feb. 2002. [Online]. Available: https://doi.org/10.1016/S0168-9002(01)02012-5

[135] P. Gianotti *et al.* (PADME Collaboration), "The calorimeters of the PADME experiment," *Nuclear Instruments and Methods in Physics Research Section A: Accelerators, Spectrometers, Detectors and Associated Equipment*, vol. 936, pp. 150–151, Aug. 2019. [Online]. Available: https://doi.org/10.1016/J.NIMA.2018.09.058

[136] R. Sumner *et al.* (L3 Collaboration), "The L3 BGO electromagnetic calorimeter," *Nuclear Instruments and Methods in Physics Research Section A: Accelerators, Spectrometers, Detectors and Associated Equipment*, vol. 265, no. 1, pp. 252–257, Mar. 1988. [Online]. Available: https://doi.org/10.1016/0168-9002(88)91078-9

[137] F. Ferroni, "The L3 BGO electromagnetic calorimeter at LEP," *Nuclear Physics B - Proceedings Supplements*, vol. 23, no. 1, pp. 100–106, July 1991. [Online]. Available: https://doi.org/10.1016/0920-5632(91)90036-E

[138] D. Anderson *et al.*, "Lead fluoride: An ultra-compact Cherenkov radiator for em calorimetry," *Nuclear Instruments and Methods in Physics Research Section A: Accelerators, Spectrometers, Detectors and Associated Equipment*, vol. 290, no. 2, pp. 385–389, May 1990. [Online]. Available: https://doi.org/10.1016/0168-9002(90)90553-I

[139] S. Baunack *et al.*, "Real-time calibration of the A4 electromagnetic lead fluoride (PbF_2) calorimeter," *Nuclear Instruments and Methods in Physics Research Section A: Accelerators, Spectrometers, Detectors and Associated Equipment*, vol. 640, no. 1, pp. 58–68, June 2011. [Online]. Available: https://doi.org/10.1016/j.nima.2011.02.099

[140] U. Buchner *et al.*, "Performance of a scintillating glass calorimeter for electromagnetic showers," *Nuclear Instruments and Methods in Physics Research Section A: Accelerators, Spectrometers, Detectors and Associated Equipment*, vol. 272, no. 3, pp. 695–706, Nov. 1988. [Online]. Available: https://doi.org/10.1016/0168-9002(88)90750-4

[141] Schott AG, "Optical Glass – Collection Datasheets," Sep. 2021, Accessed: Dec 8, 2022. [Online]. Available: https://mss-p-009-delivery.stylelabs.cloud/api/public/content/56f885e7281e469b8d1ded0c593600d6?v=5e72c5c3

[142] Strategic Elements, "Ceroxid | CeO2 | Cer(IV)-oxid," 2019, Accessed: Dec 8, 2022. [Online]. Available: https://www.strategic-elements.com/produkte/ceroxid/

[143] P. A. Williams *et al.*, "Optical, thermo-optic, electro-optic, and photoelastic properties of bismuth germanate ($Bi_4Ge_3O_{12}$)," *Applied Optics*, vol. 35, no. 19, pp. 3562–3569, July 1996. [Online]. Available: https://doi.org/10.1364/AO.35.003562

[144] B. Tatian, "Fitting refractive-index data with the Sellmeier dispersion formula," *Applied Optics*, vol. 23, pp. 4477–4485, Dec. 1984. [Online]. Available: https://doi.org/10.1364/ao.23.004477

[145] M. J. Weber, *Handbook of optical materials*. Boca Raton, Florida, United States: CRC press, 2003.

[146] Photonis, "Photonis – Photomultiplier Tubes Catalogue," 2007, Accessed: Dec 8, 2022. [Online]. Available: https://hallcweb.jlab.org/DocDB/0008/000809/001/PhotonisCatalog.pdf

[147] Saint-Gobain Crystals, "Assembly Materials – BC-642 PTFE Reflector Tape," 2021, Accessed: Dec 8, 2022. [Online]. Available: https://www.crystals.saint-gobain.com/radiation-detection-scintillators/assembly-materials

[148] Donaldson Company, Inc., "Tetratex® membrane filter media," 2022, Accessed: Dec 8, 2022. [Online]. Available: https://www.donaldson.com/en-us/membranes/

[149] M. K. Yang *et al.*, "Optical properties of Teflon® AF amorphous fluoropolymers," *Journal of Micro/Nanolithography, MEMS, and MOEMS*, vol. 7, no. 3, p. 033010, July 2008. [Online]. Available: https://doi.org/10.1117/1.2965541

[150] M. Janecek, "Reflectivity Spectra for Commonly Used Reflectors," *IEEE Transaction on Nuclear Science*, vol. 59, no. 3, pp. 490–497, Jun. 2012. [Online]. Available: https://doi.org/10.1109/TNS.2012.2183385

[151] Eljen Technology, "Silicone Grease EJ-550, EJ-552," July 2021, Accessed: Dec 8, 2022. [Online]. Available: https://eljentechnology.com/images/products/data_sheets/EJ-550_EJ-552.pdf

[152] M. Mauch, "Entwicklung und Einsatz eines FPGA-basierten Trigger-Systems an MAMI," Master's thesis, Johannes Gutenberg-Universität, Institut für Kernphysik, Mainz, Jan. 2019.

[153] LeCroy Corporation, "428F Quad Linear Fan-In/Fan-Out," Sep. 1995, Accessed: Dec 8, 2022. [Online]. Available: https://teledynelecroy.com/lrs/dsheets/428.htm

[154] J. E. Gaiser, "Charmonium spectroscopy from radiative decays of the J/Ψ and Ψ'," PhD thesis, Stanford Linear Accelerator Center, Stanford University, Aug. 1982.

[155] Saint-Gobain Crystals, "BGO Bismuth Germanate Scintillation Material," June 2018, Accessed: Dec 8, 2022. [Online]. Available: https://www.crystals.saint-gobain.com/files/881/download

[156] LeCroy Corporation, "IP-2 Instapulser®," Sep. 1995, Accessed: Dec 8, 2022. [Online]. Available: https://teledynelecroy.com/lrs/dsheets/ip2.htm

[157] R. Batchelor *et al.*, "The response of organic scintillators to fast neutrons," *Nuclear Instruments and Methods*, vol. 13, pp. 70–82, Aug.-Oct. 1961. [Online]. Available: https://doi.org/10.1016/0029-554X(61)90171-9

[158] H. Schlagheck, "Konstruktion und Kalibration eines Bleiglaskalorimeters für ultrarelativistische Schwerionenreaktionen," Diploma thesis, Westfälische Wilhelms-Universität, Institut für Kernphysik, Münster, Apr. 1994, Accessed: Dec 8, 2022. [Online]. Available: https://www.uni-muenster.de/imperia/md/content/physik_kp/agwessels/thesis_db/ag_santo/schlagheck_1994_diplom.pdf

[159] G. Schepers, "Entwicklung und Erprobung eines LED-gestützten Monitorsystems für ein modulares Bleiglasspektrometer," Diploma thesis, Westfälische Wilhelms-Universität, Institut für Kernphysik, Münster, May 1994, Accessed: Dec 8, 2022. [Online]. Available: https://www.uni-muenster.de/imperia/md/content/physik_kp/agwessels/thesis_db/ag_santo/schepers_1994_diplom.pdf

[160] A. Claussen, "Einsatz des Bleiglaskalorimeters LEDA zur Untersuchung ultrarelativistischer bleiinduzierter Schwerionenreaktionen in Hinblick auf die Produktion inklusiver Photonen," PhD thesis, Westfälische Wilhelms-Universität, Institut für Kernphysik, Münster, 1996, Accessed: Dec 8, 2022. [Online]. Available: https://www.uni-muenster.de/imperia/md/content/physik_kp/agwessels/thesis_db/ag_santo/claussen_1996_dissertation.pdf

[161] H. Baumeister *et al.* (CERN-SPS WA80 Collaboration), "Design and performance of the SAPHIR lead-glass calorimeter," *Nuclear Instruments and Methods in Physics Research Section A: Accelerators, Spectrometers, Detectors and Associated Equipment*, vol. 292, no. 1, pp. 81–96, June 1990. [Online]. Available: https://doi.org/10.1016/0168-9002(90)91736-U

[162] T. Peitzmann *et al.*, "A new monitoring system for the photon spectrometer LEDA in the WA98 experiment," *Nuclear Instruments and Methods in Physics Research Section A: Accelerators, Spectrometers, Detectors and Associated Equipment*, vol. 376, no. 3, pp. 368–374, July 1996. [Online]. Available: https://doi.org/10.1016/0168-9002(96)00224-0

[163] D. Drechsel and L. Tiator, "Threshold pion photoproduction on nucleons," *Journal of Physics G: Nuclear and Particle Physics*, vol. 18, no. 3, pp. 449–497, Mar. 1992. [Online]. Available: https://doi.org/10.1088/0954-3899/18/3/004

[164] Semiconductor Components Industries, LLC, 2014, "MICROC-SERIES/D Rev.9 – Datasheet," Feb. 2022, Accessed: Dec 8, 2022. [Online]. Available: https://www.onsemi.com/pdf/datasheet/microc-series-d.pdf

[165] M. Lauß *et al.*, "Electron beam studies of light collection in a scintillating counter with embedded fibers," *Nuclear Instruments and Methods in Physics Research Section A: Accelerators, Spectrometers, Detectors and Associated Equipment*, vol. 1012, p. 165617, Oct. 2021. [Online]. Available: https://doi.org/10.1016/j.nima.2021.165617

[166] J. D. Bjorken *et al.*, "New Fixed-Target Experiments to Search for Dark Gauge Forces," *Physical Review D*, vol. 80, p. 075018, Oct. 2009. [Online]. Available: http://doi.org/10.1103/PhysRevD.80.075018

[167] C. F. v. Weizsäcker, "Ausstrahlung bei Stößen sehr schneller Elektronen," *Zeitschrift für Physik*, vol. 88, pp. 612–625, Sep. 1934. [Online]. Available: https://doi.org/10.1007/BF01333110

[168] E. J. Williams, "Nature of the High Energy Particles of Penetrating Radiation and Status of Ionization and Radiation Formulae," *Physical Review*, vol. 45, pp. 729–730, May 1934. [Online]. Available: https://doi.org/10.1103/PhysRev.45.729

[169] K. J. Kim and Y.-S. Tsai, "Improved Weizsäcker-Williams Method and Its Application to Lepton and W-Boson Pair Production," *Physical Review D*, vol. 8, pp. 3109–3125, Nov. 1973. [Online]. Available: https://doi.org/10.1103/PhysRevD.8.3109

[170] S. N. Gninenko *et al.*, "Search for Dark Sector Physics with NA64," *Physics of Particles and Nuclei*, vol. 51, no. 5, pp. 829–858, Sep. 2020. [Online]. Available: https://doi.org/10.1134/S1063779620050044

[171] A. Aguilar-Arevalo *et al.* (MiniBooNE-DM Collaboration), "Dark Matter Search in a Proton Beam Dump with MiniBooNE," *Physical Review Letters*, vol. 118, p. 221803, May 2017. [Online]. Available: http://doi.org/10.1103/PhysRevLett.118.221803

[172] J. P. Lees *et al.* (BaBar Collaboration), "Search for Invisible Decays of a Dark Photon Produced in e^+e^- Collisions at BaBar," *Physical Review Letters*, vol. 119, p. 131804, Sep. 2017. [Online]. Available: http://doi.org/10.1103/PhysRevLett.119.131804

[173] D. Akimov *et al.*, "First Probe of Sub-GeV Dark Matter Beyond the Cosmological Expectation with the COHERENT CsI Detector at the SNS," Oct. 2021. [Online]. Available: https://doi.org/10.48550/arXiv.2110.11453

[174] R. Essig *et al.*, "First Direct Detection Limits on Sub-GeV Dark Matter from XENON10," *Physical Review Letters*, vol. 109, p. 021301, July 2012. [Online]. Available: https://doi.org/10.1103/PhysRevLett.109.021301

[175] L. Marsicano *et al.*, "Dark photon production through positron annihilation in beam-dump experiments," *Physical Review D*, vol. 98, p. 015031, July 2018. [Online]. Available: https://doi.org/10.1103/PhysRevD.98.015031

[176] D. P. Snowden-Ifft *et al.*, "Directional light-WIMP time-projection-chamber detector for electron beam-dump experiments," *Physical Review D*, vol. 99, p. 061301, Mar. 2019. [Online]. Available: https://doi.org/10.1103/PhysRevD.99.061301

[177] D. P. Snowden-Ifft and J. L. Harton, "Beam-Dump Dark Matter Search Utilizing a Low-Threshold, Directional Dark Matter Detector (BDX-DRIFT) at Jefferson Lab," *JLab PAC*, vol. 47, pp. PR12–19–005, July 2019, Accessed: Dec 8, 2022. [Online]. Available: https://indico.jlab.org/event/332/contributions/5196/attachments/4305/5223/BDX-DRIFT_PAC47_Talk.pdf

[178] C. Janas, "Experimentelle Studien zu einem Bleiglas-Schauerdetektor als Myon-Veto für MAGIX," Bachelor's thesis, Johannes Gutenberg Universität, Institut für Kernphysik Mainz, Sep. 2022.

[179] M. Bondi *et al.*, "Fully Geant4 compatible package for the simulation of Dark Matter in fixed target experiments," *Computer Physics Communications*, vol. 269, p. 108129, Dec. 2021. [Online]. Available: https://doi.org/10.1016/j.cpc.2021.108129

[180] K. Grimm, "Aufbau eines Lichtauslesesystems für ein Bleifluorid-Kalorimeter zur Messung der Paritätsverletzung in der elastischen Elektronenstreuung," PhD thesis, Johannes Gutenberg-Universität, Institut für Kernphysik, Mainz, Feb. 2002, Accessed: Dec 8, 2022. [Online]. Available: https://www.blogs.uni-mainz.de/fb08-ag-maas/files/2017/06/grimm.diss_.pdf